JAEA-Review
2010-065

JAEA-Review

JAEA Takasaki Annual Report 2009

(Ed.) Shigeru TANAKA

Takasaki Advanced Radiation Research Institute

January 2011

Japan Atomic Energy Agency

日本原子力研究開発機構

本レポートは独立行政法人日本原子力研究開発機構が不定期に発行する成果報告書です。
本レポートの入手並びに著作権利用に関するお問い合わせは、下記あてにお問い合わせ下さい。
なお、本レポートの全文は日本原子力研究開発機構ホームページ（http://www.jaea.go.jp）
より発信されています。

独立行政法人日本原子力研究開発機構　研究技術情報部　研究技術情報課
〒319-1195　茨城県那珂郡東海村白方白根 2 番地 4
電話 029-282-6387, Fax 029-282-5920, E-mail:ird-support@jaea.go.jp

This report is issued irregularly by Japan Atomic Energy Agency
Inquiries about availability and/or copyright of this report should be addressed to
Intellectual Resources Section, Intellectual Resources Department,
Japan Atomic Energy Agency
2-4 Shirakata Shirane, Tokai-mura, Naka-gun, Ibaraki-ken 319-1195 Japan
Tel +81-29-282-6387, Fax +81-29-282-5920, E-mail:ird-support@jaea.go.jp

© Japan Atomic Energy Agency, 2011

JAEA-Review 2010-065

JAEA Takasaki Annual Report 2009

(Ed.) Shigeru TANAKA

Takasaki Advanced Radiation Research Institute

Japan Atomic Energy Agency

Watanuki-machi, Takasaki-shi, Gunma-ken

(Received November 11, 2010)

JAEA Takasaki annual report 2009 describes research and development activities performed from April 1, 2009 to March 31, 2010 with Takasaki Ion Accelerators for Advanced Radiation Application (TIARA, four ion accelerators), and electron/gamma-ray irradiation facilities (an electron accelerator and three ^{60}Co gamma-ray irradiation facilities) at Takasaki Advanced Radiation Research Institute, Japan Atomic Energy Agency (JAEA Takasaki). These activities are classified into four research fields: 1) space, nuclear and energy engineering, 2) environmental conservation and resource security, 3) biotechnology and medical application, and 4) advanced materials, analysis and novel technology. This annual report contains 165 reports consisting of 157 research papers and 8 status reports on operation/maintenance of the irradiation facilities described above, and a list of publications, patents, related press-releases, TV programs, and the type of research collaborations as Appendices.

Keywords: TIARA, Ion Accelerators, Electron Accelerator, Gamma-ray Facilities, Nuclear and Energy Engineering, Environmental Conservation, Resource Security, Biotechnology, Medical Application, Advanced Materials, Analysis, Novel Technology, Materials for Space, Semiconductors, Inorganic Materials, Organic Materials, Functional Materials, Radiation Chemistry, Radiation Biology, Radioisotope Production, Nuclear Chemistry, Material Analyses, Solid State Physics, Microbeam Technology, Accelerator Technology, Accelerator Operation, Safety Control

(Editorial committee) Shigeru TANAKA, Atsushi TANAKA, Masao TAMADA,
Takuji KOJIMA, Kazumasa NARUMI, Shimpei MATSUHASHI,
Kiyoshi MIZUHASHI, Yutaka FUKUTA and Yoshiteru NAKAMURA

高崎量子応用研究所研究年報 2009

日本原子力研究開発機構 高崎量子応用研究所
（編） 田中 茂

（2010 年 11 月 11 日受理）

高崎量子応用研究所研究年報 2009 は、同研究所にある TIARA 施設（イオン加速器 4 基）及び電子・ガンマ線照射施設（電子加速器 1 基、^{60}Co ガンマ線照射施設 3 棟）を利用して 2009 年 4 月 1 日から 2010 年 3 月 31 日までの間に行われた研究・技術開発成果をまとめたものである。この研究年報には、1）宇宙・原子力・エネルギー、2）環境・資源、3）バイオ技術・医学応用、4）先端材料・計測・基盤技術の 4 分野に分類した 157 編の論文及び 8 編の施設の運転・管理状況報告からなる合計 165 編を収録する。また、論文リスト、出願特許、新聞発表、テレビ放映及び研究実施形態・利用施設の一覧表を付録として含む。

高崎量子応用研究所：〒370-1292 群馬県高崎市綿貫町 1233
編集委員：（著者代表）田中 茂、田中 淳、玉田 正男、小嶋 拓治、
鳴海 一雅、松橋 信平、水橋 清、福田 豊、中村 義輝

PREFACE

This report covers research and development activities in Takasaki Advanced Radiation Research Institute, JAEA, during the period from April 2009 to March 2010 conducted with TIARA (Takasaki Ion Accelerators for Advanced Radiation Application), electron beam and Co-60 gamma-ray irradiation facilities.

This annual report contains 165 papers in the fields of

1) Space, Nuclear and Energy Engineering,
2) Environmental Conservation and Resource Security,
3) Biotechnology and Medical Application,
4) Advanced Materials, Analysis and Novel Technology,
5) Status of Irradiation Facilities.

In the field of Space, Nuclear and Energy Engineering, radiation induced degradation of semiconductors such as solar cells, SiC devices and so on have been examined in the irradiation field which is simulated as cosmic space by using high energy electrons, protons and heavy ions to accelerate the practical application of semiconductors to the next generation electronic systems in space. Additionally, radiation stabilities of organic extractants, resins, glove rubber, barrier material for geological disposal and steels for the next generation reactors have been evaluated for the purpose of practical use in nuclear processing. The radiation-resistant polymer, lighting and cable have been developed respectively for ITER, gamma irradiation cell and J-PARC. Electrolyte membranes for fuel cells have been developed by using track etching pores and radiation grafting. Grafting leads a new anion-exchange membrane, poly(ether ether ketone)-based membrane, fabrication of nanostructure in membrane.

In the filed of Environmental Conservation and Resource Security, fibrous materials have been developed with radiation grafting technique and applied to catalyst for biodiesel production, decolonization of waste water from livestock urine, and recovery of precious metals. Furthermore, grafting was used for surface modification of vulcanized rubber, also. Monolithic column can be applied to the separation of catecholamines. Hydro-gels produced by crosslinking of hydroxypropyl cellulose have been investigated to improve the mechanical strength. In the case of carboxymethyl chitosan, basic ESR study has been carried out. R&Ds of the decomposition of persistent pharmaceuticals in waste water using gamma-rays have been performed to develop new process technologies for environmental conservation.

In the field of Biotechnology and Medical Application, studies on DNA damage and mutational effects of ion beams were progressed at molecular level. The ion beam breeding has been applied for many kinds of plants and microorganisms such as flowers, crops, yeast

and biofertilizer microorganisms to obtain new useful varieties. Among the ion-beam induced 'Sake yeast' mutants, sake was test-brewed with two promising mutants characterized by sweetness and uniqueness in flavor. Heavy-ion microbeam cell-targeting irradiation revealed that the formation of DNA double strand break signals in the unirradiated cells 6 hours after irradiation in the target colony and in the untargeted colonies was suppressed by the addition of chemical scavenger of free radicals or NO scavenger, respectively, suggesting that reactive oxygen species and NO are initiators/mediators for evoking heavy-ion induced bystander responses. The positron imaging system has been applied to various practical topics in agriculture. The symbiotic nitrogen fixation in the nodules of intact soybean plant was first visualized quantitatively using ^{13}N-labeled N_2 gaseous tracer, whose result leads to a way to test activity of each nodule under various agricultural conditions. Radiopharmaceuticals for diagnosis of non-small cell lung cancer and neuroendocrine tumors, i.e., ^{76}Br-labeled *m*-bromobenzylguanidine and ^{64}Cu-labeled trastuzumab, were successfully prepared as a new positron emission tomography (PET) probe and evaluated for basic biological studies. The in-air micro particle-induced X-ray emission (micro-PIXE) system has been utilized mainly to investigate behavior of intracellular trace elements in bio-medical samples, such as asbestos lung-tissues, brain slices of restraint stress mice, human cancerous tissue and so on. The 3D-micro-PIXE system was developed and the 3D-elemental imaging of a biological sample was demonstrated on this system.

In the field of Advanced Materials, various materials were developed by applying ion- or electron-irradiation effect: WO_3 films with hydrogen gasochromism, α-rhombohedral B superconductors with carrier doping, SiC nanotubes, polymer optical waveguides, hydrogen-storage alloys, diluted-magnetic semiconductors, polycarbosilane nanofibers, SiC membranes with gas permeation, nano porous SiC, polymer nanowires and nano-crystallines of metallic glasses. As for the Material Analysis, Rutherford-backscattering spectrometry (RBS) with the channeling technique, a powerful tool especially for analysis of thin films, has been used to examine the lattice disorder at the interface between an epitaxially-grown full Heusler alloy Fe_2MnSi layer and a Ge(111) substrate: The former is important for a spin injector toward realization of a spin field effect transistor. The RBS technique was also applied for observation of atomistic mass-transport process in Au/Cu films under centrifugal forces. On the other hand, a positron-microbeam has recently been developed and applied for micro-analysis of the vacancy-type defect of nuclear-reactor-related materials. Super structures on a clean Si(111) surface has been investigated with the use of the reflection-high-energy-positron-diffraction (RHEPD) technique. A nuclear-reaction-analysis technique combined with the ion-microbeam technique has been applied for imaging light elements in matrices such as B in Fe. As for the Novel Technology, radiation chemistry studies on radiolysis of metal ions and organics were carried out using both ^{60}Co gamma-rays

and pulsed heavy ion beams involving the development of radiolysis techniques. Different kinds of detectors/fluence monitor systems were developed for measurement of high-energy or cosmic-ray neutrons, 110 keV electrons and specific X-rays of medical radioisotopes. The fundamental studies for various MeV/atom cluster ions ranging of C_1-C_{10} and Au_1-Au_3 were performed on the basis of the measurement of secondary ions/electrons or luminescence emitted from target materials and that of change in magnetic hysteresis of the target material. The Proton-Beam-Writing (PBW) technique was also applied to the nano-structure fabrication for various devices. Technical development of fast single-ion hit, wide uniform beam formation, quick beam change at the cyclotron, and new beam generation/irradiation of C_{10} or C_{60} at the electrostatic accelerators were in progress. The development of a new highly spin-polarized positron source was also attempted.

About the Status of Irradiation Facilities, all the accelerators in TIARA, namely the AVF cyclotron, the 3-MV tandem accelerator, the 3MV single-ended accelerator and the 400-kV ion implanter, have been operated steadily and safely as well as an electron accelerator and irradiation systems in Co-60 gamma-ray irradiation facilities. A system for measuring large-area uniform beams by means of beam-induced fluorescence is being developed in order to evaluate beam characteristics such as beam shape, size, and uniformity in real time. Total operation times of the tandem accelerator, the single-ended accelerator, and the ion implanter were 32,422, 36,875, and 28,875 hours, respectively, since the beginning of their operation. The total number of experiments made by various users using the AVF cyclotron was 8,125 from the first beam extraction in 1991 to March 2010, as a result of continuous efforts such as regular maintenance and trouble shooting.

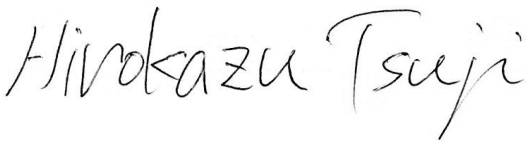

Hirokazu Tsuji,
Director General
Takasaki Advanced Radiation Research Institute
Japan Atomic Energy Agency

This is a blank page.

Contents

1. Space, Nuclear and Energy Engineering ····· 1

1-01 Radiation Resistance of InGaP/GaAs Dual-Junction Thin-Film Space Solar Cell ····· 5
1-02 Detection of Photons Induced by a Single Ion Strike ····· 6
1-03 Evaluation of Soft Error Rates in SOI SRAM with a Technology Node of 90 nm Using Oxygen Ion Probe ····· 7
1-04 Feasibility Study on a 90 nm Bulk CMOS Process for Applicability to Space Environments ····· 8
1-05 Heavy-ion Induced Current in SOI p^+n Junction Diode ····· 9
1-06 Study of Ion-Implantation Condition Effects for AlGaN/GaN-Based Light Emitting Device ····· 10
1-07 Total Ionizing Dose Tolerance of SiC Buried Gate Static Induction Transistors up to 10 MGy ····· 11
1-08 Evaluation of Radiation Tolerance of General Electronic Devices ····· 12
1-09 Evaluation of Single Event Effects on Commercial-off-the-Shelf Semiconductors for Space Flight Applications ····· 13
1-10 Mechanisms of Changes of Hole Concentration in Al-doped 6H-SiC by Electron Irradiation and Annealing ····· 14
1-11 Hydrogen Diffusion in a-Si: H Thin Films due to High Temperature Ion Irradiation ····· 15
1-12 NV Centers in Diamond Irradiated with High Energy Nitrogen Ions and 2 MeV Electrons ····· 16
1-13 Alpha-radiolysis of Organic Extractants for Separation of Actinides ····· 17
1-14 A Study on Complete Decomposition of Pyrrolidone Precipitants by γ-Ray Irradiation ····· 18
1-15 Study on Stability of Cs•Sr Solvent Impregnate Resin against Gamma Irradiation ····· 19
1-16 Hydrogen Generation in the System of Water-Adsorbent Containing the Organic Extractant by Gamma-Ray Radiation ····· 20
1-17 Irradiation Effect of Gamma-Rays on Cyanate Ester/Epoxy Resins ····· 21
1-18 Development of Radiation-Resistant Lighting ····· 22
1-19 Development of Radiation Resistant Cable ····· 23
1-20 Development of Penetration Part Processing Industrial Method in Radiation Controlled Area ····· 24
1-21 Alpha-Ray Irradiation Damage on Rubber Applied for Glove Box for Plutonium Powder Treatment ····· 25
1-22 Touch-Down Test of Magnetic Bearing Type Centrifugal Contactor with Irradiated Touch-Down Bearing ····· 26

1-23 Studies on Microstructure and Elemental Distributions of Barrier Materials for Geological Disposal of Radioactive Waste ····· 27
1-24 Behavior of Eu during Culture of *Paramecium bursaria* with Yeast Cells Sorbing Eu ····· 28
1-25 Effect of Groundwater Radiolysis on the Disposal System of High-level Radioactive Waste ····· 29
1-26 Effect of Temperature Change on Irradiation Hardening of Ferritic and Austenitic Steels during Ion-irradiation ····· 30
1-27 Simulation of Neutron Damage Microstructure in Extra High Purity Fe-25Cr-35Ni Austenitic Stainless Steels ····· 31
1-28 Effects of Radiation Damage and Helium on Swelling and Microstructure of EHP Ni-base Superalloy ····· 32
1-29 Irradiation Hardening in Ion-irradiated Hafnium ····· 33
1-30 Conductometric Analysis of Track Etching in Poly(vinylidene fluoride) ····· 34
1-31 Preparation of Anion-Exchange Membranes for Fuel Cell Applications by γ-ray Pre-Irradiation Grafting ····· 35
1-32 Enhanced Reactivity of Ion-track Grafting for Fuel-cell Electrolyte Membranes ····· 36
1-33 Radiation-Induced Graft Polymerization of Styrene into a Poly (ether ether ketone) Film for Polymer Electrolyte Membranes ····· 37
1-34 Nanoscale Structures of Radiation-Grafted Polymer Electrolyte Membranes Investigated by Dissipative Particle Dynamics Simulation ····· 38

2. Environmental Conservation and Resource Security ····· 39

2-01 Fibrous Catalyst for Biodiesel Production Synthesized by Radiation-induced Graft Polymerization ····· 41
2-02 Development of Zwitterionic Monolithic Column for Hydrophilic Interaction Liquid Chromatography and its Application to the Separation of Catecholamines and Related Compounds ····· 42
2-03 Decolorization of Secondary Treated Water from Livestock Urine Waste ····· 43
2-04 Modification of Hydroxypropyl Cellulose Hydrogels by Blending Poly (vinyl alcohol) ····· 44
2-05 Effect of Grafting Conditions on Radiation-induced Graft Polymerization ····· 45
2-06 The Recovery of Precious Metals Using Biomass Adsorbents ····· 46
2-07 Surface Modification of Vulcanized Rubber by Radiation Co-grafting ····· 47
2-08 ESR Study on Carboxymethyl Chitosan Radicals in Aqueous Solution ····· 48
2-09 Decomposition of Persistent Pharmaceuticals by Ionizing Radiation ····· 49

3. Biotechnology and Medical Application ····· 51

3-01 Damage Spectrum of DNA Strand Break Termini Induced by $^{4}He^{2+}$ Ion Beam Compared with that by ^{60}Co γ-rays ····· 57
3-02 Mutagenic effects of He ion particles in *Escherichia coli* ····· 58
3-03 Mutational Effect of Gamma-rays and Carbon Ion Beams on *Arabidopsis* Seedlings····· 59
3-04 Functional Analysis of Flavonoid Accumulation Genes of *Arabidopsis thaliana* ····· 60
3-05 Ion Beam Irradiation with Rice Seeds for the Mutation Breeding Project of the Forum for Nuclear Cooperation in Asia (FNCA) ····· 61
3-06 Generation New Ornamental Plant Varieties Using Ion Beams····· 62
3-07 Development of New Gunma Original Variety of Chrysanthemum by Ion Beam Irradiation ····· 63
3-08 Stability of Flower-colour Mutants of Delphinium 'Momoka' After Propagation by Tissue Culture ····· 64
3-09 Red–purple Flower due to Delphinidin 3,5-diglucoside, a Novel Pigment for *Cyclamen* spp., Generated by Ion-beam Irradiation ····· 65
3-10 Effects of Heavy Ion beam Irradiation in Citrus····· 66
3-11 Effect of Ion Beam Irradiation for *Asclepias* Species ····· 67
3-12 Producing New Gene Resources in Chrysanthemum Using Ion-beam Irradiation ····· 68
3-13 Ion Beam Breeding of Sugarcane Cultivar "Ni17"····· 69
3-14 Production of Soybean Mutants with Pale-Green-Leaf Phenotype by Ion Beam Irradiation ····· 70
3-15 Induction of Fusarium Wilt Resistant by Ion Beam Irradiation in Strawberry (*Fragaria* × *ananassa*) Leaf Explants ····· 71
3-16 Assessment of Irradiation Treatments on a Salt-tolerant Arabidopsis, Zu-0 and *Thellungiella* ····· 72
3-17 Effects of Ion-beam Irradiation on Germination and Growth of Seedlings of Red Pepper 'Hirosaki zairai' ····· 73
3-18 Effect of Different LET Radiations on Root Growth of *Arabidopsis thaliana* ··· 74
3-19 Phenotypic Improvement of *Bradyrhizobium japonicum* USDA 110 into a High Temperature Tolerant Strain in terms of Ion-beam Microbial Mutation-breeding Technology ····· 75
3-20 Fungicide Tolerant Mutation of Entomopathogenic Fungi Induced by Carbon Ion Beams ····· 76
3-21 Improvement of Endophytic Bacteria Using Ion Beams ····· 77
3-22 FACS-based Screening of Yeast Strain Highly Expressing Cellulase····· 78
3-23 Molecular Analysis of Carbon Ion Induced Mutations in Yeast *Saccharomyces cerevisiae* Cells ····· 79

3-24 Lethal Effects of Different LET Radiations in *Deinococcus radiodurans* ····· 80
3-25 Analysis of Mutation Induced by Ion Beams and Gamma-Rays in Vacuum-dried Conidia of *Aspergillus oryzae* ····· 81
3-26 Ion Beam Breeding of "Sake Yeast" and Test Brewing ····· 82
3-27 The Effect of γ-Sterilization of Carrier Materials on the Shelf Life of Biofertilizer ····· 83
3-28 Electron Spin Relaxation Behaviors of Radicals Induced in Gamma-irradiated Food ····· 84
3-29 Dose-dependency of Electron Spin Relaxations in Irradiated Fresh Mangoes ··· 85
3-30 Target Irradiation of Individual Cells Using Focusing Heavy-Ion Microbeam of JAEA-Takasaki ····· 86
3-31 A Quantitative Study of DNA Double-strand Breaks Induced by Heavy-ion Beams: a Problem on the Conventional DNA-sample Preparation ··· 87
3-32 Carbon-ion Microbeam Induces Behavioral Changes in the Salt Chemotaxis Learning of *C. elegans* ····· 88
3-33 Combination Effect of the Heat Shock Protein Inhibitor, 17-AAG, with Carbon-beam and X-ray Irradiation for Squamous Cell Carcinomas *in Vitro* ····· 89
3-34 Biological Effects of Carbon Ions on Glioblastoma Cell Lines ····· 90
3-35 Analysis of Molecular Mechanisms for Radiation-induced Bystander Effects Using Heavy Ion Microbeams ····· 91
3-36 Difference in Bystander Lethal Effect in Human Tumor Cell Lines Depending on *p53* -gene Status Induced by Carbon-ion Microbeams ····· 92
3-37 Heavy-ion Irradiation Induces Autophagy in Irradiated C2C12 Myoblasts and Their Bystander Cells ····· 93
3-38 Analysis of Lethal Effect Mediated by Low Dose Irradiation Induced-Secreted factors in Glioma cells ····· 94
3-39 Ion Beam Irradiation Has Different Influences on the Expression of p53 in Cultured Human Retinal Vascular Endothelial Cells Exposed to L-dopa among ^{20}Ne, ^{12}C and ^{4}He ····· 95
3-40 Irradiation with Carbon Ion Beams Induces Apoptosis, Autophagy, and Cellular Senescence in a Human Glioma-derived Cell Line ····· 96
3-41 Effects of Heavy Ion Irradiation on the Precursor Hemocytes of the Silkworm, *Bombyx mori* ····· 97
3-42 Expression of Two Gelsolins in Response to Heavy-ions Irradiation and Desiccation in the Sleeping Chironomid *Polypedilum vanderplanki* ····· 98
3-43 Nuclear Localization of a FOXO Transcriptional Factor DAF-16 in *C. elegans,* which is Required in a Response to IR Irradiation ····· 99
3-44 Analysis of Bystander Cell Signaling Pathway Activated by Heavy Ion-Microbeam ····· 100
3-45 Carbon Translocation in a Whole Plant Body by Using Positron Emitting Tracer Imaging System (PETIS) and Carbon-11-labeled Carbon Dioxide ($^{11}CO_2$) ····· 101

3-46 Quantitative Evaluation of Rice Varieties in Cadmium Uptake Activities for Remediation of Cadmium-contaminated Soil ····· 102
3-47 Quantitative Study for Nitrogen Fixation in Intact Soybean Plant from PETIS Imaging ····· 103
3-48 Visualization of ^{107}Cd Accumulation in Oilseed Rape Plants Treated with Glutathione ····· 104
3-49 Noninvasive Imaging of Zinc Dynamics in an Intact Plant Using the Positron-emitting Tracer ^{65}Zn ····· 105
3-50 Uniformity Measurement of Newly Installed Camera Heads of Positron-emitting Tracer Imaging System ····· 106
3-51 PET Studies of Neuroendcrine Tumors by Using ^{76}Br-*m* -Bromobenzylguanidine (^{76}Br-MBBG)····· 107
3-52 Imaging and Biodistribution of Her2/Neu Expression in Non-Small Cell Lung Cancer Xenografts with ^{64}Cu-labeled Trastuzumab PET ····· 108
3-53 Production of No-carrier-added Lu-177 for Radioimmunotherapy ····· 109
3-54 Improvement of Spatial Resolution of PIXE-CT at TIARA ····· 110
3-55 The Analysis of Trace Metal in a Slice of Subjected Restraint Stress Mice by In-Air Micro-PIXE ····· 111
3-56 The Optimum Conditions in the Analysis of Boron Micro-Distribution in Tumor Cells Using PIXE and PIGE ····· 112
3-57 Measurement of Strontium Distribution in Carious Enamel and Dentin around a Fluoride-containing Material ····· 113
3-58 Evaluation of Cisplatin Concentration in Response to Tumor Hypoxia in Esophageal Squamous Cell Carcinoma ····· 114
3-59 Improvement of Microcapsules that Reslease Core Contents via Radiation ····· 115
3-60 Analysis of Asbestos Bodies and Fas or CD163 Expression in Asbestos Lung Tissue by In-Air Micro-PIXE ····· 116
3-61 Preparation of Human Erythrocytes for In-Air Micro-PIXE Analysis ····· 117
3-62 Sensitivity of Micro Beam PIXE System in TIARA for Several Trace Elements ····· 118

4. Advanced Materials, Analysis and Novel Technology ····· 119

4-01 Hydrogen Gasochromism of WO_3 Films Prepared by Reactive Sputtering ····· 125
4-02 Li Ion Implantation into α-rhombohedral Boron: Carrier Doping for Superconduction ····· 126
4-03 Synthesis of Single-Crystalline and Amorphous SiC Nanotubes by Ion-Irradiation Technique ····· 127
4-04 Polymer Optical Waveguides Fabricated by Using Proton Beam Writing ····· 128
4-05 Synergy Effects in Electron/Ion Irradiation and Alkaline Pretreatment on Hydriding Property of Hydrogen Storage Alloys ····· 129
4-06 Atomistic Study of Irradiation-induced Mass Transport Process ····· 130

4-07 Fabrication of Diluted Magnetic Semiconductor Crystals by Ion-Implantation Technique ····· 131
4-08 Synthesis of Functional Polycarbosilane Nano-fiber by Ion Beam Induced Graft Polymerization ····· 132
4-09 Gas Permeation Characteristics of Silicon Carbide Membrane Prepared by Radiation-curing of Polycarbosilane Film ····· 133
4-10 Investigation of Nano Porous SiC Based Fibers Synthesized by Precursor Method ····· 134
4-11 Control of Radial Size of Polymer Nanowire Formed by Ion Beam Irradiation ·· 135
4-12 Nano-crystalline Formation of Metallic Glasses by Ion Implantation ····· 136
4-13 Behavior of N Atoms in Nitriding Processes of Evaporated-Ti Thin Films due to Ion Implantation ····· 137
4-14 The Effects of Displacement Damage and Transmutation Atoms on Microstructure of SiC: The Effects of H Atom on Dimensional Change of SiC ····· 138
4-15 Annealing Behavior of Vacancy-type Defects in Electron-irradiated Si_xGe_{1-x} Bulk Crystals at Low Temperature ····· 139
4-16 RBS Analysis of Mass-transport Process in Au/Cu Film on Sapphire Treated by Centrifugal Forces ····· 140
4-17 Low Temperature Ion Channeling of Fe_2MnSi Film Epitaxially Grown on Ge(111) ····· 141
4-18 Vacancy Generation around an SCC Crack Tip in Stainless Steels Probed by a Positron Microbeam ····· 142
4-19 Radiation-Induced Electrical Degradation in CeO_2 Ceramics Irradiated with 10 MeV Ni ····· 143
4-20 Incident Energy Dependence of Nuclear Reaction Imaging of Boron Doped in Iron ····· 144
4-21 Study on Cu Precipitation in Energetic Electron Irradiated FeCu Alloy by Means of X-ray Absorption Spectroscopy ····· 145
4-22 Cathodoluminescence of Albite Activated by Alpha-particle Induced Luminescence Centers ····· 146
4-23 Evaluation of Fluorescence Materials for Pulsed-neutron Imaging ····· 147
4-24 Positron Beam Study on Vacancy Defects in GaCrN Grown by Molecular Beam Epitaxy ····· 148
4-25 Evaluation of the ZrC Layer for Coated Fuel Particles Probed by a Positron Microbeam ····· 149
4-26 Surface Structure of Si(111)-$\sqrt{21}\times\sqrt{21}$-(Ag, Cs) studied by Reflection High-Energy Positron Diffraction ····· 150
4-27 Structure Analysis of K/Si(111)-$\sqrt{3}\times\sqrt{3}$-B Surface by Reflection High-Energy Positron Diffraction ····· 151
4-28 Radiation-induced H_2 Production and Reactions of OH Radical in Aqueous Solutions Containing Ceramic Oxides ····· 152

4-29 LET Effect on the Radiation Induced Polymerization of Maleimide ····· 153
4-30 Observation of Heavy Ion Induced Transient Species in Water by Spectroscopic Technique ····· 154
4-31 Stabilization of Measurement System of the Heavy Ion Beam Pulse Radiolysis Using Scintillator ····· 155
4-32 Development of a Head Module for Multi-Head Si/CdTe Compton Camera System ····· 156
4-33 Systematic Measurement of Neutron and Gamma-ray Yields on Thick Targets Bombarded with 18 MeV Protons ····· 157
4-34 Establishment of Neutron Fluence Monitoring Techniques for Quasi-monoenergetic Neutron Calibration Fields of High Energy at TIARA ··· 158
4-35 Measurement of Neutron Fluence in the Comparison between TIARA and CYRIC High Energy Neutron Facilities ····· 159
4-36 Study on High Energy Neutron Dosimetry Using Solid State Track Detector ··· 160
4-37 Evaluation of the Response Characteristics of a Portable Cosmic-ray Neutron Monitor ····· 161
4-38 Dose Measurement for 110 keV Electron Beam ····· 162
4-39 Relationship between Internuclear Distance and Charge State of Constituent Ions Resulting from Foil-induced Dissociation of C_2^+ ions ····· 163
4-40 Simultaneous Measurement of Secondary-electron Emission and Coulomb Explosion Imaging for 250-keV/u C_2^+ Ions Bombarded to Thin Carbon Foils··· 164
4-41 Analysis of Radiation Damage at a Si Surface Bombarded with a Single 10-, 50- and 400-keV C_{60} Ion ····· 165
4-42 Effect of Au Cluster Ion Irradiation on Magnetic Properties of FeRh Thin Films ····· 166
4-43 Positive Secondary Ion Emission from PMMA upon Energetic C_8 Cluster and Mo Ion Impacts ····· 167
4-44 Secondary Electron Emission from Carbon Induced by MeV/atom Carbon Cluster Bombardment ····· 168
4-45 Ion Induced Luminescence from Sapphire Irradiated with Swift Cluster Ion Beams ····· 169
4-46 Processing of an Upstanding Nano-Wire Array Using Ion-Beam Lithography ·· 170
4-47 Fabrication of Dielectrophoretic Devices Using Poly-dimethylsiloxane Microstructures by Proton Beam Writing ····· 171
4-48 Development of Neutron Optics Devices Using Proton Microbeam ····· 172
4-49 Fast Single-Ion Hit System for Heavy-Ion Microbeam at TIARA Cyclotron (III) ····· 173
4-50 Status Report on Technical Developments of the AVF Cyclotron ····· 174
4-51 Development of Beam Generation and Irradiation Technology for Electrostatic Accelerators ····· 175
4-52 Production of Highly Spin-Polarized Positron Source ····· 176

5. Status of Irradiation Facilities 2009 ····· 177

5-01 Safety Measures, Utilization Status and Machine Time Proportion at TIARA Facility ····· 179
5-02 Operation of the AVF Cyclotron ····· 180
5-03 Operation of the Electrostatic Accelerators ····· 181
5-04 Operation of Electron Accelerator and Gamma-ray Irradiation Facilities ····· 182
5-05 Utilization of Electron Accelerator and Gamma-ray Irradiation Facilities ····· 183
5-06 FACILITY USE PROGRAM in Takasaki Advanced Radiation Research Institute ····· 184
5-07 Radiation Control in TIARA ····· 185
5-08 Radioactive Waste Management in TIARA ····· 186

Appendix ····· 187

Appendix 1 List of Publication ····· 189
Appendix 2 List of Related Patents ····· 210
Appendix 3 List of Related Press-Release and TV Programs ····· 212
Appendix 4 Type of Research Collaboration and Facilities Used for Research ····· 214
Appendix 5 A Typical Example of Abbreviation Name for Organizations in Japan Atomic Energy Agency (JAEA) ····· 216

1. Space, Nuclear and Energy Engineering

1-01 Radiation Resistance of InGaP/GaAs Dual-Junction Thin-Film Space Solar Cell ····· 5
M. Imaizumi, S. Sato, T. Ohshima, M. Takahashi and K. Kibe
1-02 Detection of Photons Induced by a Single Ion Strike ····· 6
S. Onoda, T. Makino and T. Ohshima
1-03 Evaluation of Soft Error Rates in SOI SRAM with a Technology Node of 90 nm Using Oxygen Ion Probe ····· 7
S. Abo, N. Masuda, F. Wakaya, S. Onoda, T. Makino, T. Hirao, T. Ohshima, T. Iwamatsu, H. Oda and M. Takai
1-04 Feasibility Study on a 90 nm Bulk CMOS Process for Applicability to Space Environments ····· 8
A. Maru, H. Shindou, S. Kuboyama, T. Hirao and T. Ohshima
1-05 Heavy-ion Induced Current in SOI p^+n Junction Diode ····· 9
Y. Takahashi, A. Ohwaki, H. Takeyasu, T. Hirao, S. Onoda and T. Ohshima
1-06 Study of Ion-Implantation Condition Effects for AlGaN/GaN-Based Light Emitting Device ····· 10
H. Okada, T. Hata, M. Kondo, Y. Furukawa, A. Wakahara, S. Sato and T. Ohshima
1-07 Total Ionizing Dose Tolerance of SiC Buried Gate Static Induction Transistors up to 10 MGy ····· 11
S. Onoda, Y. Tanaka, A. Takatsuka, T. Yatsuo and T. Ohshima
1-08 Evaluation of Radiation Tolerance of General Electronic Devices ····· 12
N. Sasaki, Y. Kakimi, T. Nakao, K. Ogawa, T. Ohshima, T. Hirao and S. Onoda
1-09 Evaluation of Single Event Effects on Commercial-off-the-Shelf Semiconductors for Space Flight Applications ····· 13
I. Kato, S. Matsuda, S. Baba, T. Hirose, J. Ohya, H. Okamoto, H. Katayama, M. Naitoh, M. Harada, M. Suganuma and Y. Tange
1-10 Mechanisms of Changes of Hole Concentration in Al-doped 6H-SiC by Electron Irradiation and Annealing ····· 14
H. Matsuura, H. Yanagisawa, K. Nishino, Y. Myojin, T. Nojiri, Y. Matsuyama, S. Onoda and T. Ohshima
1-11 Hydrogen Diffusion in a-Si:H Thin Films due to High Temperature Ion Irradiation ····· 15
S. Sato, T. Ohshima and M. Imaizumi
1-12 NV Centers in Diamond Irradiated with High Energy Nitrogen Ions and 2 MeV Electrons ····· 16
J. Isoya, T. Umeda, N. Mizuochi, T. Ohshima, S. Onoda, S. Sato and N. Morishita

1-13 Alpha-radiolysis of Organic Extractants for Separation of Actinides・・・・・・・・・ 17
Y. Sugo, M. Taguchi, Y. Sasaki, K. Hirota and Y. Morita
1-14 A Study on Complete Decomposition of Pyrrolidone Precipitants by γ-Ray Irradiation ・・・・・・・・・

1-26 Effect of Temperature Change on Irradiation Hardening of Ferritic and Austenitic Steels during Ion-irradiation ····· 30
S. Jitsukawa, M. Ando, I. Ioka, Y. Abe, T. Onitsuka, N. Ishikawa and N. Okubo
1-27 Simulation of Neutron Damage Microstructure in Extra High Purity Fe-25Cr-35Ni Austenitic Stainless Steels ····· 31
I. Ioka, Y. Ishijima, H. Ogawa and Y. Nakahara
1-28 Effects of Radiation Damage and Helium on Swelling and Microstructure of EHP Ni-base Superalloy ····· 32
G. H. Kim, K. Shiba, I. Ioka, T. Sawai and S. Yamashita
1-29 Irradiation Hardening in Ion-irradiated Hafnium ····· 33
Y. Chimi and J. Ogiyanagi
1-30 Conductometric Analysis of Track Etching in Poly(vinylidene fluoride) ····· 34
T. Yamaki, H. Koshikawa, S. Sawada, S. Hasegawa, M. Asano and Y. Maekawa
1-31 Preparation of Anion-Exchange Membranes for Fuel Cell Applications by γ-ray Pre-Irradiation Grafting ····· 35
H. Koshikawa, T. Yamaki, M. Asano and Y. Maekawa
1-32 Enhanced Reactivity of Ion-track Grafting for Fuel-cell Electrolyte Membranes ····· 36
T. Sekine, S. Sawada, T. Yamaki, H. Koshikawa, M. Asano, Y. Maekawa, A. Suzuki and T. Terai
1-33 Radiation-Induced Graft Polymerization of Styrene into a Poly (ether ether ketone) Film for Polymer Electrolyte Membranes ····· 37
S. Hasegawa, K. Sato, T. Narita, Y. Suzuki, S. Takahashi, N. Morishita and Y. Maekawa
1-34 Nanoscale Structures of Radiation-Grafted Polymer Electrolyte Membranes Investigated by Dissipative Particle Dynamics Simulation ····· 38
S. Sawada, T. Yamaki, A. Suzuki, T. Terai and Y. Maekawa

This is a blank page.

1-01 Radiation Resistance of InGaP/GaAs Dual-Junction Thin-Film Space Solar Cell

M. Imaizumi [a)], S. Sato [b)], T. Ohshima [b)], M. Takahashi [a)] and K. Kibe [a)]

[a)] Institute of Aerospace Technology, JAXA,
[b)] Environment and Industrial Materials Research Division, QuBS, JAEA

Increasingly, solar panels are being required to have less weight and volume, namely, higher specific power in W/kg and lower stowage volume in W/m^3. There are two ways to meet these requirements. One is to improve the solar cell efficiency, and the other is to reduce the weight and/or thickness of solar cells. However, if a thin-film III-V multi-junction solar cell can be achieved, it realizes both properties of high-efficiency and lightweight. We have developed an InGaP/GaAs thin-film dual-junction (TF2J) solar cell [1),2)]. In this paper, we present comparison of the radiation resistance of the TF2J cell and conventional 3J cells [3),4)].

A hundred of the TF2J cells were prepared for proton irradiation experiment. No laminating film was applied on the front surface of the cell. The initial efficiency of the cells was in the range of 20-23% under AM0, 1sun (136.7 mW/cm^2) at 25 °C. Also, a conventional InGaP/GaAs/Ge triple-junction (3J) space solar cell was prepared for comparison. The thicknesses of the InGaP and GaAs sub-cells in the TF2J and the 3J cells are equivalent.

The cells were subjected to proton irradiation at the following energies; 100 keV, 200 keV, 380 keV, 1 MeV, 3 MeV, and 6 MeV with varied fluences. The current-voltage (I-V) output characteristics and the external quantum efficiency (EQE) of the cells before and after irradiation were measured. The results of the TF2J cell were compared with those of the 3J cell.

The remaining factors of the short-circuit current (Isc), the open-circuit voltage (Voc) and the maximum power (Pmax) of the TF2J and the space 3J cells irradiated with various energies of protons are compared in Fig. 1. The fluence of all energies of protons is equal (1×10^{12} cm^{-2}). In the energy range of 200 - 400 keV, radiation resistance of the TF2J cell is superior to that of the 3J cell. Protons in this energy range stop in the GaAs sub-cells according to TRIM simulation [3)]. Therefore, the energy range is the most destructive to space 3J cells [4)]. In the case of 380 keV-proton irradiation, the value of Isc of the TF2J cell after the irradiation is significantly higher than that of the 3J cell. In addition, the Voc values of the two types of cell irradiated are almost equivalent although the TF2J cell has dual-junction structure. These facts result in higher Pmax value for the TF2J cell after the irradiation.

Typical degradation in EQE of InGaP and GaAs sub-cells in the TF2J cell and the 3J cell before and after the 380 keV-proton irradiation were compared. It reveals that the better radiation resistance of Isc of the TF2J cell is attributed to higher radiation resistance of the GaAs sub-cell in the TF2J cell.

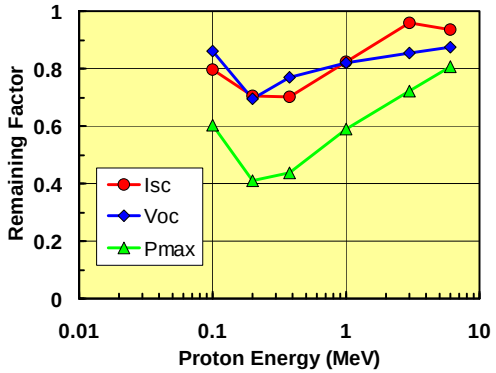

(a) TF2J cell

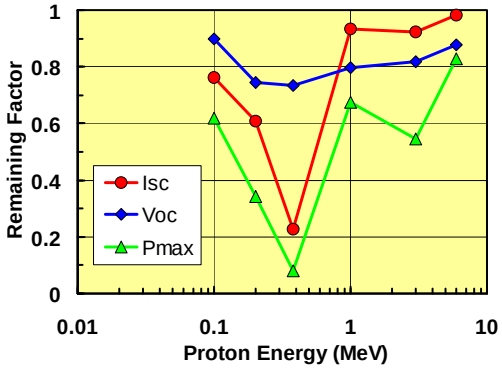

(b) #502 3J cell

Fig. 1 Dependency of remaining factors of Isc, Voc and Pmax of (a) TF2J cell and (b) #502 3J cell on irradiated proton energy. The fluence of each energy proton is 1×10^{12} cm^{-2}.

From these results, the TF2J cell is thought to require less radiation-shielding materials such as coverglass or other laminating films than conventional 3J cells. This is a great advantage for developing lightweight and flexible solar panels.

References

1) T. Takamoto et al., Proc. 31st IEEE Photovoltaic Specialists Conf. (2005) 519-524.
2) T. Takamoto et al., Proc. 4th World Conf. of Photovoltaic Energy Conversion (2006) 1769-1772.
3) M. Imaizumi et al., Proc. 29th IEEE Photovoltaic Specialists Conf. (2002) 990-993.
4) T. Sumita et al., Proc. World Conf. of Photovoltaic Energy Conversion (2003) CD 3P-B5-10.

1-02 Detection of Photons Induced by a Single Ion Strike

S. Onoda, T. Makino and T. Ohshima

Environment and Industrial Materials Research Division, QuBS, JAEA

Single Event Effects (SEEs) are well known as a malfunction of microelectronics devices caused by the impact of the Galactic Cosmic Ray (GCR) such as high energy heavy ions. Generally, SEEs are triggered by unexpected transient currents induced by an ion incidence. The focused ion microbeam has a key advantage in evaluating the transient currents at specific region of a device with a high resolution. Therefore we have developed the system of transient current mapping by using the heavy ion microbeams connected with both 3 MV tandem and AVF cyclotron accelerators [1]. These are called the Transient Ion Beam Induced Current (TIBIC) systems. The powerful advantage of TIBIC mapping is the ability to determine the position dependence of the event due to an ion incidence. Although the microbeam has a lot of advantages for SEE testing, the transporting and optimizing microbeam require a lot of time and effort. Therefore the mapping system with less effort is required. A different way to perform mapping has been proposed by Sandia National Laboratory (SNL) [2]. It is called the Ion Photon Emission Microscopy (IPEM). To observe mapping using IPEM, it is not necessary to focus the MeV ions at all. Instead of microbeam, the position where ions strike the sample is recorded together with the ion induced charge. The position signals are detected by a Position Sensitive Detector (PSD). In this study we used the high-sensitive cooled Charge Coupled Device (CCD) Camera and the Image Intensifier (I.I.) instead of PSD.

Figure 1 shows the photograph of measurement system developed at TIARA facility. This system contains following; (1) a beam extraction window (Kapton film) under the mirror, (2) a sample (phosphor on Si diode) on micro XYZ stage, (3) an electronics for charge measurements including amplifier, bias supply and oscilloscope, and (4) a photon detection equipments including the microscope (Olympus, BX51M), I.I. (Hamamatsu, C8600), and Cooled CCD camera (Hamamatsu, C4880-50-26A). The 150 MeV Ar beams accelerated by the AVF Cyclotron are extracted from vacuum to air via the Kapton film. The extracted Argon (Ar) ion penetrates the phosphor on diode. The photons from phosphor are detected by cooled CCD camera. At the same time the ion induced charge in diode is recorded by the oscilloscope.

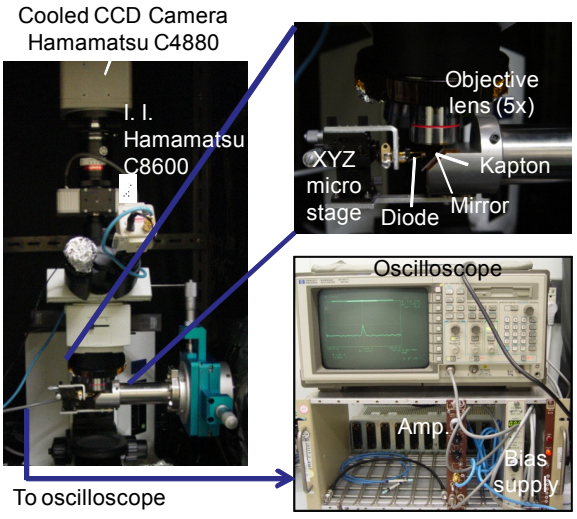

Fig. 1 Photograph of measurement system.

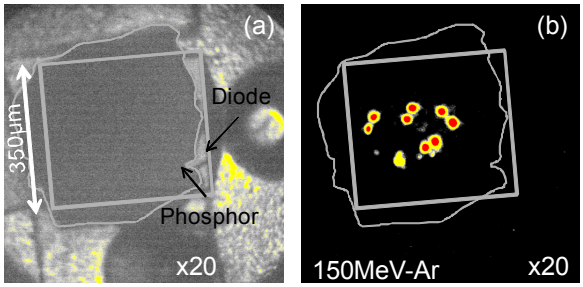

Fig. 2 Micrograph of the phosphor on diode (a) and the image of cooled CCD camera when the 150 MeV Ar ions penetrate the phosphor on diode (b). White lines indicate the contours of phosphor and diode.

Figure 2 shows the micrograph of phosphor on diode and image of cooled CCD when 150 MeV Ar ions penetrate the phosphor on diode. As shown the nine spots are detected and each spot can be distinguished. Of course, applying the beam attenuator the number of spots per one frame can be controlled. The position where ion hit the sample can be observed from the center of mass of each spot. The diameter of spot is about 50 μm. Since the spot size determines the resolution of map, it is necessary to find another luminescence sheet. At the same time of CCD image, the corresponding charge signal is measured by oscilloscope. Combining the position and charge signal, two dimensional map of charge collection on diodes can be observed.

References

1) T. Hirao et al., Nucl. Instrum. Meth. B 267 (2009) 2216.
2) B. L. Doyle et al., Nucl. Instrum. Meth. B 181 (2001) 199.

Acknowledgement

The part of this study was supported by the Grant-in-Aid for Young Scientists (B) No. 20760051 from the Ministry of Education, Culture, Sports, Science and Technology of Japan.

1-03 Evaluation of Soft Error Rates in SOI SRAM with a Technology Node of 90 nm Using Oxygen Ion Probe

S. Abo [a)], N. Masuda [a)], F. Wakaya [a)], S. Onoda [b)], T. Makino [b)], T. Hirao [b)], T. Ohshima [b)], T. Iwamatsu [c)], H. Oda [c)] and M. Takai [a)]

[a)] Center for Quantum Science and Technology under Extreme Conditions, Osaka University,
[b)] Environment and Industrial Materials Research Division, QuBS, JAEA,
[c)] Advanced Device Development Department, Renesas Technology Corporation

A soft error or bitstate upset due to the excess charge carriers generated by high energy incident particles becomes a serious problem in advanced semiconductor devices. A silicon-on-insulator (SOI) device has an advantage over the conventional bulk device for the soft error, in which a device region is insulated from the silicon substrate by a buried oxide (BOX) layer and the excess charge carriers in the silicon substrate are not accumulated to the drain electrode. However, the generated excess carriers in a SOI body are kept at the channel region in the SOI body or accumulated to the drain and source electrodes. The generated holes in the channel region of an n-channel SOI metal oxide semiconductor field effect transistor (MOSFET) increase the SOI body potential, which results in a floating body effect and the soft error. The floating body effect can be suppressed by a body-tie structure, in which the SOI body regions are connected to the source electrode. The body electrode subtracts the generated excess carriers from the channel region and suppresses the floating body effect.

In this study, the difference in soft error rates (SERs) of SOI SRAM with a technology node of 90 nm was investigated by oxygen ion probes with energies ranging from 9.0 to 18.0 MeV. The memory cell included 4 n-MOSFETs sand 2 p-MOSFETs. The memory cell size, the memory capacity and the critical charge of SOI SRAM were 1.25 μm^2, 8 Mbits and 1.8 fC, respectively. The thicknesses of the SOI body and the BOX layer were 75 and 145 nm. The over-layers were 4 copper metal and polyimide passivation layers without top plastic mould. The body-tie structure was used for suppressing the floating body effect. The amount of soft error in SRAM was monitored after oxygen ion probe irradiation. The dose rates of oxygen probes for each of the energies were monitored by a solid state detector before irradiation. The minimum and maximum dose rates were 50 and 930 cps. The beam spot sizes were less than 1 μm. The scanned areas were calculated from secondary electron images. The minimum and maximum scanned areas were 220×187 μm^2 and 327×275 μm^2, respectively. The irradiation time was adjusted for less than 1 oxygen ion hit to 1 SRAM cell from the dose rate and the scanned area.

Figure 1 shows SERs as a function of oxygen ion energy in SOI SRAM. The values of SER were normalized to the error bits for those by 12 MeV oxygen ion irradiation. No soft error occurred in SOI SRAM with oxygen ion energies of less than 10.0 MeV. This indicates that the oxygen ions with energies of less than 10.0 MeV were shielded by the over-layers of MOSFET. Soft error rates started to increase at 10.5 MeV and gradually saturated with energies above 13.5 MeV. Figure 2 shows the generated charge in the SOI body in SOI SRAM as a function of oxygen ion energy simulated by SRIM code. The energy loss through the over-layers was corrected by the designed thickness. The oxygen ions with energies less than 12.5 MeV generated less excess charge carriers than the critical charge. Therefore the soft error in SOI SRAM by oxygen ion irradiation with energies at end below 12.5 MeV shown in Fig. 1 occurred by the floating body effect due to the generated excess charge carriers in the channel regions. The oxygen ions with energies at end above 13.0 MeV generated more excess charge carriers than the critical charge, in which the soft error was induced by both the floating body effect and these excess carriers at the storage nodes.

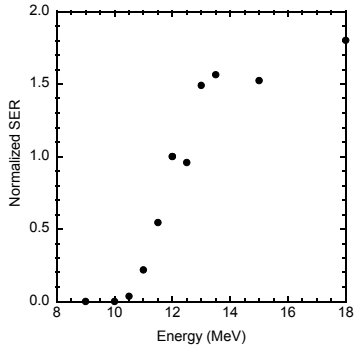

Fig. 1 SERs as a function of oxygen ion energy for the SOI SRAMs. The values of SER were normalized to the error bits by 12 MeV oxygen ion irradiation.

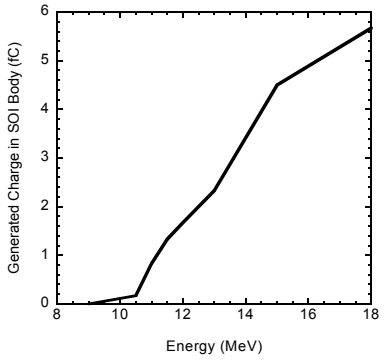

Fig. 2 Generated charge in the SOI body as a function of oxygen ion energy in the SOI SRAM.

1-04 Feasibility Study on a 90 nm Bulk CMOS Process for Applicability to Space Environments

A. Maru [a)], H. Shindou [a)], S. Kuboyama [a)], T. Hirao [b)] and T. Ohshima [b)]

[a)] Aerospace Research and Development Directorate, Japan Aerospace Exploration Agency (JAXA),
[b)] Environment and Industrial Materials Research Division, QuBS, JAEA

Recently, due to the requirements for higher density integration and device scaling, the logical circuits have been designed with < 100 nm design rule. Single-Event Upset (SEU) and Single-Event Transient (SET) phenomena are serious problems for those integrated circuits, because their supply voltage and the threshold to the phenomena are also decreasing. It is said that DICE (Dual Interlocked Storage Cell) circuit is the hardened topology against SEU [1,2]. The DICE circuit keeps data using two memory nodes, and if data inversion has occurred by incident particles on the one hand memory node, the correct data is rewritten by the other hand memory node. Therefore, DICE circuit has excellent radiation tolerance. However, in the highly integrated circuits, it is occurred that two neighboring transistors are simultaneously inverted by an incident particle due to the charge sharing mechanism. Therefore, it is important for the design of those circuits to estimate the extent of the charge sharing.

In this feasibility study, the applicability to space environments of a 90 nm bulk CMOS process was evaluated by heavy ions and the SEU cross section was calculated. For detailed evaluation, we also performed the angled irradiation. The experimental results suggested there are the critical angles in the DICE memory circuit.

At first, we evaluated the effectiveness of RHBD apploarch for 90 nm CMOS process, by using the heavy ions delivered from the AVF cyclotron at JAEA. As shown in Fig. 1, the latch cell with RHBD methodology for 90 nm, the DICE topology, has excellent radiation hardness.

However, it is said that if two critical off state transistors in the DICE circuit upset simultaneously, the memorized data in the DICE memory is lost. Therefore we performed the angled irradiation for DICE memory circuit and the SEU cross section against incident angle was calculated.

Figure 2 shows SEU cross-sections as a function of incident angle when Kr (LET= 40.3 MeV/mg/cm^2) particles were irradiated. In our DICE circuit, the most critical angle is estimated to be 52 degree. So, if the irradiated heavy ion incidents from that angle, the particle pass through the two critical transistors in the DICE circuit. Therefore, although it is considered that the actual distance of the two adjacent transistors in the off state to hold the logic state is one of the critical parameters to prevent SEUs, in addition to this parameter, some artifice to prevent SEUs by the angled irradiation is necessary. In future work, we plan to design the circuit that optimized the actual layout and added the countermeasure against the angled irradiation in order to achieve SEU immunity up to 64 MeV/(mg/cm^2) of LET.

References

1) M.P.Baze, et al., EEE Trans. Nucl. Sci., Vol. 55 (2008) 3295.
2) Kuande Wang, et al., Canadian Conference on Electrical and Computer Engineering, (2009) 1076.

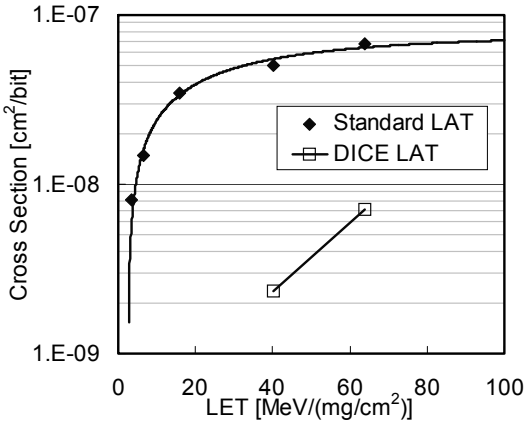

Fig. 1 SEU cross-sections as a function of Linear energy transfer for Standard and DICE latch circuits.

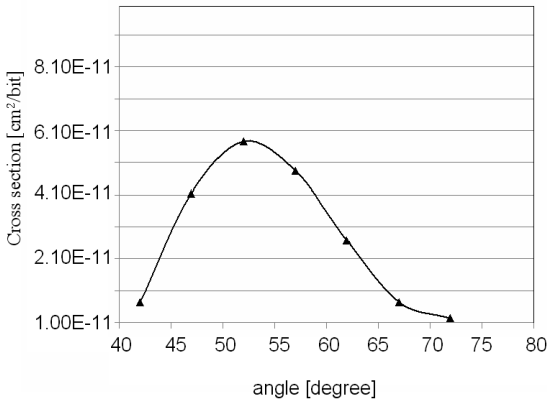

Fig. 2 SEU cross-sections against incident angle.

1-05 Heavy-ion Induced Current in SOI p^+n Junction Diode

Y. Takahashi [a)], A. Ohwaki [a)], H. Takeyasu [a)],
T. Hirao [b)], S. Onoda [b)] and T. Ohshima [b)]

[a)] Nihon University, [b)] Environment and Industrial Materials Research Division, QuBS, JAEA

One of the most detrimental effects on semiconductor devices in radiation environments is the single-event effect (SEE). Recently, silicon-on-insulator (SOI) technology has been developed to reduce SEE, because it was believed that the charge collection is suppressed by the existence of a buried oxide (BOX) layer[1]. However, anomalous charge collection through the BOX layer was also reported[2]. So it is important to clarify the charge collection mechanism through the oxide layer. In the present work, we have investigated the heavy-ion induced transient gate currents in MOS structures and we concluded that the transient current through an oxide layer is dominated by a displacement current[3]. In this study, the heavy-ion induced transient current in SOI p^+n junction diode was investigated, in order to discuss the features of transient current in SOI devices.

The Al gate p^+n junction diodes with the junction area of 100 μm in diameter were fabricated on a SOI substrate as shown in Fig. 1. The donor concentration of each silicon layer is about 10^{15} cm^{-3} and the thicknesses of active SOI layer and BOX layer are 1.5 μm and 0.3 μm, respectively. The transient currents in diodes induced by 15 MeV Oxygen ions were measured. The LETs and project range of the ions are 6.5 MeV/(mg/cm^2) and 12.3 μm, respectively. Heavy-ion irradiation tests were carried out using the Single Ion hit (SIH) system in JAEA and the transient current caused by the single ion was measured by Transient Ion Beam Induced Current (TIBIC) measurement system.

Figure 2 shows the transient current and the total collected charge, the integration value along a time after irradiation, of each electrode in the device, in which the reverse bias of 10 V is applied during irradiation test. The peak height of the current signal of p^+ electrode, anode electrode, is 24 μA and the maximum collected charge is 230 fC. These values correspond to 1/20 and 1/3 of the diode fabricated on bulk Si substrate, respectively[4]. These results indicate that the SEE effects can be reduced using the SOI devices. On the other hand, the current of n^+ electrode, cathode electrode, is almost 0 and the amount of collected charge of back electrode is almost the same as that of anode electrode. These results show that the charges collected by anode electrode were mostly caused by the radiation induced generated charges in handle Si substrate and these charges were collected through the BOX layer as a displacement current. So it is important to reduce the displacement current in order to suppress the SEE effects of SOI device.

It is considered that the displacement current can be reduced by decrease the width of depletion layer at the surface of handle Si substrate. We evaluated the heavy-ion induced current in SOI p^+n diodes using device simulation. By the results of simulation, it was found that the width of depletion layer was changed by the impurity concentration of the handle Si substrate and the collected charge could be reduced using the handle Si substrate with low resistivity.

References

1) O. Musseau, IEEE Trans. Nucl. Sci., NS-43, 2 (1996) 603-613.
2) T. Hirao et al., Nucl. Instrum. Meth. Phys. Res., B-206 (2003) 457-461.
3) Y. Takahashi et al., Nucl. Instrum. Meth. Phys. Res., B-260 (2007) 309-313.
4) Y. Takahashi, Abst. 4th Takasaki Adv. Radiat. Res. Symp. (2009) 41.

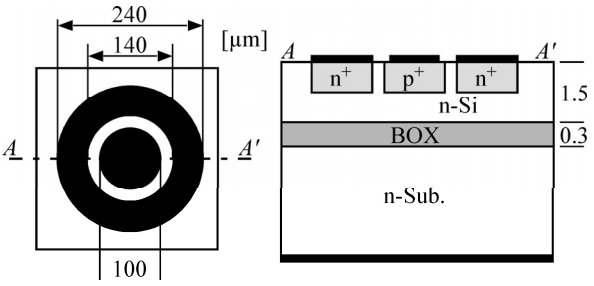

Fig. 1 Device structure of SOI p^+n junction diode.

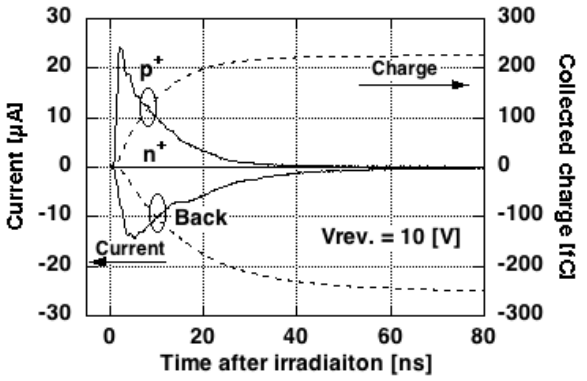

Fig. 2 Transient current and total collected charge in a SOI p^+n junction diode. Solid lines show the current and dashed lines show the amount of collected charges.

1-06 Study of Ion-Implantation Condition Effects for AlGaN/GaN-Based Light Emitting Device

H. Okada [a)], T. Hata [a)], M. Kondo [a)], Y. Furukawa [a)], A. Wakahara [a)], S. Sato [b)] and T. Ohshima [b)]

[a)] Toyohashi University of Technology,
[b)] Environment and Industrial Materials Research Division, QuBS, JAEA

Effects of ion-implantation conditions were studied for new type light emitting device based-on AlGaN/GaN high electron mobility transistor (HEMT) structure having selective doping of Eu in the channel of the transistor. Drastic decrease of the channel conductance was observed in Eu implanted samples. This decrease is explained by decrease of electron mobility, rather than decrease of the sheet carrier density from Hall effect measurement. It was confirmed that the clear red electroluminescence observed in the fabricated device originated from Eu ion with luminescence peak at 620 nm suggesting $^5D_0 \rightarrow {}^7F_2$ transition in Eu. The results suggest that ion-implantation condition affects electrical and electroluminescence properties of the proposed light emitting device.

我々は窒化物半導体ヘテロ構造である AlGaN/GaN 高電子移動度トランジスタ(HEMT)構造にイオン注入法により希土類元素を添加した三端子型発光素子を提案・試作し、その発光を報告している[1)]。このデバイスは希土類元素の内殻遷移に基づく発光を利用するもので、単色性に優れ、温度消光が少ない発光デバイスが期待でき、光通信素子、光を使った分析装置に有用な発光素子を実現できる。これまで、デバイス試作時に用いたイオン注入条件は、過去に行ったフォトルミネセンス(PL)やカソードルミネセンス(CL)などの光励起法による発光特性の結果を参照して設定してきたが、電流注入発光(EL)素子として良好な特性を実現するためには、デバイス作製条件と電気的特性・発光特性との関連を検討する必要がある。今回、希土類元素のイオン注入量、加速エネルギーと、素子の電気的特性、発光特性との関係に注目し、検討を行った。

今回の素子作製には有機金属化学気相成長法により Si 上にエピタキシャル成長させた AlGaN/GaN ウェハを用いた。室温におけるシートキャリア濃度は 1×10^{13} cm^{-2}、移動度は 1,450 cm^2/Vs であった。まず反応性イオンエッチングにより素子領域を分離する。次にイオン注入の保護膜として形成した SiO_2 層の一部に注入窓をエッチングにより形成した。試料への Eu イオン注入には、TIARA の 400 kV イオン注入装置を使用した。その後注入による欠陥の回復熱処理を行い、保護膜の SiO_2 をエッチングにより除去しソース・ドレイン電極を電子ビーム蒸着とリフトオフにより形成した。最後にゲートを同様に形成した。

Table 1 にチャネルコンダクタンス g の測定結果を示す。チャネルコンダクタンスは Eu イオン注入により大幅に減少した。この高抵抗化は注入量の増加とともにより顕著に現れた。Eu 注入量 1×10^{16} cm^{-2} では若干コンダクタンスの上昇が見られているが、この原因は不明である。イオン注入による高抵抗化の要因について検討するために、Van der Pauw 法によるホール効果測定を行った。Eu ドーズ量を変化させたサンプルについて評価したところ、シートキャリア濃度は 10^{14}～10^{16} cm^{-2} のドーズ量に対して大きな変化はみられず、ドーズ量の増加とともに電子移動度の低下がみられた。この振る舞いは、HEMT のチャネルコンダクタンスから見積もった実効移動度と数値的にもよく一致した。適切な注入量の設定により、注入領域の高抵抗化による電界集中が生じ、加速された電子による Eu イオンの衝突励起発光を引き起こすことができると考えられる。

次に、作製したデバイスの EL 発光特性について評価した。ソースードレイン間バイアス V_{DS} = 100 V により注入部分に赤色発光が得られた。注入量を変化させた実験から、注入量の増加とともに明確な赤色発光が認められることがわかった。Fig. 1 に加速エネルギー 200 keV、注入量 1×10^{15} cm^{-2} の条件で作製したデバイスの EL 発光写真を示す。分光器によるスペクトル分析から、Eu イオンの内殻遷移 $^5D_0 \rightarrow {}^7F_2$ に対応する 620 nm 付近にピークをもつスペクトルが得られ、作製したデバイスにおいて希土類元素からの発光が得られていることが確認できた。今後、ここで得られたイオン注入条件や、デバイス構造、作製条件の最適化により、希土類元素の発光に基づくユニークな発光素子の高効率化を行う。

Table 1 Eu dose dependence on channel conductance of fabricated FET with V_{acc}=70 keV.

Eu dose [cm^{-2}]	g [μS]
No implantation	7,000
1×10^{13}	190
1×10^{14}	37.1
1×10^{15}	31.7
1×10^{16}	62.4

Fig. 1 Electroluminescence (EL) image of fabricated device (V_{DS} = 100 V, V_{GS} = 0 V).

Reference

1) H. Okada et al., Phys. Status Solidi C6 S2 (2009) S631-634.

1-07 Total Ionizing Dose Tolerance of SiC Buried Gate Static Induction Transistors up to 10 MGy

S. Onoda [a)], Y. Tanaka [b)], A. Takatsuka [b)], T. Yatsuo [b)] and T. Ohshima [a)]

[a)] Environment and Industrial Materials Research Division, QuBS, JAEA,
[b)] National Institute of Advanced Industrial Science and Technology

Silicon Carbide (SiC) is regarded as one of the candidate materials for devices with radiation hardness, owing to its superior radiation resistance as well as excellent physical properties and chemical stability. Ohshima et al.[1)] reported that the electrical properties for 6H-SiC Metal-Oxide Field Effect Transistors (MOSFETs) with steam-annealed gate oxide did not degrade by gamma-ray irradiation at 200 kGy in spite that H_2-annealed ones showed the degradation above 40 kGy. These results suggest that the ionizing radiation response of MOSFETs is strongly affected by their fabrication processes especially gate oxidation. Instead of SiC MOSFETs, in this study, the Total Ionizing Dose (TID) effects on SiC Buried Gate Static Induction Transistors (SiC-BGSITs) involving no silicon dioxide are evaluated up to the absorbed dose of 10 MGy(SiO_2). For comparative purpose, we also evaluated the TID effects on commercial Si-MOSFET (17N80C3) and Si-IGBT (5J301).

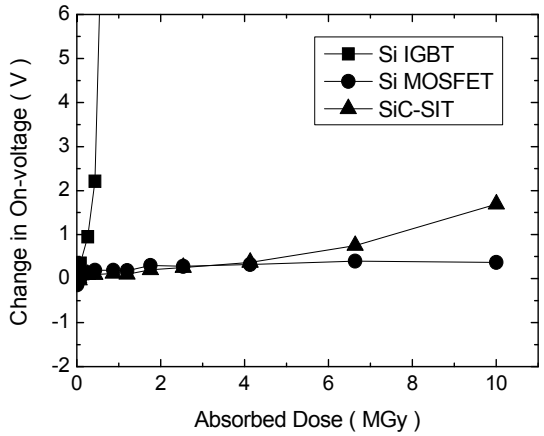

Fig. 1 Change in on-voltage of SiC-SIT, Si MOSFET, and Si IGBT after gamma-ray irradiation up to the absorbed dose of 10 MGy.

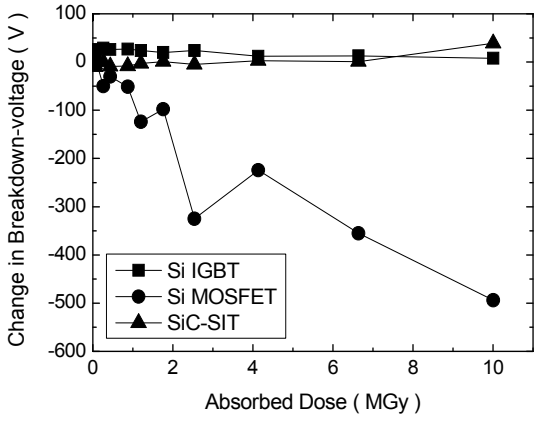

Fig. 2 Change in breakdown voltage of SiC-SIT, Si MOSFET, and Si IGBT after gamma-ray irradiation up to the absorbed dose of 10 MGy.

The SiC-BGSITs are developed by AIST [2, 3)] for the evaluation of radiation hardness. All devices including both SiC and Si transistors were mounted in TO220 packages. The gamma-ray irradiation from ^{60}Co source in JAEA was performed at the dose rate of 8.8 kGy(SiO_2)/h up to the total dose of 10 MGy. During the gamma-ray irradiation, the devices were floating. After each irradiation, the on-state, the threshold, and the blocking characteristics of each device were measured. The on-state characteristics were measured at the gate voltage (V_G) of +15 V for Si-IGBT and Si-MOSFET and that of +2.5 V for SiC-BGSIT. The on-voltage (V_{on}) was defined as the drain voltage (V_D) at the drain current (I_D) of 10 A. The threshold voltage (V_{th}) was derived from I_D-V_G characteristic measured at V_D of +0.3 V. The blocking characteristics were measured at V_G of 0 V for Si-IGBT and Si-MOSFET and that of -10 V for SiC-BGSIT.

Figure 1 and 2 show the change in on- and breakdown voltage as a function of gamma-ray absorbed dose. The V_{on} of Si-IGBT degraded excessively at the early stage of the irradiation (>~0.1 MGy(SiO_2)) due to the bulk damage produced by Compton electrons. Although not shown here the V_{th} of Si-MOSFET is very sensitive against the radiation. The blocking characteristics of Si-MOSFET degraded significantly against the radiation as shown in Fig. 2. The reduction in V_{on} of Si-IGBT and the degradation of blocking characteristics of Si-MOSFET are very serious problems to use these devices for the application under high radiation environment. On the other hand, we successfully confirmed that SiC-BGSIT has very high radiation hardness and can operate stably under harsh environment.

References

1) T. Ohshima et al., Mater. Sci. Forum 1093 (2002) 389-393.
2) Y. Tanaka et al., Mater. Sci. Forum 1219 (2006) 527-529.
3) Y. Tanaka et al., IEEE Elect. Dev. Lett. 908 (2006) 27.

Acknowledgement

This study was carried out under the Strategic Promotion Program for Basic Nuclear Research by the Ministry of Education, Culture, Sports, Science and Technology of Japan.

1-08 Evaluation of Radiation Tolerance of General Electronic Devices

N. Sasaki [a)], Y. Kakimi [a)], T. Nakao [a)], K. Ogawa [a)],
T. Ohshima [b)], T. Hirao [b)] and S. Onoda [b)]

[a)] Advanced Engineering Services Co.,Ltd.
[b)] Environmental and Industrial Materials Research Division, QuBS, JAEA

We are developing a small-satellite that will be launched in several years, and small-satellite's equipments for example "Power Control Unit", "Gyro Unit", etc. At these developments, using general electronic devices is very efficient to reduce the cost, to shorten the development period and to comply with a request of various missions. So, we have been evaluating general electronic devices about radiation tolerance related to single event since 2008. These results show a good possibility that they can be used on the space environment. This report shows a result of evaluation about FeRAM (Ferroelectric Random Access Memory) and MPU (Micro Processing Unit).

我々は、数年後の打上げを目標に 50 cm 級小型衛星の開発を進めている。また、小型衛星搭載用電力制御装置をはじめ、様々な搭載機器の開発も行っている。小型衛星を利用することの利点は、短期間、低コストで、様々な新しいミッションを実現できるということである。しかし、宇宙用電子部品の多くは、入手性や価格、部品のバリエーションの面で、この利点に大きな制限をかけてしまう。従って、小型衛星の開発において、民生電子部品を利用することは、開発期間の短縮、低コスト化や、多様なミッションへの対応等、小型衛星の利点を活かすのに必須となる。そこで、我々は 2008 年度より、小型衛星での使用を想定した、レギュレータや通信ドライバ等の民生電子部品の重粒子線照射試験を行い、シングルイベントに関し、宇宙環境への適合性評価を行ってきた。その結果、シングルイベントの発生頻度は、500 year/event 以上であり、民生電子部品の宇宙環境での使用の可能性について良い結果を得ることができた。本稿では、2009 年度に行った、FeRAM（強誘電体メモリ）、MPU（マイクロプロセッサ）の試験結果について報告する。

照射試験は、AVF サイクロトロン 散乱ビーム照射試験装置を用いて実施した。使用したイオン種を Table 1 に示す。試料は、予めパッケージをデキャップしておき、内部の半導体素子を露出した状態としている。FeRAM についての評価は、SEL（Single Event Latch-up）と RAM での SEU（Single Event Up-set）の発生頻度に関して、MPU についての評価は、SEL と内部レジスタ、FlashROM での SEU の発生頻度に関して行った。発生頻度の算出には、CREME96 を用いている。想定している軌道条件は、高度 700 km、衛星構体は 2 mm 厚アルミニウム、運用期間 1 年である。

Table 1 Particle Energy and LET.

	$^{15}N^{3+}$	$^{20}Ne^{4+}$	$^{40}Ar^{8+}$	$^{84}Kr^{17+}$
E [MeV]	56	75	150	322
LET [MeV/mg/cm^2]	3.0	5.9	14.0	34.0

FeRAM の試験では、同ロットの試料 3 つに対し同時に照射を行い、デバイスの消費電流より SEL を、SEU の発生は別途搭載した監視用マイコンにより監視した。また、SEU に関しては全ビットが 1 と 0 の 2 通りの状態について行った。以下に結果を示す。

① SEL 耐性
SEL の発生は、Kr でのみ確認された。この時の有効総フルエンスは 10^5 count/cm^2 であるので、その発生頻度は概算として 3,000 year/event であると見積もられ、SEL への耐性は非常に高い。

② SEU 耐性
本試験では、SEU の発生は確認されなかった。SEU への耐性は非常に高い。

③ その他
Ar、Kr において FeRAM と SEU 監視用マイコン間で通信異常を確認した。異常動作は電源のリセットにより正常復帰した。その発生頻度は 100 year/event である。

上記の結果から、試験に用いた FeRAM は SEL、SEU に対し、高い耐性を持っていると考えられる。実際の使用においては、異常動作時の対策としてリセット回路の実装等の工夫が必要である。

MPU の試験は、試料は 1 つとし、FeRAM と同様に消費電流により SEL の監視を行っている。SEU については、MPU に実装したプログラムにより内部レジスタの状態を常時モニタ PC へ送信し、監視を行った。また、照射終了後、FlashROM の読み出しを行い、FlashROM での SEU の有無を確認した。レジスタ、FlashROM の空き領域にはそれぞれ、予め 0 と 1 が半分ずつ書き込まれている。現在までに取得できているデータは、N、Ne、Ar についてである。結果を Table 2 に示す。

Table 2 MPU Result.

	Fluence Rate [count/cm^2/s]	SEL	SEU @Register	SEU @FlashROM
$^{15}N^{3+}$	1,449	0	3	0
$^{20}Ne^{4+}$	1,242	4	4	0
$^{40}Ar^{8+}$	2,329	4	—	0

FeRAM のシングルイベント発生頻度は 3,000 year/event 以上であり、放射線への耐性は高いという結果を得ることができた。また、MPU については、さらに照射試験を実施し、評価を行う予定である。今後、現在使用を検討している民生電子部品について、さらに照射試験を実施し、小型衛星やその搭載機器の開発への利用を積極的に進めていきたい。

1-09 Evaluation of Single Event Effects on Commercial-off-the-Shelf Semiconductors for Space Flight Applications

I. Kato [a)], S. Matsuda [a)], S. Baba [b)], T. Hirose [b)], J. Ohya [b)], H. Okamoto [b)], H. Katayama [c)], M. Naitoh [c)], M. Harada [c)], M. Suganuma [c)] and Y. Tange [c)]

[a)] Space System Department, Kamakura Works, Mitsubishi Electric Corporation,
[b)] Quality Assurance Division, Ryoei Technica Corporation,
[c)] Earth Observation Research Center, Japan Aerospace Exploration Agency

Nowadays, there are increasing interests in applying the commercial-off-the-shelf (COTS) devices widely used in the ground-based systems to space satellites, which may reduce the size and cost of satellite systems as well as shorten the time for development. However, one has to intensively evaluate potential risks of using them in the space radiation environment before they are put on board for actual flights.

We are developing a compact infra-red camera (CIRC) for the earth observation from the space, in which we utilize the design of an already developed one for the ground use with some appropriate modifications. Its preliminary design was known to contain 9 COTS semiconductor devices whose sensitivity to the single event effects (SEEs) was unknown. Hence, we performed heavy-ion irradiation test on them to evaluate it. Among variations of SEEs, we have concentrated in this test on such effects that could cause fatal failure resulting in potential permanent loss of system functions, such as Single Event Latch-up (SEL). The test was conducted at TIARA in TARRI, JAEA.

Nine COTS devices tested were as listed in Table 1; a driver/receiver, a gate inverter (Gate Inv.), a reset IC, a thermoelectric cooler (TEC) driver, a multiplexer (MUX), a synchronous static random access memory (SSRAM), a flash memory (Flash), an analog-to-digital converter (ADC) and a digital-to-analog converter (DAC). The devices under test (DUT) were set in JAXA's irradiation chamber installed in the HD2 course in TIARA facility and a cocktail ion beam with M/Q = 5 was irradiated on them. Every DUT was powered during the irradiation and the supply current was monitored to detect possible SEL event. The device temperature was nominally kept at 80 °C during the irradiation, while it was at 40-65 °C in some cases. For each device, 3 samples were exposed to $^{129}Xe^{23+}$ beam with a linear energy transfer (LET) value of 69.2 MeV-cm^2/mg. Irradiation was continued until the total fluence reached 1×10^5 ions/cm^2, or otherwise until enough number of detected SEL events was accumulated when happened. After irradiation, samples were tested for its functionality. When SEL event was detected during the irradiation and/or a sample was found to be functionally broken at the post-irradiation test about a certain device, additional irradiations were performed on that device using other species of ions, where we used either $^{84}Kr^{17+}$ (LET = 39.9 MeV-cm^2/mg), $^{40}Ar^{8+}$ (LET = 15.3 MeV-cm^2/mg), or $^{20}Ne^{4+}$ (LET = 6.3 MeV-cm^2/mg) ions depending on what kind of SEE was observed.

Among 9 devices tested, the driver/receiver, the Gate inv., the MUX, the TEC driver and the reset IC showed no evidence of SEL event happening during $^{129}Xe^{23+}$ beam irradiation. They also passed the functional testing after the irradiation. The results mean the SEL cross-section for them is below 1×10^{-5} cm^2 at LET = 69.2 MeV-cm^2/mg. Some SEL signals were detected during $^{129}Xe^{23+}$ irradiation on the other 4 devices. They, except for the DAC, were found to be functioning in the post-irradiation testing, indicating that they are recoverable by a power cycle even if SEL happens. The DAC was found not to be functional.

Additional irradiation was conducted with $^{40}Ar^{8+}$ ion on 4 devices which had shown the SEL sensitivity above. Neither the SSRAM nor Flash shows any evidence of SEL, indicating that their SEL threshold lies between 15.3 and 69.2 MeV-cm^2/mg. They also passed functional tests after irradiation. The ADC and DAC showed some SEL signals. The ADC was properly functioning after the irradiation, while the DAC was not. The ADC and DAC were further irradiated by other ion species. The ADC showed no SEL evidence during $^{20}Ne^{4+}$ irradiation, indicating its SEL threshold lies between 6.3 and 15.3 MeV-cm^2/mg. Its functionality is recoverable by a power cycle when SEL happens. Further DAC samples were devoted for $^{84}Kr^{17+}$ irradiation in order to evaluate consequent risks to a single SEL event. It was observed that a device temperature rose by about 10 °C from nominal after a single SEL occurred, which could be due to the increased current caused by the SEL. The DAC failed the post-irradiation testing, again.

In summary, 4 out of 9 devices tested were found to be SEL-sensitive at some level, as shown in Table 1. Except for the DAC, they are recoverable from SEL events by a power cycle. The DAC was found to lose its functions after an SEL. We have evaluated possible risks of using them in the space based on the above results and properly reflected them to the CIRC's design to avoid the risks.

Table 1 Summary of SEE test results for 9 COTS devices.

DUT	SEL threshold	Reflection to design
Driver/Receiver Gate Inverter Reset IC TEC driver Multiplexer	> 69.2 [MeV-cm^2/mg]	Use as is (Function recoverable from SEL by power cycle)
SSRAM Flash memory	15.3 - 69.2	
ADC	6.3 - 15.3	
DAC	< 15.3	To be replaced

1-10 Mechanisms of Changes of Hole Concentration in Al-doped 6H-SiC by Electron Irradiation and Annealing

H. Matsuura [a)], H. Yanagisawa [a)], K. Nishino [a)], Y. Myojin [a)], T. Nojiri [a)], Y. Matsuyama [a)], S. Onoda [b)] and T. Ohshima [b)]

[a)]Dept. of Electric and Electronic Engineering, Osaka Electro-Communication University,
[b)]Environment and Industrial Materials Research Division, QuBS, JAEA

By comparing electron-radiation damage in p-type 4H-SiC with that in p-type Si,[1, 2)] it was found that the reduction in the temperature-dependent hole concentration p(T) in Al-doped p-type 4H-SiC by electron irradiation was much larger than in Al-doped p-type Si. From p(T) for lightly Al-doped 6H-SiC epilayers, an acceptor species with E_V+0.2 eV, which is ascribed to an Al atom at a Si sublattice site, was observed. In heavily Al-implanted p-type 6H-SiC layers, the removal cross section of Al acceptors (κ_{Al}) for 1 MeV electron irradiation was determined to be 6.4×10^{-18} cm^2 [2, 3)].

A 4.9 μm-thick lightly Al-doped p-type 6H-SiC epilayer on n-type 6H-SiC (resistivity: 0.027 Ωcm) was cut to a 1×1 cm^2 size. The sample was irradiated with 200 keV electrons with total fluences (Φ) of 0, 1.0, 2.0, and 3.0×10^{16} cm^{-2} at room temperature. The value of p(T) were obtained by Hall-effect measurements. Since the p(T) at Φ of 3.0×10^{16} cm^{-2} could not be obtained, the sample was annealed at 500 °C for 2 min in an Ar atmosphere. The densities and energy levels of acceptors were determined by free carrier concentration spectroscopy (FCCS)[1-4)] from p(T).

Figure 1 shows the experimental p(T) before irradiation (○) and after irradiation with 200 keV electrons with Φ of 1.0×10^{16} cm^{-2} (▲) and 2.0×10^{16} cm^{-2} (□). The value of p(T) in the annealed sample is denoted by + in Fig. 1. Using p(T), the densities (N_{Al} and N_{DA}) and levels (E_{Al} and E_{DA}) of Al and deep acceptors were determined by FCCS.

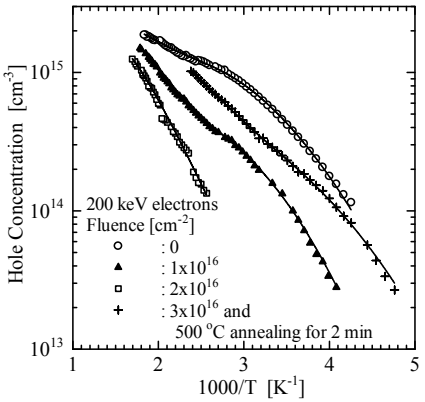

Fig. 1 Temperature dependence of hole concentration for Al-doped p-type 6H-SiC before and after irradiation with three difference Φ of 200 keV electrons. The p(T) for the annealed sample was shown by +. The solid lines represent p(T) simulations with N_{Al}, E_{Al}, N_{DA}, E_{DA}, and N_{comp} obtained by FCCS.

Since each p(T) simulation (solid line) with the obtained values is in good agreement with the corresponding experimental p(T), the values obtained by FCCS are reliable.

Figure 2 shows the dependence of N_{Al} and N_{DA} on Φ, denoted by ○ and Δ, respectively. At Φ of 3.0×10^{16} cm^{-2}, N_{Al} and N_{DA} in the 500 °C-annealed sample were shown by ● and ▲, respectively. Although N_{Al} and N_{DA} in the sample irradiated with Φ of 3×10^{16} cm^{-2} could not be determined, they are expected to be 4.3×10^{13} and 2.1×10^{15} cm^{-3}, respectively, by simulation[4)] with κ_{Al} of 1×10^{-16} cm^2 and κ_{DA} of 9×10^{-18} cm^2. The simulations of the dependence of N_{Al} and N_{DA} on Φ represent the solid and broken lines in Fig. 2, respectively. After annealing the sample at 500 °C for 2 min, N_{Al} and N_{DA} could be determined to be 4.0×10^{14} and 1.5×10^{15} cm^{-3}, respectively. By annealing at 500 °C, N_{Al} is increased, and N_{DA} is decreased. From Fig. 2, furthermore, the increment of N_{Al} is nearly equal to the decrement of N_{DA}. These suggest that the 500 °C annealing transforms the deep acceptors into the Al acceptors.

References

1) H. Matsuura et al., Jpn. J. Appl. Phys. **45** (2006) 2648.
2) H. Matsuura et al., Physica B **376-377** (2006) 342.
3) H. Matsuura et al., Jpn. J. Appl. Phys. **47** (2008) 5355.
4) H. Matsuura et al., J. Appl. Phys **104** (2008) 043702.

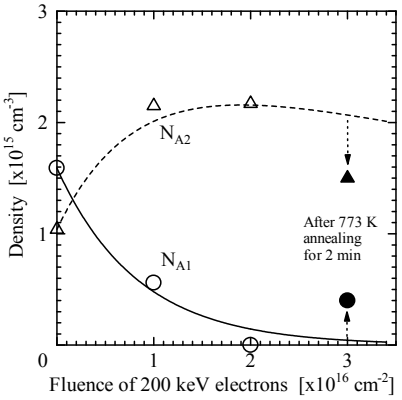

Fig. 2 Dependence of N_{Al} and N_{DA} on Φ of 200 keV electrons. Since N_{Al} and N_{DA} in the sample irradiated at Φ of 3×10^{16} cm^{-2} could not be obtained, the sample was annealed at 500 °C for 2 min. N_{Al} and N_{DA} in the annealed sample are denoted by ● and ▲, respectively. The dependence of N_{Al} and N_{DA} on Φ, simulated with κ_{Al} of 1×10^{-16} cm^2 and κ_{DA} of 9×10^{-18} cm^2, are shown by solid and broken lines, respectively.

1-11 Hydrogen Diffusion in a-Si:H Thin Films due to High Temperature Ion Irradiation

S. Sato [a], T. Ohshima [a] and M. Imaizumi [b]

[a] Environment and Industrial Materials Research Division, QuBS, JAEA,
[b] Aerospace R&D Directorate, JAXA

I. Introduction

Thin film hydrogenated amorphous silicon (a-Si:H) solar cells are one of major candidates for 'flexible' space solar cells, and thus studies of radiation effect on a-Si:H thin films are very important for the space applications [1]. However, radiation effects on electrical properties of a-Si:H semiconductors are less understood compared to crystalline type semiconductors such as silicon, gallium arsenide, and so on. In this context, our group have been studying about radiation effects on a-Si:H thin films, especially focusing on the electrical properties [2] and the hydrogen diffusion behavior.

Hydrogen diffusion and emission rates in a-Si:H depend on the hydrogen bonding state. Clustered (not isolated) hydrogen atoms are relatively easily diffuse or emit in amorphous network compared to isolated hydrogen atom [3]. Since it is well known that clustered hydrogen atoms deteriorate the electrical properties of a-Si:H thin films, it may be possible to evaluate a change in the electrical properties by investigating the hydrogen behavior due to irradiation.

The aim of this study is to observe hydrogen diffusion in ion-irradiated a-Si:H thin films with varying temperatures. Previously, we developed the *in-situ* Elastic Recoiled Detection (ERD) system following ion irradiation at low temperature condition in the dual beam irradiation chamber (MD2) [4]. Since the chamber connected to both the 400 kV Ion Implanter and from the 3 MV Single-Ended Accelerator, ERD measurement using beams from the former one can be performed for a sample just after the ion irradiation (implantation) from the latter one. In this study, we have additionally installed a sample heating system for irradiation under elevated temperature, and have observed hydrogen behavior in a-Si:H thin films irradiated with Si ions.

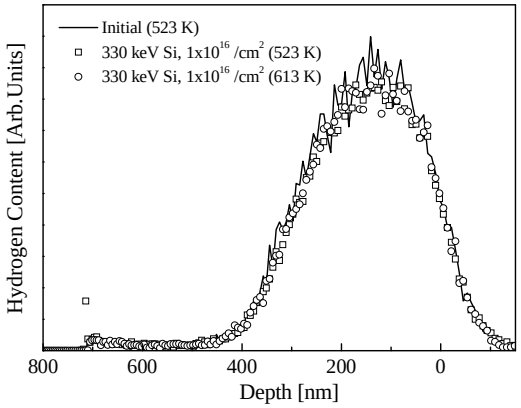

Fig. 1 ERD spectrum of an a-Si:H thin film before and after 330 keV Si ion irradiation at 1.0×10^{16} /cm^2 at 523 K. The sample temperature was raised to 613 K after the irradiation. No significant hydrogen diffusion was observed in this condition.

II. Experimental

The samples used in this study were device grade a-Si:H thin films fabricated on crystalline silicon (c-Si) substrates by Plasma Enhanced Chemical Vapor Deposition (PECVD) at National Institute of Advanced Industrial Science and Technology (AIST). The thickness of the a-Si:H thin film and the hydrogen content were estimated to be 300 nm and 11.3 at%, respectively.

Figure 1 shows the results of the ERD measurements before and after 330 keV Si ion irradiation at the fluence of 1.0×10^{16} /cm^2. The incident beam angle was 55^o from the sample plane. It was expected from the TRIM calculation that Si ions were implanted in the vicinity of the a-Si:H/c-Si interface and the average displacement per atom in the film was 12 dpa. The sample temperature was kept at 523 K during the irradiation for 4.5 hours. Elastic recoiled detection measurement after the irradiation was also carried out at 523 K. No specific change of the hydrogen distribution was observed between before and after the irradiation. The sample temperature was increased to 613 K after the irradiation and the ERD measurement was carried out again. However, no significant hydrogen diffusion was still observed. The result indicates that the hydrogen diffusion was under the detection limit even if it was enhanced due to the ion irradiation and that the samples used in this study were high quality films for electric device use. Higher temperature or longer annealing time is needed in order to observe the hydrogen diffusion.

Finally, we would like to thank Hitoshi Sai of AIST for fabricating the a-Si:H samples.

References

1) N. Wyrsch et al., J. Non-Cryst. Solids **352** (2006) 1797-1800.
2) S. Sato et al., Proc. 34th IEEE PVSC, (2009) 002354-002358.
3) X.-M. Tang et al., Solid State Commun. **74** (1990) 171-174.
4) S. Sato et al., JAEA Takasaki Ann. Rep. **2008** (2009) 11.

1-12 NV Centers in Diamond Irradiated with High Energy Nitrogen Ions and 2 MeV Electrons

J. Isoya [a], T. Umeda [a], N. Mizuochi [a], T. Ohshima [b], S. Onoda [b], S. Sato [b] and N. Morishita [b]

[a] Graduate School of Library, Information and Media Studies, University of Tsukuba,
[b] Environment and Industrial Materials Research Division, QuBS, JAEA

The NV (nitrogen-vacancy) center（S=1, C_{3v} symmetry）in diamond is a negatively charged state ($[NV]^-$) of a pair of substitutional nitrogen and adjacent vacancy. With the remarkable properties such as extremely long coherence time and the ability to initialize and readout individual spins optically at room temperature, the NV center is a potential candidate for solid state devices of quantum information processing. In the quantum computing, scalability (i.e. the increase of qubits) is attainable by fabrication of a chain-like array of NV centers with a separation (~50 nm) long enough for individual addressing. With such a long separation, the weak dipole-dipole interaction which is used for 2-qubit CNOT gate necessitates a long coherence time (T_2). The long T_2 is attained by the enrichment of ^{12}C isotope having zero nuclear spin and lowering paramagnetic nitrogen impurity (isolated substitutional nitrogen $[N_s]^0$ called P1). In ion implantation, which is a key technology for position controlled incorporation of NV centers, yield optimization to convert nitrogen atoms implanted to NV and elimination of residual unwanted defects having electron spins which shorten T_2 of implantation-produced NV centers are required. For understanding defect behaviors, in the present work, conversion from P1 to NV with minimizing residual unwanted defects by using 2 MeV electron irradiation has been also studied.

(1) 2 MeV electron irradiation

In HPHT (high pressure high temperature) synthesis of diamond, the concentration of P1is controlled from ~1 ppb to ~300 ppm by varying the composition of the metal solvent. Electron irradiation creates vacancy. Vacancy starts to diffuse in the lattice above 600 °C. Thus, NV centers are formed by trapping the vacancy by P1 during thermal annealing (800 °C). Since the negative charge of NV centers is attained by donation of an electron from the P1 center, the P1 centers are converted to $[NV]^-$ and $[N_s]^+$ (S=0).

Since a part of vacancies created is used for recombination with interstitials, a large dose is required for a full conversion of P1 to $[NV]^-$ if the initial concentration of P1 is high. We used electron irradiation at 450 °C to eliminate excess accumulation of unwanted defects before annealing. We have achieved various concentration of NV from 0.1 ppm to 15 ppm by using various HPHT crystals with various concentrations of P1. Under an excess dose of electron irradiation, a fraction of nitrogen-vacancy pair in the neutral charge state ($[NV]^0$) increases, since the negative charge requires for an electron donated from P1. It has been revealed that the conversion ratio from P1 to NV is different for different P1 concentrations. Thus, for attaining a full conversion of P1 to $[NV]^-$ without remaining P1, the dose of electron irradiation has been carefully chosen.

Here, we demonstrate how the conversion ratio depends on the P1 concentration by using a HPHT crystal which has two growth sectors with different P1 concentrations. The spins excited by the microwave pulses contribute to the instantaneous spectral diffusion. By using the instantaneous spectral diffusion effect in the 2-pulse echo decay, the dipolar broadening among the P1 spins and that among the $[NV]^-$ spins were extracted. With two different concentrations of P1/$[NV]^-$, the 2-pulse echo decay of P1/$[NV]^-$ exhibited to be biexponential. By plotting b (the inverse of the time constant) of the 2-pulse decay as a function of $\sin^2(\theta_p/2)$ where θ_p is the flipping angle of the second pulse, the dipolar broadening of each sector is obtained from the slope. From the dipolar broadening, the concentration was estimated. It has been found that the conversion ratio from P1 to NV is different for the two sectors with different P1 concentrations.

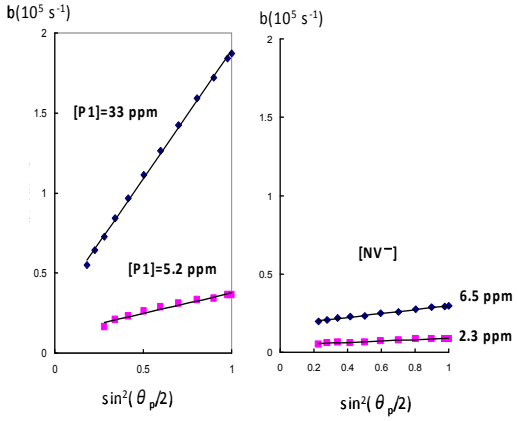

Fig. 1 Instantaneous diffusion of electron-irradiated (5.6×10^{18} e/cm^2, 450 °C) and annealed (800 °C, 2 h) type Ib crystal.

(2) High energy nitrogen ion implantation

To search a condition which optimizes the yield of $[NV]^-$ and minimizes the remaining unwanted defects, nitrogen implantation (1×10^{13} cm^{-2} for each of 7 steps of energy between 4 MeV and 13 MeV for both sides of 4.5×4.5×0.5 mm^3 substrate) at high temperatures (800 °C, 1,000 °C, and 1,200 °C) was carried out. High sensitivity ESR (electron spin resonance) technique detects 1.1×10^{12} spins of the P1 center in the high-purity ([P1]=0.6 ppb) CVD single crystal substrate (Element6) before implantation. After implantation of 2.4×10^{13} nitrogen ions, the increase of the signal intensity of P1 was not detected. PL measurements suggest that nitrogen ions are likely to be incorporated dominantly as nitrogen-vacancy pair below 1,000 °C. At the irradiation temperature of 1,200 °C, it is noticed that the production of the H3 center (N-V-N) increases. For the identification of the charge state of nitrogen-vacancy pairs produced by ion implantation, further studies (ESR under light illumination, PL with excitation laser with longer wavelength) are being carried out.

1-13 Alpha-radiolysis of Organic Extractants for Separation of Actinides

Y. Sugo [a)], M. Taguchi [b)], Y. Sasaki [a)], K. Hirota [b)] and Y. Morita [a)]

[a)] Division of Fuels and Materials Engineering, NSED, JAEA,
[b)] Environment and Industrial Materials Research Division, QuBS, JAEA

1. Introduction

Alpha-radiolysis study of organic extractants for the separation of actinides using an actinide radionuclide has some experimental problems as follows; a long-term exposure to actinides is required, and the extractants are contaminated with the radionuclide. In the previous work [1)], these problems were solved by irradiation with helium ions. It was also found that the radiation chemical yield for the degradation of *N,N,N′,N′*-tetraoctyldiglycolamide (TODGA) in *n*-dodecane by helium ions was less than that by gamma-rays.

In this study, the influence of coexisting oxygen on the radiolysis of TODGA was investigated with helium ions provided by a cyclotron accelerator in the TIARA facility.

2. Experimental

TODGA was dissolved in *n*-dodecane, and purged with nitrogen or oxygen gas. The solution was irradiated with helium ions according to the previous report [2)] under various atmospheres. The irradiated sample was diluted in acetone containing tri-*n*-butyl phosphate (TBP), which was used for the internal standard, and analyzed using a capillary gas chromatograph (GC) equipped with a flame ionization detector (FID) or a mass spectrometer (MS).

3. Results and Discussion

The concentration of TODGA in *n*-dodecane after irradiation with 48.6 MeV helium ions under air, oxygen, and nitrogen is logarithmically plotted against dose in Fig. 1. It was observed the yield for the degradation of TODGA in the presence of oxygen was slightly less than that in the nitrogen-saturated system.

Next, a difference in the degradation products according to the existence of oxygen was examined by GC/MS analysis. Figure 2 shows the changes in gas chromatograms before and after irradiation under air, oxygen, and nitrogen conditions. The peaks at the retention time of 5.6 and 14.2 min are assigned to TBP and TODGA, respectively. A number of new peaks appeared after irradiation in the range of 3.9-4.2 and 7.9-9.2 min are both assigned to the degradation products of *n*-dodecane. The former large peaks at 3.9-4.2 min, which are assigned to the oxidation products of *n*-dodecane such as ketones and alcohols, were appeared only in the presence of oxygen.

This result suggests the intermediate species of *n*-dodecane such as radical cations are liable to react with oxygen. It is therefore considered that the yield for the degradation of TODGA is slightly reduced in the presence of oxygen.

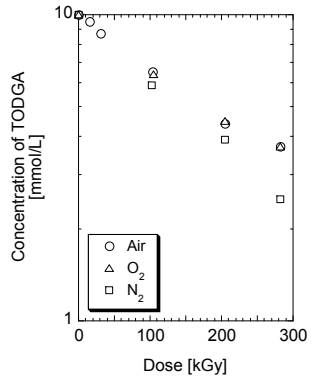

Fig. 1 Degradation of TODGA in *n*-dodecane by irradiation with 48.6 MeV helium ions under various atmospheres.

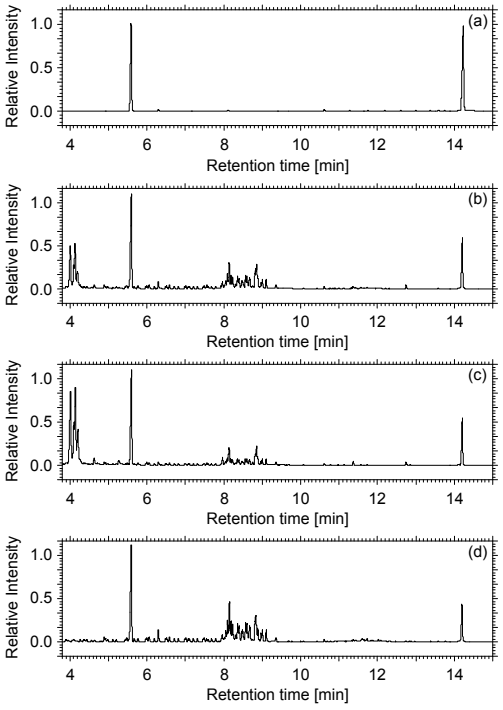

Fig. 2 Changes in the gas chromatograms (a) before and after irradiation under (b) air, (c) O_2, and (d) N_2 conditions.

References

1) Y. Sugo et al., Radiat. Phys. Chem., 78(12) (2009) 1140-1144.
2) Y. Sugo et al., JAEA Takasaki Ann. Rep. 2007 (2008) 161.

1-14 A Study on Complete Decomposition of Pyrrolidone Precipitants by γ-Ray Irradiation

M. Nogami [a)], Y. Sugiyama [a)], T. Kawasaki [a)], M. Harada [a)], Y. Kawata [b)], Y. Morita [b)], T. Kikuchi [c)] and Y. Ikeda [a)]

[a)] Research Laboratory for Nuclear Reactors, Tokyo Institute of Technology,
[b)] Division of Fuels and Materials Engineering, NSED, JAEA, [c)] Mitsubishi Materials Corporation

We have been developing a novel reprocessing system for spent FBR fuels based on two precipitation processes[1)]. In this system, only U(VI) species are firstly precipitated in nitric acid solutions dissolving spent fuels by using a pyrrolidone derivative (NRP) with low hydrophobicity and donicity which bring lower precipitation ability. Secondly the residual U(VI) and Pu(IV, VI) are precipitated simultaneously using another NRP with higher precipitation ability. Use of a slight excess amount of the precipitants is inevitable for complete precipitation of U and Pu species due to the solubility of the precipitates. Therefore, the residual precipitants included in the highly active waste solution (HAW) generated after the second precipitation treatment should be completely removed or decomposed for safer disposal of the waste.

As one of candidate methods for the purpose mentioned above, γ-ray irradiation to NRPs in HNO_3 of higher concentration was examined in this study, because NRPs in HNO_3 of 6 mol·dm^{-3} (= M) is found to be decomposed easily with γ-ray irradiation compared with in HNO_3 of lower concentration ranges[2)]. This method has advantage that no special equipments are necessary for the treatment, because an increase in the concentrations of HNO_3 of HAW is possible by inletting NOx gas or condensation.

A 9 M HNO_3 solution containing 0.1 M *N*-*n*-butyl-2-pyrrolidone (NBP) which is one of the NRPs with lower precipitation ability was put into a Pyrex glass tube. Gamma-ray irradiation by the ^{60}Co source was performed at 11.8 kGy/h up to 210 kGy at room temperature under ambient atmosphere. The irradiated sample solutions were analyzed by ^{1}H and ^{13}C NMR (JEOL 400 MHz, solvent: dimethyl sulfoxide-d_6). Pyridine was added as the internal standard for determining the decomposition ratio of NBP.

The dependence of decomposition ratio of NBP on dose is shown in Fig. 1. Approximately 70 % and 90 % of NBP are found to be decomposed after the irradiation of 20 kGy and 210 kGy, respectively. This suggests that the γ-ray irradiation to NBP in HNO_3 of higher concentration is effective for its decomposition.

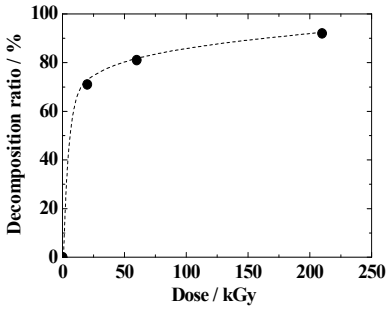

Fig. 1 Dependence of decomposition ratio of NBP on dose in 9 M HNO_3 by γ-ray irradiation.

^{1}H NMR spectra also showed a possibility of the existence of acetic acid (ca. 2.1 ppm, CH_3, singlet) and propionic acid (ca. 1.1 ppm, CH_3, triplet) in the irradiated samples. The signal at 2.1 ppm was found to increase with increasing dose. In the ^{13}C NMR spectra of the irradiated samples, the signal which should be attributed to the carbon atom of oxalic acid was detected at ca. 161 ppm. The above results support our proposal for the degradation mechanism of NBP in HNO_3 by γ-ray irradiation[2)]. Namely, the degradation of NBP starts from the cleavage of the pyrrolidone ring by the addition of oxygen atom originating from HNO_3, followed by the formation of chain monoamides and C4 compounds by the continuous addition of oxygen, finally leading to the generation of oxalic acid. It is expected that acetic acid is produced from the side butyl group through propionic acid. It was also revealed from the NMR analyses that the abundance ratios of degradation products which are not decomposed to oxalic acid or propionic acid, *i.e.*, the above-mentioned chain monoamides and C4 compounds, are small.

These facts indicate that the complete decomposition of NBP was not achieved under the present irradiation condition. Further optimization of the condition for decomposing organic acids such as acetic acid and oxalic acid is necessary. The combination with heating is expected to be effective for the practical use.

Acknowledgment

Present study is the result of "Development of Advanced Reprocessing System Using High Selective and Controllable Precipitants" entrusted to Tokyo Institute of Technology by the Ministry of Education, Culture, Sports, Science and Technology of Japan (MEXT). The authors also greatly thank Dr. R. Yamagata, Department of Advanced Radiation Technology, TARRI, JAEA, for his help at the irradiation facility.

References

1) Y. Morita et al., J. Nucl. Sci. Technol. 46 (2009) 1129.
2) M. Nogami et al., JAEA Takasaki Ann. Rep. 2008 (2009) 25.

1-15 Study on Stability of Cs·Sr Solvent Impregnate Resin against Gamma Irradiation

H. Hoshi [a)], T. Kikuchi [a)], Y. Morita [a)] and T. Kimura [b)]

[a)] Division of Fuels and Materials Engineering, NSED, JAEA,
[b)] Division of Environment and Radiation Sciences, NSED, JAEA

Minimization of radioactive waste from reprocessing process of spent nuclear fuel is strongly desired. We have developed an advanced technology for separation of heat generating elements (Cs and Sr) from high level waste to optimize radioactive waste by its characteristics. Recently, some analogues of calix-crown or crown ether extractant were reported on specific selectivity for Cs or Sr, respectively[1,2]. In our previous study, prepared adsorbents indicated promising ability to separate Cs and Sr from other typical fission products dissolved in nitric acid solution; besides they maintained significant selectivity for Cs or Sr after gamma irradiation. Decreasing ratio of static adsorption capacity by irradiation was also estimated. In this work, gamma irradiation effect on dynamic adsorption capacity was examined for the conceptual designing.

An extractant and a modifier were impregnated into porous silica, which is embedded styrene divinyl benzene polymer on the surface. These adsorbents contacting with nitric acid solution were exposed to gamma ray in a vial. The dynamic adsorption capacity was examined by using irradiated adsorbents. The irradiated adsorbent was packed in a glass column as slurry state. After the packed column was filled with 3 M HNO_3, a break through curve was obtained by feeding HNO_3 solution containing 10 mM Cs or Sr.

Initial dynamic adsorption capacity was estimated in advance and was 70.2 mmol/L, which was obtained by the product of Cs concentration and the difference between the break through point and the dead volume. Figure 1 shows the break through curve of Cs adsorbent, which was irradiated 29.1 kGy in 3 M HNO_3. The breakthrough point was estimated at 54.9 cm^3 by linear regression (dotted line). The dynamic adsorption capacity of irradiated adsorbent was 73.5 mmol/L, which was almost as same as initial one. This result indicated that this adsorbent has rather high stability against gamma irradiation.

Figure 2 shows the break through curve of Sr adsorbent, which was irradiated 29.1 kGy in 3 M HNO_3. While initial dynamic adsorption capacity was 125 mmol/L, that of irradiated adsorbent was 87.1 mmol/L; the dynamic adsorption capacity decreased by around 30%. Thus, some refinement of process design will be required.

It is concluded that Cs adsorbent maintained its dynamic adsorption capacity and Sr adsorbent kept 70% of initial capacity. Decreasing ratio of dynamic adsorption capacity by irradiation can be estimated from these results. It contributes significantly for the conceptual design of separation plant.

Present study is the result of "Development of separation technology of transuranium elements and fission products by using new extractants and adsorbents" entrusted to JAEA by the Ministry of Education, Culture, Sports, Science and Technology of Japan (MEXT). We are very grateful to Mr. Yamagata for his valuable cooperation in this study.

References

1) P. V. Bonnesen et al., Solve. Extr. Ion Exch. 18 (2000) 1079.
2) J. F. Dozol et al., EUR 19605EN, 2000.

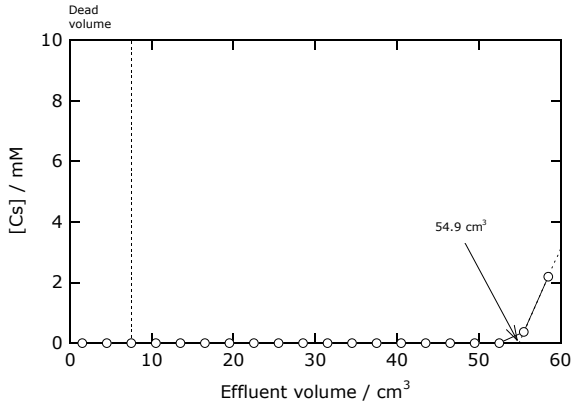

Fig. 1 Breakthrough curve of Cs adsorbent after gamma irradiation. Dose rate: 1.82 kGy/h; duration: 16 h; Dose: 29.1 kGy; soaked in 3 M HNO_3. Column: i.d. 10 mm × 100 mm height (bed height: 82 mm); flow rate: 1 cm^3/min; mobile phase: 10 mM Cs-3 M HNO_3.

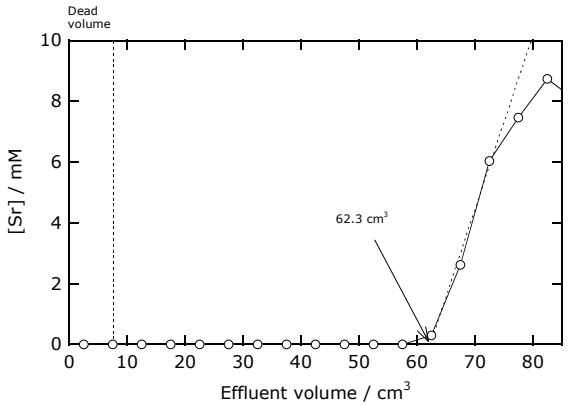

Fig. 2 Breakthrough curve of Sr adsorbent after gamma irradiation. Dose rate: 1.82 kGy/h; duration: 16 h; Dose: 29.1 kGy; soaked in 3 M HNO_3. Column i.d.: 10 mm × 100 mm height (bed height: 80 mm); flow rate: 1 cm^3/min; aq. phase: 10 mM Sr-3 M HNO_3.

1-16 Hydrogen Generation in the System of Water–Adsorbent Containing the Organic Extractant by Gamma-Ray Radiation

Y. Koma, K. Matsumura, S. Watanabe, K. Nomura and Y. Sano

Advanced Processing Unit, ANSRD, JAEA

The extraction chromatography is a promising technique for Am and Cm separation from a highly radioactive solutions of spent fuel reprocessing and employs the adsorbent composed of the porous silica particle, polymer and an extractant [1]. In the system, water and the adsorbent will generate hydrogen by gamma radiation. Generation of hydrogen should be considered for explosion safety, thus, was studied using several extractants.

Adsorbents containing CMPO (n-octyl(phenyl)-N,N-diisobutylcarbamoylmethylphosphine oxide), TODGA (N,N,N'N'-tetraoctyl-3-oxapentane-1,5-diamide), HDEHP (bis(2-ethylhexyl)hydrogen phosphate), R-BTP (2,6-bis(5,6-di-isohexyl-1,2,4-triazine-3-yl)pyridine) and TRPEN (N,N,N',N'-tetrakis((5-octyloxypyridin-2-yl)methyl)ethylen ediamine), were irradiated with gamma-ray of Co-60 in water at room temperature. The mixture of water and the adsorbent was contained in a vial for static irradiation whereas the stainless steel vessel for irradiation with Ar gas bubbling. The dose rate was about 3 kGy/h. Gas was sampled and analyzed by gas chromatography.

When CMPO adsorbent is immersed in water with the ratio of mass of adsorbent and volume of water up to 0.36 g/cm^3, G value is increased comparing the value for water and this suggests a synergy effect in hydrogen production. At the ratio of 0.50 g/cm^3, G value is suppressed about 40% of the value for water. It seems that hydrogen generated is retained longer and/or consumed in the system.

Figure 1 shows G values obtained for the water–adsorbent system at the ratio of 0.01 g/cm^3 in the static irradiation. The G value is increased for the two-phase system when compared with that of water, and the extent is depends on the adsorbent. This implies that addition of support particle denoted as 'SiO_2-P' as well as extractant enhances radiolysis. Nitric acid helps to suppress G value of H_2 for water [2] and this is also applied to the system.

Stirring the system with Ar during irradiation increases G value, on the other hand, it diminishes the difference in G value as shown in Fig. 2 except for the case of HDEHP. Irradiation at standing induces distribution of hydrogen in the system and takes long time to reach a steady state.

Based on the G values obtained, it is expected that hydrogen generated in the separation column packed with the adsorbent will be dissolved into the mobile phase and discharged to resulting in safety for explosion.

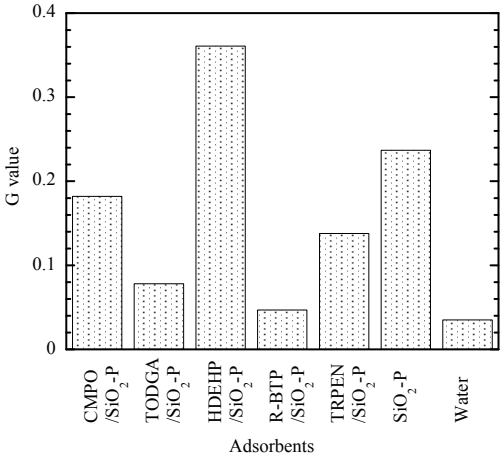

Fig. 1 G values for the water–adsorbent system at 0.01 g/cm^3. The adsorbent–water mixture was irradiated for 1 h at standing.

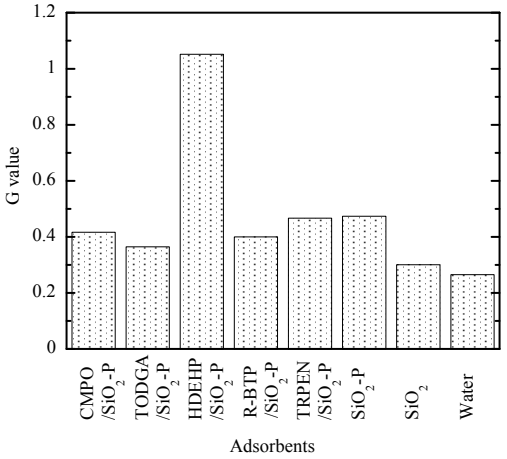

Fig. 2 G values for the water–adsorbent system at 0.1 g/cm^3 obtained after 1.25 h irradiation. The adsorbent–water mixture was stirred with Ar during irradiation.

Acknowledgements

We would like to thank Mr. R. Yamagata at Irradiation Service Section in TARRI for his assistance on the experiment. Present study is the result of "Development of Extraction Chromatography for Am and Cm Recovery" entrusted to JAEA by the Ministry of Education, Culture, Sports, Science and Technology of Japan (MEXT).

References

1) H. Funasaka and M. Itoh, Global 2007, Boise, USA (2007) 259.
2) F. J. Miner and J. R. Seed, Chem. Rev., 67, (1967) 299.

1-17 Irradiation Effect of Gamma-Rays on Cyanate Ester/Epoxy Resins

A. Idesaki [a)], H. Uechi [b)], Y. Hakura [b)], T. Nakagawa [b)], T. Ohshima [a)], S. Matsuda [b)] and H. Kishi [b)]

[a)] Environment and Industrial Materials Research Division, QuBS, JAEA,
[b)] Graduate School of Engineering, University of Hyogo

JAEA has developed a cyanate ester/epoxy resin as an insulating material for ITER superconducting coil[1,2]. Since the cyanate ester/epoxy resin shows higher radiation resistance than a pure epoxy resin, it is expected to be applied to insulating material of magnet systems used in accelerators such as J-PARC. In order to realize the application of the cyanate ester/epoxy resins, suitable resin composition has to be selected. However, there are several kinds of resins with different molecular structure for each cyanate ester and epoxy and the relationship between combination of them and their radiation resistance has not been clarified. In this work, the effect of molecular structure of epoxy on the properties of cyanate ester/epoxy resins such as gas evolution and glass transition temperature (Tg) after γ-ray irradiation was investigated.

Table 1 shows the resin composition of cyanate ester and epoxy used in this work. A bis-A type cyanate ester (DCBA) and three kinds of epoxy (bis-A type (DGEBA), bis-E type (DGEBE) and bis-F type (DGEBF)) were used. The cyanate ester and epoxy were formulated by 50/50 in weight. The prepared resins were irradiated by γ-rays with dose of 5 MGy under vacuum at room temperature.

Table 1 Resin composition of cyanate ester and epoxy.

	Cyanate ester (50 wt%)	Epoxy (50 wt%)
A	DCBA	DGEBA
B		DGEBE
C		DGEBF

Curing condition: 170 °C/1 h + 230 °C/4 h.

When the cyanate ester/epoxy resins were irradiated, gases of hydrogen (H_2), carbon monoxide (CO), carbon dioxide (CO_2) and nitrogen (N_2) were evolved. Figure 1 shows the G-value of gas evolution. The G-value means the number of evolved gas molecules in case of that the energy of 100 eV is absorbed by the material. The order of G-value of total gas was sample A (DCBA/DGEBA) > sample B (DCBA/DGEBE) > sample C (DCBA/DGEBF).

Figure 2 shows change of Tg of cyanate ester/epoxy resins by γ-ray irradiation. While the Tg of all resins decreased after the irradiation, the order of decrease width was same as gas evolution (sample A > sample B > sample C).

The results of gas evolution and decrease of Tg are considered to suggest that crosslinking part between cyanate ester and epoxy is decomposed by the irradiation and that the decomposition of crosslinking depends on the molecular structure of epoxy. In this work, it was found that the combination of bis-A type cyanate ester and bis-F type epoxy gives the highest radiation resistance. In future, formulating ratio of cyanate ester and epoxy on the radiation resistance of resins will be investigated.

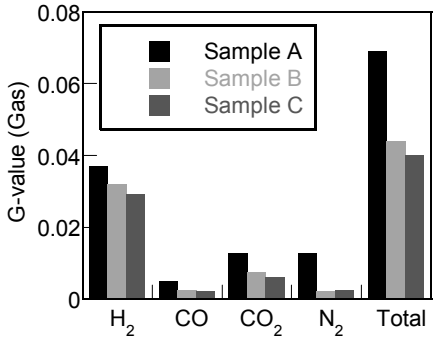

Fig. 1 Evolved gases from cyanate ester/epoxy resins by γ-ray irradiation.

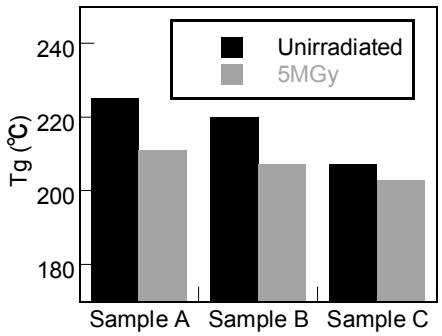

Fig. 2 Change of Tg of cyanate ester/epoxy resins by γ-ray irradiation.

Acknowledgement

We thank to Mitsubishi Gas Chemical Company, Inc. for providing cyanate ester resins.

References

1) A. Idesaki et al., Advances in Cryogenic Engineering, 54 (2008) 169.
2) Y. Shindo et al., Cryogenics, 50 (2010) 36.

1-18 Development of Radiation-Resistant Lighting

T. Tsuchida [a)], R. Yamagata [b)], H. Seito [b)], Y. Haruyama [b)], H. Kaneko [b)] and S. Kashimura [a)]

[a)] Kandenko Co., Ltd.,
[b)] Department of Advanced Radiation Technology, TARRI, JAEA

There are a lot of restrictions of electric installations in a high radiation environment. For example longevity of electric devices would be shortened remarkably in a high radiation environment. It becomes impossible also for lighting equipments to keep an original function under a high radiation environment due to deterioration of insulation resistance of ballasts and luminous flux decrease of lamps, etc.

The authors developed radiation-resistant lighting. This research aims to verify those functionality and safety under γ- ray irradiation conditions. This paper reports the progress of this research, which is planed to continue till March 2011.

１．はじめに

加速器施設・材料照射施設・核融合施設・核燃料再処理施設等は、高放射線環境となるエリアを有する。高放射線環境では多くの電気設備は寿命が著しく短くなるなど、使用に際しては制約が多い。照明器具も例外ではなく、高放射線環境下では安定器の絶縁劣化による安定器の損傷・光源部の光束低下などにより、本来の機能を保てなくなる。

そこで本課題では、放射線環境下で使用できるように独自の改良を加えた照明器具を、実際に放射線照射施設で運用した状況下で通電･点灯状態を継続することにより、それらの機能性・安全性を検証することを目的とする。

２．開発した耐放射線照明器具

今回開発した照明器具は、形状は標準の器具と変わらずに、耐放射線性能を向上させたことが特徴である。以下の主な仕様を示す。

・投光器（水銀灯 400 W）および 安定器
　定格電圧 200 V　　定格周波数 50 Hz
　定格入力電流 3.3 A　　定格消費電力 415 W
　放射線耐量 30 MGy

３．照射試験計画

Figure 1 に示すように、Co-60 照射施設 No. 2 セル内に、試験体として開発した照明器具 6 台および安定器 6 台を設置し、室内の作業用の照明器具として運用する。安定器は図に示した安定器収容盤内に設置している。既設分電盤より、照明スイッチ用に 100 V 用 1 回路、安定器用に 200 V 用 2 回路を制御盤に供給を受ける。制御盤内の漏電遮断器より安定器収容盤に 2 回路供給し、安定器からそれぞれ投光器に電源を供給する。制御盤にはアワーメータを設けており、累積点灯時間を測定する。

①試験体取付け位置での累積吸収線量 ②累積点灯時間 ③室内の照度 ④絶縁抵抗 ⑤安定器・ランプの電気特性 を 3 ヶ月毎に測定し、照明器具の特性等の劣化状況等を調べる。

４．経過

本計画は 2008 年 3 月より 3 年計画で実施しており、照射試験を開始してから、約 2 年経過している。2010 年 4 月現在、累積吸収線量は、光源部で 2 ～ 3.3 MGy、安定器取付け部で 3.1 ～ 4.5 MGy である。累積点灯時間は 1,900 時間である。室内の照度は、初期照度（465 Lx）の 63%程度(295 Lx)となった。ランプは時間経過に従い光束が減退する。このことを考慮すると、現時点での照度低下は、2%はランプの初期特性、1,900 時間の減退が 7%、残りの 28%はランプの着色や反射鏡の汚れが原因と推察される。またケーブルの絶縁抵抗の低下が確認されたが、安定器本体の絶縁性能の劣化や電気特性の変化は確認されていない。2009 年 12 月にケーブルを交換し照射試験を継続中である。

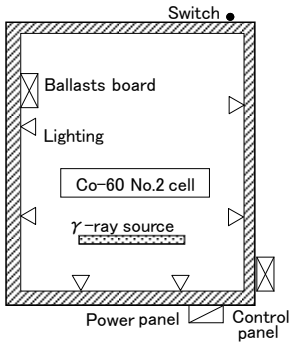

Fig. 1 Installation layout of radiation-resistant lightings.

今後は、2010 年 12 月末まで照射試験を継続した後、機器を取り外し、試験体個々の光束・電気特性などを測定し、耐放射線性能を評価する予定である。

Fig. 2 Radiation-resistant lightings (left side) and ballast (right side).

5. おわりに

本研究により、本照明器具が実際の使用条件で安定に特性を持続し利用可能であることが実証できれば、その採用により、上述の加速器施設・材料照射施設・核融合施設・核燃料再処理施設等における安全な運転の実現と、保守管理の簡便化に寄与することが期待される。具体的には、安定な照明による安全確保とともに、照明器具の交換頻度の低減により、保守作業・廃棄物処理等のランニングコストの低減に貢献できると考える。

1-19 Development of Radiation Resistant Cable

S. Ukon [a)], K. Takano [a)], K. Ishida [a)], O. Takeda [b)], N. Morishita [c)] and A. Idesaki [c)]

[a)] Power And Telecommunication Cable System R&D Center, Fujikura. Ltd,
[b)] Accelerator Division, J-PARC, JAEA,
[c)] Environment and Industrial Materials Research Division, QuBS, JAEA

We developed a radiation resistant material (RH-2.5M) based on polyolefin for Japan Proton Accelerator Complex (J-PARC). In this study, we examined material higher resistant than 2.5 MGy and ascertained the limit of a polyolefin material. As a result, the resistance of the material was able to be improved to 3 MGy, and this dose region was found to be a critical point of a polyolefin material.

Introduction

J－PARC の加速器トンネルでは、ノンハロゲン高難燃ケーブルの使用を原則としている。一般にケーブルが放射線にさらされると、絶縁体やシースなどに使用している高分子材料が損傷を受け、機械特性や難燃性が低下する。汎用のポリオレフィン難燃シース材料では、0.5 MGy の照射でシースが著しく劣化し使用に耐えなかったため、より高い耐放射線特性を持つケーブルの開発を行った。汎用のポリオレフィン難燃シース材料をベースに耐放射線処方を施した結果、2.5 MGy 照射後においても機械特性試験、及び JIS C3521 垂直トレイ燃焼試験に合格する難燃性を有する材料（RH-2.5M）を得ることができた。

本研究では更なる高耐性化及び難燃ポリオレフィン系材料の限界見極めについて検討を行った。

Experimental

高崎量子応用研究所 ^{60}Co 照射施設第 2 セルにてガンマ線を照射し（線量率：1～10 kGy/h）、照射後の試料について引張試験（破断伸び）、JIS C3521 垂直トレイ燃焼試験を実施した。試料は照射後の試験内容に応じて、シース材料のみをシート状にしたものと、ケーブルに整形したものを用意した。Fig. 1 にケーブルサンプルの照射セットアップを示す。

1. 安定剤の最適化

種々の耐候性安定剤（紫外線吸収剤・光安定剤）の効果を評価し、RH-2.5M で使用した安定剤と比較して樹脂への溶解量及び耐放射線性の効果が高い安定剤を探索した。

その結果、機械特性に対する耐放射線性の評価基準とした破断伸び 50%以上を維持できる最大照射線量を、2.5 MGy から 3 MGy に向上させることができた。引張試験の結果を、Fig. 2 に示す。

2. 難燃剤の減量

放射線に対する耐性を劣化させている要因が、材料中に含まれる添加物にあると考え、最も含有量の多い難燃剤について、減量およびそれに伴う難燃性の低下について検討を実施した。難燃剤を従来の半分程度まで減量することにより、ある程度の耐放射線性の向上が見られたが、当該の添加量ではケーブル燃焼試験に合格することができなかった。

3. ベース樹脂の検討

耐放射線性が良好だと予測されるベース樹脂の評価を行った。しかしながらケーブルのシース材料に求められる特性と耐放射線性を両立させることは困難であることがわかった。

Conclusion

ベース材料の樹脂組成の調整・難燃剤等の添加物の減量及び安定剤処方の最適化等を行い、耐性を 2.5 MGy から 3 MGy に向上させた。また、難燃性や機械特性等の維持を考慮すると、本研究で使用した難燃ポリオレフィン系の材料では 3 MGy 程度が限界であることがわかった。

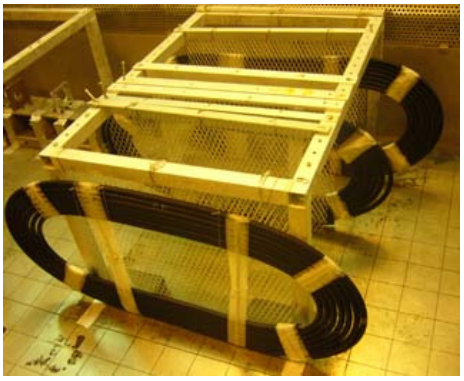

Fig. 1 The view of cable irradiation.

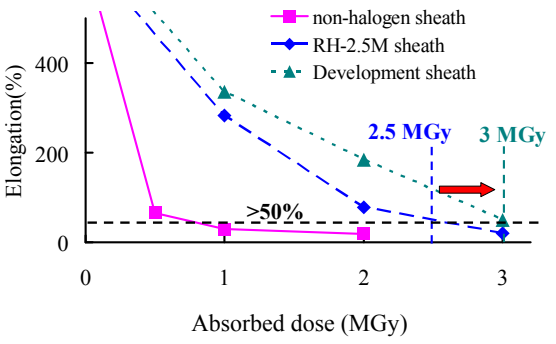

Fig. 2 Irradiation result.

1-20 Development of Penetration Part Processing Industrial Method in Radiation Controlled Area

K. Izumi [a)], M. Iguchi [a)], M. Kawasaki [a)], Y. Ohkawa [a)], K. Oka [b)] and R. Yamagata [c)]

[a)] Kandenko Co., Ltd.,
[b)] Advanced Photon Research Center, QuBS JAEA,
[c)] Department of Advanced Radiation Technology, TARRI, JAEA

At penetration parts in radiation controlled areas, such as walls and floors where cables go through, the high-airtight performance is required in order to control the negative pressure of air-conditioning. Moreover, since the cables get deteriorated by radiation, the easy replacement works are indispensable.

However, the materials in general use have neither resistance, nor any sheltering performance against radiation. In this research, we have developed radiation-resistant materials, to meet both an airtight and a sheltering performance.

１．はじめに

医療施設・加速器施設・核融合施設・原子炉施設・次世代原子炉施設等は、放射線環境となるエリアを有する。放射線エリアでは、空調の負圧管理を行うため、ケーブル・冷却水配管等の貫通部の気密性が要求される。しかし、従来の工法では、使用材料に耐放射線性がなく、遮蔽コンクリートの一部にのみ材料を流し込む構造から遮蔽性能があるとは言えない。

そこで本研究では、気密性と遮蔽性能を同時に満足する工法の開発を目的とし、本件では材料の耐放射線性能について試験を実施した。

２．放射線管理区域の貫通処理部の必要性能

放射線管理区域の貫通部は、将来の配線工事の改修等も考慮し、次の性能が必要となる。

１）容易に壊せる。
（将来の引き替え工事を容易とする。）
２）密度管理ができる。（遮蔽性能）
３）耐放射線性がある。
４）気密性能がある。

３．貫通部処理材料

試験した材料は、耐放射線性を期待して無機系の材料を中心に配合を検討し、容易に壊せ、材料の密度管理が可能な材料を照射した。

４．耐放射線性試験

Fig. 1 のような試験体（直径 5 cm×長さ 10 cm）を製作し、Co-60 照射施設にてγ線照射を行った。最大照射線量を 10 MGy として、照射した。Fig. 2 に照射状況を示す。

Fig. 1 Production situation of examination body.

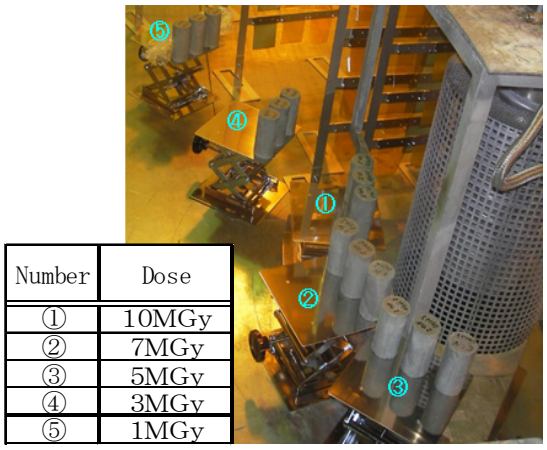

Number	Dose
①	10MGy
②	7MGy
③	5MGy
④	3MGy
⑤	1MGy

Fig. 2 Irradiation structure of examination body.

５．試験結果

照射試験の結果、照射前と照射後で、体積、密度、材料強度についてほぼ変化がなかった事から、本材料は、10 MGy までの耐放射線性があると言える。

データの一部として体積の変化を Fig. 3 に示す。

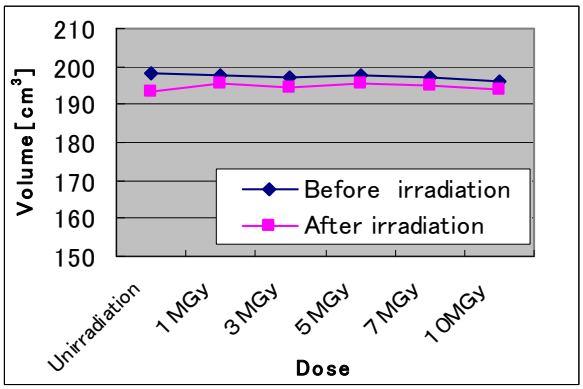

Fig. 3 Relationship between volume and dose.

６．今後

本試験により本材料は、10 MGy の耐放射線性がある事がわかった。しかし、材料が乾燥する事により約 1%体積が収縮することがわかっている。材料の収縮は、気密性能に影響することから、今後は実際のケーブルを貫通させた模擬試験体を製作し、気密性能試験を実施する。

1-21 Alpha-Ray Irradiation Damage on Rubber Applied for Glove Box for Plutonium Powder Treatment

K. Saito, Y. Nogami and H. Endo

Plutonium Fuel Development Center, NFCEL, JAEA

Currently, for economical reasons, newly improved long-lasting glove is desired and under development at Plutonium Fuel Development Center (Pu center), Tokai, JAEA. For the basic step of the development, helium ion irradiation experiments have been conducted in order to evaluate α-ray effects against the glove rubber material. In these experiments[1, 2], not only dose (ion fluence) but also temperature increase caused by ion flux was suggested as one of the possible factors of material deterioration. The separation of the factors is important to apply experimental data to glove box condition. Therefore, the experiment was conducted to confirm the effect of the temperature increase.

Sample material is chlorosulfonated polyethylene (CSM) glove which SANKO CHEMICAL INDUSTORY CO. Ltd. manufactures and Pu center mainly employs. JIS K 6251-7 dumbbell-shaped pieces cut from the rubber materials were irradiated in a vacuum with $^4He^{2+}$ ion beam generated from 3MV tandem accelerator in TIARA. The kinetic energy of the accelerated ion was 5 MeV close to the average energy of α rays emitted from plutonium isotopes. To evaluate the effect of temperature increase caused by irradiation, ion flux was varied while fluence was kept constant. Fluence was set at the level of 0.2 ~ 3 years by 2.9 MBq/cm^2 of α-contamination, i.e. $0.9 \sim 14 \times 10^{13}$ cm^{-2}. Flux, duration, the corresponding absorbed dose and its rate were $1.3 \sim 15 \times 10^{10}$ p/cm^2/s, 2~180 min, 1.9~28 MGy and 9.4~111 MGy/h, respectively. Four sample pieces were simultaneously irradiated for one condition and the irradiated samples are sent to visual inspection and two tensile tests: tensile strength and elongation at break. Experiments were divided into two parts and tensile tests were performed at July and November. Since temperature may impact the result of tensile tests, non-irradiated samples were tested in each experiment.

Up to the fluence of 1.4×10^{14} cm^{-2}, there are no differences observed in surface appearance for various flux levels as shown in Fig. 1. The results of tensile tests are shown in Table 1. Tensile strength decreases with increase of fluence, and elongation at break slightly does. However, there is not the obvious indication of the differences from flux variation.

In the experiments, the direct measurement of sample temperature was desired, but it is not easy because of the irradiation chamber geometry and instrumentation. Therefore, consideration about sample temperature was given with indirect evidences, such as the decomposition temperature of CSM and the pressure of the irradiation chamber, on the supposition that the specific heat of the rubber is constant. The consideration indicates that the possible maximum temperature is 31 °C at the minimum ion flux irradiation in the present study. This temperature is within the range of ordinary environmental condition in plutonium-charged glove boxes. In conclusion, experimental data is available only in view of fluence.

Another “cold” experiment of tensile test was performed to strengthen the interpretation of the results described above. The target of this test is non-irradiated samples with surface incision whose depth has variation. Some reduction of tensile strength and little change of elongation at break were observed for interpolated 30 μm-depth-incised samples. This result fairly agrees with the ones of irradiated samples which have about 30 μm-thickness damaged layer by ion bombardment, and bolsters the conclusion of the irradiation experiments.

The obtained data are unexampled and quantitative ones for α damage of glove and its material.

References

1) K. Saito et al., JAEA Takasaki Ann. Rep. 2007 (2008) 20.
2) K. Saito et al., JAEA Takasaki Ann. Rep. 2008 (2009) 28.

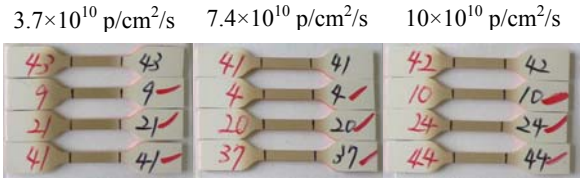

Fig. 1 Photographs of irradiated surface with the fluence of 1.4×10^{14} cm^{-2}.

Table 1 Results of tensile tests.

[Relative values*]

	Ion flux (cm^{-2} s^{-1})	Fluence (cm^{-2})		
		9.1E+12	4.6E+13	1.4E+14
Tensile strength	3.7E+10	93.8%	88.8%	80.1%
	7.4 E+10	92.0%	88.2%	80.6%
	1.0 E+11	92.3%	90.1%	76.6%
Elongation at break	3.7E+10	98.7%	96.9%	97.5%
	7.4 E+10	98.9%	98.7%	97.5%
	1.0 E+11	99.3%	99.5%	95.8%

*Normalized to non-irradiated samples.

1-22 Touch-Down Test of Magnetic Bearing Type Centrifugal Contactor with Irradiated Touch-Down Bearing

H. Ogino, K. Fujisaku and H. Hirano

Nuclear Cycle Engineering Department, NFCEL, JAEA

The centrifugal contactor has excellent phase separation and a smaller hold-up volume than any other contactor type such as mixer-settler and pulsed column. These characteristics lead to "rapid start-up and shut-down", "compact design" and "less solvent degradation". Therefore, the centrifugal contactor is said to be advantageous for reprocessing a fast breeder fuel of high burn-up and high Pu-enrichment[1], and study and development have been progressed since the 1960s.

In JAEA, the rolling bearing type centrifugal contactor with anti-corrosion design (include air purge system, ceramic-bearing and others) has been developed and has achieved to 5,000 hours of operation without significant troubles. However, the grease becomes deteriorated by acid mist, temperature and other environmental factors, and that also affects the service life[2]. To provide a possible resolution to this technical issue, we have developed the centrifugal contactor of non-contact journaled construction using magnetic bearings without grease[3]. A magnetic bearing has the construction in which the attractive force of electromagnets is exerted to levitate a rotor without mechanical contact. Figure 1 shows the overview of irradiated magnetic bearing type centrifugal contactors and the structure of magnetic bearing.

We carried out the gamma-ray irradiation test of centrifugal contactor with magnetic bearing system to estimate the radiation resistance in 2008. The equipments stopped several times under irradiation, and were not finally reactivated of two different factors, one was abrasion of the touch-down bearing and adhesion to the main shaft (shown in Fig. 2), the other was a trouble of IC. Accumulated dose of the equipments was 3.7- 4.7×10^8 R. Therefore, the present work is intended to investigate whether the cause of the stop with the touch-down bearing is an influence of gamma-ray irradiation.

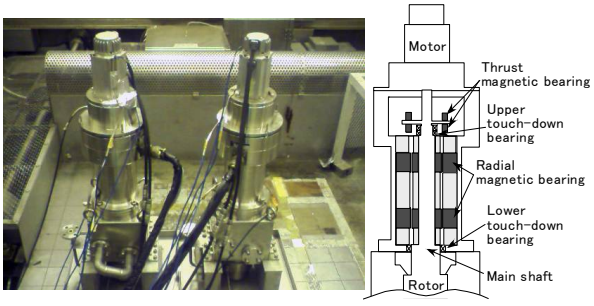

Fig. 1 Irradiated magnetic bearing type centrifugal contactors and structure of magnetic bearing.

The touch-down test were continuously carried out 6 runs (1run: 5 times touch-down) using the magnetic bearing type centrifugal contactor to which irradiated the lower touch-down bearing (a slide bearing formed of polyimide resin) was put in. So we observed the touch-down bearing, the main shaft, etc and monitored the control situation of magnetic-bearing after the touch-down test. Gamma-ray was irradiated to the lower touch-down bearing up to about 10^9 R at a rate of 17.3 kGy/h at room temperature. Figure 3 shows the observation result after the touch-down test (6 runs, 1×10^9 R). As shown in Fig. 3, neither abrasion of the touch-down bearing nor adhesion to the main shaft was observed. Moreover, the problem did not occur to control situation of the magnetic-bearing. Based on these results, we concluded that polyimide resin was a material which could be used under these system requirements. In the future, we will carry out gamma-ray irradiation test of improvement equipment which reflected these results again.

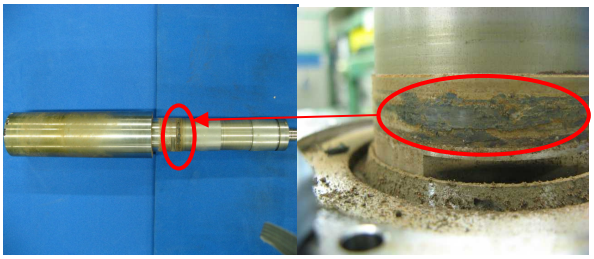

Main shaft and adhesion material

Fig. 2 Main shaft of No.1 equipment after the irradiation test (4.7×10^8 R).

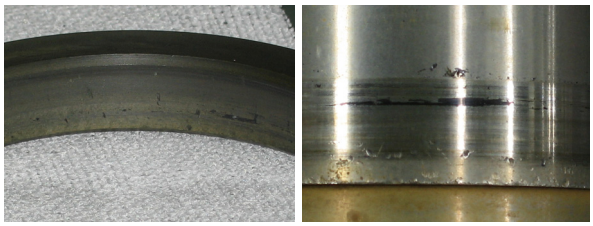

Lower touch-down bearing Main shaft

Fig. 3 Main shaft and lower touchdown bearing after the touch-down test (6 runs, 10^9 R).

References

1) G. J. Bernstein et al., ANL-7969 (1973).
2) T. Washiya et al., Proc. Global 2005 (2005).
3) N. Okamura et al., Proc. Global 2007(2007).

1-23 Studies on Microstructure and Elemental Distributions of Barrier Materials for Geological Disposal of Radioactive Waste

N. Miyasaka [a)], K. Yoshi [a)], T. Kozaki [b)], S. Sato [b)], N. Kozai [c)], M. Kohka [d)], T. Satoh [d)] and T. Kamiya [d)]

[a)] Graduate School of Engineering, Hokkaido University, [b)] Faculty of Engineering, Hokkaido University, [c)] Advanced Science Research Center, JAEA, [d)] Department of Advanced Radiation Technology, TARRI, JAEA

A compacted Na-bentonite, of which major mineral is montmorillonite having high swelling ability and low hydraulic conductivity, is a candidate buffer material in geological disposal of high-level radioactive waste. However, Na-bentonite would change if its exchangeable cations of Na^+ are replaced with Fe^{2+} which can be released from corrosion of carbon steel waste containers. Therefore, the performance as the buffer should be evaluated in a proper way not only for Na-bentonite but also for Fe(II)-bentonite. In a hydraulic conductivity measurement for Fe(II)-bentonite, Fe^{2+} in the sample are easily oxidized and precipitated under the presence of oxygen. Similarly, some fraction of Fe^{2+} in the sample may be precipitated as a result of hydrolysis if the sample is kept contact with fresh water for long time. Therefore, the stability of Fe(II)-bentonite during the measurement is a key issue to be studied so as to evaluate its hydraulic conductivity. In this study, Fe(II)-montmorillonite before and after the hydraulic conductivity measurements were characterized by chemical analyses. In addition, a micro-PIXE analysis was conducted for the samples to find the precipitation of iron in the samples.

The Fe(II)-montmorillonite was prepared from Na-montmorillonite by a modified ion-exchange reaction using Fe(II)-nitrilotriacetate complex solution. Total amounts of exchangeable cations in the samples before and after the hydraulic conductivity measurement were determined by ICP-AES after extracted with 0.1 M KCl solution. The ratios of Fe(II) to total Fe extracted from the samples were determined by colorimetry. Detail procedures of the chemical analyses are described elsewhere [1)]. The samples for micro-PIXE analyses were prepared by drying the suspension of the sample which had been dropped on a graphite plate. The hydraulic conductivity measurements by constant head method were conducted at dry densities of 0.8 and 1.0 Mg m^{-3} for about 30 days under a room temperature. Amount of distilled water passed through the sample during the experiment was 3.6×10^{-5} m^3 and 2.5×10^{-6} m^3 per 1 g-clay at dry densities of 0.8 and 1.0 Mg m^{-3}, respectively. The samples were handled under oxygen-free condition except a moment to set the sample on a sample holder of the micro-PIXE system.

Table 1 shows the results of chemical analyses for Fe(II)-sample before and after the hydraulic conductivity measurement at the dry density of 0.8 Mg m^{-3}. Although no oxidation of Fe(II) occurred, Fe content was found to decrease during the measurement. Figure 1 shows two-dimensional elemental mappings of Si, Al and Fe for the Fe(II)-sample after the hydraulic conductivity measurement. The region where only Fe has high content (as indicated with circles in the figure) appeared after the hydraulic conductivity measurement. These findings suggest that small fraction of Fe(II) ions in the Fe(II)-sample are precipitated between montmorillonite particles during the measurement.

In general, Fe^{2+} ions precipitated in micro pores may reduce the hydraulic conductivity, whereas Fe^{2+} ions precipitated over montmorillonite particles may inhibit their swelling, resulting in high hydraulic conductivity. However, the hydraulic conductivities observed were kept constant during the whole period of the measurement at both dry densities. This suggests that at least small amount of the precipitation has no or negligibly small impact on the hydraulic conductivity.

Reference

1) J. Manjanna et al., J. Nucl. Sci. Tech. 44 (2007) 929.

Table 1 Exchangeable cations and Fe(II)/Fe(total) ratio of Fe extracted from Fe(II)-samples before and after hydraulic conductivity measurement at dry density of 0.8 Mg m^{-3}.

	Exchangeable cation [meq/100g]			Fe(II)/Fe(total)
	Na	Ca	Fe	[%]
Before	3	2	101	100
After	1	3	92	100

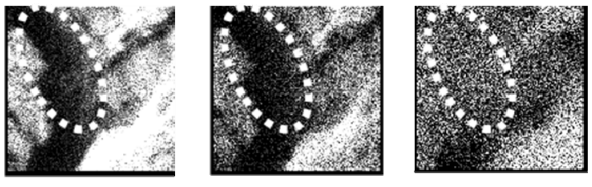

Fig. 1 Two-dimensional elemental mappings of Si, Al and Fe for Fe(II)-sample after hydraulic conductivity measurement at dry density of 0.8 Mg m^{-3}.

1-24 Behavior of Eu during Culture of *Paramecium bursaria* with Yeast Cells Sorbing Eu

N. Kozai [a)], T. Ohnuki [a)], M. Kohka [b)], T. Satoh [b)], T. Kamiya [b)] and F. Esaka [c)]

[a)] Advanced Science Research Center, JAEA,
[b)] Department of Advanced Radiation Technology, TARRI, JAEA,
[c)] Division of Environment and Radiation Sciences, NSED, JAEA

It is known that activity of microorganisms such as bacteria, algae, and yeasts has a great impact on the geological migration of the radionuclides leached from the radioactive waste forms buried underground. Retardation of the radionuclide migration by adsorption and mineralization on the cells is the most desirable function of those microorganisms. It is also known that protozoa, who prey those microorganisms, are found not only in surface water and soil but also in deep ground water. Protozoa defined as one-celled (unicellular) organisms control the number of those bait-microorganisms. However, no knowledge on the role of protozoa on the radionuclide migration is available. The chemical forms of the radionuclides sorbed on or taken up by those bait-microorganisms may change during the process of digestion and absorption by protozoa. Protozoa may take up radionuclides directly from water. The objective of this study is therefore to elucidate the role of protozoa in the migration of radionuclides. This study selected paramecia as model protozoa. Paramecia are the most common species of protozoa in fresh waters and most extensively used in research of behavior, heredity, and so on. Depending on the species, paramecia are 70-350 μm length and several tens of μm wide. This size is suitable for micro-PIXE analysis considering the special resolution, less than 1 μm, of the micro-PIXE analyzing system in the TIARA facility.

In the first year of this study, uptake or sorption of metals in aqueous solutions at pH 7 by *Paramecium bursaria* was investigated [1)]. It was found that Sr, Eu, and Pb were hardly adsorbed on living cells of *P. bursaria*. It is very interesting why Eu and Pb, which are very adsorptive to bacterial cell surfaces, are not adsorbed on *P. bursaria* cells. No evidences for mineralization of those metals on cell surfaces of *P. bursaria* were also obtained. In the second year of this study, we investigated behavior of Eu during culture of *P. bursaria* in media containing yeast sorbing Eu. Yeast, *Saccharomyces cerevisiae*, was used as a food source and Eu(III) was used as simulant of trivalent actinides.

Yeast cells were precultured in a nutrient medium, collected by centrifuge, and washed with an inorganic aqueous medium containing 200 mg/L $Ca(NO_3)_2 \cdot 4H_2O$, 20 mg/L $MgSO_4 \cdot 7H_2O$, 0.8 mg/L $Fe_2(SO_4)_3 \cdot nH_2O$, and 590 mg/L NaCl (Medium A) repeatedly. The yeast cells were contacted with an aqueous solution containing 0.5 mM $Eu(OCOCH_3)_3 \cdot nH_2O$ for four days at 25 °C. After the contact, the cells were separated from aqueous phase by centrifuge and washed with Medium A repeatedly. Cells of *P. bursaria* were precultured, collected, and washed with Medium A repeatedly. Finally, *P. bursaria* cells were statically cultured with the above prepared yeast cells in flasks containing Medium A at 23 °C. The culture was stirred only before periodic sampling of the *P. bursaria* cell culture. The cells in the sampled culture were quickly washed with Medium A and fixed with a fixative containing 4% glutaraldehyde and 60 mM sodium cacodylate. The cells fixed were washed with purified water, dried on a carbon foil in air at room temperature, and analyzed by micro-PIXE.

A part of the Eu adsorbed on yeast cells was precipitated as phosphate nano-particles on the cell surfaces and the rest of the Eu seemed to be adsorbed on the cell membrane. Soon after introducing of the Eu-adsorbing yeast cells Eu concentrations in the aqueous phase increased up to about 1 μM but quickly decreased to an almost constant level, less than 0.1 μM, after the second day of the culture. The amount of Eu leached into the aqueous phase was less than 0.1% of the Eu on the yeast cells. As culture time advances, membranous precipitates formed. These membranous precipitates contained undigested and digested yeast cells and dense membranous organic substance filling gaps between those cells. At the end of culture, numerous nano-particles of Eu phosphate were observed on digested yeast cells in the membranous precipitates. These results indicate that the Eu fixed on yeast cells mostly transitioned into membranous precipitates through growth of *P. bursaria* cells and thus suggest that *Paramecium sp*. do not impair actinide-retardation action of bait-microorganisms.

Eu was detected by micro-PIXE for the *P. bursaria* cells collected at inductive phase of growth (up to the first four days of the culture). As culture time advances, Eu was not detected for any cells. It is very interesting that Eu was specifically concentrated in the *P. bursaria* cells at inductive phase despite the fact that Eu was toxic to paramecium. It seemed that the Eu spread throughout the cells at inductive phase. This Eu is supposed to be in the interior of the cells because the first year study revealed that adsorption of Eu on cell surfaces of *P. bursaria* is very unlikely. We will investigate intracellular distribution of Eu concentrated in *P. bursaria* cells by 3D-micro-PIXE.

Reference

1) N. Kozai et al., JAEA Takasaki Ann. Rep. 2008 (2009) 31.

1-25 Effect of Groundwater Radiolysis on the Disposal System of High-level Radioactive Waste

M. Yamaguchi [a] and M. Taguchi [b]

[a] Geological Isolation Research Unit, GIRDD, JAEA,
[b] Environment and Industrial Materials Research Division, QuBS, JAEA

High-level radioactive waste (HLW) is planned to be disposed of in a deep underground repository. In the current Japanese design concept of the HLW disposal system, a canister of HLW is encapsulated in a carbon steel overpack. After the overpack finally loses its integrity and the porewater comes into contact with the HLW (it is typically assumed 10^3 years in performance assessment for the disposal system in Japan), alpha-radiolysis would occur and it is anticipated that radiolytic products such as H_2O_2 and O_2 may accelerate migration of radionuclides which are more soluble and less sorptive to barriers in oxidized states.

Actual alpha-radiolytical process of groundwater would be sensitive to some factors in the surrounding conditions during system evolution. In particular, high concentrated and dissolved H_2 which may arise due to anoxic corrosion of overpack, would suppress radiolytic formation of oxidizing species, since its effect is well known for low-LET radiolysis of water. However, there are few experiments on the effect under high-LET radiolysis of water such as alpha-particles and model calculation could not explain the absence of any effects by dissolved H_2 observed by 5 MeV He^{2+} irradiation [1]. Thus we have examined the effect of dissolved H_2 by using helium ion beam from the AVF cyclotron in TIARA and also performed model simulations on the effect of the dissolved H_2.

Sample cells were 40 mm i.d. and 5 mm in depth and cover glasses (0.15 mm thick) were attached with epoxy adhesive. Gas saturated aqueous solutions were prepared by bubbling either argon or hydrogen and they were transferred to sample cells. H_2O_2 solutions (100 μmol dm^{-3}) were prepared by adding small aliquots of stock solution to the cells. Samples were irradiated with $^4He^{2+}$ ion beam accelerated to 50 MeV by the AVF cyclotron. Incident energy was adjusted to approximately 15 MeV by placing an aluminum sheet (0.6 mm thick) on a sample cell. Ion beam was scanned over 50 × 50 mm to cover the whole area of the sample. Maximum irradiation time was 10 minutes and the accumulated doses were estimated to be about several kGy.

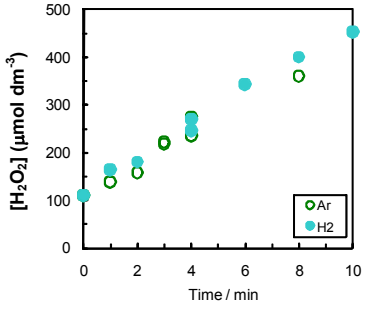

Fig. 1 Hydrogen Peroxide concentration after helium ion beam irradiation as a function of irradiation time: (open) argon bubbled samples (solid) hydrogen saturated samples.

Preliminary experiments were performed by using sample cells made of Plexiglas. H_2O_2 was decomposed almost completely in solutions saturated with H_2 by helium ion beam radiolysis. However, experimental data were scattered and decomposition of H_2O_2 after irradiation was suspected [2]. New sample cells made of quartz glass were prepared. Figure 1 shows the result with this setup. H_2O_2 concentration in degassed samples and samples saturated with H_2 increased almost linearly with accumulated dose at the same rate, indicating no effect of dissolved H_2 as reported by Pastina and LaVerne [1].

Recently Trummer and Jonsson have pointed out that the absence of the effect of dissolved H_2 on high-LET radiolysis of water can be explained by assuming the dose rate of the actual irradiation volume which is about four orders larger than the value averaged over the whole volume of the sample [3]. Figure 2 shows this dose rate dependence also hold for our experimental condition with 15 MeV He^{2+} by homogeneous model calculation.

This study is a part of the Project for assessment methodology development of chemical effects on geological disposal system funded by the Ministry of Economy, Trade and Industry, Japan.

References

1) B. Pastina and J. LaVerne, J. Phys. Chem. A105 (2001) 9316.
2) M. Yamaguchi and M. Taguchi, Radiation Chemistry in the 21st Century, P47 (2009).
3) M. Trummer and M. Jonsson, J. Nucl. Mater., 396 (2010) 163.

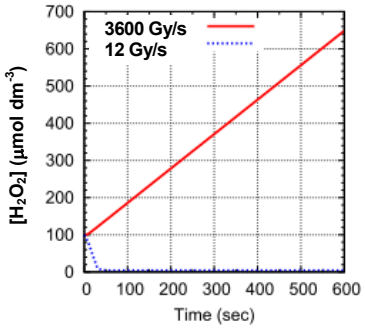

Fig. 2 Calculated Hydrogen peroxide concentration as a function of irradiation time at different dose rates.

1-26 Effect of Temperature Change on Irradiation Hardening of Ferritic and Austenitic Steels during Ion-irradiation

S. Jitsukawa [a)], M. Ando [b)], I. Ioka [a)], Y. Abe [a)], T. Onitsuka [a, c)], N. Ishikawa [a)] and N. Okubo [a)]

[a)] Division of Fuels and Materials Engineering, NSED,
[b)] Division of Fusion Reactor Engineering, FRDD, [c)] NSRC, JAEA

It has been reported that change of irradiation condition (e.g. irradiation temperature and damage rate) affects microstructural and property changes of metals and alloys[1)]. It may accelerate irradiation hardening to reduce residual ductility leading quasi-brittle fracture. Effect of temperature change on the irradiation hardening is examined.

An 8Cr-2W (0.1C-8Cr-2W-VTa) reduced activation ferritic steel F82H (developed by JAEA and JFE corporation), F82H doped with 1wt%-Ni (F82H+1Ni) and a type 316 stainless steel 316F (0.04C-0.04Si-17Cr-14Ni-2Mo) were used. Both F82H and F82H+1Ni were normalized at 1313 K. This was followed by tempering at 1023 K for 1.5 h. 316F was used after solution annealing at 1323 K for 1 h. Plates of the alloys were cut into those of 3 mm × 6 mm × 0.75 mm in size, and irradiation was conducted on the rectangular surfaces of 6 mm × 0.75 mm at temperatures of 523 K to 653 K with 10.5 MeV Fe^{3+} ions as well as He and H ions. Average damage rate was 1.0E-3 dpa/s at a depth of 1 μm; the projected range for Fe^{3+} ions was of about 2 μm.

Two accumulated damage levels of 9 dpa (displacement of atom) and 20 dpa were selected. For 9 dpa specimens, irradiation temperatures of 573 K and 648 K were applied. Also, temperature was changed for some of the specimens between these temperatures during irradiation. For 20 dpa specimens, 523 K and 653 K were applied. Temperature was changed between these two temperatures for some of the specimens. Temperature changes were performed at every 3 dpa, as seen in Fig. 1. The number of temperature changes were 3 and 6 for 9 dpa and 20 dpa specimens, respectively.

Ultra-micro hardness testing was conducted after irradiation at the ion-incident surfaces. Penetration depth of 1 μm was kept for all the tests to minimize the effect of the depth distribution of the irradiation damage. The Ultra-micro-hardness testing machine of EMT-1100a (Elionics) was used for the tests.

Hardness values after irradiation was shown in Fig. 2. The figure indicates the increment of hardness during irradiation. Both temperature dependence and damage level dependence of hardening for 316F was relatively small, although it exhibited hardening by 1.5 GPa. F82H specimens irradiated at temperatures cyclically changed exhibited maximal hardening. The response of F82H+1Ni specimens was rather complicated. Hardening attained maximal after 20 dpa by temperature change, while it was smaller than the others at 9 dpa.

Temperature dependence of hardness after irradiation to 10 dpa for F82H was plotted in Fig. 3. Figure indicates that irradiation hardening attained maximal after irradiation to 10 dpa at temperatures of 673 K. It was also indicated that hardening by ion-irradiation tends to exhibit maximal at temperatures of between 623 K and 673 K for these steels[4)]. These suggest that temperature change enhanced irradiation hardening. It has been also reported that temperature change during irradiation caused acceleration of irradiation induced microstructural change and hardening [1-5)]. Several authors have reported that the effects decreased with damage levels. Results in Fig. 2, however, indicated different tendencies.

Irradiation hardening often reduces residual ductility and fracture toughness of the materials. Results by fission reactor irradiation experiments indicate that residual ductility is not small and the margin to ductile fracture remains to be reasonable level even after irradiation to some tens of dpas at temperatures where irradiation hardening occurs[6,7)]. However, it should be noted that residual capability of work hardening is also rather limited and the additional hardening may reduce residual ductility to a considerable degree.

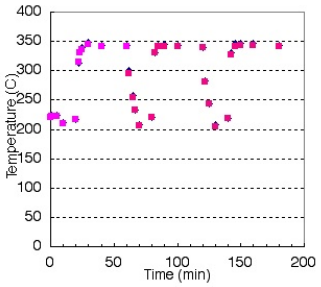

Fig. 1 Pattern of the temperature change. Temperature was reduced every 3 dpa and recovered.

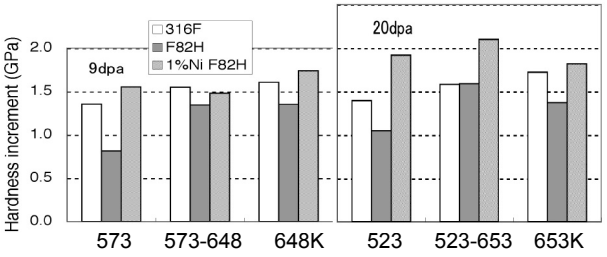

Fig. 2 Hardening at constant and cyclically changed temperature.

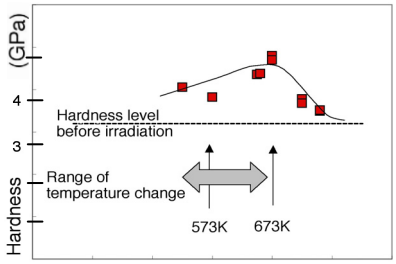

Fig. 3 Temperature dependence of hardening at 10 dpa.

References

1) Y. Yoshida et al., J. Nucl. Mater. 212-215 (1994) 471-475.
2) S. Jitsukawa et al., J. Nucl. Mater. 307-311 (2002) 179-186.
3) S. Jitsukawa et al., J. Nucl. Mater. 329-333 (2004) 39-46.
4) M. Ando, private communication.
5) S. Jitsukawa et al., J. Nucl. Mater. 367-370 (2007) 539-543.
6) K. Suzuki et al., Nucl. Eng. Design 240 (2010) 1290-1305.
7) S. Jitsukawa et. al., Nuclear Fusion 49 (2009) 115006.

1-27 Simulation of Neutron Damage Microstructure in Extra High Purity Fe-25Cr-35Ni Austenitic Stainless Steels

I. Ioka [a)], Y. Ishijima [b)], H. Ogawa [b)] and Y. Nakahara [b)]

[a)] Nuclear Engineering Research Collaboration Center, JAEA,
[b)] Division of Fuels and Materials Engineering, NSED, JAEA

The ultra high burn-up of LWR is considered to be an important technology for establishing nuclear power plants as one of the most promising future energy systems from a view-point of reducing radioactive waste and greenhouse gas. Cladding materials with the long excellent performance under heavy irradiation are required to these developments. The high chromium and high nickel austenitic stainless steel (Extra high purity (EHP) alloy) [1)] was selected as one of candidates that are possible to be made by the new engineering technology.

Microstructural evolution induced by irradiation is believed to be the key variables responsible for degradation of materials in LWR. Months to years of irradiation time are required to obtain a change in microstructure of materials at dozens of dpa. Charged particle simulation with accelerated damage rate is often used in such situations as to forecast the behavior of neutron-irradiated materials. By establishing the correlation between charged particle- and neutron- irradiated microstructures of EHP alloy, the results from charged particle-irradiation can be used to provide valuable information on microstructure evolution in EHP alloy in LWR cores.

This work is focused on investigating the microstructure of EHP alloy irradiated with charged particle under condition relevant to LWR cores. The behavior of dislocation loop is determined as a function of irradiation temperature, and is compared to those for neutron irradiations of EHP alloy.

The materials were Fe-25Cr-35Ni and Fe-25Cr-20Ni EHP alloys. The chemical compositions are shown in Table 1. The configuration of specimen is 3 mm in diameter and 0.2 mm in thickness. The surface of specimen was mechanically and electro-chemically polished to a specular finish before irradiation.

The specimens were irradiated in triple (12 MeV Ni^{3+}, 1.1 MeV He^{+}, 380 keV H^{+}) ion beam mode at temperatures of 573, 673, 773 K using the triple ion beam facility (TIARA). The temperature of the specimen was measured by an infrared thermometer. The displacement damage in the specimen was mainly attributed to Ni^{3+} ion irradiation. The dose was about 15 dpa around 1.2 μm. He^{+} and H^{+} ions were implanted in depth ranges from 1.0 to 1.5 μm using aluminum foil energy degraders. The concentrations of He^{+} and H^{+} ions in the implanted range were 45 appmHe and 450 appmH, which correspond to LWR condition.

Figure 1 shows the bright field image of Fe-25Cr-20Ni at each irradiation temperature. The images show irradiation defects such as dislocation loops are induced by charged particle-irradiation. Figure 2 shows the number density and the average diameter of dislocation loops of irradiated Fe-25Cr-20Ni and Fe-25Cr-35Ni. The dislocation loop density of Fe-25Cr-35Ni was less than that of Fe-25Cr-20Ni. There is little difference in average diameter. It is considered that Ni is effective to suppress the initiation of irradiation defects. The dislocation loop density and the average diameter of Fe-25Cr-35Ni by neutron irradiation (572 K) were about 2.2×10^{21} n/m^3 and 21 nm, respectively [2)]. The dislocation loop density and the average diameter were almost the same for both neutron irradiation and ion irradiation. It seems that more neutron irradiation data as a function of irradiation temperature are necessary.

References

1) K. Kiuchi et al., IAEA-TECDOC-1299 (1999)112.
2) I. Ioka et al., JAEA Takasaki Ann. Rep. 2008 (2009) 35.

Table 1 Chemical composition of EHP alloys.

Material	Fe	Cr	Ni	Ti	C	O
Fe-25Cr-35Ni	bal.	24.85	35.05	0.17	0.0018	0.0009
Fe-25Cr-20Ni	bal.	24.23	21.61	0.21	0.0006	0.0005
	N	Si	Mn	P	S	B
Fe-25Cr-35Ni	0.002	<0.005	0.001	0.001	0.001	-
Fe-25Cr-20Ni	0.001	<0.01	<0.01	0.001	0.002	<.0005

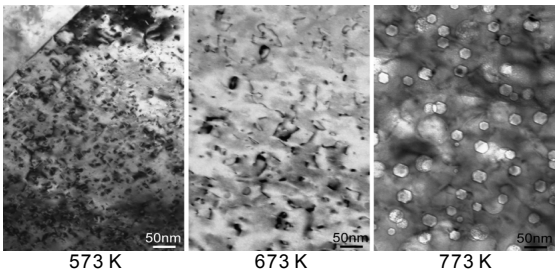

Fig. 1 Bright field image at each irradiation temperature.

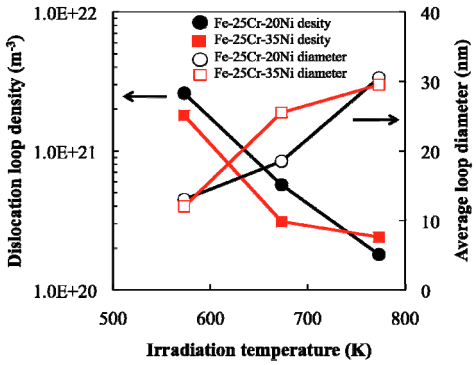

Fig. 2 Dumber density and average diameter of dislocation.

1-28 Effects of Radiation Damage and Helium on Swelling and Microstructure of EHP Ni-base Superalloy

G. H. Kim [a)], K. Shiba [a)], I. Ioka [a)], T. Sawai [b)] and S. Yamashita [c)]

[a)] Nuclear Engineering Research Collaboration Center, JAEA,
[b)] Research Coordination and Promotion Office, NSED, JAEA,
[c)] Division of Fuels and Materials Engineering, NSED, JAEA

1. Introduction

Cladding materials of a nuclear reactor are required to have the long excellent performance under the irradiation environment. In this experiment, irradiation performance of extra high purity (EHP) Ni-base superalloys designed as the MA doped MOX fuel claddings for the sodium cooled fast reactor was examined. In this alloy, impurities, such as C, O, N, P, S were reduced to less than 100 ppm in total to improve workability, irradiation embrittlement, and inter-granular corrosion.

Neutrons in the FBR core produce about 1 or 2 appmHe/dpa in high nickel alloys. It is less than that in fusion reactors or than that even in light water reactors considering the two-step reaction of Ni-58 in stainless steels [1, 2)]. Small amount of helium may, however, affect the microstructural evolution especially in EHP alloys where C, O, N impurities are extremely low. Because cavity nucleation in such high purity alloys is very difficult due to the high surface energy of cavities [3)] and helium gas pressure will drastically change the stability of cavity nuclei. Dual-ion-irradiation is, therefore, essential for the adequate evaluation of EHP alloys under radiation environment.

This work is focused on investigating the effects of helium injection on the cavity development and the dislocation evolution in EHP Ni-base superalloys by the irradiation experiments using a dual beam of iron and helium ions.

2. Experimental procedures

The EHP alloy (Fe-40Ni-25Cr-1.5Ti-1.5Al) was used for the irradiation experiments. The irradiations of samples were carried out by using Takasaki Ion Accelerators for Advanced Radiation Application (TIARA) facility. Ions of 10.5 MeV Fe^{3+} were injected to produce radiation damage and 1.05 MeV He^{2+} ions were implanted to simulate the He production. Single (Fe^{3+}) and dual (Fe^{3+} + He^{2+}) ion beam irradiation were conducted up to ~50 dpa and ~150 appmHe at 825 K. The irradiation of helium was controlled using an Al foil energy degrader to implant over the depth range from about 0.9 to 1.5 μm. The nominal displacement damage and ion-implantation depth were calculated using TRIM code. Thin foils for transmission electron microscopy (TEM) were fabricated with a focused ion beam (FIB) micro-sampling system. TEM observation was carried out for the evaluation of cavity and dislocation structures.

3. Results and discussions

Figure 1 shows the cross-section views of single and dual ion irradiated EHP alloys up to 50 dpa at 825 K. Under single beam irradiation, high density of dislocation structure was observed in the depth region 0-2.2 μm of the projected range of iron ion. Cavities were not founded. On the other hand, for dual beam irradiation to EHP alloy, the density of dislocation structure relatively decreased in the projected range of iron ion. But, the presence of helium produced many small polyhedral cavities of 25 nm in average diameter in the depth region of 0.9-1.5 μm. In this region, the displacement damage level and the He ion concentration increased from 15 dpa and 100 appm to 33 dpa and 150 appm, respectively. This result means that helium exceeding 100 appm can produce cavities.

In future, void swelling and microstructural evolution of dual-ion beam irradiated EHP Ni-base superalloy will be analyzed at the lower dose.

References

1) A. A. Bauer et al., J. Nucl. Mater. 91 (1972) 42.
2) L. R. Greenwood, J. Nucl. Mater. 137 (1983) 115.
3) E. H. Lee et al., J. Nucl. Mater. 79 (1979) 83.

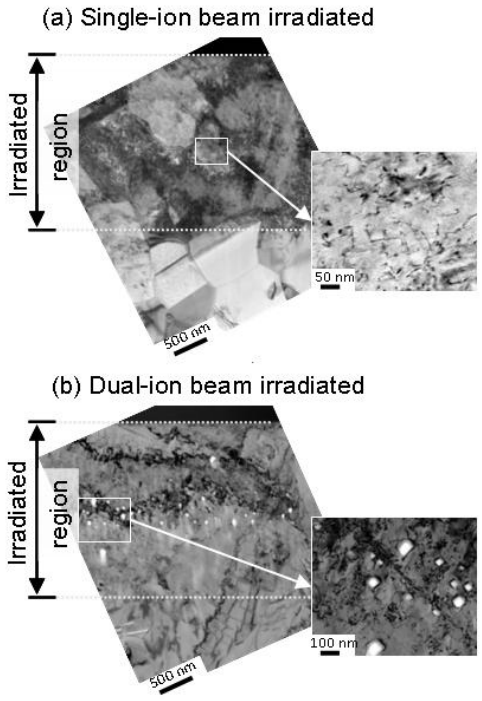

Fig. 1 Bright field images of (a) single and (b) dual ion irradiated EHP alloy up to 50 dpa at 825 K.

1-29 Irradiation Hardening in Ion-irradiated Hafnium

Y. Chimi and J. Ogiyanagi

LWR Long-term Reliability Research Unit, NSRC, JAEA

Pure hafnium metal is used as one of the neutron absorbers for control rods in commercial light water reactors, due to long nuclear lifetime and good corrosion resistance. In recent years, many cracks on the stainless steel sheath of control rods using hafnium plates have been found in Japanese boiling water reactors. The cracks might be caused by irradiation-assisted stress corrosion cracking (IASCC) due to the tensile stress originated from the irradiation growth of hafnium. However, the irradiation behavior of hafnium has been hardly reported in literature so far. We have investigated the defect production behavior of hafnium irradiated with energetic electrons, and the displacement threshold energy for hafnium was estimated as E_d=28 eV [1]. In the present work, in order to study the irradiation behavior of mechanical properties in hafnium, the irradiation hardening in hafnium irradiated with energetic heavy-ions has been investigated.

Polycrystalline hafnium plates and rods were used as specimens. Hafnium plates with ~1 mm in thickness were cut into small pieces (~5 mm × 5 mm), and hafnium rods with ~5 mm and ~3 mm in diameter (denote as "rod-1" and "rod-2", respectively) were cut into disk shape with ~1 mm in thickness. A plane surface of each specimen was mechanically and chemically polished.

Ion irradiation of the specimen was performed with 12.0 MeV $^{56}Fe^{4+}$ ions at 290 °C up to the ion fluence of 9.4×10^{15} cm^{-2} by using a 3-MV tandem accelerator in TIARA, JAEA-Takasaki. The projected range of the ions is ~2.5 μm and the maximum damage cross-section is 2.5×10^{-15} cm^2 at a depth of 2.4 μm from the specimen surface, based on the calculation using SRIM code (using E_d=28 eV [1]). Therefore, the maximum irradiation dose and dose rate are estimated to be ~23 dpa and $\sim 7 \times 10^{-4}$ dpa/s, respectively. In order to eliminate the effect of temperature history of the specimen, a part of each specimen was masked by thick metal plate not to be irradiated.

For observation of irradiation hardening in the ion-irradiated specimen, indentation tests were performed at room temperature using the UMIS-2000 (CSIRO, Australia) ultra micro-indentation testing system with Berkovich-type indenter tip. Indentation depth of 500 nm (corresponding to indentation load of around 25 mN) was adopted to observe only the damaged region in the specimen. Indentation measurements were carried out ~10 times at intervals of 20 μm in both the irradiated and un-irradiated regions for each specimen.

The results of micro-indentation hardness for ion-irradiated hafnium specimens are shown in Fig. 1 as a function of ion fluence. For hafnium plate specimen, the values of micro-hardness are higher than those for rod specimens because of the difference of texture caused by the different manufacturing processes between plate and rod materials. A large increase in micro-hardness was observed at the ion fluence of $\sim 4 \times 10^{14}$ cm^{-2}, corresponding to ~1 dpa at a peak of damage profile. Above $\sim 4 \times 10^{14}$ cm^{-2}, micro-hardness shows gradual increase with ion fluence, and has not been saturated even at 9.4×10^{15} cm^{-2} (~23 dpa).

For comparison, results for a hafnium rod specimen irradiated at 190 °C are also shown in Fig. 1. The micro-hardness for 190 °C irradiation is a little smaller than those for 290 °C irradiation, whereas the values of micro-hardness in the un-irradiated region are in the same range for both 190 °C and 290 °C irradiations.

Irradiation hardening behavior we have observed for pure hafnium metals is strongly concerned with the evolution of point defects, defect clusters and dislocation loops, which is affected by the irradiation temperature, dose and dose rate. In order to evaluate and clarify the irradiation behavior including irradiation hardening and also irradiation growth, it is necessary to understand the relationship between mechanical property change and microstructural evolution.

Reference

1) Y. Chimi et al., JAEA Takasaki Ann. Rep. 2008 (2009) 37.

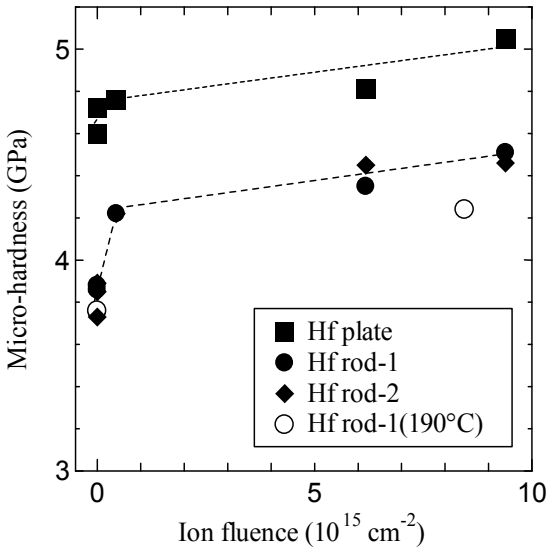

Fig. 1 Ion fluence dependence of micro-hardness for ion-irradiated hafnium (Hf) plate and rods. Dotted lines are guides for the eye.

1-30 Conductometric Analysis of Track Etching in Poly(vinylidene fluoride)

T. Yamaki, H. Koshikawa, S. Sawada, S. Hasegawa, M. Asano and Y. Maekawa

Environment and Industrial Materials Research Division, QuBS, JAEA

We have recently been working on ion-track membranes of poly(vinylidene fluoride) (PVDF) because they have attracted a renewed interest for their applications to fuel cells. Researchers previously employed a concentrated alkaline solution with a $KMnO_4$ additive at high temperatures to produce visible tracks in the PVDF films. These severe conditions provided irreversible chemical damage all over the film including the non-irradiated part. On the other hand, we have attempted to prepare PVDF-based ion-track membranes efficiently without any oxidant additives [1-3]. The aim of this study is to investigate the formation of the PVDF track membranes in detail by conductometric analysis. Interestingly, instead of the oxidant agent-induced activation, high-voltage application to the conductometry cell was found to increase the etch rate, governing the pore sizes and shapes, which is indicative of pore development affected by the etching products [4].

A 25 μm-thick PVDF film was irradiated at room temperature with 450 MeV ^{129}Xe from the TIARA cyclotron. The fluence was fixed at 3×10^7 ions/cm^2. Track etching was performed by mounting the irradiated film as a dividing wall in the conductometry cell made of Teflon containing a 9 mol/dm^3 aqueous KOH solution at 80 ºC. The electrical conductance of the solution through the film, $g(t)$, was monitored between two platinum electrodes as a function of the etching time under a sine AC voltage with a frequency of 1 kHz using an LCR meter. Assuming cylindrical pores, we calculated the effective pore diameter, d_{eff}, at any given time by

$$d_{eff} = (4Lg(t)/\pi KNS)^{1/2},$$

where L is the membrane thickness, K is the specific conductivity of the KOH etchant, N is the pore density generally corresponding to the ion fluence (corrected for the contribution of the microscopically-nonhomogeneous irradiation), and S is the area of the measured sample. The amplitude of the voltage between the electrodes was constant at either 0.3, 1.0 or 2.0 V.

Figure 1 compares the conductometry results obtained at the different applied voltages. Basically, there were several characteristic regions during the course of the etching. In the beginning, the plateau at a nearly zero diameter represented the process of etchant penetration into tracks and approach of the etched cones from both sides of the film. As soon as these two approaching cones made contact with each other, the d_{eff} suddenly increased. The time associated with this contact is called the breakthrough time, T_B. After the pore breakthrough, the d_{eff} increased, in other words, the pores grew in the transverse direction. Lastly, the rate of the d_{eff} increase became negligibly low, and eventually the curve reached the second plateau. Chemical etching in the unmodified area, that is, bulk etching occurred beyond the width of the latent track.

As also seen in (a), a T_B value is estimated to be 4.2 h at an applied voltage of 0.3 V. When the applied voltage was increased from 0.3 to 1.0 V, we did not see any significant change in the curve. When we further increased the voltage to 2.0 V, the curve exhibited a shorter T_B and time taken until the d_{eff} value started to level off, while it still showed an invariant growth rate and final d_{eff}. In other words, the etching seemed to be accelerated at the higher voltages. Cornelius et al. [5] similarly found that the etch rate for the polycarbonate-based track membranes varied with the applied voltage. As a probable cause, they took into account the creation of dissolution products during the etching process which should attach to the pore walls and affect further etching. If the dissolved species are ionic or polar, they are possibly more efficiently pulled out of the pore due to electrophoretic migration, reducing the effect of their adsorption on the inner pore surface. That is, pore development will finally be activated by a concurrent decrease in the susceptibility of the materials to chemical attack, and this activating effect due to voltage application worked well for only the etching before the breakthrough.

References

1) T. Yamaki et al., Kobunshi Ronbunshu 65 (2008) 273.
2) R. Rohani et al., Nucl. Instrum. Meth. Phys. Res. 267 (2009) 554.
3) T. Yamaki et al., GSI Sci. Rep. 2008 (2009) 350.
4) N. Nuryanthi et al., Electrochemistry 78 (2010) 146.
5) T.W. Cornelius et al., Nucl. Instrum. Meth. Phys. Res. 265 (2007) 553.

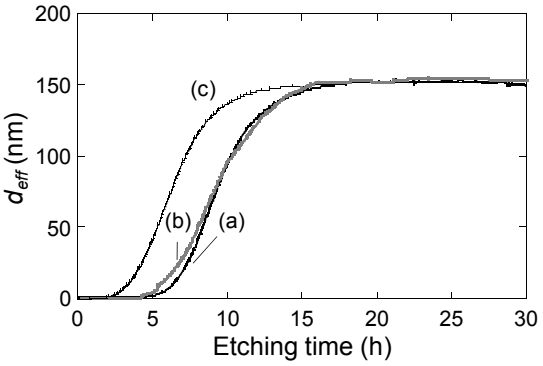

Fig. 1 Plots of the d_{eff} value as a function of the etching time. The voltage applied to the conductometry cell was (a) 0.3, (b) 1.0, or (c) 2.0 V.

1-31 Preparation of Anion-Exchange Membranes for Fuel Cell Applications by γ-ray Pre-Irradiation Grafting

H. Koshikawa, T. Yamaki, M. Asano and Y. Maekawa

Environment and Industrial Materials Research Division, QuBS, JAEA

Fuel cells are considered as large sources of clean energy because they do not emit any toxic substances and carbon dioxide. However, their widespread commercialization has been hindered by economic problems associated with the extensive use of platinum as well as by many restrictions due to much additional infrastructure and insufficient hydrogen storage capacity. In order to overcome such difficulties, worldwide researchers have recently been developing anion-exchange membrane fuel cells (AEMFCs), which do not need expensive platinum catalysts in the electrodes. We report here the preparation of new membranes for applications to "hydrazine-fueled" AEMFCs [1] by the γ-ray pre-irradiation grafting method [2,3].

Our membrane preparation involved the grafting of chloromethylstyrene (CMS) into poly(ethylene-*co*-tetrafluoroethylene) (ETFE) films and subsequent quaternization (Fig. 1) [2]. A 50 μm-thick ETFE film was pre-irradiated at room temperature in an Ar atmosphere with a ^{60}Co γ-ray at doses of 10, 20, 30 and 50 kGy. Graft polymerization was performed by immersing the irradiated ETFE film in the CMS/xylene 50/50 vol% solution in a N_2 atmosphere at 60 ºC for 1-24 h. The ETFE-*g*-CMS film was then quaternized in a 30% trimethylamine (TMA) solution at room temperature for 24 h. After the membrane was washed several times in water and in a 1 mol/dm^3 HCl solution for 24 h (to remove residual TMA), the chloride form of the membrane was converted to the alkaline form in a 1 mol/dm^3 aqueous KOH solution for 12 h.

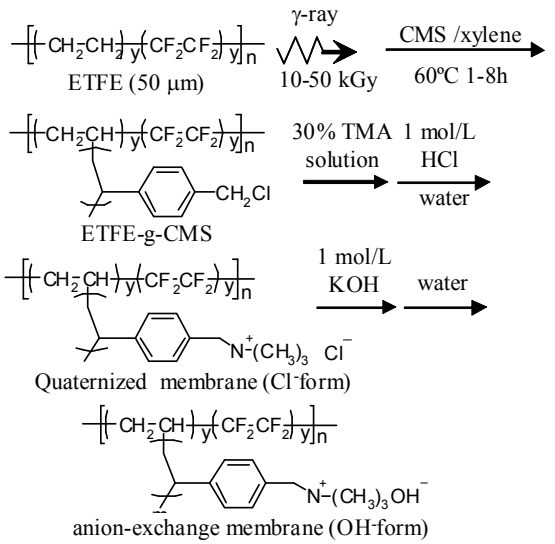

Fig. 1 The scheme for the preparation of anion-exchange membranes.

Figure 2 shows the degree of grafting *vs.* time curves for CMS grafting into ETFE films pre-irradiated with the γ-ray at the different doses. The degree of grafting was calculated as $(W_g - W_0)/W_0 \times 100$, where W_0 and W_g are the film weights before and after the grafting, respectively. The degree of grafting increased during the course of reaction for up to 8 h. We obtained higher degree of grafting as the pre-irradiation dose became higher. The highest degree of grafting reached 101% at a dose of 50 kGy for 8 h.

The ratio of chloride-to-alkaline conversion, related to the ion exchange capacity of the resulting anion-exchange membrane, was estimated from a weight change between before and after the treatment with the KOH aqueous solution and by the titration technique. The conversion ratios were approximately 60 and 50% for the above-mentioned grafted film, respectively although the reason for such low conversion efficiency has not yet been given. The hydroxide ion conductivity was 0.044 S/cm at room temperature and a relative humidity of 100%. This value is higher than or comparable to that of the previous radiation-grafted anion-exchange membranes (0.027 S/cm) [4].

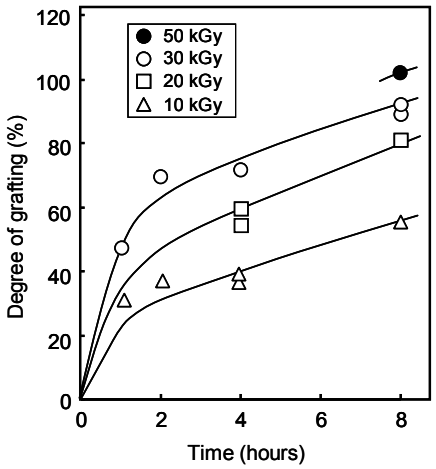

Fig. 2 The degree of grafting *vs.* time curves for CMS grafting into ETFE films irradiated with γ-rays at doses of 10, 20, 30, and 50 kGy.

References

1) K. Asazawa et al., J. Electrochem. Soc. 156 (2009) B509.
2) H. Koshikawa et al., 59th SPSJ Ann. Meet. (2010) 1239.
3) T. Yamaki, J. Power Sources, in press.
4) J.R. Varcoe et al., Chem. Mater. 19 (2007) 2686.

1-32 Enhanced Reactivity of Ion-track Grafting for Fuel-cell Electrolyte Membranes

T. Sekine [a, b], S. Sawada [a], T. Yamaki [a], H. Koshikawa [a], M. Asano [a], Y. Maekawa [a], A. Suzuki [b] and T. Terai [b]

[a] Environment and Industrial Materials Research Division, QuBS, JAEA,
[b] Department of Nuclear Engineering and Management, The University of Tokyo

Ion-track grafting involves irradiation of a base polymer film with swift heavy ions and the subsequent graft polymerization directly into the latent tracks. We have recently applied this technique to the development of proton exchange membranes (PEMs)[1]. A key for success here is to achieve high graft levels in as small a number of tracks as possible because it is very important to keep a balance between proton conductivity (prefers higher graft levels) and mechanical strength (prefers lower fluences) of the resulting membrane. We found that a mixture of water and isopropanol (H_2O/*i*PrOH) is an effective medium for enhancing the reactivity of the ion-track grafting of styrene.

A 25 μm-thick poly(ethylene-*co*-tetrafluoro- ethylene) (ETFE) film was bombarded by 3.5 MeV/n ^{129}Xe from the TIARA cyclotron. The fluence was 3.0×10^7 or 3.0×10^8 ions/cm^2, at which almost no ion tracks overlapped. Just after ion-beam irradiation, the film was exposed to air to produce peroxide groups, and then immersed in a grafting solution (a volume ratio of styrene to the grafting medium was 1:4) at 60 °C for 1-48 hours. The percentage composition of the H_2O/*i*PrOH mixture, $R_{H2O/iPrOH}$, was varied from 0 (pure *i*PrOH) to 100% (pure H_2O). The degree of grafting (*DOG*) was calculated by: $DOG(\%) = (W_g - W_0)/W_0 \times 100$, where W_g and W_0 denote the weights of the styrene-grafted and as-irradiated films, respectively.

Figure 1 plots the *DOG* of the films irradiated at 3.0×10^8 ions/cm^2 and styrene-grafted for 6 hours, as a function of $R_{H2O/iPrOH}$. All of the obtained *DOG*s were higher than that for the medium-free grafting (i.e., in neat styrene) (8.4%, a result not shown) and, interestingly, the *DOG* peaked at $R_{H2O/iPrOH}$ = 36%. Rager et al.[2] and Gürsel et al.[3] similarly used the H_2O/*i*PrOH mixture for γ-ray pre-irradiation grafting of styrene into a fluorinated base film. Our results agree with their previous ones, and can be discussed by considering the well-known Trommsdorff effect[3], in which poor solubility of the grafted polystyrene in polar media leads to an increased polymerization rate due to a slower termination rate. The lower $R_{H2O/iPrOH}$ yielded a homogeneous and compatible grafting solution, though, in contrast, the higher $R_{H2O/iPrOH}$ gave an immiscible grafting mixture, which composed a lower water-rich phase with the ETFE base film and a upper styrene-rich phase. The creation of these two phases would reduce the monomer accessibility within the base film. This is probably why the *DOG* decreased at $R_{H2O/iPrOH} > 36\%$.

Figure 2 shows the *DOG vs.* time curves for the films irradiated at fluences of 3.0×10^7 and 3.0×10^8 ions/cm^2 and styrene-grafted at $R_{H2O/iPrOH}$ = 36%. The *DOG* increased during the first 24 hours and then leveled off at a saturated value. At the same grafting time, the *DOG* was naturally smaller at the lower fluence because the number of peroxides acting as a starting point of graft polymerization is proportional to the fluence. It should be mentioned here that, for the first time, we obtained a *DOG* of > 10% even at the lower fluence of 3.0×10^7 ions/cm^2. This *DOG* corresponds to an ion exchange capacity of > 0.9 meq/g, which is comparable to that of a benchmark fuel-cell PEM called Nafion. We thus expect that the obtained result could be the technical breakthrough for PEMs endowed with both of high proton conductivity and mechanical strength. Characterization of the sulfonated membranes is now in progress.

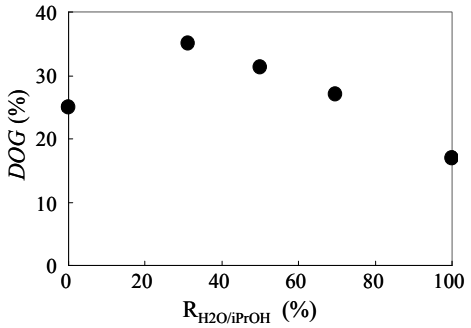

Fig. 1 The *DOG* as a function of $R_{H2O/iPrOH}$. The styrene grafting was performed for 24 hours after the ^{129}Xe irradiation at 3.0×10^8 ions/cm^2.

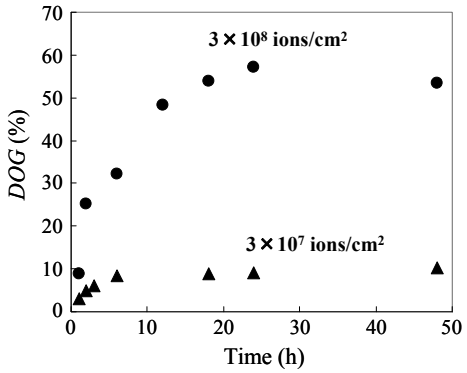

Fig. 2 The *DOG* as a function of grafting time at fluences of 3.0×10^7 and 3.0×10^8 ions/cm^2. The ^{129}Xe-irradiated films underwent the styrene grafting at $R_{H2O/iPrOH}$ = 36%.

References

1) T. Yamaki, J. Power Sources, in press.
2) T. Rager et al., Helv. Chim. Acta, 86 (2003) 1966.
3) S.A. Gürsel et al., Nucl. Instrum. Meth. Phys. Res. 265 (2007) 198.

1-33 Radiation-Induced Graft Polymerization of Styrene into a Poly(ether ether ketone) Film for Polymer Electrolyte Membranes

S. Hasegawa [a)], K. Sato [b)], T. Narita [b)], Y. Suzuki [a)], S. Takahashi [a)], N. Morishita [a)] and Y. Maekawa [a)]

[a)] Environment and Industrial Materials Research Division, QuBS, JAEA,
[b)] Graduate School of Engineering, Saitama Institute of Technology

Radiation-induced graft polymerization is a unique technique for direct grafting of a new functional polymer phase (grafts) into polymer films (substrate), in which functional polymers keep their characteristics such as thermal stability, mechanical strength, electronic properties, and crystallinity [1)]. There have been many attempts for basic researches to reveal graft polymerization mechanisms and for making new grafts into various polymer substrates including chemical transformation of grafts [2)] to be applied for battery separators, absorber resins, and polymer electrolyte membranes (PEMs) [3)]. Recently, we reported that the grafting of styrene into PEEK film pre-irradiated with 30 kGy was accelerated by using 1-propanol as a grafting solvent at 80 °C to obtain styrene-grafted PEEK with a grafting degree of more than 60% [4)]. Thus, we investigated the changes in morphology of PEEK films such as crystallinity and phase separation caused by grafting of styrene and subsequent sulfonation using differential scanning calorimetry (DSC), thermogravimetry (TGA), X-rays diffraction analysis (XRD), and electron spin resonance spectroscopy (ESR).

Judging from the similar endothermic heat of melting of the original and styrene-grafted PEEK (grafted PEEK) films, there was no change in crystallinity during the graft polymerization of styrene up to a grafting degree of 51%. Furthermore, lower glass transition temperature (T_g) than the original PEEK film in the DSC profile (Fig. 1) and no extra halo originating from amorphous polystyrene grafts being found in XRD strongly indicate that the grafting of crystalline region. These results indicate that styrene to have crystalline PEEK films proceeds in the amorphous region of PEEK without destroying the crystalline region.

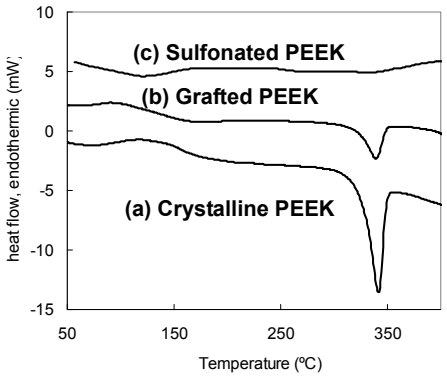

Fig. 1 DSC profiles of original PEEK (a), grafted PEEK with 51% GD (b), and PEEK-based PEM (sulfonated form of film b) with 93% SD (c).

This is because polystyrene grafts have similar hydrocarbon structures to a base PEEK polymer, so that these grafts are compatible to the amorphous phase of the PEEK films.

The ESR spectra of the original PEEK film and the film irradiated with 200 kGy in vacuo at room temperature were measured at room temperature (Fig. 2). The ESR signal in the irradiated film was observed at a *g*-value of 2.0074 with density of 5.23×10^{16} /g, which was 12 times larger than that of the original film.

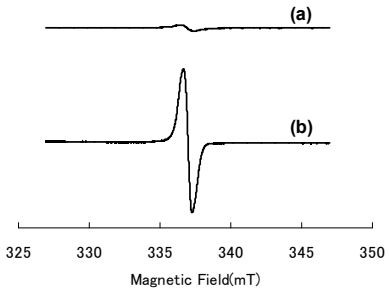

Fig. 2 ESR spectra of the original PEEK film (a) and the film irradiated with 200 kGy in vacuo at room temperature (b) were measured at room temperature.

The grafted PEEK films can be converted to PEEK-based PEM by subsequent sulfonation of the polystyrene grafts. By changing the sulfonation time in the sulfonation of polystyrene grafts at 0 ˚C in 0.05 M of chlorosulfonic acid in dichloroethane, the ion exchange capacity of the PEM can be controlled to a relatively low value. However, PEM with conductivity of more than 0.01 S/cm exhibited higher water content, above 100%. The degree of crystallinity of the grafted PEEK was found to drastically decrease with the sulfonation reaction of the grafts. The DSC and XRD observations indicated that the sulfonation reaction proceeded not only at the graft layers but also at the crystalline and amorphous phases of PEEK.

References

1) A. Chapiro, Radiation Chemistry of Polymeric System, Interscience Publishers, John Wiley & Sons, New York, 1962, Chap. XII.
2) M. M. Nasef et al., Prog. Polym. Sci. 29 (2004) 499.
3) K. Saito et al., Radiat. Chem.: Present Status and Future Trends, Elsevier, 439(2001) 671.
4) S. Hasegawa et al., Radiat. Phys. Chem. 77 (2008) 617.

1-34 Nanoscale Structures of Radiation-Grafted Polymer Electrolyte Membranes Investigated by Dissipative Particle Dynamics Simulation

S. Sawada [a)], T. Yamaki [a)], A. Suzuki [b)], T. Terai [b)] and Y. Maekawa [a)]

[a)] Environment and Industrial Materials Research Division, QuBS, JAEA,
[b)] Graduate School of Engineering, The University of Tokyo

A radiation-grafting method is one of the promising techniques for preparing polymer electrolyte membranes (PEMs) for fuel cell applications. In the research of the radiation-grafted PEMs, much effort has been devoted to improve their properties (proton conductivity, chemical stability, mechanical strength, etc.) by the best combination of base polymer films and graft monomers. As part of their basic science studies, we investigated the nanoscale structures of the PEMs by a dissipative particle dynamics (DPD) simulation. The simulation target was our original PEM synthesized by the radiation grafting of styrene into crosslinked-polytetrafluoroethylene (PTFE) and subsequent sulfonation [1-3].

According to our recent report [4], we modeled the grafted electrolyte polymers with ion exchange capacities (IECs) of 0.89 - 2.2 meq/g. Based on the molecular structures, the atom groups of $-(CF_2)_6-$, $-CH(C_6H_4SO_3H)CH_2-$, and 7 water molecules were represented as particles A, B and W, respectively. The interaction parameters between the two particles of the A-B, A-W, or B-W pair were calculated by a full-atomistic simulation. The molecular architecture (*e.g.*, the length of PTFE main chains, the length of graft chains, and the number of graft chains per molecule) was determined based on the experimental data. As the initial state, the electrolyte polymers and a fixed number of particles W were randomly located in a cubic cell with the three-dimensional periodic boundaries. After 50,000 time steps, all the systems reached the equilibrated states. For comparison, a DPD simulation was also performed on Nafion [5].

Figure 1 shows the snapshots of the simulation results in the equilibrated states. As in both (a) and (b), particles W appeared to be mixed with particles B while, in contrast, particles W in Nafion aggregated alone to grow larger. This finding indicates that, unlike Nafion, in which water clusters were excluded from any polymer parts, the water-filled regions were not clearly separated from the poly(styrene sulfonic acid) (PSSA) graft chains.

In order to obtain quantitative information on nanoscale structures, we calculated the radial distribution function between particles W, $G_{WW}(r)$. The $G_{WW}(r)$ was defined as:

$$G_{WW}(r) = \frac{n_W}{4\pi r^2 \Delta r \varphi_W}, \qquad (1)$$

where n_W is the average number of particles W existing in the distance between r and r +Δr from any particle W.

Figure 2 shows the $G_{WW}(r)$ for the hydrated electrolyte polymers. In the case of Nafion, there were sharp peaks at r = 0.60, 1.0 and 1.5 nm. These three peaks are considered to originate from the first, second and third nearest W particles, respectively, in the same cluster. At r = 3.4 nm, the $G_{WW}(r)$ dropped to under 1, which suggests the edge of a water cluster [5]. Accordingly, the diameter of the water cluster, d_C, was twice as much as this value, *i.e.*, 6.8 nm. For the grafted electrolyte polymers, the $G_{WW}(r)$ dropped to under 1 at r = 0.88 nm, corresponding to d_C of 1.8 nm. This result is in good agreement with the diameter obtained previously by the small-angle X-ray scattering analysis (1.7 nm [6]). It was found that a low of these small clusters would exist surrounded by PSSA graft chains. Such unique nanoscale structures were possibly related to the high proton conductivity and low water diffusivity of the grafted PEMs.

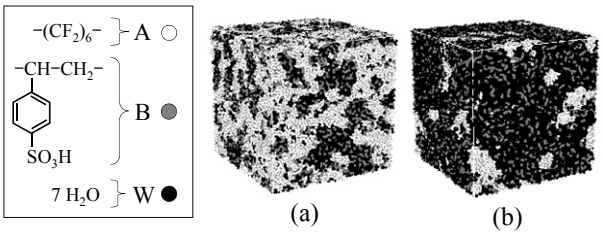

Fig. 1 Snapshots of the simulated polymer electrolyte in the IEC of (a) 0.89 and (b) 2.2 meq/g.

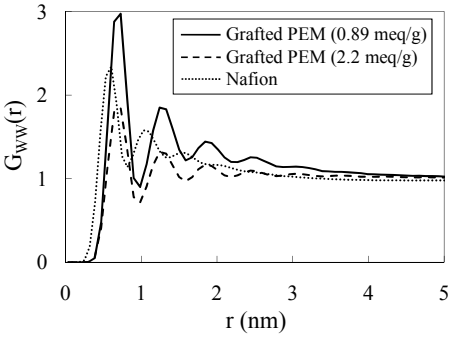

Fig. 2 The $G_{WW}(r)$ as a function of r.

References

1) T. Yamaki et al., Polymer 45 (2004) 6569.
2) S. Sawada et al., Trans. Mater. Res. Soc. Jpn. 30 (2005) 943.
3) S. Sawada et al., Solid State Inoics 179 (2008) 1611.
4) S. Sawada et al., Kobunshi Ronbunshu 67 (2010) 224.
5) S. Yamamoto et al., Polym. J. 35 (2003) 519.
6) M. Elomaa et al., J. Mater. Chem. 10 (2000) 2678.

2. Environmental Conservation and Resource Security

2-01 Fibrous Catalyst for Biodiesel Production Synthesized by Radiation-induced Graft Polymerization ····· 41
Y. Ueki, N. H. Mohamed, N. Seko and M. Tamada
2-02 Development of Zwitterionic Monolithic Column for Hydrophilic Interaction Liquid Chromatography and its Application to the Separation of Catecholamines and Related Compounds ····· 42
Y. Kamiya, S. Shin, A. Sabarudin, T. Umemura, Y. Ueki and M. Tamada
2-03 Decolorization of Secondary Treated Water from Livestock Urine Waste ····· 43
M. Takigami, N. Nagasawa, A. Hiroki, N. Kasai, F. Yoshii, M. Tamada, S. Takigami, T. Shibata, Y. Aketagawa and M. Ozaki
2-04 Modification of Hydroxypropyl Cellulose Hydrogels by Blending Poly (vinyl alcohol) ····· 44
A. Hiroki, T. Sato, N. Nagasawa and M. Tamada
2-05 Effect of Grafting Conditions on Radiation-induced Graft Polymerization ····· 45
Y. Ueki, N. C. Dafader, N. Seko and M. Tamada
2-06 The Recovery of Precious Metals Using Biomass Adsorbents ····· 46
D. Parajuli, N. Seko and K. Hirota
2-07 Surface Modification of Vulcanized Rubber by Radiation Co-grafting ····· 47
N. Mizote, A. Katakai and M. Tamada
2-08 ESR Study on Carboxymethyl Chitosan Radicals in Aqueous Solution ····· 48
S. Saiki, N. Nagasawa, A. Hiroki, N. Morishita, M. Tamada, H. Kudo and Y. Katsumura
2-09 Decomposition of Persistent Pharmaceuticals by Ionizing Radiation ····· 49
A. Kimura, M. Taguchi and K. Hirota

This is a blank page.

2-01 Fibrous Catalyst for Biodiesel Production Synthesized by Radiation-induced Graft Polymerization

Y. Ueki [a)], N. H. Mohamed [b,c)], N. Seko [a)] and M. Tamada [a)]

[a)] Environment and Industrial Materials Research Division, QuBS, JAEA,
[b)] Radiation Processing Technology Division, Malaysian Nuclear Agency,
[c)] Department of Chemistry and Chemical Biology, Graduate School of Engineering, Gunma University

1. Introduction

Fossil fuel resources are decreasing daily. Biodiesel, which is produced from vegetable oils and animal fats, has been attracting attention as an alternative to petroleum diesel fuel, since it is a non-toxic, biodegradable, renewable and carbon-neutral fuel. At present, the homogenous alkali-catalyzed method using NaOH or KOH as a catalyst is the mainstream for the industrial production of biodiesel. Recently, novel synthesis techniques, such as acid-, ion-exchange resin-, lipase-, and metal oxide-catalyzed method and non-catalytic supercritical methanol method, have been investigated and developed by numerous researchers. In this study, fibrous catalyst for biodiesel production was synthesized by using radiation-induced graft polymerization.

2. Experimental

The graft polymerization was carried out by contacting the nonwoven fabric irradiated by 100 kGy electron beam with 5 wt% aqueous emulsion, which consisted of 4-chloromethylstyrene, polysorbate 20 and deionized water, in a deaerated glass ampoule for 4 h at 40 ºC. After grafting, the grafted fabric was treated with 0.25 M trimethylamine (TMA) at 50 ºC to introduce a quaternary ammonium group, and then resulting fabric was further treated with 1 M NaOH to replace Cl^- with OH^-, before use.

3. Results and Discussion

The catalytic performance of the grafted polymer was evaluated through the transesterification of triolein (purity: 60%) and ethanol. The transesterification was performed by adding grafted polymer (weight: 0.5 g, capacity: 3.5 mmol-TMA/g-polymer) in a homogenous reaction solution (triolein: 2.8 g, ethanol: 7.2 g, decane (auxiliary solvent): 10.0 g) at 50 ºC. As seen in Fig. 1, the triglycerides were consumed with the lapse of time, and on the other hand the biodiesels were produced with time. These results confirm that the grafted polymer functions as a catalyst for biodiesel production. The conversion ratio of triglycerides in different reaction times reached 23%, 48%, 70%, 82%, and 95% at 10 min, 30 min, 1 h, 2 h, and 4 h, respectively.

Triglycerides in Fig. 1 is specifically noted; and the conversion ratio of triglycerides relative to the reaction time is plotted as in Fig. 2. In Fig. 2, the data with a commercial granular anion exchange resin (Diaion PA306S, particle size: 150–425 μm, capacity: 3.4 mmol-TMA/g- resin) are also shown for comparison. The grafted polymer promoted the transesterification at a reaction speed higher by at least 3 times than that with the granular resin, and it was found that the grafted polymer produced biodiesel efficiently within a shorter period of time. The conversion ratio of triglycerides in a reaction time of 2 h was 82% with the grafted polymer and 26% with the granular resin.

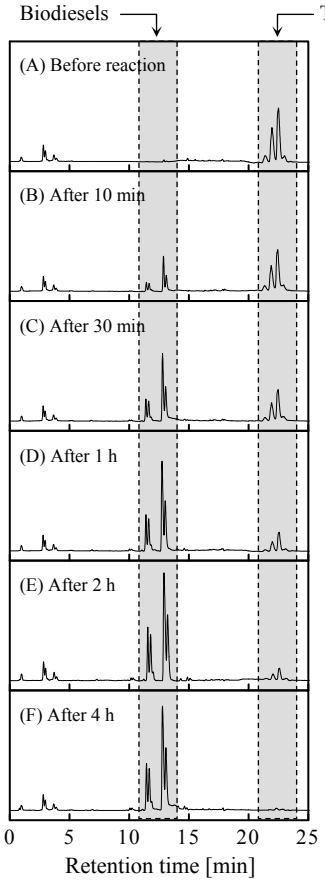

Fig. 1 Biodiesel production using grafted polymer synthesized by radiation-induced graft polymerization.

Transesterification conditions
Reactant: triolein (2.8 g), ethanol (7.2 g), decane (auxiliary solvent) (10.0 g); catalyst: grafted polymer (weight: 0.5 g, capacity: 3.5 mmol-TMA/g-polymer; reaction time: 0 ~ 4 h, reaction temperature: 50 ºC.

Measurement conditions
Sample: biodiesel solution (10 times dilution); injection volume: 5.0 μL; column: octadecyl bonded column (size: 2.1 mm i.d. × 150 mm long, particle size: 5 μm); mobile phase: A: water, B: acetonitrile, C: 2-propanol–hexane (5:4, v/v); flow rate: 0.5 mL/min; linear gradient: 30%A + 70%B (0 min) → 100%B (10 min) → 50%B + 50%C (20 min) → 50%B + 50%C (25 min); column temperature: 40ºC; detection: UV absorption at 205 nm.

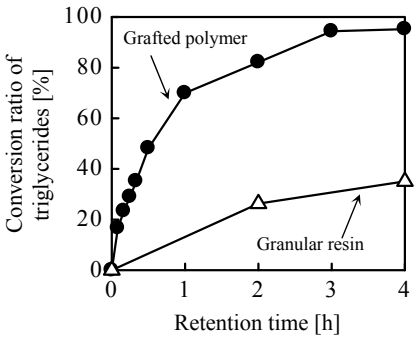

Fig. 2 Comparison of catalytic performance of grafted polymer and granular resin for biodiesel production.

2-02 Development of Zwitterionic Monolithic Column for Hydrophilic Interaction Liquid Chromatography and its Application to the Separation of Catecholamines and Related Compounds

Y. Kamiya [a)], S. Shin [a)], A. Sabarudin [a)], T. Umemura [a)], Y. Ueki [b)] and M. Tamada [b)]

[a)] EcoTopia Science Institute, Nagoya University,
[b)] Environment and Industrial Materials Research Division, QuBS, JAEA

1. Introduction

Monolithic columns have attracted increasing attention and interest in the last decade, due to the low flow-resistance and excellent mass transfer. The authors have so far been researching monolithic columns, and have succeeded in developing organic polymer-based monolithic columns for reversed phase liquid chromatography and ion chromatography. For the purpose of further expansion of column choice, in the present study, the development of a zwitterionic monolithic column for hydrophilic interaction liquid chromatography (HILIC) was attempted by γ-ray induced polymerization, and its separation performance was investigated.

2. Experimental

0.7 g of [2-(Methacryloyloxy) ethyl]dimethyl-(3-sulfopropyl)ammonium hydroxide (SPE) and 0.3 g of ethylene dimethacrylate (EDMA) were dissolved uniformly into 2.0 g of methanol. After degassing with nitrogen for 5 min, the monomer solution was immediately filled into a silicosteel tubing (0.5 mm i.d. × 100 mm long), whose inner surface was pretreated with 3-methacryloxypropyltrimeth-oxysilane to provide anchoring sites for the polymer. The tube was sealed with septa at both ends, and then irradiated at 10 kGy (dose rate: 5 kGy/h) using γ-rays from a ^{60}Co source at 0 °C. After polymerization, the resulting monolithic column was washed with ethanol and with water, and provided as the zwitterionic monolithic column for HILIC.

3. Results and Discussion

The zwitterionic monolithic column possessing adequate separation efficiency and high permeability was prepared by γ-ray induced polymerization of SPE and EDMA in the silicosteel tubing. Observation by scanning electron microscopy revealed that the radiationally-produced zwitterionic monolithic column had a more uniform 3D framework structure than the thermally-produced zwitterionic monolithic column. The radiationally-produced zwitterionic monolith was composed of interconnected homogeneous globules of ~2 μm in diameter and the through-pores of ~2−10 μm. Figure 1 shows the separations of common anions (IO_3^-, NO_2^-, NO_3^-) on the radiationally- and thermally-produced zwitterionic monolithic column. As can be seen in Fig. 1, the column efficiency of the radiationally-produced zwitterionic monolithic column was five times higher than that of thermally-produced zwitterionic monolithic column. This result could be ascribed to the improvement of specific surface area that contributed to separation of sample and the suppression of sample diffusion within the column by the use of more uniform monolith. As a practical application, the separation of urinary catecholamines and related compounds (creatinine; Cre, homovanilic acid; HVA, vanillylmandelic acid; VMA) was attempted by using the zwitterionic monolithic column, and the results are shown in Fig. 2. When laboratory reagents were used as analyses, a series of analyses were baseline separated. Furthermore, three compounds in a human urine sample could be separated and its chromatogram provided good analytical signal and enough sensitivity for peak identification.

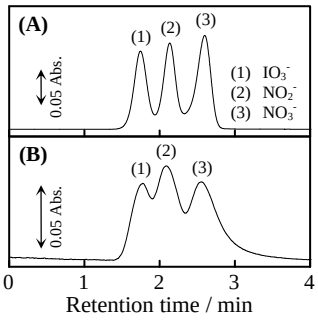

Column size: 0.5 mm i.d. × 100 mm long, mobile phase: water, flow rate: 12 μL/min (corresponding to a linear velocity of 1 mm/s), pressure drop: (A) 0.5 MPa and (B) 0.3 MPa, sample: 10 mM each of IO_3^-, NO_2^- and NO_3^-, sample volume: 0.2 μL, column temperature: 20 °C, UV detection at 210 nm.

Fig. 1 Separations of three anions on (A) radiationally- and (B) thermally-produced zwitterionic monolithic columns.

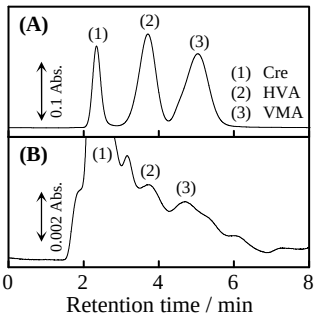

Column size: 0.5 mm i.d. × 100 mm long, mobile phase: acetonitrile–5 mM ammonium acetate (80:20, v/v), flow rate: 12 μL/min (corresponding to a linear velocity of 1 mm/s), pressure drop: 0.3 MPa, sample: (A) 10 mM each of laboratory reagents and (B) human urine sample (5 times dilution), sample volume: 0.2 μL, column temperature: 20 °C, UV detection at 214 nm.

Fig. 2 Separations of catecholamines and related compounds in a human urine.

2-03 Decolorization of Secondary Treated Water from Livestock Urine Waste

M. Takigami [a)], N. Nagasawa [b)], A. Hiroki [b)], N. Kasai [b)], F. Yoshii [b)], M. Tamada [b)], S. Takigami [c)], T. Shibata [d)], Y. Aketagawa [d)] and M. Ozaki [e)]

[a)] Gunma Industry Support Organization, [b)] Environment and Industrial Materials Research Division, QuBS, JAEA, [c)] Gunma University, [d)] Weegl Co., [e)] Maebashi Institute of Technology

Rivers in Gunma Prefecture are the sources of water supply to the Metropolitan area. There are many swine farmers near the rivers and the treated waste water from the farmers comes into the river. There is no regulation of color of the drainage, however, one of the biggest concerns of the farmers is the color of the waste water. They have removed the colored substances using coagulant [1-3)], absorption by activated carbon [4)] or soil [5)], decomposition using ozone or hydrogen peroxide [6)] and decomposition by specific microorganisms [7)]. They are effective, however, an easier and cheaper method is expected to reduce the color in the secondary treated water.

The color is thought to be a metabolite of microorganisms and not easy to be removed. Reducing the color of the waste water is expected by the farmers and local governments. Gunma Prefecture started a project, "Prefecture Collaboration of Regional Entities for the Advancement of Technological Excellence" sponsored by Japan Science and Technology Agency (JST). We collaborate to develop a material and a system to reduce the color in drainage from the farmers.

The colored substances caused by the metabolites of microorganisms are thought to include humic substances such as humic acid and fulvic acid. As acids are expected to be absorbed on anion exchange resins, we decided to develop an absorbent which is cationic, easy to desorb absorbed materials, durable for repeated use, easy to handle and not expensive. To develop an absorbent which fulfills the conditions mentioned above, we targeted a radiation-induced graft polymerization onto fabric materials.

Poly(vinyl alcohol) fabric mesh was irradiated with γ-rays at 60 kGy under reduced pressure and grafted with *N*-[3-(dimethylamino) propyl] acrylamide. The degree of grafting is expressed as a ratio of weight increase (%) by graft polymerization to the initial weight of the fabric mesh. The grafted material with degree of grafting exceeding 100% was used as an absorbent to remove color in secondary treated water. The color was effectively removed by immersing the absorbent in the secondary treated water as shown in Fig. 1. Chemical oxygen demand (COD) of the treated water decreased to 30% of the initial secondary treated water. The absorbent was effective to reduce the chromaticity and COD of the secondary treated water.

The colored materials on the absorbent were easily removed using salt solution. The absorbent after desorption was washed with water and used repeatedly for the decolorization of the secondary treated water. The colored materials were precipitated adding acid to the desorbent (salt solution). The precipitation was collected and used as a fertilizer. Leaves and roots of plants such as rice, spinach and buckwheat grew well using the fertilizer. The desorbent after removing precipitation and adjusting pH to neutral could be used repeatedly.

As mentioned above, a new system which can be attached to the present waste water purification system was proposed to treat secondary treated water from livestock urine waste without discarding usable materials.

Acknowledgment

The authors are grateful for the financial support of JST to perform the research.

References

1) I. Kobayashi, Treatment method of organic matter-containing sewage, 2005-319448A, Japan, Sep. 7, 2004.
2) N. Ozaki, Colored waste water treatment method, 2004-098042A, Japan, Sep., 6, 2002.
3) T. Suzuki, Method for Decolorizing colored waste water, 2003-181491A, Japan, Dec. 14, 2001.
4) Y. Yabuki, et al., Nihon Chikusan Gakkaiho, 78(3) (2007) 339-344.
5) R. Suzuki, et al., Res. Bull. Aichi. Agric. Res. Ctr., 38 (2006) 181-185.
6) H. Lee et al., J. Hazard. Mater. 153 (2008) 1314-1319.
7) Y. Sakamoto, et al., Method for treating colored waste water, H06-39392A, Japan, Apr. 17, 1992.

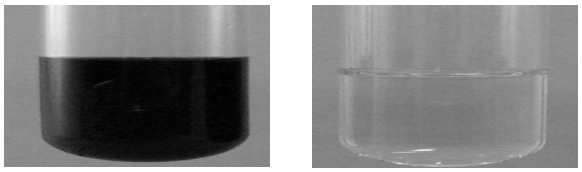

Fig. 1 Secondary treated water (left) and decolorized water using absorbent prepared by radiation-induced graft polymerization (right).

2-04 Modification of Hydroxypropyl Cellulose Hydrogels by Blending Poly(vinyl alcohol)

A. Hiroki [a)], T. Sato [b)], N. Nagasawa [a)] and M. Tamada [a)]

[a)] Environmental and Industrial Materials Research Division, QuBS, JAEA,
[b)] NIPPON CONTACT LENS INC

Hydrogels of polysaccharide derivatives such as carboxymethyl starch and hydroxypropyl cellulose (HPC) are prepared by gamma or electron beam irradiation with their high concentrated aqueous solution [1, 2)]. We have promoted the use of the obtained biodegradable hydrogels in various fields such as medicine and agriculture. However, their application range is limited because the hydrogels are hard to expand and are splintery generally. Polymer blending is most widely used technique to modify the original properties of polymer. Poly(vinyl alcohol) (PVA) exhibits not only excellent physical properties but also biodegradability, which has been applied in a tough wound dressing. In this work, the modification of mechanical properties of HPC hydrogels by blending PVA was investigated.

HPC, which is the grade of 1000-4000 cP, was purchased from Wako Pure Chemical Industries, Ltd., Japan. PVA-117 was supplied by Kuraray Co. Ltd, Japan. HPC/PVA aqueous solutions as a paste state were prepared to 20 wt% of HPC, and the PVA content was adjusted in the range of 0.4 to 4.0 wt%. The HPC/PVA blend samples with 0.5 mm thickness formed by cold pressing were irradiated with electron beam to obtain gel membranes. The irradiations were carried out using Cockcroft Walton electron accelerator at the Takasaki Advanced Radiation Research Institute, JAEA. Gel fraction of the obtained gel membranes was determined gravimetrically by measuring insoluble part after water extraction of sol. The swelling of the blend hydrogels was calculated from weight ratio between the swollen and dried hydrogels. The tensile strength and the elongation at break were measured by expanding HPC/PVA hydrogels cut into strip specimen.

Figure 1 shows the gel fraction of HPC/PVA blend hydrogels as a function of dose. The gel fraction of the blend hydrogels increased sharply up to 10 kGy and reached a constant value at 50 kGy. Increase in the PVA content especially decreased the gel fraction in the dose range up to 50 kGy. Meanwhile, the swelling of the HPC/PVA blend hydrogels decreased with increasing the dose, but increased slightly when the PVA content increased. This is due to the inhibition of the crosslinking reaction occurred by radical quenching of PVA.

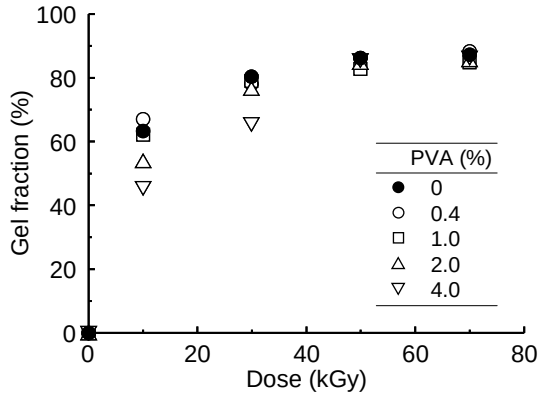

Fig. 1 The gel fraction of HPC/PVA blend hydrogels as a function of dose.

The effect of the PVA content on the elongation at break of the HPC/PVA blend hydrogels obtained at 50 kGy is shown in Fig. 2. The elongation at break of the blend hydrogel showed a minimum (45%) at 0.4 wt% of PVA content, and then, it gradually increased with increasing the PVA content beyond 0.4 wt%. Consequently, the elongation at break of the blend hydrogel with 4 wt% PVA reached 125%, which exhibited about 1.8 times larger than that of the pure HPC hydrogel. This would be due to the formation of network structure crosslinked between HPC and PVA.

From the above mentioned results, it was found that the HPC hydrogels with desired mechanical properties were obtained by the combination of PVA blending with the radiation crosslinking technique. Therefore, the HPC/PVA blend hydrogels could be used as a material to touch directly by hand.

References

1) F. Yoshii et al., Nucl. Instrum Meth. B **208** (2003) 320-324.
2) R. A. Wach et al., Macromol. Mater. Eng. **287** (2002) 285-295.

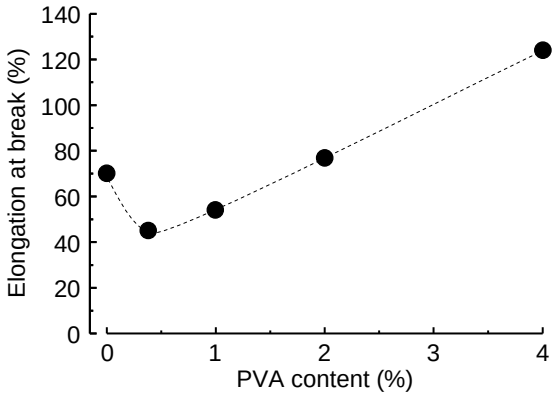

Fig. 2 The Effect of the PVA content on the elongation at break of the HPC/PVA blend hydrogels obtained at 50 kGy.

2-05 Effect of Grafting Conditions on Radiation-induced Graft Polymerization

Y. Ueki [a], N. C. Dafader [b], N. Seko [a] and M. Tamada [a]

[a] Environment and Industrial Materials Research Division, QuBS, JAEA,
[b] Nuclear and Radiation Chemistry Division, Institute of Nuclear Science and Technology, Bangladesh Atomic Energy Commission

1. Introduction

Radiation-induced graft polymerization, one of the surface modification techniques of polymer materials, has recently been attracting attention as a refined artifice because the adsorption rate of a grafted polymer is 10 - 100 times higher than that of a commercial granular resin. However, the radiation-induced graft polymerization is not very popular because this technique requires troublesome procedure and some skill. The objective of this study is to investigate the effect of grafting conditions, especially oxygen, on radiation-induced graft polymerization for the establishment of simplified grafting procedure.

2. Experimental

The nonwoven polyethylene fabric was irradiated with an electron beam up to 100 kGy. The irradiated nonwoven fabric was contacted with 5 wt% emulsion, which was composed of glycidyl methacrylate, polysorbate 20 and deionized water, in a deaerated glass ampoule at 40 °C. The degree of grafting (Dg) was evaluated by the increased weight after grafting.

3. Results and Discussion

Typically, to achieve higher Dg, the irradiation process was carried out under ideal condition (oxygen-free condition) allowing little or no deactivation of radicals that were generated by irradiation of electron beam. In order to protect the created radicals from deactivation caused by oxygen in the air, the trunk polymer was packed into a hermetically-sealed container such as a polyethylene bag, and then the air in the sample bag was substituted with inert gases such as nitrogen gas. Firstly, the effect of air in sample bag on the Dg was investigated. In this experiment, volume ratio of trunk polymer to inner volume of the polyethylene bag was controlled within a range from 1 : 1 (polymer : bag) to 1 : 100, and the inside of sample bags was filled with air. After grafting for 4 h, the Dg of 100 kGy reached 501, 505, 496, 487, and 494% at polymer/bag volume ratio of 1 : 1, 1 : 2, 1 : 5, 1: 10, 1 : 20, and 1 : 100, respectively. These results showod that air in the sample bag had little effect on the Dg, because irradiation time was very short and the radical deactivation by oxygen didn't happen very often during irradiation process.

It is also well-known that dissolved oxygen has a significant influence on the Dg, and therefore the effect of dissolved oxygen concentration in emulsion on the Dg was investigated. The dissolved oxygen concentration was controlled by passing nitrogen gas in emulsion before grafting and the Dg after grafting for 3 h relative to the dissolved oxygen concentration is plotted as in Fig. 1. In this experiment, the grafting reaction was tested under two conditions; vacuum and air atmospheric condition. As seen in Fig. 1, the Dg gradually increased with reduction of initial dissolved oxygen concentration in emulsion as expected and additionally the Dg of the vacuum condition was higher than that of the air atmospheric condition. The atmospheric effect results beam differences of oxygen concentration in the emulsion that participated in the actual graft polymerization. In other words, these were because, under the vacuum condition, the enormous proportion of dissolved oxygen in emulsion was spontaneously and immediately released into vacuum vapor phase, and consequently the deactivation of radicals was prevented. Under the vacuum condition, the dissolved oxygen concentration in emulsion was reduced from 8.3 to 1.5 mg/L within only one minute. On the other hands, the converse phenomena occurred under the air atmospheric condition. Under the air atmospheric condition, when the initial dissolved oxygen concentration became less than 1 mg/L, the Dg of 50 kGy reached about 100% and that value was enough to use as a metal adsorbent precursor. Based on the above results, it was found that the graft polymerization under air atmospheric condition could be achieved in the following conditions; the dissolved oxygen concentration in emulsion before grafting was 1.0 mg/L or less, and the irradiation dose was more than 50 kGy.

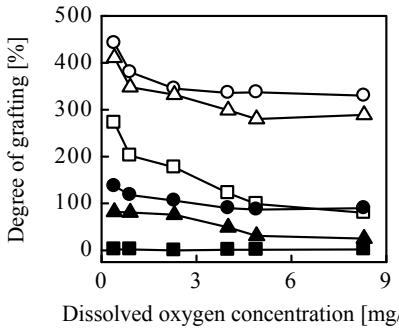

Fig. 1 Effect of dissolved oxygen concentration in emulsion before grafting on Dg. Polymerization condition:
○ dose of 100 kGy, grafting at vacuum atmosphere;
● dose of 100 kGy, grafting at air atmosphere;
△ dose of 50 kGy, grafting at vacuum atmosphere;
▲ dose of 50 kGy, grafting at air atmosphere;
□ dose of 20 kGy, grafting at vacuum atmosphere;
■ dose of 20 kGy, grafting at air atmosphere.

2-06 The Recovery of Precious Metals Using Biomass Adsorbents

D. Parajuli, N. Seko and K. Hirota

Environmental and Industrial Materials Research Division, QuBS, JAEA

1. Introduction

The recovery of precious metals from electric and electronic wastes, urban mine, is very important for the elemental strategy of Japan because we don't have few mineral resources. Conventional methods for recovery of precious metals from urban mine are solvent extraction and use of ion exchange resins. However, these methods have disadvantages of huge chemical and energy requirement, lack of required selectivity, and costly [1]. Biomass adsorbents is expected to be superior materials for recovering precious metals with lower capital cost and higher efficiency [2]. In the present work, lignophenol modified with ethylenediamine by electron-beam irradiation was uses as biomass adsorbents. Their performance for the recovery of precious metals has been studied and the results are compared with that of chemically modified derivative.

2. Experimental

2-1 Synthesis of Biomass Adsorbents

Lignophenol was extracted from cedar wood powder[3] and treated with paraformaldehyde to obtain crosslinked lignophenol gel (CLP). In order to obtain ethylenediamine modified crosslinked lignophenol, the CLP matrix was irradiated by electron beam at a dose of 20 kGy and then directly treated with ethylenediamine in dimethylsolfoxide (DMSO) as shown in Scheme 1. It is named as EN-CLP(EB). Chemically modified CLP with ethylenediamine group (EN-CLP(Chem)) was also prepared by following the same scheme without pre-irradiation for comparison of adsorption performance with EN-CLP(EB).

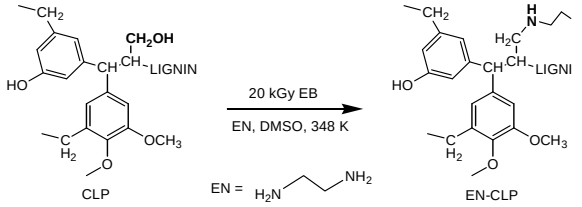

Scheme 1 Preparation of EN-CLP using electron beam.

2-2 Adsorption Test

The adsorption performence of the EN-CLP(EB), EN-CLP(Chem) was tested batchwise by mixing 5 mL of 0.5 mM different metal chloride solutions at various hydrochloric acid concentrations with 10 mg sorbents. The sorbents at 10 mg in the sample solution was continuously shaked for 24 h at 303 K in a thermostatic shaking incubator. After filtration, the amount adsorbed was evaluated by measuring the residual metal concentration in the filtrate solution. Similarly, the adsorption isotherm was examined to evaluate the maximum loading capacities of the sorbents for Au(III), Pt(IV), and Pd(II).

3. Results and Discussion

The adsorption behavior of various metals on EN-CLP(EB) modified by electron-beam irradiation at varying hydrochloric acid concentration in Fig. 1. The adsorption of Au(III) and Pt(IV) was more than 80 % even at 5 M hydrochloric acid medium. However, Pd(II) adsorption was decreased with an increase in acid concentration. Interestingly, the adsorption of other metal ions is near around zero. It was found that the sorbent of EN-CLP(EB) can be used for adsorption of gold and platinum even in highly acidic condition.

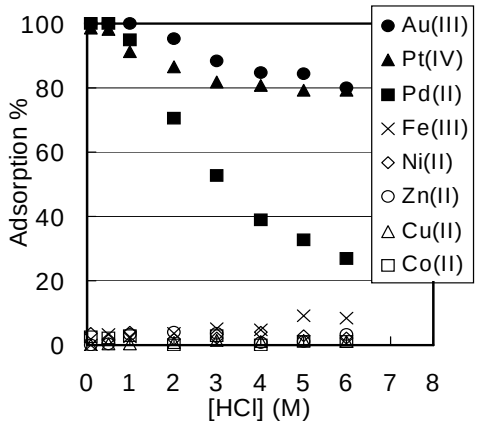

Fig. 1 Adsorption behavior of EN-CLP(EB) for various metals in hydrochloric acid. Sorbent: 10 mg, solution: 5 mL of 0.5 mM each metal.

The maximum loading capacity for Au(III), Pt(IV), and Pd(II) were found to be 3.1, 2.3, and 0.85 mol/kg for EN-CLP(EB). These capacity was higher than those of 2.4, 1.9, and 0.42 mol/kg for EN-CLP(Chem). These differences suggest that the degree of modification can be enhanced by the application of electron beam.

References

1) Y. Goksungur et al., Bioresource Technol. 96 (2005) 103.
2) C. Mack et al., Biotechnol. Adv. 25 (2007) 264.
3) M. Funaoka, Polymer International, 47 (1998) 277.

2-07 Surface Modification of Vulcanized Rubber by Radiation Co-grafting

N. Mizote [a], A. Katakai [b] and M. Tamada [b]

[a] Mitsuba Co. Ltd.,
[b] Environmental and Industrial Materials Research Division, QuBS, JAEA

In this study, hydrophilic monomer, 2-hydroxyethyl methacrylate (HEMA), and hydrophobic monomer, 3-(Methacryloyloxy) propyltris (trimethylsiloxy) silane (MPTS), were co-grafted on vulcanized rubber surface by simultaneous electron beam irradiation. Monomer solution was prepared by mixing of HEMA and MPTS. Composition of graft layer was investigated by ATR-FTIR and SEM-EDX. As a result, it was found that graft polymer of MPTS was eccentrically located in the near-surface region in the case that MPTS concentration of monomer solution was about 90 weight percent.

加硫ゴム製品は摩擦、粘着性、耐摩耗性等の向上を目的として塩素化処理やコーティングなどの表面処理が行われている。しかしこれらの表面処理は、塩素による環境負荷やコーティング剥離による耐久性の問題を有するため、新しい表面改質が求められている。我々は電子線照射グラフト重合法による加硫ゴム表面改質を検討している。本研究では、親水性モノマーの HEMA と疎水性モノマーMPTS の電子線同時照射共グラフトによるゴム表面改質特性について評価した。

ゴム基材として、カーボンブラックを配合した厚さ 2 mm の架橋 EPDM ゴム用いた。HEMA と MPTS を所定の割合で混合したモノマー溶液を用い、加速エネルギー2 MeV、電流値 1 mA、照射線量 7 kGy の照射条件で電子線同時照射グラフト重合を行った。グラフト重合した基材表面の組成を、ATR-FTIR 法で得られた MPTS グラフトポリマーの Si-C 吸収(845 cm^{-1})と EPDM の C-H_3 吸収（1375 cm^{-1}）の吸光度比により評価した。表面改質層の深さ方向の分布は、断面の SEM-EDX で測定した Si 元素分布により評価した。

Fig. 1 にモノマー溶液の MPTS 濃度と、ATR-FTIR で求めた MPTS グラフトポリマー由来の Si-C 吸光度比の関係を示す。Si-C 吸光度比は MPTS 濃度に対し直線的に増加せず、MPTS 濃度 90 wt%付近で極大ピークを示した。Fig. 2 にモノマー溶液の MPTS 濃度と SEM-EDX により求めたグラフト層深さの関係を示す。MPTS 濃度の増加に伴いグラフト層深さはおおむね一様な増大を示しており、ATR-FTIR で得られた結果のような MPTS 高濃度域での特異的な変化は見られなかった。MPTS 高濃度領域での Si 元素デプスプロファイルの比較を Fig. 3 に示す。MPTS 100 wt%では表面から内部へ緩やかに Si 検出強度が低下していくのに対し、HEMA が少量添加された MPTS 90 wt%、95 wt%では表面から 10 μm 程度のごく浅い領域に強いピーク状の Si 強度プロファイルが見られた。この結果は、MPTS 100%よりも HEMA が少量含まれたほうがより表面近傍に MPTS が偏在することを示しており、ATR-FTIR の結果と一致する。

これまでの研究で、HEMA グラフト層は 10 μm 程度の厚さであることが確認されており、MPTS は HEMA グラフト層に選択的に取り込まれると考えられる。

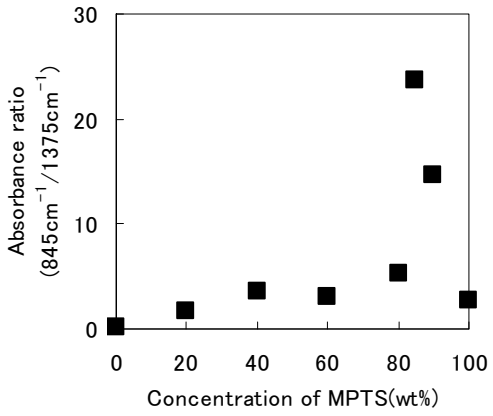

Fig. 1 Relationship between absorbance ratio of Si-C and MPTS concentration.

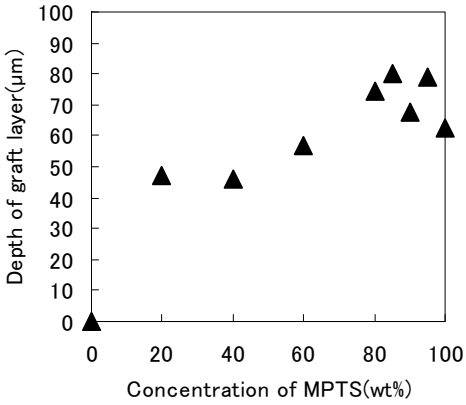

Fig. 2 Relationship between depth of graft layer and MPTS concentration.

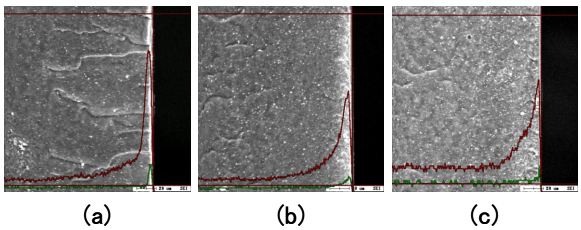

Fig. 3 Cross-sectional SEM micrograph of graft layer and depth profile of Si: (a) 90 wt% MPTS, (b) 95 wt% MPTS, (c) 100 wt% MPTS.

2-08 ESR Study on Carboxymethyl Chitosan Radicals in Aqueous Solution

S. Saiki [a)], N. Nagasawa [a)], A. Hiroki [a)], N. Morishita [a)], M. Tamada [a)], H. Kudo [b)] and Y. Katsumura [b)]

[a)] Environment and Industrial Materials Research Division, QuBS, JAEA,
[b)] Graduate School of Engineering, The University of Tokyo

Carboxymethylated polysaccharides such as carboxymethyl cellulose, carboxymethyl starch and carboxymethyl chitosan (CMCTS, as shown in Fig. 1) at highly concentrated aqueous solution undergo crosslinking reactions by ionizing irradiation, though polysaccharides are generally classified to radiation-degradation polymer[1)]. Radiation-induced crosslinking and degradation of polymer aqueous solution are generally caused by OH radical derived from water radiolysis. In order to understand the radiation-induced reaction mechanism in carboxymethyl polysaccharide aqueous solution, it is important that the initially-formed radical by the hydrogen abstraction of OH radical is identified. In this study, to identify CMCTS radical produced by reaction with OH radical in an aqueous solution, ESR spectra of CMCTS radical were observed using UV photolysis of H_2O_2.

ESR measurements were carried out at room temperature with an X-band ESR spectrometer (JES-TE200, JEOL Ltd.). Ten mM CMCTS/10 mM H_2O_2 aqueous solution was prepared at room temperature as a sample solution. The solution was bubbled with N_2 gas in a continuous flow system through a flat cell set in the ESR cavity by a peristaltic pump at a rate of 0.2 mL/min (Fig. 2). Measurements were taken continuously during irradiation with ultra high mercury lamp (USH-250D, 350 W, Ushio Inc.).

ESR spectrum of CMCTS radicals were successfully observed as shown in Fig. 3. As it can be seen, there are large split and small split, and the left-and-right spectra are not of the same shape. It was assumed that a number of radicals were overlapped in this spectrum.

To assign the radical site, we should consider the candidate of radical sites from a point of view of chemical structure. Considering the hydrogen abstraction of OH radical, radicals are possibly located on carbon atom of glucopyranose rings or of carboxymethyl group or of acetoamido group, or on nitrogen atom of amino group or of acetoamido group. Comparing the splitting pattern and width of the experimental spectra with those of the radicals which have similar chemical structure around radicals with these candidates, the case of radicals on nitrogen atom and on carbon atom of glucopyranose rings and of acetoamido group were not coincident with experimental results. Therefore, it was speculated that those radicals were not included in experimental results. On the other hand, as for radicals on carboxymethyl groups, the splitting pattern and width of the similar radical, benzyl ethyl ether radicals, were almost coincident with experimental results.

In conclusion, experimental ESR spectrum of CMCTS radicals was identified as radicals on carboxymethyl groups.

Reference

1) F. Yoshii et al., Nucl. Instrum. Meth. Phys. Res. B 208 (2003) 320-324.

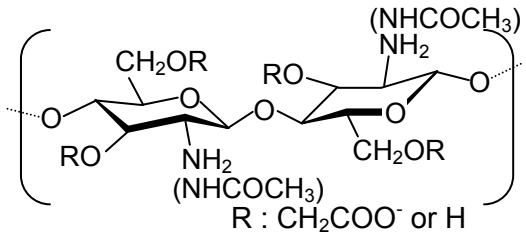

Fig. 1 Structure of carboxymethyl chitosan.

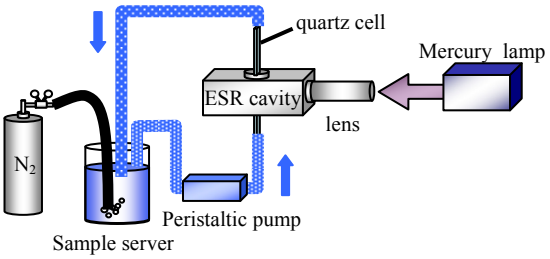

Fig. 2 ESR measurement system.

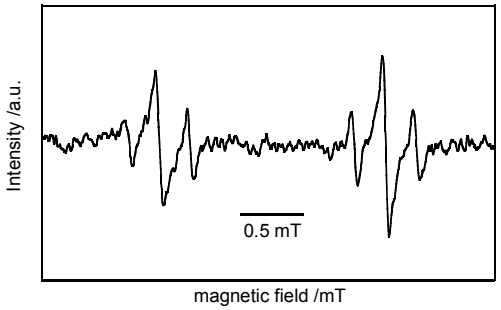

Fig. 3 ESR spectra of CMCTS radicals.

2-09 Decomposition of Persistent Pharmaceuticals by Ionizing Radiation

A. Kimura, M. Taguchi and K. Hirota

Environment and Industrial Materials Research Division, QuBS, JAEA

Introduction

Many kind of water pollutants have been widely spread in the water environment. These chemicals such as halogenated organic compounds (dioxin and PCBs), endocrine disruptors (natural hormones and akylphenols), and heavy metals were persistent, high toxic and have a low biodegradability. The risk evaluation of these pharmaceuticals and personal care products are studied recently [1]. Some pharmaceuticals would give ill effects on human and aquatic animals because of its chronic and reproduction toxicities, and the concentrations of them in the water environment increased gradually because of population growth and the diversification of advanced medical worldwide. However, it is difficult to manage the environment risk of the pharmaceuticals having great benefits for human life, and the development of direct removal methods are considered for them.

The pharmaceuticals have been also detected at the downstream of water treatment facilities, indicating that the activated sludge system could not decompose them completely. Persistent organic pollutants in wastewater could be effectively decomposed by ionizing radiation, which produces reactive species, for example, hydroxyl radicals homogeneously in water [2]. The purpose of this work is to treat the pharmaceuticals in combination of ionizing radiation with activated sludge.

Experimental

Oseltamivir, aspirin, ibuprofen, carbamazepine, mefenamic acid, ketoprofen, chlofibric acid, and dichlofenac were selected as experimental samples because they were reported to be consumed a lot worldwide and detected in the water environment [1]. Each pharmaceutical was dissolved at 10 μmol dm^{-3} in wastewater at pH value of 7.45 and the amount of Total Organic Carbon at about 0.05 g dm^{-3}, which was collected at an influent of a water treatment facility. Activated sludge solution was supplied from the wastewater treatment plant and used for the biodegradation of the pharmaceuticals. This sludge was acclimated by adding 1 g/dm^{-3} of glucose and/or granulated sugar of 500 dm^{-3}/day for 2 days. The sludge solution of 50 dm^{-3} was mixed with the equal amount of the pharmaceutical solution, and stirred at 100 rpm with aeration at 100 mL/min for 8 hours, which is the average aeration time of real wastewater treatment plant with activated sludge system. The γ-ray irradiation of the sludge and pharmaceutical solution at 5 μmol dm^{-3} was carried out at 298 K using ^{60}Co γ-ray sources. Each pharmaceutical solution after biodegradation and γ-ray irradiations was analyzed by HPLC (High Perfomemance liquid chlomatography).

Results and Discussion

The pharmaceuticals were treated first only by the activated sludge. Oseltamivir as aliphatic pharmaceutical was easy to be decomposed and eliminated at 2 hours. Decomposition yield of aspirin and ibprofen was obtained more than 90% for 2 and 4 hours, respectively. On the other hand, carbamazepine, ketoprofen, and mefenamic acid were not decomposed for 8 hours completely. Decomposition yield of chlofibric acid and dichlorfenac was obtained at about 20% after the biodegradation for 8 hours. Additional water treatment methods, therefore, would be required to decompose these persistent pharmaceuticals completely.

Decomposition of carbamazepine, ketoprofen, mefenamic acid in wastewater was investigated by γ-ray irradiation as shown in Fig. 1a. Concentration of carbamazepine was decreased exponentially as a function of dose and was almost zero up to 1 kGy, while mefenamic acid and ketoprofen were decomposed at 2 kGy. Electron-rich carbamazepine, substituted azepine group, would be easily decomposed by hydroxyl radicals. The decomposition yields of ketoprofen and mefenamic acid, which have carbonyl and carboxy groups as electron acceptors, were lower than that of carbamazepine. Concentration of chlofibric acid and dichlofenac decreased as a function of dose, and were eliminated at 1 kGy as shown in Fig. 1b. As the phenyl group of dichlofenac is substituted not only two chlorine groups as a electron accepter but also amino groups as an electron donor, decomposition curve of dichlofenac would be almost the same with that of chlofibric acid. Persistent pharmaceuticals which were difficult to treat by the activated sludge system could be decomposed by the ionizing radiation method.

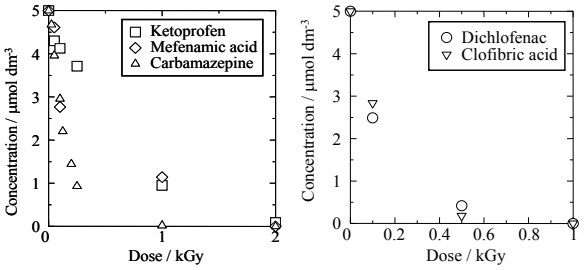

Fig. 1 Decomposition of persistent pharmaceuticals in wastewater by γ-ray irradiation. a) diaromatics (left), b) chlorinated compounds (right).

References

1) K. Fent et al., Aquatic Toxicology 76 (2006) 122-159.
2) A. Kimura et al., Radiat. Phys. Chem. 76 (2007) 699-706.

This is a blank page.

3. Biotechnology and Medical Application

3-01 Damage Spectrum of DNA Strand Break Termini Induced by $^{4}He^{2+}$ Ion Beam Compared with that by ^{60}Co γ-rays ····· 57
K. Akamatsu and K. Saito
3-02 Mutagenic effects of He ion particles in *Escherichia coli* ····· 58
T. Suzaka, H. Tauchi, N. Shikazono, K. Fujii and A. Yokoya
3-03 Mutational Effect of Gamma-rays and Carbon Ion Beams on *Arabidopsis* Seedlings····· 59
R. Yoshihara, Y. Hase, S. Nozawa, A. N. Sakamoto and I. Narumi
3-04 Functional Analysis of Flavonoid Accumulation Genes of *Arabidopsis thaliana* ····· 60
S. Kitamura, F. Matsuda, T. Tohge, K. Yonekura-Sakakibara, M. Yamazaki, K. Saito and I. Narumi
3-05 Ion Beam Irradiation with Rice Seeds for the Mutation Breeding Project of the Forum for Nuclear Cooperation in Asia (FNCA) ····· 61
A. Tanaka, S. Nozawa, Y. Hase, I. Narumi, H. Ishikawa and A. Koike
3-06 Generation New Ornamental Plant Varieties Using Ion Beams····· 62
A. H. Affrida, A. Zaiton, A. M. Salahbiah, S. Shakinah, R. Yoshihara, I. Narumi, Y. Hase and Y. Oono
3-07 Development of New Gunma Original Variety of Chrysanthemum by Ion Beam Irradiation ····· 63
T. Okada, H. Ikeda, Y. Oono, R. Yoshihara, Y. Hase and I. Narumi
3-08 Stability of Flower-colour Mutants of Delphinium 'Momoka' After Propagation by Tissue Culture ····· 64
S. Kitamura, S. Chinone, K. Tokuhiro, K. Nakatsubo, S. Nozawa, Y. Hase and I. Narumi
3-09 Red–purple Flower due to Delphinidin 3,5-diglucoside, a Novel Pigment for *Cyclamen* spp., Generated by Ion-beam Irradiation ····· 65
E. Kondo, M. Nakayama, N. Kameari, N. Tanikawa, Y. Morita, Y. Akita, Y. Hase, A. Tanaka and H. Ishizaka
3-10 Effects of Heavy Ion beam Irradiation in Citrus····· 66
Y. Matsuo, Y. Hase, S. Nozawa, R. Yoshihara and I. Narumi
3-11 Effect of Ion Beam Irradiation for *Asclepias* Species ····· 67
N. Kobayashi, S. Sasaki, K. Tasaki, A. Nakatsuka, S. Nozawa, Y. Hase and I. Narumi
3-12 Producing New Gene Resources in Chrysanthemum Using Ion-beam Irradiation ····· 68
I. Asami, T. Tsuji, T. Hasegawa, S. Fukuta, S. Kuroyanagi, Y. Hase, R. Yoshihara and I. Narumi
3-13 Ion Beam Breeding of Sugarcane Cultivar "Ni17"····· 69
Y. Takenoshita, J. Nagai, T. Nagatani, M. Ooe, Y. Hase, A. Tanaka and I. Narumi

3-14 Production of Soybean Mutants with Pale-Green-Leaf Phenotype by Ion Beam Irradiation ····· 70
S. Arase, J. Abe, S. Nozawa, Y. Hase, I. Narumi and A. Kanazawa
3-15 Induction of Fusarium Wilt Resistant by Ion Beam Irradiation in Strawberry (*Fragaria × ananassa)* Leaf Explants ····· 71
M. Yotoriyama, J. Takano, K. Namai, R. Yoshihara, S. Nozawa, Y. Hase and I. Narumi
3-16 Assessment of Irradiation Treatments on a Salt-tolerant Arabidopsis, Zu-0 and *Thellungiella* ····· 72
T. Taji, A. Horiguchi, A. Ikeda, C. Nakajima, Y. Sakata, R. Yoshihara, S. Nozawa, Y. Hase and I. Narumi
3-17 Effects of Ion-beam Irradiation on Germination and Growth of Seedlings of Red Pepper 'Hirosaki zairai' ····· 73
M. Tomikawa, T. Maeda, K. Honda, K. Saga, R. Ishikawa, Y. Akita, R. Yoshihara, S. Nozawa and I. Narumi
3-18 Effect of Different LET Radiations on Root Growth of *Arabidopsis thaliana* ··· 74
R. Yoshihara, S. Nozawa, H. Saika, M. Teranishi, S. Toki, J. Hidema and A. N. Sakamoto
3-19 Phenotypic Improvement of *Bradyrhizobium japonicum* USDA 110 into a High Temperature Tolerant Strain in terms of Ion-beam Microbial Mutation-breeding Technology ····· 75
K. Takeda, K. Tejima, K. Satoh, I. Narumi and T. Yokoyama
3-20 Fungicide Tolerant Mutation of Entomopathogenic Fungi Induced by Carbon Ion Beams ····· 76
T. Saito, K. Satoh and I. Narumi
3-21 Improvement of Endophytic Bacteria Using Ion Beams ····· 77
M. Aino, K. Satoh and I. Narumi
3-22 FACS-based Screening of Yeast Strain Highly Expressing Cellulase····· 78
K. Ninomiya, H. Soda, K. Satoh, I. Narumi and N. Shimizu
3-23 Molecular Analysis of Carbon Ion Induced Mutations in Yeast *Saccharomyces cerevisiae* Cells ····· 79
K. Shimizu, Y. Matuo, Y. Izumi, Y. Hase, S. Nozawa, A. N. Sakamoto and I. Narumi
3-24 Lethal Effects of Different LET Radiations in *Deinococcus radiodurans* ····· 80
K. Satoh, K. Tejima and I. Narumi
3-25 Analysis of Mutation Induced by Ion Beams and Gamma-Rays in Vacuum-dried Conidia of *Aspergillus oryzae* ····· 81
K. Ito, Y. Hanya, K. Satoh and I. Narumi
3-26 Ion Beam Breeding of "Sake Yeast" and Test Brewing ····· 82
T. Masubuchi, O. Kamiyama, K. Satoh, Y. Hase and I. Narumi
3-27 The Effect of γ-Sterilization of Carrier Materials on the Shelf Life of Biofertilizer ····· 83
K. Tejima, T. Yokoyama, K. Satoh and I. Narumi

3-28 Electron Spin Relaxation Behaviors of Radicals Induced in Gamma-irradiated Food ····· 84
M. Ukai, H. Kameya, H. Nakamura, M. Kikuchi and Y. Kobayashi
3-29 Dose-dependency of Electron Spin Relaxations in Irradiated Fresh Mangoes ··· 85
M. Kikuchi, T. Sakashita, T. Funayama, M. Ukai,
Y. Shimoyama and Y. Kobayashi
3-30 Target Irradiation of Individual Cells Using Focusing Heavy-Ion Microbeam of JAEA-Takasaki ····· 86
T. Funayama, T. Sakashita, Y. Yokota and Y. Kobayashi
3-31 A Quantitative Study of DNA Double-strand Breaks Induced by Heavy-ion Beams: a Problem on the Conventional DNA-sample Preparation ·· 87
Y. Yokota, T. Funayama, Y. Mutou, T. Sakashita, M. Suzuki,
M. Kikuchi and Y. Kobayashi
3-32 Carbon-ion Microbeam Induces Behavioral Changes in the Salt Chemotaxis Learning of *C. elegans* ····· 88
T. Sakashita, M. Suzuki, Y. Mutou, Y. Yokota, T. Funayama, N. Hamada,
K. Fukamoto and Y. Kobayashi
3-33 Combination Effect of the Heat Shock Protein Inhibitor, 17-AAG, with Carbon-beam and X-ray Irradiation for Squamous Cell Carcinomas *in Vitro* ····· 89
A. Musha, Y. Yoshida, T. Nonaka, T. Takahashi, T. Funayama,
Y. Kobayashi, H. Ishikawa, H. Kawamura, K. Ando, S. Yokoo and T. Nakano
3-34 Biological Effects of Carbon Ions on Glioblastoma Cell Lines ····· 90
Y. Yoshida, S. Ishiuchi, T. Funayama, Y. Kobayashi and T. Nakano
3-35 Analysis of Molecular Mechanisms for Radiation-induced Bystander Effects Using Heavy Ion Microbeams ····· 91
H. Matsumoto, M. Hatashita, M. Tomita, K. Otsuka, T. Funayama,
T. Sakashita and Y. Kobayashi
3-36 Difference in Bystander Lethal Effect in Human Tumor Cell Lines Depending on *p53* -gene Status Induced by Carbon-ion Microbeams ····· 92
M. Suzuki, T. Funayama, Y. Yokota, Y. Mutou, C. Tsuruoka,
Y. Furusawa and Y. Kobayashi
3-37 Heavy-ion Irradiation Induces Autophagy in Irradiated C2C12 Myoblasts and Their Bystander Cells ····· 93
M. Hino, N. Hamada, Y. Tajika, T. Funayama, Y. Morimura, T. Sakashita,
Y. Yokota, K. Fukamoto, Y. Mutou, Y. Kobayashi and H. Yorifuji
3-38 Analysis of Lethal Effect Mediated by Low Dose Irradiation Induced-Secreted factors in Glioma cells ····· 94
S. Wada, A. Baden, E. Nakagawa, T. Kakizaki, T. Funayama, T. Sakashita,
Y. Kobayashi and N. Ito
3-39 Ion Beam Irradiation Has Different Influences on the Expression of p53 in Cultured Human Retinal Vascular Endothelial Cells Exposed to L-dopa among ^{20}Ne, ^{12}C and ^{4}He ····· 95
K. Akeo, T. Funayama, N. Hamada, Y. Kobayashi and Y. Akeo

3-40 Irradiation with Carbon Ion Beams Induces Apoptosis, Autophagy, and Cellular Senescence in a Human Glioma-derived Cell Line ····· 96
A. Oue, N. Shimizu, N. Hamada, S. Wada, A. Tanaka, M. Shinagawa, T. Ohtsuki, T. Mori, M. N. Saha, A. S. Hoque, S. Islam, T. Funayama, Y. Kobayashi and H. Hoshino
3-41 Effects of Heavy Ion Irradiation on the Precursor Hemocytes of the Silkworm, *Bombyx mori* ····· 97
S. Kobayashi, K. Fukamoto, K. Kiguchi, T. Funayama, Y. Yokota, T. Sakashita, Y. Kobayashi and K. Shirai
3-42 Expression of Two Gelsolins in Response to Heavy-ions Irradiation and Desiccation in the Sleeping Chironomid *Polypedilum vanderplanki* ····· 98
O. Gusev, T. Kikawada, T. Sakashita, T. Funayama, Y. Kobayashi and T. Okuda
3-43 Nuclear Localization of a FOXO Transcriptional Factor DAF-16 in *C. elegans,* which is Required in a Response to IR Irradiation ····· 99
T. Kimura, T. Takanami, T. Sakashita, Y. Kobayashi and A. Higashitani
3-44 Analysis of Bystander Cell Signaling Pathway Activated by Heavy Ion-Microbeam ····· 100
M. Tomita, H. Matsumoto, K. Otsuka, M. Maeda, T. Funayama, Y. Yokota, Y. Mutou, T. Sakashita and Y. Kobayashi
3-45 Carbon Translocation in a Whole Plant Body by Using Positron Emitting Tracer Imaging System (PETIS) and Carbon-11-labeled Carbon Dioxide ($^{11}CO_2$) ····· 101
N. Kawachi, N. Suzui, S. Ishii, S. Ito, N. S. Ishioka, H. Yamazaki, A. Iwasaki, K. Ogawa and S. Fujimaki
3-46 Quantitative Evaluation of Rice Varieties in Cadmium Uptake Activities for Remediation of Cadmium-contaminated Soil ····· 102
S. Ishikawa, N. Suzui, S. Ito, S. Ishii, H. Yamazaki, N. Kawachi, N. S. Ishioka and S. Fujimaki
3-47 Quantitative Study for Nitrogen Fixation in Intact Soybean Plant from PETIS Imaging ····· 103
S. Ishii, N. Suzui, S. Ito, N. S. Ishioka, N. Kawachi, N. Ohtake, T. Ohyama and S. Fujimaki
3-48 Visualization of ^{107}Cd Accumulation in Oilseed Rape Plants Treated with Glutathione ····· 104
S. Nakamura, N. Suzui, S. Ito, N. Kawachi, N. S. Ishioka, H. Rai, H. Hattori, M. Chino and S. Fujimaki
3-49 Noninvasive Imaging of Zinc Dynamics in an Intact Plant Using the Positron-emitting Tracer ^{65}Zn ····· 105
N. Suzui, H. Yamazaki, N. Kawachi, S. Ishii, N. S. Ishioka and S. Fujimaki
3-50 Uniformity Measurement of Newly Installed Camera Heads of Positron-emitting Tracer Imaging System ····· 106
N. Kawachi, N. Suzui, S. Ishii, H. Yamazaki and S. Fujimaki

3-51 PET Studies of Neuroendcrine Tumors by Using ^{76}Br-*m* -Bromobenzylguanidine (^{76}Br-MBBG)・・・

This is a blank page.

3-01 Damage Spectrum of DNA Strand Break Termini Induced by $^{4}He^{2+}$ Ion Beam Compared with that by ^{60}Co γ-rays

K. Akamatsu and K. Saito

Division of Environment and Radiation Sciences, NSED, JAEA

1. Introduction

Chemical structures of DNA lesions and their distribution are quite important to clarify following biological repair procedures. In case of ionizing radiations, especially, it is expected that three-dimensional distribution of DNA damages is diversified as well as their chemical structures, and the diversity makes investigations of physicochemical processes in radiation effects difficult. In fact, double-strand breaks produced by high linear energy transfer (LET) alpha particles are more difficult to rejoin in living cells than those produced by low LET ^{137}Cs γ-rays[1]. So far, we have investigated difference of DNA damage spectrum between radiations using existing and/or newly developed analytical method[2]. Here, we reveal the results of strand break termini induced by $^{4}He^{2+}$ (He) ion beam in comparison with that by ^{60}Co γ-rays (7cell, Takasaki). The ion beam used was obtained from TC in TIARA.

2. Experiments

Sample preparation and irradiation

Linear formed pUC19 plasmid DNA digested by Sma I, (pUC19/Sma I) was used. pUC19/Sma I aqueous solution was mounted on a silicon plate and dried thoroughly in vacuum under P_2O_5. For γ-irradiation, the dried DNA sample on a plate was put into a glass tube sealed in vacuum to achieve secondary electron equilibrium. Each sample was irradiated at a dose (dose rate) of 40 (0.333), 100 (0.833), 400 (3.33), 900 (7.50), and 1,800 kGy (15.0 kGy/h) at r.t., respectively. For He ion beam, the DNA- mounted plate was fixed in a cylindrical chamber (39 mmϕ, height: 22 mm) with a Kapton® window (8 μm) under argon gas. Each sample was irradiated with ~ 67 keV/μm of the beam, which was controlled using a depth-tunable cell irradiation equipment, was irradiated at doses of 50, 100, 200, 400, and

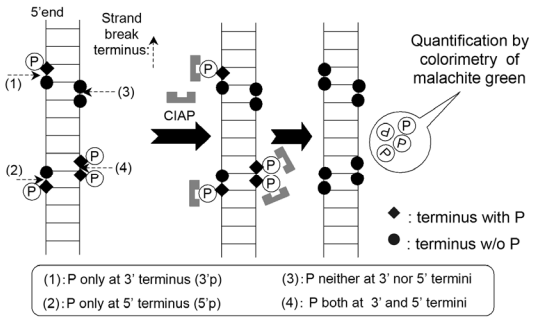

Fig. 1 Protocol for quantification of DNA strand break termini with phosphate.

Table 1 Spectra of strand break termini in DNA irradiated with $^{4}He^{2+}$ ion beam and ^{60}Co γ-rays.

Categories of termini †	Yield (nmol/J, x 10^{-12} $Gy^{-1}Da^{-1}$)		He / γ
	^{60}Co γ-rays	$^{4}He^{2+}$(~ 67 keV/μm)	
3'p + 3' OH (1)	91 (16) ※	212 (37)	2.3 (0.6)
3'OH (2)	26 (3)	16 (5)	0.6 (0.3)
3'p (3)	65 (16)	196 (37)	3.0 (0.9)
3'p + 5'p ≈ total termini(4)	130 (11)	338 (24)	2.6 (0.3)
5'p (5)	65 (19)	142 (37)	2.2 (0.9)
3'X (6)	39 (19)	126 (37)	3.2 (1.8)

†: (1), (2): obtained by SVPD method, (4): by terminal P method directly. (3) = (1) – (2), (5) = (4) – (3), (6) = (4) – (1).

900 kGy at r.t.. The irradiated DNA samples were recovered by water at 0 °C. The aqueous solutions were lyophilized and kept at -20 °C until use.

Analytical methods

To obtain strand break terminal spectra, SVPD method[2] and terminal phosphate analysis method[3] were used. The latter protocol was illustrated in Fig. 1. This method is bases on a known quantification technique of free phosphate using colorimetry of malachite green. As CIAP can hydrolyze terminal phosphate groups both at 3' and 5' ends, all strand break termini with phosphate can be quantified by the method in principle.

3. Results and Discussion

The results of these analyses of DNA irradiated with He ion beam and ^{60}Co γ-rays are summarized in Table 1 (3'X means 3'termini neither with OH nor phosphate). At a glance, the yields of all categorized termini for He ion beam were around 2-3 times larger than those for γ-rays except for the yields for 3'OH. This result suggests that high-LET radiation such as He ion beam is likely to decompose sugar moieties in DNA compared with low-LET one at least in case of the direct radiation effects.

4. Acknowledgments

We would like to gratefully thank Dr. Y. Sugo for operating the TC line, and also thank Drs. M. Kikuchi and Y. Kobayashi for γ-ray irradiation experiments.

References

1) C. M. deLala et al., Radiat. Res. 144 (1995) 43.
2) K. Akamatsu, Anal. Biochem. 362 (2007) 22.
3) K. Akamatsu, Radiat. Chem. 89 (2010) 3.

3-02 Mutagenic effects of He ion particles in *Escherichia coli*

T. Suzaka [a, b], H. Tauchi [a], N. Shikazono [b], K. Fujii [b] and A. Yokoya [b]

[a] Department of Environmental Sciences, Faculty of Science,
[b] Advanced Science Research Center, JAEA

Non-DSB type of clustered damage is induced by ionizing radiation and is proposed to cause deleterious effects to cells[1]. Their yields and configurations likely depend on the radiation qualities, such as particle energy or ionization density along the particle track characterized by LET (linear energy transfer)[1,2]. To date, the biological consequences of radiation of both low and high LETs have been extensively studied in various organisms, including bacteria, yeasts, higher plants, and mammalian cells. It is, however, still not clear on the features of the induced DNA damage in cells as well as how and to what extent the damage is processed and thus related to biological consequences, especially to mutation. In this project, we aim to find out the significance of clustering of DNA damage in mutagenesis. Here, we present the results of lacZ reversion assay of wild type cells after irradiation of soft X-rays and He ion particles with different LETs.

The cells of CC104 (wild type *E. coli*) were incubated in 0.2% glucose minimal medium at 37 °C unless otherwise stated. An order of 10^8 of cells were filtered through a nitrocellulose membrane of a diameter of 1.3 cm. To prevent cells from drying, the membrane was placed on a filter paper pre-wetted with 300 μL of 0.15 M NaCl solution with 20% glycerol. Subsequently, the membrane with the filter paper was placed on 0.15 M NaCl agar in a Petri dish, and then the dish was covered with a polyimide film (Kapton film) of 7.5 μm thickness. Cells on the membrane were irradiated with soft X-rays (tungsten target, tube voltage 150 kV, tube current 6 mA) at a dose rate of 0.47 Gy/s, and He ion particles at dose rates of 1～4 Gy/s. LETs of He ions were altered by placing a Ni foil in front of the sample. After irradiation, recovered cells were plated and incubated overnight. The fraction of survived cells was determined by dividing the number of survived cells by that of unirradiated cells. In this study, the reverse mutation frequency of *lacZ* was measured. G to T transversion in the *lacZ* gene reverts the cells so that they could grow on a medium with lactose as the only carbon source[3]. In determining the mutation frequency, irradiated cells were initially propagated in 0.2% glucose minimal medium at 37 °C for 16 hours to fix mutations. Cells were plated on a 0.2% lactose/glucose minimal medium, and were incubated at 37 °C for 40 hours. The reverse mutation frequency was determined by dividing the number of colonies on the lactose plate by that on the glucose plate.

Lethal and mutagenic effects of radiations with different qualities were assessed from dose response curves. Lethal effects of soft X-rays and He ion particles at LETs of 18 and 89 keV/μm did not show significant differences, indicating that the lethality of *E.coli* is largely independent on the LET (data not shown). The result suggests that the amount of unreparable lethal damage is similar after irradiation of different qualities of radiation in wild type *E.coli* cells. Dose response curves of mutation induction, however, differed significantly for each type of radiation (Fig. 1). Unexpectedly, the mutation frequencies increased and then leveled off with increasing dose for all types of radiation. The amount of dose to show the leveling off seemed to depend on the LET and the dose appeared to get smaller with increasing LET (Fig. 1). We do not have a clear explanation for these dose responses of mutation induction in *E.coli* at present, but similar dose response curves that show leveling offs at higher doses are also found in yeasts and in fungi[4, 5]. Studies with another target gene (*lacI* gene) for mutation induction are now underway.

References

1) N. Shikazono et al., J. Radiat. Res. 50 (2009) 27.
2) H. Nikjoo et al., Radiat. Res. 156 (2001) 577.
3) C.G. Cupples and J.H. Miller, Proc. Natl. Acad. Sci. USA 86 (1989) 9163.
4) Y. Matsuo et al., Mutat. Res. 602 (2006) 7.
5) Y. Toyoshima et al., JAEA Takasaki Ann. Rep. 2006 (2008) 93.

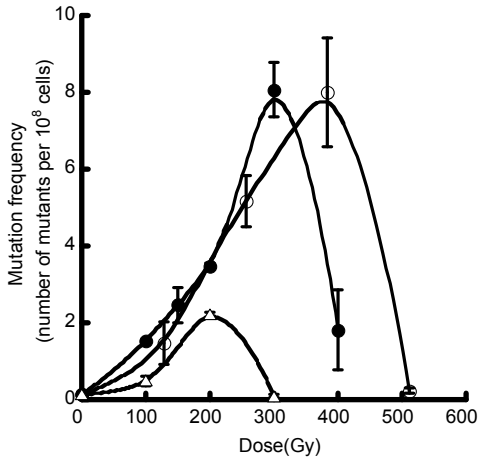

Fig. 1 Reverse mutation frequencies of wild type *E. coli* (CC104) at the *lacZ* gene. Cells were exposed to soft X-rays (○), He ions with an LET of 18 keV/μm (●), and 89 keV/μm (△).

3-03 Mutational Effect of Gamma-rays and Carbon Ion Beams on *Arabidopsis* Seedlings

R. Yoshihara, Y. Hase, S. Nozawa, A. N. Sakamoto and I. Narumi

Radiation-Applied Biology Division, QuBS, JAEA

It is expected that ion beams confer different mutational effects from low LET radiations such as gamma-rays. Indeed, ion beams have been used to produce many valuable cultivars. However, little is known about the mutational effects of ion beams on higher plants. Understanding mutational effects of ion beams is important for improvement of ion beam breeding technique. Therefore, to elucidate the molecular mechanisms of mutagenesis by ion beams in higher plants, effects of ion beams on DNA damage, DNA repair and mutation were investigated in this study.

Radiation induces various types of DNA lesions. Especially, DNA double strand break (DSB) and oxidative DNA damages (for example oxidized guanine) are major DNA lesions. In animal and bacteria, it has been proved that DSB and oxidized guanine induced deletion and base change mutations, respectively[1]. In our previous study, we showed that the incidence of mutation induced by oxidized guanine was quite low in *Arabidopsis* dry seed[2]. Thus, we speculated that atypical condition in dry seed such as low water content and cell proliferation activity affected mutation induced by oxidized guanine.

In this study, *Arabidopsis* seedlings were exposed to 220 MeV carbon ion beams (220 MeV $^{12}C^{5+}$). They were separately irradiated with gamma-rays as a control of low LET radiation. One-week-old seedlings were exposed to radiations and sensitivity of seedlings was estimated by the measurement of 5th leaf formation rate (Fig. 1). *Arabidopsis* seedlings showed higher sensitivity to 220 MeV $^{12}C^{5+}$ than gamma-rays.

For mutation spectrum analysis, Arabidopsis/rpsL[3] plants were irradiated with 80% of shoulder dose of each radiation. Mutant frequency was increased by the irradiation of both radiations (Table 1). Deletion/insertion and G to A transition were major mutations induced by both radiations in *Arabidopsis* seedlings. These types of mutations are also induced in *Arabidopsis* dry seed by both radiations. Our mutation spectrum analysis also showed that base change mutations induced by oxidized guanine (G to T and A to C) were not increased in *Arabidopsis* seedlings like dry seed (Table 2), suggesting the effects of oxidized guanine induced by ionizing radiation may be lower in plant than in other organisms, irrespective of LET. We will analyze mutation spectrum induced by radiation in DNA repair deficient *Arabidopsis* to investigate effects of DNA repair system on mutagenesis by oxidized guanine.

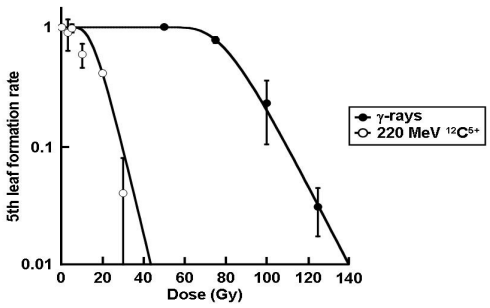

Fig. 1 Sensitivity of *Arabidopsis* seedling to gamma-rays and 220 MeV $^{12}C^{5+}$. Sensitivity of *Arabidopsis* seedlings to radiations were estimated by counting plants which formed 5th leaf by 7 days after irradiation. Shoulder doses of gamma-rays and 220 MeV $^{12}C^{5+}$ were 64 Gy and 17 Gy, respectively.

Table 1 Mutant frequency in *Arabidopsis* seedling.

	Mutant	Total clone	MF ($\times 10^{-5}$)
Background	20	575,879	3.4 ± 0.9
Gamma-rays	32	259,372	12.8 ± 6.3**
220 MeV $^{12}C^{5+}$	13	96,874	16.4 ± 10.3**

MF is Mutant frequency (Mutant / Total clone). Statistical analysis was performed by *t*-test (**: $p<0.01$).

Table 2 Mutation spectra induced in *Arabidopsis* seedling.

	Background	Gamma-rays	220 MeV $^{12}C^{5+}$
Transition			
G to A	5.2	34.7**	51.6**
A to G	1.7	3.9	0
Transversion			
G to T	1.7	3.9	0
G to C	1.7	7.7	0
A to T	3.5	3.8	0
A to C	0	0	0
Deletion/insertion	20.8	69.4**	103.2**

Data are presented as mutation frequency (the number of mutations occurred / the number of total analyzed clones). Statistical analysis was done between background and irradiated group according to Poisson distribution (**: $p<0.01$).

References

1) S. Bjelland & E. Seeberg, Mutat. Res. 531 (2003) 37.
2) R. Yoshihara et al., Int. J. Radiat. Biol. 86 (2010) 125.
3) R. Yoshihara et al., J. Radiat. Res. 47 (2006) 223.

3-04 Functional Analysis of Flavonoid Accumulation Genes of *Arabidopsis thaliana*

S. Kitamura [a)], F. Matsuda [b)], T. Tohge [c)], K. Yonekura-Sakakibara [b)], M. Yamazaki [c)], K. Saito [b, c)] and I. Narumi [a)]

[a)] Radiation-Applied Biology Division, QuBS, JAEA, [b)] RIKEN PSC, [c)] Chiba University

Plant cells have the potential to produce thousands of secondary metabolites, the production of which is finely regulated by developmental programs and environmental stimuli for each cell type. Flavonoids are one of the most widely found secondary metabolites in the plant kingdom, and show multiple functions *in planta* such as contributing to the attractive color of flowers and fruit and protection against UV-light and microbes. Flavonoids are synthesized at the cytoplasmic surface of endoplasmic reticulum (ER) within the cells. On the other hand, the final accumulation sites of some flavonoid end-products such as anthocyanins and proanthocyanidins (PAs) are known to be located in the central vacuole. This suggests that plant cells have mechanisms by which flavonoids are transported from the ER (synthesis site) to the vacuole (accumulation site). We previously isolated ion-beam-induced *Arabidopsis* mutant *tt19*, which showed aberrant accumulation pattern of anthocyanins and PAs. Physiological analysis indicates that *TT19* gene is involved in intracellular flavonoid transport. Here, in order to address the flavonoid transport mechanism more deeply, flavonoid accumulation mutants of *Arabidopsis* were analyzed at the cell biological and metabolomic levels.

TT19 gene was expressed as a fusion protein with GFP. GFP-TT19 proteins were observed only in anthocyanin- and PA-accumulating cells, implying a correlation between TT19 function and flavonoids. Within PA-accumulating cells, GFP-TT19 proteins were detected in the cytosol. This suggests that TT19 functions before vacuolar uptake of flavonoids. Vacuolar uptake of PAs is executed by a transporter protein TT12. The *tt12* mutant could not accumulate PAs in the vacuoles, whereas the *tt19* mutant could accumulate them in small vacuolar-like structures. In *tt12 tt19* double mutant, PAs were observed outside the vacuolar-like structures. These results indicate that formation of the vacuolar-like structures harboring PAs is TT12-dependent. Given the function of TT12 as a PA transporter, it is conceivable that the vacuolar-like structures in *tt19* are small "vacuoles".

We next observed PA-accumulating cells by differential interference contrast microscopy. Under this observational condition, *tt19* mutant specifically showed unique, thick spheres. These spheres were not detected in wild-type and other mutants. Histochemical analysis demonstrated that distribution pattern of these spheres overlapped the pattern of PA-accumulating small vacuoles in *tt19*. These findings prompted us to speculate that the composition and/or conformation of the PAs in the vacuoles differed between *tt19* and wild-type. To investigate this, PAs were analyzed by acid-hydrolysis and LC-MS. We found higher levels of solvent-insoluble PAs in *tt19* compared with wild-type. Metabolic profiling of the solvent-soluble fraction by LC-MS demonstrated that PA derivatives such as epicatechins and epicatechin oligomers, although highly accumulated in wild-type, were absent in *tt19*. We also revealed that *tt12* specifically accumulated glycosylated epicatechins, the putative transport substrates for TT12.

Based on these metabolic and cytological characteristics of mutants, we propose a model concerning the PA pathway (Fig. 1). The *Arabidopsis* PA precursor epicatechins, synthesized by anthocyanidin reductase (ANR) in the cytosol, are at least in part converted to epicatechin-hexosides by glycosyltransferase (GT). Following the synthesis of epicatechins and epicatechin-hexosides, cytosolic TT19 protein functions to protect the chemical properties of these precursors. Epicatechin-hexosides are taken up in the vacuoles by transporter proteins such as TT12, and the hexose moiety is removed by glycosidase in the vacuoles to polymerize the PA precursors. TT19 is required for the synthesis of regular PA polymers, but it may not be essential for the vacuolar accumulation of PA derivatives via TT12. This model will help to create plants possessing novel flavonoid constitution.

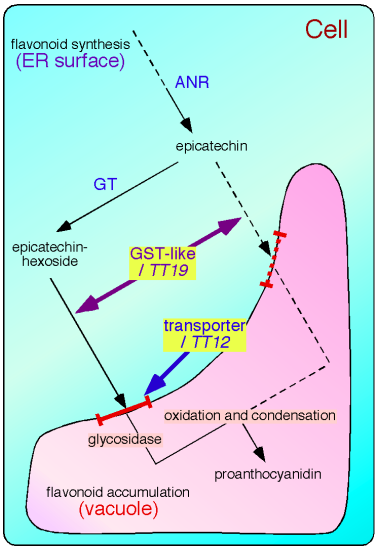

Fig. 1 A model concerning PA accumulation pathway. Putative steps are indicated as dotted arrows. Abbreviations used: ANR, anthocyanidin reductase; GT, glycosyltransferase; GST, glutathione *S*-transferase.

3-05 Ion Beam Irradiation with Rice Seeds for the Mutation Breeding Project of the Forum for Nuclear Cooperation in Asia (FNCA)

A. Tanaka [a)], S. Nozawa [a)], Y. Hase [a)], I. Narumi [a)], H. Ishikawa [b)] and A. Koike [b)]

[a)] Radiation-Applied Biology Division, QuBS, JAEA, [b)] Nuclear Safety Research Association

1. Introduction

For the spread of radiation application and development of ion beam breeding technique, ion beams have been utilized under the Mutation Breeding Project of the Forum for Nuclear Cooperation in Asia (FNCA) of MEXT (Ministry of Education, Culture, Sports, Science and Technology). This project contributes to increase food production and to improve food quality in Asia, by developing new mutant varieties with disease resistance, insect resistance, and drought tolerance of important crops, such as rice, bananas, orchids, sorghum, and soybeans, by using ionizing radiation. As the Sub-Project on Composition or Quality in Rice, utilization of ion beams has been started in 2009. Eight participant countries, i.e., Bangladesh, China, Indonesia, Korea, Malaysia, Philippines, Thailand and Vietnam joined the ion beam irradiation with rice seeds.

2. Materials & Methods

In order to obtain fruitful results, the clear and common protocol for all participant countries was firstly drawn up as shown in Fig. 1.

Outline of Protocol for Ion Beam Breeding of Rice in FNCA

1. First irradiation for sensitivity test of the sample
   - Rice dry seeds: 0, 10, 20, 40, 60, 80, 100, 120, 160, 200 Gy
   - 150 seeds per test-dose (totally 1,500 seeds)
2. Sensitivity test *
   - Survival & Growth rate (e.g. planted for 3 weeks)
   - 50 seeds for each experiment X3 replications per test-dose
   * follow Hidema's method (JAERI-Review 2003)
3. Determine the best dose:
   - usually at around the shoulder end of survival curve
4. Irradiation for mutagenesis (Second irradiation)
   - basically as many seeds as possible you can desirably more than 5,000 seeds (=M1)
5. Establishment of M2 lines
   - 1-3 M2 seeds per 1 plant (basically followed by one-plant-one-grain method)
   e.g. 3 x 5,000 = 15,000 M2 are tested

Fig. 1 Outline of protocol for the ion beam irradiation.

In general, hulled dry seeds of a rice cultivar (cv.) of participant country was irradiated with 320 MeV carbon ion beams in TIARA. About 70-100 seeds were set on a 50 mm petri-dish and irradiated within 30-90 seconds for any doses ranged from 10 to 200 Gy. After irradiation, seeds were rightly sent back to the participant countries and grown to obtain survival curves and the offspring.

3. Results and Discussion

The purpose of rice breeding should be high yield and good quality in term of low amylose content or high protein content and other characters. For this purpose, ion beam irradiation should be effective but not too much, in order not to induce bad characters or abnormalities of a mutant plant. To determine the optimal doses for mutation induction is the first and most important work for mutation breeding. Radiation sensitivity strongly depends on not only sub-species (indica or japonica) but also their cultivars. Therefore, precise data should be necessary for each cultivar. The growth and survival curves have been obtained to evaluate the best dose for mutation induction (Fig. 2). For example, in the case of indica cv. Ashal, proper dose would be 30-40 Gy because these doses caused the shoulder end of the survival curve that would be proper to induce mutants without bad characters from our sufficient experiences. Several countries have already obtained survival curves and identified the optimal doses for mutation induction. The other countries will continue sensitivity tests and determination of the optimal doses for mutagenization.

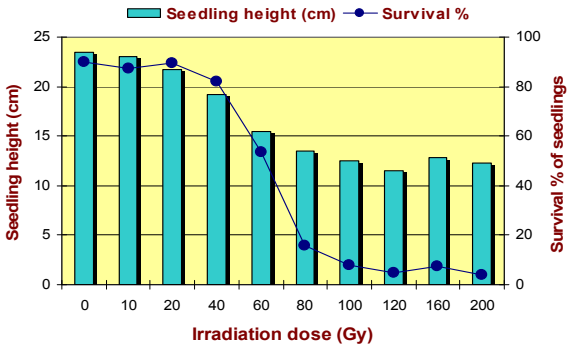

Fig. 2 The growth and survival data of indica cv. Ashal seeds irradiated with carbon ions (courtesy of Dr. Md. Lokman Hakim, Bangladesh).

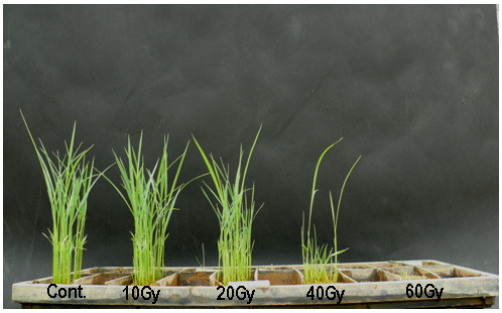

Fig. 3 Three-week-old plant of japonica cv. Ilpum irradiated with carbon ions (courtesy of Dr. Si-Yong Kang, Korea).

3-06 Generation New Ornamental Plant Varieties Using Ion Beams

A. H. Affrida [a)], A. Zaiton [a)], A. M. Salahbiah [a)], S. Shakinah [a)], R. Yoshihara [b)], I. Narumi [b)], Y. Hase [b)] and Y. Oono [b)]

[a)] Agrotechnology and Biosciences Division, Malaysian Nuclear Agency,
[b)] Radiation-Applied Biology Division, QuBS, JAEA

Chrysanthemum is one of the leading temperate flowers in Malaysia, and contributes 22.62% of the total value of cut flower production[1)]. The export values of chrysanthemum cut flowers are increasing every year. New variety of local chrysanthemum is needed to reduce dependence on foreign varieties. The objectives of this research are to develop an effective method for mutation induction of local varieties chrysanthemum using ion beams and to determine the optimum dose for callus formation using petals.

Petals of *Chrysanthemum morifolium* cv Reagan Red (Fig. 1) were surface-sterilized and cultured on 6-cm sterile petri dishes containing MS medium[2)] supplemented with 0.5 mg/L α-naphthalene acetic acid (NAA) and 2.0 mg/L 6-benzylaminopurine (BAP). The samples covered with Kapton films were irradiated with 320 MeV $^{12}C^{6+}$ ion beams at 0, 0.2, 0.5, 1.0, 2.0, 5.0, 8.0, 10.0, 15.0, 20.0 and 30.0 Gray (Gy) from the TIARA AVF Cyclotron. The irradiated petals were transferred onto fresh media and incubated at 25 ± 2 °C under 16-hour photoperiod for proliferation. Data on the number of petals that were able to produce callus and regenerate into shoots was recorded at 4th and 8th weeks after the irradiation.

The dose response curves at 4th and 8th weeks are shown in Figs. 2 and 3, respectively. From these curves, petal survival dose could be determined at week 4, in which more than 80 percent of the petals produced callus at 6.5 Gy and below. The percentage of survived petals decreased drastically at doses above 10 Gy. At this stage, only less than 35 percent of the cultures for each dose could regenerate into shoots. Therefore, no significant pattern could be concluded on the correlation between shoot regeneration and dose at week 4.

After 8 weeks, the percentages of petals that were able to maintain callus viability decreased drastically to less than 52% at 15 Gy and higher. At this stage, more cultures developed shoots or shoot buds. The 80% Regeneration Dose (RD80) is between 0.5-1.5 Gy. Irradiation dose of 15 Gy and higher was found to adversely affect the capability of the petal cultures to form shoots as the percentage of shoot regeneration were less than 5%.

As a conclusion, petal survival dose could be determined 4 weeks after irradiation whilst regeneration dose was obtained after 8 weeks of irradiation.

References

1) H. J. Lim et al., http://www.fao.org /docrep/005/ac452e /ac452e06.htm (1998).
2) T. Murashige and F. Skoog, Physiol. Plant, 15 (1962) 473.

Fig. 1 *Chrysanthemum morifolium* cv Reagan Red.

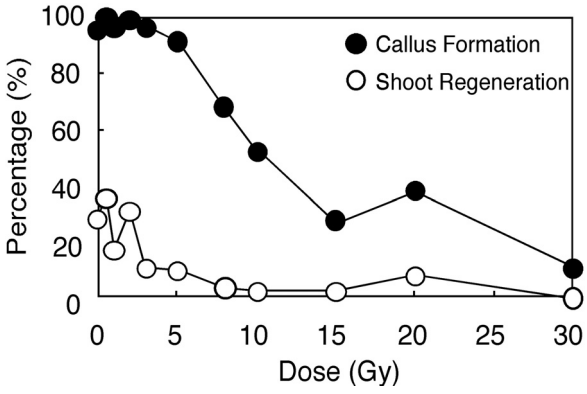

Fig. 2 Percentage of callus formation and shoot regeneration from petal cultures after 4 weeks of irradiation.

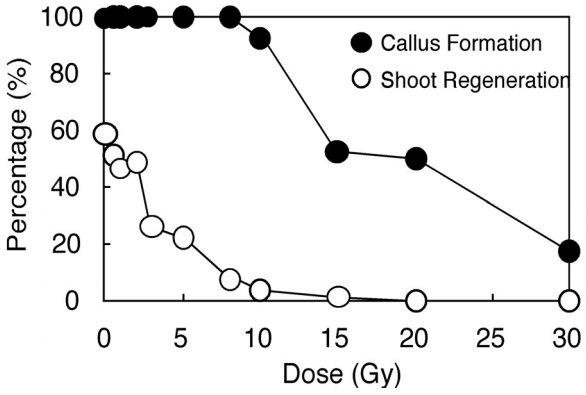

Fig. 3 Percentage of callus formation and shoot regeneration from petal cultures after 8 weeks of irradiation.

3-07 Development of New Gunma Original Variety of Chrysanthemum by Ion Beam Irradiation

T. Okada [a)], H. Ikeda [b)], Y. Oono [c)], R. Yoshihara [c)], Y. Hase [c)] and I. Narumi [c)]

[a)] Gunma Agricultural Technology Center, [b)] General Agricultural Office, Gunma West Area Regional Administration Center, [c)] Radiation-Applied Biology Division, QuBS, JAEA

'Konatsunokaze' is a white chrysanthemum variety, which has a good flower type and plant type. The purpose of this study is to obtain red and yellow flower color variants that maintain flower type and plant type of 'Konatsunokaze'. Leaf sections of 'Konatsunokaze' were irradiated with $^{12}C^{5+}$ (220 MeV) and $^{12}C^{6+}$ (320 MeV) beams at a range of doses from 0.1 to 5.0 Gy. In the $^{12}C^{5+}$ beams, the plant regeneration rate was 71.7% at 0.1Gy and decreased to 3.3% at 2 Gy. In the $^{12}C^{6+}$ beams, the regeneration rate was 23.7% at 0.1 Gy and decreased to 1.9% at 2 Gy. This result shows that irradiation with $^{12}C^{5+}$ beams is effective for obtaining regenerated plants. Now, the regenerated plants are under investigation for mutation.

１．はじめに

コギク「小夏の風（仮称）」は、群馬県の気象条件に適応し、8 月上中旬に安定して開花し、花形、草姿に非常に優れている白色花弁の品種として群馬県農業技術センターが開発したものである（2008 年 1 月品種登録出願）。コギクの品種のブランド化を目指す上では、更に黄色、赤色の花色セットとすることが必要であり、また、「小夏の風」の優れた花形、草姿を維持して、花色を変化させた品種の育成が望まれている。本センターは「小夏の風」に続き、交配育種により黄色品種として「小夏の月（仮称）」を育成したが（2009 年 12 月品種登録出願）、花形、草姿は異なっている。

イオンビームは花色変異誘導に有効で、局所的変異を誘発しやすいことが知られている [1, 2]。そこで、イオンビーム照射により「小夏の風」の形を維持したまま、赤色、黄色の品種の育成を目指すことにした。

今回の試験では「小夏の風」の葉片培養体へのイオンビーム照射を行うことで、エネルギー及び線量が植物体再生へ及ぼす影響を調査し、変異誘導に適した照射条件を検討した。

２．材料及び方法

（１）イオンビーム照射材料の調整

供試材料として「小夏の風」の葉片を用いた。葉片は 5 mm 角程度に切断し、植物ホルモンとして BA 5.0 mg/L、NAA 3.0 mg/L を添加した MS 培地（ショ糖 3%、寒天 0.8%、pH 5.8）を加えた 60 mmφシャーレ上に置床した。置床後 2～5 日培養した後にイオンビーム照射を行った。

（２）イオンビーム照射

原子力機構高崎量子応用研究所の AVF サイクロトロンを用いて、調整した材料にイオンビーム照射を行った。照射条件は加速粒子として $^{12}C^{5+}$（エネルギー 220 MeV)及び $^{12}C^{6+}$（エネルギー 320 MeV）を用い、線量を 0、0.1、0.5、1.0、2.0、5.0 Gy で照射を行った。

（３）植物体再生及び順化

イオンビームを照射した葉片は、照射 1 日後に（１）と同じ培地上に継代し、不定芽が確認されたものから随時、ホルモンフリー培地へ移植し生育を促した。培養開始から 60 日後に不定芽形成率を調査した。培養を継続し順調に生育した植物体は順化後、ガラス温室内で養生した後、ほ場へ定植した。

３．結果及び考察

「小夏の風」へのイオンビーム照射の結果、$^{12}C^{5+}$（220 MeV）での照射の場合、0.5 Gy 以上で植物体再生率が下がり始め、2 Gy では植物体の再生は 3.3%となり、$^{12}C^{6+}$（320 MeV）では、0.1 Gy で再生率が 23.7%と大きく下がり、2 Gy では 1.7%まで下がった（Fig. 1）。$^{12}C^{5+}$、$^{12}C^{6+}$のどちらも吸収線量に依存して植物体再生率は低下したが、$^{12}C^{6+}$では線量の増加が植物体再生に及ぼす影響が極めて強いことが示唆された。このことから、「小夏の風」へのイオンビーム照射は $^{12}C^{5+}$で行うことが適していると考えられた。

今後は、ほ場での慣行栽培で開花させ、開花時期や花色、花型、草姿等の線量等による変異発生率の影響を調査し、最適な照射条件を検討したい。

また、今回、無照射区を含めて葉片 1 枚あたりから再生した植物体が 1～2 個体程度であったため、葉片の再分化条件を再検討し、品種育成に重要となる母集団の増加を図りたい。

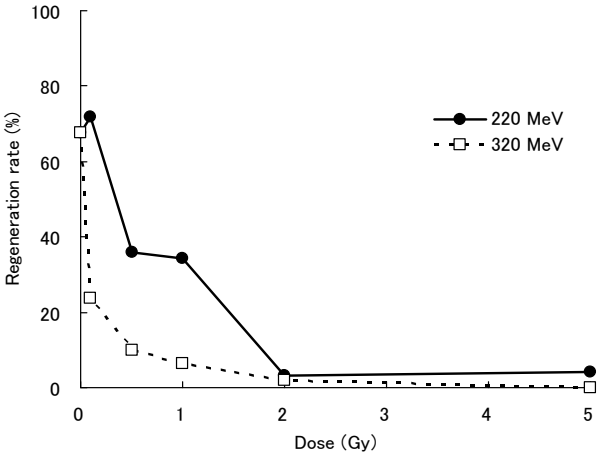

Fig. 1 Effect of $^{12}C^{5+}$ (220 MeV) and $^{12}C^{6+}$ (320 MeV) irradiation on shoot regeneration.

References

1) T. Okada et al., JAEA Takasaki Ann. Rep. 2008 (2009) 73.
2) M. Iizuka et al., JAEA Takasaki Ann. Rep. 2007 (2008) 65.

3-08 Stability of Flower-colour Mutants of Delphinium ‘Momoka’ After Propagation by Tissue Culture

S. Kitamura [a)], S. Chinone [a)], K. Tokuhiro [a)], K. Nakatsubo [a)], S. Nozawa [b)], Y. Hase [b)] and I. Narumi [b)]

[a)] Kaneko Seeds CO., LTD., [b)] Radiation-Applied Biology Division, QuBS, JAEA

We previously reported that 9 flower-colour mutants were obtained in delphinium ‘Momoka’ using ion beam irradiation. After propagation by tissue culture, 6 of them exhibited the same flower colour with their parental mutants but 3 of them exhibited different colour. Our study shows that ion beam breeding is useful for Delphinium, although stability of flower-colour mutation needs to be investigated.

前報において、花色変異体の獲得を目的にカネコ種苗㈱育成のデルフィニウム濃ピンク品種‘ももか’の葉身に、炭素イオン（$^{12}C^{6+}$, 320 MeV）0.5～1.0 Gyを照射し、再生した植物体から9個体の花色変異体を獲得したことを報告した[1, 2]。今回、獲得した花色変異体（薄ピンク 6個体、黄色がかったピンク2個体、赤味の強いピンク1個体）について、主茎の腋芽から培養増殖を行い、変異の安定性について調査した結果を報告する。

2009年9月14日に、増殖した植物体を1系統5株ずつガラスハウスに定植し、12月に開花検定を行った（Table 1）。花色が増殖後も安定して発現した系統は6系統、変化した系統が3系統あった。‘7P-IB-01’は薄ピンクの花色変異体であったが、増殖後に5株中3株が濃ピンクに変化した。‘7P-IB-04’は薄ピンクから赤味の強いピンクに、‘7P-IB-10’は黄色がかったピンクから薄ピンクに全ての株で花色が変化していた。

以上より、イオンビーム照射によって誘導された花色の変異は培養増殖後も比較的安定しているものと思われ、イオンビームによるデルフィニウム‘ももか’の改良が可能であることが示された。しかしながら、花色が培養増殖後に変化する系統も見られることから、獲得した変異の安定性についての調査は不可欠であるものと思われる。

今後、黄色がかったピンク色を呈する‘7P-IB-09’を有用な系統として再度培養増殖し、規模を拡大して変異が安定しているかの確認を行う予定である。

Fig. 1 Flower-colour mutants obtained in this study.
A: Deep pink (Original cv. ‘Momoka’),
B: Red pink,
C: Light pink,
D: Yellow pink.

References

1) S. Chinone et al., JAEA Takasaki Ann. Rep. 2007 (2008) 68.
2) S. Chinone et al., JAEA Takasaki Ann. Rep. 2008 (2009) 74.

Table 1 Stability of flower-color mutants induced by carbon-ion irradiation.

Line	Dose (Gy)	Flower colour	
		At selection	After propagation
‘Momoka’	—	Deep pink	Deep pink
7P-IB-01	1.0	Light pink	Light pink or Deep pink
7P-IB-02	0.5	Red Pink	Red Pink
7P-IB-03	1.0	Light pink	Light pink
7P-IB-04	0.5	Light pink	Red Pink
7P-IB-05	0.5	Light pink	Light pink
7P-IB-07	1.0	Light pink	Light pink
7P-IB-08	0.5	Light pink	Light pink
7P-IB-09	0.5	Yellow pink	Yellow pink
7P-IB-10	0.5	Yellow pink	Light pink

3-09 Red–purple Flower due to Delphinidin 3,5-diglucoside, a Novel Pigment for *Cyclamen* spp., Generated by Ion-beam Irradiation

E. Kondo [a], M. Nakayama [b], N. Kameari [a], N. Tanikawa [b], Y. Morita [b], Y. Akita [c], Y. Hase [c], A. Tanaka [c] and H. Ishizaka [a]

[a] Horticultural Laboratory, Saitama Prefecture Agriculture and Forestry Research Center,
[b] National Institute of Floricultural Science (NIFS), National Agriculture and Food Research Organization (NARO),
[c] Radiation-Applied Biology Division, QuBS, JAEA

We previously bred fragrant cyclamens by hybridization between cultivars of *Cyclamen persicum* and wild species *C. purpurascens*. One of these fragrant cultivars, Kaori-no-mai, blooms purple flowers containing malvidin 3,5-diglucoside as the major anthocyanin. Here, to increase flower color variation, we irradiated etiolated petioles of Kaori-no-mai with 0-16 Gy of 320-MeV carbon-ion beams. Some M_2 plants derived from self-pollination of M_1 plants irradiated at 2 Gy were flower-color mutants that retained desirable flower shape, flower size, and leaf color. One of the mutants bloomed novel red-purple flowers, the major anthocyanin of which was delphinidin 3,5-diglucoside. Loss of methylation activity at the anthocyanin 3′- and 5′-hydroxyl groups with little influence on anthocyanin concentration was attributed to the mutation.

シクラメンの栽培種（*Cyclamen persicum*, $2n$=$2x$=48）と芳香性野生種（*C. purpurascens*, $2n = 2x = 34$）の種間交雑と染色体倍加により複二倍体（$2n = 4x = 82$）の芳香シクラメンを育成し、その中の一品種、‘香りの舞い’へのイオンビーム照射による変異の拡大を検討した。

‘香りの舞い’の種子を無菌的に培地に置床し、暗黒下で発芽させた。発芽した黄化葉柄由来の 1,647 個の切片を 1/2-N MS（MS 培地の KNO_3 と $(NH_4)NO_3$ を 1/2 に減量）+ショ糖（90 g/L）+2,4D（1 mg/L）+BA（0.5 mg/L）+ジェランガム（3 g/L），pH 5.8 の培地に置床後、原子力機構高崎量子応用研究所の TIARA において 320 MeV 炭素イオンビーム 0～16 Gy を照射し、培養を継続した。得られた 222 個の M_1 開花個体では花色変異は見られなかった。次に、M_1 個体の自家受粉により得られた 2,936 粒の M_2 種子のうち 800 粒を播種し、271 個の M_2 個体を育成した。その中で、2 Gy 照射由来の 68 個から 9 個の花色に関する変異体が得られた（Table 1）。‘香りの舞い’の花色は紫であったが、変異体の花色は赤紫色であった。変異体では花色以外の変異は見られなかった（Fig. 1）。

シクラメンの花弁は、先端部（スリップ；Fig. 1, arrowheads）と基部（アイ；Fig. 1, arrows）で色調が異なることが多い。‘香りの舞い’と1個の変異体の花弁をアイとスリップに切り分け、10%酢酸により色素を抽出し高速液体クロマトグラフィー（HPLC）で分析した。また、抽出物はn-ブタノール：酢酸：水=4:1:2混合液および10%酢酸を用いた薄層クロマトグラフィーで分析するとともに、エレクトロスプレーイオン化法による質量分析を行った。その結果、‘香りの舞い’のスリップとアイの主要色素は既知のマルビジン3,5ジグルコサイドであったが、変異体の主要色素はシクラメンでは新規のデルフィニジン3,5ジグルコサイドであった（Fig. 2）。以上の結果は、変異体ではデルフィニジンの3’および5’位の水酸基のメチル化酵素をコードする遺伝子がイオンビームの影響を受け、マルビジンへの代謝が阻害されていることを示唆する。

本研究は生研センター異分野融合研究事業および農水省先端技術高度化事業の支援を受けた。

Table 1 Effects of carbon ion beam irradiation on regeneration rate and mutation induction in *in vitro* cultures of etiolated petiole of fragrant cyclamen (*Cyclamen persicum* × *C. purpurascens*) ‘Kaori-no-mai’.

Irradiation dose (Gy)	Number of plantlets generated (%)	Number of M_1 plants grown to bloom	Number of M_2 seeds obtained	Number of M_2 plants grown to bloom
0	270 (92)	58	767 (200) [1]	52 (0) [2]
0.5	372 (94)	53	740 (200)	61 (0)
1	452 (86)	75	892 (200)	90 (0)
2	196 (82)	30	537 (200)	68 (9)
4	54 (67)	3	0	-
8	39 (53)	1	0	-
16	7 (19)	2	0	-

[1] Number of M_2 seeds sown for examination.
[2] Number of M_2 plants producing red–purple flowers.

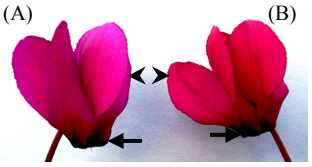

Fig. 1 Flowers of ‘Kaori-no-mai’(A) and mutant (B).

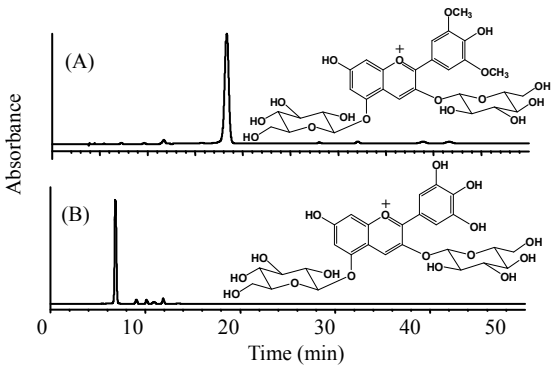

Fig. 2 HPLC elution profiles detected by absorbance at 530 nm and structures of anthocyanins in slip of (A) ‘Kaori-no-mai’ and (B) mutant.

3-10 Effects of Heavy Ion beam Irradiation in Citrus

Y. Matsuo [a)], Y. Hase [b)], S. Nozawa [b)], R. Yoshihara [b)] and I. Narumi [b)]

[a)] Saga Prefectural Agricultural Fruit Tree Experiment Station,
[b)] Radiation-Applied Biology Division, QuBS, JAEA

Radiation breeding is one of the useful methods to develop new varieties of fruit trees. To apply radiation breeding for citrus, we examined the radiation sensitivity of three citrus varieties. In “Kawata wase”, the regeneration rate from hypocotyls was 48.0% at 0 Gy and the regeneration rate decreased to 25.0% at 4 Gy. In “Imamura unsyuu”, the regeneration rate was more than 50% up to 2 Gy and was 47.6% at 4 Gy. In case of trifoliate orange, we irradiated imbibed seeds because regeneration rate from hypocotyls was low. The germination rate of irradiated seeds was more than 70% up to 12 Gy and was 53.8% at 16 Gy. Our results show that there is a difference in radiation sensitivity and shoot regeneration potential between citrus varieties.

果樹等木本植物は、栄養繁殖を中心に増殖が行われており、放射線を利用し突然変異を効率よく誘発する育種法は、果樹育種において重要な品種改良の一つである。しかし、カンキツにおいてはイオンビーム等を利用した突然変異誘発事例の報告は少ない。これまでにユズをはじめとして、福原オレンジ、ニンポウキンカン、川野ナツダイダイ等への照射試験を実施し放射線感受性の程度を調査してきた。本試験では、カンキツ生産量の大半を占める温州ミカンについての感受性程度を調査した。またカラタチについては、胚軸切断面よりカルス発生しにくいため、種子への照射試験を実施した。

供試品種は、川田早生、今村温州を用いた。種子を1/2MS培地に播種後、3週間目に胚軸を2 cm程度残し切断した。さらに、1週間後に切断面より発生したカルスにイオンビームを照射した。照射イオン種はCイオン（$^{12}C^{6+}$、加速エネルギー320 MeV）を用い、線量は2～32 Gyの5線量区とした。また、同様に中庸系カラタチの吸水種子（1週間前播種）へ照射を実施した。線量は2～32 Gyの10線量区とした。照射施設は原子力機構高崎量子応用研究所のAVFサイクロトロンを用いた。照射後、出芽・伸長を開始した個体は、馴化培地へ継代し、更に培土に鉢上げを実施し、ガラス室で育苗した。温州ミカンについては、照射4週間後の再分化率、再分化植物伸長量等の調査を行った。カラタチについては、2ヶ月後の発芽率、4ヵ月後植物伸長長等を調査した。

温州ミカンについては、両品種とも前回のゆら早生への照射試験を基準にイオンビームを照射した。再分化率は品種によりばらつきがみられた（Table 1）。川田早生の4週間後の再分化率については、対照でも50%以下となったため、播種後の生育環境を再検討する必要がある。2 Gy区では、対照とほぼ変わらなかったが、4 Gy以上となると、対照の50%程度となった。今回の照射では、全体の再分化率が低かったが、8 Gy区では、対照の50%以下となり、実用線量は2～4 Gy程度が適切であると考えられる。今村温州の再分化率については、全般的に川田早生よりも高く、4 Gy区でも対照の70%程度であった。また、8 Gy区では26%程度で16 Gy以上では、全て再分化しなかった。このため、今村温州の適正線量は4 Gy程度であると考えられる。

カラタチ種子へ照射をおこなった場合の発芽率は、12 Gy区までは70%以上であった。16 Gy区以上では50%以下程度となった（Table 2）。

照射4ヵ月後の線量毎の平均伸長は、高線量区と低線量区との明確な伸長量の差は認められなかった。しかし、個々の伸長量は、非常にばらつきが大きく、引き続き今後の経過についての調査を行う必要がある。

以上より、カラタチへは種子への照射にて変異個体を獲得できる可能性があることがわかった。また、線量は、急激に発芽率が低下する直前あたりが適正線量と思われるため、次回試験からは12 Gyから16 Gyの間で照射試験を実施する。

References

1) Y. Matsuo et al., Hort. Res. 6 (Suppl. 1) (2007) 40.
2) Y. Matsuo et al., JAEA Takasaki Ann. Rep. 2007 (2008) 74.
3) Y. Matsuo et al., JAEA Takasaki Ann. Rep. 2008 (2009) 76.

Table 1 Regeneration rate from hypocotyls of Satuma mandarin “Kawata wase” and “Imamura unsyuu” irradiated with carbon ions.

Cultivar	Absorbed dose (Gy)					
	0	2	4	8	16	32
Kawata wase	48.0	43.9	25.0	22.5	-	-
Imamura unsyuu	67.9	51.3	47.6	17.7	0.0	0.0

Table 2 Germination rate of trifoliate orange seeds irradiated with carbon ions and plant height at 4 months after Irradiation.

Absorbed dose (Gy)	0	2	4	6	8	10	12	16	20	24	32
Germination rate (%)	96.7	90.3	77.1	77.1	83.3	72.4	70.6	53.8	28.0	18.5	6.9
Plant height (cm)	10.3	10.2	11.4	12.9	10.8	9.5	8.7	6.1	8.1	9.7	9.5

3-11 Effect of Ion Beam Irradiation for *Asclepias* Species

N. Kobayashi [a)], S. Sasaki [a)], K. Tasaki [a)], A. Nakatsuka [a)],
S. Nozawa [b)], Y. Hase [b)] and I. Narumi [b)]

[a)] Faculty of Life and Environmental Science, Shimane University,
[b)] Radiation-Applied Biology Division, QuBS, JAEA

1. Introduction

Asclepias is one of the perennial ornamentals native to Central America, using for cutting, potting and bed flowers. For the purpose to obtain flower and/or plant form mutation[1–2], *Asclepias curassavica* seeds were irradiated by ion beams and researched its effect[3–5]. In this study using *A. incarnara* L. and *A. tuberosa*, the seed germination rates, growth and survival rate of seedlings obtained from ion beam irradiated seeds are investigated.

2. Materials and Methods

Asclepias incarnara L. and *A. tuberosa* L. were irradiated with carbon ion beams (220 MeV $^{12}C^{5+}$) at 12.5, 25, 50, 100 and 150 Gy on September 2009 and at 30, 45, 60, 75 and 90 Gy on October 2009.

Irradiated seeds were sowed in a green house and germinated seedlings were transplanted into pots. Germination rate was investigated on 20 days after germination. Leafing and survival rate were investigated on 30 and 40 days after germination, respectively.

3. Results and Discussion

Seed germination rate decreased from 100 Gy irradiation with increasing doses and any seeds could not germinate in 150 Gy for both *Asclepias* species. Survival rate of seedlings decreased below 50% of lethal rate in more 50 Gy (Fig. 1 upper). Rate of germination becomes 50% between 75 to 90 Gy for *A. incarnate* and between 60 to 90 Gy for *A. tuberosa* in November (Fig. 1 lower) and these seedlings could not survive because of their dormancy phase at low temperature. In the case of *A. curassavica* seed, irradiation of 50 to 200 Gy was optimal[5]. It is needed to consider the optimal irradiation dose and life cycle to get mutants for these species.

References

1) N. Kobayashi et al., JAEA Takasaki Ann. Rep. 2006 (2008) 87.
2) N. Kobayashi et al., JAEA Takasaki Ann. Rep. 2007 (2008) 70.
3) S. Kano et al., Abst. Chugoku-Shikoku Br., Japan. Soc. Hort. Sci. 46 (2007) 40.
4) S. Kano et al., Hort. Res. 7 (Suppl. 2) (2008) 583.
5) N. Kobayashi et al., JAEA Takasaki Ann. Rep. 2008 (2009) 77.

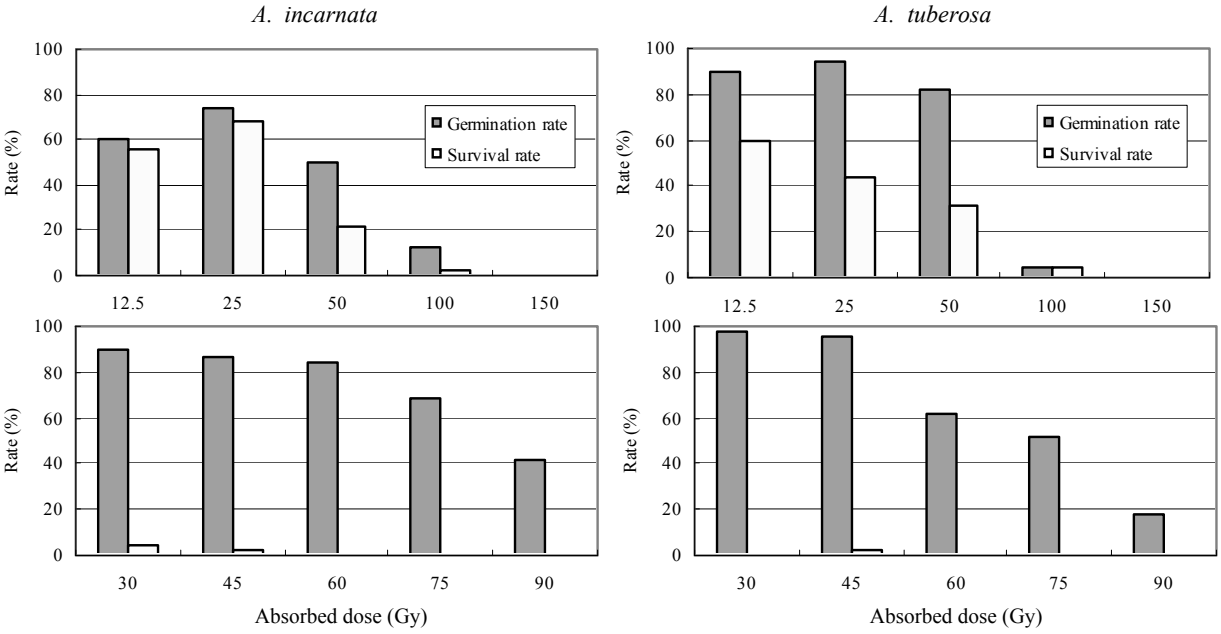

Fig. 1 Effects of ion beam irradiation for seed germination and survival rates in *Asclepias*. *A. incarnate* (left) and *A. tuberosa* (right). Data are from irradiation in September (upper) and October (lower).

3-12 Producing New Gene Resources in Chrysanthemum Using Ion-beam Irradiation

I. Asami [a)], T. Tsuji [a)], T. Hasegawa [a)], S. Fukuta [a)], S. Kuroyanagi [a)], Y. Hase [b)], R. Yoshihara [b)] and I. Narumi [b)]

[a)] Aichi Agricultural Research Center,
[b)] Radiation-Applied Biology Division, QuBS, JAEA

The goals of our study are to produce new gene resources in standard type chrysanthemum by mutation induction with ion-beam irradiation, such as agronomical characters with less lateral buds for saving the farmer's labor and also flowering in low temperature to save the cost of heating. In vitro buds of chrysanthemum cv. 'Hakusui' were irradiated with carbon ion beams (320 MeV, $^{12}C^{6+}$) at the TIARA. Irradiated plantlets were pinched for 3-times, about 3,000 herbaceous cuttings were grown in greenhouse and 22 individuals were selected for less-lateral buds in summer. The line selections with 22 individuals were performed by flowering in December, and three lines were selected with good flower shape. About 5,000 herbaceous cuttings were grown in greenhouse with minimum night temperature of 12 °C by flowering in March, 12 lines were selected for flowering in low temperature with good flower shape.

緒言

(独)日本原子力研究開発機構と鹿児島県が共同で育成した白一輪ギク「新神」及び「新神 2」は無側枝性(芽無し性：側蕾を摘む作業の削減）と低温伸長・低温開花性（低い設定温度による暖房費節減）を有し、イオンビーム照射が低コスト・省エネルギー品種の育成に有効であることが示された [1)]。この実績を愛知県育成白一輪ギク品種「白粋」に応用し、生産額全国 1 位の愛知県のキク生産農家が望む新品種を育成する。

材料及び方法

(1) 無側枝性有望候補の選抜と開花調査

前年度に「白粋」培養苗の茎頂に 1 Gy の炭素イオンビームを照射し、馴化後、屋外で越冬栽培した約 300 個体を用いた。摘心（頂芽を摘み取る）して側枝（脇芽）を伸長させることを 3 回繰り返して得た約 3 千本の茎頂部をセルトレイに挿し芽し、夏季の温室内で側枝発生の有無を調べた（セルトレイ選抜法 [2)]）。選抜した有望個体を無加温で温室栽培し、12 月に開花調査した。

(2) 低温伸長・低温開花性有望候補の選抜

上記と同様な方法で得られた約 5 千本の苗を最低夜温 12 ºC で栽培し、3 月に開花調査した。

結果

(1) 無側枝性有望候補系統の選抜と開花調査

摘心後の腋芽発生が少ない無側枝性有望候補 22 個体を得た（データ未掲載）。それらを実際に温室栽培して原品種と比較したところ、花型が原品種に似た個体は側蕾数が多く、側蕾数が少ないものは花型が良くない傾向があったが、その中で側蕾数が少なく花型が良い 3 候補を選んだ（Table 1）。

Table 1 Characteristics of the selected lines for less-lateral buds.

Line No.	NDF	Plant height	Number of lateral flower	Number of florets	Flower diameter
		cm			cm
1-2	55	51	4	274	11.9
2-2-8	51	59	9	305	13.2
3-1	58	46	7	297	12.0
Original 'Hakusui	51	44	10	301	13.3
'Zimba'	55	42	8	266	12.4
'Arajin-2	54	42	8	353	12.9

NDF : The number of days to flowering.

(2) 低温伸長・低温開花性有望候補の選抜

11 月 26 日と 12 月 20 日に定植した二つの温室で栽培したところ、元品種より開花が早く花型も同等に良い 12 候補を選んだ（Table 2）。

Table 2 Characteristics of the selected lines for flowering in low temperature.

Line No.	NDF	Plant height	Number of node	Stem diameter	Flower diameter
House A		cm		mm	cm
09LT-1-1	49	105	51	7.1	13.3
09LT-1-2	53	110	54	7.3	15.2
09LT-1-3	54	117	53	8.5	14.5
09LT-1-4	55	104	47	7.6	15.5
09LT-1-5	55	136	60	7.7	14.1
09LT-1-6	56	114	56	7.6	14.6
09LT-1-7	57	117	57	7.8	14.6
09LT-1-8	59	124	55	7.2	13.2
09LT-1-9	59	135	65	9.1	13.9
09LT-1-10	59	123	55	8.6	14.1
Original 'Hakusui'	60	120	61	8.1	14.1
House B					
09LT-2-1	54	118	58	7.5	15.1
09LT-2-2	52	131	53	7.5	13.5
Original 'Hakusui'	56	123	60	7.6	13.1

NDF : The number of days to flowering.

References

1) 今給黎征郎ら、鹿児島農試研報 34 (2006) 15.
2) 浅見逸夫ら、高崎量子応用研究シンポジウム要旨集 4 (2009) 128.

3-13 Ion Beam Breeding of Sugarcane Cultivar "Ni17"

Y. Takenoshita [a)], J. Nagai [b)], T. Nagatani [a)], M. Ooe [a)],
Y. Hase [c)], A. Tanaka [c)] and I. Narumi [c)]

[a)] Kagoshima Biotechnology Institute, [b)] Kagoshima Prefectural Institute for Agricultural Development Tokunoshima Branch, [c)] Radiation-Applied Biology Division, QuBS, JAEA

Sugarcane cultivar "Ni17" has hard hairs on its leaf sheath. We have intended to induce hairless or few hair mutants using ion beam irradiation to cultured tissue of leaf explants. As a result of nursery selection, individual selection, and line selection, we have selected one line ("KaB07-22") among the 10,410 regenerated plants. This line has a few hairs on its leaf sheath, and its growth and yield is higher than "Ni17" by spring planting. We are planning to investigate further detail characteristics of "KaB07-22" by ratooning planting.

さとうきび品種「Ni17」は、株出萌芽性、風折抵抗性に優れ[1)]、本県では「NiF8」に次いで栽培されているが、葉鞘部に着生する粗剛な毛群が収穫や採苗時に手に刺さる等の問題があり改良の必要がある。そこで、我々は2003年度からイオンビームを利用した変異誘発によって毛群の少ない「Ni17」優良系統の育成に取り組んでいる。これまで我々は、個体再生率並びに圃場生育からみたイオンビームの適正吸収線量を明らかにした[2–3)]。また、2004年度に選抜した「KB04-25」は、「Ni17」に比べ毛群が少なく、収量は19%～21%増加した系統であったが[4)]、「Ni17」に比べ茎が細く、また本県主力品種である「NiF8」に比べ収量が劣ったため品種化までには至っていない。今回、新たに2006年度に変異誘発を行った個体群から「Ni17」に比べ毛群が少なく、収量性でも有望と考えられる系統が得られたので、その選抜経過と特性について報告する。

「Ni17」の茎頂付近の幼葉切片に、日本原子力研究開発機構高崎量子応用研究所のAVFサイクロトロンにより発生させたイオンビーム（320 MeV・$^{12}C^{6+}$）を0 Gy（無照射）及び1～4 Gy照射し、カルスから不定胚を経由し10、410個体の再生植物体を育成した。再生植物体はガラスハウス内においてポリポットで育苗し、2007年5月に幼苗時の毛群の発生程度を調査し、2007年6月に毛群の発生程度が無～極少であった351個体を圃場に定植して個体選抜試験に供試した。2007年10月に毛群の発生程度と茎長、茎数、茎径を調査して24個体を選抜し、2007年11月から南西諸島の徳之島支場において系統選抜試験に供試した。2009年2月に毛群の発生程度、茎長、茎数、茎径を調査して5系統を選抜した。2009年3月から選抜した5系統について、さらに徳之島支場において、さとうきび栽培における一般的な作型である春植え栽培試験に供試し、2010年3月に毛群の発生程度と併せて詳細な特性並びに収量調査を行った。春植え栽培における特性調査の結果、供試した5系統から1系統（系統名「KaB07-22」）を選抜した。

「KaB07-22」は、1 Gy照射した個体群から得られた（Table 1）。「KaB07-22」は春植え栽培において「Ni17」に比べ毛群が少なかった（Table 1）。また、「KaB07-22」は「Ni17」に比べ茎数が約15%少ないものの、茎径が「Ni17」並であり、茎長が25 cm長くなったことから1茎重は29%増加した。その結果、茎数×1茎重である収量は「Ni17」に比べ10%増加し、また「NiF8」と比較しても4%増加した（Table 1）。

以上の結果から、今回選抜した「KaB07-22」は、以前の選抜系統「KB04-25」で問題となった細茎化が認められず、また収量は元品種「Ni17」並びに本県主力品種「NiF8」以上であったことから有望と考えられた。今後は、株出し栽培に供試し、毛群の発生程度のほか、他品種との収量性比較など更に詳細な特性調査を行う計画である。

References

1) 竹牟ら、鹿児島県農業試験場研究報告 32 (2004) 81.
2) F. Tohjima et al., JAEA Takasaki Ann. Rep. 2005 (2007) 83.
3) F. Tohjima et al., JAEA Takasaki Ann. Rep. 2006 (2008) 73.
4) Y. Takenoshita et al., JAEA Takasaki Ann. Rep. 2007 (2008) 66.

Table 1 Characteristics of the selected line 「KaB07-22」 by spring planting (2009).

Line Cultivar	Dose (Gy)	Hair	Number of millable stalks (number/a)	Millable stalk length (cm)	Stalk diameter (mm)	Weight per stalk (g/number)	Weight of millable stalks (kg/a)
KaB07-22	1	few	800	150	23.0	641	513
Ni17(control)	-	many	942	125	22.8	496	468
NiF8(comparison)	-	ー	858	149	23.3	576	494

3-14 Production of Soybean Mutants with Pale-Green-Leaf Phenotype by Ion Beam Irradiation

S. Arase [a)], J. Abe [a)], S. Nozawa [b)], Y. Hase [b)], I. Narumi [b)] and A. Kanazawa [a)]

[a)] Research Faculty of Agriculture, Hokkaido University,
[b)] Radiation-Applied Biology Division, QuBS, JAEA

Soybean (*Glycine max*) is an important crop in terms of production of food, oil, and forage. However, existing mutant lines of soybean is very limited, which is a constraint on performing a genetic study and breeding of this plant. Soybean is considered to have derived from ancestral plant(s) that have a tetraploid genome, and as a consequence, more than 90% of nucleotide sequence in the soybean genome is duplicated [1)]. It is conceivable that such a duplicated nature of the genome brought about a low frequency of mutant production by conventional methods for mutagenesis such as γ-ray or X-ray irradiation as well as chemical treatments. In these circumstances, we have started to examine whether ion beam irradiation is effective in producing a mutant in soybean because ion beam irradiation is expected to cause genomic changes that are more drastic than those induced by conventional mutagenesis.

We have previously analyzed the effects of ion beam irradiation on plant growth and morphology in soybean by exposing dried seeds to the 320 MeV carbon ions with the range of 0.2−25 Gy [2)]. The irradiated seeds were sown on soil and plants were grown for three weeks in a greenhouse. We found that irradiation doses higher than approximately 5 Gy affected plant growth rate. In order to establish a plant population that can be available for screening mutants, we further examined the effects of irradiation by growing plants in a field. We found that both plant height and the ratio of the number of plants that survived until seed-setting per the number of seeds sown in the field depended on the doses of irradiation. We tentatively concluded that irradiation doses around 2.5 Gy are suitable for producing mutants [3)].

Based on these results we grew plants from irradiated seeds in a large scale to obtain a population of M_2 seeds: 3,200 seeds and 3,320 seeds irradiated at 5 Gy and 2.5 Gy, respectively, were sown in the field and seeds were harvested. The harvested M_2 seeds were sown in the field next year and generation of individuals with visibly altered phenotypes was examined [4)].

We detected plants with a visibly altered phenotype. The observed change was a chlorophyll deficiency, as evidenced by pale-green leaves (Fig. 1). Frequency of this type of change was 0.10% (n=1,911) and 0.19% (n=1,038) for M_2 plants irradiated with 2.5 Gy and 5.0 Gy, respectively. We confirmed that this phenotypic change was heritable by growing the progeny of M_2 plants with the altered phenotype. The M_3 progeny of four out of six M_2 plants maintained the altered phenotype (Fig. 1; the progeny of 'D-2,' 'B-1,' 'B-2,' and 'C-2' plants). Thus, at least these four M_2 plants had stable heritable change(s) that caused the altered phenotype, demonstrating that ion-beam irradiation at 2.5–5.0 Gy can induce mutation.

The frequency of the chlorophyll-deficient phenotype was comparable to that observed in other plants. For example, the frequency of the mutation in petunia was 0.4% when irradiated at half the dose that caused a decrease in survival rate but which generated various mutants [5)]. Thus, we consider that the irradiation conditions, including doses, to obtain mutants for use as breeding materials were effectively optimized in our study.

References

1) R. C. Shoemaker et al., Genetics 144 (1996) 329.
2) A. Kanazawa et al., JAEA Takasaki Ann. Rep. 2006 (2008) 88.
3) A. Kanazawa et al., JAEA Takasaki Ann. Rep. 2007 (2008) 71.
4) A. Kanazawa et al., JAEA Takasaki Ann. Rep. 2008 (2009) 68.
5) Y. Hase et al., Plant Biotechnol. 27 (2010) 99.

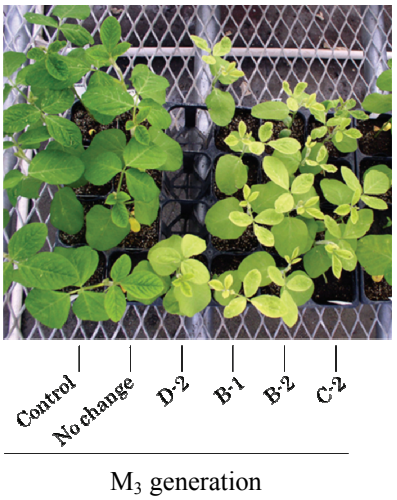

Fig. 1 Inheritance of the pale-green-leaf phenotype. Four progeny plants from each M_2 plant are shown (except D-2, for which one progeny plant is shown): from left to right, non-irradiated control, progeny of M_2 plant with no visible change, progenies of D-2, B-1, B-2, and C-2 plants.

3-15 Induction of Fusarium Wilt Resistant by Ion Beam Irradiation in Strawberry (*Fragaria* × *ananassa*) Leaf Explants

M. Yotoriyama [a)], J. Takano [a)], K. Namai [a)],
R. Yoshihara [b)], S. Nozawa [b)], Y. Hase [b)] and I. Narumi [b)]

[a)] Tochigi Prefectural Agricultural Experiment Station,
[b)] Radiation-Applied Biology Division, QuBS, JAEA

In order to obtain Fusarium wilt resistant mutant in strawberry cultivar "Tochiotome", 1,516 leaf explants were irradiated with 320-MeV carbon ion beams. Regeneration rate was in the range of 11.7 - 15.3%. Three mutants that showed stronger resistance to Fusarium wilt were selected from 1.0 Gy and 2.5 Gy irradiated group.

栃木県が育成したイチゴ品種「とちおとめ」は、作付面積が全国一であり、優れた果実品質を有するが、最重要病害の萎黄病に罹病性であるため[1)]、生産者から耐病性品種の育成が強く望まれている。イオンビームによる変異誘発は、原品種の特性を維持しつつ、一部の特性を改良するのに適している。そこで本研究では、イオンビームを用いた「とちおとめ」の萎黄病耐病性個体を作出することを目的とした。

イオンビームは日本原子力研究開発機構、イオン照射施設（TIARA）のAVFサイクロトロンを用いて、炭素イオン（$^{12}C^{6+}$, 加速エネルギー 320 MeV）を0.5, 1.0, 2.5 Gyの線量で照射した。

とちおとめ無菌培養苗の葉片を約5 mm角に調製し、TDZ 1.0 mg/L、2,4-D 0.1 mg/Lおよびブドウ糖18 g/Lを添加した1/3MS改変培地（前培養培地）で1日間液体培養した。その後、前培養培地に0.8%寒天を添加した培地（カルス誘導培地、60 mm径シャーレ）に置床し、イオンビーム照射まで4日間培養した。照射後、同様なカルス誘導培地（90 mm径シャーレ）で約1ヵ月間培養し、TDZ 1.0 mg/Lおよびブドウ糖18 g/Lを添加したMS培地に移植して再分化を誘導した。その後、発根誘導培地（ショ糖30 g/L、寒天0.8%を含むMS培地）に移植し、約2ヵ月間培養した。発根した苗はバーミキュライトを含む50穴セルトレイで1～2ヵ月間順化した。培養条件は、カルス誘導時の光強度が7 μmol m^{-2} s^{-1}、再分化誘導培養以降は40 μmol m^{-2} s^{-1}とし14時間日長、25 ºCで管理した。再分化率は、再分化誘導1ヵ月後に調査した。萎黄病菌（FOF-10S菌株）はマングビーン培地で室温、110 rpm、10日間振とう培養後、滅菌二重ガーゼでろ過した。得られた胞子様菌体は、滅菌蒸留水で2.2×10^6 bud cells/mLに調製し、1株当たり15 mLずつ灌注接種した。萎黄病菌接種苗は、人工気象器内で28 ºC、14時間日長で管理した。接種77日後に発病程度(0：病徴無し、1：小葉のわずかな奇形、2：小葉に奇形・黄化、3：軽度の萎縮、4：萎縮・萎凋、5：枯死)を調査した。なお、対照に多芽体由来の「とちおとめ」および「アスカウェイブ(萎黄病抵抗性)」順化苗を用いた。

本年度、萎黄病耐病性検定まで終了した供試葉片は非照射（312葉片）まで含めると1,828葉片であった。全照射区における再分化率は、11.7～15.3%（平均値は13.7%）であった（Fig. 1）。また、萎黄病耐病性検定による結果、対照の多芽体由来「とちおとめ」に比較して発病程度の軽かった1.0 Gy照射区の2個体、2.5 Gy照射区の1個体の計3個体を選抜した（Table 1）。

Reference

1) Y. Ishihara et al., 栃木県農業試験場研究報告 44 (1996) 109.

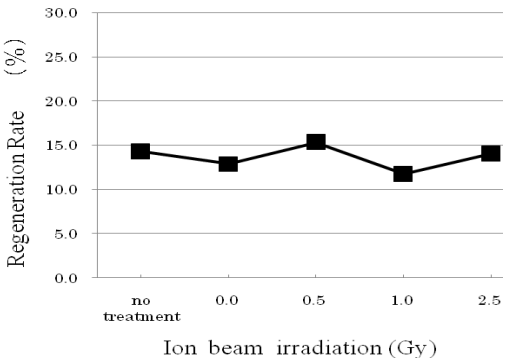

Fig. 1 Relationship between regeneration rate and ion beam irradiation.

Table 1 Degree of disease resistance to Fusarium wilt in regenerated plants derived from irradiated Tochiotome leaves.

	Degree of disease resistance to Fusarium wilt						
	0	1	2	3	4	5	Total
No treatment					2	7	9
0 Gy					1	12	13
0.5 Gy					16	30	46
1 Gy			[2]		14	7	23
2.5 Gy				[1]	14	26	41
Control*							
Tochiotome					4	13	17
Asuka wave	6						6

*: Growing points of runners were treated as a control of disease resistance.
□: Selected plants.

3-16 Assessment of Irradiation Treatments on a Salt-tolerant Arabidopsis, Zu-0 and *Thellungiella*

T. Taji [a)], A. Horiguchi [a)], A. Ikeda [a)], C. Nakajima [a)], Y. Sakata [a)], R. Yoshihara [b)], S. Nozawa [b)], Y. Hase [b)] and I. Narumi [b)]

[a)] Department of Bioscience, Tokyo University of Agriculture,
[b)] Radiation-Applied Biology Division, QuBS, JAEA

Heavy-ion beam mutagenesis is generally accepted as an effective method for mutation breeding. Accelerated particles of heavy-ion beams are thought to produce closely positioned DNA damage and double strand breaks (DSBs) upon piercing DNA strands. In plants, the DNA mutations caused by heavy-ion beams have been investigated in the model plant Arabidopsis[1]. However, it is known that the mutation frequency is different among plant species. Here, we assess the effect of carbon ion beams on plant development and sterility in salt-tolerant Arabidopsis accession, Zu-0 and *Thellungiella* to generate the mutagenized seeds for genetic screenings. In performing mutagenesis experiments, Arabidopsis Zu-0 and *Thellungiella* seeds were irradiated with carbon ion beams in the range of doses from 25 to 250 Gy. The secondary leaf developments or the sterility of Zu-0 and *Thellungiella* were inhibited more than 100 Gy and 50 Gy, respectively. Thus, we determined the irradiation treatments of Zu-0 and *Thellungiella* at doses of 50 Gy and 25 Gy, respectively, which are half doses giving inhibition on plant development and sterility.

自然界には塩に対して極めて高い耐性を示す植物が存在する。特に海水程度の高塩濃度でも生育可能な植物を塩生植物といい、マングローブなどが知られている。このような実際に高い耐性を示す植物の耐性メカニズムが、モデル植物より明らかとなってきた耐性メカニズムを用いて得られているのか、あるいは独自のメカニズムによって得られているのか非常に興味深い。これまでにも塩生植物を用いた研究はなされているものの、その形態や生活環から、分子レベル、ゲノムレベル、あるいは遺伝学を利用した研究は非常に困難であった。ところが最近、Arabidopsis に近縁の塩生植物、*Thellungiella halophila* が発見された。

Thellungiella は Arabidopsis と同様に、植物体が小さい、生活環が 3 ヶ月と短い、種子多産と遺伝学に向く形質を示す。また、多くの塩生植物で見られる塩腺のような形態的な特性が無いにもかかわらず、海水程度の塩濃度下でも生育可能な程の著しい耐塩性を示すほか、極めて高い凍結・オゾン・高温ストレス耐性を示すことが明らかとなってきた。

一方、モデル植物である Arabidopsis のエコタイプ（accessions）は世界中で 1,000 種近く発見されている。これらのエコタイプ間には数百塩基に 1 塩基の違いしかないにもかかわらず、近年の研究によりストレス耐性にも大きな違いがあることが明らかとなってきた。理研 BRC では、350 種の Arabidopsis のエコタイプが収集されている。申請者はこの 350 種のエコタイプについて耐塩性評価を行った結果、極めて高い耐塩性を示すエコタイプを発見した。

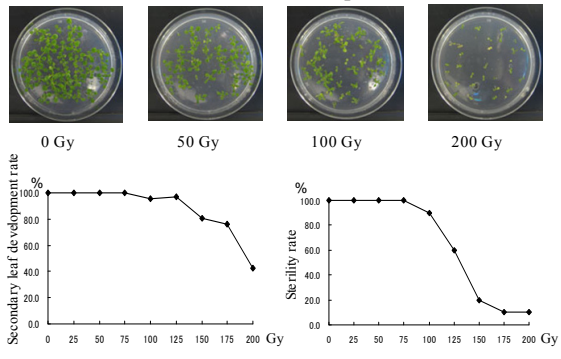

Fig. 1 Assessment of irradiation treatments on Arabidopsis Zu-0.

本研究では、このような自然界で高い耐性を示す植物の耐性メカニズムを遺伝学的に明らかにするため、これらの植物に様々な線量のイオンビームを照射し、変異誘導に最適な線量を本葉の展開率と稔性を指標に検討した。

その結果、Arabidopsis Zu-0 においては、100 Gy で、*Thellungiella* においては 50 Gy で本葉の展開率が低下し始めることが明らかとなった。また、Arabidopsis Zu-0 においては本葉の展開と同様、100 Gy で稔性の低下も認められた（Fig. 1, 2）。これまでの知見から、遺伝学的に用いるイオンビームの吸収線量は本葉の展開や稔性の低下が認められる線量の半分程度が最適とされている。そこで、Arabidopsis Zu-0 および *Thellungiella* 種子に変異を誘導させるイオンビーム吸収線量をそれぞれ 50 Gy, 25 Gy に決定した。

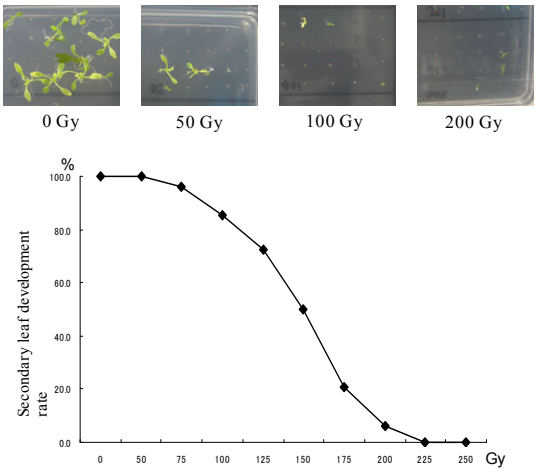

Fig. 2 Assessment of irradiation treatments on *Thellungiella.*

Reference

1) N. Shikazono et al., J. Exp. Bot. 56 (2005) 587.

3-17 Effects of Ion-beam Irradiation on Germination and Growth of Seedlings of Red Pepper 'Hirosaki zairai'

M. Tomikawa [a)], T. Maeda [a)], K. Honda [a)], K. Saga [a)], R. Ishikawa [a)], Y. Akita [b)], R. Yoshihara [b)], S. Nozawa [b)] and I. Narumi [b)]

[a)] Faculty of Agriculture and Life Science, Hirosaki University,
[b)] Radiation-Applied Biology Division, QuBS, JAEA

Red pepper (*Capsicum annuum* L.) 'Hirosaki zairai' is a local variety grown around Hirosaki city in Aomori prefecture, and it has been promoted as one of the 'valuable local brands'. In this study, we tried to create additional values on this unique variety via mutation breeding using ion beam irradiation which has been widely adopted on many crops[1–3].

Seeds of 'Hirosaki zairai' placed on petri dishes were irradiated with 220-MeV carbon-ion beams accelerated by a TIARA AVF cyclotron (JAEA, Takasaki, Japan), at the doses of 0, 10, 20, 30, 40, 50, 60, 70, 80, 100, 200 and 300 Gy. One hundred seeds were irradiated at each dose. All the treated seeds were sown on ϕ 90 mm petri dishes with moistened filter papers (25 seeds on each dish × 4 replication), and incubated at 25 °C. Germinated seeds were counted daily, and then were transplanted to 128-hole cell tray and cultivated in a greenhouse at Hirosaki University. Effects of the ion beam irradiation on M_1 plants were evaluated by examining the shapes of cotyledons, plants and fruits. Plant height and number of joints were measured once a week from 40 days after sowing. Ten M_1 seedlings from each dose were transplanted to #7 plastic pots in a greenhouse, and the rest of the seedlings were transplanted on the research field of Hirosaki University after 90 days from sowing. Immature green fruits (10 fruits per each dose) were collected from M_1 plants growing both in greenhouse and open field at 20 days after flowering. Red fruits were also collected after fully matured. Length, width in the middle part, width in the shoulder part and weight of each fruit were measured. All the irradiated plants were examined on the indication of mutation by visual judgment. Some flowers in a green house were covered with mesh net for self-pollination. Same treatment was conducted on the visually–mutated plants.

Delay of germination was observed in accordance with dosage, however, germination rates were more than 96 %, and no visual mutation was observed in the shape of radicles in all the treatments. Curled cotyledons were observed only in the ion-beam irradiated plants, and degree of the curl got larger in accordance with dosage. Both emergence rates of shoot and survival at 60 days after sowing got lower at the doses over 50 Gy, and almost all seedlings died over 70 Gy (Fig. 1). Plant heights were rather lower in the plants irradiated with high dosage at May 20 (72 days after sowing): however, the differences in plant heights got smaller at June 18 (101 days after sowing). No significant difference was observed in the number of joints. These results suggested that the physical energy of ion beam irradiation, especially over 50 Gy, was seemed to cause significant effects on the growth of young seedlings. Some irregular plants in the shape were observed over 10 Gy, such as dwarfing, short internode, and one short internode plant was found to have much more fruits in comparison with non-irradiated control. We successfully earned M_2 seeds from such 'visibly-mutated' plants. Further investigation was needed whether such mutations were genetically fixed. No significant difference was observed in the shape of fruits within the plants from which the green or red fruits: however, some extremely small fruits and 'doubly–fruited' i.e. prolificated fruits (a small fruit was formed in a fruit) were observed in 40-Gy irradiated samples. This result suggested that ion beam irradiation also affected on fruiting. The results of this study showed that ion beam irradiation seemed to be applicable on the mutation breeding of red pepper 'Hirosaki zairai', and that mutation could be caused at the absorbed dose of over 10 Gy.

References

1) I. Honda et al., Euphytica. 151 (2006) 61.
2) H. Yamaguchi et al., Breeding Sci. 59 (2009) 169.
3) E. Kondo et al., Plant Biotech. 26 (2009) 565.

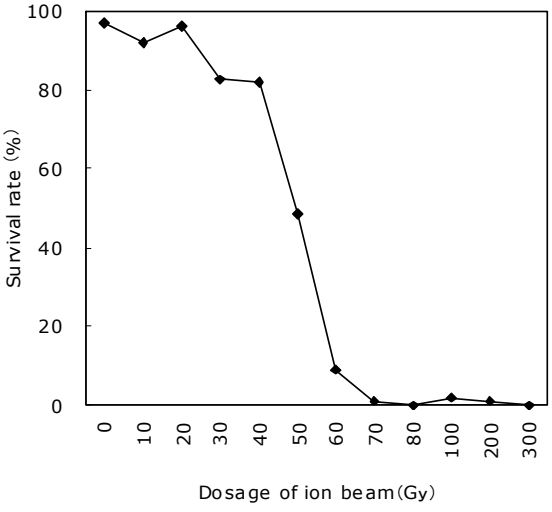

Fig. 1 Effect of ion beam irradiation on the survival rate of the seedlings of red pepper 'Hirosaki zairai' at 60 days after sowing.

3-18 Effect of Different LET Radiations on Root Growth of *Arabidopsis thaliana*

R. Yoshihara [a)], S. Nozawa [a)], H. Saika [b)], M. Teranishi [c)],
S. Toki [b,d)], J. Hidema [c)] and A. N. Sakamoto [a)]

[a)] Radiation-Applied Biology Division, QuBS, JAEA, [b)] Plant Genetic Engineering Research Unit, National Institute of Agrobiological Sciences, [c)] Graduate School of Life Sciences, Tohoku University, [d)] Kihara Institute for Biological Research, Yokohama City University

Biological effects of ion beams have been mainly studied in animal or bacterial systems because of the need of ion-beam application in medical treatments. Concurrently, ion beams have been used as a remarkable mutagen in the mutation breeding for useful agricultural or garden products. Although many valuable cultivars have been produced in the ion-beam breeding, little is known about the mechanism of ion-beam mutagenesis in higher plants. In this study, we aim to elucidate the effects of ion beams on higher plants. We focus on two points: i) what kinds of damage are produced by ion beams, and ii) what kinds of cellular processes are involved to turn the damage into mutations. Such information will lead to great advancement of ion-beam breeding techniques.

To analyze the effects of ion beams on higher plants, we first quantified the growth inhibitory effects by ion-beam irradiation. We irradiated the model plant *Arabidopsis thaliana* with 220 MeV carbon ion beams (220 MeV C, LET: 112 keV/μm), 50 MeV helium ion beams (50 MeV He, LET: 16.8 keV/μm) or γ-rays (LET: 0.2 keV/μm), and root growth was measured after each treatment.

Arabidopsis seeds were sown on Murashige and Skoog (MS) ager plates aseptically. The plates were held vertically in the 23 °C growth chamber for three days so that roots grew along the surface of plates, ensuring of accurate irradiation. The plants were exposed to ion-beam or γ-ray radiations. After grown for another 3 days, the root length was measured. Root elongation rate is shown as the rate of root length of irradiated plant to that of non-irradiated plant.

Root elongation rates of wild-type *Arabidopsis* exposed to 50 MeV He were indistinguishable with those exposed to γ-rays. This result let us speculate that the both radiations induce comparable quantity and/or quality of DNA lesions that inhibit the root growth (Fig. 1 [A]).

However, root elongation rates of plants exposed to 220 MeV C were significantly lower (Fig. 1 [A]). This result suggests that 220 MeV C may induce more numbers of DNA lesions or more severe types of DNA lesions than γ-rays and 50 MeV He.

In prior studies, it was suggested that ion beams induce DNA double-strand breaks (DSBs) in plant. The DSBs are known as one of the most severe DNA lesions and repaired by non-homologous end-joining (NHEJ) or homologous recombination (HR) pathways in many organisms. *Arabidopsis* also posses a series of genes involved in the NHEJ and HR pathways. Therefore, we prepared a mutant *Arabidopsis* that is deficient in NHEJ and exposed it to ion beams to examine whether the ion-beam induced DNA lesions are repaired by the NHEJ pathway.

When the wild-type and NHEJ deficient plants were exposed to γ-rays or 50 MeV He, the root elongation rate of NHEJ deficient mutant was more severely inhibited than the wild type (Fig. 1 [B], [C]). However, the root elongation rate of the mutant exposed to 220 MeV C was almost the same as that of the wild type (Fig. 1 [D]). These results suggest that the considerable amount of DNA lesions induced by γ-rays or 50 MeV He are repaired by NHEJ, but the majority of DNA lesions induced by 220 MeV C are not repaired by NHEJ. From this observation, we propose a hypothesis that the types of DNA lesions induced by relatively low LET radiations such as γ-rays or 50 MeV He and those by extremely high LET radiations such as 220 MeV C are inherently different. The difference in types of DNA lesions could affect the variety of mutation induced. We will next analyze the mutation spectrum in various repair-deficient plants to elucidate the mechanism of ion beam mutagenesis in higher plants.

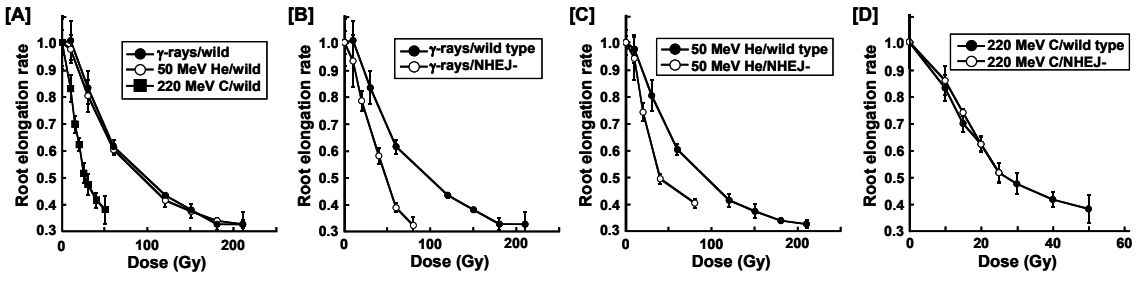

Fig. 1 Root elongation rate of wild type and mutant *Arabidopsis*.
[A] Root elongation rate of wild type plants exposed to γ-rays, 50 MeV He and 220 MeV C,
[B], [C], [D] Inhibitory effect on root elongation in mutant plants by γ-rays [B], 50 MeV He [C] and 220 MeV C [D].

3-19 Phenotypic Improvement of *Bradyrhizobium japonicum* USDA 110 into a High Temperature Tolerant Strain in terms of Ion-beam Microbial Mutation-breeding Technology

K. Takeda [a)], K. Tejima [b)], K. Satoh [b)], I. Narumi [b)] and T. Yokoyama [c)]

[a)] Graduate school of Agriculture, Tokyo University of Agriculture and Technology,
[b)] Radiation-Applied Biology division, QuBS, JAEA,
[c)] Institute of Agriculture, Tokyo University of Agriculture and Technology

In order to supply food to increasing population in Asia, agricultural production should be increased and a large amount of nitrogen fertilizer is required. Most of the nitrogen fertilizers are chemical nitrogen fertilizers. They are produced by oil and natural gas in terms of the Haber–Bosch process, which exhausts a large amount of CO_2. Furthermore, the economically minable period of the fossil resources is estimated to be around 40 years, therefore a reduction of chemical nitrogen fertilizer input is required in agricultural practices.

In Asian countries, in order to increase crop yield under low input of chemical nitrogen fertilizers, many researchers in agricultural institutes are trying to develop biofertilizers, which contain beneficial soil microorganisms and increase availability of plant nutrients from soils. However, several researchers point out constraints on application of biofertilizers. Major constraint of biofertilizer utilization in agricultural practice is a serious deterioration of qualities in biofertilizers under both storage and transportation conditions. In other words, exposing high temperature and drought stress causes a viability loss of beneficial microorganisms in biofertilizers. This becomes a serious problem on the dissemination of biofertilizer in southeastern Asia. Therefore, in order to prevent deterioration in variability of inoculants in biofertilizers exposed to high temperature, we are trying to improve a phenotypic character concerning high temperature tolerant in *Bradyrhizobium japonicum* USDA 110, which is a worldwide superior inoculant to soybean. In this study, ion-beam microbial mutation-breeding technology is used to generate high temperature tolerant mutants.

B. japonicum USDA 110 was cultivated in YM liquid medium until they reached to a concentration of 10^8 cells/mL. Cells were harvested by centrifugation and resuspended in a solution containing 10% skim milk and 1.5% sodium glutamate. The suspension was then subjected to vacuum-freeze drying (Fig. 1) to minimize the effect of water radiolysis during irradiation. Freeze-dried cells of *B. japonicum* USDA 110 were irradiated with carbon ion beams (220 MeV $^{12}C^{5+}$) at TIARA in JAEA. Irradiation dose was ranged from 0 to 800 Gy. Survival rates were changed as follows: 10% at 100 Gy, 0.7% at 300 Gy, and 0% at 800 Gy. Aliquots of irradiated cells were proliferated on YM-agar plate in order to fix mutations. Mutant frequency was determined by measuring the number of rifampicin resistant colonies (Fig. 2; rifampicin resistance is conferred by a mutation in *rpoB* gene encoding RNA polymerase β subunit) in total number of viable colonies. The highest frequency value of mutants was obtained from cells irradiated at 300 Gy. In general, *B. japonicum* USDA110 cannot survive at 40 °C. In order to obtain high temperature tolerant mutants, the irradiated cells were put on the YM agar plate and keep for over 1 month at 45 °C in several times. But, we couldn't find any proliferated colony. Therefore, we developed a new method to screen survival cells at 45 °C. In the new method, the irradiated cells were incubated in YM liquid medium at 45 °C for 5 days, and the cultures were put on YM-agar. Consequently, we obtained high temperature tolerant mutants of *B. japonicum* USDA 110, which can survive at 45 °C for 5 days. Now, we are characterizing these mutants in terms of differences in several phenotypic properties.

Fig. 1 Preparation of freeze-dried cells of *B. japonicum* USDA 110.

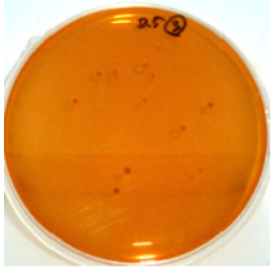

Fig. 2 Refampicin resistant colonies of *B. japonicum* USDA 110 on YM-agar plate supplemented by 400 μg/mL of rifampicin.

3-20 Fungicide Tolerant Mutation of Entomopathogenic Fungi Induced by Carbon Ion Beams

T. Saito [a)], K. Satoh [b)] and I. Narumi [b)]

[a)] Faculty of Agriculture, Shizuoka University, [b)] Radiation-Applied Biology Division, QuBS, JAEA

Entomopathogenic fungi, *Isaria fumosorosea*, *Beauveria bassiana* and *Verticillium lecanii*, are important agents to control insect pests, but the fungi are highly susceptible to conventional fungicides for plant diseases such as powdery mildew. The purpose of this study is to generate mutants tolerant to fungicides using carbon ion beams. In order to determine a suitable dose of ion beam radiation to induce the fungi mutate efficiently, fungal conidia were irradiated with ion beams in the 50 to 400 Gy range. The dose that gives 10% conidial survival was approximately 150 Gy in *I. fumosorosea*, 150 to 300 Gy in *B. bassiana* and 150 to 350 Gy in *V. lecanii*. Irradiated conidia were cultured on Sabouraud dextrose agar supplemented by fungicides, benomyl (500 ppm) and triflumizole (150 ppm). Fungicide-tolerant mutants were obtained from *B. bassiana* and *V. lecanii*, but not *I. fumosorosea*. The mutants were obtained in a dose-independent manner. The results indicate that ion-beam irradiation is greatly useful for making fungicide-tolerant mutants of entomopathogenic fungi.

化学合成農薬は数多くの課題を抱えていることから、IPM（総合的害虫管理技術）の普及が急務とされている。このIPMの基幹技術と目されているのが天敵昆虫や天敵微生物などを用いる生物的防除法である。天敵微生物については昆虫病原糸状菌が商品化されているが、殺菌剤と併用しにくいという難題を抱えている。たとえば、農作物を栽培すれば「うどんこ病」などの病気が発生するが、殺菌剤の散布は昆虫病原糸状菌に対して悪影響を与えてしまう。この抜本的な解決策として、殺菌剤の影響を受けにくいという新機能を有する昆虫病原糸状菌を創出することが考えられる。本研究の目的は、イオンビームによる突然変異育種技術を用いて、昆虫病原糸状菌の殺菌剤耐性変異体を創出することである。

研究初年度は、炭素イオンビームの吸収線量を決定するため、代表的な昆虫病原糸状菌3種（*Isaria fumosorosea*、*Beauveria bassiana* 及び *Verticillium lecanii*）を供試して、照射線量と分生子生存率の関係を調べた。また、殺菌剤耐性変異体選抜の予備試験を行った。

各供試菌は、サブロー寒天培地で20日間（20 °C）培養し、得られた分生子を0.1% Tween 80を含む蒸留水に懸濁し、ろ過装置を用いてメンブレンフィルター（直径 4.5 cm）上に分生子を集めた。このメンブレンフィルターをプラスチックシャーレ（直径6 cm）に入れ、シャーレ上面をカプトン膜で覆ったのち、炭素イオンビームを照射した。吸収線量は、8段階（50～400 Gy、50 Gy 間隔）とした。

分生子生存率の調査方法は次の通りである。イオンビーム照射後のフィルターをサブロー液体培地が入ったサンプル瓶（10 mL 用）に投入し、撹拌棒を用いてフィルターから分生子を離脱させた。フィルターを取り除いた後、液体培地の分生子濃度を測定した。生存率は、分生子を懸濁させた液体培地（100 µL）をサブロー寒天培地上に塗布し、20 °C で培養した後のコロニー数をもとに算出した。

殺菌剤耐性変異体の選抜方法は次の通りである。殺菌剤は、市販のベンレート水和剤（50%ベノミル）とトリフミン乳剤（15%トリフルミゾール）を供試した。各殺菌剤を添加（1,000倍）したサブロー寒天培地上にイオンビーム照射後の分生子懸濁液 200 µL を塗布し、20 °C で3週間程度培養後、発育良好なコロニーを殺菌剤耐性変異体として分離した。この操作は、イオンビームの照射区ごとに行った。

イオンビーム吸収線量と分生子生存率の関係をTable 1に示した。生存率が10%程度となる吸収線量は、*I. fumosorosea* が150 Gy、*B. bassiana* が150～300 Gy 及び *V. lecanii* が150～350 Gy であり、実験によってばらついた。

殺菌剤耐性変異体の獲得状況を Table 2 に示した。*I. fumosorosea* ではベノミル耐性変異体は得られたが、著しい奇形を呈したことから、期待される変異体とは認められなかった。また、トリフルミゾール耐性変異体も得られなかった。一方、*B. bassiana* ではベノミル耐性変異体が得られ、トリフルミゾール耐性変異体も少数ながら得られた。*V. lecanii* でも両剤に対する耐性変異体が得られた。吸収線量と耐性変異体出現頻度に一定の傾向はみられなかった。

以上のことから、イオンビームは昆虫病原糸状菌の殺菌剤耐性変異体の作出に利用できると考えられる。得られた殺菌剤耐性変異体の病原力については、今後、検討する予定である。

Table 1 Percent survival of fungal conidia treated with carbon ion beams.

Dose (Gy)	*I. fumosorosea*			*B. bassiana*		*V. lecanii*	
	1st	2nd	3rd	1st	2nd	1st	2nd
400	0	0		0		6.1	
350	0	0	0	0.1	5.0	36.0	
300	0	0	0.6	0.6	12.8	50.5	0.1
250	0.3	0.6	1.9	3.1	24.2	61.3	2.0
200	3.2	1.1	3.8	5.0	52.1	62.4	4.5
150	10.2	6.0	6.9	13.5	75.1	69.9	13.8
100	53.2	25.5	20.1	44.5	59.6	80.2	80.6
50	91.4	70.8	34.0	90.9	83.2	91.2	

Table 2 Fungicide-tolerant mutation induced by carbon ion beams.

Fungicide	*I. fumosorosea*	*B. bassiana*	*V. lecanii*
Benomyl	Deformed	Obtained	Obtained
Triflumizole	None	Obtained	Obtained

3-21 Improvement of Endophytic Bacteria Using Ion Beams

M. Aino [a)], K. Satoh [b)] and I. Narumi [b)]

[a)] Hyogo Prefectural Center for Agriculture, Forestry and Fisheries,
[b)] Radiation-Applied Biology Division, QuBS, JAEA

The endophytic bacteria produce various kinds of bioactive substances, by which the plants grow well and exhibit resistance to diseases and environmental stress. In this study, we investigated survival rate, mutation frequency for kanamycin resistance and antagonistic effect against tomato bacterial wilt of endophytic bacteria, *Pseudomonas fluorescens* FPH 9601, that was irradiated with ion beams. The absorbed dose range was 10 to 300 Gy. Irradiation over 100 Gy resulted in a significant decrease in cell survival, whereas irradiation below 10 Gy had no effect on cell survival. The kanamycin resistant bacteria appeared only in 300-Gy irradiated cells at a rate of 1.8%. We could successfully obtain mutants that have enhanced suppressiveness against the tomato bacterial wilt by ion-beam irradiation. These results suggest that ion-beam irradiation is a useful method to obtain mutants of Pseudomonads.

内生細菌は種々の生理活性物質を産生し、これらの働きによって感染した植物の生育が促進されたり、病害に対して抵抗性になったり、環境ストレスに対して耐性になったりする。これらの現象は内生細菌の植物への親和性に依存すると考えられる。一方、*Pseudomonas* 属細菌の中には植物に内生能を示す菌株が多く存在し、現在、生物農薬として販売されている「セル苗元気」（トマト・ナス・ピーマンの青枯病に効果を示すバイオ農薬）の原体微生物として用いられている。本生物農薬に含まれる *Pseudomonas* 属細菌を用い、イオンビーム突然変異育種の技術を用いて植物への定着や抗菌活性能力の増強が可能かどうかを検討した。

供試菌株は *Pseudomonas fluorescens* FPH9601 を用い、標準寒天培地上で 28 °C、24 時間培養後、滅菌蒸留水に懸濁した。懸濁液（約 10^8 cfu/ml）2 mL を直径 47 mm の酢酸セルロースメンブランフィルター（ADVANTEC 社）でろ別した。ろ別後、直ちに直径 60 mm シャーレにフィルターを入れ、凍結乾燥を行った。保護剤等は添加せず行った。凍結乾燥後、シャーレ上面をカプトン膜で覆った。

イオンビーム照射は TIARA の AVF サイクロトロンを用い、$^{12}C^{5+}$（220 MeV）で 10～300 Gy の範囲で凍結乾燥菌体を照射した。照射後、試料を滅菌蒸留水と共に試験管に入れ、30 分間振とう後、懸濁液を菌体原液とし、以下の試験に供試した。

①吸収線量と生存率の関係：上記原液を基とし、希釈平板法を用いて生存菌数を計測した。供試培地は標準寒天培地を用いた。28 °C で 24 時間後に形成されたコロニーを計測し、生存数とした。

②吸収線量とカナマイシン耐性変異株の出現との関係：カナマイシンを 125、250 及び 500 ppm を含む標準寒天培地を流し込んだシャーレ（直径 90 mm）に上記原液 0.1 mL を塗布し、28 °C で 48 時間後にそれぞれのシャーレに生じたコロニーを計測した。

③植物病害に対する発病抑制効果の増強株の検出：上記原液（吸収線量 300 Gy）を 100 倍に希釈し、標準寒天培地を流し込んだシャーレに塗布し、28 °C、48 時間後に生じたコロニーをかき取り、再度、標準寒天培地上で 28 °C、48 時間培養した。培養菌株を 15%グリセロール溶液に懸濁し、–80 °C で保存した。凍結保存菌株（100 菌株）を標準液体培地に植菌し、28 °C で 24 時間培養し、シードリングバイオアッセイチャンバー法を用いて、トマト青枯病（*Ralstonia solanacearum*）に対する発病抑制効果を検定した。

吸収線量と生存率の関係は、10 Gy では非照射と変わらずコロニーが出現したが 25 Gy から急激に生存数が減少し 100～300 Gy の照射では、非常に高感受性を示した（Fig. 1）。カナマイシン耐性株の出現は、カナマイシン 250 及び 500 ppm では各線量とも耐性株は出現しなかったが、125 ppm の場合、300 Gy 照射時のみに 1.8%の割合で耐性菌が出現した。イオンビーム照射によるトマト青枯病に対する発病抑制効果の変化は、親株と比べ、59 株が効果低下し、41 株が効果増強した（Fig. 2）。これらの内 4 株は、親株よりも 5 倍以上の高い発病抑制効果を示した。これらの結果からイオンビームを用いた *Pseudomonas* 属細菌の突然変異育種は可能と推定された。

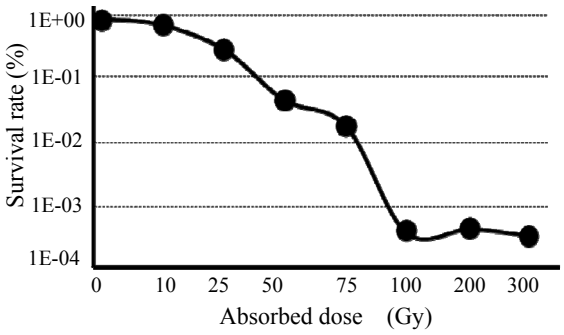

Fig. 1 Cell survival after irradiation with carbon ion beams in *P. fluorescens* FPH9601.

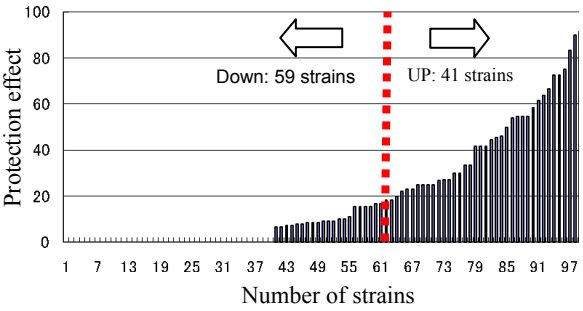

Fig. 2 Suppression of tomato bacterial wilt by ion beam irradiated *P. fluorescens* FPH.

3-22 FACS-based Screening of Yeast Strain Highly Expressing Cellulase

K. Ninomiya [a)], H. Soda [a)], K. Satoh [b)], I. Narumi [b)] and N. Shimizu [a)]

[a)] Division of Material Engineering, Graduate School of Natural Science and Technology, Kanazawa University, [b)] Radiation-Applied Biology Division, QuBS, JAEA

By using immunocytochemistry and fluorescence-activated cell sorter (FACS), yeast population highly expressing cellulase on the cell surface was enriched from the mutant population prepared by irradiation with carbon ion beams (220 MeV $^{12}C^{5+}$, 100 Gy). The cellulase activity of selected yeasts was 5.2×10^{-3} U/OD unit, whereas cellulase activity of parental strain was 1.6×10^{-3} U/OD unit.

近年、非食用バイオマスであるセルロースを原料としたエタノール発酵生産への関心が高まっている。セルロース糖化酵素であるセルラーゼを発現する酵母を用いた“セルロースからの直接エタノール発酵生産”では、酵母のセルラーゼ発現量が生産コストを下げるための律速段階の 1 つと言われている。本研究では、セルラーゼ高発現酵母を育種するために、細胞表層に発現したセルラーゼの酵素量を蛍光免疫染色で蛍光強度に置き換えることにより、fluorescence-activated cell sorter（FACS）を用いて、セルラーゼ高発現株を蛍光強度の高い細胞集団として high-throughput に分取することを目的とした。

使用菌株：3 種のセルラーゼ endoglucanase II（EGII）、cellobiohydrase II（CBHII）ならびに β-glucosidase を細胞表層に発現した酵母 *Saccharomyces cerevisiae* MT8-1/pEG23u31H6/pFCBH2w3/pBG211 株 [1]（MT8-1III 株）を用いた。また、MT8-1III 株に炭素イオン（220 MeV $^{12}C^{5+}$）を線量 100 Gy で照射し（以下、重イオンビーム照射）、変異株集団を調製した。酵母の培養は SD 培地を用いて 30 °C で行った。

蛍光免疫染色および FACS：酵母表層のセルラーゼ分子の量を蛍光量として評価するため、EGII ならびに CBHII のタグとして融合発現させた $RGSHis_6$ および FLAG に対する一次抗体、それぞれの一次抗体に特異的な Alexa Fluor 488（FITC）および R-phycoerythrin（PE）標識二次抗体を用いて二重染色を行った。蛍光免疫染色を行った酵母株は、FACS を用いて蛍光強度を測定し、FITC ならびに PE の蛍光強度の高い細胞集団を目的株として細胞分取を行なった。

セルラーゼ活性測定：酵母表層の EGII ならびに CBHII の総括のセルラーゼ活性を、カルボキシメチルセルロース（CMC）を基質として測定した。CMC が加水分解されることにより生じる還元末端の増加速度を 3,5-dinitrosalicylic acid（DNS）法を用いて測定し、セルラーゼ活性として評価した。1 min で 1 μmol の還元末端を生じる酵素活性を 1 U、また、波長 600 nm における濁度 $OD_{600}=10$ の酵母細胞懸濁液 1 mL を 1 OD unit と定義し、酵母細胞の持つセルラーゼ活性を U/OD unit で表した。

Figure 1(A)に親株である MT8-1III 株の蛍光免疫染色の結果を示す。FITC ならびに PE の蛍光強度（EGII ならびに CBHII の発現量に相当）の相対値が 10^4 以上の領域（P4 領域）に分布する細胞は全体の 1.6%であった。一方、Fig. 1(B)には、親株 MT8-1III 株に対して「重イオンビーム照射による変異導入」と「FACS による P4 領域の細胞集団の選抜」を行なった酵母の蛍光免疫染色の結果を示す。P4 領域に存在する細胞は全体の 6.9%に増加することが分かった。

親株 MT8-1III 株と、重イオン変異と P4 領域の選抜を行なった酵母について、セルラーゼ活性を測定した。その結果、親株 MT8-1III 株のセルラーゼ活性が 1.6×10^{-3} U/OD unit であったのに対し、選抜された酵母集団のセルラーゼ活性は 5.2×10^{-3} U/OD unit へ向上していることが分かった。

Reference

1) Y. Fujita et al., Appl. Environ. Microbiol. 68 (2002) 5136.

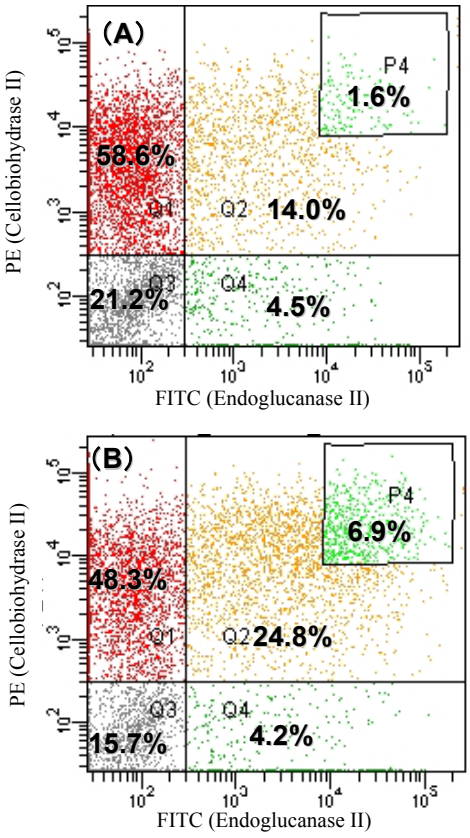

Fig. 1 Scatter plots of FITC and PE fluorescence corresponding to EGII and CBHII expression on yeast cells, respectively. (A) Parental yeast strain of MT8-1III. (B) Selected yeast from P4 region cells sorted from ion-beam irradiated MT8-1III.

3-23 Molecular Analysis of Carbon Ion Induced Mutations in Yeast *Saccharomyces cerevisiae* Cells

K. Shimizu [a)], Y. Matuo [a, b)], Y. Izumi [b)], Y. Hase [c)], S. Nozawa [c)], A. N. Sakamoto [c)] and I. Narumi [c)]

[a)] Radioisotope Research Center, Osaka University, [b)] Research Institute of Nuclear Engineering, University of Fukui, [c)] Radiation-Applied Biology Division, QuBS, JAEA

1. Introduction

This study is intended to elucidate the molecular mechanism of the mutagenesis caused by ion beam irradiation. Ion beam irradiation is expected to increase mutation frequency and spectrum, since it has a high linear energy transfer (LET). However, the detailed molecular mechanism of its action has not been proven.

Recently, we reported that the main mutations induced by high-LET carbon-ion irradiation were GC to TA transversions[1)]. DNA adducts such as 8-oxodG, which are produced by interactions of reactive oxygen species (ROS) with these molecules, can create various pairing formations in DNA molecules, for example, pairing with dA in the syn conformation to produce a GC to TA mutation[2)]. In this study, we used the yeast mutant strains *ogg1* and *msh2*, which are deficient in mismatch repair mechanisms. Mutations involving 8-oxodGs were caused by ion beam irradiation in the *ogg1* and *msh2* mutant strains.

2. Materials and methods

2.1. Yeast strains

S. cerevisiae haploid strains used in this study were S288c (*MATα*, *RAD*), *rad52* (*MATα*, *G160/2b*), *ogg1* (*MATα*, *ΔOGG1*) and *msh2* (*MATα*, *Δmsh2*).

2.2. Irradiation methods

To determine the biological effectiveness of high LET ion beam irradiation, yeast cells were exposed to heavy ions accelerated at the AVF cyclotron (TIARA; JAEA Takasaki, Takasaki, Japan).

As for the physical properties of the carbon ions, the mean LET in the yeast was estimated to be 107 keV/μm water equivalent. This LET value was calculated by means of the ELOSS code program, which uses the elementary composition and the density of the target to calculate the energy loss of ion particles.

3. Results and Discussion

One of the most common consequences of ROS exposure is the incorporation of oxidized nucleotides such as 8-oxodG into the genome. Mismatch repair has been shown to repair oxidative damage by lowering the level of 8-oxodG that is incorporated into the genome, presumably by recognizing mismatches different from those recognized by base excision repair.

The distribution of the mutations induced by carbon ion beam irradiation is shown in Fig. 1. In the *ogg1* mutant strain, there were minor hot spots at positions 330, 515, 602, and 745 (Fig. 1 (C)). The mutations in *msh2* mutant were distributed evenly for base substitution, except for a minor hot spot at position 345. These results suggest that the incorporation of damaged nucleotides was not uniform. In comparison with the surrounding sequence context of mutational base sites, the C residues in the 5'- (A/T) C (A/T) -3' sequence were found to be easily mutated (data not shown). These observations are in agreement with results obtained in wild type cells.

References

1) Y. Matuo et al., Mutat. Res. 602 (2006) 7.
2) M. Inoue et al., J. Biol. Chem. 273 (1998) 11069.

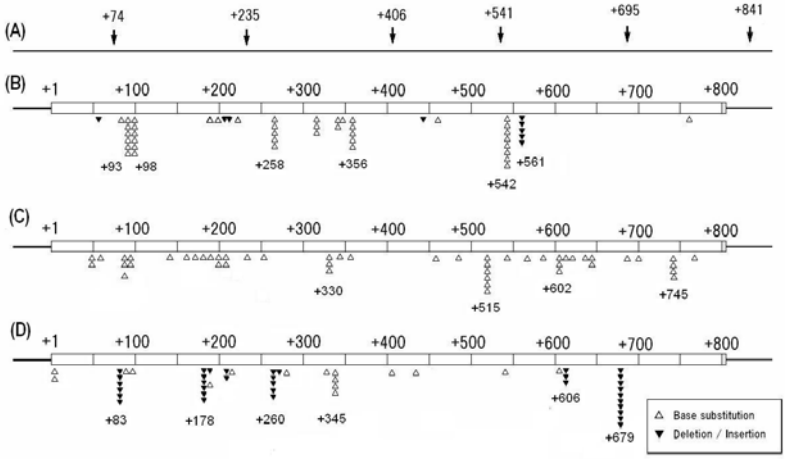

Fig. 1 The mutation spectra induced by carbon ion beam irradiation of yeast. White triangles: base substitute mutations, inverted black triangles: deletion/insertions. (A) nucleotide position number of *URA3* gene; (B) mutation spectrum of wild type; (C) *ogg1*; (D) *msh2*.

3-24 Lethal Effects of Different LET Radiations in *Deinococcus radiodurans*

K. Satoh, K. Tejima and I. Narumi

Radiation-Applied Biology Division, QuBS, JAEA

Introduction

Ionizing radiation induces DNA double-strand breaks (DSBs), which is a particularly serious form of DNA damage and has an especially deleterious effect on cells. The radiosensitivity of organisms varies extensively depending on the species. Ion beams have a high linear energy transfer (LET, keV/μm) and give DNA damage containing DSBs locally (clustered damage) than gamma rays do. In mammalian cells, plants and *Escherichia coli*, the relative biological effectiveness (RBE) depends on LET and exhibits the peak at a range of LET from about 100 to 200 keV/μm [1-3].

While, *Deinococcus radiodurans* exhibits extraordinary resistance to the lethal effects of ionizing and UV radiations, as well as many other DNA damaging agents. This resistance has been attributed to its highly proficient DNA repair capacity[4]. The most noteworthy characteristic of *D. radiodurans* is its capacity for repairing ionizing radiation-induced DSBs. However, LET-dependent biological effect in *D. radiodurans* is poorly understood. In this study, we investigated lethal effects and relationship between LET and RBE for different LET radiations.

Experimental procedures

D. radiodurans cells were cultivated at 30 °C in TGY medium with agitation to early stationary phase. Cells were harvested, washed and resuspended in 100 mM Tris-HCl (pH 7.0) containing 2.5% glycerol (TG buffer). Aliquots (1 mL) of the cell suspensions were adhered onto cellulose membrane, frozen at −80 °C and dried *in vacuo*. The freeze-dried cells were irradiated with four kind of ion beams ($^{4}He^{2+}$ [50 MeV; 19.4 keV/μm], $^{12}C^{5+}$ [220 MeV; 121.8 keV/μm], $^{20}Ne^{8+}$ [350 MeV; 441 keV/μm], $^{40}Ar^{13+}$ [460 MeV; 1,650 keV/μm]) accelerated by AVF cyclotron, or with ^{60}Co gamma rays (0.2 keV/μm) at Food Irradiation Facility, JAEA. The irradiation dose ranged from 1 to 15 kGy. Irradiated cells were harvested, diluted appropriately with the TG buffer, spread onto TGY agar, and incubated at 30 ˚C for 3 days prior to the enumeration of colonies. The RBE was calculated from the equation: RBE = D_{10} of gamma rays (Gy) / D10 of ion beams (Gy), where D_{10} is the dose quantity necessary for decreasing the survival fraction to 10%.

Results and discussion

To determine the cell condition for ion beam irradiation, the sensitivities for gamma rays were compared between the freeze-dried and wet cells. The freeze-dried cells exhibited a higher resistance to gamma-irradiation than the wet cells (Fig. 1), indicating that the effect of water radiolysis was relieved under the freeze-dried condition. From this result, the freeze-dried cells were used for ion beam irradiation.

As shown in Fig. 1, the radioresistances of freeze-dried cells to He, C and Ne ion beams were almost equal to that of the gamma-irradiated cells. On the other hand, the high-LET Ar ion-irradiated cells exhibited a much higher resistance than those of other radiations at high doses (10 to 15 kGy). This higher resistance to Ar ion beams was attributed to overkill effect. Unlike other organisms, *D. radiodurans* did not show the dependence of LET on RBE at a range of LET from about 0.2 to 441 keV/μm (Fig. 2). These results suggest that *D. radiodurans* could repair the clustered damages effectively.

References

1) N. Hamada et al., Radiat. Res. 166 (2006) 24.
2) Y. Hase et al., Int. J. Radiat. Biol. 78 (2002) 799.
3) M. Imamura et al., J. Gen. Appl. Microbiol. 43 (1997) 175.
4) I. Narumi, Trends Microbiol. 11 (2003) 422.

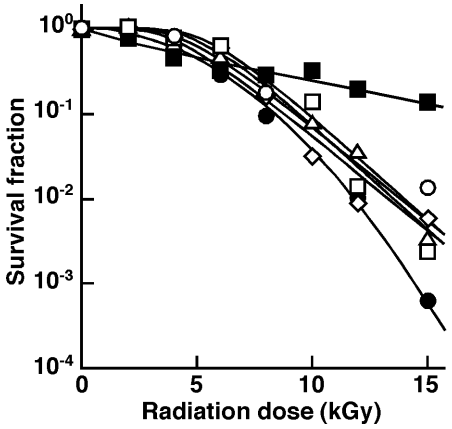

Fig. 1 Survival curves to different LET radiations. Symbols: closed circles, gamma rays (wet cells); open circles, gamma rays (freeze-dried cells); open triangles, $^{4}He^{2+}$; open lozenges, $^{12}C^{5+}$; open squares, $^{20}Ne^{8+}$; closed squares, $^{40}Ar^{13+}$.

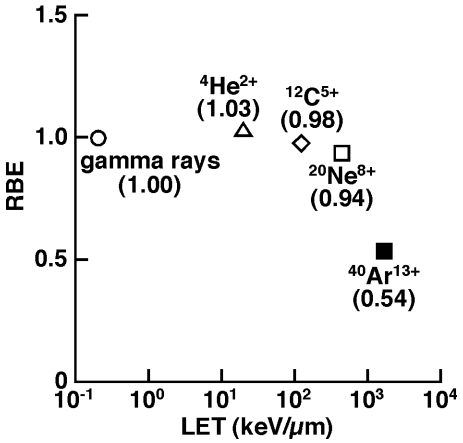

Fig. 2 The relationship between LET and RBE in *D. radiodurans*.

3-25 Analysis of Mutation Induced by Ion Beams and Gamma-Rays in Vacuum-dried Conidia of *Aspergillus oryzae*

K. Ito [a)], Y. Hanya [a)], K. Satoh [b)] and I. Narumi [b)]

[a)] R&D Division, Kikkoman Corp., [b)] Radiation-Applied Biology Division, QuBS, JAEA

Introduction

It is known that the mutation spectrum varies depending on the mutation methods and conditions. We demonstrated that ion-beam mutagenesis had a high mutation frequency and a broad mutation spectrum compared to UV irradiation in *Aspergillus species*, previously [1–2)]. However, those irradiation experiments were carried out against germinated conidia growing on Malts agar plate, which generated easily hydroxyl radicals that influence the mutation spectrum. One way to maximize the characteristics of ion-beam mutagenesis is to irradiate organisms in a dry form, by which hydroxyl radicals generated by water radiolysis, is kept to the minimum. In this report, we obtained 5FOA (5-fluoroorotate) resistant mutants from vacuum-dried conidia as a dry form to investigate the effect of irradiation condition (irradiation to a wet form or to a dry form) on mutation pattern. Moreover, we investigated mutagenesis of vacuum-dried conidia that were irradiated with gamma rays for a comparison purpose.

Materials and Methods

(1) Survival rate

Survival rate was calculated by counting the number of colonies regenerated from constant number of conidia with or without irradiation. The suspension containing 1×10^6 conidia (*A. oryzae* RIB40) was filtrated on a membrane filter (pore size was 0.45 μm) and dried up in a vacuum desiccator. The vacuum-dried conidia were irradiated with $^{12}C^{5+}$ (220 MeV, 121.8 keV/μm) ion beams in a range of dose from 100 to 400 Gy, or with gamma rays in a range from 100 to 1,200 Gy. Irradiated conidia were resuspended in 0.01% Tween80 solution. The suspension were diluted and spread on Malts agar plate. The number of colonies was counted after incubation at 30 °C for 3 days.

(2) Isolation of 5FOA resistant mutants

5FOA resistant mutants were isolated using the same procedure previously described [2)].

(3) DNA analysis of 5FOA resistant mutants

The *pyrG* gene (orotidine 5'-phosphate decarboxylase) and *pyrF* gene (orotate phosphoribosyl transferase) were amplified from 5FOA resistant mutants by PCR. The amplified fragments were cloned and sequenced to detect mutation pattern.

Results and Discussion

(1) Survival rate and isolation 5FOA mutants from vacuum-dried conidia irradiated with ion beams or gamma rays

Figure 1 shows the survival rate of vacuum-dried conidia irradiated with ion beams and gamma rays. The survival rate of gamma irradiation was much higher than that of ion-beam irradiation at the higher dose (over 300 Gy). Twenty mutants that resisted to 5FOA with uracil auxotrophy were obtained from ion-beam irradiated conidia. On the other hand, no mutant was obtained from conidia irradiated with gamma rays. In vacuum-dried conidia, induction of mutation by ion beams might be more powerful tool than gamma rays.

(2) Mutation analysis of 5FOA mutants from the vacuum-dried conidia irradiated with ion beams

Among 20 mutants, either *pyrG* gene or *pyrF* gene was not amplified in 8 mutants, and both of genes were not amplified in 5 mutants. The large structural genomic alteration, such as deletion, inversion or translocation, might occurred around the region of each gene in these mutants. Those mutants were not obtained from germinated conidia that were irradiated with ion beams[2)]. Although *pyrG* gene and *pyrF* gene locates on different chromosome, it is interesting that the mutants without amplification of both genes were obtained. The spatial arrangement of each gene might be close in nucleus. Among other 7 mutants, 5 mutants had deletion mutations (2 mutants were *pyrG* deficient and 3 mutants were *pyrF* deficient). A lot of mutants from germinated conidia with ion-beam irradiation were single base substitution [2)], whereas only one mutant from the vacuum-dried conidia was so.

In conclusion, the mutation pattern varied with irradiation condition and complex structural genomic alteration induced by ion-beam irradiation tended to occur in the vacuum-dried conidia (a dry form) rather than germinated conidia (a wet form).

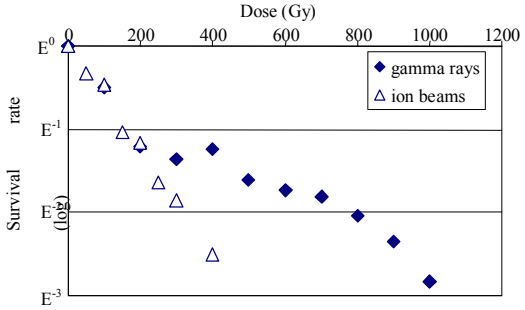

Fig. 1 Survival rate of vacuum-dried conidia after irradiation with ion beams and gamma rays in *A. oryze* RIB40.

References

1) K. Ito et al., JAEA Takasaki Ann. Rep. 2006 (2008) 94.
2) K. Ito et al., JAEA Takasaki Ann. Rep. 2007 (2008) 86.

3-26 Ion Beam Breeding of “Sake Yeast” and Test Brewing

T. Masubuchi [a)], O. Kamiyama [a)], K. Satoh [b)], Y. Hase [b)] and I. Narumi [b)]

[a)] Gunma Industrial Technology Center,
[b)] Radiation-Applied Biology Division, QuBS, JAEA

We are trying to obtain high ethyl caproate producing Sake yeast by carbon ion-beam irradiation. Freeze-dried yeast was irradiated with carbon ion beams (220 MeV) in a range of dose from 50 to 300 Gy by AVF cyclotron at JAEA. We isolated 887 cerulenin resistant mutants of sake yeast “Kyokai-901”, “G2” and “No.227 (Ion beam mutant strain)”. Sake was brewed on 57 kg-scale Test Brewing with 2 mutants that had been isolated by last year’s irradiation experiments. No.227 seemed to hold enormous promise as a new type of yeast for quality sake because of its sweetness and uniqueness in flavor.

群馬県では現在オリジナルの吟醸用清酒酵母として「群馬KAZE酵母」を既に実用化しているが、消費者の嗜好の変化に対応した新たな酵母の開発をすべく、平成20年度よりイオンビーム照射による変異処理を行い、優良株の選抜を試みている。平成21年度は、更に優良な変異株を得るべく選抜を継続すると共に、それまでに得られた優良株の試験醸造を行い、醸造適性の確認を行った。選抜の指標は従来同様に吟醸酒の主要な香気成分であるカプロン酸エチルの生成能とした。

【変異株の選抜】

イオンビーム照射に供する試料の調製、照射後の処理は前報に準じて行った[1)]。照射は、TIARAのAVFサイクロトロンを用いて加速した炭素イオン（220 MeV $^{12}C^{5+}$）を50～300 Gy照射した。本年度は従来用いたきょうかい901号の他にG2酵母（群馬県保存株）、No.227酵母（平成20年度にイオンビーム照射で得られた優良株）を親株として用いた。

カプロン酸エチル高生成株を取得するための選択培地は、市川ら[2)]の方法に準じセルレニン12.5～37.5 μMを含むYPD寒天培地を用いた。これに生育したセルレニン耐性変異株を齋藤ら[3)]の方法を改変した発酵試験に供し、15 ℃で7日間の培養後に重量減少量（CO_2放出量）を測定し発酵力の目安とした。また、得られた上清をヘッドスペースガスクロマトグラフにより、イソアミルアルコール、酢酸エチル、酢酸イソアミル、カプロン酸エチルの各成分を定量して香気生成能を評価した。

発酵試験は887株について実施したが、G2酵母からは優良株を得ることはできなかった。良好な香気生成能を示す変異株は主として100～150 Gyの照射区分で得られた。発酵試験で良好な17株について、布宮ら[4)]の変即二段仕込みを改変した方法で小仕込み試験（総米200 g）を行った。いずれも対照とした群馬KAZE酵母（2号）よりも良好な香気生成能を示したため、発酵能などを考慮した上で次年度の試験醸造に供したい。

【試験醸造】

平成20年度に得られた変異株のうち、香気生成能が良好だったNo.231およびNo.227酵母を試験醸造に供した。対照として群馬KAZE酵母（2号）を用いた。試験醸造は群馬産業技術センター保有の醸造設備を用い、40%精白山田錦を原料とした総米57 kgの吟醸造りを行った。

No.231酵母は、醪の発酵状態を示す指標であるBMD値の経時曲線が群馬KAZE酵母とあまり変わらなかったが、No.227酵母は醪後半のキレが緩やかであり、群馬KAZE酵母より発酵力は弱い（Fig. 1）。一方、No.227酵母の醪中のカプロン酸エチル量は三者の中で最も多い（Fig. 2）。上槽した清酒を官能評価すると、No.227酵母は甘さ、ふくらみなどの面で新しい香り傾向を示し、新たな吟醸酵母として期待が持てる。

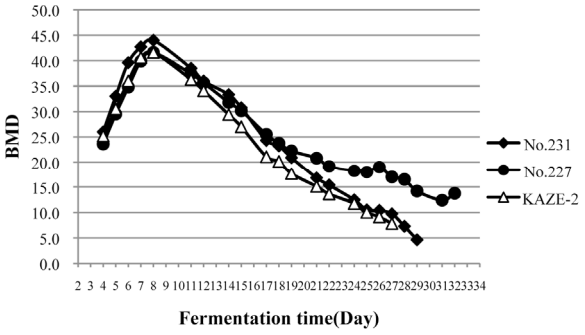

Fig. 1 BMD in sake-moromi by Test brewing.

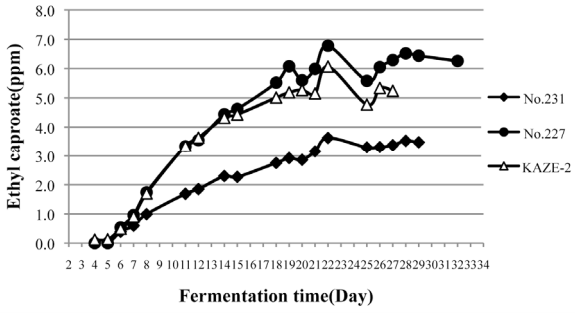

Fig. 2 Ethyl caproate in sake-moromi by Test brewing.

References

1) T. Masubuchi et al., JAEA Takasaki Ann. Rep. 2008 (2009) 84.
2) 市川 英治 et al., 1988年度日本農芸化学会大会講演要旨集、435.
3) 齋藤 久一 et al., 醸協 87 (1992) 915.
4) 布宮 雅昭 et al., 醸協 90 (1995) 217.

3-27 The Effect of γ-Sterilization of Carrier Materials on the Shelf Life of Biofertilizer

K. Tejima [a)], T. Yokoyama [b)], K. Satoh [a)] and I. Narumi [a)]

[a)] Radiation-Applied Biology Division, QuBS, JAEA,
[b)] Institute of Agriculture, Tokyo University of Agriculture and Technology

Numerous studies on the inoculation technique of beneficial microorganisms to plants at agricultural fields have been carried out worldwide. However, except in a case of a low competition with native microbes, the practical technique that shows remarkable effect on the plant growth has not been established. Biofertilizer is a substance that holds beneficial microorganisms for plant growth (e.g. Rhizobia) in the carrier such as peat, perlite, charcoal and soil [1)]. To use biofertilizer more efficiently, it is necessary to keep the amount of viable inoculants in the biofertilizer for a definite period of time. The inoculants survival in the biofertilizer could be affected by the physical and chemical properties of carrier materials and by the competition with native microbes in the carrier. Gamma-irradiation is expected to sterilize the carrier materials without changes in physical and chemical properties. In an effort to demonstrate the advantage of γ-sterilization, the survivals of inoculants were monitored to assess the shelf life of biofertilizer.

Two kinds of peat (commercial sterilized peat moss from Canada and Japanese peat soil: Named "P1" and "P2", respectively), Japanese forest subsoil of the Kanto Loam Formation (Named "L"), and three kind of Japanese cultivated soil (topsoil of the Andosol, Gray Paddy soils and Brown Fluvic soils: Named "S1", "S2" and "S3", respectively) were prepared. Except P1, the soil samples were air-dried and passed through a 2 mm sieve. All soil samples were stored at room temperature in the dark. In order to optimize the γ-ray dose to sterilize soils for the purpose of use as a biofertilizer's carrier material, the survival rate of native microbes in the prepared soils were determined. P2, L, S1 and S2 were packed in plastic bags and irradiated with 1 k, 5 k, 10 k, 20 k, 30 k and 50 kGy of γ-rays. As a result, 50 kGy was determined to be suitable to sterilize soil (Fig. 1). This result was confirmed by additional experiments where P1 and S3 were also sterilized completely by 50 kGy γ-irradiation.

As carrier materials, P1, P2, S1 and S3 were chosen. To make the soil-based artificial carriers, the S1 and S3 were mixed with charcoal powder (3:1) (Named "CS1" and "CS3", respectively). Following the addition of 20 mL of sterilized water per 100 g of the carriers (P1, P2, CS1 and CS3), they were sterilized by 50 kGy γ-irradiation or autoclaving at 121 °C for 40 min. After that, water suspension (20 mL) of *Bradyrhizobium japonicum* strain USDA110 was inoculated to sterilized or non-sterilized carriers. The final density of inoculants in the biofertilizer was 6.6×10^7 cells g^{-1}. The biofertilizer was packed in plastic bags and stored for one month in the 4 °C or 30 °C. Before and after storage, viable inoculants in the biofertilizer were enumerated by the dilution plate method.

Relative ratios of viable inoculants in the biofertilizer stored for one month are shown in Table 1. The relative ratio at pre-storage is defined as 1. As a result of storage at 30 °C, the relative ratio increased in the biofertilizer made from γ-sterilized or autoclave-sterilized carrier, though it tended to decrease in the biofertilizer made from non-sterilized carrier. The γ-sterilization was superior to the autoclave-sterilization in enhancing the inoculants survival. For P1, the relative ratio was high irrespective of sterilization treatment in this study because P1 had already been sterilized during manufacturing process. On the other hand, only a small change in the relative ratio was detected in the biofertilizer stored at 4 °C.

Reference

1) K. Senoo and I. Narumi, FNCA Biofertilizer Manual (2006) 41.

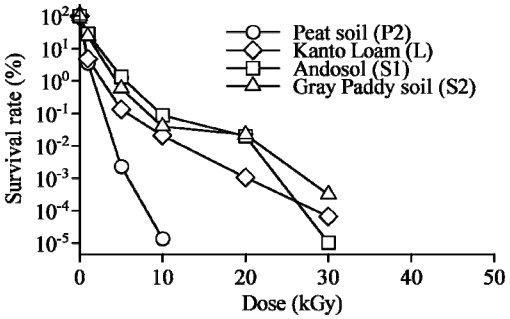

Fig. 1 Survival rates of native microbes in the different kinds of soils after γ-irradiation. Survival microbes were not detected at 50 kGy irradiation.

Table 1 Relative ratios of the viable inoculants in the biofertilizer.

	carrier	Pre-storage	One month storage	
			4°C	30°C
γ-sterilized	P1	1.00	0.83	34.47
	P2	1.00	5.60	19.25
	CS1	1.00	3.09	10.21
	CS3	1.00	4.67	8.17
Autoclaved	P1	1.00	1.01	48.44
	P2	1.00	2.40	3.71
	CS1	1.00	2.26	3.42
	CS3	1.00	3.85	5.91
Non-sterilized	P1	1.00	1.12	46.66
	P2	1.00	0.24	0.25
	CS1	1.00	0.92	0.12
	CS3	1.00	0.96	0.21

3-28 Electron Spin Relaxation Behaviors of Radicals Induced in Gamma-irradiated Food

M. Ukai [a)], H. Kameya [a)], H. Nakamura [a)], M. Kikuchi [b)] and Y. Kobayashi [b)]

[a)] Hokkaido University of Education, [b)] Radiation-Applied Biology Division, QuBS, JAEA

Irradiation of food by various electromagnetic waves or rays of elementary particles is gaining wide applications [1)]. It has been proved that irradiation eliminates pathogen and reduces food borne illness. Since irradiation may induce free radicals, electron spin resonance (ESR) spectroscopy has been applied to reveal the irradiation history and dosage in a wide variety of foods. Ukai et al. have reported radiation response of the irradiated foods using ESR [2-4)]. In order to determine the relaxation behaviors of radicals in irradiated foods, we varied the microwave strength to obtain progressive saturation behavior (PSB). These microwave saturation ESR spectra showed that an organic free radical signal is quite readily saturated, and thus has a long relaxation time. The time scale of magnetic relaxations reflects existence of organic free radicals. We also have reported the detection protocol of irradiated food based on radical relaxation phenomena [4)].

The theory for continuous microwave saturation for homogenously and inhomogeneously broadened paramagnetic systems was developed decades ago [5)]. The measurement procedures have later been refined and employed to estimate the spin-lattice and spin-spin relaxation times T1 and T2 from the saturation curves in various model cases characterized by inhomogeneous broadening [6)]. The saturation parameters and relaxation times were obtained by employing diagrams that utilized a few selected points on the saturation curve. To our knowledge, an analysis employing all data on a saturation curve has not been carried out previously.

In the present work, a computer program [7)] to analyze the microwave power dependence of inhomogeneously broadened ESR lines using all data points on a saturation curve was therefore applied. Using this theoretical analysis, the relaxation behaviors of radicals were revealed by microwave saturation ESR spectra.

The specimen was commercial available nutmeg which was proven to be no irradiation history. Irradiation was carried out at JAEA at room temperature (ca. 300 K). We used the gamma ray from ^{60}Co as an irradiation source. The irradiation doses used for the sample were 1, 3 and 5 kGy. ESR measurements were carried out with an ESR spectrometer (JEOL, JES-FA3XG, Akishima). All the ESR spectra were recorded at the X-band (9.3 GHz).

Figure 1 shows the typical ESR spectra of nutmeg. ESR spectra obtained before irradiation consisted of three signal components. The sharp intense signal (P1) is due to an organic free radical. The P2 signal in the vicinity of P1 is attributable to a signal with hyperfine (hf) interaction of Mn^{2+}. Furthermore, the signal (P3) detected at g=4.0 may be originated from the ferric (Fe^{3+}) ion. The signal intensity of P1 is increased by irradiation. The PSB curves shows that the intensity of the P1 signal increased linearly with microwave power and met the threshold at the 4 - 8 mW range. After the thresholds, the P1 signal intensities decreased. As radiation dosage increased, the signal intensity became higher. By PSB we could evaluate relaxation times of T1 and T2 (Table 1). Irradiation induced radicals of nutmeg yielded relaxation times, T1 in the μsec and T2 in nsec ranges, respectively. Upon the irradiation, T1 shortened, and T2 lengthened.

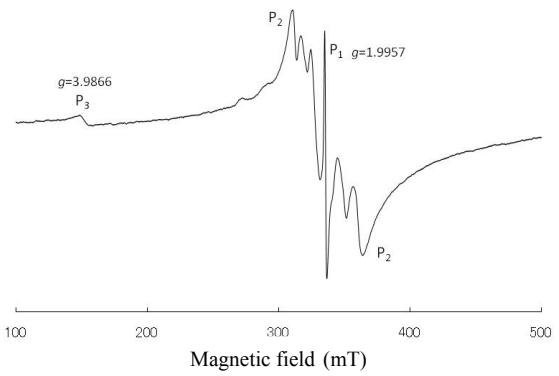

Fig. 1 Typical ESR spectra of nutmeg.

References

1) T H. Delincée, Radiat. Phys. Chem. 63 (2002) 455-458.
2) M. Ukai et al., Appl. Magn. Reson. 24 (2003) 1-11.
3) H. Nakamura et al., Spectrochim. Acta 63(4) (2006) 883-887.
4) M. Ukai et al., Spectrochim. Acta 63(4) (2006) 879-882.
5) T. G. Castner Jr., Phys. Rev. 115 (1959) 1506-1519.
6) J. Maruani, J. Magn. Reson. 7 (1972) 207-215.
7) A. Lund, Radiat. Res. 172 (2009) 753-760.

Table 1 Relaxation times (T1 and T2).

Irradiation	T1(μs)	T2 (ns)
non-irradiation	16	90
1 kGy	7	130
3 kGy	7	130
5 kGy	7	130

3-29 Dose-dependency of Electron Spin Relaxations in Irradiated Fresh Mangoes

M. Kikuchi [a)], T. Sakashita [a)], T. Funayama [a)], M. Ukai [b)], Y. Shimoyama [c)] and Y. Kobayashi [a)]

[a)] Radiation-Applied Biology Division, QuBS, JAEA, [b)] Hokkaido University of Education, [c)] Muroran Institute of Technology

The irradiation to tropical fruits is used as a quarantine treatment against fruit flies in the world. Distinguishing the irradiation is required to endorse the reliability of labels for consumers. Recently, we have found that the radiation-induced radicals remain in irradiated fresh mangoes 9 days after the irradiation [1)]. Since lifetime of radicals is related to where unpaired electrons are in the surroundings, interactions of the unpaired electrons are investigated for rough water-rich environments.

To measure ESR spectra of irradiated fresh mangoes, we employed the freeze-dry method, a gentle treatment for the biological samples. ESR spectroscopy was performed with an RE-3X (Jeol) at room temperature using the X-band microwave frequency (9.44 GHz). To estimate interaction of the electrons, the relaxation times of T_1 and T_2 were evaluated by a program code developed by Lund, *et al.* [2)].

Figure 1 shows progressive saturation behaviors (PSB) for the main peak of dried specimens prepared from irradiated water-rich mango fleshes at various microwave powers. The PSB hits the maximum in the vicinity of 3 mW. The *g*-value (g=2.004) and the PSB of the mango specimens indicated a signal consisted of organic free radicals.

The relationships between the relaxation times and the irradiation doses are observed (Fig. 2). Generally, relaxation time T_1 relates to the energy transfer through the chemical bonds by the interactions between the electron spin and the lattice. The relaxation time T_2 relates the interaction between the spins. Therefore, no difference between irradiated and non-irradiated samples for T_1 values indicates the existence of the energy transfer pathways through chemical bonds. Dose-dependency of T_2 in flesh and skin indicates that longer T_2 is induced by weaker interactions. This interaction should be related to the inter-electron distance. Moreover, these responses may be affected by the different water contents in the mango organs, since torsional motion of biopolymers is easy in the water-rich surroundings. Therefore, conformational changes of some biopolymers with radicals were occurred in the water-rich fruit after the increase of flexibility by chemical bond breaks (Fig. 3). In seed that is of a semi-dried, the increase of unpaired electron contents after γ-irradiation causes stronger interactions, leading to shorter T_2.

ESR spectroscopy on freeze-dried powdered specimens of irradiated fresh mangoes can measure whole radicals including both mechano-radicals and γ-induced radicals. Additional relaxation time analyses might be possible to distinguish the contribution of ESR signals by radiation-induced radicals from that by whole radicals. Finding of stable radicals in fresh fruits enables one to know γ-induced radicals with novel methodology of T_2 dose-dependency [3)].

References

1) M. Kikuchi et al., Spectrochim. Acta A 75 (2010) 310-313.
2) A. Lund et al., Radiat. Res. 172 (2009) 753-760.
3) M. Kikuchi et al., Food Irradiat. Jpn. 44 (2009) 9-13.

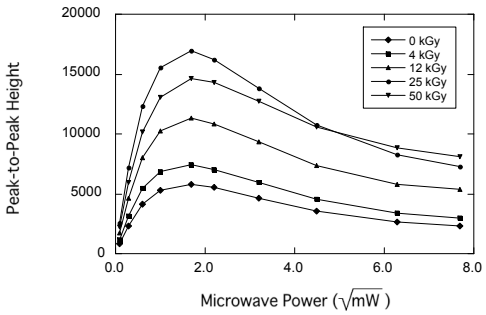

Fig. 1 Progressive saturation curves of freeze-dry specimens prepared from irradiated mango fleshes.

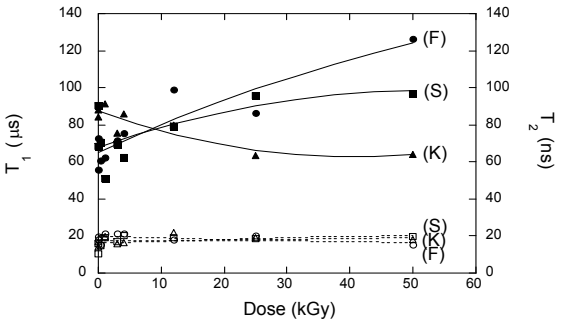

Fig. 2 Dose dependency of relaxation times for irradiated mango fleshes (F), skins (S) and seeds (K). Dotted and solid lines were fitted by the least square method using T_1 and T_2 values, respectively.

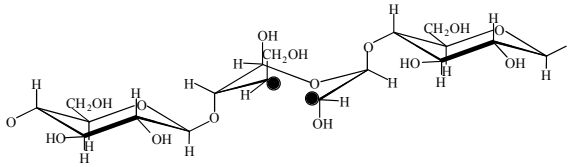

Fig. 3 A model as for a spin-spin interaction in the cellulose biradical. Black dot corresponds an unpaired electron in free radical.

3-30 Target Irradiation of Individual Cells Using Focusing Heavy-Ion Microbeam of JAEA-Takasaki

T. Funayama, T. Sakashita, Y. Yokota and Y. Kobayashi

Radiation-Applied Biology Division, QuBS, JAEA

Heavy-ion beam is utilized for heavy-ion cancer therapy and ion beam breeding because of its unique biological effectiveness. However the elucidation of mechanisms underlying biological response of heavy-ion radiation is necessary to advance these useful applications. Localized irradiation of specific regions within organisms using heavy-ion microbeam systems provides an attractive means of investigating the mechanism of heavy-ion radiation action. Therefore, we had developed the heavy-ion collimating microbeam system at the facility of Takasaki Ion Accelerator for Advanced Radiation Application (TIARA) of the Japan Atomic Energy Agency (JAEA), and utilized for analyzing heavy-ion induced biological effects[1].

However, there is a difficulty in generating finer beam that is capable for carrying out precise subcellular irradiation in our current system, because of inevitable scattering of ions at the edge of micro collimator. The scattering ions do not hit on the targeted cells, thus made mishit cells in the sample. On the other hand, there are little scattering ions when microbeam is generated by focusing system using magnetic lens, thus the system is expected to target and irradiate cells accurately. Therefore, we developed new focusing microbeam line at another vertical beam line of AVF cyclotron of TIARA, JAEA[2].

New system can focus heavy-ion beam to minimum one micrometer in vacuum using a quadruplet quadrupole lens system, and equipped with an X, Y beam scanner for fast hitting of single ion to micron scaled samples. To irradiate this finer microbeam to the specific region of individual cells, a cell targeting system was designed and installed under the beam extraction window. The system was consisted of inverted microscope and automatic stages of 7 axes. The system can be controlled completely from remote preparation room. For avoiding vibration, the system is installed on the rigid frame that is hanged and fixed to the magnetic lens. At the bottom port of the microscope, a high sensitivity cooled CCD camera was installed for detecting weak fluorescence of scintillator and stained target cells.

The position of focusing microbeam was detected under microscopic view using CaF_2(Eu) scintillator. The ions irradiated to the sample were detected by solid state ion detector installed on the objective revolver of the microscope, and counted by counter NIM module to control a fast beam shutter.

Using the system, irradiation of HeLa cells were carried out. The cytoplasm of cells were stained with CellTracker Orange fluorescent dye (Invitrogen) and inoculated on a film of ion track detector, CR39, of 100 μm thick. For avoid drying, the sample was covered by Kapton film of 8 μm in thick and sealed by petrolatum. The positions of each target cell were extracted from the fluorescent cell image using self-developed image analysis code, which is optimized for analyzing CellTracker-stained cell image (Fig. 1). The cells were, thereafter, targeted and irradiated with focusing Ne ion beam (13.0 MeV/u, LET = 380 keV/μm). The irradiation was carried out by moving the cells to the position of beam spot using automatic stage system. The ions were irradiated from up above, and the number of ion irradiated was counted by solid stage detected installed under sample stage.

After irradiation, the tracks of traversed ion were visualized by etching of CR39 film and hit positions of irradiated ion were confirmed. The ions were well focused and hit on targeted cells precisely. Therefore, we concluded that the new system can target and irradiate individual cultured cells by focusing heavy-ion microbeam.

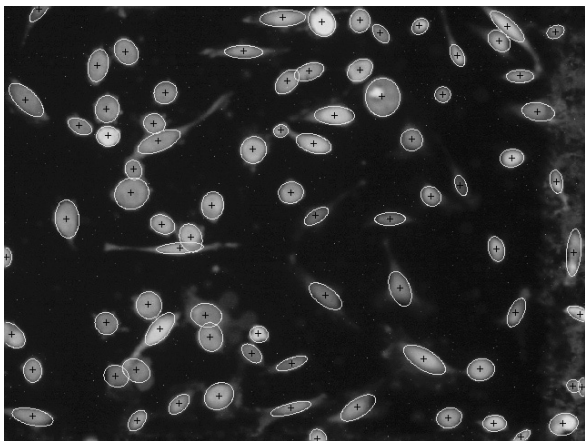

Fig. 1 Detection of cell target position using image analysis code optimized for CellTracker-stained cell image.

References

1) T. Funayama et al., J. Radiat. Res. 49 (2008) 71-82.
2) M. Oikawa et al., Nucl. Instrum. Meth. Phys. Res. B 260 (2007) 85-90.

3-31 A Quantitative Study of DNA Double-strand Breaks Induced by Heavy-ion Beams: a Problem on the Conventional DNA-sample Preparation

Y. Yokota, T. Funayama, Y. Mutou, T. Sakashita, M. Suzuki, M. Kikuchi and Y. Kobayashi

Radiation-Applied Biology Division, QuBS, JAEA

Linear energy transfer (LET) is an important factor of radiation quality. Biological effects (e.g. chromosomal aberration and cell death) per absorbed dose are greater in high-LET heavy ions than in low-LET radiation such as X-rays and γ-rays [1]. It is a general consensus of the underlying mechanism that heavy ions induce irreparable DNA damage in irradiated cells more frequently than low-LET radiation. In computer simulation studies, the interaction between the high-density ionization along a particle track of heavy ions and higher-order chromosomal structure is predicted to induce clustered DNA damage in irradiated cells.

DNA double-strand breaks (DSBs) are believed to be the most serious DNA damage induced in irradiated cells because DSBs make a chromosome into fragments and destroy the genome information of organisms. Since 1990s, DSBs have been quantified with pulsed-field gel electrophoresis (PFGE) technology. PFGE can separate DNA fragments with sizes up to several mega base pairs (bp) by changing the direction of electric field periodically[2]. In conventional studies, genome DNA preparation from irradiated cells was performed in agarose plugs for avoiding excess DNA fragmentation during experimental procedures[3].

The length and the number of radiation-induced DNA fragments are measured to determine the space of neighboring DSBs on a chromosome and the number of induced DSBs, respectively. However, this DNA fragment analysis could not measure the DNA fragments shorter than 10 kbp (similar to gene sizes) correctly [4]. So, heavy-ion-induced DNA fragmentation in irradiated cells is not totally understood. The purpose of our study is to quantify the DNA fragments shorter than 10 kbp in the cells irradiated with heavy ions.

In the last year, we have found that DNA fragments are partly lost from the agarose plug into surrounding buffer during the conventional DNA preparation procedure (Fig. 1). In our experiment, DNA molecular size standards (mixture of 500 bp and 5 kbp ladders) were used as a substitute of genome DNA. They were suspended in 0.75% high-purity agarose and $1.0 \times 0.5 \times 0.15$ mm^3 agarose plugs were casted with a plug mold. Then, agarose plugs were incubated in 0.5 M EDTA for 24 h and in 0.5 × TBE buffer for 2 h before PFGE assay (a mock procedure of the conventional DNA preparation). After PFGE, electrophoresis gel was incubated in SYBR Green I solution to stain DNA with fluorescent dye. DNA band pattern was visualized on a UV transilluminator (Fig. 1A). Gel image was recorded with a cooled CCD video camera. DNA content of each band was measured based on the fluorescence intensity and normalized to that of the agarose plug (Fig. 1B). The smaller the bands compared between both lanes were, the larger the difference in normalized DNA content became. This means that the loss of DNA fragments from the agarose plug is dependent on band sizes. This phenomenon makes difficult to reveal the total number of DNA fragments in irradiated cells.

In future, we will develop the new method for collecting DNA fragments totally from irradiated cells to characterize heavy-ion-induced DSBs. An expectant approach is to lyse irradiated cells in a test tube and capture the various sizes of DNA fragments with an anion-exchange resin.

References

1) Y. Yokota et al., Int. J. Radiat. Biol. 79 (2003) 681-685.
2) D. C. Schwartz et al., Cell 37 (1984) 67-75.
3) Y. Yokota et al., Radiat. Res. 163 (2005) 520-525.
4) Y. Yokota et al., Radiat. Res. 167 (2007) 94-101.

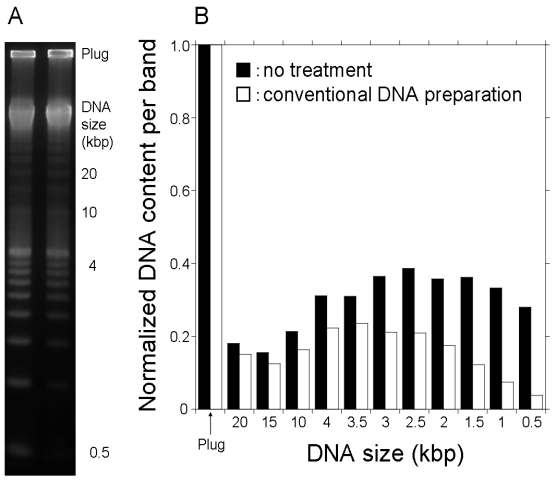

Fig. 1 Loss of DNA fragments from agarose plugs is dependent on size. (A) DNA molecular size standards are embedded in agarose plugs and run in PFGE. Left lane: no treatment, right lane: the plug was incubated in 0.5 M EDTA buffer for 24 h and in 0.5 × TBE buffer for 2 h (a mock procedure of the conventional DNA preparation) before PFGE. (B) DNA content of each band was measured and normalized to that of the plug.

3-32 Carbon-ion Microbeam Induces Behavioral Changes in the Salt Chemotaxis Learning of *C. elegans*

T. Sakashita [a)], M. Suzuki [a)], Y. Mutou [a)], Y. Yokota [a)], T. Funayama [a)], N. Hamada [b)], K. Fukamoto [c)] and Y. Kobayashi [a)]

[a)] Radiation-Applied Biology Division, QuBS, JAEA,
[b)] Radiation Safety Research Center, Central Research Institute of Electric Power Industry,
[c)] Faculty of Textile Science and Technology, Shinshu University

Introduction

An increasing body of data indicates that ionizing radiation affects the nervous system and alters its function [1)]. Chemotaxis of *C. elegans* during the salt chemotaxis learning was modulated by gamma irradiation [2)]. Our preliminary results showed the similar response of the salt chemotaxis learning to whole-body carbon-ion irradiation. However, we have no direct evidence for the interaction of ionizing radiation with the central neuronal tissue (nerve ring) in *C. elegans*. Microbeam irradiation is useful to analyze direct radiation effects at a cellular or tissue level. Thus, we investigate the effects of energetic carbon ions ($^{12}C^{5+}$, 18.3 MeV/u, LET = 119 keV/μm) on the salt chemotaxis learning of *C. elegans* using microbeam irradiation to its nerve ring and also combined effects with anesthesia that inhibits nerve function.

Materials and Methods

Well-fed adults of *C. elegans* grown at 20 ˚C on the plate spread with *E. coli* OP50 were used in all experiments. The area of nerve ring, "Head", of non-anesthetized *C. elegans* with S-basal (100 mM NaCl, 50 mM KPO_4 pH 6.0, and 5 mg/L cholesterol) in a ditch of the micro total analysis systems (μTAS)[3)] was irradiated with 12,000 carbon ions corresponding to 500 Gy at 20 μmφ micro-aperture area (Fig. 1). Immediately after irradiation, chemotaxis to NaCl during learning was measured. The TaKaRa Slide Seal (Fig. 2; TKR 9066, TaKaRa Bio Inc., Shiga, Japan) was used for the microbeam irradiation of anesthetized animals [4)]. Irradiation effects during learning could not be evaluated in anesthetized animals, so that the ability of the salt chemotaxis learning was tested. Using the assay plate with a gradient of NaCl concentration, we evaluated chemotaxis based on the chemotaxis index (CI) that was calculated as {(number of animals at the high-concentration spot) – (number of animals at the control spot)}/ (total number of animals in the assay plate) [5)]. The results of CI were evaluated as mean ± 95% confidential interval.

Results and Discussion

To investigate direct radiation effects, non-anesthetized animals was irradiated with carbon-ion microbeam, and showed the modulation of the chemotaxis to NaCl during learning (CI: 0.26±0.12 in non-irradiated animals, -0.13± 0.09 in "Head" locally irradiated animals). It demonstrates the direct evidence by the hit of carbon ions at the nerve ring. Also, to test the effects of carbon ion-induced damage in Head area, we evaluated defects in the salt chemotaxis learning of anesthetized animals. The ability of the salt chemotaxis learning was not affected by carbon ions (CI: 0.33±0.07 in non-irradiated animals, 0.32±0.10 in "Head" locally irradiated animals). Our findings indicate that the modulation of the salt chemotaxis learning is induced by the direct hit of ionizing radiation at the nerve ring of *C. elegans*, and the salt chemotaxis learning in anesthetized *C. elegans* is not affected by microbeam irradiation.

References

1) T. Sakashita et al., J. Radiat. Res. 51 (2010) 107.
2) T. Sakashita et al., FASEB J. 22 (2008) 713.
3) Lockery et al., J. Neurophysiol. 99 (2008) 3136.
4) Sugimoto et al., Int. J. Radiat. Biol. 82 (2006) 31.
5) Saeki et al., J. Exp. Biol., 204 (2001) 1757.

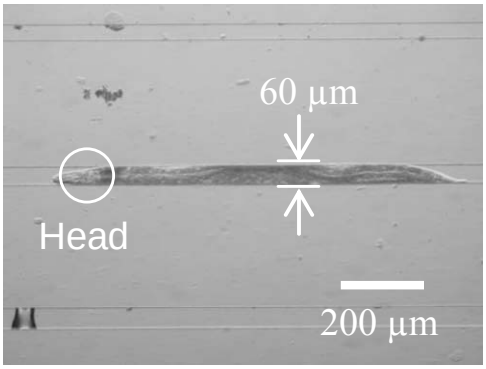

Fig. 1 Non-anesthetized *C. elegans* in a ditch of μTAS. Circle shows the area of nerve ring, "Head".

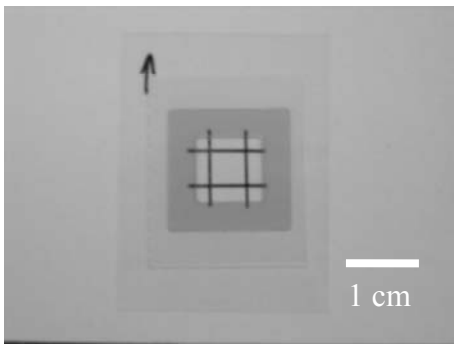

Fig. 2 Image of TaKaRa Slide Seal which is a gray frame, and 25 μL buffer with anesthetized *C. elegans* is instilled into this area.

3-33 Combination Effect of the Heat Shock Protein Inhibitor, 17-AAG, with Carbon-beam and X-ray Irradiation for Squamous Cell Carcinomas *in Vitro*

A. Musha [a,b], Y. Yoshida [c], T. Nonaka [d], T. Takahashi [a], T. Funayama [e], Y. Kobayashi [e], H. Ishikawa [a], H. Kawamura [c], K. Ando [c], S. Yokoo [b] and T. Nakano [a,c]

[a] Department of Radiation Oncology, Graduate School of Medicine, Gunma University, [b] Department of Stomatology and Oral Surgery, Graduate School of Medicine, Gunma University, [c] Gunma University Heavy Ion Medical Center, [d] Department of Radiation Therapeutics, Kanagawa Cancer Center, [e] Radiation-Applied Biology Division, QuBS, JAEA

Heat shock protein 90 (Hsp90) is a molecular chaperone that plays a critical role in cellular stress signaling pathways. The Hsp90 inhibitor, 17- allylamino-17-demethoxygeldanamycin (17-AAG), binds to the ATP binding site of Hsp90 protein and specifically inhibits its chaperone functions in tumor cells. We investigated whether 17-AAG has any radio-sensitization effects *in vitro*. We used two squamous cell carcinoma cell lines, LMF4 (oral cancer cell line) and TE1 (esophageal cancer cell line). Cells were irradiated with a FAXITRON RX-650 X-ray machine at a dose rate 1.1~ 1.3 Gy/min at Gunma University and irradiated with the broad beam of carbon particles by the AVF cyclotron of TIARA (Takasaki Ion Accelerators for Advanced Radiation Application) at Japan Atomic Energy Agency, operating 18.3 MeV/u, 108 keV/μm. Cells were treated with 100 nM 17-AAG for 24 hours before irradiation. Cell survival was measured by colony formation assay. Specifically, cells were irradiated with X-ray (0-10 Gy) and irradiated with the broad beam of carbon particles (0-4 Gy), trypsinized, diluted, counted, and seeded in 60-mm dishes at various cell densities. After 2 weeks of incubation, colonies were stained with crystal violet. Survival curves for both cell lines treated with X-ray irradiation and 17-AAG demonstrated an additive effect. However, this radio-sensitization effect seen with X-ray irradiations was not seen in the carbon beam irradiations. A radiation dose to reduce surviving fraction to 10% (D_{10}) was 7.09 Gy or 7.73 Gy for TE1 or LM4 cells, respectively. Furthermore, treatment of cells with carbon-beam irradiation reduced D_0 values to 0.5 Gy and 0.6 Gy for TE1 and LM4 cells, respectively. RBE (Relative Biological Effectiveness) was 5.14 and 5.12 for TE1 cells and LMF4 cells, respectively. Treatment of cells with 17-AAG alone reduced the surviving fraction to 0.6 and 0.7 in TE1 and LMF4 cells, respectively. 17-AAG showed radio-sensitization in cell killing of the two squamous cell lines in the X-irradiation. However, the carbon beam irradiation plus 17AAG treatment did not show a radio-sensitization effect. These results suggest that Hsp90 may be an appropriate target for selectively enhancing the radio-sensitivity of tumor cells in the X-irradiation. However, the carbon beam irradiation suggests that Hsp90 may not be an appropriate target for selectively enhancing the radio-sensitivity of tumor cells. The carbon-beam irradiation treatment is more effective than chemoradiotherapy for locoregional treatment.

【目的】熱ショックタンパク質 90（Hsp90）は多くの腫瘍細胞で高発現しており、シグナル伝達で重要な役割をもつ。Hsp90 阻害剤の 17-AAG とX線、炭素線の併用による放射線増感効果について *in vitro* にて検討した。

【材料および方法】細胞は口腔扁平上皮癌細胞株 LMF4 と食道扁平上皮癌細胞株 TE1 を用いた。X線単独、炭素線単独、ならびに 17-AAG 併用群において、コロニー形成法により細胞生残率を解析した。併用群は 17-AAG を 24 時間接触後に照射を施行した。

【結果】生存率 10%となる線量(D_{10})はX線単独が TE1 では 7.09 Gy、LMF4 では 7.73 Gy であり、X 線+17-AAG はそれぞれ 4.49 Gy と 4.69 Gy であった。炭素線単独が TE1 では 1.38 Gy、LMF4 では 1.51 Gy であり、炭素線+17-AAG はそれぞれ 0.95 Gy と 1.32 Gy であった。X 線では両細胞とも 17-AAG による放射線増感効果を示したが(Fig. 1)、炭素線では、顕著な増感効果は認められなかった(Fig. 2)。両細胞の RBE（Relative Biological Effectiveness）は、TE1 では 5.14、LMF4 では 5.12 であった。

【結論】両細胞とも X 線で認められた 17-AAG 併用による増感効果は、炭素線では認められなかった。上記の結果より、炭素線に比べ X 線において HSP90 に関連した増感効果の機序が存在することが示唆された。

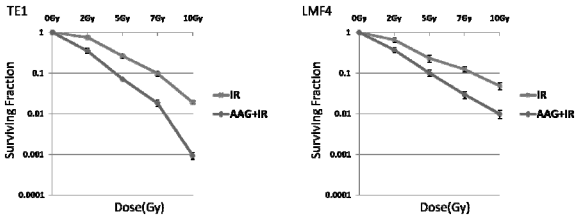

Fig. 1 Cell survival (X-ray irradiation).
HSP90 inhibitor 17-AAG radio-sensitizes two squamous cell carcinoma cell lines (LMF4 and TE1).

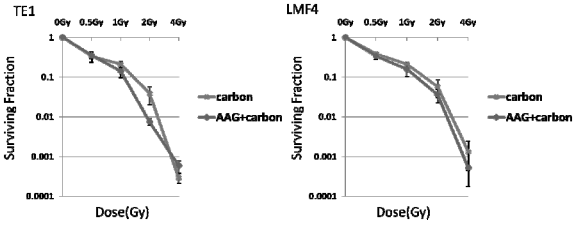

Fig. 2 Cell survival (carbon beam irradiation).
Carbon-beam irradiation plus 17AAG treatment did not show a radio-sensitization effect.

3-34 Biological Effects of Carbon Ions on Glioblastoma Cell Lines

Y. Yoshida [a)], S. Ishiuchi [b)], T. Funayama [c)], Y. Kobayashi [c)] and T. Nakano [a)]

[a)] Gunma University Heavy Ion Medical Center, [b)] Department of Neurosurgery, University of the Ryukyus Faculty of Medicine, [c)] Radiation-Applied Biology Division, QuBS, JAEA

Glioblastoma (GBM) is one of the most common and the most malignant tumors occurring in the central nervous system. GBM is notorious for high growth and invasive behavior and makes the surgical intervention ineffective. Recently, though there are many reports about the effectiveness of carbon ion therapy, little is known about effects of carbon ion therapy for GBM. In addition, almost all of GBM patients has not satisfied with treatment of the carbon ion alone for GBM.

Temozolomide (TMZ) is a cytotoxic alkylating agent which has shown an activity in the recurrent anaplastic glioma and GBM. Combining TMZ with radiotherapy has been reported to improve outcome compared with radiation alone, and this treatment is currently considered as the standard treatment for GBM. Hence, in this study, we investigated the effectiveness of combining TMZ with carbon ion therapy for GBM.

【目的】難治性腫瘍の一つである神経膠芽腫は遊走・浸潤性が非常に高いことから正常な脳細胞との境界が不鮮明であり、手術により腫瘍を全摘出することが困難である。また、X 線や抗がん剤に対して非常に抵抗性であるため、集学的治療を行っても根治は絶望的である。神経膠芽腫において、新規抗がん剤である temozolomide（TMZ）は細胞毒性を示すアルキル化剤に分類される抗悪性腫瘍剤であり、経口投与で脳脊髄液に良好に移行し、治療効果をもたらすことが報告されている。X 線との併用療法群において、X 線単独療法群に比べ、平均生存期間を延長させることが明らかとなっているが、重粒子線照射との併用に関しては、基礎研究も含めて報告がない。今後の重粒子線治療との併用療法の適用に向けて、抗腫瘍効果や正常組織への影響についての基礎的なデータを得ることは、非常に重要であると考える。

【方法】U87MG と CGNH-PM を用いて細胞実験を行った。細胞への照射は TIARA にて炭素イオン線（18.3 MeV/amu, 108 keV/μm, 0~10 Gy）、群馬大学にて X 線（120 kVp, 4.5 mA, 0~10 Gy）を照射した。TMZ は照射約 1 時間前に単回投与した。評価は主にコロニー形成法により細胞生残率の測定を行った。また、炭素線照射前後の細胞を経時的に固定して PI にて染色して細胞周期について Flow-cytometry にて解析した。

【結果】

(1) U-87MG 細胞および CGNH-PM 細胞を用いて炭素イオン線照射（0~10 Gy）単独群と炭素イオン線＋TMZ 群における細胞生存率をコロニー形成法により測定した結果、炭素イオン線への TMZ の併用はそれぞれの腫瘍細胞において相加効果を示した。

(2) 細胞周期について解析した結果、炭素イオン線照射後にいずれの細胞においても顕著な G2 ブロックが認められた（Fig. 1）。しかし炭素イオン線単独群と炭素イオン線＋TMZ 併用群との間に明らかな差異は確認できなかった。

(3) CGNH-PM 細胞の浸潤能について Wound-healing assay を用いて検討した結果、炭素イオン線単独、TMZ 単独、炭素イオン線＋TMZ 群、各群において顕著な浸潤能の低下は認められず、むしろ炭素イオン線照射により遊走能が亢進している傾向にあった（Fig. 2）。

【まとめと考察】炭素イオン線へのTMZの併用は相加的に腫瘍増殖抑制効果を認めるが、腫瘍細胞の遊走性については抑制効果が認められなかった。今後さらなる解析を行い、炭素線へのTMZ併用の有用性について明らかにする。

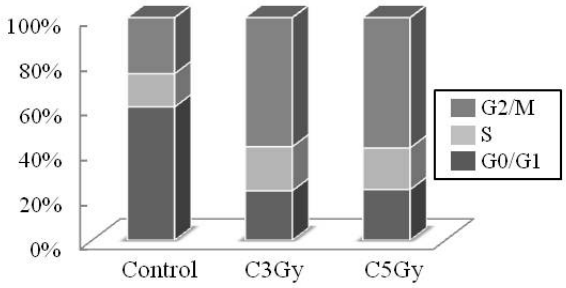

Fig. 1 Cell cycle distribution of CGNH-PM cells at 24 hours after irradiation.

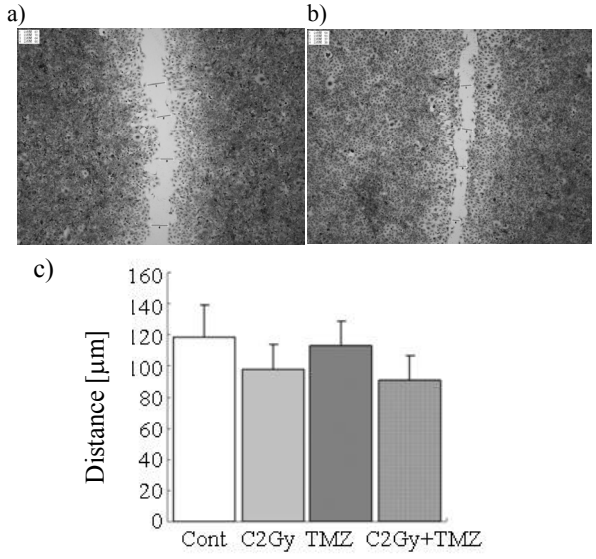

Fig. 2 Wound-healing assay of CGNH-PM cells at 24 hours after irradiation. a) control, b) carbon ion irradiated, c) width of wound field.

3-35 Analysis of Molecular Mechanisms for Radiation-induced Bystander Effects Using Heavy Ion Microbeams

H. Matsumoto [a)], M. Hatashita [a)], M. Tomita [b)], K. Otsuka [b)], T. Funayama [c)], T. Sakashita [c)] and Y. Kobayashi [c)]

[a)] Faculty of Medical Science, University of Fukui, [b)]Central Research Institute of Electric Power Industry, [c)]Radiation-Applied Biology Division, QuBS, JAEA

The objective of this project is to elucidate molecular mechanisms of the bystander response using heavy ion microbeams in JAEA. We found that the foci of γH2AX and pNBS1 were formed in the unirradiated cells in the target colony including the irradiated cell 6 h after irradiation with 460 MeV ^{40}Ar beams and that this formation of the foci was almost completely suppressed by the addition of DMSO or Lindane. Also we found that the foci of γH2AX and pNBS1 were formed in the unirradiated cells in the untargeted colonies 6 h after irradiation and that this formation of the foci was almost completely suppressed by the addition of aminoguanidine or c-PTIO. Our findings strongly suggested that ROS and NO are initiators/mediators for evoking heavy ion microbeam-induced bystander responses.

低線量／低線量率放射線に対して生物が示す特異的な応答様式の一つに放射線誘発バイスタンダー応答がある[1)]。我々は、細胞局部照射装置を用いて、この放射線誘発バイスタンダー応答の分子メカニズムを明らかにすることを計画した。

1. 実験方法

(1)細胞：ヒト正常線維芽細胞(AG1522 細胞)を用いた。

(2)培養：開孔（径 12 mm）35 mm ディッシュの内面中央に 20 mm 四方の collagen コートした CR-39 をパラフィンで固定したものを使用した。2×10^5 cells/mL の細胞懸濁液 5 μL を CR-39 樹脂上に 5 箇所スポットし(1,000 cells/colony)、15~20 時間培養したものを照射実験に供した。

(3)照射：Funayama ら[2)]の方法に従って、中央にスポットしたコロニーの細胞 1 個に 5 粒子の 460 MeV $^{40}Ar^{13+}$を HZ1 ポートにおいて照射した。

(4)細胞の蛍光免疫染色：照射後、細胞を 37 °C で培養し、6 時間後にメタノールで固定し、抗 γH2AX 抗体および抗 pNBS1 抗体を用いた蛍光抗体染色法により染色し、蛍光顕微鏡下で観察した[3)]。標的細胞を含む正方形枠（250×250 μm; C）内、そこから右方向に設定した 3 個の正方形枠（250×250 μm）の内部、および遠隔に存在するサテライトコロニーの中心部の正方形枠（250×250 μm）内のフォーカス形成頻度を測定した。

2. 結果および考察（Fig. 1）

(1)Ar 線マイクロビームの照射により、照射された細胞(標的細胞)において γH2AX および pNBS1 のフォーカス形成が認められ、それらは同所局在していた。

(2)Ar 線マイクロビーム照射により、バイスタンダー細胞においても γH2AX および pNBS1 のフォーカス形成が認められ、それらは同所局在していた。従って標的細胞から分泌されたバイスタンダー因子によりバイスタンダー細胞に DNA 二本鎖切断が誘発されていることが示唆された。またバイスタンダー細胞におけるこれらのフォーカス形成は標的細胞から離れるに従ってその頻度は漸次減少した。

(3)距離に依存したバイスタンダー因子の変化：Ar 線マイクロビーム照射により、バイスタンダー細胞における γH2AX および pNBS1 のフォーカス形成が DMSO（0.1%）、Lindane（40 μM）、Aminoguanidine（AG, 10 μM）および c-PTIO（10 μM）によって抑制された。DMSO による抑制は、標的細胞周辺において顕著であり、それ以外の部位では抑制効果は認められなかった。Lindane による抑制効果は標的細胞近傍においてのみ顕著であった。AG および c-PTIO による抑制効果は、標的細胞から離れるに従って顕著に認められた。

以上の結果より、ギャップ結合を移行しているバイスタンダー因子および標的細胞近隣の細胞に培地を介して作用しているバイスタンダー因子は活性酸素種（ROS）であることが示唆された。一方、遠隔的に作用しているバイスタンダー因子は活性窒素種（RNS）、特に NO ラジカルであることが示唆された。

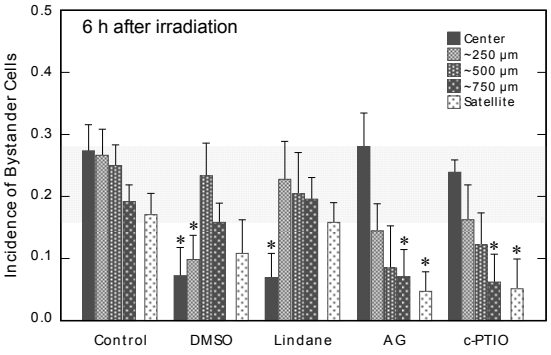

Fig. 1 Changes in bystander factors with depending on the distance from the targeted cell.

References

1) H. Matsumoto et al., J. Radiat. Res. 50 Suppl. (2009) A67.
2) T. Funayama et al., Radiat. Res. 163 (2005) 241.
3) A. Takahashi et al., Cancer Res. 64 (2004) 8839.

3-36 Difference in Bystander Lethal Effect in Human Tumor Cell Lines Depending on *p53*-gene Status Induced by Carbon-ion Microbeams

M. Suzuki [a)], T. Funayama [b)], Y. Yokota [b)], Y. Mutou [b)], C. Tsuruoka [a)], Y. Furusawa [a)] and Y. Kobayashi [b)]

[a)] Research Center for Charged Particle Therapy, NIRS,
[b)] Radiation-Applied Biology Division, QuBS, JAEA

Since 1994, a Phase I/II clinical study and cancer radiotherapy have been begun using carbon-ion beams generated with the Heavy Ion Medical Accelerator in Chiba (HIMAC) at National Institute of Radiological Sciences [1)]. In the field of fundamental biological studies for high-LET radiations, there are many reports regarding bystander cellular effects after exposure to alpha particles derived from ^{238}Pu or He-ion microbeams. However, only limited sets of studies have examined bystander effects after exposure to different ion species heavier than helium. We have been studying bystander lethal and mutagenic effects in normal human fibroblasts irradiated with carbon-ion microbeams using the 256(16×16)-cross-stripe irradiation method past 3 years. This year we examined the bystander lethal effect using 1 normal human cell and 3 different human tumor cell lines derived from different origins and considered the relationship between bystander effect and *p53*-gene status.

Two different astrocytoma cell lines with wild- and mutated-type *p53* gene distributed by Institute for Fermentation in Japan, amelanotic melanoma with mutated-type *p53* gene distributed by Health Science Research Resources Bank in Japan and normal human skin fibroblasts with wild-type *p53* gene obtained from RIKEN BioResource Center in Japan were used in this study. Carbon-ion microbeams ($^{12}C^{5+}$, 220 MeV) were generated with the HZ1 port of TIARA. Approximately 8×10^5 exponentially growing the 4 different human cell types were inoculated into each of microbeam dish, which was made of acrylic resin ring with 36 mm diameter and attached 7.5 μm-thick polyimide film on the bottom of the ring, 2 days before the microbeam irradiation. In order to block up cell-cell communication, half of the sample dishes were treated with a specific inhibitor of gap-junction mediated cell-cell communication (40 μM of gamma-isomer of hexachloro- cyclohexane) one day before the irradiation. Irradiation was carried out using the 256(16×16)-cross-stripe irradiation method described in the previous report[2)]. The linear energy transfer (LET) of carbon-ion microbeams was estimated to be 103 keV/μm at the sample position. Microbeams of 20 μm in diameter were irradiated in each point with 8 delivered ions. Cell-killing effect was detected using a colony formation assay as a reproductive cell death.

Figure 1 showed cell-killing effect in 4 different human cell types with different *p53*-gene status irradiated by carbon-ion microbeams. The surviving fraction in the cells with wild-type *p53* gene (C, D) in microbeam-irradiated dishes (IR) was around 0.90, while almost 1.0 was detected in microbeam-irradiated dishes with a specific inhibitor of gap-junction mediated cell-cell communication (L+IR). On the other hand, the surviving fraction in the cells with mutated-type *p53* gene (A, B) was the same between IR and L+IR. The results show that bystander lethal effect was observed in normal and tumor cells harboring wild-type *p53* gene, but not in *p53*-mutated tumor cells. Moreover, observed bystander effect was suppressed by treating with a specific inhibitor of gap-junction mediated cell-cell communication. There is evidence that both *p53*-mediated cellular response and gap-junction-related bystander effect are an important for carbon-ion induced bystander lethal effect.

References

1) H. Tsuji et al., J. Radiat. Res. 48 (2007) 1.
2) M. Suzuki et al., JAEA Takasaki Ann. Rep. 2006 (2008) 107.

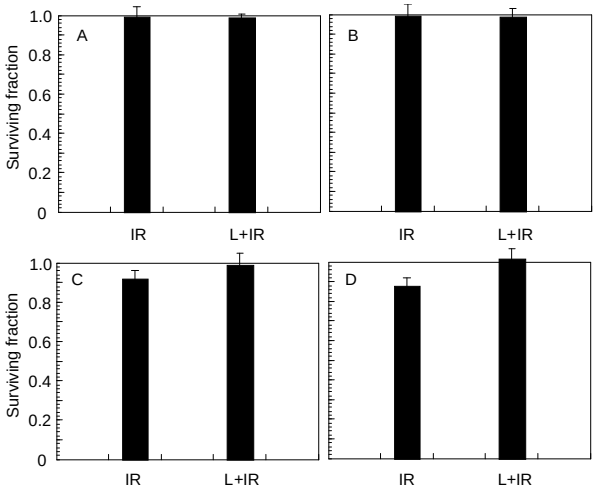

Fig. 1 Cell-killing effect in 4 human cell types with different origin. A&B; Human tumor cell lines harboring mutated-type *p53* gene, C&D; Normal human fibroblasts (C) and human tumor cell line (D) harboring wild-type *p53* gene. Cells were irradiated with carbon-ion microbeams treated with (L+IR) / without (IR) a specific inhibitor of gap-junction mediated cell-cell communication. The results are the means and standard errors from 3 independent beam times.

3-37 Heavy-ion Irradiation Induces Autophagy in Irradiated C2C12 Myoblasts and Their Bystander Cells

M. Hino [a)], N. Hamada [b)], Y. Tajika [a)], T. Funayama [c)], Y. Morimura [a)], T. Sakashita [c)], Y. Yokota [c)], K. Fukamoto [d)], Y. Mutou [c)], Y. Kobayashi [c)] and H. Yorifuji [a)]

[a)] Department of Anatomy, Graduate School of Medicine, Gunma University, [b)] Radiation Safety Research Center, Nuclear Technology Research Laboratory, Central Research Institute of Electric Power Industry, [c)] Radiation-Applied Biology Division, QuBS, JAEA, [d)] Faculty of Textile Science and Technology, Shinshu University

The C2C12 myoblasts were irradiated with ^{40}Ar (11.2 MeV/u) and ^{20}Ne (12.8 MeV/u) and the induction of autophagy was assayed by electron microscopy, immunofluorescence staining using LC-3 antibody and LysoTracker Red staining. These morphological observations showed that autophagy is induced in the irradiated C2C12 myoblasts. In addition to irradiated cells, bystander cells were also positive with LysoTracker Red staining. Altogether, these results suggest that heavy ion-irradiation induces autophagy not only in irradiated myoblasts but also in their bystander cells.

我々はこれまでに骨格筋単離筋線維の重粒子線照射による構造変化を電子顕微鏡を用い解析を行ってきた[1,2]。その結果照射領域の細胞膜では不規則な突起と陥凹、基底板の断片化が見られた。また照射領域の細胞質では筋原線維の配向の乱れ、筋小胞体の内腔の拡大が見られた。またオートファジー小体が多数観察された。

オートファジーは真核生物に普遍的な現象で、細胞質の一部を新たに形成された膜系が取り囲み、隔離し分解する機構である。オートファジーの基本的な生理的機能は、栄養飢餓状態で自己の細胞質を分解することでアミノ酸などの栄養素を産生することとされている。一方で一定の領域の細胞質やミトコンドリア等のオルガネラをまとめて分解することができる機構であることから飢餓応答以外にも障害をうけた細胞質領域やオルガネラをバルクに除去することで細胞質のホメオスタシスを維持していると考えられている。

今回我々は、重粒子線照射により誘導されるオートファジーについてマウス由来の骨格筋芽細胞 C2C12 株を用いてより詳細な検討を行った。

(1) C2C12 細胞に重粒子線 (^{40}Ar, 11.2 MeV/u; ^{20}Ne, 12.8 MeV/u)を照射した後 30 分までの各時点で細胞を固定し透過型電子顕微鏡による観察を行った。その結果照射細胞においてオートファジー小体が観察された。

(2) LC-3 はオートファジーの初期に隔離膜が細胞質を隔離する過程に必須の因子である。オートファジーが活性化した細胞ではLC-3の抗体染色像の増強が見られることからオートファジーの初期過程のマーカーとして用いられている。そこで C2C12 細胞に重粒子線を照射後 30 分の時点で固定し、抗 LC-3 抗体を用いて蛍光抗体染色を行った。重粒子線照射により蛍光強度の増強が見られた。

(3) オートファジー小体ではリソソームと融合することで内容物の分解が行われるため、成熟したオートファジー小体の内側は酸性である。C2C12 細胞を酸性オルガネラのマーカーである LysoTracker 試薬存在下で培養し、重粒子線を照射後 30 分の時点で細胞を固定し、オートファジー小体形成を観察した。重粒子線照射により LysoTracker 染色の蛍光強度の増強が見られた。

以上三点の結果は筋芽細胞 C2C12 において重粒子線照射がオートファジーを誘導することを示している。

(4)バイスタンダー効果は被ばくした細胞から周辺の直接は被ばくしなかった細胞へ遠隔的に被ばくの情報が伝えられる現象である。重粒子線によるオートファジー誘導がバイスタンダー細胞に引き起こされるか検討した（Fig. 1）。その結果、オートファジーの誘導はバイスタンダー細胞にも引き起こされることが明らかになった。また、このバイスタンダー効果は周辺の細胞と物理的に接触していない細胞でも観察されたことから液性因子の関与が示唆される。

近年がんに対する放射線治療においてアポトーシスと並んでオートファジー性細胞死が注目を集めている。重粒子線によるオートファジー誘導の解明は重粒子線治療の効果を高める上でも有意義と考えられる。

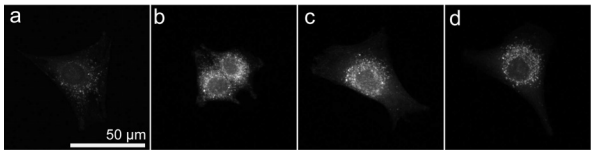

Fig. 1 LysoTracker Red staining of irradiated and bystander cells. Cells were sham-irradiated or 2 Gy-irradiated with or without shielding. Cells were fixed at 30 min after irradiation. (a) Sham-irradiated controls. (b) 2 Gy-irradiated cells without shielding. (c) 2 Gy-irradiated cells in the irradiated area of partially shielded sample. (d) Non-irradiated bystander cells in the shielded area of 2 Gy-irradiated sample.

References

1) M. Hino et al., Cell Struct. Funct. 32 (2007) 51.
2) M. Hino et al., Cell Struct. Funct. 34 (2009) 11.

3-38 Analysis of Lethal Effect Mediated by Low Dose Irradiation Induced-Secreted factors in Glioma cells

S. Wada [a)], A. Baden [a)], E. Nakagawa [a)], T. Kakizaki [a)], T. Funayama [b)] , T. Sakashita [b)], Y. Kobayashi [b)] and N. Ito [a)]

[a)] Department of Veterinary Medicine, Kitasato University,
[b)] Radiation-Applied Biology Division, QuBS, JAEA

So far, we clarified that low dose ion beam irradiation induced enhanced lethal effect and this phenomenon related with sphingomyelinase (SMase). In this study we investigated if the enhanced lethal effect induced by low dose ion beams was involved in secreted materials, so-called bystander effect. In medium transfer experiments surviving fraction by X-ray and carbon beam irradiation decreased and DNA damage by low dose X-ray irradiation was induced. On the other hand, these effects were inhibited by SMase inhibitor. This result indicates that bystander effect considerably contributes enhanced lethal effect induced by low dose radiation and SMase effects at the upstream of this signal transduction.

1. はじめに

これまでに低線量炭素線照射による生存率は、高線量域の生存曲線からの外挿値よりも低い値を示し、低線量炭素線照射でも高い細胞致死効果が得られることを明らかにし、この低線量炭素線照射による細胞致死効果の増強のメカニズムには細胞膜応答分子のスフィンゴミエリナーゼが関与することを明らかにしてきた。さらに、放射線照射後に細胞内にラジカル種が産生されることとこのラジカル種の産生はスフィンゴミエリナーゼ阻害剤によって抑制されることも明らかにしてきた。しかしながら、この細胞致死効果の増強メカニズムが直接照射を受けた細胞に過剰なシグナル伝達が誘導されたためか、照射細胞からの何らかのシグナル伝達因子によって（バイスタンダー効果）細胞内に過剰なシグナル伝達が誘導されたかは明かでない。

そこで、細胞致死効果の増強メカニズムの細胞外からのシグナル伝達因子の影響について解析した。特に、腫瘍細胞では細胞外からのシグナル伝達においてギャップジャンクションの様な細胞間伝達機構は破綻していることが多いため、細胞外に放出される液性因子の関する機構について解析を行った。

2．実験方法

グリオーマ細胞を用い、AVF サイクロトロンによって加速された 220 MeV C^{5+}（LET=108 keV/μm）を照射した。また、対照の放射線として X 線を用いた放射線応答も解析した。細胞外放出因子による細胞致死効果を解析するため、X 線および炭素線照射した細胞を 1 時間培養後、その培養液のみを回収し、非照射細胞に添加し 1 時間培養後に colony formation assay を用いて、細胞致死効果を算出した（培養液交換実験）。さらに、細胞外放出因子による細胞致死効果のスフィンゴミエリナーゼの関与を解析するため、スフィンゴミエリナーゼ阻害剤による細胞致死効果の解析も行った。また、低線量 X 線照射について細胞外放出因子による細胞障害を DNA2 本鎖切断についてγH2AX のリン酸を観察することにより評価した。

3. 結果および考察

低線量域での X 線および炭素線照射における細胞外放出因子による細胞致死効果を観察した（Fig. 1）。いずれの放射線においても、培養液交換によって生存率の有意な低下が観察された。さらに、照射細胞をスフィンゴミエリナーゼ処理したとき、非照射細胞に誘導される細胞死が抑制され、生存率がコントロールレベルまで回復した。この結果は、いずれの放射線も低線量照射によって細胞外放出因子によって細胞死が誘導され、この細胞致死誘導機構にもスフィンゴミエリナーゼが関与することを示唆している。これまでに照射後にラジカル種の産生とそのラジカル種の産生にはスフィンゴミエリナーゼが関与したため、非照射細胞に生成される DNA 損傷を観察したとき（Fig. 2）、培地交換 90 分後に DNA 損傷が生成され、この DNA 損傷生成はスフィンゴミエリナーゼ阻害剤によって抑制された。

これらのことから、低線量放射線照射による細胞致死効果増強機構にはいずれの放射線においてもバイスタンダー効果の寄与が大きいと考えられ、さらに、この機構にはスフィンゴミエリナーゼがシグナル伝達過程のかなり上流で関与することが推察された。

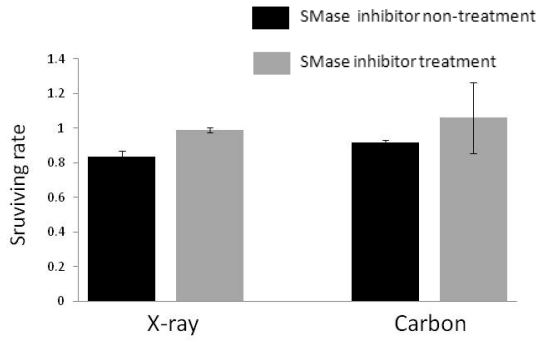

Fig. 1 Killing effect of media transfer from irradiated culture.

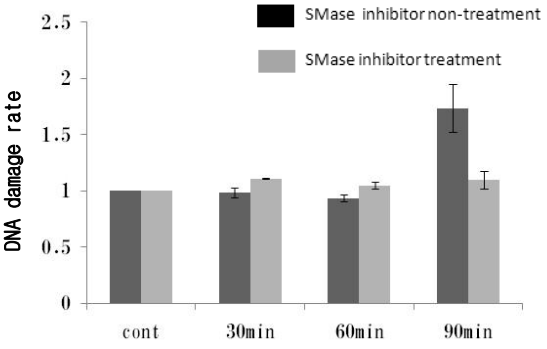

Fig. 2 DNA damage induction in non-irradiated culture by transferring media from X-ray irradiated culture.

3-39 Ion Beam Irradiation Has Different Influences on the Expression of p53 in Cultured Human Retinal Vascular Endothelial Cells Exposed to L-dopa among ^{20}Ne, ^{12}C and ^{4}He

K. Akeo [a,b], T. Funayama [c], N. Hamada [d], Y. Kobayashi [c] and Y. Akeo [a]

[a] Akeo Eye Clinic, [b] Department of Ophthalmology, Keio University School of Medicine,
[c] Radiation-Applied Biology Division, QuBS JAEA,
[d] Radiation Safety Research Center, Central Research Institute of Electric Power Industry

Deficiency of L-dopa causes degeneration of the substantia nigra in the brain and L-dopa is used in the treatment of Parkinson's disease. We proved that L-dopa produced NO and superoxide, and had the cytotoxic effects on the retinal pigment epithelial cells [1]. L-dopa injected into the vitreous of the rats dilated the vena in the ciliary body [2]. We wondered if RE cells could be exposed to oxidative stress by administrated L-dopa. We already reported that oxidative stress such as hyperoxia [3] augmented the cytotoxicity of the aortic endothelial cells by L-dopa.

Glutathione peroxidase (GPX), a selenium-dependent and lipid peroxide-scavenging enzyme that effectively reduces lipid peroxides with the concomitant oxidation of glutathione is distributed in mitochondria [4]. Faucher et al. measured the expression of two bcl-2 family members, bax and bcl-2, in a human endothelial like cell-line overexpressing the organic hydroperoxide-scavenging enzyme GPX, in the absence of any apoptotic/oxidant stimulus, and showed that overexpressing an antioxidant gene such as GPX in endothelial cells is able to change the basal mRNA and protein bax levels without affecting those of p53 and bcl-2. This phenomenon could be useful to antiatherogenic therapies which use antioxidants with the aim of protecting the vascular wall against oxidative stress injury [5].

Exposure to L-dopa inhibited the expression of GPX in RE cells. Ion beam irradiations both of ^{4}He and ^{12}C decreased the expression more remarkably than ^{20}Ne. The expression of GPX in RE cells incubated with L-dopa decreased significantly after 8 h of exposure to ^{4}He, and after 4 and 24 h of exposure to ^{12}C. On the contrary, ion beam irradiation of ^{20}Ne increased the expression of GPX in RE cells incubated with L-dopa after 4 h of the exposure of the irradiation significantly. We considered the different accumulation of the energy irradiated at a point by various ions could be concerned with the effects on the expression GPX in RE cells incubated with L-dopa.

Established human RE cells in vitro incubated with L-dopa (250 μM) for 2 h were exposed to ionization radiation that is induced by acceleration of the ionizing atom of 350 MeV ^{20}Ne, 220 MeV ^{12}C, and 50 MeV ^{4}He. We obtained the RE cells after 0, 4, 8, 24 h of the irradiation and extracted total cellular RNA to synthesize cDNA. We used the Primer3 website to design the primers for RT-PCR amplification of the cDNA of p53 and 18S RNA. The reactions were carried out at the following temperature: 95 ºC, for denaturation; 60 ºC, for annealing; and 72 ºC, for extension for 17–27 cycles. After mixing the cDNA, primer, and SYBR green, the expression of 18S RNA and p53 was measured using the LightCycler system. The technology of this system is extremely innovative and enables rapid and simultaneous evaluation PCR experiments. Fluorometric analysis of the formed PCR products was performed as a real-time measurement either continuously or at specifically defined time points during each PCR cycle.

The expression of p53 in RE cells significantly was not influenced by only exposure to L-dopa, but increased just after the irradiation both of 350 MeV ^{20}Ne and 50 MeV ^{4}He in those cells incubated with L-dopa. Ion beam irradiation caused the induction of apoptosis in RE cells damaged by lipid peroxidation with L-dopa.

References

1) K. Akeo et al., Pigment Cell Res. 13 (2000) 80.
2) S. A. Amaki et al., Pigment Cell Res. 14 (2001) 256.
3) K. Akeo et al., Exp. Eye Res. 49 (1989) 335.
4) K. Watanabe, Tran. Soc. Pathol. Jpn. 76 (1986) 39.
5) K. Faucher et al., Mol. Cell Biochem. 277 (2005) 81.

3-40 Irradiation with Carbon Ion Beams Induces Apoptosis, Autophagy, and Cellular Senescence in a Human Glioma-derived Cell Line

A. Oue [a,b], N. Shimizu [a], N. Hamada [b,c,d,e], S. Wada [b,c,d,f], A. Tanaka [a,b], M. Shinagawa [a,b], T. Ohtsuki [a,b], T. Mori [a,b], M. N. Saha [a], A. S. Hoque [a], S. Islam [a,b], T. Funayama [c], Y. Kobayashi [b,c,d] and H. Hoshino [a,b]

[a] Department of Virology and Preventive Medicine, Graduate School of Medicine, Gunma University, [b] The 21st Century Center of Excellence Program for Biomedical Research Using Accelerator Technology, [c] Radiation-Applied Biology Division, QuBS, JAEA, [d] Department of Quantum Biology, Division of Bioregulatory Medicine, Graduate School of Medicine, Gunma University, [e] Present address: Radiation Safety Research Center, Central Research Institute of Electric Power Industry, [f] Present address: School of Veterinary Medicine and Animal Science, Kitasato University

Introduction

Carbon, neon, and other heavy ions are charged particles with high linear energy transfer (LET), and their irradiation have shown higher relative biological effectiveness than low LET radiation such as X-rays. In addition, the dose distribution of heavy ion beams exhibits a steep fall-off after the Bragg peak, and thus, more precise dose localization can be achieved. Consequently, cancer radiotherapy using heavy ion beams have shown that serious damages to surrounding normal tissues can be reduced markedly. For clinical trials, carbon ion beams (C-ions) have been selected and the efficacy of C-ions therapy has been demonstrated in various cancers.

In this study, to elucidate the biological responses of cultured cells to irradiation with C-ions, we examined the induction of apoptosis, autophagy, and cellular senescence in human glioma cells [1].

Methods and Materials

A human glioma-derived cell line, NP-2, was irradiated with C-ions. Apoptotic cell nuclei were stained with Hoechst 33342. Induction of autophagy was examined either by staining cells with monodansylcadaverine (MDC) or by Western blotting to detect conversion of microtuble-associated protein light chain 3 (MAP-LC3) (LC3-I) to the membrane-bound form (LC3-II). Cellular senescence markers including induction of senescence-associated β-galactosidase (SA-β-gal) were examined. The mean telomere length (MTL) of irradiated cells was determined by Southern blot hybridization. Expression of tumor suppressor p53 and cyclin/cyclin-dependent kinase inhibitor $p21^{WAF1/CIP1}$ in the irradiated cells was analyzed by Western blotting.

Results

When NP-2 cells were irradiated with C-ions at 6 Gy, the major population of the cells died due to apoptosis and autophagy. The residual fraction of attached cells (less than 1% of initially irradiated cells) could not form colony: however, they showed a morphological phenotype consistent with cellular senescence, that is, enlarged and flattened appearance. The senescent nature of these attached cells was further indicated by staining for SA-β-gal. The MTL was not changed after irradiation with C-ions. Phosphorylation of p53 at serine 15 as well as the expression of $p21^{WAF1/CIP1}$ was induced in NP-2 cells after irradiation. Furthermore, we found that irradiation with C-ions induced cellular senescence in a human glioma cell line lacking functional p53.

Conclusions

In summary, we found that the major population of human glioma cells died due to apoptosis and autophagy after irradiation with C-ions. C-ion exposure also induced cellular senescence in the minor population of the irradiated cells. Elucidation of a gene(s) and regulatory mechanism(s) of cell death and cellular senescence in response to C-ions irradiation should contribute to develop new therapeutic protocols to improve the efficacy of cancer radiation therapy using heavy ion beams.

Reference

1) A. Jinno-Oue et al., Int. J. Radiat. Oncol. Biol. Phys. 76 (2010) 229.

3-41 Effects of Heavy Ion Irradiation on the Precursor Hemocytes of the Silkworm, *Bombyx mori*

S. Kobayashi [a)], K. Fukamoto [a)], K. Kiguchi [a)], T. Funayama [b)] Y. Yokota [b)], T. Sakashita [b)], Y. Kobayashi [b)] and K. Shirai [a)]

[a)] Division of Applied Biology, Faculty of Textile Science and Technology, Shinshu University, [b)] Radiation-Applied Biology Division, QuBS, JAEA

When compared with bacteria, insects are evolutionarily much closer to mammals. Thus the response systems against irradiation of the insect cells should be similar to that of mammalian cells. Nevertheless, like bacteria, insect cells are generally known to be quite resistant to radiation compared with mammalian cells. However, the detailed mechanisms (or reasons) of this resistance of insect cells have not been fully understood.

Heavy ion beams can deposit more energy in target organs than X-rays or gamma rays, and the irradiation system of heavy ion beams in QuBS make it possible to irradiate the desired region of the small biological samples. Therefore, this system is an extremely useful tool to inactivate specific organs or tissues such as larval imaginal discs in insects.

We have been studying the effects of heavy ion irradiation on the hemopoietic organs of *Bombyx mori* by using heavy ion beams [1)]. From the results obtained to date, we have shown that the hemopoietic organs can be regenerated following the radio-surgery, even after irradiation with 100 Gy carbon ions [2)].

For the regeneration of the irradiated hemopoietic organs, the apoptotic cell death of damaged precursor hemocyte in the hemopoietic organs is the first and an important step. However, it has also been made apparent that the insect cells, such as epidermal cells of *B. mori* or cultured cells (Sf9 cells), are more resistant to the irradiation including the carbon ions. No effect of carbon ion irradiation on the viability of these cells was observed even at a dose of 400 Gy. Therefore, the information obtained from studies on the induction mechanisms of apoptosis in the precursor hemocytes in the irradiated hemopoietic organs would contribute to the further understanding of the radiation response in insect cells. In this report, we have investigated the effects of heavy ion irradiation for the precursor hemocyte.

The viability of the irradiated precursor hemocytes up to 4 days after the irradiation was studied using carbon ions. Apoptotic cells were observed from 2 days to 4 days after irradiation with 100 Gy. The number of detected apoptotic cells had increased after irradiation, peaked at 2 days after irradiation, and gradually decreased afterwards. Whereas at a dose of 1 or 10 Gy, no cell death was induced by the heavy ion irradiation.

DNA replication in the irradiated precursor cells was examined using thymidine analog, BrdU. This analog is incorporated into DNA chains of the cells that are just duplicating the genome DNA. At a dose of 100 Gy, BrdU labeled cells had decreased remarkably at 2 days after irradiation. No significant effect on incorporation of BrdU was observed within the specimens irradiated with 1 or 10 Gy (Fig. 1).

Finally, the developmental change of cell numbers in the irradiated hemopoietic organs was evaluated and compared with those of non-irradiated organs. When the hemopoietic organs were irradiated with 100 Gy of carbon ions, proliferation of the irradiated precursor hemocytes in the organs had almost stopped and the number of cells was static until 3 days after irradiation. Moreover radiation-induced cellular hypertrophy was clearly observed in the cells at 3 days after irradiation. Whereas, at a dose of 1 or 10 Gy, the number of cells in the organs had increased along with larval development and no remarkable effect was observed.

Initially, it had seemed to us that precursor hemocytes were not resistant to heavy ion beams. However, these results indicate the responses to heavy ion irradiation of precursor hemocyte are quite similar to those of other insect cells, such as epidermal cells and Sf9 cells.

References

1) K. Kiguchi et al., Nucl. Instrum. Meth. Phys. Res. B210 (2003) 312.
2) E. Ling et al., J. Insect Biotechnol. Sericol. 72 (2003) 95.

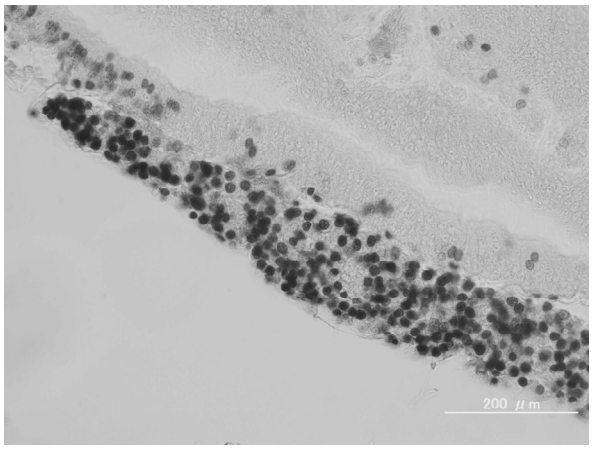

Fig. 1 BrdU labeling of precursor hemocytes in the irradiated hemopoietic organ.

3-42 Expression of Two Gelsolins in Response to Heavy-ions Irradiation and Desiccation in the Sleeping Chironomid *Polypedilum vanderplanki*

O. Gusev [a)], T. Kikawada [a)], T. Sakashita [b)], T. Funayama [b)], Y. Kobayashi [b)] and T. Okuda [a)]

[a)] Anhydrobiosis Research Unit, National Institute of Agrobiological Sciences,
[b)] Radiation-Applied Biology Division, QuBS, JAEA

Larvae of the sleeping chironomid *Polypedilum vanderplanki* survives prolonged complete desiccation and high-dose irradiations [1, 2)]. We found earlier that both desiccation and heavy ion irradiation cause severe DNA damage in cells of the larvae and post-anhydrobiosis and post-irradiation recovery of nucleic acids takes at least a few days. During the DNA recovery, cells of the larvae do not undergo apoptosis, but the mechanism of preventing apoptosis is still unknown. Gelsolin is one of the potential inhibitors of apoptosis, and a key protein for cell-motility processes, but its activity in insects is yet to be studied [3)]. At the present study we have analyzed mRNA expression of two members of gelsolin family in the larvae subjected to anhydrobiosis and irradiation.

We used the doses of ion beams which were previously found to be ID_{50} (median inhibitory dose) for adult emergence (70 Gy) of the chironomid [1,2)]. The larvae were exposed to 50 MeV ^{4}He (LET_∞=16.2 keV/μm) ion beam delivered from the azimuthally-varying-field cyclotron at TIARA. Total RNA from hydrated, dehydrating, rehydrated, and irradiated larvae was extracted using Trizol (Invitrogen) and the RNeasy Mini Kit (Qiagen, Hilden, Germany), and reverse transcribed using Ready-To-Go™ T-Prime First-Strand Kit (GE Healthcare Bio-Sciences, Piscataway, NJ). The RNA samples from dehydrating and rehydrating larvae were named "D" and "R", respectively, and numbers correspond to the hours of treatment. Real-time PCR was performed using a LightCycler ® 2.0 Real-Time PCR apparatus (Roche Diagnostics, Basel, Switzerland) with SYBR® Green PCR Master Mix (TaKaRa, Ohtsu, Japan).

Two members of gelsolin family were different in number of functional gelsolin domains: gelsolin-1 (Fig. 1) contained three domains and gelsolin-2 (Fig. 2) had six functional domains. Both gelsolins we up-regulated after irradiation with 70 Gy ion beams and gelsolin-1 showed two clear wave of expression during the anhydrobiosis cycle, while gelsolin-2 was up-regulated only during rehydration of the larvae. Initial, approximately 10-fold increase of gelsolin-1 gene expression was observed in the beginning of dehydration of the larvae (Fig. 1) and then the up-regulation of the expression was observed during the larvae rehydration reaching peak (>70 folds compared to control wet larvae, i.e. 0 h of D and IR) at 12 hours of rehydration.

Members of gelsolin family may play important roles in anhydrobiosis, i.e. first increase of gelsolin-1 expression during initial stage of dehydration related to trial of the organism to neutralize negative effect of molecular crowding on cell motility in dehydrating larvae and the second wave of expression of both gelsolins upon rehydration might also be related to restoration of activity of muscle proteins and general cell motility in the reviving larvae. As they occurred after irradiation, we assume that they are also involved in the suppression of apoptosis upon irradiation and anhydrobiosis by blocking cytochrome-C release from mitochondria in a same way as it was found in mammalian cells [3)].

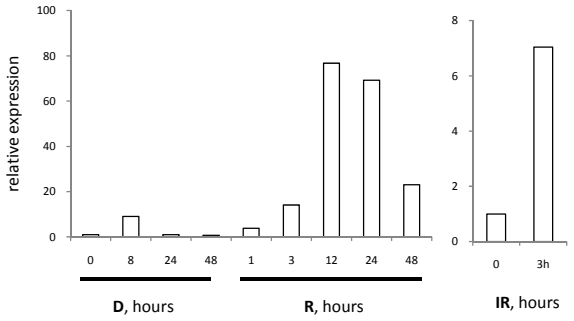

Fig. 1 Relative expression of gelsolin-1 in the larvae of *P. vanderplanki*: during desiccating (D) and following rehydration (R), and in non-desiccated larvae after irradiation with 70 Gy of ^{4}He (IR).

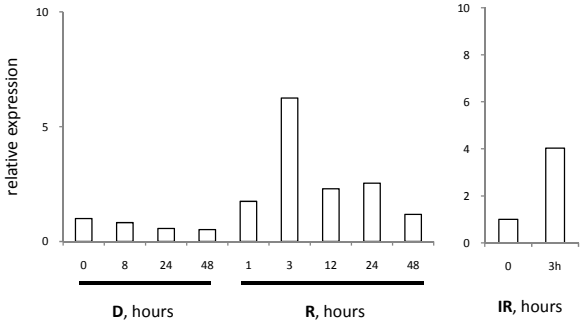

Fig. 2 Relative expression of gelsolin-2 in the larvae of *P. vanderplanki* during desiccating (D) and following rehydration (R), and in non-desiccated larvae after irradiation with 70 Gy of ^{4}He (IR).

References

1) Watanabe et al., Int. J. Radiat. Biol. 82 (2006) 587.
2) Watanabe et al., Int. J. Radiat. Biol. 82 (2006) 835.
3) Silacci et al., Cell. Mol. Life Sci. 61 (2004) 2614.

3-43 Nuclear Localization of a FOXO Transcriptional Factor DAF-16 in *C. elegans*, which is Required in a Response to IR Irradiation

T. Kimura [a)], T. Takanami [a)], T. Sakashita [b)], Y. Kobayashi [b)] and A. Higashitani [a)]

[a)] Graduate School of Life Sciences, Tohoku University,
[b)] Radiation-Applied Biology Division, QuBS, JAEA

We have identified that certain genes including *F49F1.6* induced by ionizing radiation (IR). Also, their induction has been observed during infection of *Psudomonas aeruginosa* as innate immune response [1)]. *F49F1.6* gene product has a signal peptide and Metridin-like ShK toxin domain and shows good similarity to the N-terminal region of mammalian Mucin-2 precursor [2)]. We have also found consensus sequences for GATA-1 and DAF-16 transcriptional factors in the transcriptional promoter region. By using RNAi technology, ELT-2 (a GATA-type transcription factor) is required specifically for responses to IR and bacterial infection. In this study, we analyzed the function of another transcription factor DAF-16 in response to IR.

DAF-16 codes the Forkhead box O (FoxO) transcription factor family that acts in an insulin-mediated pathway to affect dauer formation, and that also affects life span, innate immunity and reproduction [1,3)]. It is orthologous to human FOXO1, -3, -4 and -6. In the *daf-16* mutant, induction levels of *F49F1.6* gene following IR irradiation were decreased as compared with those of wild type (Fig. 1). Oppositely, those of the *daf-2* mutant were increased (Fig. 1). It has been reported that DAF-2 signals negatively regulate the activity of DAF-16 [3)]. These results indicate that DAF-16 functions as a transcriptional factor to induce certain genes including *F49F1.6* in response to IR irradiation.

The *daf-16* gene is broadly expressed in most cells except for the cells in the pharynx and in the somatic gonad [2,4)]. In addition, its nuclear transport in response to environmental stress such as high temperatures is described [4)]. We therefore investigated whether DAF-16 translocates from cytoplasm to nuclei following IR irradiation by using a recombinant strain expressed a DAF-16::GFP fusion protein. The results shown in Fig. 2A indicated that strong signals of DAF-16::GFP were revealed in cytoplasm of gut and body wall cells of control animals. Following IR irradiation, the signals were translocated into nuclei of these cells as well as those of high temperatures treatments (Fig. 2B, C). It clearly indicates that IR caused nuclear localization of DAF-16 protein, and it might act as a transcription factor for certain genes including *F49F1.6* in response to IR.

We are now attempting to study whether the nuclear localization caused by IR is driven through either oxidative stress or DNA damage response. Moreover, in addition to ELT-2 (GATA) and DAF-16 (FoxO), PMK-1 (p38 MAPK) is required for *F49F1.6* induction by IR irradiation. The next challenge is to resolve the complex regulatory mechanism with these factors.

References

1) E.R. Troemel et al., PLoS Genet. 2 (2006) e183.
2) WormBase., http://www.wormbase.org/.
3) C.L. Kurz &M-W. Tan, Aging Cell 3 (2004) 185.
4) S.T. Henderson & T.E. Johnson, Curr. Biol. 11 (2001) 1975.

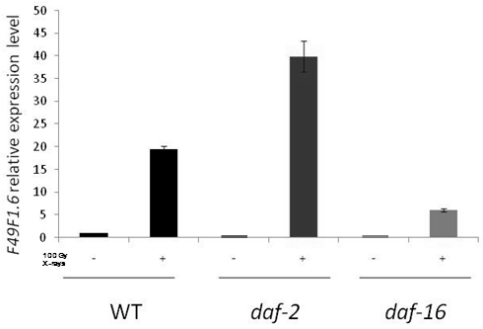

Fig. 1 A FoxO factor DAF-16 is required for *F49F1.6* gene expression induced by 100 Gy X-ray irradiation.

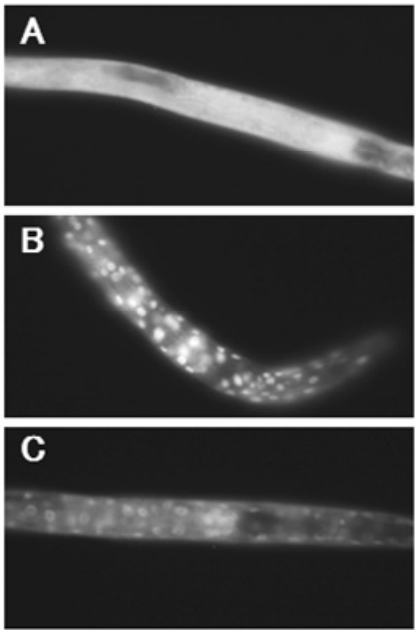

Fig. 2 Nuclear localization of DAF-16 following IR irradiation. A: control of DAF-16::GFP in TJ356 strain, B: high temperature treatment at 35 °C for 2 h, C: 4 h after 1,000 Gy X-rays irradiation.

3-44 Analysis of Bystander Cell Signaling Pathway Activated by Heavy Ion-Microbeam

M. Tomita [a)], H. Matsumoto [b)], K. Otsuka [a)], M. Maeda [a)], T. Funayama [c)], Y. Yokota [c)], Y. Mutou [c)], T. Sakashita [c)] and Y. Kobayashi [c)]

[a)] Central Research Institute of Electric Power Industry, [b)] University of Fukui, [c)] Radiation-Applied Biology Division, QuBS, JAEA

Radiation-induced bystander responses are defined as responses in cells that have not been directly targeted by radiation but are in the neighborhood of cells that have been directly exposed. In our study we aim to clarify the cell signaling pathway activated by high-LET radiation in the bystander cells. Normal human fibroblast WI-38 cells were cultured to form 5 colonies on CR-39 based dish. One cell in the targeted colony was irradiated with 460 MeV ^{40}Ar beams. Focus formation of DNA double-strand break (DSB) repair related proteins could be observed in the unirradiated cells in the untargeted colonies. Our present results suggest that several kinds of DSB repair related proteins are colocalized in the vicinity of DSBs induced in the bystander cells.

低線量放射線による生物影響は、高線量放射線の場合とは大きく異なることが明らかになりつつある。近年、低線量放射線のリスクを評価する上で注目されているのが、DNA 初期損傷量に依存しない「非標的効果」である。中でも、放射線誘発バイスタンダー応答は、もっとも特徴的な非標的効果であり、放射線に直接曝露された細胞の近傍に存在する全く放射線に曝露されていない細胞において観察される応答である [1)]。本研究は、原子力機構の細胞局所照射装置を利用し、バイスタンダー細胞に生じるシグナル伝達経路の変化を、ヒト正常細胞を用いて明らかにすることを目的とする。

細胞をマイクロビームで照射するために、ディッシュ中心部に直径 14 mm の穴があいている 35 mm ディッシュの内側に、20 mm 角にカットした CR-39 をパラフィンで接着した。細胞試料として、ヒト胎児肺由来正常線維芽細胞 WI-38 を用いた。WI-38 を CR-39 上で培養するために、さまざまな試行を繰り返した結果、以下の方法を確立した。まず、CR-39 を細胞接着因子であるファイブロネクチンでコーティングした後、一晩紫外線下で乾燥させた。次に、5×10^5 cells/mL に調整した WI-38 細胞の懸濁液 5 μL を、CR-39 上に 5 箇所スポットした後、周辺に 200 μL の培養液を入れ、一晩培養した。翌日、細胞が接着していることを確認し、培養液を加え、さらに 1 日培養したものを、照射試料とした。作成した試料を、クリスタルバイオレッドで染色した写真を Fig. 1 に示す。

5 個のコロニーの内、中央にあるコロニー内の細胞 1 個にのみ、5 粒子の 460 MeV $^{40}Ar^{13+}$を、HZ1 ポートにおいて照射した [2)]。照射 6 時間後に、細胞を 4%パラホルムアルデヒド/PBS 溶液を用いて固定した。0.1% Triton X-100/PBS 溶液で処理した後、53BP1、リン酸化ヒストン H2AX (γ-H2AX)、リン酸化 ATM、NBS1 などの抗体を用いて免疫蛍光染色を行い、細胞核は DAPI で染色した。その後、ディッシュから CR-39 をはがし、スライドグラスに細胞接着面を張り合わせた後、CR-39 をエッチング処理した。

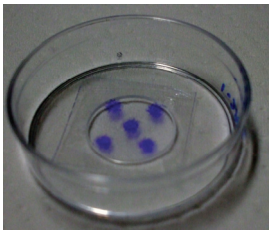

Fig. 1 Colony formation of normal human fibroblast WI-38 cells on CR-39 dish. Five colonies (center and 4 satellites) were formed.

共焦点レーザー顕微鏡を用い、細胞に Ar イオンがヒットしていることを確認した後、非照射の 4 個のコロニー内にある細胞に生じたフォーカスを観察した。

Figure 2 に示すように、非照射細胞において、53BP1 のフォーカス形成が観察された。同様に、γ-H2AX、NBS1、リン酸化 ATM のフォーカス形成も認められた。これらの結果から、照射によって直接生じた DNA2 本鎖切断と同様に、バイスタンダー細胞に生じた切断部位にも、複数の修復タンパク質が集積していることが示唆された。現在、バイスタンダー細胞におけるフォーカス数の増加について定量的な解析を進めている。

今後は、細胞周期チェックポイントや生存シグナル、アポトーシス誘導等に関与するタンパク質について、順次解析を進める。

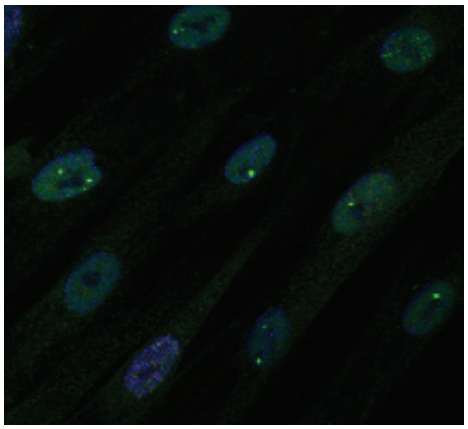

Fig. 2 Foci formation of 53BP1 in the unirradiated cells in the untargeted satellite colony.

References

1) H. Matsumoto et al., J. Radiat. Res. 50 (2009) A67.
2) T. Funayama et al., Radiat. Res. 163 (2005) 241.

3-45 Carbon Translocation in a Whole Plant Body by Using Positron Emitting Tracer Imaging System (PETIS) and Carbon-11-labeled Carbon Dioxide ($^{11}CO_2$)

N. Kawachi [a)], N. Suzui [a)], S. Ishii [a)], S. Ito [a)], N. S. Ishioka [a)], H. Yamazaki [a,b)], A. Iwasaki [c,d)], K. Ogawa [c,d)] and S. Fujimaki [a)]

[a)] Radiation-Applied Biology Division, QuBS, JAEA, [b)] Faculty of Science and Technology, Tokyo University of Science, [c)] Plant Redox Regulation Research Group, Research Institute for Biological Sciences Okayama, [d)] Core Research for Evolutional Science and Technology, JST

Elucidation of carbon kinetics in a plant is important from viewpoint of environmental reduction in the amounts of atmospheric carbon dioxide (CO_2) and from an agricultural viewpoint in terms of the growth and development of the plant body. In particular photosynthetic CO_2 fixation and photoassimilate translocation are important topics for understanding the mechanisms underlying carbon kinetics. In this study, we have developed a new method to investigate the carbon kinetics in a whole body by using one of the most powerful radionuclide-based imaging techniques for plant study, that is, the positron emitting tracer imaging system (PETIS).

Carbon-11-labeled carbon dioxide ($^{11}CO_2$) and PETIS enable video imaging of tracer dynamics of carbon fixation, photosynthesis, and translocation [1, 2)]. Because of a large field of view (FOV; 120.8 mm width, 186.8 mm height) provided by the PETIS and the sufficiently small size of soybeans (*G. max* cv. Jack) that fit in the FOV, dynamic quantitative PETIS data of gradual changing in ^{11}C activity and ^{11}C distribution throughout the entire intact plant body after pulse-chase $^{11}CO_2$ treatment was acquired. Figure 1(a) shows an experimental setup of this method. All aerial part of the soybean was covered by a large exposure cell, and was positioned between two opposite detectors of PETIS.

The treatment of the $^{11}CO_2$ exposure and air containing an ambient concentration (~350 ppm) of nonradioactive carrier CO_2 gas led to the cell at flow rate of 1,000 mL/min. The positron emitting ^{11}C-radioisotope was produced by bombarding a nitrogen gas target with approximately 10 MeV protons from AVF cyclotron at TIARA. The $^{11}CO_2$ gas was synthesized 20 MBq at the time when PETIS began acquiring images. The noninvasive imaging experiments were repeatable to scan at fertilizer application level and various environmental conditions of temperature, light intensity, and humidity from a single individual.

Figure 1(b) shows an example of serial PETIS images of carbon dynamics re-sorted in the sequence from 0–5 to 35–40 min in a soybean of whole plant. All the images were corrected for ^{11}C radioactive decay (half life = 1,223.1 sec). Total activity of the ^{11}C in the images was stable over the acquisition, so that the image data followed the law of carbon nutrient conservation in a plant body. This conservation in serial images indicates the successful imaging of CO_2 photoassimilate translocation from the time of infusion into leafs to that of distribution of the whole plant body; further, carbon kinetics is analyzable to understand plant physiology and nutrition.

References

1) N. Kawachi et al., IEEE TNS 2991 (2006) 53.
2) K. Kikuchi et al., J. J. S. Horti. Sci. 199 (2008) 77.

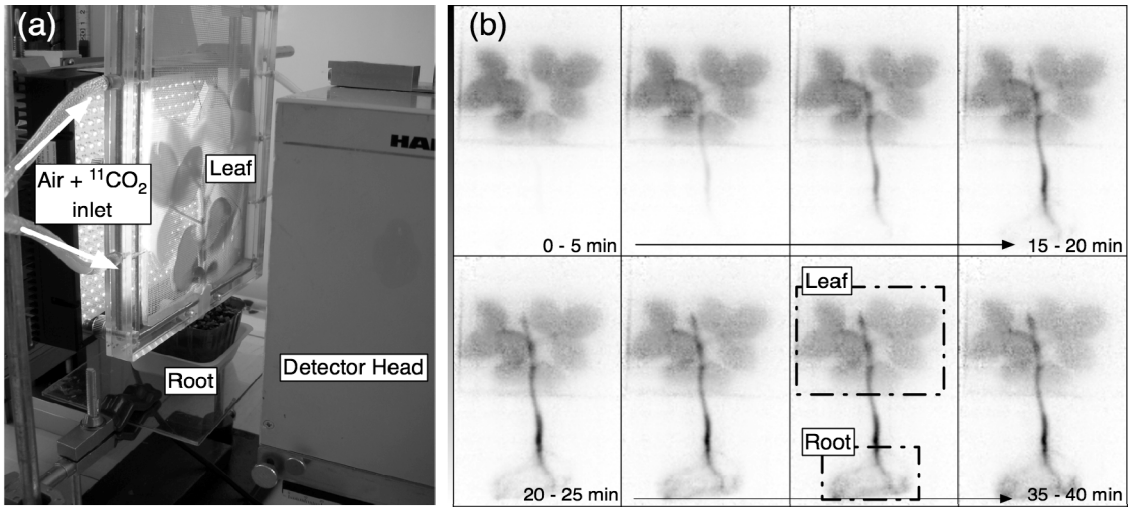

Fig. 1 (a) Photograph of an experimental setup. (b) The PETIS image data re-sorted in the sequence from 0−5 to 35−40 min (from left to right).

3-46 Quantitative Evaluation of Rice Varieties in Cadmium Uptake Activities for Remediation of Cadmium-contaminated Soil

S. Ishikawa [b)], N. Suzui [a)], S. Ito [a)], S. Ishii [a)], H. Yamazaki [a),c)] N. Kawachi [a)], N. S. Ishioka [a)] and S. Fujimaki [a)]

[a)] Radiation-Applied Biology Division, QuBS, JAEA,
[b)] Soil Environment Division, National Institute for Agro-Environmental Sciences,
[c)] Faculty of Science and Technology, Tokyo University of Science.

Introduction

Contamination of arable soil with cadmium (Cd) is one of the most serious problems in Japan. Rice is the most major source of Cd intake for Japanese people, therefore, a lot of efforts have been taken and many future plans are discussed to reduce Cd content in rice grain. The idea called "phytoremediation" is considered one of the most feasible and effective plans to reduce the contamination of soil with Cd in Japan. The project employs rice plants which are NOT edible but intensively absorb Cd from the soil and accumulate it in their aerial part to be harvested. To drive this approach forward, National Institute for Agro-Environmental Sciences (NIAES) has been selecting rice varieties with good potentials for intensive accumulation of Cd. However, two subjects should be completed to establish the practical rice cultivar for phytoremediation. First, physiological activities on Cd translocation of the test plants should be evaluated quantitatively to find best candidates. Second, the biological mechanisms which provide differences of such activities among the varieties should be elucidated.

On the other hand, the movement of Cd in intact rice plants was first visualized by JAEA in 2005 using a positron-emitting tracer imaging system (PETIS). Recently, the translocation of Cd in the whole rice plant body, for instance, absorption by roots, transport towards the aerial parts, transfer from the xylem (route to the leaves) to the phloem (to the grains) and accumulation to the spikelets, was described quantitatively using PETIS [1)]. In this study, we evaluated the activities on Cd translocation of a few candidate varieties and analyzed the biological mechanisms using PETIS.

Results and Discussion

Positron-emitting cadmium tracer, ^{107}Cd, was produced and purified as described previously [2)]. In this study, three common rice cultivars, Nipponbare, Koshihikari and Sasanishiki and three candidate varieties were subjected. We equally fed the hydroponic culture solution including ^{107}Cd to the six test plants and obtained the serial images of the Cd distribution in the aerial parts every 4 min for 36 h using PETIS, as described previously [1)].

Figure 1 shows the result as an integrated image. It was found that the three candidate plants accumulated Cd in their aerial parts approximately two times as common cultivars. It was also found that almost all Cd in the culture solution was absorbed by all the tested plants (data not shown). Therefore, this result indicates that the difference was due to greater activities of the candidates in the process to export Cd from the root tissue to the aerial parts, but not in the process of absorption from the culture. This strongly supports the previous report by Uraguchi et al., NIAES [3)].

It should also be stressed that the candidates tested in this study are foreign varieties and NOT suitable for cultivation in Japan. Practical cultivar for phytoremediation must be established by crossing these candidates with cultivars adequate for cultivation in Japan. Each physiological process of Cd translocation is considered to be executed by molecular machinery programmed by specific genes, and thus our result leads to the conclusion that the genes of the candidates related to the Cd export process from the root should be introduced into the progeny in order to realize the desired rice cultivar. We will continue the evaluation of the crossed progeny, which are genetically suggested to have the related genes derived from the candidates, with the PETIS-based method established in this study.

References

1) S. Fujimaki et al., Plant Physiol. 152 (2010) 1796-1806.
2) N. S. Ishioka et al., TIARA Ann. Rep. 2004 (2006) 277-279.
3) S. Uraguchi et al., J. Exp. Bot. 60 (2009) 2677-2688.

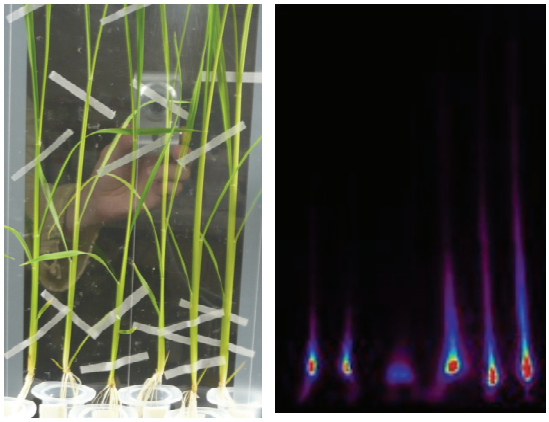

Fig. 1 Photograph of the tested plants (left) and the integrated PETIS image of Cd translocation in the same area (right). From the left, Nipponbare, Koshihikari, Sasanishiki, and three varieties of candidates were set.

3-47 Quantitative Study for Nitrogen Fixation in Intact Soybean Plant from PETIS Imaging

S. Ishii [a)], N. Suzui [a)], S. Ito [a)], N. S. Ishioka [a)], N. Kawachi [a)], N. Ohtake [b)], T. Ohyama [b)] and S. Fujimaki [a)]

[a)] Radiation-Applied Biology Division, QuBS, JAEA,
[b)] Graduate School of Science and Technology, Niigata University

The nodule is a symbiotic organ of leguminous plants with rhizobium. Soybean plants utilize nitrogen (N) fixed by nodules from atmospheric N_2. Until now, ^{15}N, a stable isotope, has long been used for studies of N_2 fixation. However, because this method is invasive, it has been difficult to analyze an instant response to environmental (ex. temperature, light) changes.

The purpose of our study is to image the N_2 fixation noninvasively and analyze the kinetics quantitatively and by using nitrogen gas labeled with ^{13}N (half life: 10 min), a positron emitting isotope, and PETIS (positron-emitting tracer imaging system). Previously, we succeeded development of a new method of production of pure ^{13}N-labelled nitrogen gas and the imaging of nitrogen fixation [1)]. To know the kinetics of nitrogen fixation rate, it was required to establish the quantitative method from PETIS data. In this paper, we report the quantitative analysis of nitrogen fixation from image data.

We produced ^{13}N-labeled nitrogen gas, and fed it as a mixture of N_2, O_2 and He (10:20:70) to the underground part of intact nodulated soybean plants for 10 min. Then the tracer gas was flushed out by flowing fresh ambient air. The serial images by PETIS were collected for 1 h (360 frames $\times$ 10 second).

As a result, serial images of distribution of the fixed ^{13}N were obtained (Fig. 1). We quantified nitrogen fixation rates of assimilated nitrogen in the root nodules using the PETIS data. Regions were set on the clump of nodules on the image data and a time-activity curve was generated from the time-course of radioactivity within the region. The average value of activity (Bq) in the first 10 frames after the ^{13}N-labeled nitrogen tracer gas was flushed out was calculated and then converted into the amount of total nitrogen (mol N_2) using the specific activity of the fed gas (1.7×10^{11} Bq mol^{-1} N_2). This value indicates the amount of total nitrogen fixed by the nodules during 10 min of exposure and was used to estimate the rate of nitrogen fixation (μmol N_2 h^{-1}). The rate of nitrogen fixation was estimated be 0.29 μmol N_2 h^{-1} (Table 1; plant No. 6). The rates of nitrogen fixation of the six test plants were estimated to be 0.17 ± 0.10 μmol N_2 h^{-1} in the same way (Table 1). To analyze the export of nitrogen from the nodules, a linear fit was carried out on the data points of the time-activity curve of each sample for 20 min from the end of flushing out of the tracer gas. The slope of the line (Bq min^{-1}) was converted to the decreasing rate (μmol N_2 h^{-1}) using the specific activity. The decreasing rates estimated for the six test plants are shown in Table 1. The large variability in the fixation rates may be attributed to differences in the size of the plants and/or in the number of nodules.

In conclusion, we estimated nitrogen fixation rates quantitatively in intact soybean plants.

References

1) S. Ishii et al., JAEA Takasaki Ann. Rep. 2008 (2009) 106.
2) S. Ishii et al., Soil Sci. Plant Nutr. 55 (2009) 660-666.

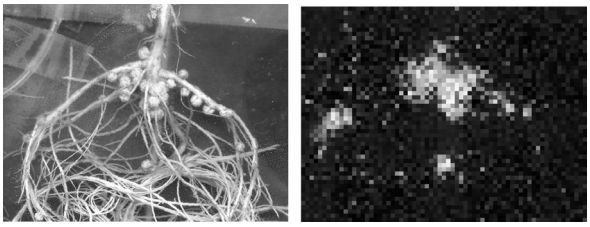

Fig. 1 Photograph of the tested plant (left) and the integrated PETIS image of nitrogen fixation in the same area (right).

Table 1 Estimated values for the rates of nitrogen fixation and decreasing rate.

Plant No.	Fixation rate (μmol h^{-1})	Decreasing rate (μmol h^{-1})
1	0.08	0.006
2	0.09	0.033
3	0.06	<0.001
4	0.33	0.003
5	0.25	0.005
6	0.29	0.016
Mean±SD	0.17±0.10	0.012±0.011

3-48 Visualization of ^{107}Cd Accumulation in Oilseed Rape Plants Treated with Glutathione

S. Nakamura [a)], N. Suzui [b)], S. Ito [b)], N. Kawachi [b)], N. S. Ishioka [b)], H. Rai [a)], H. Hattori [a)], M. Chino [a)] and S. Fujimaki [b)]

[a)] Faculty of Bioresource Sciences, Akita Prefectural University,
[b)] Radiation-Applied Biology Division, QuBS, JAEA

Cadmium (Cd) is one of toxic heavy metals. Cd accumulation in human bodies leads to serious health problems. Cd accumulates in human bodies mainly through consumption of agricultural products. It is necessary to reduce Cd accumulation in agricultural products in order to inhibit Cd accumulation in human bodies. However, critical technologies to reduce Cd accumulation in agricultural products have not yet been realized. To realize these technologies, it is needed to understand mechanisms of Cd long-distance transport and Cd accumulation in higher plants. However, these mechanisms are not well understood so far. Glutathione (GSH) is a major low molecular weight thiol tripeptide, consisting of cysteine, glutamic acid, and glycine. GSH is involved in many aspects of metabolism in plants. In our previous work, GSH concentration in the phloem sap collected from oilseed rape plants increased by Cd treatment [1)]. These results suggested that GSH might be playing important roles in controlling Cd long-distance transport and accumulation in plants. In this work, we investigated effects of GSH to Cd long-distance transport and accumulation by using positron emitting tracer imaging system (PETIS). PETIS is a planner imaging system. We can obtain serial images of distribution of positron emitting molecules in the plant body non-invasively [2)]. We already have succeeded in visualizing Cd absorption, transport and accumulation in rice plants by using PETIS [3)].

^{107}Cd (half-life: 6.5 h) was used as positron-emitting radioactive tracer in our PETIS experiments. ^{107}Cd was produced by bombarding silver plate with an energetic proton beam delivered from AVF cyclotron at TIARA (Takasaki Ion Accelerators for Advanced Radiation Application). Produced ^{107}Cd was purified, following the method of Ishioka et al [4)]. Purified ^{107}Cd was used for PETIS experiments. Oilseed rape plants (*Brassica napus*) were grown hydroponically in a growth chamber where the plant growth conditions were controlled completely for two weeks after sowing. PETIS experiments were also performed in the growth chamber under controlled growth conditions. After setting two week old oilseed rape plants in the chamber, PETIS experiments were started by adding purified ^{107}Cd in the nutrient solutions which were including GSH. In these experiments, 10 μM Cd was added to hydroponic solutions as a carrier. Time-series images of the ^{107}Cd distribution were obtained every four minute for 36 h. After PETIS experiments, ^{107}Cd accumulation in the plant body of oilseed rape plants were investigated thoroughly by using an imaging instrument (BAS-1500; Fujifilm, Tokyo, Japan).

We succeeded to obtain fine serial images of Cd transport and accumulation in oilseed rape plants (data not shown). We also succeeded to obtain images of ^{107}Cd accumulation in these plants by using an imaging instrument (Fig. 1). ^{107}Cd signals were observed in the shoot and root of oilseed rape plants. In the shoot, Cd accumulation was inhibited by GSH treatment (Fig. 1A and 1B). However, we could not see any difference in the Cd accumulation in the root of oilseed rape plants (Fig. 1C and 1D). Further research enables us to understand effects of GSH on Cd long-distance transport and accumulation in oilseed rape plants.

References

1) S. Nakamura et al., Sulfur Transport and Assimilation in Plants in the Post Genomic Era (2005) 229-232.
2) S. Fujimaki, ITE Let. (2007) 8, C1-C10.
3) S. Fujimaki et al., Plant Physiol. 152 (2010) 1796-1806.
4) N. S. Ishioka et al., JAEA Takasaki Ann. Rep. 2005 (2006) 162.

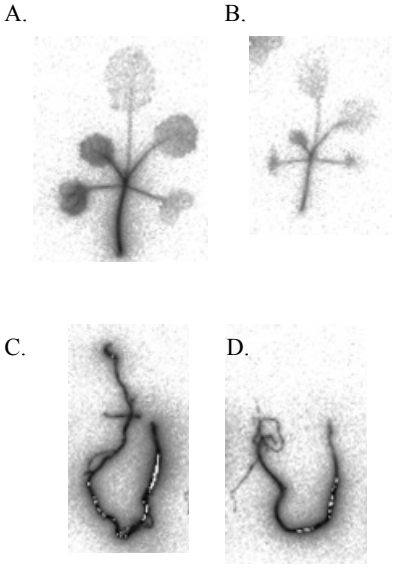

Fig. 1 ^{107}Cd accumulation in the plant body of oilseed rape plants. These images were obtained by using an imaging instrument (BAS-1500). A; Shoot of oilseed rape plant (Control), B; Shoot of oilseed rape plant (GSH treated), C; Root of oilseed rape plant (Control), D; Root of oilseed rape plant (GSH treated).

3-49 Noninvasive Imaging of Zinc Dynamics in an Intact Plant Using the Positron-emitting Tracer ^{65}Zn

N. Suzui [a)], H. Yamazaki [a),b)], N. Kawachi [a)], S. Ishii [a)], N. S. Ishioka [a)] and S. Fujimaki [a)]

[a)] Radiation-Applied Biology Division, QuBS, JAEA,
[b)] Faculty of Science and Technology, Tokyo University of Science

Introduction

Zinc is an essential element for all living organisms including higher plants. Zinc deficiency of crops is one of the most serious problems in food production in the world. Therefore, it is important to understand how plants regulate zinc uptake. In attempt to elucidate the mechanism of zinc uptake, noninvasive imaging of zinc dynamics has been a powerful tool. In the past decade, we have employed a positron-emitting tracer imaging system (PETIS), which provides serial time-course images of the two-dimensional distribution of a radioisotope (e.g. ^{11}C, ^{13}N, ^{52}Fe, ^{64}Cu, ^{107}Cd) in an intact plant without contact [1,2]. Noninvasive imaging of zinc by PETIS has been conducted using ^{62}Zn (half-life: 9.2 hours), which was produced with an energetic proton beam delivered from AVF cyclotron at TIARA (Takasaki Ion Accelerators for Advanced Radiation Application) [3,4]. Although ^{62}Zn is a weak positron emitter (7%), its daughter ^{62}Cu (half-life: 9.7 min) decays with 97.8% by positron emission, and therefore it was thought that the image of ^{62}Zn could be obtained by PETIS with high efficiency. However, because it is possible that ^{62}Cu migrates differently from ^{62}Zn in a plant body, there has been the argument that the positron imaging using ^{62}Zn correctly reflects zinc dynamics in plants.

On the other hand, one of other zinc radioisotopes, ^{65}Zn (half-life: 244 days) is commercially available and frequently used as a zinc tracer in plants. ^{65}Zn decays with 98.6% by electron capture and 1.4% by positron emission to stable ^{65}Cu. Because of its weak positron emission, ^{65}Zn was thought to be unsuitable for positron imaging, but there has been no verification of the possibility. Thus, in this study, we examined whether positron imaging of zinc is possible using ^{65}Zn and PETIS.

Results and Discussion

First, a filter paper (5 mm in diameter) containing 60 kBq ^{65}Zn (RIKEN) was monitored by PETIS, and obvious image of ^{65}Zn was obtained with counting efficiency of 6.1×10^{-4} cps/Bq. Then, the tracer solution containing 400 kBq ^{65}Zn was fed to a rice plant (Oryza sativa L.) and the dynamics of ^{65}Zn in plant was monitored by PETIS. As a result, serial images of ^{65}Zn distribution were successfully obtained every 5 minutes for 48 hours (Fig. 1). In addition, the uptake kinetics (Km/Vmax) and the translocation velocity of zinc in plant were determined from the image data.

These results indicate that ^{65}Zn is a suitable radioisotope for noninvasive imaging by PETIS. By taking advantage of the long half-life, ^{65}Zn translocation can be visualized all through the life of plants. Furthermore, the commercial availability of ^{65}Zn makes it possible to conduct noninvasive imaging of zinc in facilities without cyclotron, accelerating the research of zinc dynamics in plants.

References

1) S. Fujimaki, ITE Let. 8 (2007) 404-413.
2) S. Fujimaki et al., Plant Physiol. 152 (2010) 1796-1806.
3) S. Watanabe et al., Radiochim. Acta 89 (2001) 853-858.
4) M. Suzuki et al., Plant Mol. Biol. 66 (2008) 609-617.

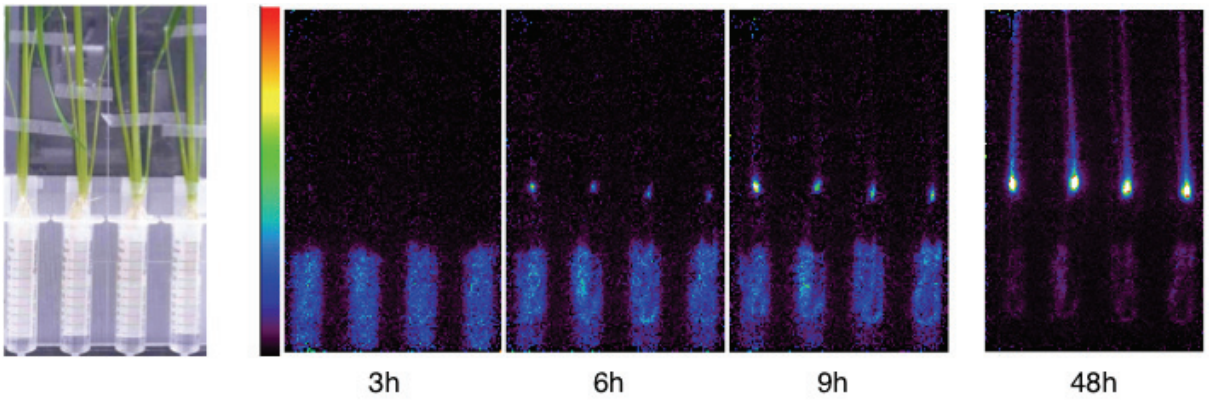

Fig. 1 Photograph of the tested rice plants (left) and the integrated PETIS image of ^{65}Zn in the same area (right). Each image is integration of 36 original frames, corresponding to 3 hours.

3-50 Uniformity Measurement of Newly Installed Camera Heads of Positron-emitting Tracer Imaging System

N. Kawachi [a], N. Suzui [a], S. Ishii [a], H. Yamazaki [a,b] and S. Fujimaki [a]

[a] Radiation-Applied Biology Division, QuBS, JAEA,
[b] Faculty of Science and Technology, Tokyo University of Science

A positron-emitting tracer imaging system (PETIS) is the most promising device that can be used for radiotracer imaging in plant studies. Elucidation of nutrient dynamics in a plant is important from an agricultural viewpoint in terms of the growth and development of a plant body; this helps in understanding the mechanisms underlying nutrient kinetics using the PETIS. Here, we have performed phantom experiments for the quarterly maintenance of the uniformity and sensitivity correction of the PETIS to assess the performance of its newly installed detector head and maintain a sufficiently high image quality for plant study. In order to quantitatively acquire the analyzable dynamic data of PETIS images, it is mandatory to begin a scheduled work for constant quality control.

We prepared a flat uniform phantom containing a radioactive solution of Na-22 (half-life; 2.6 years), and the radioactivity of the solution was 16.3 kBq/mL. The phantom had a thickness of 3 mm, a width of 90 mm, and a height of 90 mm. We have operated three types of the PETIS detector head (Hamamatsu Photonics Co. [1]). Newly installed PETS No. 4 and elderly PETIS No. 2, which has a large field of view, and No. 3, which has fine detector module, acquired for 5 min to image the phantom in this maintenance experiment. All images were corrected for detector geometry and counting rate losses. To analyze the image quality of the phantom data, we estimated the mean value (MEAN), standard deviation (SD), and the root mean square uncertainty (RMSU) of a selected region of interest (ROI) in the images. %RMSU is defied as follows,

$$\%RMSU = \frac{100 \times \sigma}{\bar{x}}$$

where σ is the standard deviation, and $\bar{x}$ is the mean value of the count in ROI.

Figure 1 shows the imaging results of the phantom experiments performed with PETIS No. 3 and No. 4. The phantom image acquired with PETIS No. 3 has a sharper pattern than those acquired with PETIS No. 4; on the other hand, the phantom image obtained with PETIS No. 4 has more uniformity than that obtained with PETIS No. 3. The crosshatching pattern on the image of PETIS No. 3 indicates that the errors of geometry correction and sensitivity dispersions are caused by the aged deterioration of the detector modules. Results of uniformity analysis of MEAN, SD, and %RMSU for an active image area are summarized in Table 1. The analyzed data support the impression of the visualized phantom images. PETIS No. 4 exhibited excellent uniformity performance for plant study.

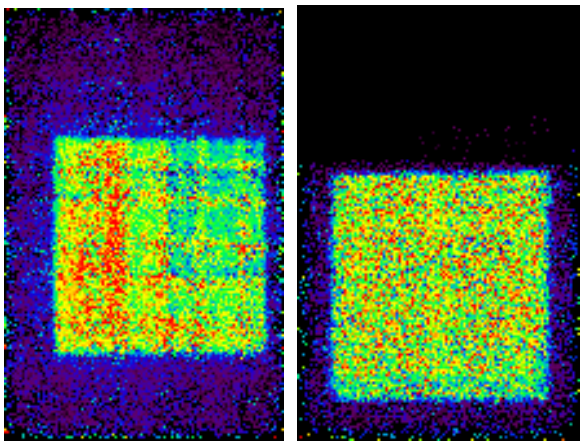

(PETIS No. 3) (PETIS No. 4)

Fig. 1 Images of radioactive flat phantom (^{22}Na; 390 kBq) acquired for 5 minutes with PETIS No. 3 (left) and PETIS No. 4 (right).

Table 1 Analyzed performance of MEAN, SD, and %RMSU for the active image area of the PETIS detector head of No. 2, No. 3, and No. 4.

	PETIS No. 2	PETIS No. 3	PETIS No. 4
MEAN	6.89×10^{-4}	7.14×10^{-4}	3.56×10^{-4}
S. D.	7.63×10^{-5}	1.23×10^{-4}	1.46×10^{-5}
%RMSU	11.1	17.2	4.11

The %RMSU is expected to increase in the activity of the images; therefore, the measurements of %RMSU dependence on the counting rate in each detector head are now in progress. These works on the maintenance of PETIS quality control ensure quantitative kinetic analysis and support many other plant physiological experiments of PETIS studies.

Reference

1) H. Uchida et al., Nucl. Instrum. Meth. A 516 (2004) 564.

3-51 PET Studies of Neuroendcrine Tumors by Using ^{76}Br-*m*-Bromobenzylguanidine (^{76}Br-MBBG)

Sh. Watanabe [a)], H. Hanaoka [b)], J. X. Liang [a)], Y. Iida [b)], Sa. Watanabe [a)], K. Endo [b)] and N. S. Ishioka [a)]

[a)] Radiation-Applied Biology Division, QuBS, JAEA,
[b)] Graduate School of Medicine, Gunma University

Introduction

^{131}I-*m*-Iodobenzylgunanidine (^{131}I-MIBG), functional analogue of norepinephrine, has been employed for the therapy of neuroendcrine tumors which express norepinephrine transporter (NET). ^{123}I-MIBG scintigraphy has been also used for diagnosis of NET positive tumors such as detecting metastasis, investigating suitability and monitoring response to the treatment with ^{131}I-MIBG. However, ^{123}I-MIBG scintigraphy has limitation to diagnose small legions due to lower sensitivity and resolution. Since positron emission tomography (PET) is superior to spatial resolution and quantitative capability compared to scintigraphy, positron emitter labeled MIBG has potential to improve diagnostic ability of NET positive neuroendcrine tumors. Then, we have reveal the utility of positron emitter ^{76}Br ($t_{1/2}$ = 16.1 h, β^+ = 57%) labeled *m*-bromobenzyl-guanidine (^{76}Br-MBBG) as a PET tracer for NET positive tumor. In this study, we have performed PET imaging by using ^{76}Br-MBBG and ^{18}F-FDG.

Materials and Methods

No-carrier-added ^{76}Br was produced using enriched $Cu_2{}^{76}Se$ target (99.7% enrichment, 365 mg) at JAEA-TIARA AVF cyclotron. ^{76}Br-MBBG was synthesized from MIBG in the presence of *in situ* generated Cu^+ catalyst [2)]. Characterization was carried out with HPLC analysis. (Mobile phase: 15% acetonitrile in 0.01 M Na_2HPO_4 solution; Flow rate: 3 mL/min.; Column: μBondapak C-18 300 mm × 7.6 mm i.d., Waters). For PET studies, rat pheochromocytoma (PC-12) xenografted mice were intravenously administered 5 MBq of FDG. The mice were anesthetized with sodium pentobarbital solution, and PET scans were performed at 1 h after administration by using an animal PET scanner (Inveon; Siemens) with 20 min emission scanning. Two days after FDG-PET, the tumor-bearing mice were intravenously administered 7 MBq of ^{76}Br-MBBG and also anesthetized with sodium pentobarbital solution. PET scans were then performed at 1 h, 3 h, and 6 h after administration.

Results and Discussions

^{76}Br-MBBG was synthesized with 20-50% of labeling efficiency. Retention time of ^{76}Br-MBBG in HPLC analysis was 27 min, which are identical to non-radioactive MBBG. Radiochemical purity was >97%. Animal PET demonstrated that the transplanted PC-12 tumor was successfully imaged at 3 h after administration (Fig. 1). In mouse A, high accumulation was also observed at this time point in the bladder, after which ^{76}Br-MBBG was gradually cleared from these non- target organs. On the other hand, FDG failed to detect an even larger tumor. In mouse B, however, there were two tumors which showed differential uptake of ^{76}Br-MBBG and FDG. That is, ^{76}Br-MBBG showed high accumulation in the lower tumor, but FDG showed high accumulation in the upper tumor (Fig. 1B). Animal PET studies demonstrated that ^{76}Br-MBBG could image NET expressing tumors clearly at 3 h after administration. The accumulation patterns of MBBG and FDG in the tumors differed from mouse to mouse and even from lesion to lesion within individual animals. Histological staining of the excised tumors after PET studies indicated that MBBG-strong and FDG-weak tumors were well-differentiated and MBBG-weak and FDG-strong tumors were poorly differentiated, which agrees well with the clinical data. Thus, the variation of tumor differentiation was considered to have contributed to the variation in the accumulation level of MBBG.

Conclusion

In the present study, MBBG showed a higher level of tumor accumulation than MIBG. In PET studies, MBBG provided a clear image with high sensitivity, and its accumulation pattern was distinct from that of FDG. These results indicated that ^{76}Br-MBBG would be a potential tracer for imaging NET-expressing neuroendocrine tumors.

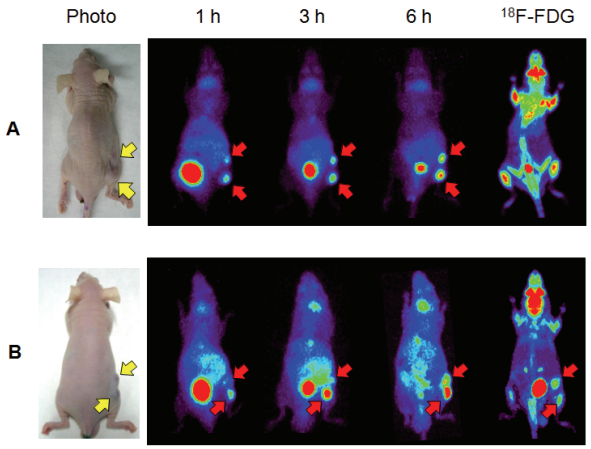

Fig. 1 PET imaging of PC-12 xenografted nude-mice A and B by using ^{76}Br-MBBG and ^{18}F-FDG. Yellow allows indicate the position of xenografted tumor, and red allows show the tumor detected by PET imaging.

References

1) S. Watanabe et al., JAEA Takasaki Ann. Rep. 2008 (2009) 107.
2) S. Watanabe et al., J. Nucl. Med. (2010) in press.

3-52 Imaging and Biodistribution of Her2/Neu Expression in Non-Small Cell Lung Cancer Xenografts with ^{64}Cu-labeled Trastuzumab PET

P. Paudyal [a)], B. Paudyal [a)], H. Hanaoka [a)], N. Oriuchi [a)], Y. Iida [a)], H. Yoshioka [a)], H. Tominaga [a)], Sa. Watanabe [b)], Sh. Watanabe [b)], N. S. Ishioka [b)] and K. Endo [a)]

[a)] Graduate School of Medicine, Gunma University,
[b)] Radiation-Applied Biology Division, QuBS, JAEA

Lung cancer is one of the leading causes of death with a 5-year survival rate of less than 10%. Activation of human epidermal growth factor receptor 2 (Her2/neu) genes is encountered in subpopulations of non-small cell lung carcinomas (NSCLC). NSCLC overexpress the Her2/neu gene in approximately 59% of cases. Trastuzumab, a humanized monoclonal antibody, interferes with Her2 signaling and is approved for the treatment of Her2/neu overexpressing breast cancer. However, its therapeutic use in Her2/neu overexpressing NSCLC remains obscure[1].

^{64}Cu with half-life 12.7 h labeled monoclonal antibody has been garnering interest in the field of targeted imaging due to its emission of both β^+ (17.4%) and β^- (41%)[2]. The present study aimed to determine the role of ^{64}Cu-labeled trastuzumab positron emission tomography (PET) for non-invasive imaging of Her2/neu expression in NSCLC.

Methods: Trastuzumab was conjugated with the bifunctional chelator 1, 4, 7, 10-tetraazacyclododecane-1, 4, 7, 10-tetraacetic acid (DOTA) and radiolabeled with ^{64}Cu. The molecular specificity of DOTA-trastuzumab was determined in NSCLC cell lines with Her2/neu overexpression (NCI-H2170) and negative expression (NCI-H520). $^{64}CuCl_2$ was provided in a dry state and was dissolved in sodium acetate buffer (0.25 M, pH 6.0). Thirty μg of DOTA-trastuzumab was added and the mixture was incubated at 40 ºC for 1.5 h. Then, 10 mM EDTA was added and the above solution was incubated for 15 min at 45 ºC. The labeling yield was checked with thin layer chromatography (TLC). The final purification was done using a Bio-Spin 6 Tris column. Imaging of Her2/neu expression was performed in NCI-H2170 tumor-bearing mice with ^{64}Cu-DOTA-trastuzumab PET and ^{64}Cu-DOTA-IgG. Size exclusion HPLC (SE-HPLC) was used to evaluate the *in vitro* and *in vivo* stability of ^{64}Cu-DOTA-trastuzumab. For *in vitro* stability, ^{64}Cu-DOTA-trastuzumab was mixed with murine serum and the solution was incubated at 37 °C and the aliquots were analyzed at 1 h, 24 h and 48 h. For *in vivo* analysis, blood was drawn from the mice injected with ^{64}Cu-DOTA-trastuzumab at 1 h and 48 h and the sample was analyzed by SE-HPLC.

Results: The labeling efficiency of ^{64}Cu-DOTA-trastuzumab was 92% without purification and 99% after purification, which should allow the specific uptake of the conjugate. The number of DOTA chelator molecule attached to the trastuzumab was 5-6 per mole of trastuzumab. Incubation of ^{64}Cu-DOTA-trastuzumab in murine and *in vivo* revealed that the conjugate existed only in the intact form (retention time : 19-20 min) and no transchelation to protein was seen until 48 h which confirmed the stability of the conjugate as shown in the Fig. 1. The retention time of the sample, serum and blood was 19-20 min. *In vitro* studies revealed specific binding of DOTA-trastuzumab in the Her2/neu positive NCI-H2170 cells, while no binding was seen in the Her2/neu negative NCI-H520 cell line. Biodistribution and PET studies revealed a significantly high accumulation of ^{64}Cu-DOTA-trastuzumab in the Her2/neu overexpressing NCI-H2170 tumor at 24 h and 48 h post-injection (21.4 ± 1.4% and 23.2 ± 5.1% injection dose/gram (% ID/g), respectively) as shown in the Fig. 2. PET imaging of Her2/neu negative NCI-H520 tumors showed much less uptake of ^{64}Cu-DOTA-trastuzumab (4.0% ID/g). The NCI-H2170 tumor uptake of ^{64}Cu-DOTA-trastuzumab was significantly higher than that of ^{64}Cu-DOTA-IgG ($p<0.0001$)[3].

Conclusion: ^{64}Cu-DOTA-trastuzumab showed a very clear image of a Her2/neu positive tumor and appeared to be effective as a PET tracer for imaging of Her2/neu gene expression in NSCLC, suggesting its potential clinical use for identifying patients that might benefit from trastuzumab-based therapy. Since lung cancer is the leading cause of death throughout the world, it would be of great significance if even a small percentage of patients would respond to the trastuzumab-based therapy.

References

1) A. Micheli et al., Ann. Oncol. 13 (2002) 840-65.
2) C. J. Anderson et al., J. Nucl. Med. 33 (1992) 1685-91.
3) P. Paudyal et al., Cancer Sci. 101 (2010) 1045-1050.

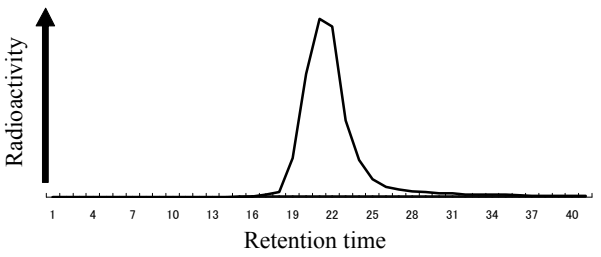

Fig. 1 Radioactivity profile of ^{64}Cu-DOTA-trastuzumab PET after incubation in murine serum at 48 h. The protein was found in intact form.

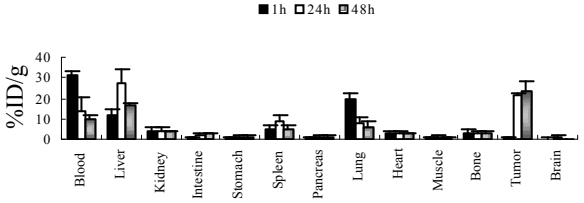

Fig. 2 Biodistribution of Her2/neu overexpressing non-small cell lung cancer, NCI-H2170 xenografts at different time points. The uptake in tumor increased with time while it is decreased in normal organs.

3-53 Production of No-carrier-added Lu-177 for Radioimmunotherapy

Sa. Watanabe [a)], K. Hashimoto [a)], H. Hanaoka [b)], K. Endo [b)] and N. S. Ishioka [a)]

[a)] Radiation-Applied Biology Division, QuBS, JAEA,
[b)] Graduate School of Medicine, Gunma University

Lutetium-177 is considered to have potential for application in radioimmunotherapy, because it emits β-particles ($E_{\beta,max}$=498 keV) suitable to penetrate small tumors and its physical half-life of 6.734 days is long enough for ^{177}Lu-labeled antibodies to accumulate to tumor sites. In addition, real time imaging of biodistribution can be done by using the ^{177}Lu, because the energy of γ-rays (E_γ=113 keV and 208 keV) emitted from ^{177}Lu is particularly suitable for imaging by single photon emission computed tomography. We have succeeded in the production of high purity no-carrier-added (nca) ^{177}Lu of capable of labeling antibodies using reversed-phase ion-pair liquid chromatography. However, in this separation, nca ^{177}Lu could not be completely separated from more than 2.5 mg of Yb_2O_3 target. For this reason, the radioactivity of nca ^{177}Lu produced by our separation method is limited less than GBq. Therefore, for the realization of the large scale production, we considered the adoption of a coarse separation between Lu and Yb by using LnResin column before reversed-phase ion-pair liquid chromatography. In the present paper, the maximum weight of Yb_2O_3 capable of the separation between Lu and Yb by using LnResin column chromatography followed by reversed-phase ion-pair liquid chromatography was investigated.

For the production of nca ^{177}Lu, the ^{176}Yb(n, γ)^{177}Yb ($T_{1/2}$=1.911 h) → ^{177}Lu process was used. An enriched $^{176}Yb_2O_3$ target (^{176}Yb:97.6%) in a quartz ampoule was irradiated for 7 hours at JAEA JRR-3 with a thermal neutron flux of 1×10^{14} n·cm^{-2}·s^{-1}. The weight of Yb_2O_3 target was varied from about 2 to 15 mg. Ytterbium-175 ($T_{1/2}$=4.185 d) was also produced due to the ^{174}Yb content in the target, and was used as a tracer of ytterbium. The irradiated $^{176}Yb_2O_3$ target was allowed to stand for a few days for the decay of ^{177}Yb ($T_{1/2}$=1.911 h). The irradiated $^{176}Yb_2O_3$ was then dissolved in a mixture containing both 3 mL of 6 M HCl and 2 mL of 30% H_2O_2 with heating. The solution was evaporated to dryness and the residue was dissolved in a few mL of 0.1 M HCl. The solution was loaded on a LnResin column (Eichrom technologies, 50-100 mesh, 300 mm × 8 mm ϕ). Elution was done with 1000 mL of 2 M HCl, 30 mL of 3 M HCl and 150 mL of 6 M HCl. Ytterbium is mainly eluted in 2 M and 3M HCl and Lu is in 3 M and 6 M HCl. The effluent was taken as three fractions of 2 M, 3 M and 6 M HCl and the radioactivity of each fraction was measured with a calibrated HPGe detector.

The results of elution of the LnResin column were shown in Table 1. In 2.0, 5.7 and 10.3 mg of Yb_2O_3 targets loaded on the LnResin column, the weight of Yb_2O_3 in 3 M and 6 M HCl fraction was less than 2 mg. On the other hand, in 15.0 mg of Yb_2O_3 target, the weight of Yb_2O_3 in 3 M and 6 M HCl fraction was more than 5 mg. Since, in the reversed-phase ion-pair liquid chromatography, nca ^{177}Lu could not be completely separated from more than 2.5 mg of Yb_2O_3 target, the 15 mg of Yb_2O_3 target is too much. Therefore about 10 mg of Yb_2O_3 target was considered to be maximum weight of Yb_2O_3 capable of the separation between Lu and Yb by using LnResin column followed by reversed-phase ion-pair liquid chromatography.

By irradiation of 10 mg of Yb_2O_3 for 10 days at JRR-3 with a thermal neutron flux of 1×10^{14} n·cm^{-2}·s^{-1}, 3.6 GBq of ^{177}Lu can be produced as calculated value. Therefore, a large scale production of ^{177}Lu (GBq order) for the clinical application can be theoretically achieved. For future plan, a large scale production of ^{177}Lu will be carried out by the combination of the coarse separation by using LnResin column and the fine separation by using reversed-phase ion-pair liquid chromatography.

Acknowledgments

A part of this study is the result of "Development of RI-DDS for advanced cancer diagnosis and therapy" carried out under the Strategic Promotion Program for Basic Nuclear Research by the Ministry of Education, Culture, Sports, Science and Technology of Japan.

Table 1 Distribution of ^{175}Yb and ^{177}Lu in 3 M and 6 M HCl fraction by LnResin column chromatography. The First column shows the weight of Yb_2O_3 target loaded on the LnResin column. The second column shows the percentage of ^{175}Yb in 3 M and 6 M HCl fraction in which lutetium is mainly eluted. The third column shows the weight of Yb_2O_3 in 3 M and 6 M HCl fraction, which was calculated by multiplication of weight of Yb_2O_3 target loaded on the LnResin column (first column) by the percentage of ^{175}Yb in 3 M and 6 M HCl fraction (second column). The forth column shows the percentage of ^{177}Lu in 3 M and 6 M HCl fraction. In all weight of Yb_2O_3, the percentage of ^{177}Lu is more than 90%.

Loaded Yb_2O_3 weight (mg)	^{175}Yb in 3 M and 6 M HCl fraction (%)	Yb_2O_3 weight in 3 M and 6 M HCl fraction (mg)	^{177}Lu in 3 M and 6 M HCl fraction (%)
2.0	11.3	0.23	91.5
5.7	11.4	0.65	96.2
10.3	16.4	1.7	96.0
15.0	35.2	5.3	90.3

3-54 Improvement of Spatial Resolution of PIXE-CT at TIARA

T. Satoh, M. Kohka, A. Yokoyama, T. Ohkubo, A. Yamazaki, Y. Ishii and T. Kamiya

Department of Advanced Radiation Technology, TARRI, JAEA

Introduction

We develop a technique for three-dimensional (3D) measurement of trace elements in a minute sample (e.g. a biological cell) using micro-PIXE and STIM. In our previous report [1, 2], we applied not only CT (computed tomography) technique but also STIM (scanning transmission ion microscopy) to micro-PIXE analysis for 3D measurement taking account of such parameters as the 3D densities of major elements, the energy of an incident particle, the X-ray production cross section and the X-ray attenuation coefficient, and we used FBP (filtered back projection) algorithm, with which 3D reconstruction is relatively simple and fast. As a result, the spatial resolution of about 10 μm was achieved but it is not enough for a biological cell. To make it better, we improved rotation mechanism of a sample, and used ML-EM (maximum likelihood expectation maximization) iterative algorithm instead of FBP because ML-EM is well suited to rare event analysis such as micro-PIXE.

Experiment

We used micro-PIXE system connected to the 3 MV single-ended accelerator at TIARA, and a leg of an insect was used as a test sample. It is useful for confirming spatial resolution of this 3D analysis because it has hollow tubular structure and includes various elements. It was bombarded by 3 MeV proton microbeam in micro-PIXE and STIM.

In this development, the sample must be rotated somehow in micro-PIXE and STIM. In our previous work, it was glued on a metal needle and was rotated directly by hand. The vibration of the rotation caused a bad effect on spatial resolution. Therefore, we used an ultrasonic motor because it has good rotational accuracy and very low mechanical vibration.

For STIM experiment, the surface barrier detector was placed just behind the target, while a Faraday cup was placed at the same position in the case of micro-PIXE analysis.

Result

Figure 1 shows a microscope image of the test sample. Figure 2 is the 3D image which was reconstructed from twelve micro-PIXE images using ML-EM method. The number of iteration was 10.

Cross-sectional images along the white line of Fig. 2 were shown in Fig. 3. The left and right images in Fig. 3 were reconstructed using ML-EM and FBP, respectively. As shown in Fig. 3, many radial artifacts were produced using FBP. On the other hand, we were able to get a better spatial resolution and to recognize the boundary of the sample easily because there was no artifact in case of ML-EM.

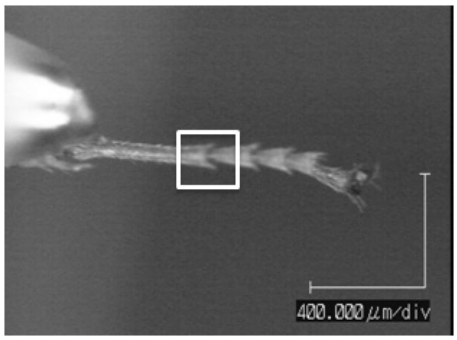

Fig. 1 Optical microscope image of the sample. It was glued on the top of a metal needle. The white rectangle shows the measured area (200 μm × 200 μm).

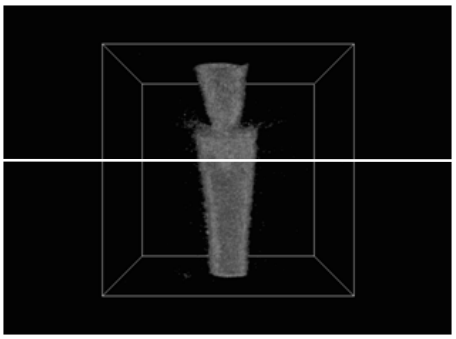

Fig. 2 The result of the 3D reconstruction from twelve micro-PIXE images with ML-EM.

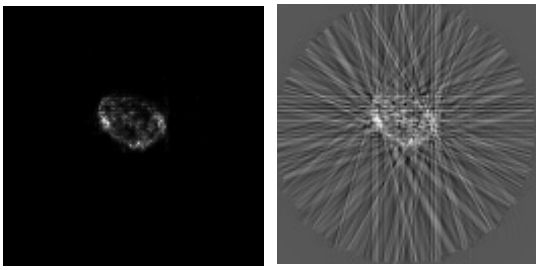

Fig. 3 Crossl-sectional image at the white line in Fig. 2. The left and right images in Fig. 3 were reconstructed using ML-EM and FBP, respectively.

References

1) T. Satoh et al., Nucl. Instrum. Meth. B 267 (2009) 2125.
2) T. Satoh et al., JAEA Takasaki Ann. Rep. 2008 (2009) 110.

3-55 The Analysis of Trace Metal in a Slice of Subjected Restraint Stress Mice by In-Air Micro-PIXE

E. Sakurai [b)], K. Yanai [b)], K. Ishii [a)], S. Okura [a)], K. Fujiki [a)], H. Yamazaki [a)], S. Matsuyama [a)], N. Okamura [b)], T. Kamiya [c)], T. Satoh [c)] and K. Arakawa [c)]

[a)] Department of Quantum Science and Energy Engineering, Tohoku University,
[b)] Department of Pharmacology, Tohoku University School of Medicine,
[c)] Department of Advanced Radiation Technology, TARRI, JAEA

Stress induces the changes of circadian rhythm sleep disorder and causes depression in human. Histaminergic neuron system has many important roles in the brain such as sleep-awake cycle, locomotor activity, learning and memory[1)]. The histamine receptor subtypes (H1, H2, H3 and H4) mediate these neuronal actions. We reported that neuronal histamine is closely associated with acute and chronic stress responses[2)]. Histamine H3 receptor exits in pre-synaptic terminals and may have alteration histamine release and modulates other neuron-systems[1)]. Therefore, we hypothecate that histamine H3 receptor knockout (H3-KO) mice may have resistance of stress. In this experiment, we examined the effects of histamine H3 receptor on restraint stress induced behavioral changes in histamine H3 receptor knockout mice and their wild type mice. Mice were treated by 50 mg/kg /day of 5-bromo-deoxyuridine (BrdU) for 5 consecutive days, 2 h before the behavioral studies. Bromine is a useful marker to detect new born cells in the brain and is used widely for neurogenesis experiments. There are some reports that the hippocampal neurogeneses are reduced by subjected restraint stress in rats. However, it is still unclear whether stress induces the distribution changes of the trace elements or not. Particle Induced X-ray Emission: PIXE is a powerful method for the analysis of trace elements. In this report, the trace element distributions in the brain slices of the H3-KO mice were measured by In-Air-Micro PIXE.

In-air micro-PIXE was developed at the Takasaki Ion Accelerators for Advanced Radiation Application (TIARA), JAEA. Micro-PIXE allows analyzing the spatial distribution of the elements quantitatively.

H3-KO mice were randomly divided into 3 groups. Mice were restrained in a mouse holder for 4 h during 5 consecutive days as a physical group, and the other mice were set next to the restrained cages as a psychological stress group. The control mice were kept in a separate room. After behavioral studies, mice brains were quickly removed and each brain was cryosectioned sagittally at 16 μm thickness.

Figure 1 shows the beam irradiation image in region of 450 × 450 μm^2 in the brain slice of control, subjected psychological stress and physiological stress mice. The image on the extreme left indicates for the control mice (no-stress). The accumulate image of sulfur, zinc and bromine were shown under micrograph of the each brain slices.

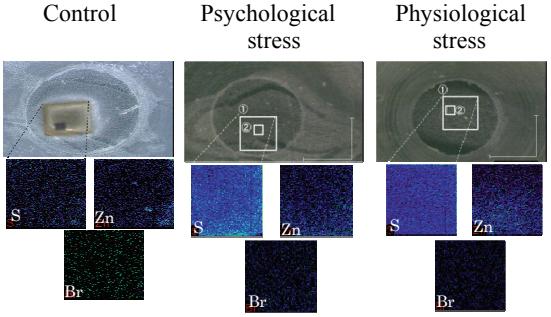

Fig. 1 Micrograph of beam irradiation, zinc and bromine image (450 × 450 μm) of H3-KO brain slices.

The amounts of trace metal in the slices are shown in Fig. 2. The amount of bromine in the slices of subjected restraint stress or psycological stress are almost same when compare with no-stress control mice. Interestedly, the amount of sulfer (data is not shown) and iron in the slice of subjected psycological stress were significant heigher than that of control or physiological stress mice. On the other hand, zinc in the slices of subjected psycological stress was significant lower than that of control or physical stress mice.

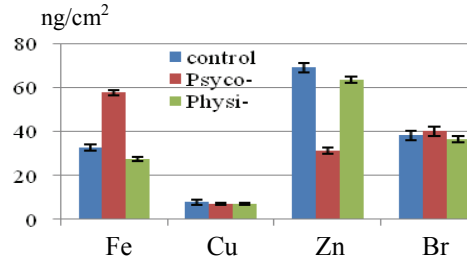

Fig. 2 Comparisons of Fe, Cu, Zn and Br levels in the brain slices of mice under stressful condition.

There are many reports that the histamine H3 receptor is a major target for development of drugs against various disorders of the brain[3)]. However the accumulations of trace element in the slices were significantly different under the each stresses condition.

These results might be useful information to drug therapy for various stress disorder.

References

1) T. Watanabe et al., Tohoku J. Exp. Med. 195 (2001) 197-217.
2) E. Sakurai et al., JAEA Takasaki Ann. Rep. 2007 (2008) 122.
3) M. B. Passani et al., Trends Pharmacol. Sci. 25 (2004) 618-625.

3-56 The Optimum Conditions in the Analysis of Boron Micro-Distribution in Tumor Cells Using PIXE and PIGE

K. Endo [a)], Y. Shibata [a)], T. Yamamoto [a)], K. Nakai [a)], A. Matsumura [a)], T. Satoh [b)], A. Yokoyama [b)], M. Kohka [b)], T. Ohkubo [b)], A. Yamazaki [b)], Y. Ishii [b)], T. Kamiya [b)] and K. Ishii [c)]

[a)] Department of Neurosurgery, Institute of Clinical Medicine, University of Tsukuba, [b)] Department of Advanced Radiation Technology, TARRI, JAEA, [c)] School of Engineering, Tohoku University

Micro particle-induced X-ray emission (micro-PIXE) was applied to determine the inter- and intracellular distribution of boron-10(^{10}B) in tumor cells. Because the energy of micro-PIXE from ^{10}B is too low, particle-induced gamma-ray emission (PIGE) was employed to detect the gamma-rays produced from the nuclear reaction of ^{10}B (p, γ) ^{7}Be.

Cultured 9L gliosarcoma cells grown on polycarbonate film were exposed to sodium borocaptate (BSH). To analyze the inter- and intra-cellular distribution of ^{10}B in 9L gliosarcoma cells, the cells were irradiated with a 1.7 MeV proton beam collimated to a 1 μm diameter and the emitted gamma-rays were detected. The inter- and intracellular distribution of ^{10}B in 9L gliosarcoma cells was directly analyzed using micro-PIGE. The results showed that the distribution of ^{10}B atoms was correctly measured. The distribution of ^{10}B should have been evenly distributed in 9L gliosarcoma cells and some ^{10}B atoms showed that distribution. However, there was a significantly high background and the detection of true ^{10}B atoms was not easy. The main purpose of this study is to determine the optimum conditions to apply this technique in an *in vitro* experiment.

Cultured 9L gliosarcoma cells were grown for 4 days on a 5 μm thick polycarbonate film. These cells were treated with 100 ppm, 250 ppm and 1,000 ppm of BSH, respectively on the 3rd and 4th day. These cells were fixed on the polycarbonate film with the acute freezing on the 5th day.

The samples were analyzed to compare the distribution image of the ^{10}B atoms using the micro-PIXE analysis system at TIARA with a 30 to 60 minutes measuring time and a measuring range from 25×25 μm to 100×100 μm, respectively.

The peak ^{10}B atom measurement was small on the measurement spectrum in comparison to the circumference background. It was possible to confirm that ^{10}B atoms were measured.

At the next step, a mask was created from the distribution of sulphur and a suitable threshold value was determined. Thereafter, a PIGE spectrum was created which was specified by the masked portion and the whole spectrum was compared to the masked spectrum.

It was possible to confirm the presence of a correlation in the distribution of sulphur (S) or phosphorus (P) (tumor cells) and the distribution of ^{10}B atoms because the peak of ^{10}B atoms appeared more clearly in the masked spectrum.

A more clear correlation was observed between the distribution of tumor cells and that of ^{10}B atoms distribution when the two images were combined. This demonstrated that the ^{10}B atom was accumulating around the tumor cells.

In this *in vitro* experiment, various conditions were compared to determine the optimum conditions to yield clear distribution images. The results showed that the tumor-^{10}B distribution was clearly demonstrated at a BSH concentration of 250 ppm. The best measurement ranges were from 50×50 μm to 100×100 μm and the optimum measurement time to obtain the clearest image using PIGE was from 30 to 60 minutes (Fig. 1).

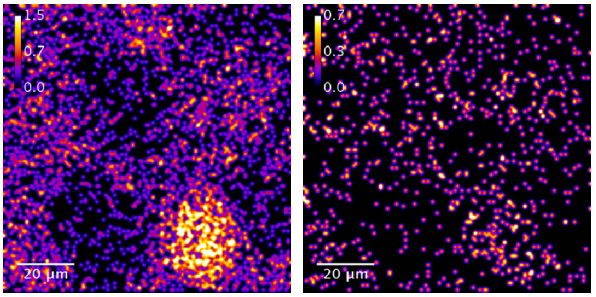

Fig. 1 Distribution of tumor cells (P) and ^{10}B(B). Measurment time was 30 minutes.

However, the intracellular micro-distribution of boron could not be clearly detected in this analysis. Improvements are therefore necessary in the technical methods of cell fixation, while the micro-PIXE analyzing system also needs to be further upgraded.

References

1) J.A. Coderre et al., Radiat. Res. 149 (1998) 163-170.
2) M. Wegden et al., Nucl. Instrum. Meth. Phys. Res. B 219-220 (2004) 67-71.
3) K. Endo et al., Oncol. Res. 16 (2006) 57-65.

3-57 Measurement of Strontium Distribution in Carious Enamel and Dentin around a Fluoride-containing Material

H. Komatsu [a)], Y. Matsuda [a)], T. Kijimura [a)], K. Okuyama [a)], H. Yamamoto [b)], Y. Iwami [b)], S. Ebisu [b)], M. Nomachi [c)], K. Yasuda [d)], T. Satoh [e)] and M. Kohka [e)]

[a)] Graduate School of Dental Medicine, Hokkaido University, [b)] Graduate School of Dentistry, Osaka University, [c)] Graduate School of Science, Osaka University, [d)] The Wakasa wan Energy Research Center, [e)] Department of Advanced Radiation Technology, TARRI, JAEA

Introduction

To estimate caries preventive effect of fluoride-containing materials (FCMs), we continue to investigate the fluorine (F) uptake in artificial caries lesion around FCM during pH-cycling as F uptake resulted from the precipitation of fluorapatite $Ca_{10}(PO_4)_6F_2$ (i.e., remineralization). Some FCMs contain strontium (Sr) in the powder component instead of calcium or as an additional ion to enhance radiopacity. The remineralization may be facilitated by the presence of strontium, as it has both chemical and physical properties close to calcium and is able to replace Ca in apatite. The purpose of this study was to measure the strontium distribution in carious enamel and dentin around a strontium-containing FCM using an in-air micro-PIXE system at TIARA.

Material and Methods

Cavities in enamel and dentin surfaces of extracted human teeth were drilled and filled with strontium-containing FCM (SI-R20607). Two 170 μm longitudinal sections including the filling material were obtained from each tooth. All tooth surfaces, except the outer surface of enamel or dentin, were coated with a wax. The pH-cycling (pH 7.0-pH 4.5) was carried out for 5 weeks for preparing artificial carious tooth using an automatic pH cycling system. Two pairs of demineralizing and remineralizing solutions of pH-cycling were prepared for simulating caries risk (Table 1). After pH-cycling, Sr distribution of the outer lesion in each specimen was evaluated using micro-PIXE system at TIARA. The strontium distributions in carious enamel or dentin were analyzed at more than 100 μm separation from the cavity wall. The outermost surface of the carious lesion was at the spot containing 5% of the calcium concentration in intact tooth. For the comparison of strontium distribution, the average strontium concentration in each specimen was calculated at area of about 20 μm from the defined surface.

Results

Figure 1 demonstrates the Sr distribution of the specimens after 5-week pH-cycling. There was a difference in Sr uptake from material between Sol-A and Sol-B of pH-cycling. Both enamel and dentin for Sol-A, Sr uptakes from material into the outer lesion were confirmed, while no uptake into the lesions of both enamel and dentin for Sol-B was detected. In the observations of Sr uptake into the intact tooth adjacent to the material, the amount of Sr in both enamel and dentin had high value compared with those in area of deeper than 100 μm in Fig. 1. In addition, the amount of Sr in enamel was higher than that in dentin.

Discussion

In this study, although the number of measured specimens was limited in each group, it can be speculated that there was a difference in Sr uptake between Sol-A and Sol-B of pH-cycling. Transverse microradiography analysis in the previous study indicated that the caries progression for the pH-cycling with Sol-A was more severe than that with Sol-A. When calcium dissolution rate of apatite crystals was high in remineralizing process with Sol-A, the rate of Sr replacement to Ca with Sol-A was higher than that with Sol-B. Therefore, it appears that Sr uptake increased with Sol-A. To estimate caries preventive effect of FCMs, Sr measurement will be useful.

Measurements for reference materials that made with a mixture of hydroxyapatite and strontium carbonate were also performed with selecting areas of uniform mixture. Results of these measurements were used for obtaining comfortable values of strontium concentration in the tooth.

Table 1 The solutions of the pH-cycling.

Solutions (Risk)	Demineralizing (pH 4.5)	Remineralaizing (pH7.0)
Sol-A (High)	0.2 M Lactic acid, 3.0 mM $CaCl_2$, 1.8 mM KH_2PO_4.	0.02 M HEPES, 3.0 mM $CaCl_2$, 1.8 mM KH_2PO_4
Sol-B (Low)	0.05 M Acetic acid, 1.5 mM $CaCl_2$, 0.9 mM KH_2PO_4	0.02 M HEPES, 1.5 mM $CaCl_2$, 0.9 M KH_2PO_4, 0.13 M KCl

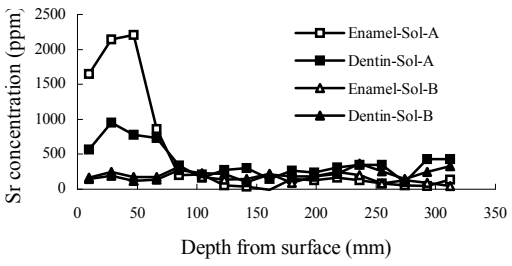

Fig. 1 Mean Sr distribution of the specimens after 5-week pH-cycling.

3-58 Evaluation of Cisplatin Concentration in Response to Tumor Hypoxia in Esophageal Squamous Cell Carcinoma

M. Sakai [a)], N. Tanaka [a)], H. Kimura [a)], T. Inose [a)], M. Sohda [a)], M. Nakajima [a)], H. Kato [a)], T. Asao [a)], H. Kuwano [a)], M. Oikawa [b)], T. Satoh [c)] and T. Kamiya [c)]

[a)] Graduate School of Medicine, Gunma University, [b)] Fundamental Technology Center, National Institute of Radiological Science, [c)] Department of Advanced Radiation Technology, TARRI, JAEA

Chemotherapy and radiotherapy can provide effective treatments for Esophageal Squamous Cell Carcinoma (ESCC). Cis-diaminedichloroplatinum (II) (CDDP) or cisplatin, a DNA-damaging agent, is widely used as a chemotherapeutic drug for the treatment of various human malignancies, including ESCC. To date, tumor hypoxia appears to be strongly associated with tumor propagation, malignant progression, and resistance to therapy, and it has thus become a central issue in tumor physiology and cancer treatment. The aim of our study is to evaluate cisplatin concentration in response to oxygenation state in a single tumor cell (TE-2: human ESCC cell line) using In-Air Micro-PIXE, the newly-developed device that enable to visualize trace element distribution in a single cell.

Cell sample preparation was performed as follows. Exponentially growing TE-2 cells were labeled with 100 μL (per 10-cm dish) bromodeoxyuridine (BrdU; BD Biosciences, San Jose, CA, USA) for 24 h. The 4-μm thick Mylar films were stretched between Pyrex glass and Viton rings, followed by immersion in 5 mol sulfuric acid for 2 h and washing with distilled water three times. Twenty-four hours after the BrdU labeling procedure, cells were trypsinized and counted using a hemocytometer, then 1×10^6 cells were seeded on a Mylar film in a culture dish for 24 h under normoxia (O2 : 21%) or hypoxia (O2 : 1%). Then, the original medium on Mylar film was replaced with CDDP containing medium (0.5-mmol CDDP). After 2 hours of CDDP containing medium exposure, this medium was removed and cells were washed five times with a tris-hydroxymethylaminomethane-HNO_3 solution (pH 7.4). The cells were then cryofixed by soaking the samples in isopentane at liquid nitrogen temperature. The frozen samples were dried for 24 h in a freeze-drier and kept in a desiccator until PIXE analysis. The In-Air Micro-PIXE analysis was performed at TIARA as described previously [1)]. We used the calibration curve constructed by Sakurai et al. [1)] for the quantitative evaluation of cisplatin.

Figure 1 shows the comparison of intracellular and nuclear CDDP concentration in TE-2 cultured under normoxia and hypoxia. Intracellular CDDP concentration in TE-2 cultured under hypoxia was significantly lower than that of under normoxia (p=0.0365). Although nuclear CDDP concentration in TE-2 had no significant deference between cultured under hypoxia and normoxia (p=0.1259), nuclear CDDP concentration in TE-2 cultured under hypoxia had a tendency to be lower than that of under normoxia. Our results show that tumor hypoxia may affect intracellular and nuclear CDDP concentration.

In the previous study [2)], we investigated several factors that affected CDDP concentration in two human ESCC cell lines (TE-2 and TE-13. TE-2 cells were more sensitive to cisplatin than TE-13 cells). Multidrug resistance protein 2 (MRP2), which belong to the ATP-binding cassette cell membrane transporter family [3)], is one of those factors. MRP2 is reported to be involved in resistance to cisplatin [4)]. We compared MRP2 expression in cisplatin-treated TE-2 cells and TE-13 cells as a chemoresistance marker for cisplatin-based therapy, using real-time reverse transcriptase-polymerase chain reaction (RT-PCR). MRP2 expression in TE-13 cells was significantly higher than that in TE-2 cells. It therefore seems likely that cell membrane transporters play an important role in affecting intracellular cisplatin concentration and its sensitivity. In our present study, the mechanism of the effect of tumor hypoxia to intracellular CDDP concentration was not fully investigated. It is clear that further studies are needed to elucidate the expression of the factors which was involved in resistance to cisplatin, such as MRP2, in ESCC under hypoxia.

References

1) H. Sakurai et al., Cancer Sci. 99 (2008) 901-904.
2) N. Tanaka et al., Cancer Sci. (2010) Feb 25.
3) M. Michael et al., Nat. Rev. Cancer 2 (2002) 48-58.
4) R. G. Deeley et al., Physiol. Rev. 86 (2006) 849-99.

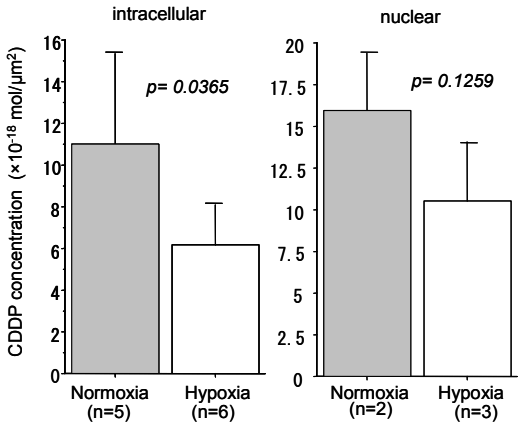

Fig. 1 Comparison of intracellular and nuclear CDDP concentration in TE-2.

3-59 Improvement of Microcapsules that Reslease Core Contents via Radiation

S. Harada [a], S. Ehara, [a] K. Ishii [b], T. Sato [c], S. Yamazaki [b], N. Matsuyama [b] and T. Kamiya [c]

[a] Department of Radiology, Iwate Medical University,
[b] Department of Quantum Science and Energy Engineering, Tohoku University,
[c] Department of Advanced Radiation Technology, TARRI, JAEA

Introduction

Since 2005, we have been developing microcapsules that release anticancer drugs during radiotherapy and anticancer drug targeting[1),2)]. The irradiated microcapsules release anticancer drugs. The released anticancer drugs along with radiation synergistically act against the tumor, resulting in increased antitumor activity. Localization of anticancer drugs by using microcapsules decreases the adverse effects of these drugs.

Previously, these microcapsules were generated by polymerizing hyaluronic acid and alginate with Ca^{2+} and Fe^{2+} ions. The mechanism of anticancer drug release by the microcapsules was as follows: radiation-induced (1) decomposition of hyaluronic acid and (2) destruction of Fe^{2+} in the polymer by conversion of Fe^{2+} into Fe^{3+}. However, the frequency of anticancer drug release was low, i.e., 72.3 ± 2.3%, at 20-Gy radiation dose.

It is known that radiation-induced breakdown of H_2O_2 releases oxygen through the following chemical reaction: $2H_2O_2 \rightarrow O_2 + 2H_2O$. If H_2O_2 is added to the microcapsules, radiation-induced release of oxygen may increase the pressure within the capsules and thus result in increased rupturing of the microcapsules. In this study, we tested whether addition of H_2O_2 increased the radiation-induced rupturing of microcapsules.

Materials and Methods

The capsules were generated by spraying a mixture of 3.0% hyaluronic acid and 2.0% alginate, supplemented with 0.3% H_2O_2, 0.2 mmol of carboplatin, and 0.5 mol/L each of $FeCl_2$ and $CaCl_2$. One million microcapsules were allowed to float in normal saline; thereafter, the capsules were irradiated with ^{60}Co γ ray at doses ranging from 0.5 to 3 Gy with 0.5 Gy interval at Iwate Medical University. The radiation-induced rupturing of the microcapsules was imaged using a micro PIXE camera in TIARA.

Results

The micro-PIXE image of microcapsules by Pt signals is shown in Fig. 1 and the frequency of radiation-induced rupturing is also shown in Fig. 2.

Before irradiation, the contours of microcapsules were round and their liquid core was distinct (Fig. 1A). After irradiation, the contours of microcapsules were made irregular and the releasing of liquid core as carboplatin could be observed (Fig. 1B).

The frequency of rupturing of the microcapsules increased with increase in the radiation dose (Fig. 2). The frequencies of rupturing of the microcapsules with H_2O_2 added was significantly increased than those of without H_2O_2 added when radiation doses was greater than 2 Gy (Fig. 2).

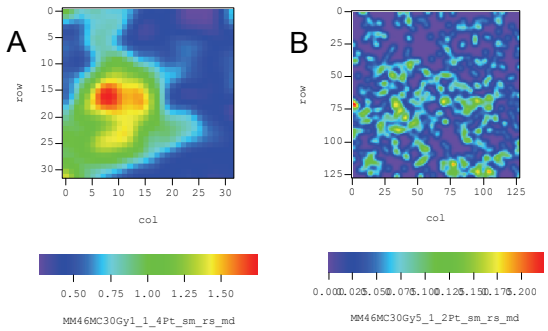

Fig. 1 Rupturing of microcapsules observed by micro PIXE camera. A: Before irradiation, B: After irradiation.

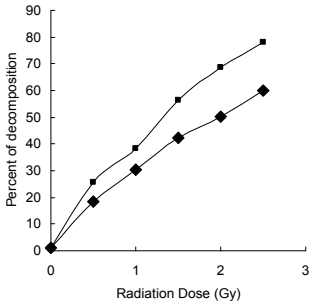

Fig. 2 Micro-PIXE images of the ruptured microcapsules by micro PIXE camera. A and the frequency of rupturing of microcapsules. (■) with H_2O_2 added, (◆) without H_2O_2 added.

Discussion

In the conventional radiotherapy, 2-Gy fractions of radiation were administered. According to our data, addition of H_2O_2 significantly increased the rupturing of microcapsules at radiation doses 2 Gy, compared with that of no addition of H_2O_2. Addition of H_2O_2 to the microcapsules is considered to be useful for their clinical application.

References

1) S. Harada et al., TIARA Ann. Rep. 2003 (2004) 276.
2) S. Harada et al., Nucl. Instrum. Meth. B 260 (1) (2007) 16.

3-60 Analysis of Asbestos Bodies and Fas or CD163 Expression in Asbestos Lung Tissue by In-Air Micro-PIXE

K. Dobashi [a)], S. Matsuzaki [b)], Y. Shimizu [b, c)], T. Nagamine [a)], T. Satoh [d)], T. Ohkubo [d)], A. Yokoyama [d)], Y. Ishii [d)], T. Kamiya [d)], K. Arakawa [d)], S. Makino [c)], M. Utsugi [b)], T. Ishizuka [b)], S. Tanaka [e)], K. Shimizu [f)] and M. Mori [b)]

[a)] Faculty of Health Science, Gunma University, [b)] Department of Medicine and Molecular Science, Graduate School of Medicine, Gunma University, [c)] World Health Organization Collaborating Center of Prevention and Control of Chronic Respiratory Diseases/Dokkyo University, [d)] Department of Advanced Radiation Technology, TARRI, JAEA, [e)] Department of General Surgical Science, Graduate School of Medicine, Gunma University, [f)] Division of Thoracic and Visceral Organ Surgery, Graduate School of Medicine, Gunma University

Inhalation of asbestos increases the risk of lung cancer and pulmonary fibrosis. It is difficult to directly assess the distribution and content of inhaled particles in lung tissue sections. We showed that in-air micro particle induced X-ray emission (in-air micro-PIXE) system is useful for assessing the distribution and quantities of asbestos fibers and other metals in lung tissue comparing to immune-related cell localizations. Furthermore, the analysis using the system confirmed that asbestos induced apoptosis by upregulating Fas expression and also revealed the accumulation of CD163-expressing macrophages in the lungs of patients with asbestosis. By quantitative comparison of the area of Fas or CD163 expression and the Fas- or CD163-negative area in asbestos lung tissue, the harmful levels which caused the expression of Fas or CD163 could be estimated on Si, Fe and Mg deposition. These results indicate that the system could be useful for investigating the pathogenesis of inhaled particle-induced immune reactions and for determining harmful levels of exogenous agents.

アスベストは、天然の鉱物繊維で長さは約 8 μm, 幅約 0.1 μm、断熱性、耐火性、防音性、耐腐食性に優れており、建築用製材などに多く用いられてきた。しかし、アスベストの吸入は、肺線維症や肺ガンの原因で、発病までの潜伏期間が数 10 年と長いことから、「静かな時限爆弾」とも言われ、大変な社会問題となっている。早期診断や病態解明には、肺内でのアスベストの種類、量、分布などを、人肺組織内で特定することが不可欠だが、今まで外科的に大きな肺組織を採取しなければならず、簡単に調べられなかった。我々は、独立行政法人日本原子力研究開発機構（以下「原子力機構」）と 21 世紀 COE プログラムの一環として共同研究を組織した。原子力機構が開発した大気マイクロ PIXE 分析技術を応用して、数 mg の肺組織の中のケイ素や金属元素の二次元分布を、1 μm の解像度で画像化する分析法を開発した。本法により世界で初めて、吸入したアスベストを肺組織中に存在したままで画像化することに成功し、2008 年 10 月に International journal of immunopathology and pharmacology に論文掲載された（文献 1）。この新方式は、気管支鏡などで簡単に採取できるわずかな肺組織があれば、肺組織中のアスベストの正確な存在や組成分析を可能にする画期的なものである。これにより、アスベスト吸引の有無を早期に診断し、その後の迅速な対処を可能にした。その他に、環境からの粉じん暴露による肺内の重金属沈着の有無の診断など、種々の応用が期待される。病態解明では、我々は、アスベストの周囲に一致して、ヘモグロビンを貪食するマクロファージ(CD163 発現細胞)の集積とアポトーシスを引き起こし肺線維化に関与する Fas の発現が増強していることを明らかとした。しかも、Fig. 1 に示すごとく、アスベスト肺患者の肺組織に Fas や CD163 が発現している部分と発現していない部分で、アスベスト成分である Si,Fe,Mg の量を S に対する比率で求めると、明らかに Fas,CD163 発現部位でこれらの元素が高値を示しており、アスベストの存在が周囲に炎症を惹起し、これらタンパク質の発現を誘導していることが示唆された（文献 2）。大気マイクロ PIXE による研究は、吸入粒子により引き起こされた免疫反応の病態解明や吸入物質の有害レベルの決定に有用である。

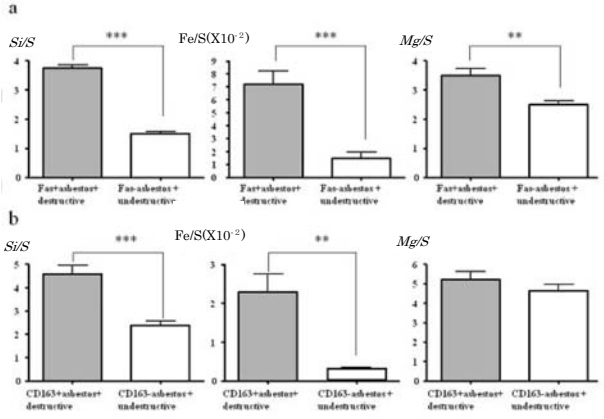

Fig. 1 The ratio of Si to S (background content in lung tissue), as well as the ratios of Fe to S and Mg to S, are shown for the Fas-expressing area (a), and the ratios of Si to S, Fe to S, and Mg to S are shown for the CD163-expressing area (b). Gray boxes indicate the ratios of elements in area of asbestos lung with Fas or CD163 expression and tissue damage, and blank boxes indicate the ratios of elements in intact areas of asbestosis lung without Fas or CD163 expression. All data are presented as mean the ratio of Si/S, Fe/S and Mg/S ± S.D. Statistical significance were shown as ** $p<0.01$ and *** $p<0.001$.

References

1) Y. Shimizu et al., Int. J. Immunopathol. Pharmacol. 2008 ; 21(3) 567-76.
2) S. Matsuzaki et al., Int. J. Immunopathol. Pharmacol. 2010; 23(1) 1-11.

3-61 Preparation of Human Erythrocytes for In-Air Micro-PIXE Analysis

Y. Tokita [a)], H. Kikuchi [a)], T. Nagamine [a)], T. Satoh [b)], T. Kamiya [b)] and K. Arakawa [b)]

[a)] School of Health Sciences, Faculty of Medicine, Gunma University,
[b)] Department of Advanced Radiation Technology, TARRI, JAEA

1. Introduction

Essential elements play a pivotal role on homeo- stasis in human body, and metal ions such as zinc, copper, and iron are assayed in the clinical samples of serum, urine and tissues. It is well known that erythrocytes (red blood cell) contain various trace elements, which are altered along with pathogenesis of disorders. Because erythrocytes can be collected via peripheral vessels non-invasively, this blood cell is a convenient sample material for in-air micro PIXE analysis.

In order to establish an appropriate preparation with erythrocytes for micro PIXE analysis, we investigated (i) whether X-ray spectra can be affected by morphological change of erythrocyte (color and shape) or ion contained in washing solution, (ii) what element is most suitable to demarcate the physical shape of erythrocyte.

2. Material and Method

Erythrocytes samples obtained from normal volunteers and a patient of Wilson disease were analyzed by in-air micro PIXE. The blood was collected via cubital vein using EDTA 2Na as anticoagulant. Equal volume of physiological saline or isotonic LiCl solution was added this blood, centrifuged (1,400 rpm, 5 min), and discard supernatant. Residual red blood cells were used for the sample preparation.

PIXE samples were prepared by two methods. (i) After washing with saline, blood sample was seep into 0.5 μm thick of mayler membrane, and floating on isopentane in a stainless cup, then this cup was put on liquid nitrogen and lyophilized by vacuum evaporation (Conventional method). (ii) Blood sample was dropped on mayler membrane, and this membrane was sunk into isopentane (-150 ºC), cooled by liquid nitrogen previously, then lyophilized by vacuum evaporation (Ortega method [1)]).

Three point zero MeV proton beams in 1-μm diameter that was generated by the TIARA single-ended accelerator at JAEA-Takasaki, was used to analyze elemental distribution of erythrocytes.

3. Results and Discussion

To confirm the optimization as PIXE sample, we compared the conventional method with the Ortega method. Elemental distributions of erythrocytes were similar between both methods. But, under optical microscope, the erythrocytes made by the conventional method colored black and changed its shape atrophic. The erythrocytes made by the Ortega method were clear and spherical. As a next step, we analyzed elemental distribution in the erythrocytes colored-black or clear; the black-colored erythrocyte indicated higher K value than that of the clear ones. This result suggests that spread of erythrocyte is needed to prepare a proper PIXE sample.

It is unclear known whether erythrocyte's X-ray spectra, especially Na, is influenced by cations contained in washing buffer, physiological saline (NaCl). Thus, to confirm this problem, we compared the erythrocyte's X-ray spectrum between the sample washed with saline and that washed with Li-contained solution. As a result, no difference was identified in two X-ray spectrums. Therefore cation contained in washing solution was not essential for sample preparation.

We compared elemental maps of three elements (Cl, Fe, and K) to confirm a suitable element to demarcate erythrocyte's shape, and distribution of Cl is well agreed with erythrocyte's shape (Fig. 1). Reproducibility is confirmed by two normal erythrocyte's data.

Reference

1) R. Ortega, Cell. Mol. Biol. 42 (1996) 77-88.

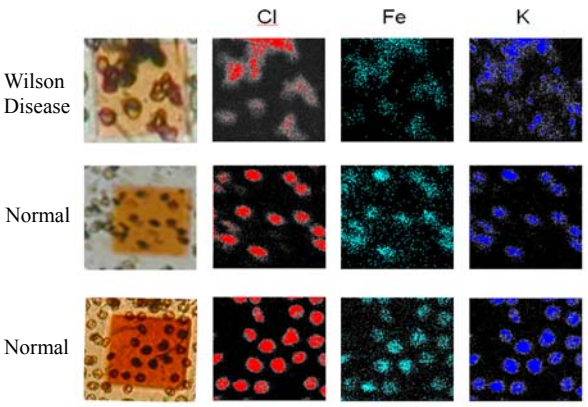

Fig. 1 Comparison of microphotograph with distribution of each element analyzed by PIXE.

3-62 Sensitivity of Micro Beam PIXE System in TIARA for Several Trace Elements

Y. Iwata [a)], K. Ishii [b)], T. Kamiya [c)] and T, Satoh [c)]

[a)] Department of Chemistry, Faculty of Education and Human Studies, Akita University, Department of Quantum Science and Engineering, [b)] Graduate School of Engineering, Tohoku University, [c)] Department of Advanced Radiation Technology, TAARI, JAEA

Standard Reference Material (SRM) for determination of platinum and zinc was made by anion-exchange resin. Macro porous cation-exchange resin, Macro-Prep 25S (BioRad) was suspended in the standard solution containing the known amount of trace elements. The concentration of those elements in the resin was 0-270 ppmv. Individual particle of the resin was subjected to 3 MeV proton bombardments by micro beam system of TIARA. It was found the macro porous nature of the resin allows trace elements to react with the exchange sites located throughout the matrix. PIXEana program was used to analyze peak count for each characteristic X-ray. Sensitivity for Al, Ca, Mn, Fe, Co, Ni, Cu, Zn, Sr and Pb was calculated by elemental abundance in the resin and does of proton. The count for characteristic X-ray per pg (element) × nC (dose) and number of sample(n) for instance was Al : 80±19 (17), Ca : 60±14 (18), Fe 25±6 (9) , Zn 8.0±1.9 (8) and Pb : 8.0±1.9 (8).

1. はじめに　PIXE分析における装置の校正や分析値の相互比較のために、イオン交換樹脂中に分析目的元素を正確量含有する標準物質（SRM）を開発してきた。これまで、粒径7-11 mmのマクロポーラス型陰イオン交換樹脂に、$PtCl_6^{2-}$ および $ZnCl_3^-$を付着させたSRMを調製し、TIARAマイクロPIXEシステムにおける白金と亜鉛の定量感度を報告した[1)]。今回は、マクロポーラス型陽イオン交換樹脂に生体関連元素のアルミニウム、カルシウム、マンガン、鉄、コバルト、ニッケル、銅、亜鉛、ストロンチウムおよび鉛を一定量含むSRMを調製し、特性X線強度と元素添加量とから、分析感度を求めたので報告する。

2. SRMの調製　純水中に沈降したマクロポーラス型陽イオン交換樹脂Macro Prep 25S（粒径25 μm、BIORAD）の体積をメスシリンダーで測定し、等しい大きさの球形の樹脂が最密充填していると仮定し、樹脂の体積を求めた。樹脂を含む懸濁液に、Al^{3+}、Ca^{2+}、Mn^{2+}、Co^{2+}、Cu^{2+}およびPb^{2+}含む標準溶液、あるいはAl^{3+}、Ca^{2+}、Fe^{3+}、Ni^{2+}、Zn^{2+}、Sr^{2+}およびPb^{2+}を含む標準溶液を加え、振とうした。樹脂体積あたりの含有量は、Al^{3+}、Ca^{2+}およびPb^{2++}は270 ppmvの一定量とし、Mn^{2+}、Fe^{3+}、Co^{2+}、Ni^{2+}、Cu^{2+}、Zn^{2}およびPb^{2+}の含有量は54、81および135 ppmvと段階的に変化させ、添加する元素の違いを含め6種類のSRMを調製した。

マイクロPIXE分析　TIARAの3 MeV 陽子ビームをサブミクロンに絞って照射した。スキャンエリアを29 × 29 μm とし、大気中300 - 400 nCの照射を行った。

3. SRMのマイクロPIXE像　マクロポーラス型の樹脂内に均一に分布したイオン交換基にAl^{3+}、Ca^{2+}が均一に分布し、その交換基と金属イオンが反応することが確かめられた。添加した元素並びにイオン交換基に含まれる硫黄の特性X線のエネルギー領域の強度から、樹脂内の元素分布を画像化できた(Fig. 1)。解析プログラム(PIXEana)により、照射したSRMの粒径を求めることができる。画像内のSRM領域(Fig. 1 網掛部分)のスペクトルから、特性X線のピーク面積をPIXEana のFitting機能で解析した。照射した10粒のSRMはほぼ球形であり、半径は、9.4 - 12.4 μmであった。

分析感度の定量化　樹脂の体積から元素量、断面積から照射電荷量および特性X線のカウントから、元素1 pgあたり1 nC照射による特性X線のカウント数を求めた(Table 1)。8-17個のSRMの結果を標準偏差とともに示した。試料間の変動が20-30％程度とやや大きいのは樹脂中の元素濃度やX線測定そのものではなく、Fig. 1で示した樹脂半径の見積もりやスペクトルの解析による誤差が大きいと判断している。調べた元素では、感度は主としてX線発生断面積の減少とともに低下している。第3周期元素については、KαとKβ線の強度比を測定した。

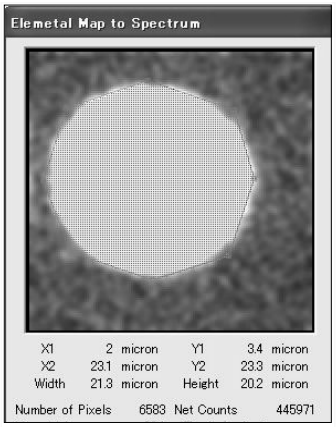

Fig. 1　Elemental mapping of S in a SRM by Microbeam PIXE and extraction of image for SRM.

今回の感度測定により、1)マイクロビームでマッピングした部分から関心領域を抽出し、その面積(Pixcel)と照射電荷量を求める。2)関心領域のX線スペクトルから目的元素の特性X線カウントを求める。そして、Table 1と1, 2)の結果から、関心領域の元素存在量を算出できることとなった。また、試料の厚さ等の形状がわかれば元素濃度を求めることが可能となった。

Table 1　Analytical sensitivity for several elements by Microbeam PIXE in TIARA.

Element (X-ray)	Sensitivity (Count / pg nC)	n
Si(Li) Detector		
Al (Kα)	80 ± 19	17
Ca (Kα)	60 ± 14	18
Mn (Kα)	27 ± 7	9
Fe (Kα)	25 ± 6	9
Co (Kα)	16 ± 7	8
Ni (Kα)	13 ± 3	8
Cu (Kα)	11 ± 3	8
Zn (Kα)	8.0 ± 1.9	8
Sr (Kα)	0.93 ± 0.35	9
Pb (Lα)	1.4 ± 0.3	17
Ge Detector [1)]		
Zn (Kα)	150 ± 10	8
Pt (Lβ)	33 ± 5	8

Reference

1) Y. Iwata et al., JAEA Takasaki Ann. Rep. 2007 (2008) 173.

4. Advanced Materials, Analysis and Novel Technology

4-01 Hydrogen Gasochromism of WO_3 Films Prepared by Reactive Sputtering ····· 125
S. Yamamoto, K. Kawaguchi, M. Sugimoto and M. Yoshikawa
4-02 Li Ion Implantation into α-rhombohedral Boron: Carrier Doping for Superconduction ····· 126
K. Kirihara, H. Hyodo, T. Nagatochi, S. Yamamoto, F. Esaka, H. Yamamoto, S. Shamoto and K. Kimura
4-03 Synthesis of Single-Crystalline and Amorphous SiC Nanotubes by Ion-Irradiation Technique ····· 127
T. Taguchi, S. Yamamoto, K. Kawaguchi, K. Kodama and S. Shamoto
4-04 Polymer Optical Waveguides Fabricated by Using Proton Beam Writing ····· 128
K. Miura, Y. Machida, M. Uehara, O. Hanaizumi, Y. Ishii, T. Satoh, K. Takano, T. Ohkubo, A. Yamazaki, A. Inouye, M. Kouka, A. Yokoyama and T. Kamiya
4-05 Synergy Effects in Electron/Ion Irradiation and Alkaline Pretreatment on Hydriding Property of Hydrogen Storage Alloys ····· 129
H. Abe, M. Kishimoto, H. Uchida and T. Ohshima
4-06 Atomistic Study of Irradiation-induced Mass Transport Process ····· 130
Y. Ikoma, T. Motooka, H. Sakita, Hafizal Yahaya, H. Naramoto, K. Narumi, S. Sakai and Y. Maeda
4-07 Fabrication of Diluted Magnetic Semiconductor Crystals by Ion-Implantation Technique ····· 131
A. Yabuuchi, M. Maekawa, A. Kawasuso, S. Entani, Y. Matsumoto, S. Sakai and S. Yamamoto
4-08 Synthesis of Functional Polycarbosilane Nano-fiber by Ion Beam Induced Graft Polymerization ····· 132
K. Yoshimura, M. Sugimoto, A. Idesaki, M. Yoshikawa and S. Seki
4-09 Gas Permeation Characteristics of Silicon Carbide Membrane Prepared by Radiation-curing of Polycarbosilane Film ····· 133
A. Takeyama, M. Sugimoto, A. Idesaki and M. Yoshikawa
4-10 Investigation of Nano Porous SiC Based Fibers Synthesized by Precursor Method ····· 134
M. Sugimoto, M. Yoshikawa, K. Kita, M. Narisawa and A. Nakahira
4-11 Control of Radial Size of Polymer Nanowire Formed by Ion Beam Irradiation ·· 135
S. Tsukuda, S. Seki, M. Sugimoto, A. Idesaki, M. Yoshikawa and S.-I. Tanaka
4-12 Nano-crystalline Formation of Metallic Glasses by Ion Implantation ····· 136
S. Nagata, Y. Murayama, B. Tsuchiya, T. Shikama, M. Sasase, A. Inouye and S. Yamamoto
4-13 Behavior of N Atoms in Nitriding Processes of Evaporated-Ti Thin Films due to Ion Implantation ····· 137
Y. Kasukabe, Y. Watanabe, Y. Chen, S. Yamamoto and M. Yoshikawa

4-14 The Effects of Displacement Damage and Transmutation Atoms on Microstructure of SiC: The Effects of H Atom on Dimensional Change of SiC ····· 138
T. Nozawa, T. Taguchi and H. Tanigawa
4-15 Annealing Behavior of Vacancy-type Defects in Electron-irradiated Si_xGe_{1-x} Bulk Crystals at Low Temperature ····· 139
Y. Nagai, K. Inoue, H. Takamizawa, T. Takeuchi, A. Kuramoto, T. Toyama, M. Hasegawa and I. Yonenaga
4-16 RBS Analysis of Mass-transport Process in Au/Cu Film on Sapphire Treated by Centrifugal Forces ····· 140
H. Naramoto, K. Narumi, T. Hao, M. Ono, S. Okayasu, S. Sakai, Y. Hiraiwa, Y. Maeda and M. Sasase
4-17 Low Temperature Ion Channeling of Fe_2MnSi Film Epitaxially Grown on Ge(111) ····· 141
Y. Maeda, K. Narumi, Y. Terai, T. Sadoh and M. Miyao
4-18 Vacancy Generation around an SCC Crack Tip in Stainless Steels Probed by a Positron Microbeam ····· 142
A. Yabuuchi, M. Maekawa and A. Kawasuso
4-19 Radiation-Induced Electrical Degradation in CeO_2 Ceramics Irradiated with 10 MeV Ni ····· 143
N. Ishikawa and K. Takegahara
4-20 Incident Energy Dependence of Nuclear Reaction Imaging of Boron Doped in Iron ····· 144
H. Shibata, Y. Kohno, T. Satoh, T. Ohkubo, A. Yamazaki, Y. Ishii, A. Yokoyama and M. Kohka
4-21 Study on Cu Precipitation in Energetic Electron Irradiated FeCu Alloy by Means of X-ray Absorption Spectroscopy ····· 145
A. Iwase, S. Kosugi, S. Nakagawa, N. Ishikawa and Y. Okamoto
4-22 Cathodoluminescence of Albite Activated by Alpha-particle Induced Luminescence Centers ····· 146
H. Nishido, M. Kayama, S. Toyoda, K. Komuro and K. Ninagawa
4-23 Evaluation of Fluorescence Materials for Pulsed-neutron Imaging ····· 147
T. Sakai, M. Taguchi, S. Kurashima, H. Sato, T. Kamiyama and Y. Kiyanagi
4-24 Positron Beam Study on Vacancy Defects in GaCrN Grown by Molecular Beam Epitaxy ····· 148
A. Kawasuso, A. Yabuuchi, M. Maekawa, S. Hasegawa, Y. Zhou and H. Asahi
4-25 Evaluation of the ZrC Layer for Coated Fuel Particles Probed by a Positron Microbeam ····· 149
M. Maekawa, A. Yabuuchi, A. Kawasuso and J. Aihara
4-26 Surface Structure of Si(111)-$\sqrt{21}\times\sqrt{21}$-(Ag, Cs) studied by Reflection High-Energy Positron Diffraction ····· 150
Y. Fukaya, I. Matsuda, A. Kawasuso and A. Ichimiya

4-27 Structure Analysis of K/Si(111)-$\sqrt{3} \times \sqrt{3}$-B Surface by Reflection
High-Energy Positron Diffraction ····· 151
Y. Fukaya, A. Kawasuso and A. Ichimiya
4-28 Radiation-induced H_2 Production and Reactions of OH Radical in Aqueous
Solutions Containing Ceramic Oxides ····· 152
Y. Kumagai, R. Yamada and R. Nagaishi
4-29 LET Effect on the Radiation Induced Polymerization of Maleimide ····· 153
S. Nakagawa, M. Taguchi and K. Hirota
4-30 Observation of Heavy Ion Induced Transient Species in Water
by Spectroscopic Technique ····· 154
M. Taguchi, Y. Sugo, S. Kurashima, A. Kimura and K. Hirota
4-31 Stabilization of Measurement System of the Heavy Ion Beam Pulse
Radiolysis Using Scintillator ····· 155
T. Kondoh, J. Yang, K. Kan, Y. Yoshida, H. Shibata,
S. Kurashima and M. Taguchi
4-32 Development of a Head Module for Multi-Head Si/CdTe Compton
Camera System ····· 156
M. Yamaguchi, T. Kamiya, T. Satoh, N. Kawachi, N. Suzui, S. Fujimaki,
H. Odaka, S. Ishikawa, M. Kokubun, S. Watanabe, T. Takahashi, H. Shimada,
K. Arakawa, Y. Suzuki, K. Torikai, Y. Yoshida and T. Nakano
4-33 Systematic Measurement of Neutron and Gamma-ray Yields on Thick Targets
Bombarded with 18 MeV Protons ····· 157
M. Hagiwara, T. Sanami, Y. Iwamoto, N. Matsuda, Y. Sakamoto, Y. Nakane,
H. Nakashima, K. Masumoto, Y. Uwamino and H. Kaneko
4-34 Establishment of Neutron Fluence Monitoring Techniques for
Quasi-monoenergetic Neutron Calibration Fields of High Energy at TIARA ···· 158
Y. Shikaze, Y. Tanimura, J. Saegusa, M. Tsutsumi, Y. Uchita,
M. Yoshizawa, H. Harano, T. Matsumoto and K. Mizuhashi
4-35 Measurement of Neutron Fluence in the Comparison between TIARA and
CYRIC High Energy Neutron Facilities ····· 159
T. Matsumoto, H. Harano, A. Masuda, Y. Unno, M. Hagiwara,
T. Sanami, J. Nishiyama, Y. Shikaze, Y. Tanimura, M. Yoshizawa,
M. Baba and K. Mizuhashi
4-36 Study on High Energy Neutron Dosimetry Using Solid State Track Detector ···· 160
T. Kosako, T. Iimoto, Y. Koike, T. Abe, M. Hirota, M. Mikhail,
K. Shimada, C. Alexandre, Le Thiem Ngoc, Y. Setoguchi and K. Tani
4-37 Evaluation of the Response Characteristics of a Portable Cosmic-ray
Neutron Monitor ····· 161
H. Yasuda, K. Yajima and A. Endo
4-38 Dose Measurement for 110 keV Electron Beam ····· 162
H. Seito, S. Matsui, T. Hakoda, M. Ishikawa, H. Hanaya, Y. Haruyama,
H. Kaneko, J. Kimura and T. Kojima

4-39 Relationship between Internuclear Distance and Charge State of Constituent Ions Resulting from Foil-induced Dissociation of C_2^+ ions ····· 163
A. Chiba, Y. Saitoh, K. Narumi, Y. Takahashi, K. Yamada and T. Kaneko
4-40 Simultaneous Measurement of Secondary-electron Emission and Coulomb Explosion Imaging for 250-keV/u C_2^+ Ions Bombarded to Thin Carbon Foils··· 164
Y. Takahashi, K. Narumi, A. Chiba, Y. Saitoh, K. Yamada, N. Ishikawa, H. Sugai and Y. Maeda
4-41 Analysis of Radiation Damage at a Si Surface Bombarded with a Single 10-, 50- and 400-keV C_{60} Ion ····· 165
K. Narumi, H. Naramoto, Y. Takahashi, K. Yamada, A. Chiba, Y. Saitoh and Y. Maeda
4-42 Effect of Au Cluster Ion Irradiation on Magnetic Properties of FeRh Thin Films ····· 166
A. Iwase, N. Fujita, S. Kosugi, Y. Saitoh and T. Matsui
4-43 Positive Secondary Ion Emission from PMMA upon Energetic C_8 Cluster and Mo Ion Impacts ····· 167
K. Hirata, Y. Saitoh, A. Chiba, K. Yamada, Y. Takahashi, K. Narumi and T. Kojima
4-44 Secondary Electron Emission from Carbon Induced by MeV/atom Carbon Cluster Bombardment ····· 168
T. Kaneko
4-45 Ion Induced Luminescence from Sapphire Irradiated with Swift Cluster Ion Beams ····· 169
H. Shibata, Y. Saitoh, A. Chiba, K. Yamada, Y. Takahashi, K. Narumi, T. Kojima and T. Kamiya
4-46 Processing of an Upstanding Nano-Wire Array Using Ion-Beam Lithography ··· 170
K. Takano, T. Satoh, T. Kamiya, Y. Ishii, T. Ohkubo, M. Kohka, M. Sugimoto, S. Seki and H. Nishikawa
4-47 Fabrication of Dielectrophoretic Devices Using Poly-dimethylsiloxane Microstructures by Proton Beam Writing ····· 171
Y. Shiine, H. Nishikawa, Y. Furuta, T. Satoh, Y. Ishii, T. Kamiya, R. Nakao and S. Uchida
4-48 Development of Neutron Optics Devices Using Proton Microbeam ····· 172
T. Sakai, R. Yasuda, H. Iikura, T. Nojima, M. Matsubayashi, M. Kohka, T. Sato, T. Ohkubo and Y. Ishii
4-49 Fast Single-Ion Hit System for Heavy-Ion Microbeam at TIARA Cyclotron (III) ····· 173
W. Yokota, T. Satoh, S. Okumura, S. Kurashima, N. Miyawaki, H. Kashiwagi, K. Yoshida, M. Kohka, K. Takano and T. Kamiya
4-50 Status Report on Technical Developments of the AVF Cyclotron ····· 174
S. Okumura, T. Yuyama, Y. Yuri, T. Ishizaka, I. Ishibori, H. Kashiwagi, S. Kurashima, N. Miyawaki, K. Yoshida, T. Nara and W. Yokota

4-51 Development of Beam Generation and Irradiation Technology for Electrostatic Accelerators ····· 175
A. Yokoyama, S. Uno, A. Chiba, K. Yamada, Y. Saitoh, Y. Ishii, T. Satoh, T. Ohkubo and T. Agematsu
4-52 Production of Highly Spin-Polarized Positron Source ····· 176
A. Kawasuso, M. Maekawa, Y. Fukaya and A. Yabuuchi

This is a blank page.

4-01 Hydrogen Gasochromism of WO_3 Films Prepared by Reactive Sputtering

S. Yamamoto, K. Kawaguchi, M. Sugimoto and M. Yoshikawa

Environment and Industrial Materials Research Division, QuBS, JAEA

The detection of gaseous hydrogen leakage below the lower explosive limit (LEL) of 4% by volume ratio of hydrogen in air, the lack of electric sparking possibilities in explosive environments, is an important technology. Gasochromic materials, coloration by gases, have considerable promise as the optical gas sensing materials. Hydrogen gasochromism of Tungsten trioxide (WO_3) films coated with noble metal (Pd, Pt) catalysts, the color changes reversibly from grayish semi-transparent to deep blue, has been investigated for the application in optical hydrogen gas sensors. In this study, we investigated the effects of crystalline structure on gasochromism of WO_3 films.

WO_3 films were prepared by a reactive rf magnetron sputtering from a W (purity 99.9%) target in an argon and oxygen mixture. WO_3 films with thicknesses of approximately 300 nm were deposited on mirror-polished SiO_2 and α-Al_2O_3 $(01\bar{1}2)$ substrates. The substrates temperatures were maintained at 200 °C for amorphous WO_3 film, and at 600 °C for oriented and epitaxial WO_3 films. Polycrystalline WO_3 films were prepared by annealing of amorphous WO_3 films at a temperature of 400 °C in air for 2 hours using an electric furnace. The films were characterized by X-ray diffraction (XRD), Rutherford backscattering spectroscopy (RBS). To examine the hydrogen gasochromic performance of WO_3 films, the films were coated with a Pd layer (15 nm) by sputtering. And then, the transmittance at a wavelength of 645 nm was measured using a spectrometer while an argon gas including 1% hydrogen.

Figure 1 shows XRD patterns for the WO_3 films on SiO_2 and α-Al_2O_3 $(01\bar{1}2)$ substrates. The film prepared on SiO_2 substrate at 200 °C has an amorphous structure, and after that the film annealed at 400 °C in air becomes a polycrystalline structure. The characteristic peaks of the XRD pattern of the annealed film can be attributed to a monoclinic WO_3 phase, as referred to in the JCPDS 43-1035 file. The WO_3 film on SiO_2 and α-Al_2O_3 $(01\bar{1}2)$ substrates deposited at 600 °C show the growth of (010)-oriented and epitaxial WO_3(001) films. The hydrogen gasochromic performance of WO_3 films with various structures was examined by optical transmission measurements. The change in optical transmittance, T/T_0 at 645 nm of Pd/WO_3 films between the initial state (T_0) and the colored state (T), was measured. Optical response curves of coloration by 1% H_2 in Ar for amorphous, polycrystalline, (010)-oriented and epitaxial WO_3 (001) films coated with a Pd layer were summarized in Fig 2. The normalized transmittance, T/T_0 of the (010)-oriented and amorphous WO_3 films on SiO_2 substrates are rapidly changing within a few minutes by exposure to 1% hydrogen gas. On the contrary, the ratio T/T_0 of the polycrystalline and the epitaxial WO_3 (001) film shows a slight change. The hydrogen gasochromic performance of amorphous and (010)-oriented WO_3 films is superior to that of polycrystalline and epitaxial WO_3 (001) films. It indicates that gasochromic performance of WO_3 films is influenced by the structure of the films.

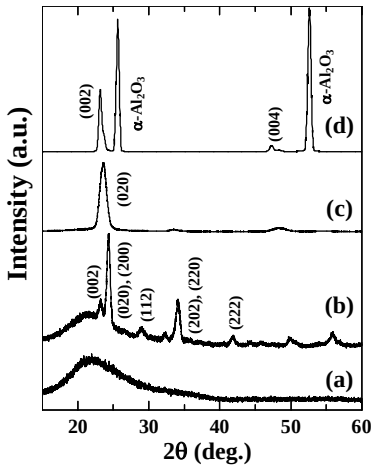

Fig. 1 XRD patterns for the WO_3 films: (a) amorphous WO_3, (b) polycrystalline WO_3, (c) (010)-oriented WO_3 and (d) epitaxial WO_3 (001).

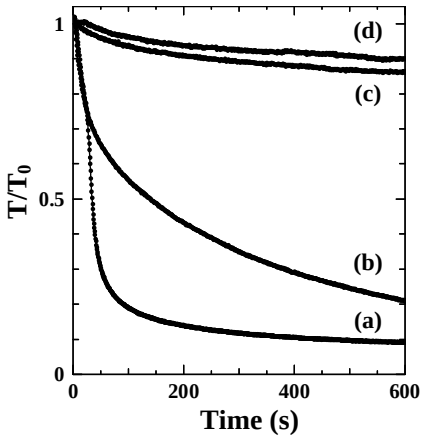

Fig. 2 Optical response curves of coloration by 1% H_2 in Ar for (a) Pd/(010)-oriented WO_3 film, (b) Pd/amorphous WO_3 film, (c) Pd/epitaxial WO_3 (001) film and (d) Pd/polycrystalline WO_3 film, respectively.

4-02 Li Ion Implantation into α-rhombohedral Boron: Carrier Doping for Superconduction

K. Kirihara [a)], H. Hyodo [b)], T. Nagatochi [c)], S. Yamamoto [d)], F. Esaka [e)], H. Yamamoto [f)], S. Shamoto [f)] and K. Kimura [c)]

[a)] National Institute of Advanced Industrial Science and Technology, [b)] Tokyo University of Science, [c)] The University of Tokyo, [d)] Environment and Industrial Materials Research Division, QuBS, JAEA, [e)] Division of Environment and Radiation Sciences, NSED, JAEA, [f)] Neutron Material Research Center, QuBS, JAEA

Carrier doping into an α-rhombohedral boron (α-r-B) crystal is expected to realize superconduction with a higher transition temperature (T_c) than that of MgB_2 [1)]. A twelve-boron-atom (B_{12}) icosahedral cluster is a building block of α-r-B structure (Fig. 1). Theoretical calculation suggested that high electronic density of states at Fermi level could be provided by appropriate carrier doping [2)]. Furthermore, high phonon frequency and strong electron-phonon coupling in boron are important factors for high T_c. Recently, we observed superconduction in Li-doped α-r-B crystal for the first time[3)]. The method of carrier doping was Li vapor diffusion. However, the amount of Li in α-r-B is still limited because of the formation of oxide barrier layer or other secondary phases and therefore T_c is still low (~7 K). Ion implantation is expected to be one of the effective methods of Li doping for realizing higher T_c than ever. In boron rich solids, very little is known about radiation damage by ion implantation. Only in boron carbide, self recovery of radiation damage in icosahedral cluster was reported in the study of He-ion implantation and post annealing [4)]. However, radiation damage in α-r-B is not reported. In this study, we report radiation damage in α-r-B by Li-ion implantation. Effect of carrier doping after post annealing is presented.

Powder sample of α-r-B was prepared by annealing of highly pure (99.99%) amorphous boron at 1,200 °C for 50 h in vacuum. The powder was formed into pellet by spark plasma sintering (SPS). Electrical conductivity σ was measured for the SPS samples by van der Pauw technique at 2~300 K. Micro-grains (3~5 μm in diameter) of a high purity single crystal were selected for the measurement of Raman spectroscopy. Implantation of Li^+ ions with energy of 150 keV was conducted at ambient temperature. We did not heat the samples during implantation in order to avoid vaporization of implanted Li.

According to the Raman spectra of micro-grains, Li implantation with a fluence of 4.5×10^{17} ions/cm^2 resulted in amorphization in the implanted region. Raman spectra of an α-r-B crystal observed after *in-situ* laser annealing, indicates recovery of the damage. The temperature of healing was estimated to be approximately 900 °C.

The ion fluence for SPS samples (3 mm×3 mm×1 mm) was 1.3×10^{18} ions/cm^2. Secondary ion mass spectroscopy (SIMS) of implanted samples revealed a maximum Li concentration of 7~8 at% at depth of ~700 nm from the surface. Since the implanted region has significant radiation damage, the temperature dependence of σ (plot (a) in Fig. 2) indicates variable range hopping conduction in Li-implanted amorphous boron. After rapid annealing of the implanted sample at 900 °C for 1 min in an Ar atmosphere, the temperature dependence of σ (plot (b) in Fig. 2) was similar to that of the vapor diffusion sample (nominal composition is $Li_{1.4}B_{12}$). Concentration of Li of the annealed sample measured by SIMS was 2 at%, in agreement with that of the vapor diffusion sample estimated by Rietveld analysis. Since the recovery of radiation damage could occur after post annealing, carrier doping into α-r-B by Li-ion implantation can be expected, similarly to the case of vapor diffusion. Additional implantation to obtain higher Li concentration is in progress.

References

1) K. Soga et al., J. Solid State Chem. 177 (2004) 498.
2) S. Gunji et al., J. Phys. Soc. Jpn. 62 (1993) 2408.
3) T. Nagatochi et al., to be submitted.
4) D. Shimeone et al., J. Nucl. Mater. 277 (2000) 1.

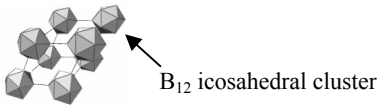

Fig. 1 Crystalline structure of α-r-B.

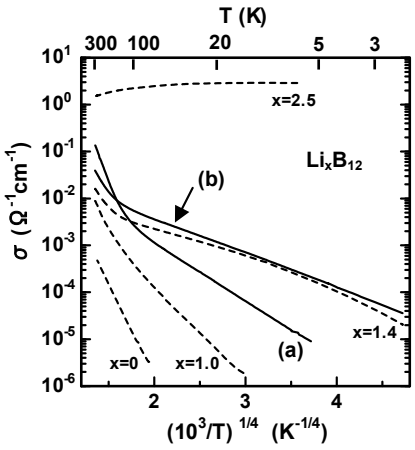

Fig. 2 Temperature dependence of electrical conductivity σ of α-r-B. Solid lines represents σ of the samples before (a) and after (b) Li ion implantation. Broken lines represents σ of the Li vapor diffusion samples. Number x is the nominal composition of Li.

4-03 Synthesis of Single-Crystalline and Amorphous SiC Nanotubes by Ion-Irradiation Technique

T. Taguchi [a)], S. Yamamoto [b)], K. Kawaguchi [b)], K. Kodama [a)] and S. Shamoto [a)]

[a)] Neutron Material Research Center, QuBS, JAEA,
[b)] Environment and Industrial Materials Research Division, QuBS, JAEA

Since the discovery of carbon nanotubes (CNTs) in 1991, significant numbers of researchers have synthesized new one-dimensional nanostructured materials such as nanotubes, nanorods and nanowhiskers for potential applications. Some of them have reported that many nanomaterials such as TiC, NbC, BN, SiO_2 and GaN nanostructures are fabricated from CNTs as the template. SiC is one of the most important wide-band-gap semiconducting materials for high temperature and high power. And SiC is also one of the most important structural materials at high temperature. Therefore, SiC offers exciting opportunities in electronic devices and in structural materials at high temperature. We reported that the C-SiC coaxial nanotubes, which were CNTs sheathed with SiC, were formed. Furthermore, the single-phase SiC nanotubes were successfully synthesized by heating the C-SiC coaxial nanotubes in air[1,2]. However, many grain boundaries exist in SiC nanotubes because SiC nanotubes fabricated in this study are polycrystalline. Grain boundaries degrade the electronic and mechanical properties of SiC nanotubes. Therefore, the synthesis of single-crystalline and/or amorphous SiC nanotubes without the grain boundary is required. The purpose of this study is to synthesize single-crystalline and amorphous SiC nanotubes by ion-irradiation technique.

Carbon nanotubes (GSI Creos Corporation, Tokyo, Japan) were used as the template. The C-SiC coaxial nanotubes were synthesized by heating CNTs with Si powder (The Nilaco Corporation, Tokyo, Japan) at 1,200 ºC for 100 h in a vacuum. Single-phase SiC nantoubes were formed by the heat treatment of C-SiC coaxial nanotubes at 600 ºC for 2 h in air. Thin films of single-phase SiC nanotubes were prepared on the alumina plates by depositing with the single-phase SiC nanotubes dispersed in ethanol. These thin films of single-phase SiC nanotubes were irradiated with 3-MeV Si^{2+} ions at 190 ºC and 900 ºC. The ion fluence was 6.4×10^{20} ions/m^2.

According to TEM observations, a few single-crystalline SiC nanotubes were formed by the ion irradiation at 900 ºC. Figure 1 shows the typical TEM image of single-crystalline SiC nanotubes. Because grain growth in the SiC nanotubes occurred by the ion irradiation at 900 ºC, polycrystalline SiC nantoubes were transformed to single crystalline SiC nanotubes. However, the number of single-crystalline SiC nanotubes synthesized by this process was very small. On the other hand, many amorphous SiC nanotubes were formed by the ion irradiation at 190 ºC. Figure 2 shows the typical TEM image of amorphous SiC nanotubes. No microstructural change in SiC nanotubes occurs only by thermal annealing up to 900 ºC because synthesis temperature is 1,200 ºC. As well as single-phase SiC nanotubes, polycrystalline C-SiC coaxial nanotubes were transformed to single-crystalline C-SiC coaxial nanotubes by the ion-irradiation at 900 ºC and to amorphous C-SiC coaxial nanotubes by the ion irradiation at 190 ºC, respectively. By the ion irradiation using a slit or a mesh, the SiC composite nanotubes with two or more different crystallinities and microstructures such as polycrystal-amorphous, single crystal-polycrystal and single crystal-amorphous in a SiC nanotube can be synthesized in the near future.

References

1) T. Taguchi et al., J. Am. Ceram. Soc. 88 [2] (2005) 459-461.
2) T. Taguchi et al., Physica E 28[4] (2005) 431-438.

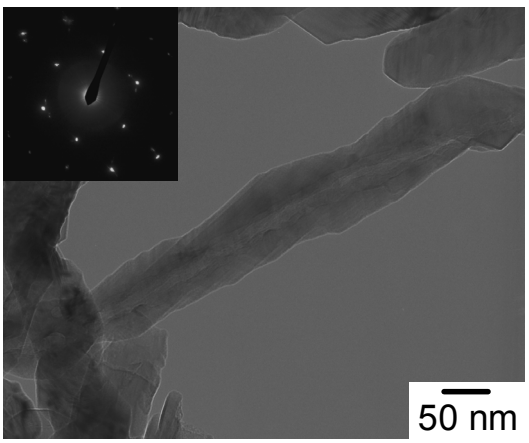

Fig. 1 TEM image of a single-crystalline SiC nanotube.

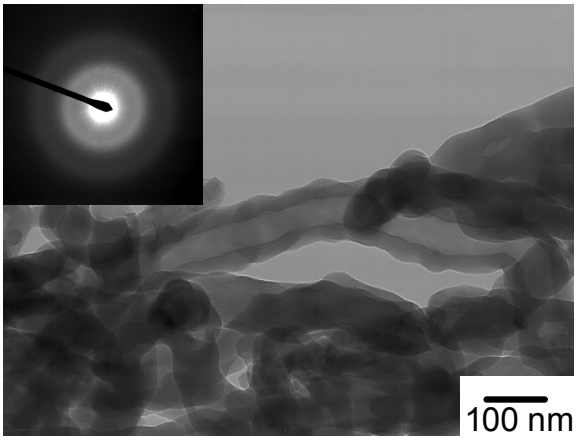

Fig. 2 TEM image of an amorphous SiC nanotube.

4-04 Polymer Optical Waveguides Fabricated by Using Proton Beam Writing

K. Miura [a)], Y. Machida [a)], M. Uehara [a)], O. Hanaizumi [a)], Y. Ishii [b)], T. Satoh [b)], K. Takano [b)], T. Ohkubo [b)], A. Yamazaki [b)], A. Inouye [b)], M. Kouka [b)], A. Yokoyama [b)] and T. Kamiya [b)]

[a)] Graduate School of Engineering, Gunma University,
[b)] Department of Advanced Radiation Technology, TARRI, JAEA

Proton beam writing (PBW) has recently attracted much attention as a next-generation micro-fabrication technology. It has many advantages compared with other technologies such as electron beam (EB) writing. PBW facilitates three-dimensional processes and has higher throughput than EB writing [1-3]. Planar polymer optical waveguides are becoming increasingly important recently in the field of optical fiber communication. In this study, we proposed and fabricated straight polymer waveguides (shown in Fig. 1) by using PBW, and obtained single-mode waveguides working at a wavelength of 1.55 μm.

An SiO_2 film was deposited as an under-cladding on an Si substrate (20 mm × 20 mm) by using radio-frequency sputtering. A PMMA (refractive index ~1.48) film was spin-coated on the SiO_2 film at 1,350 rpm for 30 sec. The sample was then baked at 120 °C for 2 min. We repeated these processes twice, and the PMMA film became 10 μm thick. Straight waveguides were drawn by using the 3 MV single-ended accelerator in TIARA. The proton irradiation energy was 1.7 MeV, the proton beam current was 60 pA, the dose was 100 nC/mm^2, and the beam size was about 1 μm$^{\phi}$. We drew seven waveguides having widths of 4, 6, 8, 10, 12, 14, and 16 μm on the PMMA film. A 10-μm thick PMMA film was deposited again on the sample as an upper-cladding by spin-coating under the same condition as the first PMMA layer. We cleaved both sides of the sample to observe near field patterns (NFPs) of the waveguides. We used a wavelength-tunable laser (Santec Ltd., ECL-210) for our NFP measurements. The laser wavelength was 1.55 μm, and the light was introduced through a single-mode fiber (SMF) to edges of the waveguides. We observed their NFPs by using a vidicon camera (Hamamatsu Photonics Ltd., C2741-03).

Figure 2 presents the NFP image of the 8-μm width waveguide. Its mode field diameter (MFD) was almost 10 μm, which is almost the same as the MFD of the SMF (vertical size ~9.8 μm, horizontal size ~10.5 μm). It is therefore considered that the coupling losses between fabricated waveguides and SMFs are low. We regarded it as a single-mode waveguide because no higher-order mode was observed when the excitation condition was changed. All waveguides were evaluated by the same method, and we found that the waveguides having widths above 12 μm were multimode waveguides. We assume that the proton beam penetrated though the PMMA and SiO_2 films to the Si substrate [4], and all waveguides work by the difference of refractive indices between the two proton-irradiated films.

We thus succeeded in fabricating straight polymer waveguides by using PBW. We are planning to measure the refractive indices of proton-irradiated PMMA and SiO_2 films, and to fabricate Y-junction waveguides and thermo-optic polymer switches based on Mach-Zehnder interferometer waveguides.

References

1) A. A. Bettiol et al., Nucl. Instrum. Meth. Phys. Res. B 231 (2005) 364.
2) F. Watt et al., Materials Today 10 (2007) 20.
3) N. Uchiya et al., Nucl. Instrum. Meth. Phys. Res. B 260 (2007) 405.
4) I. Rajta et al., Nucl. Instrum. Meth. Phys. Res. B 260 (2007) 400.

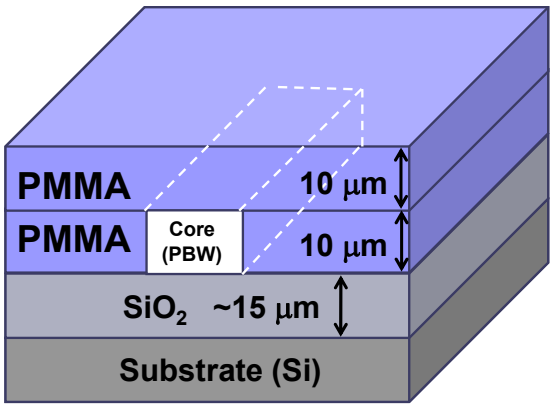

Fig. 1 Schematic figure of the PMMA waveguide utilizing the PBW technology.

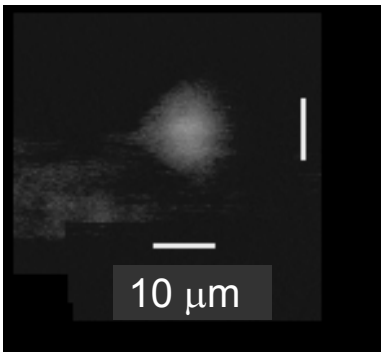

Fig. 2 Observed NFP of the 8-μm width waveguide.

4-05 Synergy Effects in Electron/Ion Irradiation and Alkaline Pretreatment on Hydriding Property of Hydrogen Storage Alloys

H. Abe [a)], M. Kishimoto [b)], H. Uchida [c)] and T. Ohshima [a)]

[a)] Environment and Industrial Material Research Division, QuBS, JAEA,
[b)] Course of Applied Science, Graduate School of Engineering, Tokai University,
[c)] Department of Energy Science and Engineering, School of Engineering, Tokai University

In previous studies [1, 2)], we reported that the alkaline pretreatment of the alloy surface using LiOH, NaOH or KOH accelerates the initial rate of hydrogen absorption of hydrogen storage alloys. Electron/ion beam irradiation is known to produce a high density of vacancy type defects in the surface region of materials and to be quite useful methods for the surface modification [3, 4)].

In this study, we examined the synergy effects of both the electron/ion irradiation and alkaline pretreatment on the Mm-Ni based alloy surface. We aimed to fabricate alloys with a higher performance of the hydrogen absorption rate by the surface modification of the alloys using electron/ion irradiation in this report. The electron/ion beam modifications are effective methods to improve the hydrogen absorption rate in metals. We also analyzed the chemical compositions at the surface of the irradiated/un-irradiated Mm-Ni based alloys, their crystal structures, and the phases of bulk. The samples used in this study were $MmNi_{3.48}Co_{0.73}Mn_{0.45}Al_{0.34}$ (Mm = $La_{0.35}Ce_{0.65}$) alloys. The samples were irradiated with either e^- at an acceleration energy of 2 MeV with a dose from 5×10^{16} to 1×10^{17} /cm^2 using the 2 MV Cockcroft-Walton electron accelerator in JAEA-Takasaki. The hydrogen absorption rate measurements were performed for the irradiated and un-irradiated Mm-Ni based alloys using the electrochemical apparatus method. An alkaline treatment was made by heating a sample at 398 K for 30 min in a 6 M-KOH solution. This treatment introduces K ions in the surface oxide layers of the alloy [3, 4)]. The hydrogen absorption rate of Mm-Ni based alloy was measured electrochemically in the 6 M-KOH with an open cell as the current density at a constant potential of -0.93 V at room temperature, from 0 to 120 minutes. These were measured after the combined with and without 6 M-KOH alkaline pretreatment respectively.

Figure 1 shows hydriding curves for samples with and without electron irradiation before electrochemical process. Samples with electron irradiations in the air exhibit much higher hydriding rates than that of a sample without irradiation. As known, electron irradiation induces vacancy type defects in the surface region of the alloy. These defects may act as hydrogen trapping sites, and increase hydrogen concentration in the surface region. This may enhance the initial hydriding rate, which was similarly observed for other metals pretreated by various charged ions [5)].

Figure 2 shows hydriding curves for samples with and without electron irradiation. After the electron irradiations in air, samples were treated in an alkaline solution of 6 M-KOH. Samples with electron irradiations show higher reaction rates than that of a sample without irradiation. The reaction rates for samples with both the irradiation and the alkaline treatment are much higher than those for samples only with electron irradiations (Fig. 1). After the irradiation, samples were exposed to air before the measurement of electrochemical hydriding rate. In this step, the surface oxidation of samples surely took place. Therefore, the additional alkaline treatment was effective to enhance the rate, because the alkaline treatment induces the K atoms in the surface oxides, and reduces the work function of electron of the surface to facilitate the dissociation of H_2O and the subsequent hydriding rate [1,2)].

Electron irradiation onto the surface of the Mm based hydrogen storage alloy was found very effective. Additional alkaline treatment was found also to contribute to the enhancement of the hydriding rate. These effects can be interpreted in terms of the induced vacancy defects by electron irradiation, and the surface oxidation of the alloy surface.

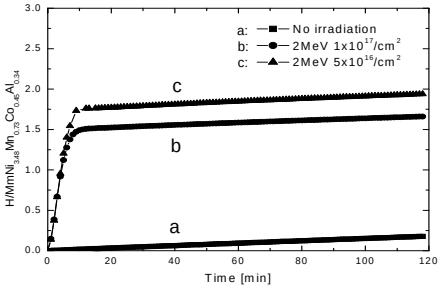

Fig. 1 Hydriding curves for samples with and without electron irradiation.

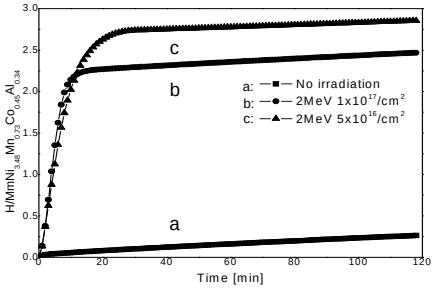

Fig. 2 Hydriding curves (a) for a sample without electron irradiation and with alkaline treatment, and (b) and (c) for samples with electron irradiations and alkaline treatment.

References

1) H. Uchida et al., J. Alloy Comp. 662 (2002) 330-332.
2) H. Uchida et al., J. Alloy Comp. 751 (1999) 293-295.
3) H. Abe et al., J. Alloy Comp. 288 (2005) 404-406.
4) H. Abe et al., J. Alloy Comp. 348 (2006) 408-412.
5) H. Abe et al., Nucl. Instrum. Meth. B, 206 (2003) 224.

4-06 Atomistic Study of Irradiation-induced Mass Transport Process

Y. Ikoma [a)], T. Motooka [a)], H. Sakita [a)], Hafizal Yahaya [a)], H. Naramoto [b)], K. Narumi [b)], S. Sakai [b)] and Y. Maeda [b,c)]

[a)] Department of Materials Science and Engineering, Kyushu University, [b)] Advanced Science Research Center, JAEA, [c)] Faculty of Engineering, Kyoto University

A nanometer-sized pores (nanopores) is of great interest for a possible application to molecular sensors such as DNA sequencers [1)]. These nanopores are fabricated using biomaterials and insulators. Especially, insulator nanopores are mainly fabricated by means of ion beam sculpting [2, 3)] or electron beam exposure [4)]. We have investigated the nanopore formations utilizing the structural change in Si and by ion irradiation [5,6)] and smart cut process by hydrogen ion implantation into nanopore-formed Silicon-on-Insulator (SOI) substrates [7)].

In the case of the ion irradiation technique, SOI(100) substrates with the top Si layer of 180 nm. The initial μm-size holes were prepared by ~30 keV Ga^+ focused ion beam irradiation using HITACHI FB-2000 at Kyushu University. Then the B^+, Si^+, P^+, and Ar^+ ions with the energy of 10 keV were implanted into the hole region at room temperature with doses of 4.4×10^{16} /cm^2, 4.3×10^{16} /cm^2, 0.9×10^{16} /cm^2, and 1.5×10^{16} /cm^2, respectively. These implantations were carried out by 400 kV ion implanter at TIARA. In order to avoid possible carbon contaminations on the sample surfaces, the irradiation chamber was kept cooled by surrounding cold shrouds.

Figure 1 shows the transmission electron microscopy (TEM) photographs obtained from the SOI samples before and after P^+ ion irradiation. The structural changes induced by ion bombardments were analyzed based on the dark-field (DF) and bright-field (BF) images combined with the selected-area diffraction (SAD) patterns. The dark-field images indicate that the hole region is crystalline before ion irradiation, but the hole region is changed to amorphous after ion irradiation. The pore area before and after ion irradiations is changed from 4.73 μm^2 to 4.56 μm^2, respectively. The shrinks of B^+, Si^+, P^+, and Ar^+ ions per dose are 0.5×10^{-25} cm^4, 1.8×10^{-25} cm^4, 1.9×10^{-25} cm^4, and 5.5×10^{-25} cm^4, respectively. It is found that the shrinkage effects can be attributed to dilation of crystalline Si upon amorphization induced by ion beam bombardments. The observed difference in ion species may be due to the difference in the number of the ion-beam-induced Frenkel-pairs, which is consistent with the D-D pair model for ion-beam-induced amorphization of Si proposed previously [8,9)].

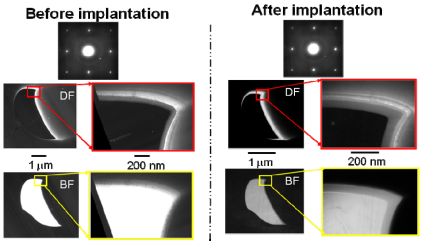

Fig. 1 TEM photographs from the SOI sample with a hole before and after the irradiation with 10 keV P^+ ions.

We also investigated the smart cut process by hydrogen ion implantation into nanopore-formed SOI substrates. The nanopore samples were fabricated by a pulse jet CVD technique described elsewhere [10)]. Separation by Implanted Oxygen (SIMOX) (100) with SOI and buried oxide (BOX) layers of 180 nm and 100 nm, respectively, were cleaned by the conventional RCA method [11)]. These substrates were introduced into the chamber after being dipped in aqueous 5% buffered HF in order to remove surface oxides. Electronic grade CH_3SiH_3 was introduced into the growth chamber using a supersonic pulse valve with a nozzle diameter of 0.8 mm. The pulse width and frequency were set at 100 μs and 10 Hz, respectively. The substrate temperature was set at 850 °C. After forming the SiC heteroepitaxial layer and the {111} faceted pits on SOI layer, these samples were dipped into 5% buffered HF solution for 10 min in order to remove the BOX layer under the pits. Hydrogen ion implantation was performed at room temperature with 1.44 MeV H_2^+ up to the dose of 1×10^{17} H/cm^2 utilizing 3 MV single-ended accelerator at TIARA. In order to separate the nanopore-grown film from SIMOX substrates, we heated the as-implanted sample at ~500 °C in air. From the scanning electron microscopy observation, it was confirmed that the sample surface was successfully cut with the depth at 10 μm from the substrate surface.

These results suggest that ion beam irradiation is promising not only for inducing the structural changes of solids but also for fabricating nanopore systems by the smart-cut technique.

References

1) M. Rhee and M. A. Burns, Trends Biotechnol. 24 (2006) 580.
2) J. Li et al., Nature 412 (2001) 166.
3) J. Li et al., Nature Mater. 2 (2003) 611.
4) A. J. Storm et al., Nature Mater. 2 (2003) 537.
5) T. Motooka et al., JAEA Takasaki Ann. Rep. 2006 (2008) 169.
6) T. Motooka et al., JAEA Takasaki Ann. Rep. 2007 (2008) 140.
7) Y. Ikoma et al., Abst. 4th Takasaki adv. Radiat. Res. Symp. (2009) 170.
8) T. Motooka, Phys. Rev. B 49 (1994) 16367.
9) T. Motooka et al., Phys. Rev. Lett. 78 (1997) 2980.
10) Y. Ikoma et al., Proc. SPIE 6984 (2008) 69841V.
11) W. Kern and D. A. Puotinen, RCA Rev. 31 (1970) 187.

4-07 Fabrication of Diluted Magnetic Semiconductor Crystals by Ion-Implantation Technique

A. Yabuuchi [a)], M. Maekawa [a)], A. Kawasuso [a)], S. Entani [a)], Y. Matsumoto [a)], S. Sakai [a)] and S. Yamamoto [b)]

[a)] Advanced Science Research Center, JAEA,
[b)] Environment and Industrial Materials Research Division, QuBS, JAEA

Ion implantation is a powerful technique for doping impurities into crystals with non-equilibrium concentration at low temperature. This technique may be used in fabrication of diluted magnetic semiconductors (DMS) that require high-concentration magnetic atom doping without a secondary phase formation. However, radiation damages are introduced by ion implantation. Recent calculation studies have suggested that a presence of vacancies affects the magnetic properties in DMS[1]. In this study, magnetic ions were implanted into compound semiconductor crystals by using an ion-implantation technique. Furthermore, we have attempted to clarify the correlation between the magnetic properties and presence of vacancy-type defects.

Hydrothermal-grown n-type ZnO(0001) single crystals were implanted with several different energy Cr^+ ions up to 380 keV to a fluence of 1×10^{16} ions/cm^2 at RT. After ion implantation, the isochronal annealing was conducted in the range up to 1,100 ^{o}C with a step of 100 ^{o}C for 30 min in a nitrogen atmosphere. The Doppler broadening of annihilation radiation (DBAR) spectra were acquired at RT after the annealing at each temperature. Moreover, after annealing up to 1,100 ^{o}C, XRD and SQUID measurements were performed.

Figure 1 shows the change in the peak intensity of a DBAR spectrum (S parameter) obtained with beam energy of 5 keV for a Cr^+-implanted ZnO crystal during isochronal annealing. From this, irradiation-induced vacancies were clustering up to 600 ^{o}C, and such vacancy clusters were annealed out at 900 ^{o}C. From XRD measurements after annealing at 1,100 ^{o}C, no secondary phase peaks were observed. SQUID measurement result for the 1,100 ^{o}C-annealed sample was shown in Fig. 2. In this sample, a clear magnetic hysteresis was not observed. In further study, evaluation of samples with higher impurity concentrations is needed.

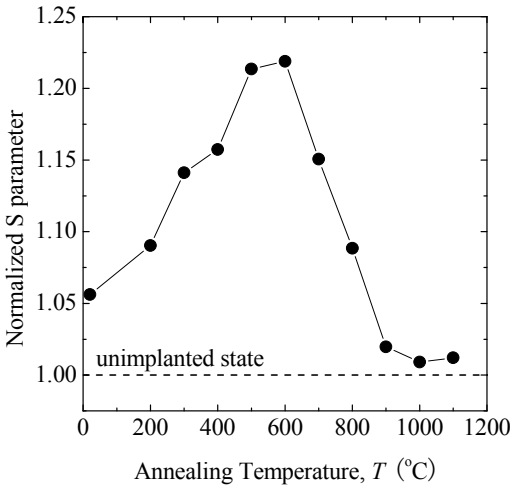

Fig. 1 The change in the S parameter for 1×10^{16} Cr^+ ions/cm^2 implanted ZnO before and during isochronal annealing. The dashed line represents a value of S for unimplanted ZnO.

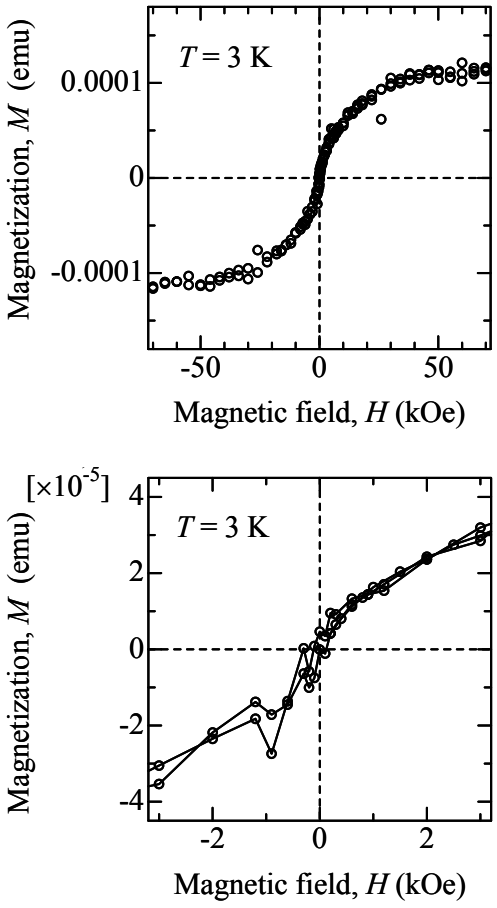

Fig. 2 Magnetization curves of a ZnO sample Cr^+-ion-implanted and annealed at 1,100 ^{o}C for 30 min in a nitrogen atmosphere.

Reference

1) L. Liu et al., Phys. Rev. Lett. 100 (2008) 127203.

4-08 Synthesis of Functional Polycarbosilane Nano-fiber by Ion Beam Induced Graft Polymerization

K. Yoshimura [a)], M. Sugimoto [a)], A. Idesaki [a)], M. Yoshikawa [a)] and S. Seki [b)]

[a)] Environment and Industrial Materials Research Division, QuBS, JAEA,
[b)] Department of Applied Chemistry, Osaka University

Recently, we have synthesized the polycarbosilane (PCS) nano fiber by ion beam irradiation and obtained silicon carbide (SiC) nano fiber by firing of this PCS nano fiber[1)]. Because of the quite large surface area of nano fiber, the metal-loaded SiC nano fiber has potential use as functional materials of catalysts. To date, radiation-induced graft polymerization and subsequent metal chelation step has been used for metal loading[2)]. In general, radiation-induced graft polymerization, which is key step of such metal loading process, is performed by electron-beam or γ-ray irradiation. For PCS nano fiber prepared by ion beam irradiation, the graft chain will be grown by induced radicals on the PCS nano fibers after ion beam irradiation. In this study, we synthesize functional PCS nano fiber by ion beam induced graft polymerization. The introduction of graft chain was examined on the basis of AFM measurement of nano fibers with and without grafting process. The SiC fiber was also prepared by firing of this material.

PCS (NIPUSI Type-A), as a ceramic precursor polymer, was purchased from Nippon Carbon Co. LTD and was spin-coated on a Si substrate. The coated PCS was irradiated using 450 MeV $^{129}Xe^{23+}$ ion beam. The irradiated films were treated by dry, degassed toluene solution of glycidyl methacrylate (GMA) and the insoluble irradiated part of the film was developed as GMA grafted PCS nano fiber. Then the samples were fired at 1,273 K in argon to obtain SiC nano fiber. The sizes and shapes of the nano fibers were observed using a SPA-400 atomic force microscope (AFM) from Seiko Instruments, Inc.

Investigations of the grafted PCS nano fiber by AFM were performed in order to identify the graft reaction proceeded. Figure 1a and 1b show the AFM micrograph of PCS nano fiber and grafted PCS nano fiber, respectively. As can be seen, the radii of grafted PCS nano fiber were larger than the PCS nano fiber. The radii of PCS nano fiber were 8 nm, while the radii of grafted PCS nano fiber were 20 nm. Generally, grafted polymer fiber was thicker than the starting polymer fiber[3)]. Therefore, increases of the radii suggest that graft polymerization proceeded on the PCS nano fiber similar to the bulk fiber. Thus, GMA grafted PCS nano fiber was successfully synthesized.

Figure 1c and 1d show AFM micrograph of SiC nano fiber produced by firing of PCS nano fiber and grafted PCS nano fiber, respectively. The PCS nano fiber shrank 30-40% reduction in the radii after firing. On the other hand, the radii of SiC nano fiber obtained from grafted PCS nano fiber were almost the same before and after firing. This result suggested that most of graft chain is converted to amorphous carbon on SiC nano fiber via firing process.

The GMA grafted PCS nano fiber and its firing material may have potential applications as nano catalyst supports and as nano catalysts.

References

1) M. Sugimoto et al., Trans. Mater. Res. Soc. Jpn. **33**, (2008) 1027.
2) N. Seko et al., Nucl. Instrum. Meth. B **265** (2007) 146.
3) A. Sekine et al., Radiat. Phys. Chem. **79** (2010) 16.

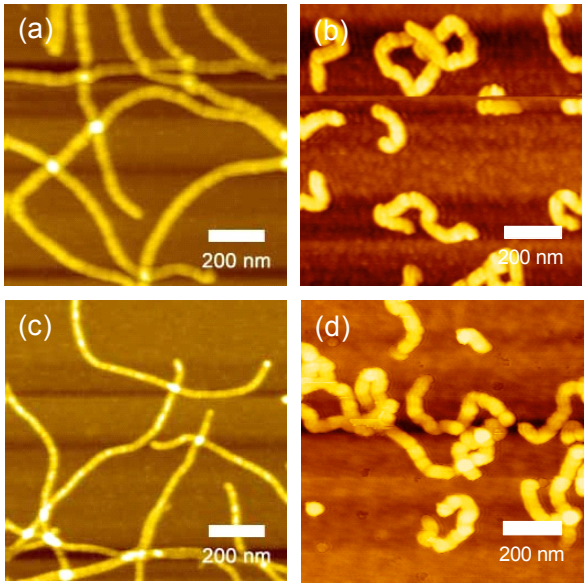

Fig. 1. AFM micrograph of (a) PCS nano fiber, (b) GMA grafted PCS nano fiber, (c) SiC nano fiber produced by firing of PCS nano fiber at 1,273 K in argon, and (d) SiC nano fiber produced by firing of GMA grafted PCS nanofiber at 1,273 K in argon. Nano fiber was formed by 450 MeV $^{129}Xe^{23+}$ ion beam irradiation at a fluence of 1×10^9 ions cm^{-2}.

4-09 Gas Permeation Characteristics of Silicon Carbide Membrane Prepared by Radiation-curing of Polycarbosilane Film

A. Takeyama, M. Sugimoto, A. Idesaki and M. Yoshikawa

Environment and Industrial Materials Research Division, QuBS, JAEA

Hydrogen has attracted much attention because it could produce energy without exhausting a popular greenhouse gas, carbon dioxide (CO_2). Hydrogen is produced industrially by use of steam reforming of methane at temperature range of 1,073 to 1,273 K, with consuming lots of energy to maintain the reactant gases at such high temperature. When the inorganic membrane is used to separate hydrogen from the product gases, it is expected the reaction equilibrium would be shifted to the product side, consequently the reaction temperature are lowered and the amount of energy required for the process is decreased. Silica (SiO_2) membranes have been expected as a candidate for such hydrogen separation because of their high H_2 permeance and selectivity, however, there is a serious issue that they are unstable in steam at high temperature.

Silicon Carbide (SiC) membrane has a potential advantage of hydrothermal stability at high temperature due to its high chemical inertness. So far, SiC membranes with lower H_2 permeance and selectivity compared than SiO_2 membranes were prepared and much effort to improve its gas permeation character have been made [2]. In this study, SiC membranes with high H_2 permeance and selectivity were prepared by the modified coating method using precursor (polycarbosilane, PCS) solution and curing of PCS film by electron beam irradiation.

Alpha alumina tubes coated with thin gamma alumina layer were used as supports. Appropriate amount of polycarbosilane (PCS) were dissolved into cyclohexane to prepare 10 mass% solution. Porous supports whose both ends were plugged were dipped in PCS solution for 60 s and drawn up by 1.5 mm/s. After drying in air, supports coated with PCS film were immersed in the same PCS solution and drawn up again. Subsequently, curing and cross-linking of PCS film was carried out by an electron beam irradiation in helium atmosphere or thermal oxidation in air at 493 K followed by the pyrolysis at 973 K for 30 minutes in argon atmosphere. Single gas permeance of hydrogen (H_2) and nitrogen (N_2) of the membrane were measured using home-made apparatus and the selectivity (H_2/N_2) was calculated.

Figure 1 shows H_2 permeance and selectivity of SiC membrane prepared from PCS film cured by electron beam irradiation or thermal oxidation. For SiC membrane prepared from thermally cured PCS film, H_2 permeance (closed circle) was almost inversely proportional to the temperature. This temperature dependence indicates H_2 molecule diffuse through pore of the membrane colliding with the pore wall by Knudsen diffusion mechanism [3]. Knudsen diffusion occurs when the pore diameter is smaller than about one tenth of the mean free path of H_2 molecule, which increase proportionally to the temperature. Therefore, the H_2 permeance and selectivity were declined as the temperature and mean free path were increased.

In contrast, H_2 permeance of SiC membrane prepared from radiation-cured PCS film (opened circle) was exponentially increased. This is typical of thermally activated diffusion of H_2 molecule by molecular sieving mechanism, indicating pore diameter of SiC membrane was smaller than that of membrane prepared from thermally cured PCS film. Considering the gas evolution behavior of SiC fiber during the pylolysis [4], for radiation-cured PCS film, smaller amount of gas evolved during the pyrolysis and this caused the formation of small pore in SiC membrane. Assuming molecular sieving mechanism, H_2 permeance at 773 K in which steam reforming of methane is performed, is calculated from plots of H_2 permeance. Extrapolated H_2 permeance is 7.6×10^{-7} mol/m^2/s/Pa and the selectivity is over 116, which shows SiC membrane prepared by modified coating method and radiation-curing have both high H_2 permeance and selectivity at the temperature preferable to H_2 production.

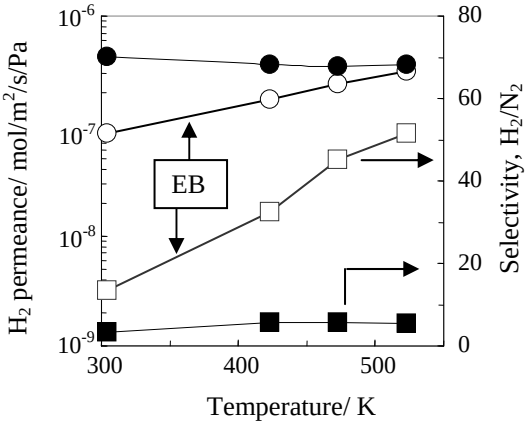

Fig. 1 H_2 permeance and selectivity of SiC membranes. Closed circles and squares are for the membrane prepared by thermally cured PCS.

References

1) T. Tsuru et al., J. Membr. Sci. 316 (2008) 53.
2) T. Nagano et al., J. Ceram. Soc. Jpn. 114 (2006) 533.
3) J. Dong et al., J. Appl. Phys. 104 (2008) 121301.
4) M. Sugimoto et al., J. Am. Ceram. Soc. 78 (1995) 1013.

4-10 Investigation of Nano Porous SiC Based Fibers Synthesized by Precursor Method

M. Sugimoto [a)], M. Yoshikawa [a)], K. Kita [b)], M. Narisawa [b)] and A. Nakahira [b)]

[a)] Environment and Industrial Materials Research Division, QuBS, JAEA,
[b)] Graduate School of Engineering, Osaka Prefecture University

Silicon carbide (SiC) based porous ceramics is one of promising thermoelectric materials, thermal generators and gas separators in high temperature. In recent years, there are many studies about Si-C base porous ceramics synthesized by polymer precursor method [1, 2]. There are, however, rare reports about porous ceramic fiber production available in a mass scale in spite of its potential application.

Recently, we have paid attention to various polysiloxanes for supplemental agents to polycarbosilane (PCS) for Si-C-O fibers [3]. The fiber derived from such polymer blend often yields characteristic porous structure. In this study, we investigate the effect of additive polymers to polycarbosilane (PCS) for controlling pore structures in the pyrolyzed fiber.

Commercialized polymethylphenylsiloxane (KF-54, Shin-Etsu Chemicals) and polymethylhydrosiloxanes (KF-99, Shin-etsu Chemicals) were blended with PCS (NIPUSI-Type A, Nippon Carbon). The blend ratios were 15 mass%. These polymer blends were melt-spun into polymer fibers at 523-578 K. The fibers including PMPhS and PMHS were identified as PS15 and HS15 respectively. The fibers were irradiated for curing by γ-ray in air or electron beam (EB) in He. The dose rate of γ-ray was 0.0057 kGy/s and the dose was 2 MGy, as for the EB, the dose rate was 1.6 kGy/s and the dose was 8 MGy. After the curing, the fibers were pyrolyzed at 1,273 K for 3.6 ks in Ar. After the pyrolysis, the pyrolyzed fibers were heated up again at 1,573-1,773 K for 1.8 ks in Ar. After the above process, the obtained ceramic fibers were observed by FE-SEM. Tensile strength and specific surface area of the fibers were also measured.

Figure 1 shows the FE-SEM images of the cross-sections of PS15 pyrolyzed at 1,573, 1,673, 1,773 K. The cross-section pyrolyzed at 1,573 K could not be observed, that of pyrolyzed at 1,673 K showed pores whose average diameter was less than 100 nm and that of PS15 pyrolyzed at 1,773 K shows pores whose average diameter was among 100 nm. The PS15 pyrolyzed at 1,773 K seems to be sintered. On the other hand, the cross-sections of PS15 cured by EB in He do not show any indication of pore formation.

The fibers cured by thermal or γ-ray oxidation maintained inner pores whose diameter was around 100 nm. Moreover, the surface area of the HS15 fiber was 12.1 g/m^2 and was larger than that of PS15 fiber. On the other hand, the fibers cured by electron beam without oxidation maintained only surface pores, while inner pores were collapsed. It was considered that the method of curing and the kind of additive polysiloxane for PCS determined the pore size in the fibers.

In the case of PS15 γ-ray oxidation curing and pyrolysis at 1,673 K was the best condition to achieve large surface area and the polymer blend with more PMPhS was appropriate to increase the specific surface area. As for the HS15, the surface area was less than that of PS15; however the tensile strength of the ceramic fiber pyrolyzed by the HS15 at 1,723 K was over 0.35 GPa. It seems that the component of polysiloxane has two effects of a deterrent to SiC crystal growth and a binder among the crystals in the porous ceramic fiber. The synthesized nano porous ceramics are promising as parts in catalyst or adsorbent for high temperature because of expected large specific surface area with high strength.

References

1) P. Colombo, and M. Modesti, J. Am. Ceram. Soc. **82**, (1999) 573-78.
2) Y. Kim et al., J. Ceram. Soc. Jpn. **11**, (2003) 863-4.
3) K. Kita et al., J. Am. Ceram. Soc. **92**, (2009) 1192-7.

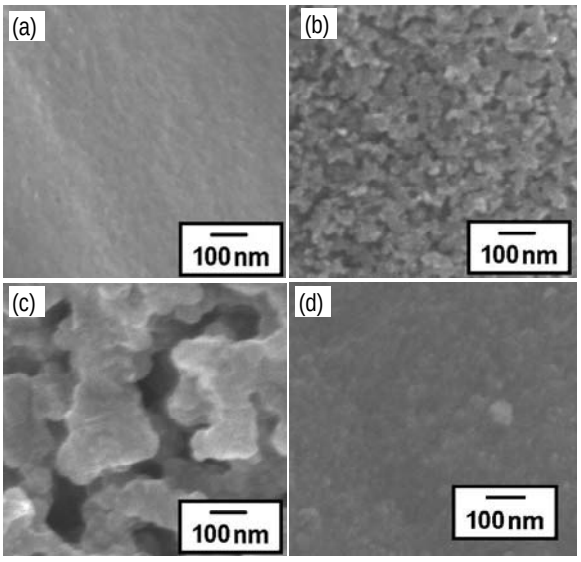

Fig. 1 SEM images of the cross sections of PS15 cured by γ-ray oxidation pyrolyzed at 1,573(a), 1,673(b), 1,773 K (c) and PS15 cured by EB without oxygen pyrolyzed at 1,673 K (d).

4-11 Control of Radial Size of Polymer Nanowire Formed by Ion Beam Irradiation

S. Tsukuda [a)], S. Seki [b)], M. Sugimoto [c)], A. Idesaki [c)], M. Yoshikawa [c)] and S.-I. Tanaka [a)]

[a)] Institute of Multidisciplinary Research for Advanced Materials, Tohoku University,
[b)] Division of Applied Chemistry, Graduate School of Engineering, Osaka University,
[c)] Environment and Industrial Materials Research Division, QuBS, JAEA

Ion irradiation at low fluence without overlapping between ion tracks produces single ion events in the target materials. Single ion bombardment can release active intermediates at high density within a limited area along the single ion track. These active intermediates form a heterogeneous spatial distribution in the ion track due to the variety of chemical reactions involved. In polystyrene (PS) and polycarbosilane (PCS), the crosslinking reactions along the ion track result in the formation of a cross-linked nanogel (nanowire) in thin films. The non-crosslinked area can be removed by development with toluene, utilizing the change in solubility due to the gelation of PS and PCS. The nanowires formed by ion bombardment can therefore be completely isolated on the substrate. It has also been reported that the radius of nanowire increased with the LET of the ion beam and molecular weight of polymer.[1-3)] In this study, 450 MeV Xe ion beam firstly irradiated to PS and polycarbosilane PCS films in order to form nanowires. Additionally, γ ray irradiation to the same film was carried out in order to control the radial sizes of nanowires. The change of radial sizes which depended on the dose was quantitatively measured, and we discussed in terms of radiation induced gel formation.

PCS and PS were spin-coated on Si substrates from the respective toluene solutions at 5 wt%. The samples were subsequently placed in a vacuum chamber and exposed to 450 MeV Xe ion beams at the Takasaki Ion Accelerators for Advanced Radiation Application (TIARA) cyclotron accelerator facility of the Japan Atomic Energy Agency.

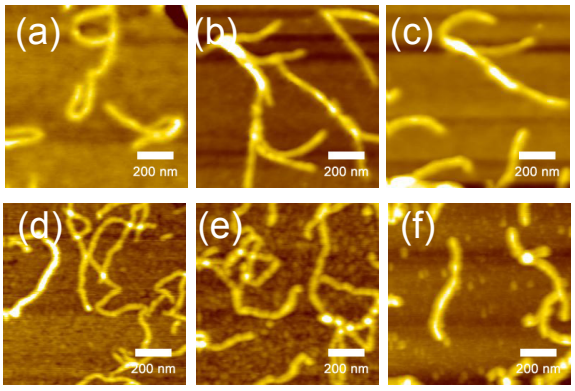

Fig. 1 AFM micrographs of nanowires based on PS (a-c) and PCS (d-f). The nanowires were formed by 450 MeV Xe ion beam irradiation at 1.1×10^9 ions/cm^2, and additional γ ray irradiation with the dose of (a, d) 22.4, (b, e) 52.2, and (c, f) 171.7 kGy, respectively.

Table 1 The radii of PCS and PS nanowires formed by the ion beam and γ ray irradiation.

	[b]Dose [kGy]			
	0[b]	22.4[b]	52.2[b]	171.7[b]
Radius (PS) *r* [nm]	5.1[a]	8.6	9.1	10.2
Radius (PCS) *r* [nm]	7.2[a]	7.8	8.2	11.5

a: These values were radius of nanowires formed by ion beam irradiation.
b: These values were the dose of γ ray irradiation.

The ion irradiated films were also exposed to γ ray with the dose 22~120 kGy. After irradiation, the samples were developed using organic solvents for 2 minutes. The direct observation of the surface of the substrates were performed using an atomic force microscope (AFM Seiko Instruments Inc.(SII) SPI-4000). The value of radial size is defined as an average radius of cross-sectional measurements of a nanowire at least 30 positions.

After the wet-development procedure, the nanowires lie prostrate on the substrate surface. These radii of PS and PCS nanowires formed by 450 MeV Xe beam irradiation were 5.1 and 7.2 nm, respectively. The γ ray irradiation to the same films with (~171.7 kGy) was carried out after 450 MeV Xe ion beam irradiation. Figure 1 shows results of additional γ irradiation with 22.4, 52.2 and 171.7 kGy, respectively. These radii of nanowires based on PS and PCS were larger than that of the original nanowires, respectively. The value of radius also increased with the dose of γ ray, as shown in Table 1. These results indicate the γ ray irradiation produces homogeneous crosslinking reactions throughout films, and the cross-linking reactions between the boundary of original nanowires and around polymer chains were caused in the solid films by the γ irradiation. Therefore, the radius (*r*) of cross-section of nanowires was increased with an increase of the radiation dose of γ ray. It is suggested that γ ray irradiation was also useful to control their radial sizes of nanowires obtained by ion beam irradiation.

References

1) S. Seki et al., Adv. Mater. 13 (2001) 1663-1665.
2) S. Tsukuda et al., J. Phys. Chem. B **108** (2004) 3407-3409.
3) S. Tsukuda, et al., Appl. Phys. Lett. **87** (2005) 233119-1-3.

4-12 Nano-crystalline Formation of Metallic Glasses by Ion Implantation

S. Nagata [a)], Y. Murayama [a)], B. Tsuchiya [a)], T. Shikama [a)], M. Sasase [b)], A. Inouye [c)] and S. Yamamoto [c)]

[a)] Institute for Materials Research, Tohoku University, [b)] The Wakasa-wan Energy Research Center, [c)] Environment and Industrial Materials Research Division, QuBS, JAEA

Metallic glasses have created considerable interest because of their excellent physical and chemical properties such as mechanical strength and corrosion resistance owing to their unique amorphous nature [1)]. Generally, the amorphous phase of an alloy can be obtained from the liquid state by rapidly cooling. Solid state amorphization techniques such as, mechanical alloying and hydrogenation have been extensively studied as novel processing methods. Ion implantation is an alternative method to form non-equilibrium phases by nuclear and electronic excitation along the trajectory of the ions, and to embed simultaneously an additional element. An advantage of this synthesis is the formation of an amorphous layer on fabricated products in a controlled way, by choosing the incident particle and its energy. Although the Zr-based glassy alloys are attractive due to high glass-forming ability, the ion beam effects on Zr-based alloy have been investigated mainly in the binary system such as Zr-Fe, or using swift heavy ions concerning extremely large electronic energy deposition. Recently we demonstrated that the ion irradiation effects on the primary precipitates during heat treatment [2)] and the ion-beam induced amorphization [3)] of the Zr-Cu-Ni-Al alloy. In this study, nano-crystalline formation and its effects on the mechanical properties were examined in Zr-Cu-Ni-Al amorphous alloy irradiated by ion beams.

The samples used in the present study were metallic glass ribbons of $Zr_{55}Ni_5Cu_{30}Al_{10}$ prepared by the melt spinning method and were amorphous films of $Zr_{65}Ni_{10}Cu_{17.5}Al_{7.5}$ deposited on NaCl substrate by the RF magnetron sputtering method. Some selected samples were prepared to thin foils using focused ion beam (FIB) technique. A master alloy was produced by arc melting method using 99.99 mass% Zr, 99.999 mass% Cu, 99.999mass% Al and 99.99 mass% Ni under purified Ar atmosphere. The crystal structure of the sample surface was investigated by X-ray diffractometry (XRD) with Cu-Kα radiation using a glancing incident angle α of 0.5 – 1.0 degree. Ions of Mg, P, and Bi with the 200 – 500 keV were implanted into the sample at room temperature. The structural and compositional changes of the ion implanted surface were investigated by transmission electron microscope (TEM), X-ray diffractometry (XRD) and Rutherford Backscattering Spectrometry (RBS).

Figure 1 shows bright-filed TEM images and selected area diffraction patterns of $Zr_{55}Al_{10}Ni_5Cu_{30}$ films. Because the calculated mean projected range of the 250 keV P ions was about 180 nm, most of the incident ions penetrated the film of 100 nm thick. For the un-implanted sample, the SAD pattern has wide halo rings without spots, while the bright-field TEM image shows a typical columnar characteristic of the microstructure of about 100 nm width. Nano-crystalline precipitates of fcc-Zr_2Cu were effectively formed with a size of 5 – 20 nm in the amorphous matrix by ion irradiation to fluences above 1×10^{16} cm^{-2}, although the long-range ordering of the structure was not observed in the X-ray diffraction patterns. The size and the concentration of the ion-induced precipitates were increased with the nuclear energy deposition of the ion, and the structure of the precipitates was independent of the ion species. No other capable structure of the precipitates, such as bct-Zr_2Cu, fcc-Zr_2Ni and Zr_6Al_2Ni, was observed. The hardness and elastic modulus estimated by the nano-indentation were proportional to the volume fraction of the ion-induced precipitates.

References

1) A. Inoue, Acta Mater. 48 (2000) 279.
2) S. Nagata et al., Nucl. Instrum. Meth. B 257 (2007) 420.
3) S. Nagata et al., Nucl. Instrum. Meth. B 267 (2009) 1514.

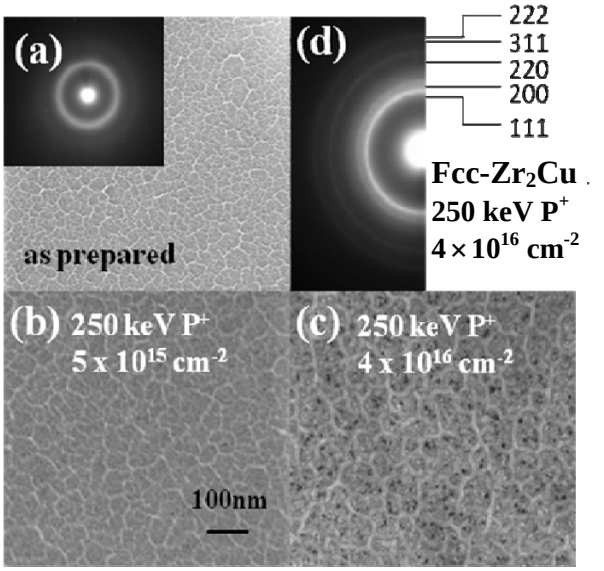

Fig. 1 Bright-filed TEM micrographs and selected area diffraction patterns of $Zr_{55}Al_{10}Ni_5Cu_{30}$ films; (a) as prepared, (b) irradiated by 250 keV P^+ to 5×10^{15}cm^{-2}, (c) irradiated by 250 keV P^+ to 4×10^{16} cm^{-2}, (d) irradiated by 250 keV P^+ to 4×10^{16} cm^{-2}.

4-13 Behavior of N Atoms in Nitriding Processes of Evaporated-Ti Thin Films due to Ion Implantation

Y. Kasukabe [a), b)], Y. Watanabe [b)], Y. Chen [b)], S. Yamamoto [c)] and M. Yoshikawa [c)]

[a)] Center for International Exchange, Tohoku University, [b)] Department of Metallurgy, Tohoku University, [c)] Environment and Industrial Materials Research Division, QuBS, JAEA

It has recently been reported that properties of non-stoichiometric titanium nitrides (TiN_y) such as electrical conduction, diffusion barrier, wear resistance, catalysis, etc. depend not only on chemical composition, but also on orientation relationships between TiN_y films and substrates. Therefore, much interest has been focused on studying atomistic-growth processes of TiN_y films [1)]. The purpose of the present paper is to clarify atomistic-growth processes of TiN_y films due to ion implantation by using in-situ transmission electron microscopy and electron energy-loss spectroscopy, along with composition analysis and with the characterization of the electronic structure by molecular orbital calculation. The ions of N_2^+ with 62 keV are implanted into deposited Ti films in the 400-kV analytic high-resolution TEM combined with ion accelerators installed at JAEA-Takasaki [2)].

Nitrogen ions (N_2^+) with 62 keV were implanted into the as-deposited Ti film composed of mainly (110)-oriented TiH_x and $(03\cdot5)$-oriented hcp-Ti at room temperature, which results in the epitaxial formation of (110)-oriented and (001)-oriented TiN_y, respectively. In order to elucidate the atomistic nitriding processes of the epitaxial transformation of Ti thin films due to N implantation in detail, DV-Xα MO calculations have been performed for the Ti_{19} cluster and $Ti_{19}N$ cluster models shown in Fig. 1(a). The Ti_{19} cluster of Fig. 1(a), which does not include a nitrogen atom indicated by an open circle G, corresponds to a part of the hcp-Ti structure. The central position G (O-site) of the octahedron with larger space as formed by A-F atoms in Fig. 1(a), has lower electron density (~1/5,000 of electron density of A-site). Thus, the O-sites have smaller repulsion for electrons of N atoms, and admit the invasion of N atoms, which leads to the formation of a $Ti_{19}N$ cluster in Fig. 1(a). The contour map of the wavefunction of the mainly Ti_{3d}-N_{2p} bonding orbital, which has the energy eigenvalue of -5.9715 eV below the Fermi level, is shown in Fig. 1(b). It can be seen from Fig. 1(b) that strong Ti-N bonds (A-G and F-G bonds) include the π-like bonds of $Ti3d_{yz}$ and $N2p_z$ orbitals, and that the $N2p_z$ orbital interacts with orbitals of Ti atom denoted by J, but hardly with those of Ti atom denoted by K. It can be considered that the interaction of the $N2p_z$ orbital with Ti atom, J, leads to the movement of the nitrogen atom, G, to other neighboring O-site of the octahedron formed by A, C, D, H, I and J atoms, midway between the A and J atoms. Since in the transformed fcc-Ti sublattice after the hcp-fcc transformation, the site, G, in Fig. 1(a) is not O-sites, the N atom denoted by G has to move into other O-sites in order to form the TiN_y. In other words, the movement (diffusion) of the N atom in the O-site of hcp to other neighboring O-site of the octahedron which is maintained during the hcp-fcc transformation of Ti-sublattice plays an important role in epitaxial growth of TiN_y. Thus, the shift of the F atom to the center of gravity of the triangle BEF promoted by the forming of the strong A-G and F-G bonds and the weakening of the C-B and D-E bonds for $Ti_{19}N$, the inheritance of square atomic arrangement formed by C, D, H and I atoms, and the movement of the N atom in the O-site of hcp-Ti to other neighboring O-site of the octahedron (from G, to other neighboring O-site of the octahedron formed by A, C, D, H, I and J atoms) can be considered to be the origin for the hcp-fcc transformation of Ti sublattices and epitaxial growth of TiN_y.

References

1) S. Hao et al., Phys. Rev. B 74 (2006) 035424-1.
2) H. Abe et al., JAERI-Research 96-047 (1996)18p.

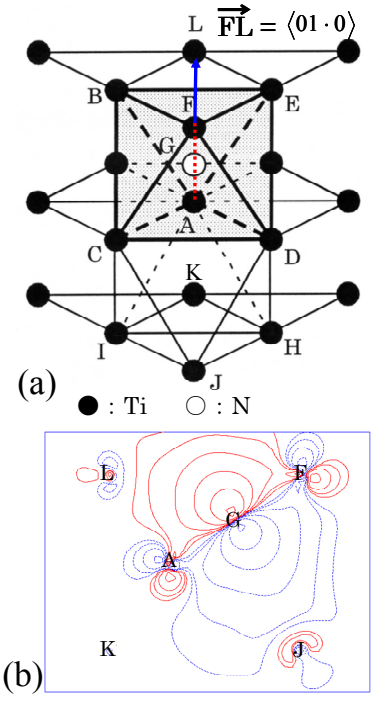

Fig. 1 (a) Schematic illustration of the Ti_{19} cluster and $Ti_{19}N$ cluster with a nitrogen atom, G. (b) The contour map of the wavefunction of the mainly Ti_{3d}-N_{2p} bonding orbital, which are drawn for the $\{\bar{2}1\cdot 0\}$ plane including A, L, F and J atoms in (a).

4-14 The Effects of Displacement Damage and Transmutation Atoms on Microstructure of SiC: The Effects of H Atom on Dimensional Change of SiC

T. Nozawa [a], T. Taguchi [b] and H. Tanigawa [a]

[a] Division of Fusion Energy Technology, FRDD, JAEA,
[b] Neutron Material Research Center, QuBS, JAEA

A SiC/SiC composite is a candidate for fusion structural material due to the inherently good irradiation resistance of SiC itself [1, 2]. Specifically, a dense and robust nano-infiltration transient-eutectic-phase sintered (NITE) SiC/SiC composite is believed to be viable due to potential high competitiveness. However, irradiation tolerance of NITE composites, which contain secondary phases composed of sintering aids, is somehow questionable considering the fact of irradiation-induced degradation for SiC with impurities [1]. In contrast, for the practical application, understanding the synergistic effects of He and H as transmutation products of a fusion reactor on microstructural evolution of SiC under irradiation is important. For instance, applying the triple ion beam irradiation by the TIARA facility, the significance of H on the He bubble formation was identified for pure SiC [3]. However, this effect on SiC with impurities is presently uncertain. This study primarily aims to identify the effects of displacement damage and transmutation atoms (He and H) on microstructure of SiC with sintering aids.

A NITE-SiC ceramic as representative matrix phase of NITE-SiC/SiC composites was tested. The sintering aids were Al_2O_3 and Y_2O_3. Triple ion beam (Si^{2+}, He^+ and H^+) irradiation was carried out up to 10 dpa at 1,000 ºC. A constant He/dpa ratio of 130 appm/dpa and varied H/dpa ratios of 0, 40 and 130 appm/dpa were applied. Figure 1 shows the calculated depth profiles of displacement damage and He, H and Si concentration. The radiation-induced dimensional change was then evaluated by the step-height measurement by the atomic force microscopy (Fig. 2). The detail of this technique was descrived elesewhere [4].

Figure 3 shows radiation-induced dimensional change as a function of the H/dpa ratio. Considering data scatter, it is speculated that the effect of the H/dpa ratio on the radiation-induced dimensional change of NITE-SiC was neglegibly small. However, for ~10 dpa, the amount of implanted H was very little to form He bubbles, which impact the magnitude of radiation-induced dimensional change. Further evaluation is, therefore, required to conclude this. The detailed analysis of the synergestic effects on microstructure of NITE-SiC is being continued.

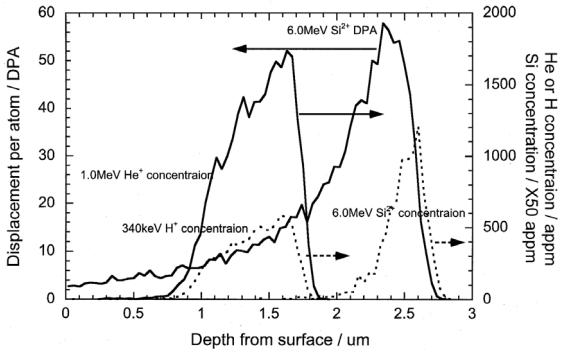

Fig. 1 Displacement damage, He, H and Si concentration as a function of depth from the surface in SiC calculated by SRIM code.

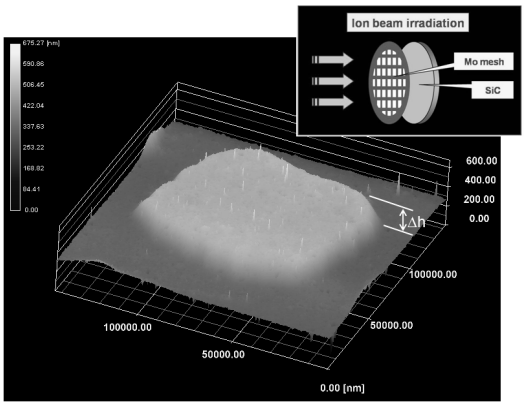

Fig. 2 Example of the step-height swelling measurement by the atomic force microscopy.

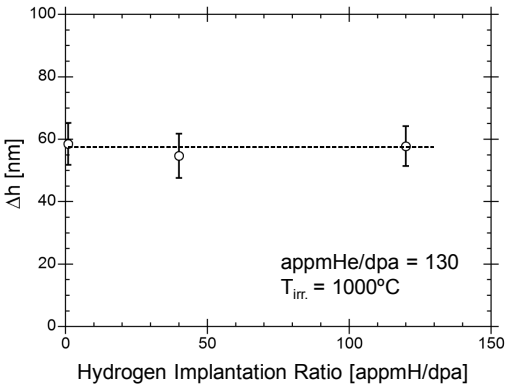

Fig. 3 The effect of H/dpa on dimensional change of SiC under triple ion beam (Si^{2+}, He^+ and H^+) irradiation.

References

1) L.L. Snead et al., J. Nucl. Mater. 371 (2007) 329.
2) T. Nozawa et al., J. Nucl. Mater. 386-388 (2009) 622.
3) T. Taguchi et al., J. Nucl. Mater. 367-370 (2007) 698.
4) Y. Katoh et al., Mater. Trans. 43 (2002) 612.

4-15 Annealing Behavior of Vacancy-type Defects in Electron-irradiated Si_xGe_{1-x} Bulk Crystals at Low Temperature

Y. Nagai [a)], K. Inoue [a, b)], H. Takamizawa [a)], T. Takeuchi [a, c)], A. Kuramoto [a)], T. Toyama [a)], M. Hasegawa [d)] and I. Yonenaga [d)]

[a)] The Oarai Center, IMR, Tohoku Univ., [b)] Kyoto Univ., [c)] JAEA, [d)] IMR, Tohoku Univ.

Vacancy-type defects in an electron-irradiated Si-Ge alloy ($Si_{0.85}Ge_{0.15}$) were investigated by positron annihilation technique. The Czochralski-growth undoped Si-Ge single crystals[1)] were irradiated at 77 K with 2 MeV electrons to a fluence of 2.5×10^{17} e/cm^2. The specimens were set to a sample chamber for positron experiments without temperature rise, and then positron lifetime and coincidence Doppler broadening (CDB) measurements were performed at 80 K. The positron trapping at monovacancies was observed for as-irradiated state. The isochronal annealing up to 250 K resulted in the increase of high momentum component fraction of CDB, which indicates that the fraction of positron annihilation with Ge electrons for the specimen annealed at 250 K was higher than that for the unirradiated specimen. On the other hand, positron lifetime showed slight decrease by the annealing. These results strongly suggest that the vacancies are stabilized by being surrounded with Ge atoms.

Si_xGe_{1-x} (0<x<1) は、全組成域で全率固溶体を形成し、バンドギャップや格子定数を Si から Ge まで連続可変なことなどから、バンドギャップ・格子定数・ひずみ制御工学材料などとして注目されており、Si に変わる高速電子デバイス材料などへの応用が期待されている。本研究では、SiGe 中の空孔型欠陥に関する基礎的な知見を得るため、Si_xGe_{1-x} 単結晶を低温電子線照射し、陽電子消滅法（陽電子寿命、同時計数ドップラー広がり法）による照射後等時焼鈍実験を行った。

試料は Czochralski 法を用いて作成された $Si_{0.85}$-$Ge_{0.15}$ 単結晶を用いた [1)]。液体窒素温度で電子線照射 (2 MeV、照射量 2×10^{17} /cm^2) した後、液体窒素温度を保持したまま試料をホルダーへ装着し、80 K で陽電子寿命および同時計数ドップラー広がり(CDB)測定を行った。さらに 90 K から 450 K まで 10 K おきに各 30 分間の等時焼鈍を行った。

Fig. 1 に、陽電子寿命の 2 成分解析結果の等時焼鈍回復挙動を（290 K～340 K では 1 成分解析の結果を平均寿命として）示す。また、Fig. 2 に CDB を用いて得られた高運動量成分割合：HMCF（$16\sim22\times10^{-3}m_0c$ 領域の割合、m_0 は電子の静止質量、c は光速）と低運動量成分割合：LMCF（$0\sim4\times10^{-3}m_0c$ 領域の割合）の相関の等時焼鈍回復挙動を示す。照射直後の長寿命成分 τ_2 の値から、陽電子は単空孔に捕獲されたものと考えられる。τ_2 は 250 K 焼鈍までは徐々に短くなっており、空孔空隙の寸法が小さくなっていることを示す。Fig. 2 では同じ焼鈍温度領域において、HMCF-LMCF 相関が未照射の点ではなく、Pure Ge の点の方向に移動していることから、Ge 電子との陽電子消滅割合が増加していることを示す。これらの結果は、焼鈍温度が上がるに従って空孔周囲には Si よりも Ge の割合が増えたこと、また、それに伴って空孔の実効サイズが小さくなったこと（Ge の原子半径は Si のそれよりも大きい）を示唆する。これらの結果から、SiGe 中の空孔は周囲にある Ge の割合が高い方が安定であることを示している [2)]。

また、330 K 以上では、陽電子寿命の増加から空孔集合体の形成が示唆される。

References

1) I. Yonenaga, J. Cryst. Growth **275** (2005) 91.
2) K. Inoue et al., to be published.

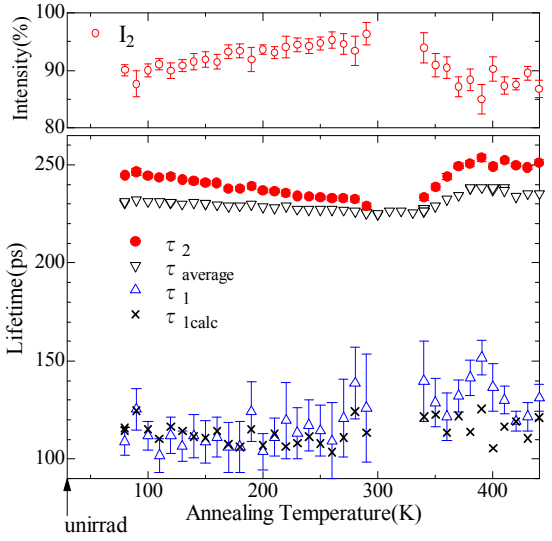

Fig. 1 Annealing behavior of positron lifetime in electron-irradiated $Si_{0.85}Ge_{0.15}$.

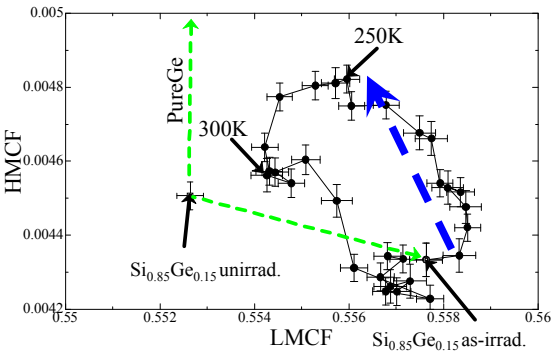

Fig. 2 Annealing behavior of LMCF-HMCF correlation of CDB measurement in electron-irradiated S.

4-16 RBS Analysis of Mass-transport Process in Au/Cu Film on Sapphire Treated by Centrifugal Forces

H. Naramoto [a)], K. Narumi [a)], T. Hao [a)], M. Ono [a)], S. Okayasu [a)], S. Sakai [a)], Y. Hiraiwa [b)], Y. Maeda [a, b)] and M. Sasase [c)]

[a)] Advanced Science Research Center, JAEA,
[b)] Faculty of Engineering, Kyoto University, [c)] Department of Research and Development, WERC

The controlled mass-transport is commonly important in materials science, and the various kinds of efforts have been made to find out the controlling parameters for that purpose. Recently, the directional mass transport has been reported under the application of the centrifugal force in the solid state, assuming the directional diffusion of vacancies [1)]. For the directional transport, it is important to consider the symmetry-lowering or the gradient field introduction by the application of external filed [2)], and this becomes more pronounced in nm system[3)]. Mass-transport process is also strongly influenced by the lattice imperfections, and the attention should be paid for the possible introduction of the lattice defects under the external fields.

In the present study, Au/Cu diffusion couple films were prepared on α-Al_2O_3(0001) substrate with the vacuum deposition method. The centrifugal force application was made at 0.61×10^6 G (denoted as MG hereafter following "million-level gravity") along the direction of the film pressing to the substrate (+MG) and also along its reverse (-MG) at 220 °C. For a comparison, the same kinds of samples were treated with the same thermal conditions. The mass-transport process is quantitatively analyzed with 2.7 MeV $^4He^+$ ion Rutherford Backscattering Spectrometry (RBS) system at TIARA, and possible microstructure changes associated with thermal annealing and/or centrifugal force application are characterized with a Scanning Transmission Electron Microscope (STEM) at WERC.

Figure 1 illustrates the results of RBS analysis for the growth of Cu layer on the surface as a function of treatment-periods for thermal annealing and also for centrifugal force application of ±MG. Even after thermal annealing with the same conditions as MG application, considerable amounts of mass-transport of Cu atoms into the surface through Au layer is observed. The similar phenomena was also observed in thin Au/Cu films with the high epitaxial nature (not shown for the simplicity), but any evidence of Cu atom localization was not confirmed within the Au layer in this case. This difference contains the important suggestion for surface diffusion along cylindrical microstructures within epitaxial films [4)]. It is also distinguished that the MG application enhances the mass-transport of Cu atoms into the surface through Au layer, and the enhancement seems to be expected to be intensified under the –MG application.

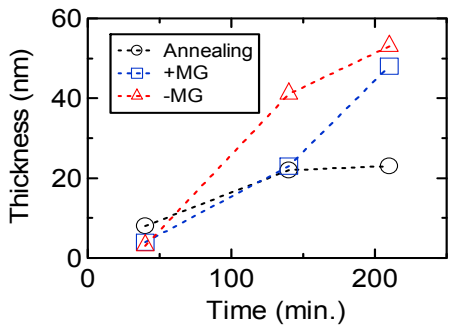

Fig. 1 The thickness changes of the transported Cu layer on the Au surface as a function of time for the annealed samples and the samples treated with +MG and -MG at 220 °C.

In order to confirm the possible introduction of the lattice defects under the centrifugal force application, the microstructure analysis was made with STEM. Figure 2 illustrates the typical STEM image of the cross-sectional area in Au/Cu film after the relevant treatment. In this case, the top Cu layer thickness amounts to 70 nm. The RBS analysis contains some ambiguity of possible opening of Au layer so as to expose the Cu layer directly to the analyzing He^+ ion beam, but the present STEM image evidences the Cu atom transport through Au layer. The growth rate of the Cu layer on the surface under the application of the +MG and -MG is higher than that of the thermal annealing. The different growth rate of the Cu layer under the application of +MG/-MG suggests the influences of lattice imperfections on the mass-transport process. The X-Ray Diffraction (XRD) analysis confirms the non-alloying even under the employed treatments. In the STEM micrograph, one can recognize the microstructural changes typically found in deformed metals, and it is inevitable to consider the influence of lattice imperfections as a next step.

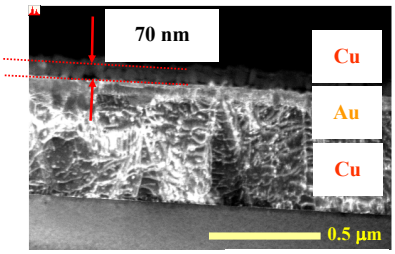

Fig. 2 STEM image of cross-sectional area in Au/Cu film after treated with +MG at 220 °C for 310 min.

References

1) T. Mashimo *et al*., Phil. Mag. Lett. **83** (2003) 687.
2) M. J. Aziz *et al*., Phys. Rev. B**73** (2006) 054101.
3) G. Dehm, Prog. in Mater. Science **54** (2009) 664.
4) A. V. Chechkin *et al*., Phys. Rev. E **79** (2009) 040105(R).

4-17 Low Temperature Ion Channeling of Fe_2MnSi Film Epitaxially Grown on Ge(111)

Y. Maeda [a, b], K. Narumi [b], Y. Terai [c], T. Sadoh [d] and M. Miyao [d]

[a] Kyoto University, [b] Advanced Science Research Center, JAEA,
[c] Osaka University, [d] Kyushu University

A full Heusler alloy $L2_1$-Fe_2MnSi is important for a spin polarized metal electrode (a spin injector) toward realization of a spin filed effect transistor: Spin-FET [1,2]. The perfect atomic rows along the <111> direction consist of periodic intervals of Fe(A), Mn(B), Fe(C), Si(D) in the $L2_1$ lattice. According to theoretical calculation of magnetic properties of Fe_2MnSi, perfect spin polarization (half metallicity) may be affected by actual occupation behavior of Mn atoms at the B site because the B site atom dominates electronic spin states near the Fermi level. Since 2007, we have successively investigated axial orientation and perfection of DO_3-Fe_3Si, Fe_4Si [2], $L2_1$-Fe_2MnSi with some compositions, Fe_2CoSi, Co_2MnSi films epitaxially grown on Ge(111) substrate. We found both cases that a lattice mismatch with the Ge substrate dominated axial orientation as observed in Fe_2MnSi [4] and that the nearest neighbor atoms around the B site or (A, C) site dominate chemical bond strength and stability of axial orientation as in Fe_2CoSi.

In this study following on the previous work, we investigate the axial orientation at the epitaxial interface of Fe_2MnSi(111)/Ge(111), then discuss the results taking into account the results on ion channeling at low temperature, where we can pass over effect of lattice vibrations on the axial orientation.

The epitaxial Fe_2MnSi layers with a thickness of ~50 nm were grown by low temperature- molecular beam epitaxy (MBE) on n-type Ge(111) substrates at 200 °C [5]. The three elements of Fe, Mn, and Si were co-evaporated with Knudsen cells. The axial channeling measurement and Rutherford backscattering spectroscopy (RBS) for analysis of composition of alloy films were carried out at either SC1 or MD2 beam lines in TIARA. The channeling measurement using 2.0 MeV-$^4He^+$ ions and a backscattering angle of 165 degrees was carried out at 300 K, 110 K and 40 K. The samples were mounted on a cooled holder.

Figure 1 shows angular yield profiles obtained by RBS at 300, 110, and 40 K. We observed evident channeling along the Ge<111> axis and obtained the minimum yield at the interface χ_{min}=0.045, 0.037 and 0.023, and the critical angle $\psi_{1/2}$=0.85, 0.94 and 1.04 degrees at each temperature.

Considering the previous results that their axial channeling at the interface of $Fe_{3-x}Mn_xSi$/Ge was affected by the lattice mismatch ratio which increased by increase of Mn content, the better channeling behavior observed at low temperature may be attributed to decrease in the lattice mismatch caused by thermal expansion. Actually, the lattice mismatch ratios calculated from thermal expansion data between Fe_2MnSi [6] and Ge [7] are 0.27% at 300 K, 0.15% at 110 K and 0.10% at 40 K. The channeling behavior being dependent upon the composition and temperature teaches us that the most dominant factor of the axial orientation at the interface is the lattice mismatch between Fe_2MnSi and Ge.

References

1) K. Hamaya et al., Phys. Rev. Lett. 102 (2009) 137204.
2) M. Miyao et al., Thin Solid Films. 518 (2010) S273.
3) Y. Maeda et al., Appl. Phys. Lett. 91 (2007) 17191.
4) Y. Maeda et al., MRS Proc. 1119E (2009) 1119-L05-02.
5) K. Ueda et al., Appl. Phys. Lett. 93 (2008) 112108.
6) G. D. Mukherjee et al., Physica B 254 (1998) 223.
7) O. Madelung, Semiconductors: Data Handbook, 3rd ed. Springer, 2003, Berlin, p.47.

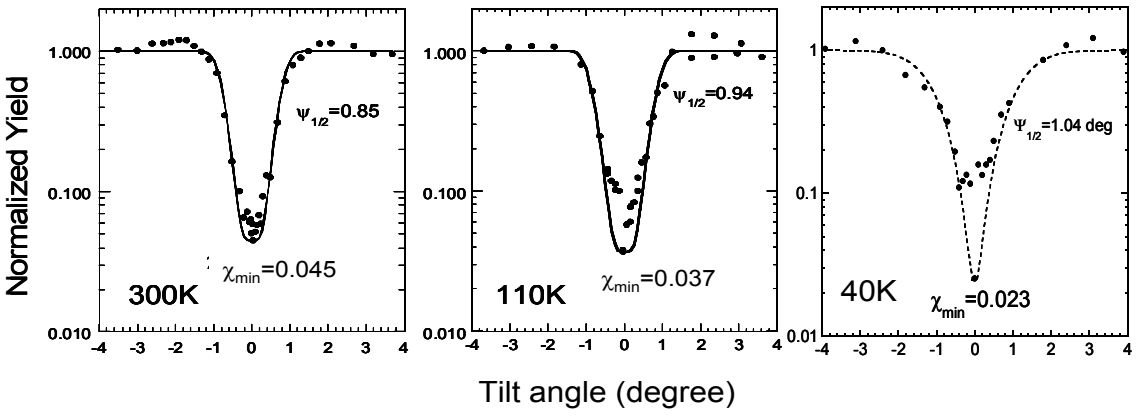

Fig. 1 Angular yield profiles along the Ge<111> axis of Fe_2MnSi/Ge(111) obtained at 300, 110, and 40 K.

4-18 Vacancy Generation around an SCC Crack Tip in Stainless Steels Probed by a Positron Microbeam

A. Yabuuchi, M. Maekawa and A. Kawasuso

Advanced Science Research Center, JAEA

In the 1970's, the stress corrosion cracking (SCC) occurred frequently in reactor materials of Type 304 austenitic stainless steels. It has been recognized that the degradation of the corrosion resistance is caused by the reduction of chromium concentration near the grain boundary due to chromium carbide formation during welding. This chromium carbide formation phenomenon is called sensitization, and nuclear-reactor materials were replaced by low-carbon stainless steels to avoid sensitization. Nevertheless, the SCC still occurs in the high-temperature pure-water reactor environment. This suggests that the suppression of the corrosion resistance degradation can not prevent the SCC failure. Recently, the SCC propagation model that the vacancy-type defects that accumulate in the crack tip play a role as a crack nucleus was proposed [1,2]. However, there is no information available on the generation or accumulation mechanism of such vacancies around the SCC crack tips. In this study, lattice defect spatial distributions around the SCC crack tip in an austenitic stainless steel have been probed by a positron microbeam.

A Type 304 stainless steel foil with 5 × 10 mm in size and 30 μm in thickness was annealed for 24 hours at 650 °C in the vacuum. The foil was attached to the compact tensile test specimen holder and tensile stress was applied. The holder was exposed into boiling $MgCl_2$ solution, so the SCC crack was introduced. The SCC crack specimen was loaded into the positron microbeam apparatus[3]. The SCC crack specimen was irradiated with a 20-keV positron microbeam. When vacancy-type defects are present in a material, annihilation gamma-ray peak intensity is increased. We have evaluated the change in peak intensity using the S parameter which increases with increasing peak intensity.

Figure 1 shows the measured S-parameter distribution map obtained from an SCC crack specimen. From this result, the increase of S parameter was observed around the SCC crack. To investigate what type of defect has caused the increase of this S parameter, the gamma-ray spectrum obtained from the surrounding of the SCC crack was compared with the spectrum obtained from the tensile test specimen. The tensile specimen was prepared from a 50-μm thick Type 316L stainless steel foil. The test piece was solution-annealed and tensile-deformed with a nominal strain of 22%. The spectra obtained from both specimen are plotted in Fig. 2 with the ratio change from the standard spectra. These two ratio curves agree well, which means that the same type of defect is included in the two specimens. Furthermore, the calculated spectrum of mono-vacancy in bcc-Fe replicates the experimental spectra. On the contrary, corrosion test revealed corrosion-induced defects were introduced only to 100 nm from the surface. These results indicate that the increase of S parameter near the SCC crack was caused by plastic-deformation-induced vacancies.

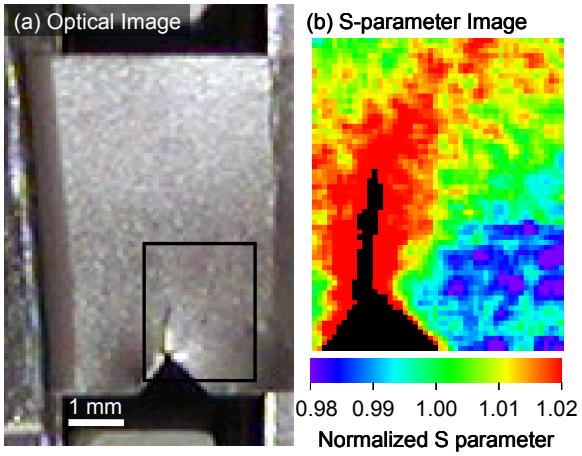

Fig. 1 (a) Optical image of the SCC crack in the sensitized Type 304 stainless steel and (b) S-parameter image around the SCC crack. The black pixel in the S-parameter image corresponds to the pre-notch and the SCC crack gap.

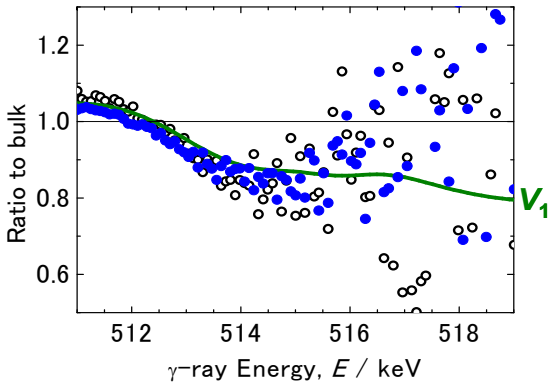

Fig. 2 The ratio curves for SCC crack specimen (●) and tensile test specimen (○). The solid line represents the calculation result with annihilating at mono-vacancy.

References

1) R.W. Staehle, "Proc. Int. Conf. Water Chem. of Nucl. React. Sys.", Jeju Is., Korea (2006).
2) K. Arioka et al., INSS Journal 13 (2006) 168.
3) M. Maekawa and A. Kawasuso, Appl. Surf. Sci. 255 (2008) 39.

4-19 Radiation-Induced Electrical Degradation in CeO_2 Ceramics Irradiated with 10 MeV Ni

N. Ishikawa and K. Takegahara

Division of Fuels and Materials Engineering, NSED, JAEA

Radiation damage is one of the important causes of degradation of thermal conductivity and serious swelling in nuclear ceramic fuels. Understanding of radiation damage in nuclear fuel is important for controlling fuel properties during burn up. One of main objectives of this study is to elucidate the irradiation parameter dominating the radiation damage of ceramics by means of accelerator experiments, and to develop the characterization method of the radiation damages. Especially for simulating the process of radiation damage by elastic displacements, low-energy particle (10 MeV Ni) irradiation experiment has been performed. The oxide ceramics target, CeO_2, which has the same crystal structure (fluorite structure) with a UO_2 nuclear fuel is adopted. In the present study, the radiation damage behavior is characterized not only by the X-ray diffraction method but also by the electrical conductivity measurement method.

Thin films of CeO_2 were prepared on Al_2O_3 single crystal substrates, and were irradiated with 10 MeV Ni ions at room temperature. After the irradiation, fluence dependence of change of X-ray diffraction (XRD) pattern was measured in the wide fluence range up to 1.0×10^{16} ions/cm^2, and also the electrical conductivity was measured up to about 1×10^{16} ions/cm^2. The film thickness was fixed to be about 0.3 μm which is thin enough to rule out the possibility of unwanted implantation effects.

Figure 1 shows the change in electrical conductivity plotted against fluence. Prominent electrical degradation is observed in the fluence range from 10^{12} to 10^{14} ions/cm^2, and it saturates in the high fluence range above 10^{14} ions/cm^2. This behavior can be understood, if the damage cross-section of around 7×10^{-15} cm^2 and electrical conductivity of damaged region of around 3×10^{-4} Ω^{-1}m^{-1} are assumed. This is demonstrated as a dotted curve in the figure.

In Fig. 2, the intensity of X-ray diffraction peak ((002) peak intensity) is plotted as a function of fluence. A sudden decrease in peak intensity is observed in the fluence range of around 10^{13} ions/cm^2. The decrease in the intensity saturates in the high fluence range over about 10^{13}-10^{14} ions/cm^2. This behavior can be understood, if the damage cross-section of around 1×10^{-13} cm^2 is assumed. This is demonstrated as a dotted curve in the figure. The damage cross-section for electrical conductivity measurement is smaller than that for XRD measurement, indicating that the damaged area responsible for electrical degradation is smaller than that responsible for crystallographic degradation.

Part of the present study is the result of "Research of highly accurate evaluation of radiation damage in advanced nuclear reactor fuel ceramics" entrusted to "Japan Atomic Energy Agency" by the Ministry of Education, Culture, Sports, Science and Technology of Japan (MEXT). Part of the present work was supported by KAKENHI (21360474).

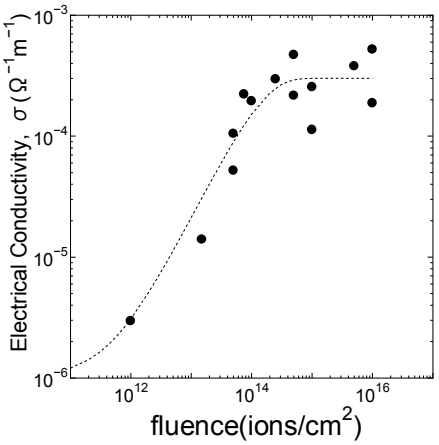

Fig. 1 Electrical conductivity of CeO_2 thin films plotted against fluence of 10 MeV Ni ions. For a dotted curve, see text.

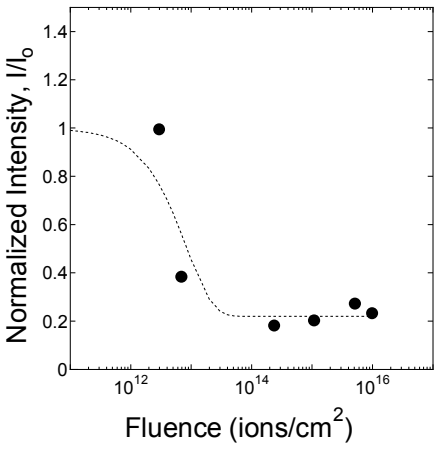

Fig. 2 Intensity of X-ray diffraction peak normalized by that of unirradiated CeO_2 thin films plotted against fluence of 10 MeV Ni ions. For a dotted curve, see text.

4-20 Incident Energy Dependence of Nuclear Reaction Imaging of Boron Doped in Iron

H. Shibata [a)], Y. Kohno [b)], T. Satoh [c)], T. Ohkubo [c)], A. Yamazaki [c)], Y. Ishii [c)], A. Yokoyama [c)] and M. Kohka [c)]

[a)] Graduate School of Engineering, Kyoto University,
[b)] Department of Materials Science and Engineering, Muroran Institute of Technology,
[c)] Department of Advanced Radiation Technology, TARRI, JAEA

An addition of a trace amount of boron to iron improves mechanical properties. Behavior of boron additive, however, is not sufficiently understood because of the difficulty of microscopic analysis, although boron treatment substantially may prevent hydrogen from segregating at grain boundaries. Recently imaging of boron distribution in a cancer cell has been also required to elucidate the buildup mechanism for boron neutron capture therapy (BNCT). These requirements to analyze the behavior of several tens ppm boron with a good spatial resolution stimulates us for developing an imaging technique of a trace amount of boron distribution by using PIGE or α-particle detection by nuclear reaction.

A proton micro-beam from 3 MV single-ended electrostatic accelerator of TIARA facility was used for microanalysis of a trace amount of boron. The imaging techniques of a trace amount of boron (several tens ppm) distribution by detecting 428 keV γ-ray emitted from ^{10}B (p, α' γ) ^{7}Be or α-particle from ^{11}B (p, α) ^{8}Be nuclear reaction have been developed. In the case of γ-ray measurement, X-rays from the same sample was also measured simultaneously for heavier elemental analysis. A typical current of several pA at the beam diameter of about 2 ~ 3 μm was used for mapping area of 250 μm × 250 μm in this experiment. The overall spatial resolution of the proton beam can be kept nearly 3 μm.

A hp-Ge γ-ray detector (Ortec 1601-1231- S-2), which has 100 cc crystal volume, is remodeled by Raytech corporation. The endcap of the detector is converted to L-shape to set the detector crystal just behind the sample. The resolution of this detector is 1.7 keV at 1.33 MeV with a cooled FET pre-amplifier. A Si(Li) detector is also installed for micro-PIXE analysis of heavier elements. The simultaneous measurements of X-ray and γ-ray can be performed in this study.

In 2009, in order to obtain information of depth profile of boron distribution, γ-ray images dependent on incident beam energy were measured. 1.5 ~ 2.3 MeV proton micro-beams were used to determine depth position of boron by measuring γ-rays from the inside of the specimen. An iron specimen (10 × 10 × 1 mm) used in this study contained 100 ppm boron and trace amounts of C, Si, Mn, P, S, N, Cr, W, Co and V.

Figure 1 shows total cross section of ^{10}B(p, α'γ)^{7}Be reaction. One broad resonance peaked at 1.5 MeV superposing smooth slope beginning from around 700 keV can be seen in this energy region. Irradiation was performed in the energy range from 1.5 to 2.3 MeV in every 200 keV interval.

Penetration depths of protons for nuclear reaction were ~ 8 μm for 1.5 MeV incident energy, ~10 μm for 1.7 MeV, ~ 13 μm for 1.9 MeV, ~15 μm for 2.1 MeV and ~19 μm for 2.3 MeV that were calculated by using SRIM considering nuclear reaction threshold of about 750 keV. The relation between these images is clearly understood because of 2 ~ 4 μm depth intervals.

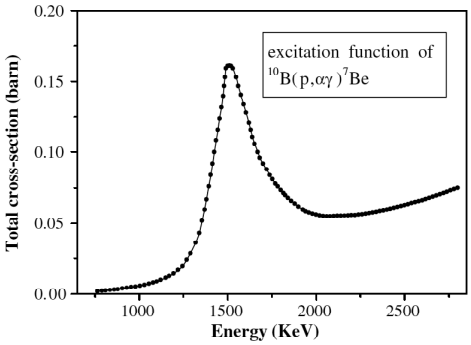

Fig. 1 Total cross-section of ^{10}B(p, α'γ)^{7}Be reaction [1)].

Typical γ-ray images taken by (a) 1.5, (b) 1.7, (c) 1.9 , (d) 2.1 and (e) 2.3 MeV proton irradiation are shown in Fig. 2. Several tens micron of segregated boron blocks were observed at each incident energy, and some correlations between boron images at different incident energies could be clearly seen. This segregation may appear along with iron grain boundaries. Sizes of these blocks are from several μm to ~10 μm. In this study, any iron grains cannot be imaged, therefore, these blocks cannot be determined their locations. As intensities of γ-ray signals does not calibrate to the absolute value of boron density, concentration of boron in a block does not estimated.

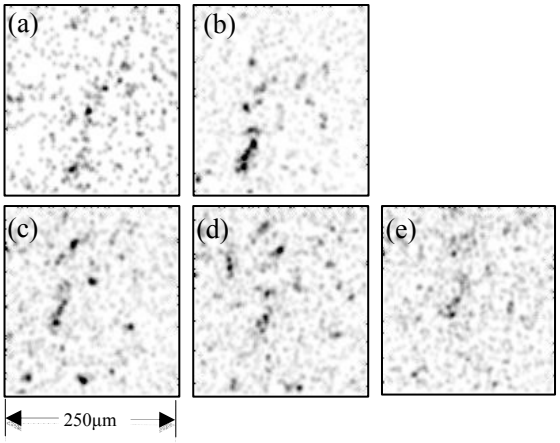

Fig. 2 Typical γ-ray images of 100 ppm boron contained steel specimen bombarded by (a) 1.5, (b) 1.7, (c) 1.9 , (d) 2. 1 and (e) 2.3 MeV proton micro-beam.

Reference

1) R. Mateus et al., Nucl. Instrum. Meth. Phys. Res. B 219-220 (2004) 519-523.

4-21 Study on Cu Precipitation in Energetic Electron Irradiated FeCu Alloy by Means of X-ray Absorption Spectroscopy

A. Iwase [a)], S. Kosugi [a)], S. Nakagawa [a)], N. Ishikawa [b)] and Y. Okamoto [c)]

[a)] Department of Materials Science, Osaka Prefecture University,
[b)] Advanced Science Research Center, JAEA,
[c)] Synchrotron Radiation Research Center, QuBS, JAEA

In the previous reports [1,2], we showed the change in Vickers hardness for electron-irradiated FeCu alloys and discussed the dependence of the hardness on electron-fluence and Cu concentration. In the present experiment, FeCu alloy specimens were irradiated with electrons up to much higher fluences and the status of Cu precipitation was studied by means of extended X-ray absorption fine structure (EXAFS) measurements.

Specimens were prepared from Fe-0.6wt.%Cu alloy. They were annealed at 850 ºC and were quenched into 0 ºC water. The specimens were irradiated with 2 MeV electrons to the fluence of 4.5×10^{19} /cm^2 using two electron accelerators at JAEA-Takasaki. After the irradiation, the micro Vickers hardness was measured as a function of electron fluence. EXAFS spectra at Cu K absorption edge were collected using the 27B beamline at the Photon Factory of High Energy Accelerator Research Organization (KEK-PF). The spectra were obtained using 7 element germanium detector in the fluorescence mode. For comparison, EXAFS spectra for pure Cu and Fe foils were also measured in the transmission mode.

Figure 1 shows the dependence of change in Vickers microhardness on electron fluence for Fe-0.6wt.%Cu specimens. The hardness increases monotonically with increasing the electron fluence, and tends to be strongly saturated at high fluence. Figure 2 shows the k^3-weighted Foulier transforms corresponding to the EXAFS spectra for pure Fe, pure Cu and Fe-0.6wt.%Cu specimens which were irradiated with electrons. For small electron fluence (2.7×10^{17} /cm^2), the shape of EXAFS spectrum for FeCu alloy is similar to that for pure Fe. With increasing the electron fluence, however, the EXAFS shapes become similar to that for pure Cu. The present result suggests that Cu precipitates with BCC structure appear by the electron irradiation with the small fluence. With increasing the electron fluence, the structure of Cu precipitates gradually change from BCC to FCC.

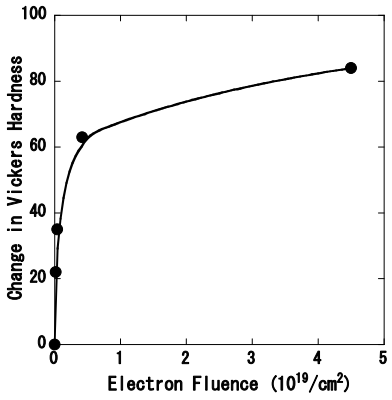

Fig. 1 Change in Vickers hardness for Fe-0.6wt.%Cu irradiated with 2 MeV electrons at 250 ºC.

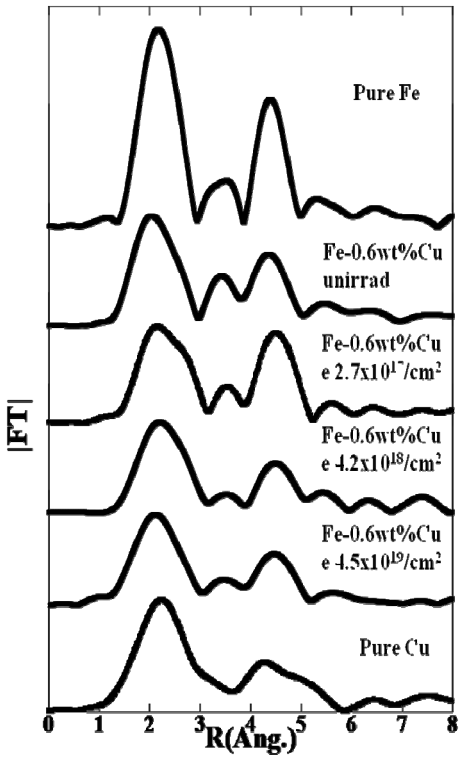

Fig. 2 Foulier transform of Cu K-edge EXAFS spectra for electron irradiated Fe-0.6wt.%Cu. For comparison, EXAFS spectra for pure Fe and pure Cu are also shown.

References

1) S. Nakagawa et al., Proc. Mater. Res. Soc. Symp. 1043-T09-04 (2008).
2) S. Nakagawa et al., JAEA Takasaki Ann. Rep. 2008 (2009) 136.

4-22 Cathodoluminescence of Albite Activated by Alpha-particle Induced Luminescence Centers

H. Nishido [a)], M. Kayama [a)], S. Toyoda [b)], K. Komuro [c)] and K. Ninagawa [b)]

[a)] Research Institute of Natural Sciences, Okayama University of Science, [b)] Department of Applied Physics, Okayama University of Science, [c)] Earth Evolution Sciences, University of Tsukuba

Cathodoluminescence (CL) is an optical phenomenon that is based on the generation of visible radiation through sample excitation by high-energy electrons. Radiation-damage halos caused by alpha-particles are recognized in mineral grains of quartz and biotite with radioactive uranium- and thorium-bearing mineral inclusions. However, the halos in feldspar minerals, most common mineral in the Earth's crust, have not been studied from the point of CL characterization, where radiation-damages are not observable with a polarized microscope. They can be detected only with a CL microscope and are called CL halos. Until now the formation of such halo has not been investigated in detail. In this study, CL of He^+ ion implanted albite in feldspar group have been measured to clarify the halo for geodosimetry and geochronology.

Single crystals of albite ($Ab_{98\sim100}Or_{2\sim0}$) from Minas Gerais, Brazil (Ab1), Niigata, Japan (Ab2) and Shiga, Japan (Ab3) were selected for CL measurements. He^+ ion implantation (dose density: $1.23\times10^{-4}\sim7.38\times10^{-4}$ C/cm^2) on the samples was performed using a 3 MV-tandem ion accelerator at the Takasaki Advanced Radiation Research Institute of the Japan Atomic Energy Agency. The energy was set at 4 MeV corresponding to the energy of alpha-particles from ^{238}U. A scanning electron microscopy-cathodoluminescence (SEM-CL), which is comprised of SEM (JEOL: JSM-5410) combined with a grating monochromator (OXFORD: Mono CL2), was used to measure CL spectra ranging from 300 to 800 nm at 15 kV acceleration voltage and a beam current of 1.0 nA. All CL spectra were corrected for total instrumental response, which was determined using a calibrated standard lamp.

CL imaging of Ab1, Ab2 and Ab3 shows CL halo on the surface of He^+ ion implanted sample. Approximately 15 μm width of CL halo in the section is consistent with theoretical range of alpha-particles from disintegration of ^{238}U in albite. Their CL spectra in the halos consist of four emission bands at around 400, 580, 660 and 730 nm. The emissions at 400, 580 and 730 nm can be assigned to Ti^{4+}, Mn^{2+} and Fe^{3+} impurity centers, respectively. The intensities of these CL emissions decrease with an increase in radiation dose of He^+ implantation. Raman spectroscopy on these albite in halo areas reveals pronounced peaks at 480, 520 and 780 cm^{-1} of which full width at half maximum (FWHM) increase with an increase in radiation dose. It implies that He^+ implantation causes a breakage of the framework, suggesting a reduction of CL emission centers assigned to Ti^{4+}, Mn^{2+} and Fe^{3+} impurity centers. In the case of an emission band at around 660 nm, however, the higher the radiation dose of He^+ implantation, the higher the intensity of CL emission at 660 nm becomes. These results suggest that CL emission at around 660 nm might be assigned to radiation induced defect center formed by He^+ ion implantation.

In general, a CL spectral peak fitted by one Gaussian curve in energy units can be assigned to one specific type of emission center. These spectra of implanted albite can be deconvoluted by Gaussian curves in energy units, resulting in four components centered at 3.05, 2.10, 1.86 and 1.56 eV, where a number of the Gaussian component can be determined by chi-square test for CL spectral data fitted with the smallest margin of error. An integral intensity of the Gaussian component at 1.86 eV positively correlates with radiation dose of He^+ implantation in the halo area of individual albite. It suggest that the component at 1.86 eV (660 nm) might be assigned to radiation-induced defect center formed by He^+ ion implantation (Fig. 1). CL line analysis along the halo section reveals that a change in the CL intensity along depth direction substantially corresponds to the Bragg's curve, implying energy loss process of specific ionization along the track of a changed particle. Therefore, the CL emission of albite related to radiation-induced defect center can be used to quantitatively evaluate the radiation dose of alpha-particles induced on feldspar minerals as an indicator applied for a geodosimeter.

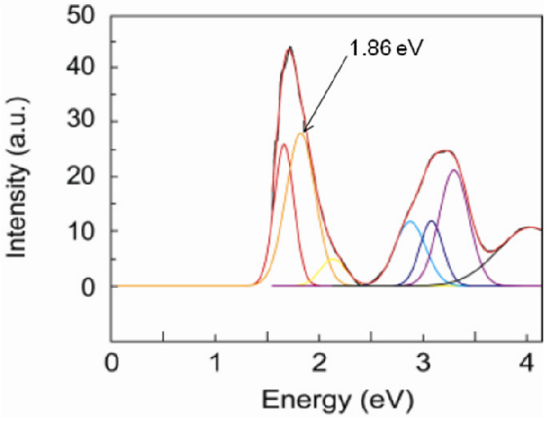

Fig. 1 Deconvolution of CL spectrum of Ab3 ($Ab_{98\sim100}Or_{2\sim0}$ from Shiga, Japan) by Gaussian curves.

4-23 Evaluation of Fluorescence Materials for Pulsed-neutron Imaging

T. Sakai [a)], M. Taguchi [b)], S. Kurashima [c)], H. Sato [d)], T. Kamiyama [d)] and Y. Kiyanagi [d)]

[a)] Materials Science Research Division, QuBS, JAEA, [b)] Environment and Industrial Materials Research Division, QuBS, JAEA, [c)] Department of Advanced Radiation Technology, TARRI, JAEA, [d)] Graduate School of Engineering, Hokkaido University

We have evaluated fluorescence lifetime of two materials those are candidates for pulsed-neutron imaging detector. The fluorescence materials are conventional ZnS(Ag) and Y_2O_2S(Eu) that is used in Color Neutron Image Intensifier. The fluorescence lifetime of former one is relatively short and suitable for pulsed-neutron detecting devices. On the other hand, the latter has fairly long fluorescence lifetime so that this material is not fit for epithermal neutron detection.

2008 年 12 月より、大強度陽子加速器施設（J-PARC）の利用運転が始まり、我が国においても本格的に大強度のパルス中性子を利用する環境が整った。その中で、中性子エネルギーによる物質の透過率の違いを観るパルス中性子ラジオグラフィ法は、従来のラジオグラフィ法では観察できなかった試料内部の応力分布や相変化などを可視化できる手法として、世界的にも注目を集めている [1)]。パルス中性子ラジオグラフィにおいては、中性子のエネルギーを飛行時間法により測定するため、空間分解能だけではなく時間分解能にも優れた検出手段が必須である。ラジオグラフィ法において、中性子の検出は、ホウ素やリチウム等の中性子を捕獲して荷電粒子を放出する核種と蛍光材料を組み合わせることで行われる。このため、残光の少ない蛍光材料を使う必要があり、その特性評価を行うため、サイクロトロンからのイオンビームにより発光特性の評価を行った。

実験は、サイクロトロンからの 50 MeV He^{2+}ビームを試験する蛍光材料に照射し、その発光スペクトルと波長毎の発光寿命を測定した。評価を行った蛍光材料は、一般的な蛍光材料として広く用いられている ZnS(Ag)と、中性子カラーイメージインテンシファイアの出力蛍光面 [2)]にも用いられている Y_2O_2S(Eu)の 2 種類である。Figure 1 に発光スペクトルを示す。

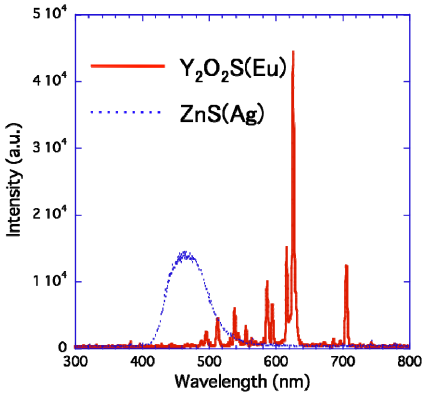

Fig. 1 Fluorescence spectra of ZnS(Ag) and Y_2O_2S(Eu).

ZnS(Ag)の発光スペクトルは、460 nm 付近にピークが観察された。そこで、発光寿命に関しては、このピーク付近の波長を測定した。また、Y_2O_2S(Eu)に関しては、多数のピークが観察され、それぞれの波長に対して発光寿命の測定を行った。発光寿命測定方法に関しては、金属干渉型バンドフィルターにより分光を行い、光電子増倍管からの出力波形を高速デジタルオシロスコープで観測した。また、励起を行う He^{2+}ビームは、静電偏向式のチョッパーで時間幅を 0.5~5 μs に制限して、蛍光材料に照射した。Figure 2, 3 に、それぞれ ZnS(Ag)と Y_2O_2S(Eu)の発光寿命測定の結果を示す。

ZnS(Ag)に関しては、発光強度がピーク値の 20%になるまでの時間が 10 μs 程度であり、比較的エネルギーの高い熱外中性子などの検出にも利用することが出来る。短波長側の発光寿命は更に短いため、よりエネルギーの高い中性子の検出にも利用できる可能性がある。一方、Y_2O_2S(Eu)に関しては、発光量の多い 630 nm 付近の発光寿命は、1 ms 程度とかなり長い。また、短波長側のピークに関しても、長波長側のピークよりは短寿命であるが、数 100 μs 程度あるため、エネルギーの高い中性子の検出には適さないと思われる。

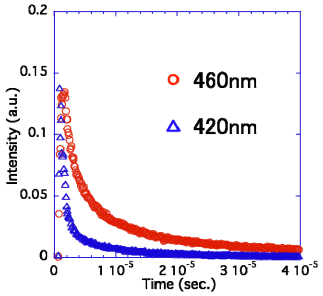

Fig. 2 The fluorescence lifetime of ZnS(Ag).

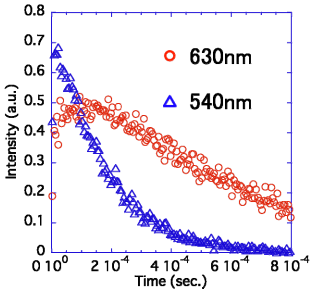

Fig. 3 The fluorescence lifetime of Y_2O_2S(Eu).

References

1) W. Kockelmann et al., Nucl. Instrum. Meth. A 578 (2007) 421-434.
2) 日塔光一 他、東芝レビュー Vol. 59 No. 10 (2004) 51-54.

4-24 Positron Beam Study on Vacancy Defects in GaCrN Grown by Molecular Beam Epitaxy

A. Kawasuso [a)], A. Yabuuchi [a)], M. Maekawa [a)], S. Hasegawa [b)], Y. Zhou [b)] and H. Asahi [b)]

[a)] Advanced Science Research Center, JAEA,
[b)] Institute of Science and Industrial Research, Osaka University

Vacancy defects in GaCrN grown by molecular beam epitaxy have been characterized by energy variable positron beam. Both positron lifetime and the Doppler broadening of annihilation radiation (DBAR) measurements show that the GaCrN film grown at 540 °C contains vacancy defects. The observed vacancy defects are identified as eight-vacancy clusters. Although the Si doping reduces such vacancy clusters probably due to the occupation of Ga sites, another type of vacancy defects still survives. From the detailed theoretical calculation, the residual vacancy defects are attributable to Si_{Ga}-V_N complexes.

GaCrN 混晶は、有望な希薄磁性半導体として精力的な研究がなされている。高温での CrN の相分離を回避するため低温成長が試みられている。しかし、低温成長条件では、空孔型欠陥の発生が問題となっている。空孔型欠陥の抑制手段として Si 添加が提案されているが、その効果は不明である。そこで本研究では、低温成長条件下で、無添加及び Si 添加 GaCrN を作製し、陽電子ビームによる空孔型欠陥の評価を行った。

化学気相成長法でサファイア基板上に成長した厚さ 2 μm の GaN 膜上に、分子線エピタクシー法により 700 °C で 40 nm のバッファ層を成長させた後、540 °C で GaCrN（Cr 濃度 0.7%）を約 500 nm で成長させ、最後に 4 nm の GaN キャップ層を 700 °C で成長させた。低速陽電子ビームを用いて、消滅ガンマ線のドップラー拡がり測定と消滅寿命測定を行った。Projector Augmented Wave 法 [1)]を用いて陽電子消滅特性の理論計算を行い、空孔型欠陥の同定に役立てた。

Figure 1 の黒丸は、低温（540 °C）で GaCrN 層を成長させた試料について得られた消滅ガンマ線ドップラー拡がりスペクトルの S パラメータの陽電子エネルギー依存性（SE 曲線）である。参照用として MOCVD 育成 GaN の SE 曲線を白丸で示している。無添加の場合、GaCrN 層に相当する陽電子打ち込みエネルギー（2-10 keV）の S パラメータが増大している。Si を添加すると、S パラメータの増大は大きく抑制されるが、依然として、参照 GaN 試料よりも高い値である。このように、低温成長条件下では、GaCrN 層に原子空孔型欠陥が導入されること、Si 添加により原子空孔濃度または種類が変化することが分かる。

上で観測された原子空孔型欠陥を同定するために、Fig. 2 に示すように、同時計数ドップラー拡がり測定を行い、理論計算と比較した。無添加の GaCrN の測定結果は、6 個から 12 個の原子空孔が集合してできたクラスターを想定することで説明できる。Si 添加した場合は、Si 原子と窒素空孔の複合体（Si_{Ga}-V_N）または窒素アンチサイトと窒素空孔の複合体（N_{Ga}-V_N）により説明できることが明らかになった。

Reference

1) P. E. Blöh, Phys. Rev. B50 (1994) 17953.

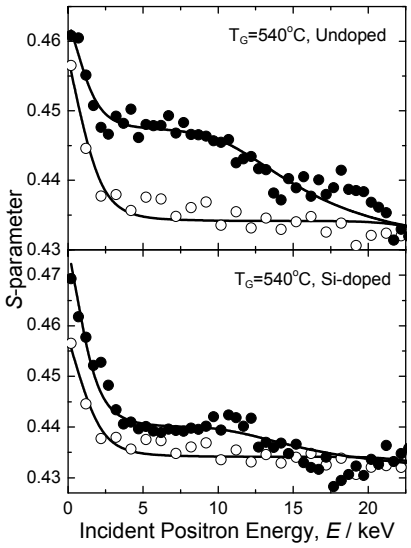

Fig. 1 S parameter of the Doppler broadening of annihilation radiation obtained for GaCrN films grown at 540 °C with and without Si doping as a function of incident positron energy.

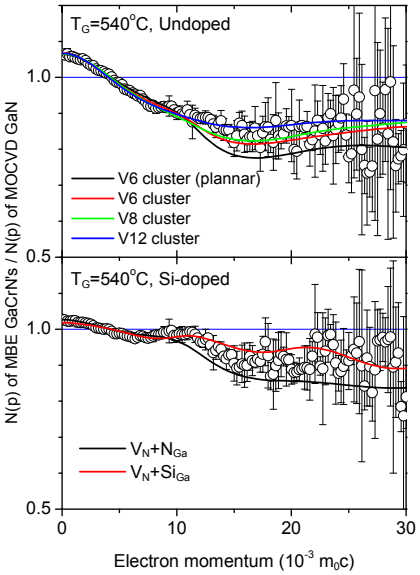

Fig. 2 The Doppler broadening of annihilation radiation spectra obtained for GaCrN films grown at 540 °C with and without Si doping. The incident positron energy is 8 keV.

4-25 Evaluation of the ZrC Layer for Coated Fuel Particles Probed by a Positron Microbeam

M. Maekawa [a)], A. Yabuuchi [a)], A. Kawasuso [a)] and J. Aihara [b)]

[a)] Advanced Science Research Center, JAEA,
[b)] Division of Fuels and Materials Engineering, NSED, JAEA

Zirconium carbide (ZrC) is known as a hard and strong material having a high melting point of 3,540 °C. The ZrC is one of the candidates of a coating material for a fuel particle of the Very High Temperature Gas-Cooled Reactor (VHTR) [1, 2]. The ZrC coating layer is formed by a chemical-vapor-deposition technique with a pyrolytic reaction of $ZrBr_4$, CH_4 and H_2 at around 1,500 °C. By transmission electron microscope (TEM) observations, many structural defects, such as carbon precipitates and/or microvoids, were found in the deposited ZrC layer. It is known that density of these defects changes drastically depending on the gas condition. However, detailed characteristics of defects and its behavior have not been fully elucidated. In this study, we attempt to evaluate open-volume type defects in the ZrC coating layer using a positron microbeam.

Figure 1 shows the cross-sectional optical image of the ZrC-coated particle. In this study, non-nuclear-surrogate particles which consist of a micro-spherical kernel of stabilized ZrO_2, carbon layer and ZrC layer were used. Table 1 shows the properties of samples. Although high C/Zr ratio increases the growth rate, density of structural defects also increases [3]. For the reference sample, commercial ZrC powder (Nilaco ZR-497201) was also measured. Doppler-broadening of annihilation quanta of the ZrC layer were measured and characterized by *S* and *W* parameters, which are defined as the peak and tail intensities, respectively. All the *S* and *W* parameters are normalized to the reference value. If defects exist and positrons are trapped to them, the *S* parameter increases and the *W* parameter decreases.

Figure 2 shows the correlation between *S* and *W* parameters for each sample. Measured *S* and *W* parameters of the sample with the lower defect density are closer to the value of the reference sample. This means that the density of structural defects observed by the TEM relates to density of the vacancy type defects. Figure 3 shows the *S* parameters as a function of C/Zr ratio. *S* parameter is increased with increase of carbon and finally seems to approach S ≈ 1.05. From a theoretical calculation, it is confirmed that the value was corresponds to a Zr vacancy in the ZrC crystal. By the heat treatment at 1,760 °C, *S* parameter decreased to 1.03; however, it did not reach to the reference value (1.00). This means that thermal annealing is not effective for recovery of the defects because of the high thermal stability of defects.

References

1) S. Ueta et. al., J. Nucl. Materials **376** (2008) 146.
2) T. Ogawa et. al., J. Am. Ceram. Soc. **75**(1992) 2985.
3) J. Aihara et. al., J. Am. Ceram. Soc. **92** (2009) 197.

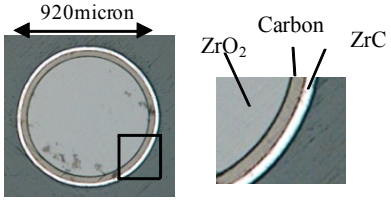

Fig. 1 Cross-sectional optical image of a ZrC-coated fuel particle.

Table 1 List of samples.

Sample name	CH4/ZrBr ratio	Growth rate (micron/h)	Density (g/cm^3)	Defect density
F1	2.12	21	6.01	large
F2	1.50	20	6.01	↑
F3	1.28	18	6.35	
F4	1.00	14	6.5	small

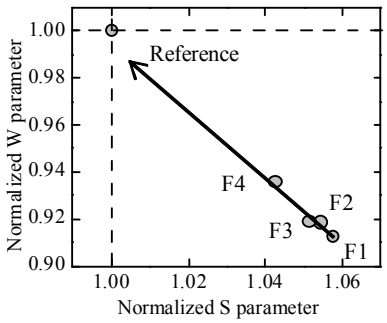

Fig. 2 S and W parameters for the each samples.

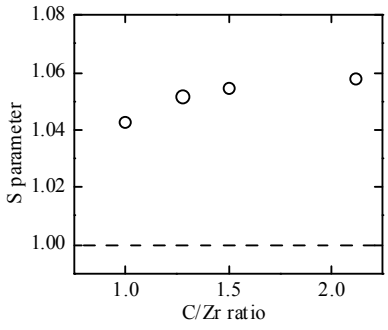

Fig. 3 S parameters as a function of C/Zr ratio.

4-26 Surface Structure of Si(111)-√21×√21-(Ag, Cs) studied by Reflection High-Energy Positron Diffraction

Y. Fukaya [a)], I. Matsuda [b)], A. Kawasuso [a)] and A. Ichimiya [a)]

[a)] Advanced Science Research Center, JAEA, [b)] The University of Tokyo

The Si(111)-√3×√3-Ag surfaces have been extensively investigated as a typical two-dimensional metal system [1)]. By the adsorption of small amounts of noble (Cu, Ag, and Au) and alkali (Na, K, and Cs) metal atoms on the Si(111)-√3×√3-Ag surfaces, the √21×√21 superstructures are formed, accompanied with a drastic increase in the surface electrical conductivity [1)]. The atomic coordinates of √21 × √21 superstructures have been studied experimentally and theoretically. In the case of the adsorption of noble metal atoms, we found that three noble atoms are situated at the center of large Ag triangles, surrounding the Si trimer [2)]. According to the scanning tunneling microscopy observations [3)], the alkali-metal-atom induced √21×√21 superstructure is considered to be different from the noble-metal-induced ones. In this study, we measured the rocking curve of reflection high-energy positron diffraction (RHEPD) from the Cs-induced √21 × √21 superstructure and analyzed the atomic height of Cs atoms by means of the dynamical diffraction theory.

The substrates (10 × 5 × 0.5 mm^3) were cut from a mirror-polished *n*-type Si(111) wafer with a resistivity of 1-10 Ωcm. To prepare clean 7 × 7 surfaces, they were heated at 670 K in several hours and flashed at 1470 K in a few seconds several times in an ultra-high vacuum (UHV) chamber with a base pressure less than 3×10^{-8} Pa. Then, 1.0 ML Ag atoms were deposited on the Si(111)-7 × 7 surfaces held at 740 K to form the √3×√3-Ag structures (1 ML = 7.83×10^{14} cm^{-2}). Finally, 0.14 ML Cs atoms were deposited on the Si(111)-√3 × √3-Ag surfaces at 230 K. The formation of well-ordered Si(111)-√21×√21-(Ag,Cs) surfaces was confirmed by reflection high-energy electron diffraction (RHEED).

The RHEPD measurements were carried out using a highly parallel and well focused positron beam generated from ^{22}Na positron source and electromagnetic lens. The positron beam energy was set at 10 keV. The diffraction patterns were magnified with a micro-channel plate with a phosphor screen and recorded with a charge-coupled-device camera. In the rocking curve measurements, the glancing angle of the incident positron beam was changed from 0.3° to 6.0° at a step of 0.1° by rotating the sample.

The open circles in Fig. 1 show the RHEPD rocking curve measured from the Si(111)-√21×√21-(Ag,Cs) superstructure at 170 K. The azimuth of the incident beam corresponds to 7.5° away from the [$11\bar{2}$] direction. Under this condition, the RHEPD intensity of specular spots is very sensitive to the atomic positions normal to the surface. In the total reflection region, two distinct dip structures are clearly observed at around 1.2° and 2.2°.

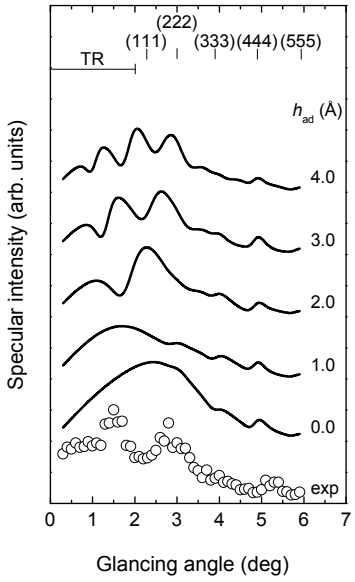

Fig. 1 RHEPD rocking curves from the Si(111)-√21 × √21-(Ag,Cs) superstructure. The open circles denote the experimental curve. The solid lines indicate the calculated curves using various heights (h_{ad}) of Cs atoms from the underlying Ag layer. TR stands for the total reflection region.

To determine the height of Cs atoms, we calculated the rocking curves based on the dynamical diffraction theory. The solid lines in Fig. 1 show the rocking curves calculated using various heights of Cs atoms from the underlying Ag layer. The shape of the curve drastically changes depending on the height of Cs atoms. From the comparison between the measured and calculated curves, the optimum height of Cs atoms from the underlying Ag layer was determined to be 3.04 ± 0.26 Å. The value is much larger than those of noble metal adsorptions (0.53-0.59 Å) [2)]. The atomic radius of Cs (2.67 Å) is much larger than that of noble metals (1.28-1.46 Å). It is considered that the large atomic radius leads to the large adsorption height. Consequently, we found that the adsorption height of Cs atoms is much higher than those of noble metals.

References

1) S. Hasegawa et al., Prog. Surf. Sci. **60** (1999) 89.
2) Y. Fukaya et al., Surf. Sci. **600** (2006) 3141.
3) C. Liu et al., Jpn. J. Appl. Phys. **42** (2003) 1659.

4-27 Structure Analysis of K/Si(111)-√3×√3-B Surface by Reflection High-Energy Positron Diffraction

Y. Fukaya, A. Kawasuso and A. Ichimiya

Advanced Science Research Center, JAEA

The K/Si(111)-√3×√3-B surface has been extensively investigated as a typical example of Mott-type insulating surfaces [1]. Recently, it has been reported that the K/Si(111)-√3×√3-B surface undergoes the phase transition from the √3×√3 to 2√3×2√3 surface at 270 K[2]. The electronic states of the Mott insulating surface have been studied in detail. In the experimental point of view, however, the atomic coordinates of the K/Si(111)- √3×√3-B surface still remain unresolved. In this study, to investigate the atomic coordinates of the Mott insulating surface, we measured the rocking curve from the K/Si(111)- √3×√3-B surface using a reflection high-energy positron diffraction (RHEPD). By means of the intensity analysis based on the dynamical diffraction theory, we determined the atomic heights of the K on Si(111)- √3×√3-B surface.

The substrates ($10 \times 5 \times 0.625$ mm^3) were cut from a mirror-polished highly B-doped Si(111) wafer. They were flashed at 1470 K a few times in an ultra-high vacuum (UHV) chamber with a base pressure less than 2×10^{-8} Pa. After the annealing at 1170 K, well-ordered √3 × √3 structure was formed. Subsequently, 1/3 ML of K atoms were deposited onto the Si(111)- √3×√3-B surface at room temperature (1 ML corresponds to the atomic density of 7.83×10^{14} cm^{-2}).

The experiments were carried out in the UHV chamber equipped with a positron source of ^{22}Na and electromagnetic lens system. The accelerating voltage of the incident positron beam was set at 10 kV. The diffraction pattern was enhanced using a micro-channel plate with a phosphor screen and taken with a charge-coupled-device camera. The glancing angle of the incident positron beam was varied from 0.3° to 6.0° at 0.1° step by rotating the sample.

Figure 1 shows the RHEPD rocking curve of specular spots from the K/Si(111)- √3×√3-B surface at 60 K. The incident azimuth corresponds to 7.5° away from the [$11\bar{2}$] direction (one-beam condition). Under the one-beam condition, the RHEPD intensity is very sensitive to the atomic coordinates perpendicular to the surface. The intense total reflection and 111 Bragg peaks are clearly observable. In the total reflection region, the dip structure at around 2.0° is also observed. Although in the previous study a 2√3×2√3 structure is observed below 270 K[2], the pattern still displays √3×√3 periodicity at 60 K. It is considered that the phase transition temperature is very sensitive to the defects on the surface[2].

We calculated the RHEPD intensity based on the dynamical diffraction theory. We optimized the atomic height of the K atoms so as to minimize the difference between the measured and calculated curves. The solid line indicates the calculated curve using the height of 1.99 ± 0.26 Å from the first Si layer. The calculated rocking curve is in good agreement with the measured one.

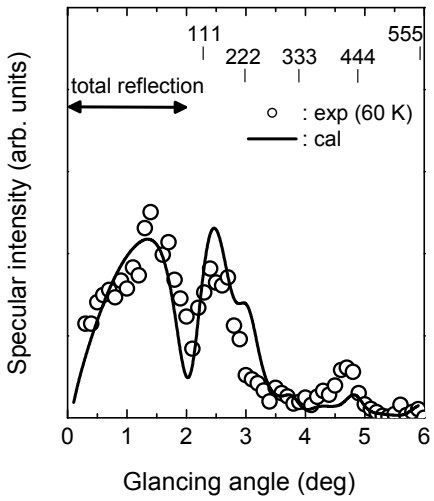

Fig. 1 RHEPD rocking curve of specular spots from the K/Si(111)- √3 × √3-B surface at 60 K. The open circles and solid line indicate the measured and calculated curves, respectively. The acceleration voltage of the incident beam is 10 kV. The incident azimuth corresponds to 7.5° away from the [$11\bar{2}$] direction (one-beam condition). The critical angle of the total reflection is estimated to be 2.0° via the Snell's equation.

According to the first principles calculations [3], the optimum heights of the K atoms at H_3 (threefold coordinated) and T'_4 (ontop) sites correspond to the 2.03 Å and 2.19 Å, respectively (see Fig. 2). The height of 1.99 Å obtained in this study is close to the theoretical value at H_3 site [3]. Therefore, it is considered that the K atoms are situated at the H_3 site. The adsorption of the K atoms at H_3 site is energetically favored theoretically [3].

References

1) H. H. Weitering et al., Phys. Rev. Lett. **78** (1997) 1331.
2) L. A. Cardenas et al., Phys. Rev. Lett. **103** (2009) 046804.
3) H. Q. Shi et al., Phys. Rev. B **70** (2004) 235325.

4-28 Radiation-induced H_2 Production and Reactions of OH Radical in Aqueous Solutions Containing Ceramic Oxides

Y. Kumagai, R. Yamada and R. Nagaishi

Division of Environment and Radiation Sciences, NSED, JAEA

Influence of coexistent solid ceramic oxide on radiation-induced reactions and their final products in aqueous solutions has been reported especially on the molecular hydrogen (H_2) production [1]. The mechanism of influence in the heterogeneous system, however, is still to be investigated in order to understand the radiation effect on water in contact with solid oxides. In the present studies, the dose rate dependence of the H_2 production and the reaction of OH radical in reduction process of dichromate ion ($Cr_2O_7^{2-}$) in the presence of ceramic oxides were conducted.

The samples were aqueous solutions containing ceramic oxides. Irradiation experiments were carried out at JAEA-Takasaki using ^{60}Co γ-ray source. The absorbed dose was measured by the CTA-film dosimeter or the dichromate chemical dosimeter.

Dose rate dependence of H_2 production

The sample for the H_2 production measurement is aqueous 0.4 mol·dm^{-3} (≡ M) sulfuric acid (H_2SO_4) solution containing 33 wt.% of alumina particles. After irradiation, produced gas was analyzed by gas chromatography. As references H_2 from aqueous solution only and pure water were also measured.

In the presence of alumina particles, the yield of H_2 depended clearly on the dose rate in the range of our experiment (0.08 – 20 kGy/h). The results are shown in Fig. 1. The yield became higher with increasing the dose rate. For the reference samples, no significant change in the yield was observed.

The peculiar dose rate dependence and the high yield of H_2 in the presence of alumina particles suggest that H_2 is produced through a reaction pathway induced by the addition of alumina particles besides the intra-spur reactions of water radiolysis. In the intra-spur reactions, the yield of H_2 is 0.047 μmol·J^{-1} and should have no dose rate dependence in this dose rate range of γ-irradiation.

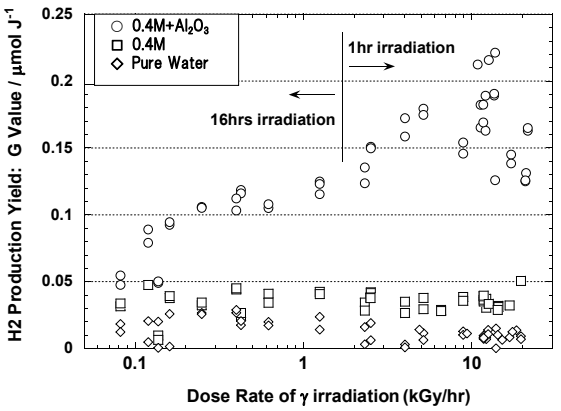

Fig. 1 Dose rate dependence of H_2 production yield in 0.4 M H_2SO_4 solution containing 33 wt.% of alumina (○), 0.4 M H_2SO_4 solution (□), and pure water (◇).

OH radical reaction in $Cr_2O_7^{2-}$ reduction process

The sample for the reaction of OH radical is aqueous 0.1 M perchloric acid ($HClO_4$) solution of 1 mM potassium dichromate ($K_2Cr_2O_7$) containing 9.1 wt.% of silica gel saturated by nitrogen. Silver perchlorate ($AgClO_4$) was added to the samples as an OH radical scavenger. After irradiation the concentration of $Cr_2O_7^{2-}$ in supernatant separated from the samples was measured by UV-Vis spectroscopy.

The observed reduction yields in the presence and absence of silica gel are shown in Fig. 2. The difference between the yields of these two series also shown in Fig. 2 indicates the addition effect of silica gel. The difference decreased with increasing concentration of Ag^+ and then seemed to reach a plateau.

The effect of silica gel increasing the reduction yield of $Cr_2O_7^{2-}$ was partially inhibited by the addition of silver ion (Ag^+). This suggests that, because scavenging of OH radical in this concentration range of Ag^+ occurs from 0.1 to 1 μs after the energy deposition, coexistence of silica gel has influences on both the chemical and earlier physicochemical stages of radiation-induced reactions, which divided at around 0.1 μs after the energy deposition by radiation.

Reference

1) R. Yamada et al., Int. J. Hydrogen Ener. 33 (2008) 929.

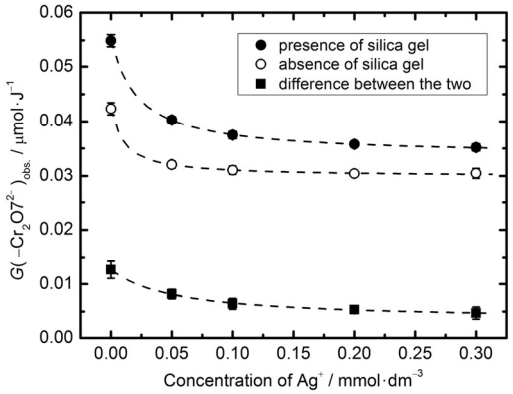

Fig. 2 Observed yield of $Cr_2O_7^{2-}$ reduction in the presence (●) and absence (○) of 9.1 wt.% of silica gel in 0.1 M $HClO_4$ solution as a function of concentration of Ag^+. Decrease of the deference of these two (■) indicates that Ag^+ inhibited the addition effect of silica gel.

4-29 LET Effect on the Radiation Induced Polymerization of Maleimide

S. Nakagawa [a)], M. Taguchi [b)] and K. Hirota [b)]

[a)] Tokyo Metropolitan Industrial Research Institute,
[b)] Environmental and Industrial Materials Research Division, QuBS, JAEA

Maleimide was irradiated in N_2-saturated 2-propanol solution with 220 MeV C-ion, 100 and 50 MeV He-ion, and 20 MeV proton beams from the AVF cyclotron in the TIARA Facility. LET effect on the radiation induced polymerization of maleimide was studied. When the 0.5 mol/L maleimide solution was irradiated, fine particles at the average degree of polymerization of 18 were produced. Though efficiency of polymer formation decreased, the relative ratio of polymers with higher molecular weight increased with heavier ion irradiation. Efficiencies of degradation of maleimide and polymer formation became 1.5 times higher, when the dose rate was 1/10 times lower.

マレイミド（$C_2H_2(CO)_2NH$）は、光化学重合反応の開始剤として研究が行われてきた。また、マレイミド類をアルコール溶媒中（>0.02 mol/L）で放射線照射したところ、溶媒ラジカルが付加した化合物が生成することがわかった[1,2]。しかし、低濃度での照射ではラジカルによる溶媒からの水素引き抜き反応が速いため、主な生成物はモノマーであり、ダイマーの生成効率は低い。そこで、0.1 mol/L 以上の高濃度溶液を重イオン照射した時の、ポリマー生成の効率を比較検討する。この結果により、活性種密度を制御して、ポリマー生成効率を制御するための知見が得られると期待される。

マレイミドを 2-プロパノールに溶かし（0.15 mol/L, 0.5 mol/L）、窒素置換した試料に、C イオン（220 MeV）, He イオン（100 MeV）,プロトン（20 MeV）を照射し、生成物の分子量分布をゲルパーミエーションクロマトグラフ（GPC）で分析した。分析試料は、真空乾燥した残留物をテトラハイドロフランで溶解したものを用いた。

0.15 mol/L 溶液では、マレイミドが 2〜8 分子程度まで重合した化合物が中心であったが、0.5 mol/L 溶液では、マレイミド 18 分子程度が重合したポリマーの微粒子が生成した（Fig. 1）。また、生成するポリマーの GPC スペクトル形状は、照射した放射線の種類によらず同じ傾向が見られた。

0.15 mol/L 溶液に C イオン及びプロトンを照射した時のマレイミド（n=1）とポリマー（n=2, 4, 6, > 8）の GPC スペクトルのピーク面積を Fig. 2 - 3 に示す。照射線量が増加し、マレイミドの濃度が減少すると、高分子ポリマーの生成効率が減少する。LET の高い重いイオン照射ほど、マレイミドの減少効率は小さいが、高分子ポリマーの生成割合は大きい。また、He イオン照射においてイオン電流を 1/10 にしたところ、マレイミドの減少効率及びポリマーの生成効率が約 1.5 倍に増加した。

これらの結果から、マレイミドのポリマー生成には、高濃度であること、溶媒ラジカルの生成濃度が高すぎないことが重要であると推測される。

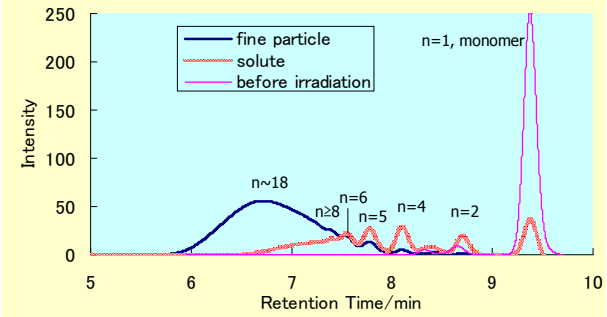

Fig. 1 GPC spectra before and after irradiation of 0.5 mol/L 2-propanol solution by 20 MeV proton.

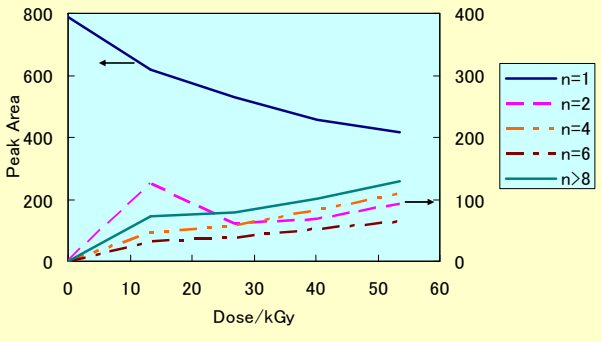

Fig. 2 The dependence of the dose and the yield of polymer irradiated by 220 MeV C-ion.

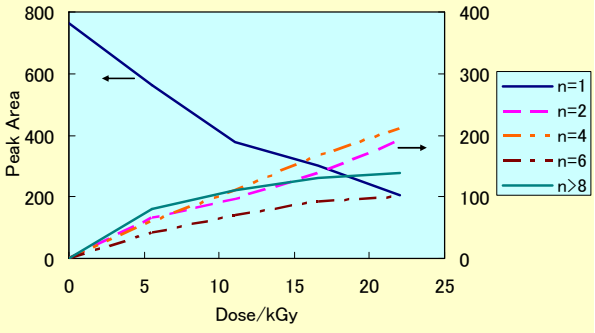

Fig. 3 The dependence of the dose and the yield of polymer irradiated by 20 MeV proton.

References

1) S. Nakagawa, Radiat. Phys. Chem. 79 (2010) 705.
2) S. Nakagawa et al, Radiat. Phys. Chem. 79 (2010).

4-30 Observation of Heavy Ion Induced Transient Species in Water by Spectroscopic Technique

M. Taguchi [a], Y. Sugo [b], S. Kurashima [c], A. Kimura [a] and K. Hirota [a]

[a] Environment and Industrial Materials Research Division, QuBS, JAEA,
[b] Division of Fuels and Materials Engineering, NSED, JAEA,
[c] Department of Advanced Radiation Technology, TARRI, JAEA

Introduction

High energy heavy ions induce unique irradiation effects, which are differ from those induced by low LET radiations, such as γ-rays or electron beam. These effects are induced by reactions of reactive species generated heterogeneously and densely around its trajectory in medium, and used as a new tool for the various basic and application studies for material and biological sciences. We decide water samples as a first target because it is the main component of living body, and radiation-induced reactions in water are well understood under low LET radiation. Hydroxyl(OH) radical is the most important species for reactions in water samples because of its high reactivity and formation yield. In a previous paper [1, 2], we decided experimentally the formation yield of the OH radicals depending on the mass and energy of incident ions, and elapsed time just after irradiation. However, in order to understand the chemical reactions in the track in more detail, a time resolved spectroscopy is a good approach for observing radical behaviors. We constructed the highly sensitive transient absorption measurement system using pulsed heavy ions from AVF cyclotron [3]. The reactions caused by the OH radical were observed by using this measurement system.

Experimental

The aqueous sample solution was poured into the metallic cell and irradiated with the pulsed heavy ions in the atmosphere, and optical absorbance was measured in online. The number of heavy ions included in the pulse was evaluated by reading the electric charge received by Faraday cup that had been set in the vacuum in the upper-stream of the irradiation cell. The fine structure of the pulse was also evaluated by measuring the luminescence from a scintillator set at the sample position. The semiconductor light source or Xe lamp was used as a probe light source. The probe light passed the sample cell twice at the angle of 20 degree toward the beam axis by mirrors above and under the sample cell, and then was detected with Si photodiode. The cell has the thickness of 2 mm and 50-μm glass windows on the top and bottom for preventing energy loss of the heavy ions and optical measurement.

Results and discussion

The absorption spectrum, which has a peak in the visible region by the heavy ion irradiation to aqueous potassium thiocyanate (KSCN) solution, was observed. This absorbance was assigned to $(SCN)_2^-$ from spectrum structure. The well-known reaction between the OH radical and SCN^- under low LET radiation is also observed by the heavy ion irradiation. In order to investigate energy or LET effects on radical behaviors, the incident energy was controlled by putting thin aluminum foils on the irradiation cell. Since H ion has 4 mm range in water, the absorbance measurements could be carried out for reactions occurred in the distinguished region, for example, plateau (○) and Bragg peak regions (◇) as shown in Fig. 1. The yield of the OH radical was estimated from the absorbance peak of $(SCN)_2^-$ just after the pulsed heavy ion irradiation. The yield in the Bragg peak region was a fraction of that in the plateau region, and this LET dependence could be explained in terms of the track structure theory.

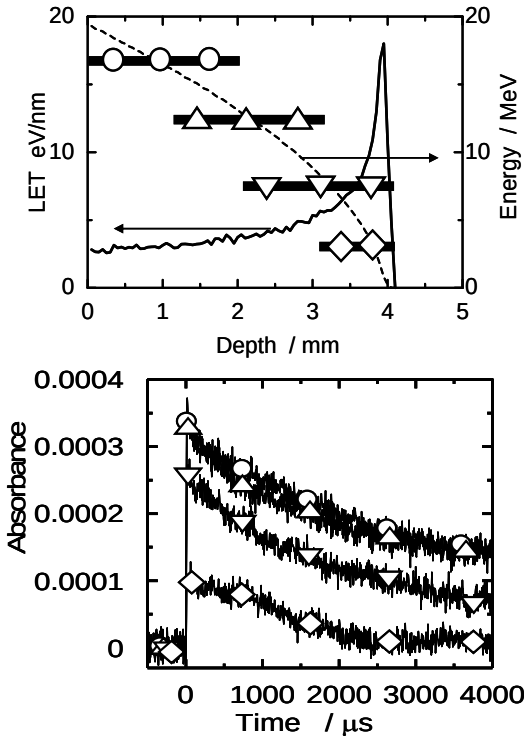

Fig. 1 Depth curves of energy and LET value of H ion in water(upper), and time profiles of absorbance at 447 nm for aqueous KSCN solution at each depth(lower).

References

1) M. Taguchi et al., Radiat. Res. 171 (2009) 254-263.
2) G. Baldacchino et al., Chem. Phys. Lett. 468 (2009) 275-279.
3) M. Taguchi et al., Radiat. Phys. Chem. 78 (2009) 1169-1174.

4-31 Stabilization of Measurement System of the Heavy Ion Beam Pulse Radiolysis Using Scintillator

T. Kondoh [a)], J. Yang [a)], K. Kan [a)], Y. Yoshida [a)], H. Shibata [b)], S. Kurashima [c)] and M. Taguchi [d)]

[a)] ISIR, Osaka University, [b)] Faculty of Engineering, Kyoto University,
[c)] Department of Advanced Radiation Technology, TARRI, JAEA,
[d)] Eenvironment and Industrial Materials Research Division, QuBS, JAEA

An ion-beam pulse radiolysis system with scintillators is being developed at TIARA facility to measure the initial process of ion-beam induced reactions in the microscopic tracks. This ion pulse radiolysis system had some problems that the measured light intensity was very unstable and the fluctuation could not be compensated by the reference. Therefore, the intensity of signal light was stabilized and the optimization of measuring the reference was carried out in last year.

イオンビームを用いたがん治療など応用技術が、近年発展し、注目されている。これらは、高LET放射線である重イオンビームが、物質に入射した時の局所的高密度励起の効果を応用したものであり、今後の発展には、局所的高密度励起と後続の反応過程を解明する必要がある。パルスラジオリシスは、パルス的に照射した放射線により物質中に生成した活性種を光吸収などで観測する手法であるが、イオンビームの場合、エネルギー付与の空間構造の特異性などから測定システムの構築は非常に困難である。さらに、高密度励起により生成した活性種は、高速に反応するため、これを解明するにはナノ秒程度の時間分解能が必要である。我々は、シンチレータをビーム軸上の試料直前に置き、イオンビームによるシンチレータの発光を分析光として、試料中の高密度励起による活性種の光吸収を測定する方法を開発している。この手法では、分析光源と励起場所がイオンビームの飛跡上なので、トラック内の活性種測定と高時間分解能を同時に実現できる。サイクロトロンの重イオンビームは、通常数10ナノ秒のパルス間隔のため化学反応の観測は困難であるが、PチョッパーとSチョッパーを同時に高度に制御することにより、220 MeV C^{5+}イオンビームのシングルパルス化に成功した。

HYポートに輸送されたビームは、サンプルセル上に設置されたシンチレータを通過した後、試料に入射して停止する。シンチレータ発光のうち試料を通過した光がフィルターで分光され光電子増倍管で検出される。光吸収測定には、それぞれの試料について光源光強度、照射時信号光強度、ビームノイズ、バックグラウンドの四つのデータが必要である。これまで、試料を変更する毎、更に一つのデータ取得中でも信号光強度が変動する問題があった。平均強度と位置の安定性が高いサイクロトロンのビームであるが、シングルパルス切り出し条件下では、ビーム強度や位置の変動が信号光に影響していると考え、試料を通過しないシンチレータ発光を測定し、光源光強度のリファレンスとして補正を試みたが、成功しなかった。この原因は、試料液面、サンプルセル、シンチレータの配置に独立性と再現性が低く、リファレンスが光源変動を反映していない事が原因と考えられる。

この問題を解決するために、今年度は測定体系の安定化対策を行った。改良した測定装置体系をFig. 1に示した。従来の体系における測定の再現性の欠如は、縦型セルとシンチレータの非独立積層型配置が原因と考えられる。各素子の直線的配置はそのままに、石英サンプルセルを横向きに使用し、フリッパーマウントに固定することにより光路長は正確に一定となり、独立かつ再現性の高い配置に変更した。また、シンチレータはコリメーター下に固定し、フリッパーマウントにより独立かつ再現性高く設置した。コリメーター下流に設置することによりコリメーターを通過したイオンビームのみがシンチレータを発光させるのでリファレンスは正確に信号光を反映する。安定化対策の後、光源変動補正のために、リファレンス測定配置の最適化を行った。CaF_2（Eu）シンチレータを用い、信号光強度とリファレンス光強度の間の相関をFig. 2に示した。信号光強度とリファレンス光強度には比例関係があり、最適化した配置ではリファレンスによる光源光強度の補正が可能となった。

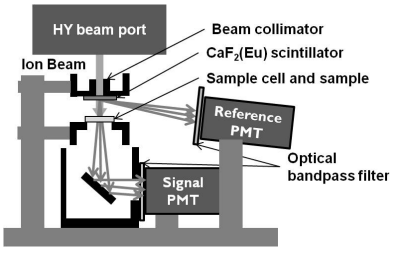

Fig. 1 New stabilized measurement system of the heavy ion beam pulse radiolysis using scintillator with reference measurement.

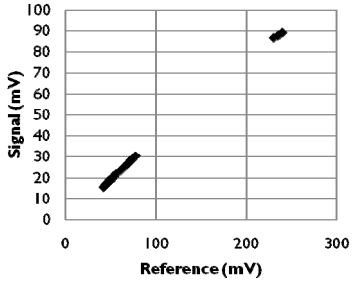

Fig. 2 Correlation between the signal (vertical axis) and the reference (horizontal axis).

4-32 Development of a Head Module for Multi-Head Si/CdTe Compton Camera System

M. Yamaguchi [a, c], T. Kamiya [a], T. Satoh [a], N. Kawachi [b], N. Suzui [b], S. Fujimaki [b], H. Odaka [c, d], S. Ishikawa [c, d], M. Kokubun [c], S. Watanabe [c, d], T. Takahashi [c, d], H. Shimada [c], K. Arakawa [a, e], Y. Suzuki [f], K. Torikai [e], Y. Yoshida [e] and T. Nakano [e, f]

[a] Department of Advanced Radiation Technology, TARRI, JAEA, [b] Radiation-Applied Biology Division, QuBS, JAEA, [c] Institute of Space and Astronautical Science, JAXA, [d] Department of Physics, University of Tokyo, [e] Gunma University Heavy Ion Medical Center, Gunma University, [f] Graduate School of Medicine, Gunma University

For the mainstream imaging techniques in the field of life science research like PET or SPECT, simultaneous imaging of multiple nuclei is difficult because the energy of the measurable gamma ray is specific or in a restricted energy range. We are constructing a three-dimensional imaging system for life science applications as a device that can provide simultaneous imaging, having high spatial and energy resolutions and wide energy range from several tens of keV to a few MeV, applying the most advanced space-observation technology, Si/CdTe semiconductor Compton camera, developed at ISAS/JAXA [1]. The Si/CdTe Compton camera was developed under the assumption of use at moderate temperature and the analog ASIC for signal processing. Moreover, because its solid and thin scattering layer allows close placement of the measured object, good angular resolution corresponds to good spatial resolution directly. These aspects allow construction of compact medical system.

In contrast to space-observation use, three-dimensional imaging ability becomes important for life science research. In order to achieve a good three-dimensional spatial resolution, modularizing the Compton camera into a small camera head, which parmits multi-angle imaging with multi-head structure, is required[2]. In this work, a head module has been developed as a prototype module of the multi-head system. Figure 1 shows the inner circuit of the prototype module. The upper part is layer of front end cards including Si/CdTe detectors and analog ASIC's. The bottom part contains DC voltage transform circuits and digital signal transform circuits. The plate in the middle part is a heat sink. Sensor and circuit modules are closely arranged and put in a compact vacuum-insulating cylindrical housing having a height of 24 cm and a diameter of 22 cm. Each of camera heads will be fixed on robot arms to adjust the position and the direction. Performance evaluation test was made for the prototype module with a sealed Ba-133 point-type source. The source was put at two positions in the measurement. We confirmed that the resultant image was almost consistent with the source positioning (see Fig. 2). The angular resolution measure was estimated to be 4.5 degrees.

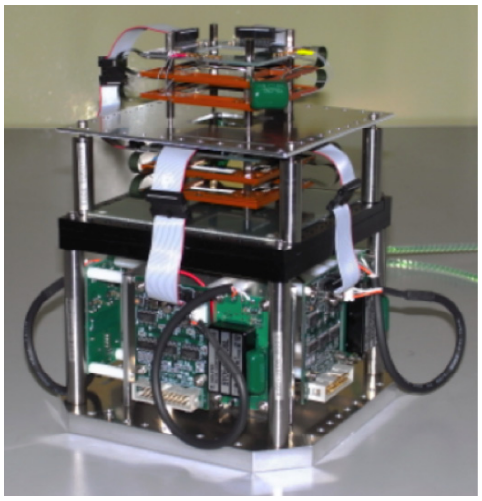

Fig. 1 A picture of the internal circuit of the prototype module.

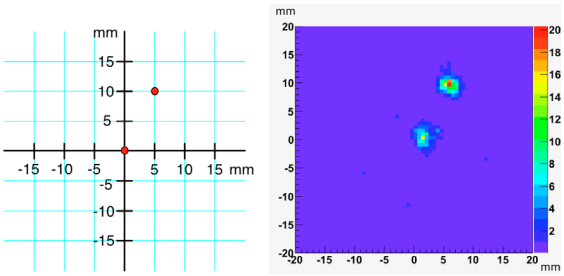

Fig. 2 A diagram of source position and the resultant image. Left diagram shows the source positions in the experiment. Red filled circles represent the source positions. During the experiment, the source was moved in two places. Right diagram represents the imaging result. The resulting image was almost consistent with the source positioning.

References

1) T. Takahashi, Exp. Astron. 20 (2006) 317-331.
2) M. Yamaguchi, et al., IEEE Nucl. Sci. Symp. Med. Imaging Conf. Record 2008, 4 (2009) 4000-4002.

4-33 Systematic Measurement of Neutron and Gamma-ray Yields on Thick Targets Bombarded with 18 MeV Protons

M. Hagiwara [a)], T. Sanami [a)], Y. Iwamoto [b)], N. Matsuda [b)], Y. Sakamoto [b)], Y. Nakane [c)], H. Nakashima [c)], K. Masumoto [a)], Y. Uwamino [d)] and H. Kaneko [e)]

[a)] Radiation Science Center, KEK, [b)] Division of Environment and Radiation Sciences, NSED, JAEA, [c)] Safety Division, J-PARC, JAEA, [d)] Nishina Center for Accelerator-Based Science, RIKEN, [e)] Department of Advanced Radiation Technology, TARRI, JAEA

Nuclear data on proton-induced neutron and γ-ray production in the energy range from 10 to 20 MeV is important to execute the shield design and to estimate activation of low-energy accelerator facilities for medical use such as production of radiopharmaceuticals in positron emission tomography (PET) and a neutron source of an accelerator-based boron neutron capture therapy (BNCT). A number of cyclotrons are installed in medical facilities to produce positron emission radioisotopes such as ^{18}F through the ^{18}O(p,n)^{18}F reaction for label tracers used in PET. The ^{9}Be(p, n) reaction is one of possible neutron sources used in an accelerator-based BNCT. These nuclear reactions simultaneously produce neutrons and γ-rays, and neutrons severely activate the accelerator components and the cyclotron room. The energy and angular distribution of neutrons should be estimated for radiation safety as well as clearance of the facility decommission.

However, the experimental data on the energy and angular distribution for neutron and γ-ray production are very scarce especially for proton energies from 10 to 20 MeV. Currently, shielding of the neutrons and γ-rays as well as activation of accelerator components and the room wall are calculated by using calculation codes such as PHITS [1)] and MCNPX [2)]. The accuracy of the codes for such a low energy region should be checked by experimental data, because most of physical models implemented in the codes were developed to describe reactions of high-energy particles. In this report, we describe the measurement of neutron and γ-ray energy spectra from various targets (^{9}Be, ^{nat}C, ^{27}Al, ^{nat}Cu and ^{181}Ta) induced by protons, and comparisons between the experimental data and calculation results.

The experiments were carried out with 18 MeV proton beams delivered to the HB-1 beam line at the AVF cyclotron of TIARA. The targets are installed in a vacuum chamber. The NE213 organic liquid scintillators (5.08 cm in diameter and 5.08 cm in length) were placed in directions of 0, 15, 30, 45, 60, 90, 120 and 150° at a distance of 2.0 - 4.0 m from the target to measure the light outputs by neutrons and γ-rays, and the time-of-flight (TOF). The events of neutrons and γ-rays were separated by using a pulse shape discrimination technique and these energy spectra were analyzed by the TOF method and the unfolding method with FERDOU code [2)], respectively. Figure 1 and 2 show the typical neutron energy spectra with comparison between measured and calculation results using MCNPX with ENDF/B-VII data library and implemented physical models (Bertini + Dresner model) for beryllium, and using PHITS with LA150 data library for aluminum. The calculation results generally well reproduce the measured energy spectra.

We will continue systematic measurements of neutron and γ-ray spectra from accelerator components induced by lower energy proton bombardment to check the accuracy of evaluated data libraries and calculation codes.

References

1) H. Iwase et al., J. Nucl. Sci. Tech. 39 (2002) 1142.
2) M. B. Chadwick et al., Nucl. Sci. Eng. 131 (1999) 293.
3) K. Shin et al., Nucl. Tech. 53 (1981) 78.

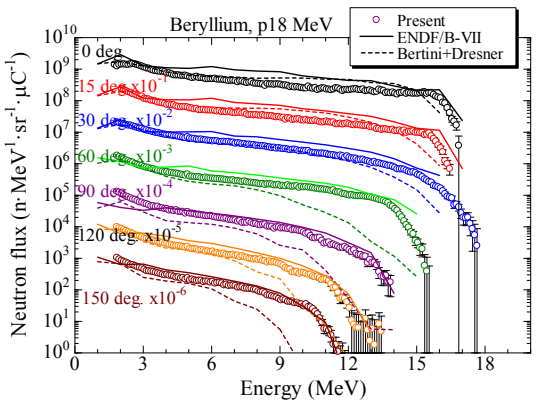

Fig. 1 Energy spectra of neutrons from thick beryllium target induced by 18 MeV proton bombardment.

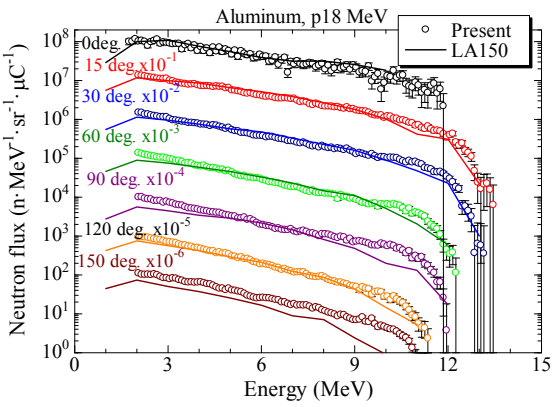

Fig. 2 Energy spectra of neutrons from the aluminum target induced by 18 MeV proton bombardment.

4-34 Establishment of Neutron Fluence Monitoring Techniques for Quasi-monoenergetic Neutron Calibration Fields of High Energy at TIARA

Y. Shikaze [a)], Y. Tanimura [a)], J. Saegusa [a)], M. Tsutsumi [a)], Y. Uchita [a)], M. Yoshizawa [a)], H. Harano [b)], T. Matsumoto [b)] and K. Mizuhashi [c)]

[a)] Department of Radiation Protection, NSRI, JAEA, [b)] National Metrology Institute of Japan, National Institute of Advanced Industrial Science and Technology, [c)] Department of Advanced Radiation Technology, TARRI, JAEA

The neutron standard fields above 20 MeV have not been established in Japan. Therefore, the calibration fields have been developed by using the quasi-monoenergetic neutron irradiation fields with 45, 60 and 75 MeV peaks at TIARA [1-3)] of Takasaki Advanced Radiation Research Institute, Japan Atomic Energy Agency. Establishment of the neutron fluence monitoring techniques was needed for use of the calibration fields. Several works were performed for the establishment as described below.

Firstly, the transmission type neutron fluence monitor[4)] was developed with a thin plastic scintillator and two photomultiplier tubes on both sides of the scintillator to monitor the neutron fluence directly. The performance test results indicated enough sensitivity and good stability of the sensitivity within ±2.7, ±1.7 and ±1.3% for the three neutron fields with 45, 60 and 75 MeV peaks, respectively.

Secondly, a user-friendly counting system was developed with PC card type fast counters (Interface CSI-632106) for the neutron fluence and beam current monitoring in calibrations and experiments. The counting system consists of the scaler and the multi-channel-scaler (MCS). The scaler is used to record the monitor counts and the integrated beam current for each measurement. The MCS is used to record time variation of them during the irradiation time. The MCS is useful to know stability of the beam and monitors, and may help off-line analysis. The incoming data are displayed by the software on the Windows PC screen (Fig. 1). The obtained data are recorded in the Microsoft Excel formatted files.

Thirdly, the calibration procedure of the neutron fluence monitor for each experiment was decided. The neutron fluence, Φ is obtained from

$$\Phi = k_{fm} \times C_{fm}, \quad (1)$$

where k_{fm} and C_{fm} are the conversion factor and the fluence monitor counts. However, the gain of the fluence monitor may slightly change every experiment although the fluence monitor shows good stability during beam time of one experiment. Therefore, the k_{fm} must be evaluated every experiment. To evaluate the k_{fm}, the ^{232}Th fission chamber with very stable gain and ease of use was employed as a standard. The conversion factors of the fission chamber, k_{fc} had been evaluated from the absolute measurements using the proton recoil counter telescope[5)]. The k_{fc} were found to be 1.63×10^8, 1.22×10^8 and 1.14×10^8 [n/sr/(fission chamber count)] for the three neutron fields with 45, 60 and 75 MeV peaks, respectively. Using the correlation with the fission chamber, the k_{fm} can be obtained from

$$k_{fm} = k_{fc} \times R_{(fc/fm)}, \quad \ldots(2)$$

where $R_{(fc/fm)}$ is the count ratio of the fission chamber to the fluence monitor. As the fluence monitor is stable during an experiment, reliable monitoring of the neutron fluence was realized by the calibration procedure.

In conclusion, the development of the neutron fluence monitor, the counting system and the calibration procedure established the neutron fluence monitoring techniques with good usability. The monitoring techniques together with the precise evaluation of the neutron fluence by the absolute measurement contributed to the establishment of the neutron calibration fields of high energy at TIARA.

References

1) M. Baba et al., Nucl. Instrum. Meth. Phys. Res. A 428 (1999) 454.
2) Y. Shikaze et al., Radiat. Prot. Dosim. 126 (2007) 163.
3) Y. Shikaze et al., J. Nucl. Sci. Tech. Suppl. 5 (2008) 209.
4) Y. Shikaze et al., JAEA Takasaki Ann. Rep. 2008 (2009) 152.
5) Y. Shikaze et al., Nucl. Instrum. Meth. Phys. Res. A 615 (2010) 211.

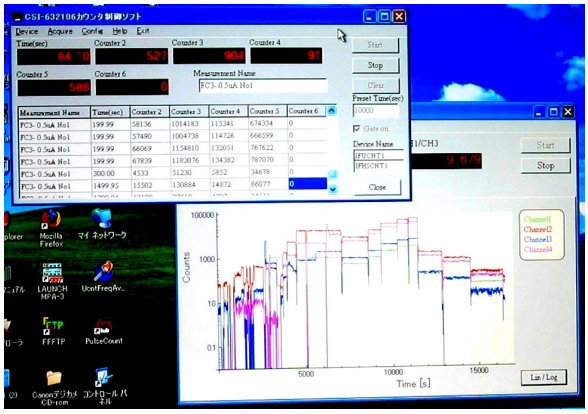

Fig. 1 The counting system for the neutron fluence and beam current monitoring. The scaler (upper left) and the multi-channel-scaler (lower right) are displayed.

4-35 Measurement of Neutron Fluence in the Comparison between TIARA and CYRIC High Energy Neutron Facilities

T. Matsumoto [a)], H. Harano [a)], A. Masuda [a)], Y. Unno [a)], M. Hagiwara [b)] , T. Sanami [b)], J. Nishiyama [a)], Y. Shikaze [c)], Y. Tanimura [c)], M. Yoshizawa [c)], M. Baba [d)] and K. Mizuhashi [e)]

[a)] National Metrology Institute of Japan, National Institute of Advanced Industrial Science and Technology, [b)]High Energy Accelerator Research Organization,
[c)] Department of Radiation Protection, NSRI, JAEA, [d)]CYRIC, Tohoku University,
[e)] Department of Advanced Radiation Technology, TARRI, JAEA

Precise measurement for high energy neutrons is important in studies on nuclear data, exposure in aircrafts, neutron induced soft error rate in semiconductor devices and the neutron dose estimation around large accelerator facilities such as J-PARC. High energy neutron fields at cyclotron facility TIARA and CYRIC are promising candidate for reference fields in order to calibrate measurement devices. However, each facility has different characteristics for the neutron field and adopts different methods for high energy neutron measurements. Therefore, comparison studies are currently being conducted between these two facilities.

In TIARA experiments, 45 MeV quasi-monoenergetic neutrons were produced from the ^{7}Li(p,n) reaction. The neutron fluence were measured with several neutron detectors, 5"×5" and 3"×3" NE213 liquid scintillators[1)], proton recoil telescope (PRT)[2)] and a spherical ^{3}He proportional counter with a spherical moderator made of polyethylene and lead[3)]. In the measurements, we used a transmission type plastic scintillator developed by JAEA as a neutron monitor. The plastic scintillator was set in the neutron flight path between the neutron source and the detector. The results of the detector with the moderator were extracted from detection efficiency and neutron spectrum obtained from the TOF measurement with the NE213. The lower energy limit in neutron spectrum measured with the TOF method is determined by repetition rate of the proton beam from the accelerator and the flight path length. The spectral component below the limit needs to be given by the extrapolation or another method of measurement. In the experiments, we obtained the spectral component below the limit with a ^{3}He loaded multi-moderator spectrometer (Bonner sphere spectrometer) that was located 12.9 m away from the neutron source. The moderators are composed of polyethylene, lead and copper. Detection efficiency for each moderator of the spectrometer is obtained from calculation with the MCNPX simulation code and experimental results measured in monoenergetic neutron fields with energy range from 100 keV to 15 MeV in AIST. Figure 1 shows low energy component in the 45-MeV neutron field obtained with the Bonner sphere spectrometer by means of an unfolding method. Experimental results for peak neutron fluence in the 45-MeV quasi monoenergetic neutron field obtained with each detector are given in Table 1. The experimental results for each detector were normalized with counts observed with the plastic scintillator. The results are in good agreement within 10 %.

The low energy component in the quasi monoenergetic neutron field will be observed with other detectors such as a sandwich spectrometer. We will also try to derive the neutron fluence and to investigate the low energy component for 60 or 75 MeV neutron field. Moreover, the results for the 45 MeV neutrons will be compared with those obtained at CYRIC.

References

1) M. Baba et al., Nucl. Instrum. Meth. Phys. Res. A 428 (1999) 454.
2) Y. Shikaze et al., Nucl. Instrum. Meth. Phys. Res. A 615 (2010) 211.
3) B. Wiegel and A. V. Alevra, Nucl. Instrum. Meth. Phys. Res. A 476 (2002) 36.

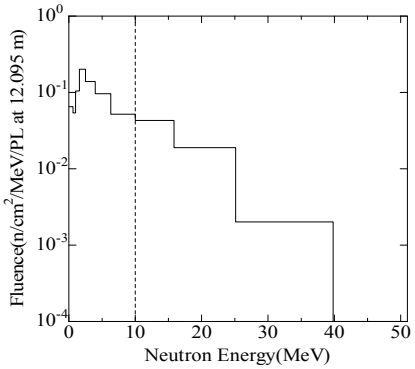

Fig. 1 Low energy component in the 45-MeV quasi monoenergetic neutron field measured with the Bonner sphere spectrometer.

Table 1 Peak neutron fluences (10^{6} n/sr/PL) in the 45 MeV quasi-monoenergetic neutron field derived from the two NE213 detectors, PRT and the spherical ^{3}He proportional counter with the moderator made of polyethylene and lead.

PRT	3"×3"NE	5"×5"NE	^{3}He
2.86	2.93	3.05	3.08

4-36 Study on High Energy Neutron Dosimetry Using Solid State Track Detector

T. Kosako [a], T. Iimoto [b], Y. Koike [c], T. Abe [a], M. Hirota [d], M. Mikhail [d], K. Shimada [d], C. Alexandre [d], Le Thiem Ngoc [d], Y. Setoguchi [d] and K. Tani [d]

[a] Nuclear Professional School, Graduate School of Engineering, The University of Tokyo,
[b] Division for Environment, Health and Safety, The University of Tokyo,
[c] Radioisotope Center, The University of Tokyo,
[d] Department of Nuclear and Management, School of Engineering, The University of Tokyo

Personal neutron dosimeters using Solid State Track Detector (CR-39) have been developed for use in workplaces of high-energy accelerator facilities. To improve sensitivity of these detectors for high energy neutrons above 10 MeV, a personal neutron dosimeter was newly designed using CR-39 covered with polyethylene and iron sheets. In the budget year of 2009, we examined the sensitivity of our developing personal dosimeter using the quasi-monoenergetic neutron field at the LC0 beam course of the TIARA cyclotron.

近年、J-PARC をはじめとした大型加速器施設が建設され、順次運転が開始している。このような施設での中性子は熱領域から GeV オーダーまでの幅広いエネルギースペクトルを持つ。その中でも人体の被ばく線量に寄与するのは主に 100 MeV 以下の成分である[1]。また、現在使用されている積算型中性子個人線量計には、CR-39 と呼ばれる固体飛跡検出器が用いられている。CR-39 は、ポリエチレンを陽子ラジエーターとして組み合わせることにより数 MeV の中性子に対して感度が増加するが、10 MeV 以上の中性子に対して感度が低下することが課題となっている。そこで本研究では CR-39 に組み合わせるラジエーターを工夫することにより、高エネルギー中性子に対する感度の増加を試みている。今年度は、TIARA サイクロトロンの LC0 ビームコースにおける準単色中性子場を用いて実験を行った。50, 68, 80 MeV の陽子を Li ターゲットに照射し、ピークエネルギーがそれぞれ約 45, 65, 75 MeV の準単色中性子を、鉄コリメータを通じて 2 層ラジエーターを装着した CR-39(Fig. 1)に照射した。CR-39 は水ファントム表面に設置し、鉄コリメータ正面から 68.5 cm の位置に固定した。準単色中性子を照射後、CR-39 に化学エッチング処理を施し、光学顕微鏡でエッチピット数を計数した。準単色中性子場は、Fig. 2 の様に中性子のエネルギースペクトルがピーク値だけでなく、ピーク値以下にも尾を引くように存在している[2]。45 MeV の中性子に対する各種ラジエーターの応答を得るために、ピーク値以外の中性子の影響を除く補正を行った。Fig. 3 に 45 MeV の中性子に対する 2 層ラジエーターの増感効果の鉄層の厚さによる変化の実験値と計算値を示す。計算値は PHITS を用いて 45 MeV 単色中性子を照射した条件で求めた。Fig. 3 より鉄の厚さが約 3 mm で極大を持つことがわかった。ポリエチレン層からの反跳陽子を 3 mm 厚の鉄で効率よく検出することが可能になることを実験と計算の両面から示した。

謝辞 本研究の遂行にあたり、JAEA 原子力基礎工学研究部門放射線防護 Gr グループリーダー遠藤章博士より多大な技術的支援をいただいた。ここに記して厚く御礼を申し上げます。

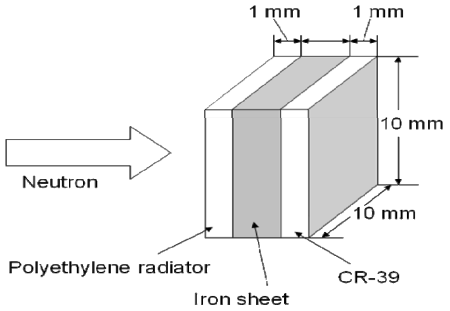

Fig. 1 Structure of CR-39 with two layer radiator.

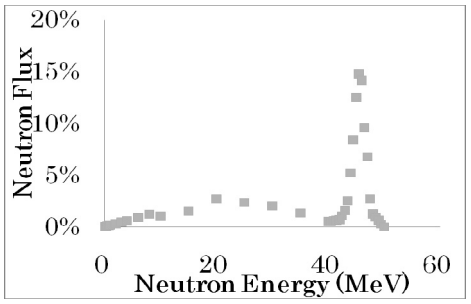

Fig. 2 ^{7}Li (p, n) source spectrum for 50 MeV protons[2].

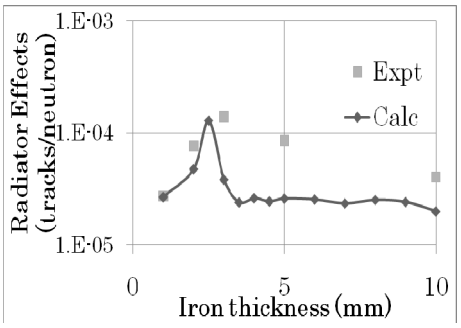

Fig. 3 Two-layer radiator effects for 45 MeV neutrons by changing iron thickness.

References

1) Y. Sakamoto et al., JAERI-Tech. 2001-042 (2001).
2) M. Baba et al., Nucl. Instrum. Meth. Phys. Res. A 428 (1999) 454.

4-37 Evaluation of the Response Characteristics of a Portable Cosmic-ray Neutron Monitor

H. Yasuda [a)], K. Yajima [a)] and A. Endo [b)]

[a)] National Institute of Radiological Sciences (NIRS),
[b)] Division of Environment and Radiation Sciences, NSED, JAEA

Introduction: Measurement-based dosimetry of cosmic radiation exposure is still difficult at high altitude because the radiation field in space and aviation is complex as the field comprises various particle species: protons, neutrons, heavy ions, electrons, photons, etc. In such fields, detector signals attributing to different radiation components are inseparably mixed.

Precise measurements of cosmic radiation usually need large detectors to determine particle species and energies. For example, cosmic-ray neutrons have been measured with proportional counters having thick moderators called "Bonner spheres". However, such bulky instruments are hardly employed for in-flight monitoring because of the space and power limitations. Liquid organic scintillators, which have been widely used for neutron/gamma separation in nuclear facilities, are not allowed in civilian aircraft mainly due to safety concerns.

Thus, we have started to develop a practical portable monitor which can measure cosmic radiation precisely in both spacecraft and aircraft.

Materials and methods: The monitoring system consists of a detector probe, a signal processing unit, a high-voltage supplier and a data analyzing program which runs on Windows PC. The detector probe, which can be flexibly replaced, is an original phoswich-type scintillation detector composed of cylindrical stillbene scintillator (special order product; Oyo-koken, Japan) with dimensions of ϕ50 mm × 50 mm covered with 15mm-thick plastic scintillator (EJ-299; Eljen Technology, USA). The decay time of scintillation from stillbene is 3.5 ns and that of the plastic scintillator is 320 ns. The probe is coupled with a 2-inch photomultiplier tube (R6041; Hamamatsu Photonics, Japan).

The phoswich scintillation probe gives different pulse shapes for different particle species; for example, long decay signal is unseen for energetic neutrons, whereas it is well recognized for charged particles. The pulse shape is analyzed with an original signal processing unit with dimensions of W150 mm × D150 mm × H50 mm. This unit has a flash ADC which converts an analogue signal (0 to 5 V, negative) from the detector probe to the digital data with 12-bit dynamic range from -20 to 400 ns from the trigger point at 2 ns intervals. The maximum processing rate is about 400 events per second. Signal voltage levels integrated for 2 ns each is transferred to a personal computer via USB2.0 interface. The total weight of the system is about 10 kg.

The characteristics of the monitor responses to cosmic-ray neutrons were partly examined using energetic neutron beams supplied at JAEA-TIARA. The responses to heavy charged particles were also examined using ~230 MeV protons and ~230 MeV/u helium ions at the Heavy Ion Medical Accelerator in Chiba (NIRS-HIMAC).

Results and Discussion: Figure 1 shows the results obtained with the vertical incident beams of 75 MeV neutrons in comparison with protons and helium ions. The X-axis of the graph is the signal integral from -20 to 50 ns (the trigger point is 0) and the Y-axis is that from 200 to 400 ns. According to the plot figure, it is considered that the newly developed monitor can detect neutrons and heavy charged particles separately. The good ability for separation between neutrons and γ-rays has already been confirmed for the stillbene scintillator.

It should be noted, however, a considerable incident angle dependence was observed, which is probably due to the physical feature of stillbene crystal and the cylindrical scintillator structure. Separation of muons and energetic electrons including calibration methods for those particles is the subjects in ongoing research. Determination of the precise energy spectra of cosmic-ray particles calls for further investigation.

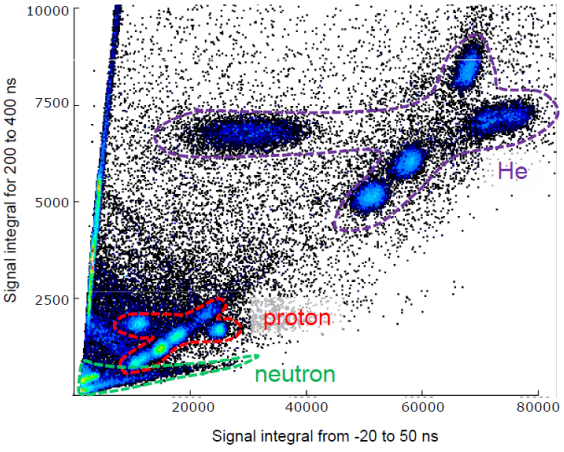

Fig. 1 Two dimensional plots of the scintillation signals integrated for different ROI ranges. The data obtained at TIARA using 75 MeV neutrons are seen in the left-lower part. The plots of neutrons were clearly separated from those of protons (~230 MeV) and helium ions (~230 MeV) obtained at NIRS-HIMAC.

Acknowledgments: The authors appreciate Dr. Yoshiaki Shikaze and other staffs of JAEA for their great help in neutron beam irradiation. A part of this study was supported by the Japan Space Forum / JAXA.

4-38 Dose Measurement for 110 keV Electron Beam

H. Seito [a)], S. Matsui [b)], T. Hakoda [a)], M. Ishikawa [b)], H. Hanaya [a)], Y. Haruyama [a)], H. Kaneko [a)], J. Kimura [b)] and T. Kojima [a)]

[a)] Department of Advanced Radiation Technology, TARRI, JAEA,
[b)] Hamamatsu Photonics K. K.

An electron beam (EB) generator of a few tens of keV is frequently used to hardening of printing ink and addition of the hydrophily for various materials. Thin radiochromic film dosimeters such as FWT-60, GAF and B3 are mainly used in low energy EB industrial processing [1)]. These dosimeters are calibrated for high energy EB or cobalt-60 gamma-rays[2)]. Consistency in dose evaluation for a few MeV electron and ten-hundred keV electron is still under discussion [3)]. This work aims to reveal consistency in dose response of film dosimeter between low and high energy EB.

The dosimetry study for 110 keV electron beams was performed at the EB generative machine called EB-ENGINE (Hamamatsu Photonics K. K). The machine is composed of electron source (filament), vacuum tube and irradiation chamber. Accelerated electrons traverse air through beryllium accelerator window. The distance from the window to the surface of film dosimeter was 40 mm as shown in Fig. 1. The dosimeters (FWT-60) were calibrated for 2-MeV electron and dose distribution in 110 keV electron beam irradiation field was evaluated by both the film dosimetry and Monte Carlo calculation code: PENELOPE. The absorbed dose distributions given by measurement and the calculation are compared in Fig. 2. The difference in dose between the measurement and calculation was found to be within ± 6 kGy. Such a difference is small, considering geometrical deviation in setting of film dosimeter. This fact suggests that calibration curve of FWT-60 film dosimeter for 2 MeV EB would be valid also for 110 keV EB. These results show that dose responses of FWT-60 film dosimeters are independent on electron energy.

As the next step, calorimetry was tested to check the film dosimetry results. A calorimeter with an aluminum absorber was designed. The calorimeter consists of mainly three parts; an absorber disk, a temperature sensitive sensor and an aluminum stage with three polycarbonate props to sustain the absorber disk. A cross section of the calorimeter is shown in Fig. 3. Energy fluence values measured by the calorimeter were slightly smaller than those estimated by the PENELOPE code calculation. The factor of this difference is under consideration. Application of calorimetry to 110 keV EB dosimetry needs to be discussed further.

References

1) ISO/ASTM 51275, 2004. Standard Practice for Use of a Radiochromic Film Dosimetry System. ASTM International, 100 Barr Harbor Drive, West Conshohocken, PA 19428-2959, USA.
2) ISO/ASTM 51261, 2002. Standard Guide for Selection and Calibration of Dosimetry System for Radiation Processing. ASTM International, 100 Barr Harbor Drive, West Conshohocken, PA 19428-2959, USA.
3) J. Helt-Hansen et al., Radiat. Phys. Chem. 74 (2005) 341.

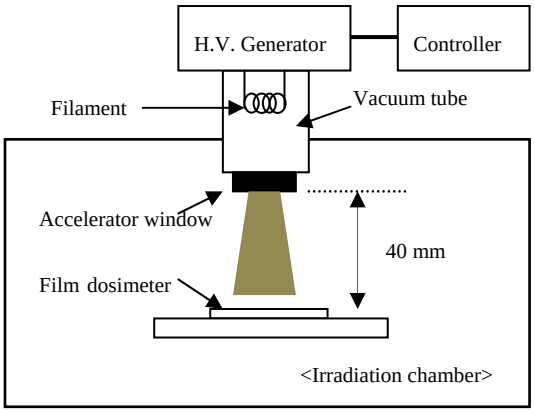

Fig. 1 Geometry of the irradiation set-up.

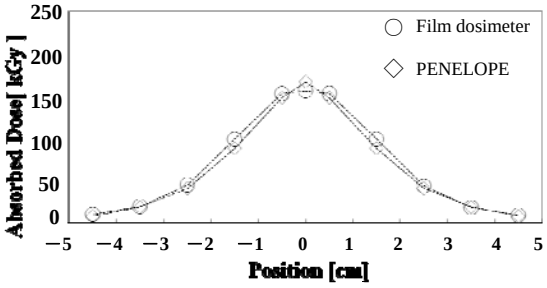

Fig. 2 Comparison of the dose distribution given by FWT-60 film dosimeter with that by PENELOPE calculation.

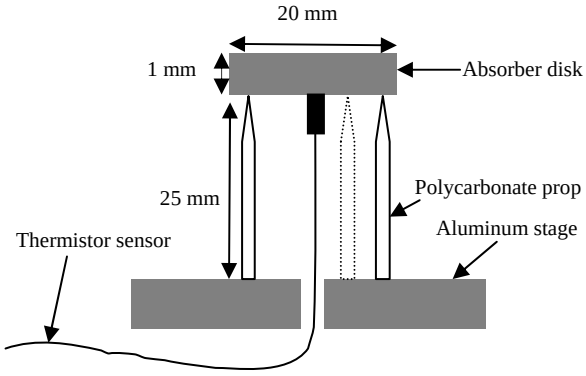

Fig. 3 Schematic drawing of the calorimeter.

4-39 Relationship between Internuclear Distance and Charge State of Constituent Ions Resulting from Foil-induced Dissociation of C_2^+ ions

A. Chiba [a)], Y. Saitoh [a)], K. Narumi [b)], Y. Takahashi [b)], K. Yamada [a)] and T. Kaneko [c)]

[a)] Department of Advanced Radiation Technology, TARRI, JAEA, [b)] Advanced Science Research Center, JAEA, [c)] Department of Applied Physics, Okayama University of Science

When a swift cluster ion penetrates a solid, the interactions between cluster constituent ions and electrons in matter give rise to the characteristic phenomena which never appear under a monatomic-ion irradiation due to the interference resulting from the spatiotemporal correlation among the closely spaced ions within the cluster, that is to say "vicinage effect". Since Brandt *et al.*[1] showed experimentally and theoretically that the energy loss per atom of a swift hydrogen cluster was different from that of a proton at the same velocity, the characteristic phenomena caused by the penetration of a heavy-atom cluster also have been frequently observed not only for the energy loss but also for the average charge state of constituent ions and for the secondly-particle emission from the target surface. These vicinage effects had been presented also theoretically by the several authors [2], and they have indicated that analysis of the charge state of the constituent ions inside matter is significant in the clarification of vicinage effect, because the interaction forces such as stopping power, wake force and Coulomb repulsion depend on the charge state of individual constituents in the cluster. The charge-state measurements of N_2^+ constituents penetrated to the various foil-thicknesses indicated that the vicinage effect in charge state gradually decreased with increasing internuclear distance due to the mutual Coulomb repulsion [3]. This fact means that the internuclear distance is extremely significant parameter for the precise evaluation in vicinage effect. Therefore, a measurement of the divergence angular distributions classified into the charge-state combination of constituent ions resulting from foil-induced dissociation of 6-MeV C_2^+ ions was carried out in order to investigate the relationship between the internuclear distance and the charge state of individual constituent ions.

The magnetically selected C_2^+ ion beam extracted from the tandem accelerator in the TIARA was pulsed and collimated by a beam chopper composed of a switching deflection plates and a pair of 0.1-mm-diam aperture, and penetrated an amorphous carbon foil of 0.5-μg/cm^2 thickness. The dissociated constituent ions from C_2^+ emerging from the foil were deflected depending on their charge state by an electric field applied to the deflection plates, and were detected by a micro-channel plate (MCP) equipped with fluorescent screen placed at 1.4 m downstream from the foil. The pictures of the luminance points on the MCP taken by a CMOS camera were saved event-by-event to the computer at the rate of approximately 50 frames per second. The divergence angle and the charge state of constituents were determined from an arrangement of a pair of luminance points on the MCP. An overall resolution of the divergence angle was less than 1.4×10^{-4} rad (FWHM).

In this experimental condition, the kinetic energy of constituent ions would be unaffected almost by the elastic collision with target nuclei. Therefore, when the incident spatial orientation of C_2^+ projectile at the foil surface is perpendicular to the beam direction, the divergence angle of these constituents would correspond to a peak value (θ_{max}) in the angular distribution geometrically because the electronic perturbation due to a wake force is negligible. Figure 1 shows the relationship between the charge-state combination $q_i \times q_j$ and θ_{max} for 6-MeV C_2^+ projectiles, where q_i and q_j are the charge state of dissociated *i*- and *j*-ion. The measured θ_{max} in each angular distribution classified into the charge state combination of constituent ions cannot be reproduced by the simple model calculation, which takes into account the interaction through a screened Coulomb repulsion. This consequence suggests that the final charge-state combination of constituents emerging from the foil depends on the initial internuclear-distance which is fluctuated due to a vibration excitation of C_2^+ ion, if this disagreement is resulting from an assumption that the initial internuclear-distance of all C_2^+ ions is an average value in this calculation.

References

1) W. Brandt et al., Phys. Rev. Lett. 33 (1974) 1325.
2) For example, T. Kaneko, Phys. Rev. A 66 (2002) 52901.
3) D. Maor et al., Phys. Rev. A 32 (1985) 105.

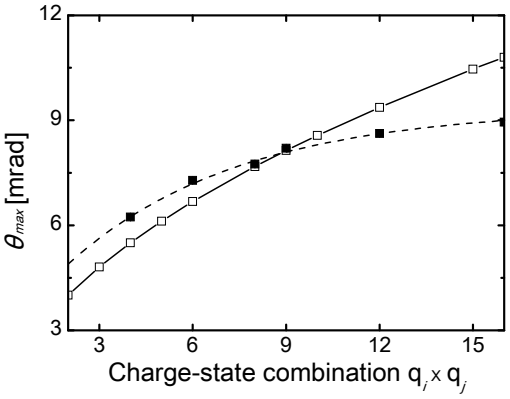

Fig. 1 Charge-state combinations $q_i \times q_j$ of dissociated ions resulting from impact of 6-MeV C_2^+ ions on 0.5-μg/cm^2 carbon foil, as a function of θ_{max}. The dashed and solid lines are fits to the experimental and calculated data, respectively.

4-40 Simultaneous Measurement of Secondary-electron Emission and Coulomb Explosion Imaging for 250-keV/u C_2^+ Ions Bombarded to Thin Carbon Foils

Y. Takahashi [a)], K. Narumi [a)], A. Chiba [b)], Y. Saitoh [b)], K. Yamada [b)], N. Ishikawa [a)], H. Sugai [a)] and Y. Maeda [c,a)]

[a)] Advanced Science Research Center, JAEA, [b)] Department of Advanced Radiation Technology, TARRI, JAEA, [c)] Department of Energy Science and Technology, Kyoto University

The origin of vicinage effect on secondary-electron emission induced by swift molecular ions or cluster ions is still an unresolved question although many studies have been performed. The secondary-electron emission under a swift monoatomic ion impact has been accounted for by a three-step process: *production* (excitation) of scattered electrons by the incident ion, *transport* of the scattered electrons in the solid, and finally, *transmission* of the scattered electrons through the surface barrier. It has been pointed out that the mechanism of the vicinage effect is mainly due to disturbance in the *transport* process by an electric potential induced by fragment ions [1)]. Under this mechanism, it is expected that the potential can strongly affect the *transport* process, and such influence may depend on the relative position of trajectories of fragment ions. In this study, we have measured the correlation between secondary-electron emission and relative position of fragment ions obtained from Coulomb explosion imaging for C_2^+ ions bombarded to thin carbon foils.

The swift C^+ and C_2^+ ions with the energies of 250 keV/u (3.2 v_0) and self-supporting amorphous carbon foils of 1.4, 2.8, 14.1 μg/cm^2 (70-700 Å) were used. The secondary-electron yield γ_n in the forward and backward directions from a carbon foil were measured simultaneously by two microchannel-plate (MCP) detectors. Fragment ions with different charge states transmitted through a foil were separated by electrostatic deflection plates, and detected as luminous points by an MCP detector equipped with a fluorescent screen. The orientational angle φ between the internuclear vector of a pair of fragment ions after the penetration of the foil and the beam direction was derived from the relative positions of the two luminous points. The $\gamma_2(\varphi)$ as a function of the orientational angle divided into three angular regions was obtained from the distribution of the number of secondary electrons for each orientational angle. We also measured γ_1 using C^+ ions with the same velocity. The orientation dependence of the vicinage effect was evaluated from the ratio of the secondary-electron yield $R_2(\varphi) = \gamma_2(\varphi)/2\gamma_1$. Appearance of the vicinage effect is presented as $R_2(\varphi) \neq 1$.

Figure 1 shows $\gamma_2(\varphi)$ in the backward and forward directions for the three foils with different thickness for a pair of outgoing C^{3+} - C^{3+} ions. The forward yield was larger when the internuclear vector of a pair of fragment ions was parallel to the beam direction than when it was perpendicular for the thinnest foil. No orientation dependence was observed for the other thicker foils in the forward direction and for all foils in the backward direction. The ratio $R_2(\varphi)$ for φ = 0-30º and φ=60-90º in the forward direction plotted as a function of the calculated internuclear distance between the fragment ions at the exit of the target is shown in Fig. 2. It indicates that the dependence vanishes at the internuclear distance of ~1.6 Å, although the vicinage effect in the *transport* process has been observed even for ~70 Å in this velocity [2)]. Hence, the present result indicates that there is little effect of the orientation in the *transport* process, and the orientation dependence observed in the forward direction for the thinnest foil could be attributed to the *production* process of electrons. No orientation dependence of the vicinage effect in the *transport* process was observed for the region of foil thickness used in this study. Therefore, it is conceivable that a response distance of the electric potentials induced by fragment ions is much larger than the transport length of electrons.

References

1) H. Arai et al., J. Phys. Soc. Jpn., 78 No. 10 (2009) 104301.
2) Y. Takahashi et al., Europhys. Lett. 88 (2009) 63001.

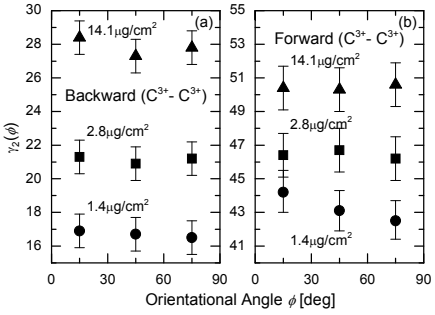

Fig. 1 $\gamma_2(\varphi)$ for (a) backward and for (b) forward emission for a pair of outgoing C^{3+}-C^{3+} ions from three foils.

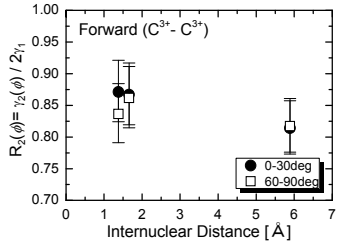

Fig. 2 Ratio $R_2(\varphi) = \gamma_2(\varphi)/2\gamma_1$ in the forward direction as a function of the internuclear distance.

4-41 Analysis of Radiation Damage at a Si Surface Bombarded with a Single 10-, 50- and 400-keV C_{60} Ion

K. Narumi [a)], H. Naramoto [a)], Y. Takahashi [a)], K. Yamada [b)], A. Chiba [b)], Y. Saitoh [b)] and Y. Maeda [a, c)]

[a)] Advanced Science Research Center, JAEA, [b)] Department of Advanced Radiation Technology, TARRI, JAEA, [c)] Department of Energy Science and Technology, Kyoto University

Bombardment effects of 10-to-100-keV C_{60} ions on a Si surface have been investigated in order to understand the unique sputtering phenomenon induced by C_{60}-ion bombardment: carbon build-up at the surface[1,2] and energy dependence of Si sputtering yield[3]. In this report, the volume affected by single-C_{60}-ion bombardment was evaluated by investigating C_{60}-ion fluence dependence of the areal density of disordered Si atoms.

Pieces of Si(100) wafer, which had been treated with a wet chemical method to remove an oxide layer and to reduce organic contaminants on a surface, were irradiated with 10- and 50-keV C_{60}^{+} and 400-keV C_{60}^{2+} ions from the 400-kV ion implanter of TIARA. The fluence of the C_{60} ion was 10^{11} to 10^{14} C_{60}/cm^2. After the irradiation, the number of disordered Si atoms was evaluated by Rutherford-backscattering spectrometry (RBS) using 2-MeV $^4He^+$ ions incident along a <100>-axial channel.

RBS spectra for Si samples irradiated with 400-keV C_{60}^{2+} ions are shown in Fig. 1. The number of Si atoms displaced from the lattice site can be determined by the integrated yield of a surface damage peak around 1.13 MeV. Obtained areal density of the disordered Si atoms is plotted as a function of C_{60}-ion fluence as shown in Fig. 2: The areal density increases with the fluence, then seems to reach a constant at a certain fluence.

In order to analyze the result, two conditions were assumed: 1) A volume affected by irradiation with one C_{60} ion is cylindrical, and 2) all Si atoms in the volume are displaced with the same probability from the lattice site.

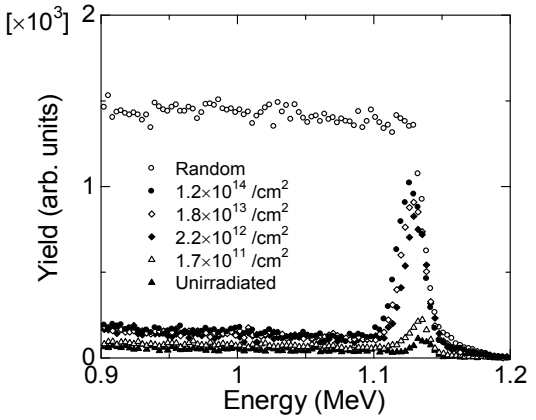

Fig. 1 RBS spectra for 2.0-MeV $^4He^+$ ions incident along a <100>-axial channel of Si samples irradiated with 400-keV C_{60}^{2+} ions. A random RBS spectrum is also shown.

The areal density N (/cm^2) of Si atoms displaced from the lattice site at the fluence ϕ (/cm^2) is given by,

$$N = b - (b - N_0)\exp(-a\phi), \qquad (1)$$

where a is the area of the cross section of the volume, b the upper limit of N, and N_0 the areal density of disordered Si atoms at an unirradiated surface, which could be caused by natural oxidation after irradiation. The obtained fluence dependence is reproduced well by eq. (1) as shown in Fig. 2, and the fitted parameters are listed in Table 1: The thickness of the disordered layer, which is the height of the volume, derived from b assuming the bulk density of Si is also shown as L. The results so far indicate that a and L of the volume affected by single-C_{60}-ion bombardment increase with the ion energy. Further analysis is in progress.

References

1) K. Narumi et al., JAEA Takasaki Ann. Rep. 2006 (2008) 166.
2) K. Narumi et al., JAEA Takasaki Ann. Rep. 2007 (2008) 175.
3) K. Narumi et al., JAEA Takasaki Ann. Rep. 2008 (2009) 163.

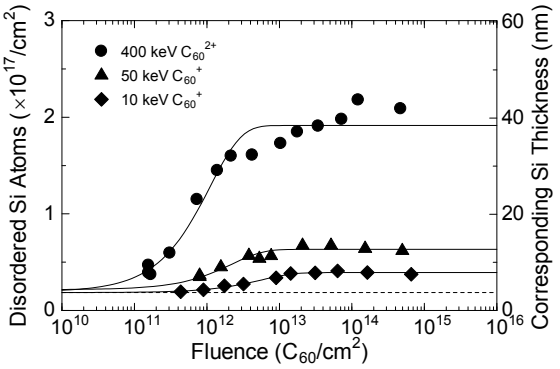

Fig. 2 Fluence dependence of areal density of disordered Si atoms. A broken line shows N_0. Results from fitting with eq. (1) are shown by solid lines. The right-hand ordinate shows Si thickness derived from the left-hand ordinate assuming the bulk density of Si.

Table 1 Fitting parameters in eq. (1) obtained from the results shown in Fig. 2.

Energy (keV)	a (nm^2)	b (/cm^2)	L (nm)
10	18	3.9×10^{16}	7.8
50	45	6.3×10^{16}	13
400	90	1.9×10^{17}	38

4-42 Effect of Au Cluster Ion Irradiation on Magnetic Properties of FeRh Thin Films

A. Iwase [a)], N. Fujita [a)], S. Kosugi [a)], Y. Saitoh [b)] and T. Matsui [a)]

[a)] Department of Materials Science, Osaka Prefecture University,
[b)] Department of Advanced Radiation Technology, TARRI, JAEA

Recently, we have found that energetic ion irradiation induces ferromagnetic state in Fe-53at% Rh alloy which intrinsically shows anti-ferromagnetic state. The irradiation induced magnetic transition is caused by the elastic interaction between irradiating ions and FeRh target[2)]. In this report, we show the effect of cluster ion irradiation on the magnetic state of FeRh thin films.

$Fe_{47}Rh_{53}$ thin films about 40 nm thick were irradiated with Au_1 ions and Au_3 cluster ions at room temperature by using a tandem accelerator at JAEA-Takasaki. Ion energies were 1.67 MeV for Au_1 ions and 5.0 MeV for Au_3 cluster ions. The fluences of Au_1 ions were 3×10^{11} Au/cm^2, 1×10^{12} Au/cm^2, and 3×10^{12} Au/cm^2. The fluences of Au_3 ions were 1×10^{11} Au_3/cm^2, 3.5×10^{11} Au_3/cm^2, and 1×10^{12} Au_3/cm^2. Before and after the irradiations, the magnetic hysteresis (M-H curves) was measured in a field range of -6 to 6 kOe at 20 K using a SQUID magnetometer.

Figure 1 shows the M-H curves for FeRh thin films irradiated with Au_1 ions. The magnetization of the FeRh films increases with increasing the ion fluence.

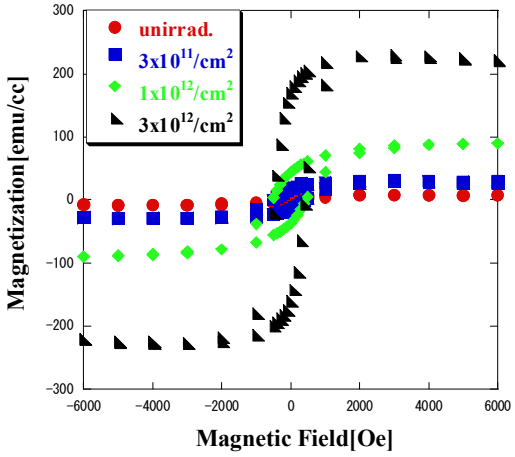

Fig. 1 M-H curves at 20 K for FeRh thin films irradiated with 1.67 MeV Au_1 ions.

Figure 2 indicates that a same trend can be observed in the effect of Au_3 cluster ion irradiation on M-H curves.

Figure 3 shows the value of saturation magnetization, Ms, as a function of the number of incident Au atoms. Even at the same number of incident Au atoms, the value of Ms for Au_3 cluster ion irradiation is larger than that for Au_1 ion irradiation. The present result implies that not only the total energy deposited through the elastic interaction but also the spatio-temporal overlapping of the interaction with each constituent atom of the cluster ions is important to understand the effect of cluster ion irradiation on the magnetic properties of FeRh alloy.

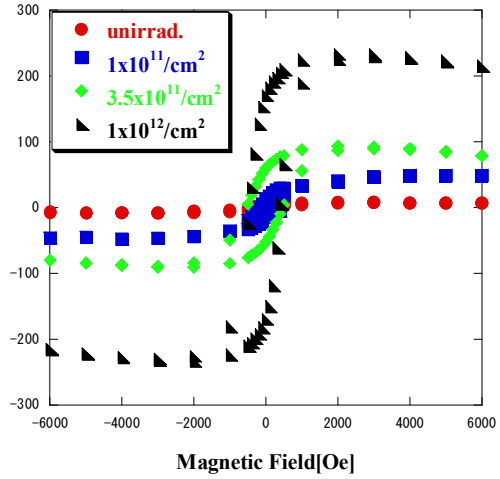

Fig. 2 M-H curves at 20 K for FeRh thin films irradiated with 5.0 MeV Au_3 cluster ions.

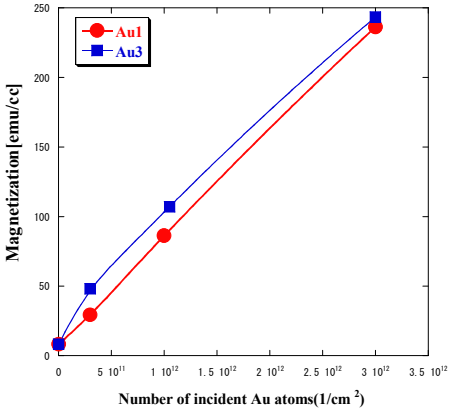

Fig. 3 Values of Ms as a function of the number of incident Au atoms for Au_1 and Au_3 cluster ion irradiations.

References

1) N. Fujita et al., Nucl Instrum. Meth. Phys. Res. B 267 (2009) 921-924.
2) N. Fujita et al., J. Appl. Phys. 107 (2010) 09^{E}302.
3) N. Fujita et al., Jpn. J. Appl. Phys. 49 (2010) in press.

4-43 Positive Secondary Ion Emission from PMMA upon Energetic C_8 Cluster and Mo Ion Impacts

K. Hirata [a)], Y. Saitoh [b)], A. Chiba [b)], K. Yamada [b)], Y. Takahashi [b)], K. Narumi [c)] and T. Kojima [b)]

[a)] National Institute of Advanced Industrial Science and Technology (AIST),
[b)] Department of Advanced Radiation Technology, TARRI, JAEA,
[c)] Advanced Science Research Center, JAEA

Secondary ions (SIs) are ejected from the surface when the primary ions bombard the target. Cluster ion impact on a target produces different SI emission yields compared with those for monoatomic ions because of their peculiar irradiation effects caused by simultaneous energy transfer from the constituent atoms of the cluster to a small area of the target surface. In this paper, we report comparison of SI emission yields from a Poly(methyl methacrylate) (PMMA) target for incident ion impacts of energetic cluster ions (0.8 MeV C_8^+, 2.4 MeV C_8^+, and 4.0 MeV C_8^+) and heavy monoatomic molybdenum ions (4.0 MeV Mo^+, and 14 MeV Mo^{4+}) with similar mass to C_8 ion by time-of-flight (TOF) SI mass analysis combined with SI electric current measurements.

SI emission yield measurements for PMMA were performed using a TOF mass analyzer combined with pulsed ion beams produced by a 3 MV tandem accelerator at the Japan Atomic Energy Agency (JAEA)/Takasaki [1)], which has been described elsewhere [2,3)]. For quantitative comparison of SI emission yields per incident ion impact, peak intensities of the TOF spectra were plotted by scaling the total count of each spectrum based on qI_s/I_o (q: incident ion charge number, I_o: incident beam electric current, I_S: positive SI current for each irradiation condition), respectively. I_o and I_s were measured by highly sensitive electrometers, respectively, connected to a Faraday cup and a movable metal plate with a grid, as described elsewhere [2)].

Figure 1 shows the positive SI TOF spectra from m/z (mass to charge ratio) = 58 to 72 of PMMA for (a) 0.8 MeV C_8^+, (b) 2.4 MeV C_8^+, (c) 4.0 MeV C_8^+, (d) 4.0 MeV Mo^+, and (e) 14 MeV Mo^{4+}, respectively. The major peaks observed in the figure can be attributed to $C_2H_3O_2^+$ (m/z=59) and $C_4H_5O^+$ (m/z=69), respectively. The total count of each spectrum was scaled based on qI_s/I_o for each irradiation condition in order to quantitatively compare the SI emission yields per incident ion impact among the spectra.

The relative SI emission yield per C_8 impact increases in the order of 4.0 MeV C_8^+ > 2.4 MeV C_8^+ > 0.8 MeV C_8^+. SI emission yields are influenced by energy transfer processes and their deposited energy densities around the impact-points. In an incident energy range of 0.1-0.5 MeV for C (corresponding to that of 0.8-4.0 MeV for C_8), the energies transferred by electronic and nuclear processes increases and decreases with increasing the incident energy, respectively, provided the transferred energies for a cluster ion with n identical atoms is n times that of a monoatomic ion with the same velocity. Considering that the relative SI emission yields are higher in the order of 4.0 MeV C_8^+, 2.4 MeV C_8^+, and 0.8 MeV C_8^+, the electronic energy transfer process dominantly contributes to the SI emission.

Comparison of the SI emission yields for the C_8 impacts with those for the Mo impacts reveals that the 4.0 MeV C_8^+ impact provides higher SI emission yields than the Mo ion impacts of not only for 4.0 MeV but also for 14 MeV. This shows that the higher SI emission yields are obtained with lower incident ion energy using cluster ions rather than swift heavy monoatomic ion. Energetic cluster ion impacts provide emission yields of the positive SIs of m/z=59 and 69 for PMMA more effectively than impacts of heavy monoatomic ion with similar mass to that of the cluster ion, which is advantageous for highly sensitive surface analysis using TOF SI mass analysis.

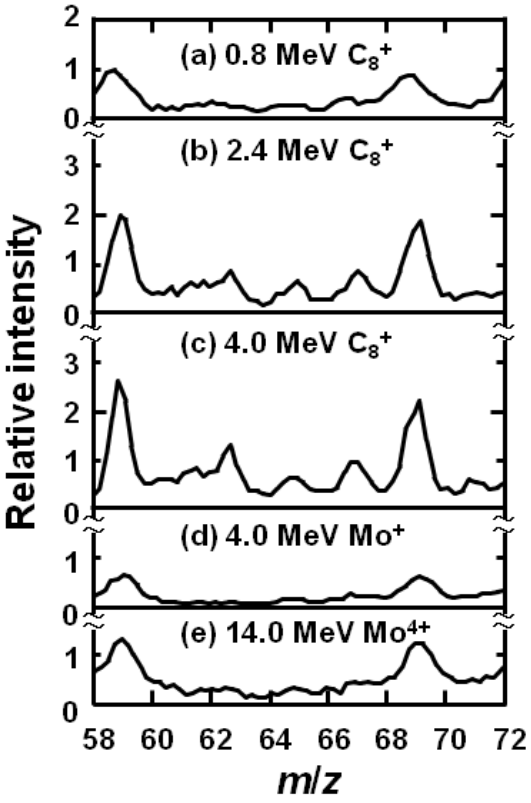

Fig. 1 Positive secondary ion TOF spectra of PMMA for (a) 0.8 MeV C_8^+, (b) 2.4 MeV C_8^+, (c) 4.0 MeV C_8^+, (d) 4.0 MeV Mo^+, and (e) 14 MeV Mo^{4+}. Peaks at m/z=59 and 69 are attributed to $C_2H_3O_2^+$ and $C_4H_5O^+$, respectively.

References

1) Y. Saitoh et al., Nucl. Instrum. Meth. Phys. Res. A **452** (2000) 61.
2) K. Hirata et al., Appl. Phys. Lett., **86**, (2005) 044105.
3) K. Hirata et al., Nucl. Instrum. Meth. Phys. Res. B in press.

4-44 Secondary Electron Emission from Carbon Induced by MeV/atom Carbon Cluster Bombardment

T. Kaneko

Department of Applied Physics, Faculty of Science,
Okayama University of Science

Sub-linear dependence of the secondary electron yield $\gamma(n)$ under the MeV/atom carbon cluster C_n^+ impact on the atom number (n) was theoretically investigated. In addition to the conventional three-step model, we newly included the electron disturbance in the electron transportation. The calculated result shows the relation of $\gamma(n)/\gamma(1) = 1 + a(n-1)$ and $a < 1$. This sub-linear dependence is in good agreement with the existing experimental data.

クラスターイオンを入射粒子とした種々の照射効果の研究が盛んである。この理由は、クラスターイオンを用いることで、クラスター構成粒子数とクラスターの空間構造という新たなビームパラメーターが加わったことによって、新たな知見が期待できるからである。最近、1 原子当たりに MeV 程度のエネルギーをもつ高速クラスターイオンを固体に照射して、100 eV 程度以下の低エネルギーの 2 次電子が放出される現象の研究が盛んである。陽子などの軽イオン入射では、この二次電子の収率はイオンの電子的阻止能に比例することが知られているが、クラスターイオン入射では、この関係が成り立たない。また、クラスターイオン入射での二次電子収率は、クラスターの構成粒子数の増加に対して線形よりも弱い依存性を示すことが報告された [1)]。この弱線形性は、入射クラスターの荷電状態とクラスターの空間構造によるものではないか、との指摘がなされた。この考えは、定性的一致を導いたものの、実験データを定量的に説明するには十分とはいえなかった [2)]。そこでわれわれは、(1) 入射粒子による標的電子の励起、(2) 励起された電子の出口表面までの伝播、(3) 励起電子の表面ポテンシャルの克服、という従来の 3 段階モデルに加えて、励起された電子の伝播過程で、それらが入射粒子によって邪魔されるのではないか、と考えて新たなモデルを構築した [3)]。

標的物質の電子系のモデルとして電子ガスモデルを採用した。この系の励起モードには個別電子励起と集団励起（プラズモン励起）が存在する。プラズモン励起には有限の寿命を仮定した。これらの励起は動的誘電関数によって記述される。一方、入射粒子であるクラスターイオンは、速度に依存した統計的電子分布をもつ個別イオンの集まりとして記述した。初期の核間距離はボーア半径の 2.4 倍、すなわち 0.127 nm に定めた。計算結果を図に示す。Fig. 1 は、C_n^+ (n=1 - 4) クラスターイオンが炭素標的に照射されたときの二次電子収率 $\gamma(n)$ を、同速の炭素イオン C^+ 照射に対する相対値で表わしたものである。図中で、正方形■と菱型◆は、それぞれ、入射エネルギーが 0.15 MeV/atom と 0.50 MeV/atom のときである。これらを関数関係 $\gamma(n)/\gamma(1) = 1 + a(n-1)$ と表わすと、前者では $a = 0.25$、後者では $a = 0.39$ となった。これらは明らかに線形依存性よりも弱いことを示している。この結果は、$0.2 \le a \le 0.4$ という実験データとよい一致を示している。

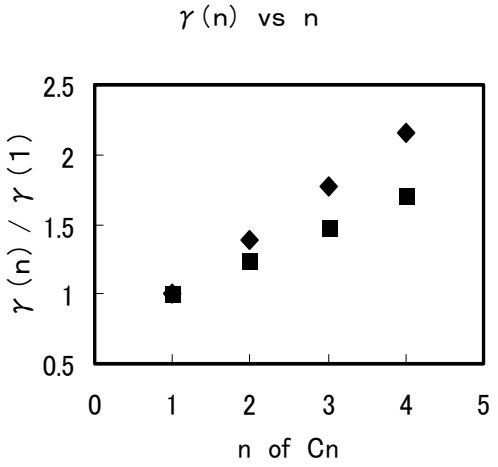

Fig. 1 Dependence of $\gamma(n)/\gamma(1)$ on the number of particles for the incident energy of 0.15 MeV/atom (■) and 0.50 MeV/atom (◆).

References

1) H. Kudo et al., Vacuum 84 (2010) 1014-1017.
2) T. Kaneko et al., J. Phys. Soc. Jpn. 75 (2006) 034717.
3) T. Kaneko et al., Fifth International Workshop on High Resolution Depth Profiling (2009).

4-45 Ion Induced Luminescence from Sapphire Irradiated with Swift Cluster Ion Beams

H. Shibata [a)], Y. Saitoh [b)], A. Chiba [b)], K. Yamada [b)], Y. Takahashi [c)], K. Narumi [c)], T. Kojima [b)] and T. Kamiya [b)]

[a)] Graduate School of Engineering, Kyoto University, [b)] Department of Advanced Radiation Technology, TARRI, JAEA, [c)] Advanced Science Research Center, JAEA

The luminescence spectra from sapphire (α-Al_2O_3) induced by 0.5-1.5 MeV/atom carbon cluster ion irradiation were measured in the wave length range of 250−800 nm as a function of ion fluence at room temperature. The luminescence was observed at 326 nm (F^+ center) and 411 nm (F center) in any cluster irradiation. Result shows sub-linear feature for cluster size dependence.

高速（高エネルギー）クラスターイオンと物質との相互作用においては、単原子イオンの集合体として個数以上、あるいは個数以下の非線形的な効果を与えることが知られている。これまでに二次イオン粒子放出に関する高速クラスターイオン照射の特徴を調べ、主に電子励起が起きるエネルギー領域ではクラスターサイズが大きくなるとともに正負二次イオンの収量が指数的に増えることがわかったが、これは表面付近での化学反応によるものと考えている。このように標的表面の分子吸着の状態に強く依存する現象を避けるため、標的の照射損傷のみに依存すると考えられる発光を測定し、クラスターイオンの照射効果を調べるのが本研究の目的である。2009 年度は炭素クラスターイオンとサファイア（α-Al_2O_3）標的との衝突で放出される発光を、時間分解マルチチャンネル分光器（Hamamatsu Photonics PMA11）で測定したので報告する。

本実験に用いたクラスターイオンは日本原子力研究開発機構高崎量子応用研究所 TIARA の 3 MV タンデム静電加速器からのエネルギー 0.5 ～ 1.5 MeV/atom（42～126 keV/u）の C_1^+～C_8^+イオンで、照射野は 3 mmφ、ビーム電流は C_1^+で 2.5 nA、C_8^+で 40 pA 程度である。試料には発光強度が強く、発光過程が比較的良くわかっているサファイアを選んだ。

発光スペクトルの測定波長範囲は 250～800 nm で、326 nm 及び 411 nm に発光が見られる。326 nm は F^+センターからの発光で、発光強度はイオンビーム照射と同時に次第に増加し、ピークに達してから少しずつ減衰する。411 nm は F センターからの発光で、これもビーム照射と同時に次第に増加し、ピークに達してから、326 nm よりも早く減衰していく。ピークに達するまでの照射量を比較すると、いずれの発光もクラスターサイズが大きくなるほど少ない照射量で最大発光量に達する。

Fig. 1 は F^+中心 rd の発光量についてクラスターイオンサイズの依存性を調べたものである。発光量には時間依存性があるので、本実験では発光量が最大に達する点での発光収量を比較することにした。0.5 MeV/atom C_1^+イオン照射下の F^+中心の発光収量を 1 として、0.5 MeV/atom クラスターイオンの発光収量に対する比を図に示した。図から発光量の比はクラスターサイズに比例して増加しており、その比例係数は約 0.9 であった。クラスターサイズに対応して線形的に増加した場合、比例係数は 1 なので、この場合はサブリニアな関係になっている。つまり F^+中心を形成する照射欠陥はクラスターサイズに比例して増加するが、クラスターの個数倍よりは若干少ない量で最大値に達する。

クラスター効果を記述する量として、n 個のクラスターイオンの反応収量 I_n を 1 個当たりの反応収量を n 倍したものとの比をとったもの（I_n= I(n) / nI(1)）がよく使われる。例えば阻止能（S = -dE/dx）では R_n= S(n) / nS(1) と表される。

図中の Theory というのはクラスターを一つの融合した原子と考えて阻止能の R_n を計算したもので、標的の種類に依存せず入射クラスターの種類と速度にのみ依存する。図には nR_n の値を図示した。図から分かるように阻止能の理論値は 0.5 MeV/atom エネルギーではサブリニアな関係を示し、クラスターサイズに対し線形的な依存性にはない。実際のクラスターの阻止能は融合した原子の阻止能と線形的な阻止能との間にあるので、実験値に近い値となり、照射損傷による発光と阻止能とは良い相関があると示唆される。

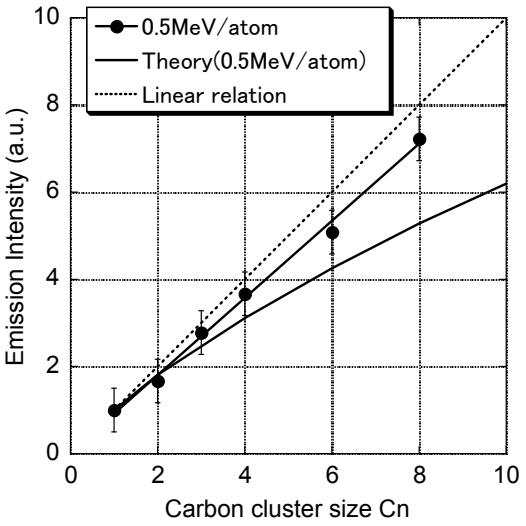

Fig. 1 The ratios of yields of luminescence from sapphire target bombarded by 0.5 MeV/atom C_1^+ ~ C_8^+ projectiles. The yield of luminescence from F^+ center of sapphire target irradiated by 0.5 MeV/atom C_1^+ ion is unity.

Reference

1) Y. Aoki et al., Nucl. Instrum. Meth. Phys. Res. B 114 (1996) 276.

4-46 Processing of an Upstanding Nano-Wire Array Using Ion-Beam Lithography

K. Takano [a)], T. Satoh [a)], T. Kamiya [a)], Y. Ishii [a)], T. Ohkubo [a)], M. Kohka [a)], M. Sugimoto [b)], S. Seki [c)] and H. Nishikawa [d)]

[a)] Department of Advanced Radiation Technology, TARRI, JAEA, [b)] Environment and Industrial Materials Research Division, QuBS, JAEA, [c)] Graduate School of Engineering, Osaka University, [d)] Department of Electrical Engineering, Shibaura Institute of Technology

Recently, heavy ion irradiation for polymer films at the energy range of hundred MeV has been expected to be a promising tool for a new micro-processing technique to fabricate wire structures with the diameter of nano meter size, nano-wire[1)]. The nano-wires are fabricated by the irradiation to induce the cross-linking reaction of the polymer within an ion track along the ion trajectory as a negative photolithography process. At the developing with an organic solvent after irradiation, the wires are lying down the substrate, flowing away, or sticking to neighbor wires. In order to avoid the lying and the flowing, a fabrication of upstanding nano-wires which are supported by bridge structure has been tried by ion beam lithography with the focusing systems of the light and heavy ion beams at the TIARA.

As the target samples, tri-layer films were fabricated by stacking of a processing layer, a buffer layer, and a substrate. The processing layer was a SU-8 negative photoresist gel which was spin-coated with 20 μm thickness. The buffer layer consists of cured SU-8 negative photoresist by irradiation of electron beam 0.5 MeV or ^{60}Co gamma ray at Takasaki. The substrate was selected clear polyethylene terephthalate sheets. The irradiation was carried out as follows; 1) the focused $^{1}H^{+}$ beam of 3 MeV, which penetrated the gel layer, was scanned with bridge pier pattern, 2) bridging between the piers was performed by drawing of girder pattern with the focused $^{1}H^{+}$ beam of 0.5 MeV, of which the penetration depth of 7 μm was shorter than the gel thickness, 3) matrix writing in air was performed by the single ion hit of $^{20}Ne^{7+}$ of 260 MeV with spot writing at 500 ions/spots, as shown in Fig. 1. After a post-baking at 95 °C for 20 min, the written films were developed by a fluidic pumping with propylene glycol monomethyl ether acetate at the flow rate of 1.4 mL/min for charge and discharge.

The fabrication of upstanding nano-wires was successful, not randomly strung but arrayed by the single ion hit between the bridge girder with long span of 80 μm and the buffer layer, as shown in Fig. 2. The buffer layer promoted the bond of the wires to the substrate. However, the neighbor wires gather mutually and sticking. In order to avoid this sticking problem, the supercritical fluid drying method with carbon dioxide or other new developing processes will be tried as the next step.

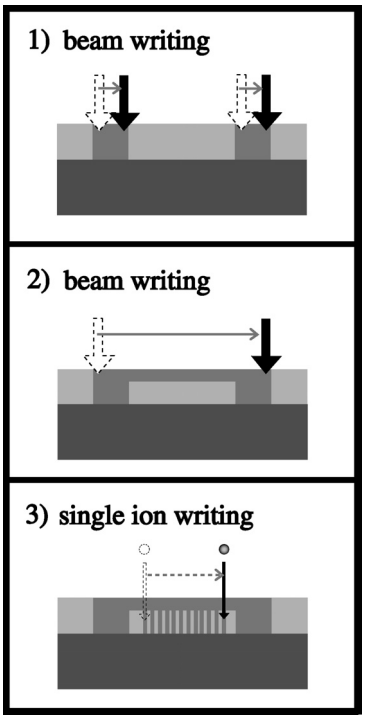

Fig. 1 Scheme of the process for upstanding nano-wire array which was supported by bridge structure in the ion beam writing. 1) 3 MeV H^{+} beam writing for the bridge pier pattern, 2) 0.5 MeV H^{+} beam writing the bridge girder pattern, and 3) wire string by single ion hit of 260 MeV $^{20}Ne^{7+}$.

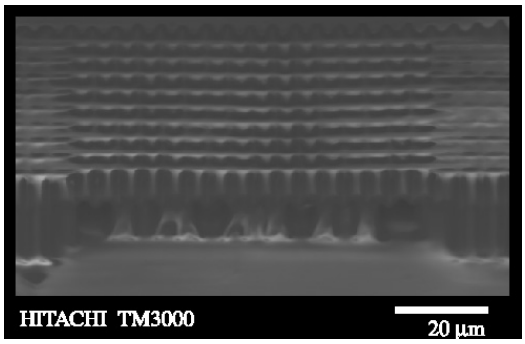

Fig. 2 SEM image of the upstanding nano-wire array which was strung between the bridge girder and the substrate by single ion hit of 260 MeV $^{20}Ne^{7+}$.

Reference

1) S. Tsukuda, et al., Appl. Phys. Lett. 87 (2005) 233119.

4-47 Fabrication of Dielectrophoretic Devices Using Poly-dimethylsiloxane Microstructures by Proton Beam Writing

Y. Shiine [a)], H. Nishikawa [a)], Y. Furuta [a)], T. Satoh [b)], Y. Ishii [b)], T. Kamiya [b)], R. Nakao [c)] and S. Uchida [c)]

[a)] Department of Electrical Engineering, Shibaura Institute of Technology,
[b)] Department of Advanced Radiation Technology, TARRI, JAEA,
[c)] Department of Electrical and Electronic Engineering, Tokyo Metropolitan University

Proton Beam Writing (PBW) is a direct write process using focused beam of MeV protons[1),2)]. The focused MeV proton beam has several advantages over other techniques using sources such as electrons, x-rays, and UV light.

When the high-aspect ratio microstructures such as pillar arrays produced by PBW were applied to dielectrophoretic (DEP) devices, it was previously demonstrated that a spatially modulated electric field can serve as an efficient trapping sites for microbes such as Escherichia coli (*E.coli)* [3)]. Since the PBW is serial and a relatively slow lithographic process, it is time consuming to expose large area of resists for the whole device including micro fluidic channels with a length of several tens of millimeters. Such a drawback can be overcome by a coupled use of soft lithography techniques [4)] with a master produced by PBW on poly-dimethylsiloxane (PDMS). In this paper, we demonstrate the fabrication of prototypes of 3D-DEP devices equipped with high-aspect-ratio pillars, which were combined with micro fluidic channels produced by a replication SU-8 master.

High-aspect-ratio pillar arrays with area of 60×1000 μm^2 were fabricated by PBW with a 13-μm thick SU-8 on a silica substrate. A master for a PDMS micro fluidic channel was fabricated by PBW on SU-8 layer on a silicon substrate. The PBW was performed at 1.0-1.7 MeV proton beam focused around 1 μm, using a dedicated PB writer at the Center for Flexible Micromachining, Shibaura Institute of Technology, or at the Takasaki Ion Accelerators for Advanced Radiation Application (TIARA), Japan Atomic Energy Agency.

Figure 1 shows a process flow of fabricating DEP devices, including (a) PBW of SU-8 layer, (b) soft lithography of micro fluidic channel, and (c) sealing the pillar arrays with the PDMS, where the silica substrate with pillar arrays is sealed with PDMS with a micro fluidic channel. Figure 2 (a) show an optical microscope image of the pillar arrays on silica, which were successfully sealed with a PDMS micro fluidic channel. Figure 2 (b) shows a photograph the DEP device with tubing at inlet and outlet ports.

A soft lithography technique with PDMS was successfully applied to the fabrication of the 3D-DEP device equipped with high-aspect-ratio pillar arrays. By the coupled use of the soft lithography technique with PBW, the fast prototyping capability of the PBW was highlighted for the development of the 3D-DEP devices.

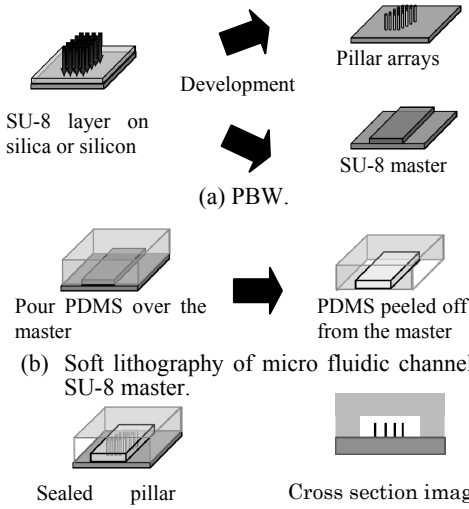

Fig. 1 Fabrication processes of a DEP device by (a) proton beam writing of SU-8 for pillar arrays and a master, coupled with (b) a soft lithography using SU-8 master on PDMS, followed by (c) sealing the pillar arrays on silica with PDMS.

References

1) F. Watt et al., Materials Today 10, 6 (2007) 20-29.
2) Y. Furuta et al., J. Vac. Sci. Tech. B. 25 (2007) 2171-2174.
3) Y. Furuta et al., Microelectron. Eng. 86 (2009) 1396-1400.
4) J. C. McDonald and G. M. Whitesides, Acc. Chem. Res. 35 (2002) 491-499.

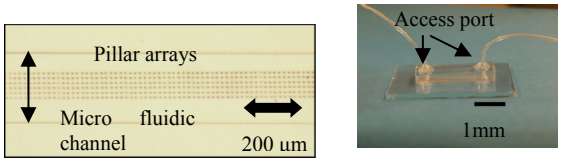

(a) Optical microscope image of pillar arrays on silica.

(b) Photograph of the sealed device.

Fig. 2 (a) Optical microscope image of a sealed pillar arrays on silica and (b) photograph DEP device.

4-48 Development of Neutron Optics Devices Using Proton Microbeam

T. Sakai [a)], R. Yasuda [a)], H. Iikura [a)], T. Nojima [a)], M. Matsubayashi [a)], M. Kohka [b)], T. Sato [b)], T. Ohkubo [b)] and Y. Ishii [b)]

[a)] Materials Science Research Division, QuBS, JAEA,
[b)] Department of Advanced Radiation Technology, TARRI, JAEA

We have developed two fundamental techniques to manufacture neutron optics devices. One is on-line beam targeting method and another is software for conversion of image data to coordinates data. Line&space test-chart for spatial resolution measurement on neutron radiography technique was successfully created.

中性子ラジオグラフィ（NRG）法は、学術研究や産業利用をはじめ、水（水素）分布を可視化する非破壊分析法として、良く用いられている手法の一つである。近年、燃料電池自動車の実用化を目指した研究開発が官民において盛んに行われているが、そのための分析手法の一つとしても、NRG 法は非常に注目されている。しかしながら中性子ビームの平行度等の問題により、現状の NRG の空間分解能は数十 μm 程度であり、燃料電池開発で要求される 10 μm 程度の空間分解能は達成できていない。そこで NRG 法の高度化を目指し、プロトンマイクロビームによる微細加工技術を利用して、中性子光学用素子の開発に着手した。

試作した素子は、中性子用のコリメーターと空間分解能を評価するためのテストチャートである。中性子は透過性が強いため、素子の厚みは極力厚い方が望ましい。そこで加工に用いるプロトンビームとしては、シングルエンド加速器の最大加速電圧である 3 MeV のビームを用いた。またコリメーターとするアクリル樹脂製試料の中心には、位置合わせ用のマーカーを機械加工により付けてあるため、その位置に正確にビームを照射する必要がある。そこで、SB ラインに設置されている光学顕微鏡の像を、マイクロ PIXE 測定用のソフトウエア [1)]上に表示できるようにし、ビーム照射位置を顕微鏡下で観察しながら調整できるようにした。これにより、ビームの照準を正確に行うことが可能になった。2009 年度においては、直径 100 μm のコリメーター作製に成功し、今後 10 μm 径のコリメーターを製作する予定である。

テストチャートの加工に関しては、空間分解能を評価するため、サイズの異なるラインペア（Line&Space）を貫通孔で作製する必要がある。パターンに関しては、CAD ソフトウエアで作成し、その画像データを座標データに変換するためのソフトウエアを開発した。このソフトでは、JPEG もしくは BITMAP 形式の画像データを読み取り、任意の閾値により二値化、座標データに変換することが出来る。Fig. 1 にテストチャートの画像パターンを示す。このデータを元に、75 μm 厚のアクリルシートにビーム照射を行い、エッチング処理を施した。その結果を Fig. 2 に示す。

本年度においては、プロトンマイクロビームを用いて中性子光学素子を作製するための要素技術の開発を行った。今後、実素子を開発し、中性子を用いて素子の特性評価試験を行う予定である。

Fig. 1 Line&space test-chart pattern for evaluation of neutron radiography spatial resolution.

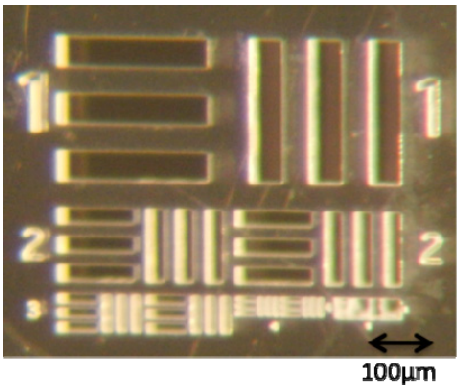

Fig. 2 Microscopic photograph of a fabricated test-chart. The line patterns are passed through the sheet.

Reference

1) T. Sakai et al., Nucl. Instrum. Meth. B 390 (1998) 136-138.

4-49 Fast Single-Ion Hit System for Heavy-Ion Microbeam at TIARA Cyclotron (III)

W. Yokota, T. Satoh, S. Okumura, S. Kurashima, N. Miyawaki, H. Kashiwagi, K. Yoshida, M. Kohka, K. Takano and T. Kamiya

Department of Advanced Radiation Technology, TARRI, JAEA,

The focusing microbeam system and the fast single-ion hit system are being developed for this decade at the TIARA cyclotron. Microbeams and single-ion hit of 260 MeV-$^{20}Ne^{7+}$ and/or 520 MeV-$^{40}Ar^{14+}$ were utilized to irradiate living biological cells for study of radiation biology, semiconductor devices for study of radiation effects such as Single Event Upset and micro-fabrication of polymer films in fiscal 2009. The experimental results of these studies are described elsewhere. The microbeam size used in those experiments was 1 - 2 μm in diameter in vacuum. It was extracted out to the atmosphere through a 0.2 μm thick silicon nitride window for biological experiment. The beam size grew several times as large mainly by scattering in air depending on the distance between the window and the target. Although these beams were generally supplied smoothly, there are still technical matters to improve for better beam quality and wider application, each of which is described below.

Instability of microbeam sometimes appeared as frequent decrease of intensity. The instability was synchronizing with change of trajectory or profile of beam on the way of beam transport from the ECR ion source to the cyclotron. Although any change related to the ion source such as intensity of light and electric potential of plasma was not observed, change in the plasma condition is the most suspicious as an origin of the instability since ECR plasma is easy to be influenced by temperature of ambient air and coolant [1]. Strict control of these temperatures will be introduced in the near future.

Miss hit, no ion hit at a targeted point, appeared on occasion at more than ten percents of the total hit number depending on tuning of beam focusing or transport as reported in the last annual report [2]. This can affect irradiation experiment seriously and it is desired to be reduced down to less than 1%. Miss hit took place obviously when an ion hit other than a targeted point, and a candidate of the cause described in the report was scattering of the ion at the micro slit (see Fig.1 for the composition of the microbeam system). Every ion focused on a target in an area of a microbeam spot size must pass both the micro slit and the divergence defining slit even if it is scattered by the micro slit. Only the possibility, therefore, that every ion reaches other than the targeted point is change of ion charge state at the micro slit, which brings different focusing force of the micro lens from that for the original charge state. The distance of ion shift was examined by applying the electrostatic scanner voltage using 260 MeV-$^{20}Ne^{7+}$ beam focused on CR-39 target by a quadrupole lens upstream. The ions concentrated in a limited area without the voltage, while the area broke up into four groups when the voltage was turned on. The distance of the shift of the groups from the original position was proportional to successive integers corresponding to the charge state. The ion concentration of each group depended on opening of the micro slit. These results clearly indicate that ion charge state was changed into the four values by scattering at the micro slit.

Expansion of ion beam species and energies is desired to proceed continuously. Development of usual beam, non-microbeam, is made for two or three ion species or energies every year. That for microbeam is more time-consuming because it includes an experiment of microbeam formation. Therefore, a new microbeam will be added every year. In fiscal 2009, 220 MeV-$^{12}C^{5+}$, required from radiation biology study, was developed and 2 μm diameter was attained. If a cocktail beam acceleration technology is applied, a number of microbeams can be developed more easily [3]. For example, a mass to charge ratio of 260 MeV-$^{20}Ne^{7+}$ is about 2.86 (≈20/7), and ions having similar ratio, such as 190 MeV-$^{14}N^{5+}$ with M/Q≈2.8, can be accelerated and focused using the similar operational parameters with less tuning.

References

1) K. Yoshida et al., Rev. Sci. Instrum. 81, 02A312 (2010).
2) Y. Yokota et al., JAEA Takasaki Ann. Rep. 2008 (2009) 165.
3) S. Kurashima et al., Nucl. Instrum. Meth. B 267 (2009) 2024.

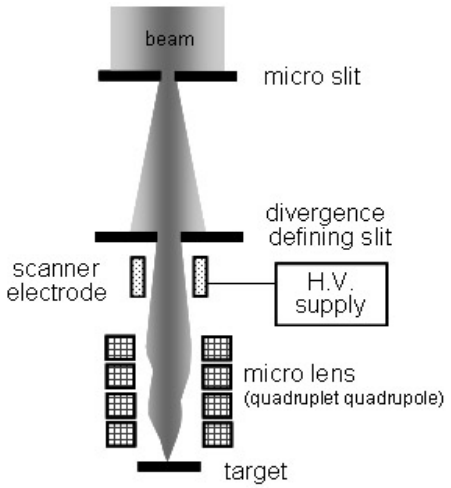

Fig. 1 Schematic diagram of the microbeam system at the TIARA cyclotron.

4-50 Status Report on Technical Developments of the AVF Cyclotron

S. Okumura, T. Yuyama, Y. Yuri, T. Ishizaka, I. Ishibori, H. Kashiwagi, S. Kurashima, N. Miyawaki, K. Yoshida, T. Nara and W. Yokota

Department of Advanced Radiation Technology, TARRI, JAEA

Uniform Irradiation of Ion Beams by Means of a Nonlinear Focusing Method

The raster scanning method is widely used for large-area uniform irradiation of ion beams at the TIARA cyclotron facility. However, some practical problems can arise because of its irradiation principle that a focused spot beam is periodically swept; e.g., the local target heating is induced by irradiation of a high-current beam, a transient phenomenon of an irradiation sample cannot be measured in real time, short-time or low-fluence irradiation of high uniformity is difficult, etc. Therefore, a multipole-magnet beam profile uniformization system (MuPUS) based on the *nonlinear focusing method*, has been developed as an alternative to the raster scanning method[1-2]. With this method, the beam profile can be made uniform by the nonlinear forces of multipole magnets. It is, thus, possible to irradiate a large-area sample or a number of samples simultaneously and continuously at a constant particle fluence rate.

We are developing a measurement system of a large-area uniform beam using beam-induced fluorescence in order to evaluate beam characteristics such as the beam size and the uniformity in real time. It is possible to observe the uniform irradiation profile of the beam in real time since the beam spot is stationary on the target, unlike the case of the scanning method where the beam spot is moving fast on the target. We have, thus, adopted some of Tb-doped Gd_2O_2S screens called DRZ (Mitsubishi Chemical) as a fluorescent screen. They are suitable for real-time tuning of a low-current-density beam since the optical decay time of light emission by beam irradiation is much shorter and the sensitivity to ion beams is higher, as compared with an ordinary Al_2O_3 screen. The fluorescence signal from the screen mounted on a target stage was detected by a CCD camera and converted to the brightness data with a LabVIEW (National Instruments) system on a Windows computer. The response of the brightness to the beam current density, i.e., the fluence rate of the beam was explored. It is possible to evaluate the uniformity of the beam intensity distribution in an arbitrary region. To monitor the uniformity of a large-area beam (typically, several tens of square centimeters) precisely, the location of the camera was also optimized.

A 6 cm × 6 cm uniform beam of 10-MeV proton was applied to the test irradiation of space-use solar cells as the nonlinear focusing method can realize a uniform irradiation field at a constant fluence rate, closer to the actual space environment. The irradiation time has been shortened to a fraction of that of raster scanning. We have demonstrated the high potential of this method. To realize the uniform-beam formation of heavy ions, R&D studies have been started.

Quick Change of the Cyclotron Magnetic Field for Reduction of Beam Changing Time

Reduction of the beam changing time is required to increase the available beam time for users. We are developing a technique for reducing the changing time of the magnetic field of the cyclotron, since a long changing time is normally required to form the magnetic field for acceleration. The most time-consuming process is a cycling of magnetic field strength, which is a start-up process of about 30 minutes for ensuring stability and reproducibility of the magnetic field. Since the settling time of the magnetic field without the cycling process is longer, as shown in Fig. 1, and the reproducibility is insufficient, we have started the development of the brief start-up process, which replaces the cycling process.

References

1) Y. Yuri et al., Phys. Rev. ST Accel. Beams **10** (2007) 104001.
2) Y. Yuri et al., Proc. Euro. Particle Accel. Conf., EPAC'08 (2008) 3077.

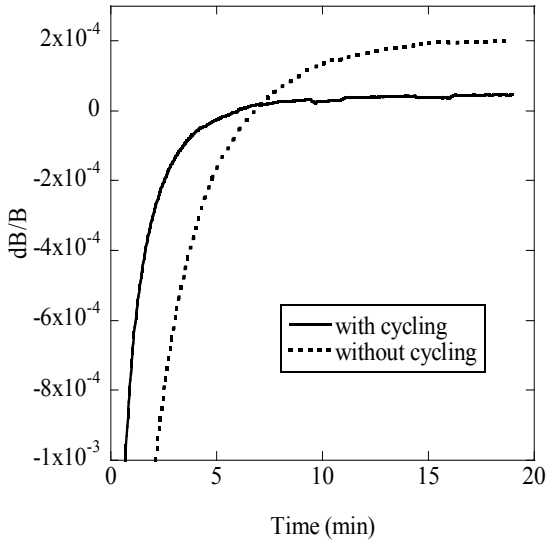

Fig. 1 Changes of the magnetic field strength (B) of the cyclotron just after the start-up process for 10 MeV proton beam acceleration.

4-51 Development of Beam Generation and Irradiation Technology for Electrostatic Accelerators

A. Yokoyama, S. Uno, A. Chiba, K. Yamada, Y. Saitoh,
Y. Ishii, T. Satoh, T. Ohkubo and T. Agematsu

Department of Advanced Radiation Technology, TARRI, JAEA

Cluster ion acceleration

The key points in accelerating cluster ions by means of a tandem accelerator are both their cross-sections of collision induced destruction and charge exchange in charge exchanging gas. Therefore the cross sections were measured for the carbon cluster ions (C_4, C_8, C_{10}), which were frequently used in irradiation experiments at our facility. Stripper gases of He, N_2 having different molecular size and valence band electrons state were tested to investigate a suitable gas for use in accelerating cluster ions with a tandem accelerator. The cross sections are deduced from a transmission probability through the tandem accelerator as a function of the stripper gas density, and the transmission probability can be written as

$$T = \alpha e^{-\sigma_d \chi}(1 - e^{-\sigma_p \chi}) \quad \cdots\cdot (1)$$

where σ_p and σ_d are the production and destruction cross sections respectively, and χ is the stripper gas density. Figure 1 shows the transmission of C_{10} as a function of stripper gas density. From eq. (1), for high stripper gas density the transmission should be proportional to $e^{-\sigma_d \chi}$. Therefore, σ_d can be taken directly form the slope of the transmission curve at high gas density and σ_p can be determined by fitting eq. (1) to the total curve [1]. As a result, the destruction cross sections of C_n are proportional to the cluster size, and those of helium are smaller than those of nitrogen, whereas the production cross sections seem to be no significant change on the cluster size and stripper gas species. The results indicate helium gas should be effective for cluster ion acceleration.

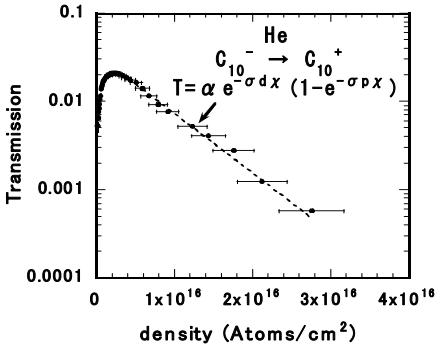

Fig. 1 Transmission of C_{10} as the function of stripper gas density.

Study of Faraday cup shapes for a fullerene beam intensity distribution monitor

We are developing an ion beam intensity distribution monitor using multi Faraday cup (MFC) [2]. Each FC unit of MFC is required a high aspect ratio to measure beam current accurately without a negative suppressor, because a large number of secondary positive ions are produced by fullerene collision and extracted by the electron-suppression field. A depth and a bottom shape of the FC unit were studied using 120 keV C_{60}^+ beam with the 400 kV ion implanter. The beam current was accurately measured using 15 mm depth FC with both flat and oblique bottom, as shown in Fig. 2.

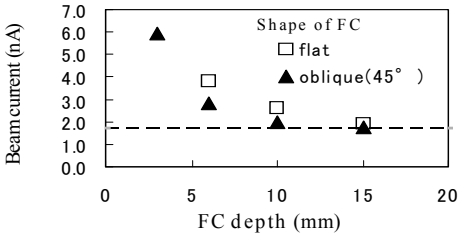

Fig. 2 The relationship between the measured beam current and FC depth. The inside diameter of FC unit is 3 mm. The accurately current was supposed with dotted lines.

Emittance measurement using scintillator luminescence induced by MeV proton beams

The emittance of the ion beams accelerated by the 3 MV single-ended accelerator is measured using an emittance monitor [3]. First, the emittance was estimated from the numerically analyzed CCD camera images of luminescence induced by proton beam injected into a scintillator, SiO_2 thin plate. There was, however, a problem of an irradiation damage of the scintillator. The YAG:Ce plate, 400 mm^2 and 0.2 mm thick, was tried instead of the SiO_2. The radiation resistance of the YAG:Ce scintillator was demonstrated by measuring the two kinds of proton beam induced luminescence intensity from several times proton irradiation area or non-irradiation one. The experiment also showed the luminescence had a good linearity to the incident proton beam current. The brightness was 0.7 A m^{-2} sr^{-1} eV^{-1} as a preliminary study. The high accuracy beam emittance will be studied using the improved emittance monitor in the next year.

References

1) F. Ames et al., Nucl. Instrum. Meth. B 112 (1996) 64.
2) K. Yamada et al., JAEA Takasaki Ann. Rep. 2008 (2009) 168.
3) A. Chiba et al., TIARA Ann. Rep. 2002 (2003) 327.

4-52 Production of Highly Spin-Polarized Positron Source

A. Kawasuso, M. Maekawa, Y. Fukaya and A. Yabuuchi

Advanced Science Research Center, JAEA

We attempt to produce the ^{68}Ge-^{68}Ga radioisotope as a highly spin-polarized positron source. We irradiated 20 MeV or 25 MeV proton beam for ^{69}Ga targets. We confirmed the production of ^{68}Ge-^{68}Ga radioisotopes by a nuclear reaction of ^{69}Ga (p, 2n) ^{68}Ge. From the magnetic field dependence of two-gamma self-annihilation intensity of positronium in a fused silica, we determined the spin polarization of emitted positrons to be more than 80 % as theoretically predicted using the positron helicity.

放射性同位元素から放出される陽電子のスピンは、弱い相互作用に伴うパリティ非保存のため、進行方向に偏極している。スピン偏極陽電子は、磁性体の新たな評価手段として期待される。しかし、十分に高いスピン偏極率と長い半減期を持つ陽電子線源が実用化されていなため、この分野の研究は立ち遅れている。そこで我々は、高エネルギーイオンビームを用いた核反応により、高スピン偏極陽電子線源を製造し、その磁性材料研究における可能性を追求している。

陽電子のスピン偏極率は、主に陽電子のヘリシティ v/c（v：放出陽電子の速度、c：光速度）で決まる。即ち、高いスピン偏極率の陽電子を得るためには、放出陽電子の速度（エネルギー）が大きい陽電子線源を用いることが重要である。本研究では、陽電子の最大エネルギーが 1.9 MeV であり、理論上のスピン偏極率が 94%である ^{68}Ge-^{68}Ga（半減期：288 日）に着目した。

効率的に ^{68}Ge-^{68}Ga を生成するために、分離精製された ^{69}Ga 安定同位体を標的物質とし、これにプロトンビームを照射することで ^{68}Ge-^{68}Ga を生成した。IRAC コードを用いた計算評価の結果、プロトンエネルギー20～25 MeV、標的物質の厚さ 0.5～1 mm が最適条件であった。そこで実験では、厚さ 0.5 mm と 1 mm の ^{69}Ga ターゲットを各 1 個作製し、それぞれに 20 MeV と 25 MeV のプロトン照射を行った。また、照射中に融解した Ga が外部に漏出しないように、特別の線源カプセルを製作した（Fig. 1）。Ga はカーボン製の皿に格納され、上部を厚さ 25 μm の Be 板で封じる構造になっている。プロトンビームは Be 板を貫通して照射される。

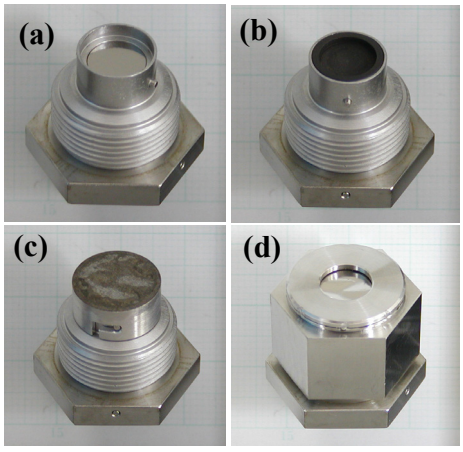

Fig. 1 Positron source capsule components: (a) pedestal, (b) carbon tray, (c) Be window and (d) outer cap with Ti window.

照射実験の結果、20 MeV と 25 MeV のプロトン照射（積算照射電流：2.91 μAh、7.31 μAh）に対して、それぞれ 0.452 MBq と 0.985 MBq の ^{68}Ge-^{68}Ga が生成していることが分かった。これらの放射能は、何れも IRAC 計算から期待されるものの 1/10～1/5 程度であった。この原因としては、ビーム電流や核反応断面積の過大評価が考えられ、今後検討すべき課題である。

陽電子を溶融石英に打ち込むことでポジトロニウム（陽電子と電子の水素様結合状態：Ps という記号で表す）が生成される。通常、S=0 のパラ状態（p-Ps）と S=1 のオルソ状態（o-Ps）が 1：3 の割合で生成する。磁場中では、p-Ps と m=0 の o-Ps は新たな二つの混合状態を形成し、これらの二光子消滅率が変化する。この変化は、陽電子スピンが偏極していると、磁場反転非対称性を示す。この性質を使うことで、逆に、陽電子の偏極率を評価することができる [1]。Fig. 2 は、上で製造した ^{68}Ge-^{68}Ga と従来の ^{22}Na から放出される陽電子を溶融石英に打ち込んだ際に観測される Ps の二光子消滅強度の磁場依存性を示している。これより、^{68}Ge-^{68}Ga に対して観測される Ps の二光子消滅強度は ^{22}Na と比較して大きな磁場反転非対称性を示すことが分かる。理論解析の結果、^{68}Ge-^{68}Ga から放出される陽電子のスピン偏極率は 80%以上であることが分かった。

Reference

1) Y. Nagai et al., Nucl. Instrum. Meth. B 171 (2000) 199.

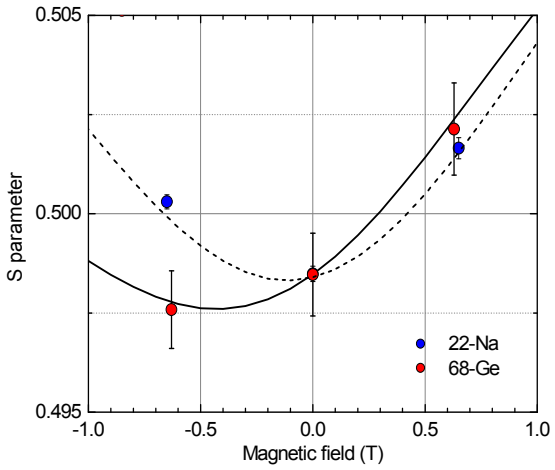

Fig. 2 Two-gamma self-annihilation intensity of Ps in a fused silica observed using ^{68}Ge-^{68}Ga (red circles) and ^{22}Na (blue circles).

5. Status of Irradiation Facilities 2009

5-01 Safety Measures, Utilization Status and Machine Time Proportion at TIARA Facility ····· 179
K. Mizuhashi, H. Takizawa, M. Hosono, K. Nishimura, Y. Nakamura, S. Kaneya, S. Mochizuki, T. Asai, M. Kawabata and K. Daikubara
5-02 Operation of the AVF Cyclotron ····· 180
T. Nara, I. Ishibori, S. Kurashima, K. Yoshida, T.Yuyama, T.Ishizaka, S. Okumura, N. Miyawaki, H. Kashiwagi, Y.Yuri, W. Yokota, K. Akaiwa, To. Yoshida, S. Ishiro, Tu. Yoshida, S. Kanou, A. Ihara, K. Takano and T. Saitoh
5-03 Operation of the Electrostatic Accelerators ····· 181
T. Agematsu, S. Uno, A. Chiba, K. Yamada, A. Yokoyama, Y. Saitoh, Y. Ishii, T. Satoh, T. Ohkubo, W. Yokota, T. Kitano, T. Takayama, S. Kanai, T. Orimo, Y. Aoki and N. Yamada
5-04 Operation of Electron Accelerator and Gamma-ray Irradiation Facilities ····· 182
Y. Haruyama, H. Hanaya, R. Yamagata, H. Seito, H. Kaneko, T. Yamaguchi, N. Yagi, M. Takagi, I. Kawashima and S. Matsuzaki
5-05 Utilization of Electron Accelerator and Gamma-ray Irradiation Facilities ····· 183
H. Kaneko, Y. Haruyama, H. Hanaya, R. Yamagata, H. Seito, T. Yamaguchi, N. Yagi, M. Takagi, I. Kawashima and S. Matsuzaki
5-06 FACILITY USE PROGRAM in Takasaki Advanced Radiation Research Institute ····· 184
Y. Fukuta, M. Hoto and D. Nogami
5-07 Radiation Control in TIARA ····· 185
Safety Section
5-08 Radioactive Waste Management in TIARA ····· 186
T. Ishibashi and T. Hosoi

This is a blank page.

5-01 Safety Measures, Utilization Status and Machine Time Proportion at TIARA Facility

K. Mizuhashi, H. Takizawa, M. Hosono, K. Nishimura,
Y. Nakamura, S. Kaneya, S. Mochizuki, T. Asai, M. Kawabata and K. Daikubara

Department of Advanced Radiation Technology, TARRI, JAEA

1. Safety Measures

Two different periodical inspections for TIARA facilities were performed every month and every three months to maintain safety of the facility.

The computer for the radiation safety data management was renewed in fiscal year 2009. This computer acquires necessary data for the radiation evaluation: concerning fourteen radiation monitors, an anemometer, operating condition of four accelerators, four environmental radiation monitors and two safety interlock systems. In case of radiation trouble, appropriate doses of radiation can be evaluated from these data. The computer for radiation safety management is shown in Fig. 1. Whenever the TIARA facilities are working, one can observe radiation dose in the entire facility with this computer system.

Fig. 1 Computer system for radiation management.

2. Utilization Status

Change of number of visitors for experiment at TIARA facility as a function of fiscal year is shown in Fig. 2. The maximum number of visitors was 1,404 in 2005. The number of visitors in fiscal year decreased from 2006 and it was 781 in 2009. It seems that the decrease of the number of visitors was related to the amount of the travel expenses budget that supports the external users. The year when the budget was the highest was 2002. Afterwards, the budget was reduced and was not provided at all after 2006. Regardless of this decrease, the total number of research subjects in these five years seems to be almost constant at 140 as shown in Fig. 2. The reason for this is that common use unrelated to travelling expenses increased after 2006. The decrease in the numbers of research subject and visitor from the peak was 92.6% and 55.6%, respectively in 2009.

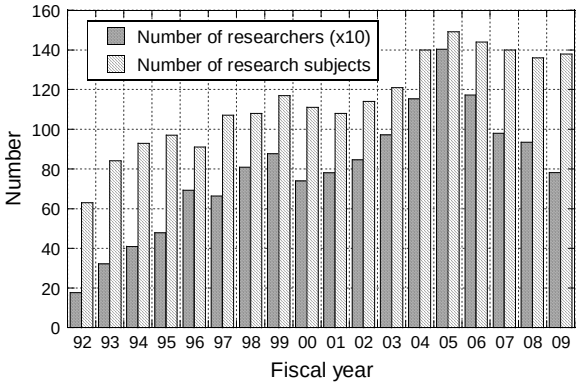

Fig. 2 Relations between the numbers of research visitors and research subjects at TIARA.

3. Machine Time Proportion

Four accelerators were used for various research subjects according to operation plan in fiscal year 2009. The proportion of the machine time used in the fields of research is shown in Fig. 3. The total of utilization time of the AVF cyclotron and the electrostatic accelerators in fiscal year 2009 was 2,272 hours and 476 days, respectively which were offered to the experiments.

The highest proportion at the cyclotron was for the field of Biotechnology-Medical application, 33.7%. At the electrostatic accelerators, the highest proportion was for the field of the Basic technology, 36.8%. The proportion for the field of RI production-Nuclear science was only 0.4%. This is because some subjects were moved from the RI production-Nuclear science field to the Biotechnology-Medical application fields.

The total proportion of “the common use” and “the promotion use” was 16.3% at cyclotron and 13.2% at electrostatic accelerator, respectively. These values were within 20% of the total machine time which is provided as “the common use” and “the promotion use” at the TIARA facility.

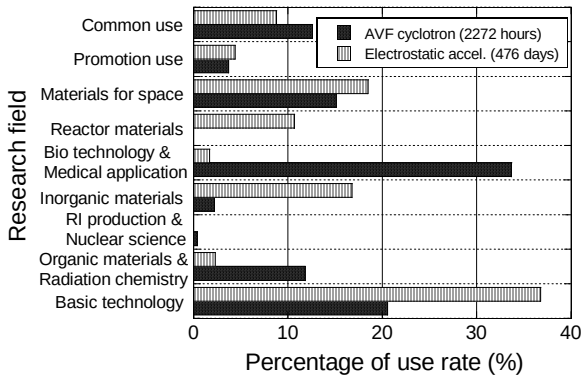

Fig. 3 Proportion of the machine time used for the fields of research.

5-02 Operation of the AVF Cyclotron

T. Nara [a)], I. Ishibori [a)], S. Kurashima [a)], K. Yoshida [a)], T. Yuyama [a)], T. Ishizaka [a)], S. Okumura [a)], N. Miyawaki [a)], H. Kashiwagi [a)], Y. Yuri [a)], W. Yokota [a)], K. Akaiwa [b)], To. Yoshida [b)], S. Ishiro [b)], Tu. Yoshida [b)], S. Kanou [b)], A. Ihara [b)], K. Takano [b)] and T. Saitoh [b)]

[a)] Department of Advanced Radiation Technology, TARRI, JAEA, [b)] Beam Operation Service, Co., Ltd.

Operation

The AVF cyclotron was steadily operated throughout fiscal 2009 and supplied various ion beams for research experiments. The cumulative operation time was 59,535 hours and the total number of experiments was 8,125 from the first beam extraction in 1991 to March 2010.

Table 1 shows the statistics of the cyclotron operation of fiscal 2009. The total operation time amounted to 3,148.3 hours, and monthly operation times are shown in Fig. 1. The percentages of operation time of the year used for regular experiments, joint-use, the innovation program, beam tuning, and beam development are 66.9%, 8.9%, 2.4%, 19.7%, and 2.1%, respectively. The number of machine troubles was 130. The only trouble that led to cancellation of experiments was a breakdown of a power supply of the cyclotron RF system.

Table 1 Statistics for cyclotron operation in fiscal 2009.

Beam service time	2,461.8 h
Machine tuning	620.9 h
Beam development	65.6 h
Total operation time	3,148.3 h
Change of particle and/or energy	238 times
Change of beam course	309 times
Change of harmonic number	56 times
The number of experiments	633
Experiment cancelled due to machine trouble	2(8.5h)

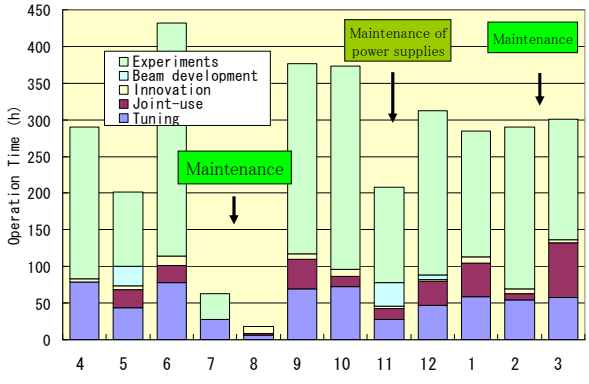

Fig. 1 Monthly operation time in fiscal 2009.

The multi-cusp ion source is used to produce H^+ and D^+ ions. For production of ions heavier than Helium, two ECR ion sources are used alternatively. Table 2 shows the operation time of each ion source. Fractional distribution of major ions used for experiments is shown in Fig. 2. The tendencies of the statistics are similar to those of the past years.

Table 2 Operation times of ion sources.

Ion source	Operation time(h)	Ratio(%)
Multi-cusp	1,041.0	30.2
ECR (OCTOPUS)	983.6	28.6
ECR(HYPERNANOGAN)	1,418.9	41.2

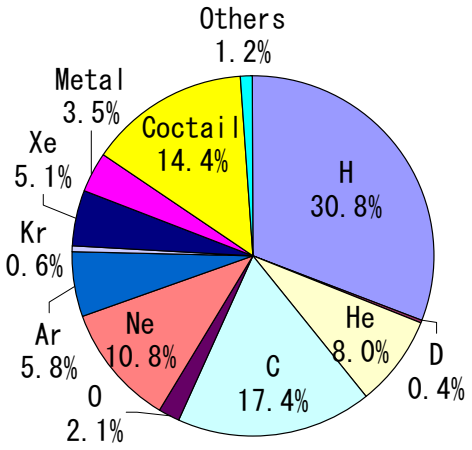

Fig. 2 Ion species used for experiments in fiscal 2009.

Maintenance

The regular yearly overhaul and maintenance were carried out. The major items were as follows: 1) Correction of the reference positions of some beam probes, the inflector, etc. 2) Replace of the sequence controllers for safety interlock system. 3) Inspection of the RF system and evaluation of its characteristics. 4) Change of lubricating oil for about 50 rotary pumps. 5) Inspection of the beam scanner power supplies. 6) Routine maintenance of the power supplies. 7) Improvement of the controller of the beam attenuator.

Technical Development

The new beam acceleration tests were carried out for 12 MeV D^+, 25 MeV H^+, 490 MeV $^{192}Os^{30+}$ and 98 MeV $^{28}Si^{5+}$, and they are ready for use in experiments.

A measurement system of a large-area uniform beam by means of beam-induced fluorescence is being developed in order to evaluate beam characteristics such as beam shape, size and uniformity in real time. Development of a technique for reducing the changing time of the magnetic field of the cyclotron is also in progress for quick change of ion species and beam energy. The details of those technical developments are described elsewhere in this annual report.

5-03 Operation of the Electrostatic Accelerators

T. Agematsu [a)], S. Uno [a)], A. Chiba [a)], K. Yamada [a)], A. Yokoyama [a)], Y. Saitoh [a)], Y. Ishii [a)], T. Satoh [a)], T. Ohkubo [a)], W. Yokota [a)], T. Kitano [b)], T. Takayama [b)], S. Kanai [b)], T. Orimo [b)], Y. Aoki [b)] and N. Yamada [b)]

[a)] Department of Advanced Radiation Technology, TARRI, JAEA,
[b)] Beam Operation Service, Co., Ltd

1. Operation and Status

Three electrostatic accelerators were operated smoothly in FY 2009, and all the planned experiments were carried out except those canceled by users. The yearly operation time of the tandem accelerator, the single-ended accelerator and the ion implanter amounted to 2,100, 2,416 and 1,866 hours respectively, similarly to past years. The total operation time of each accelerator since operation started was 32,422, 36,864 and 28,875 hours, respectively. The monthly operation time is shown in Fig. 1. Ion species used for experiments in FY 2009 are also shown in Fig. 2.

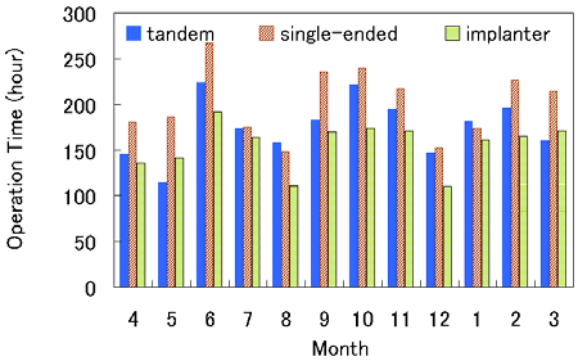

Fig. 1 Monthly operation time of each accelerator in FY 2009.

2. Maintenance

The number of troubles was smaller than that for past years. Major maintenance performed in FY 2009 is as follows;

Tandem accelerator: There was no trouble of accelerator leading to cancelation of experiments. Minor repair and scheduled maintenance were carried out.

Single-ended accelerator: The radio frequency oscillator of the ion source mounted in high-voltage terminal and the sequencer for control of the SB beam line have failed, and they were changed to new ones.

Ion implanter: The oven controller of Freeman ion source was renewed in February 2010.

3. New Beam Development

As to the ion implanter, intensity of Pt ion beam was very small and we tried to generate Pd ion as an alternative. But intensity of Pd ion beam can not be kept long time, and it is insufficient now for experiments. We will study to keep beam intensity long time.

As to the tandem accelerator, ion beam of Mn was successfully generated and accelerated at intensity of 150 nA. We also tried to generate Yb ion, which was trial development for expanding the variety of ion species as lanthanoid group. However, beam intensity of the target mass separated by analyzer magnet of accelerator was very small, and it is insufficient for experiments.

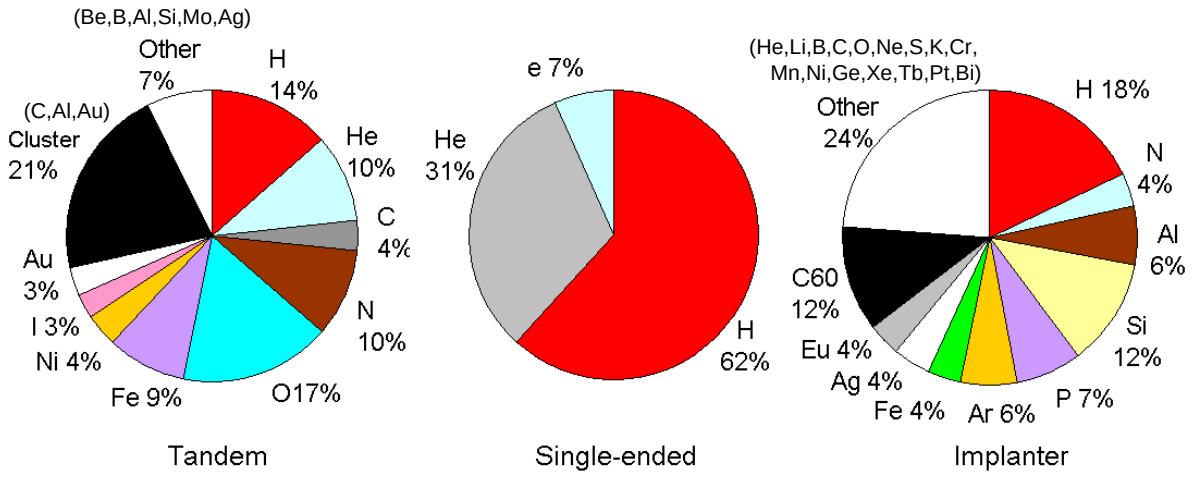

Fig. 2 Ion species used for experiments in FY 2009.

5-04 Operation of Electron Accelerator and Gamma-ray Irradiation Facilities

Y. Haruyama [a)], H. Hanaya [a)], R. Yamagata [a)], H. Seito [a)], H. Kaneko [a)], T. Yamaguchi [b)], N. Yagi [b)], M. Takagi [b)], I. Kawashima [b)] and S. Matsuzaki [b)]

[a)] Department of Advanced Radiation Technology, TARRI, JAEA,
[b)] Radiation Application Development Association, RADA

1. Operation

1.1 Electron accelerator

The electron accelerator was on service without serious trouble 9:00 - 17:30 on Monday and Friday, and 8:30 - 23:00 on Tuesday to Thursday, to satisfy the demand of operation time for users.

The annual operation time of the electron accelerator is shown in Fig. 1. Total operation time of the accelerator in FY2009 947.9 h, increased by about 10% compared with that in FY2008, and analysis of the number of research subject indicated the increase of longer-time irradiation for material for space subject.

The accelerator served mainly for graft-polymerization for new materials development, radiation effect study on semiconductors and various experiments of visiting users.

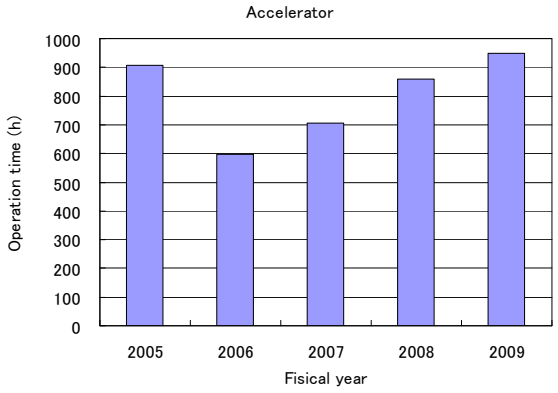

Fig. 1 Annual operation time of the electron accelerator.

1.2 Gamma-ray irradiation facilities

The Co-60 gamma-ray irradiation facilities consist of three buildings with eight irradiation rooms and cover a wide dose-rate range from 0.04 Gy/h to 20 kGy/h. The annual operation time for the first, second irradiation facilities and food irradiation facility is 15,971 h, 12,389 h and 7,681 h, respectively, as shown in Fig. 2.

The first irradiation facility served mainly for radiation-resistance testing of electric cables used in nuclear power plants and various materials used in J-PARC facility for long irradiation period. The second irradiation facility served mainly for development of new functional materials and other research subjects of visiting users, including irradiation room No.6 operated as hourly scheduled. The food irradiation facility served mainly for development of detection method for irradiated foods and radiation resistance testing at lower dose rates.

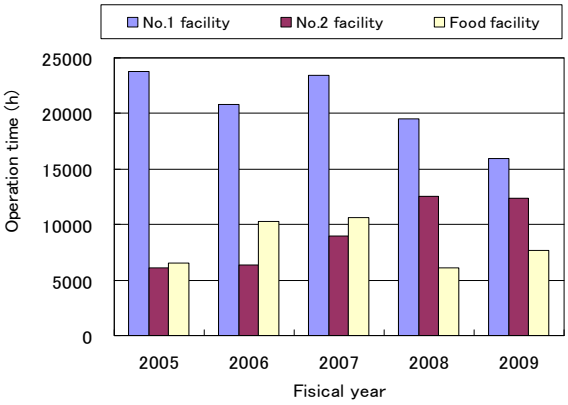

Fig. 2 Annual operation time of Co-60 gamma-ray irradiation facilities.

2. Maintenance

2.1 Electron accelerator

The regular maintenance was carried out for 7 days in October, 2009 for check on accelerator body, the conveyor and doors of irradiation room and repair of vacuum system at the vertical beam line.

2.2 Gamma-ray irradiation facilities

The regular maintenance mainly on mechanical system for radiation source transportation is performed every year at one of three gamma-ray irradiation facilities by turns. The check of the interlock system is performed two times in a year for all the facilities.

The maintenance of the first irradiation facility was done in July, 2009, for 19 days. The Cobalt-60 sources were purchased and loaded to the irradiation room No.2 in the first irradiation facility to maintain total activities of the room. The old waste sources of about 20 pieces were disposed through The Japan Radioisotope Association (JRIA).

5-05 Utilization of Electron Accelerator and Gamma-ray Irradiation Facilities

H. Kaneko [a)], Y. Haruyama [a)], H. Hanaya [a)], R. Yamagata [a)], H. Seito [a)], T. Yamaguchi [b)], N. Yagi [b)], M. Takagi [b)], I. Kawashima [b)] and S. Matsuzaki [b)]

[a)] Department of Advanced Radiation Technology, TARRI, JAEA,
[b)] Radiation Application Development Association, RADA

An electron accelerator and three gamma-ray irradiation facilities were operated for various research subjects according to the operation plan in FY 2009 without serious trouble. Distribution of research subjects and the number of experiment subjects are shown in Fig. 1 and Fig. 2, respectively. Table 1 shows irradiation time and the number of research subjects for each facility.

The number of experiment subjects at the electron accelerator increased in the research fields of materials for space and heat-resist material, and decreased in the field of basic technology and nuclear facilities. The number at gamma-ray irradiation facilities increased in the field of nuclear facilities, and decreased in the field of materials processing and resource & bio-technology.

Table 1 Irradiation time and number of experiment subjects in each research field at each facility in FY2009.

Facility / Research fields	Electron Accelerator		Gamma-ray Irradiation facilities	
	Irradiation time (h)	Subject number	Irradiation time (h)	Subject number
Material processing	167.9	326	7557	326
Heat-resist material	245.3	67	150	5
Material for space	340.8	89	10474	49
Nuclear facilities	0.0	0	35525	93
Environment	2.1	5	951	78
Basic technology	74.7	10	2166	55
Resource & Bio-technology	0	0	279	110
Joint use	117.2	36	21764	150
Total	947.9	515	78866	882

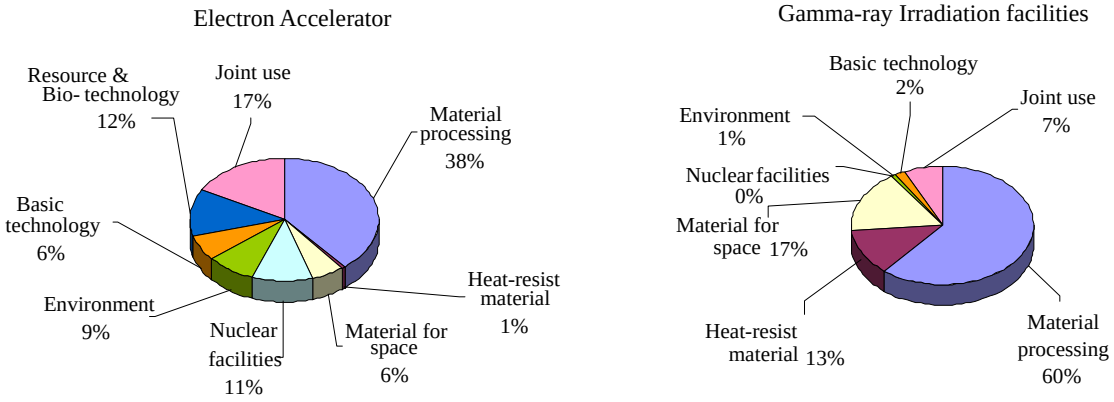

Fig. 1 Distribution of research subjects (FY 2009).

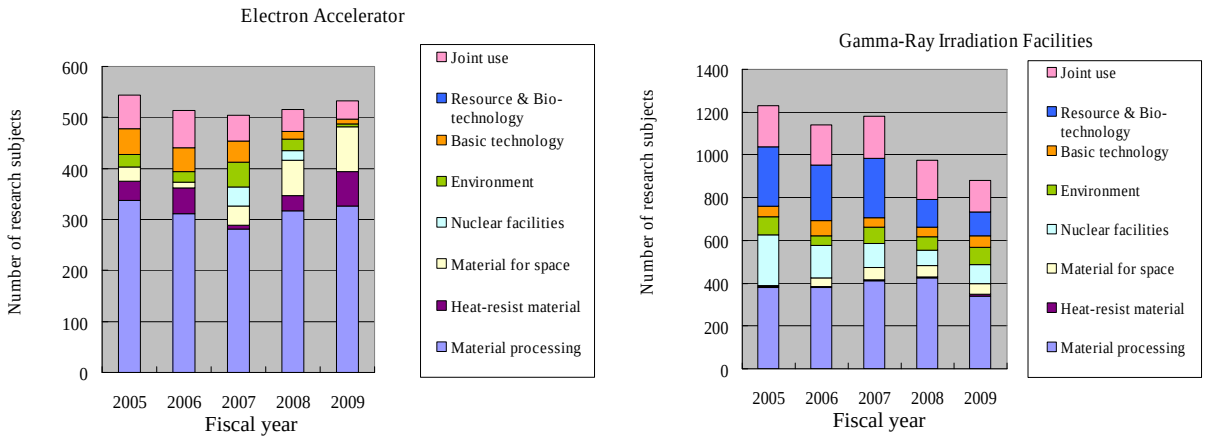

Fig. 2 The number of research subjects (FY 2005-2009).

5-06 FACILITY USE PROGRAM in Takasaki Advanced Radiation Research Institute

Y. Fukuta, M. Hoto and D. Nogami

Department of Advanced Radiation Technology, TARRI, JAEA

1. Introduction

The facilities of JAEA are widely opened to users from universities, public institutes, and the industries, etc. Taking over the former system, FACILITY USE PROGRAM started in 2006, which is the system of facility use for the user's purpose on fee-charging basis. There are 3 open use facilities in Takasaki; Co-60 Gamma-ray Irradiation Facilities, Electron Accelerator and TIARA (Takasaki Ion Accelerators for Advanced Radiation Application). In addition to them, some of the off-line devices can be used.

We round up the Research Proposals every half year. And the special committee examines carefully the availability and the validity of the experimental plan. The facility usage fee has revised from this fiscal year. The details of the fee are the admission fee, the irradiation fee, the expendables fee and the additional charge. In case of Non-proprietary research, the users must report the irradiation result to JAEA, which exempts them from the irradiation fee. JAEA opens the reports to the public. Universities can also apply through the facility use program of the University of Tokyo. Such applications are accepted as priority case. Table 1 shows the outline of the program.

Table 1 Classification of FACILITY USE PROGRAM.

Purpose	Research and development			Except R&D
Classification	General		Priority case	Commercial
Result	Non-proprietary	Proprietary		
Referee	Yes	No		
Charge*	A	B		C

*A = the admission fee + the expendables fee,
B = the admission fee + the irradiation fee,
C = the admission fee + the irradiation fee + depreciation.

2. Use in FY2009

There were 18 Research Proposals in FY2009 at Takasaki Institute, and 17 of them applied to Non-proprietary use. Including the users from priority case, we accepted 230 applications from 59 users. Table 2 shows that the percentage of the users from universities exceeds the others except for Co-60 Facilities.

Figure 1 shows classification of all 230 applications. On TIARA, Non-proprietary use occupies more than 50%, while less than few percents for the other facilities.

Table 2 User's affiliation for each facility.

Facility \ User		University	Public institute	Others	Total
TIARA	AVF cyclotron	7	1	4	12
	3MV tandem accelerator	5	0	0	5
	3MV single-ended accelerator	1	0	0	1
	400kV ion implanter	3	1	0	4
Co-60 gamma-ray irradiation facilities		5	0	17	22
Electron accelerator		4	1	10	15
Total		25	3	31	59

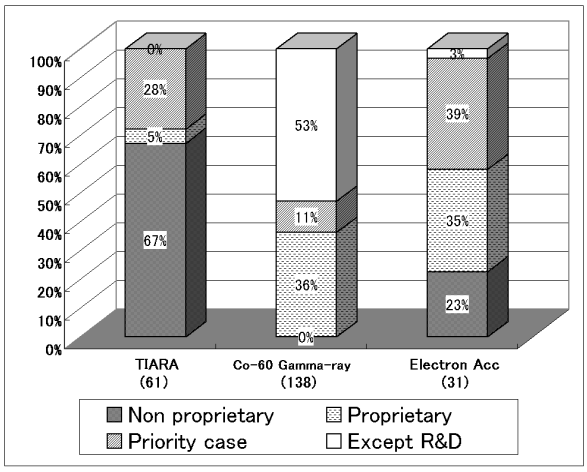

Fig. 1 Percentage of each classification. The percentage above is based on the number of application.

3. Public Relations

The information like an outline of this system, guidelines for applicants, format download etc. can be seen on JAEA website as follows: http://sangaku.jaea.go.jp/3-facility/01-intro/index-02.html.

In addition to this, we have the "Project for Promotion of Shared Use of High Technology Research Institute", which is one of the subsidiary project of Ministry of Education, Culture, Sports, Science and Technology (MEXT). This project intends that commercial users promote shared use of facilities, which develops the whole activity of science technology from Basic Research to Innovation Creation.

An outline of this project can be seen on website as follows: http://www.taka.jaea.go.jp/innovation/index.html.

5-07 Radiation Control in TIARA

Safety Section

Department of Administrative Services, TARRI, JAEA

1 Individual monitoring

(1) Individual monitoring for the radiation workers

Table 1 shows a distribution of effective dose of the radiation workers in FY 2009. The effective dose values of almost all radiation workers were below the detection limit (0.1 mSv).

The maximum dose was 0.6 mSv/y due to the overhaul of the TIARA AVF cyclotron.

Table 1 Distributions of the effective dose of the radiation workers in FY 2009.

Items \ persons		Number of persons in each periods				Total
		1st quarter	2nd quarter	3rd quarter	4th quarter	
Distribution range of effective dose HE:Effective dose *1 (mSv)	HE < 0.1	522	574	572	602	686
	0.1 ≦ HE ≦ 1.0	1	5	0	2	8
	1.0 < HE ≦ 5.0	0	0	0	0	0
	5.0 < HE ≦ 15.0	0	0	0	0	0
	15.0 < HE	0	0	0	0	0
Number of persons under radiation control (A)		523	579	572	604	694
Exposure above 1mSv	Number of persons (B)	0	0	0	0	0
	(B)/(A)×100(%)	0	0	0	0	0
Mass effective dose (Person・mSv)		0.3	1.2	0.0	0.3	1.8
Mean dose (mSv)		0.00	0.00	0.00	0.00	0.00
Maximum dose (mSv)		0.3	0.6	0.0	0.2	0.6

*1 The dose by the internal exposure was not detected.

(2) Individual monitoring for the visitors and others

Table 2 shows the number of persons who temporally entered the radiation controlled areas. The effective dose of all persons was less than 0.1 mSv.

Table 2 The number of persons who temporary entered the radiation controlled areas in FY 2009.

Periods	1st quarter	2nd quarter	3rd quarter	4th quarter	Total
Number of persons	325	312	592	384	1613

2 Monitoring of radioactive gas and dust

Table 3 shows the maximum radioactive concentrations and total activities for radioactive gases released from the stack of TIARA, during each quarter of FY 2009.

Small amount of ^{41}Ar, ^{11}C and ^{13}N were detected for some time during operation of the cyclotron or experiment, but the pulverized substances (^{65}Zn, etc.) were not detected.

Table 3 Monitoring results of released radioactive gases and dust in FY 2009.

Nuclide	Periods \ Items	1st quarter	2nd quarter	3rd quarter	4th quarter	Total
^{41}Ar	Maximum concentration	$<1.5\times10^{-4}$	$<1.5\times10^{-4}$	$<1.7\times10^{-4}$	$<1.7\times10^{-4}$	$<1.7\times10^{-4}$
	Activity	4.7×10^{8}	0	6.5×10^{6}	5.4×10^{6}	4.8×10^{8}
^{11}C	Maximum concentration	$<1.5\times10^{-4}$	$<1.5\times10^{-4}$	$<1.7\times10^{-4}$	$<1.7\times10^{-4}$	$<1.7\times10^{-4}$
	Activity	4.7×10^{7}	5.5×10^{7}	2.3×10^{8}	2.7×10^{8}	6.0×10^{8}
^{13}N	Maximum concentration	——	——	$<1.7\times10^{-4}$	$<1.7\times10^{-4}$	$<1.7\times10^{-4}$
	Activity	——	——	1.0×10^{7}	9.5×10^{6}	2.0×10^{7}
^{65}Zn	Maximum concentration	$<6.6\times10^{-10}$	$<6.4\times10^{-10}$	$<5.7\times10^{-10}$	$<5.7\times10^{-10}$	$<6.6\times10^{-10}$
	Activity	0	0	0	0	0

Unit : Bq/cm^3 for Maximum concentration, Bq for Activity.

3 Monitoring for external radiation and surface contamination

External radiation monitoring was routinely carried out in/around the radiation controlled areas and surface contamination monitoring was also carried out. Neither unusual value of dose equivalent rate nor surface contamination was detected.

Figure 1 shows a typical example of distribution of the dose equivalent rate in the radiation controlled area of the cyclotron building.

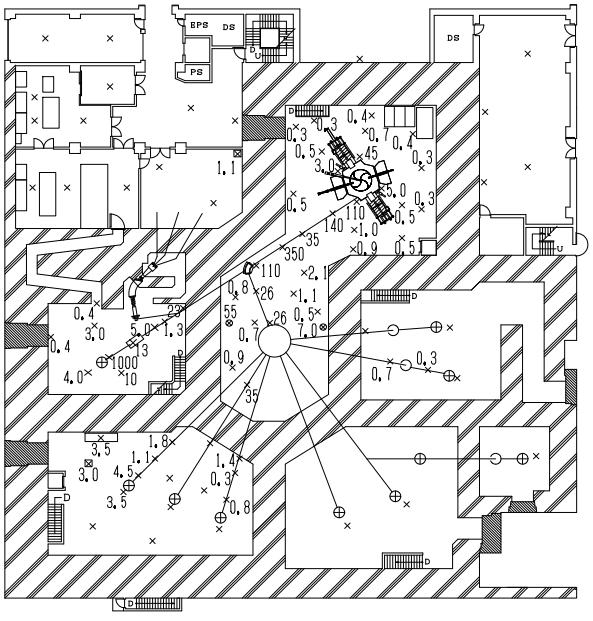

Fig. 1 Dose equivalent rate distribution in the radiation controlled area of the cyclotron building.
Measurement date : 29th and 30th March, 2010,
Measuring position : Indicated with × 1 m above floor,
Unit : μSv/h,
(The values are not indicated if they are less than 0.2 μSv/h).

5-08 Radioactive Waste Management in TIARA

T. Ishibashi and T. Hosoi

Department of Administrative Services, TARRI, JAEA

1. The radioactive wastes management

The radioactive wastes generated in TIARA are managed by Utilities and Maintenance Section. The main radioactive wastes are the solid wastes generated from the research experiment and the maintenance of the cyclotron. Other radioactive wastes are the liquid wastes such as inorganic waste fluids generated from the research experiment and the air-conditioning machines in controlled area. These wastes are managed according to their properties.

2. Solid radioactive waste

Table 1 shows the amounts of solid wastes at various properties and kinds generated in each quarter of FY 2009. The main solid waste is generated from the research experiment and the maintenance of the cyclotron.

Combustible wastes are rubber gloves, paper, and clothes, etc. Incombustible wastes are metal pieces, the glasses, and contaminated parts.

3. Liquid radioactive waste

Table 2 shows the amounts of liquid wastes generated in each quarter of FY 2009. Most of liquid waste was inorganic waste water generated from chemical experiments and condensed water from operation of air conditioning units installed in each room of the first class radiation controlled area. The largest quantity of waste water in summer season (2nd quarter) is mainly due to condensed water. After treatment by evaporation, inorganic water is reused in the controlled area. Only small amounts of concentrated liquid are generated from the evaporation.

Table 1 Radioactive solid wastes generated in FY 2009.

Amounts / Items	Amounts of generation in each periods (m^3)					Number of package /drum
	1st quarter	2nd quarter	3rd quarter	4th quarter	Total	
Category A*	0.06	0.38	0.04	0.75	1.23	
1)Combustible	0.04	0.26	0.04	0.42	0.76	6**
2)Incombustible	0.02	0.12	0.00	0.33	0.47	0
Compressible	0.02	0.12	0.00	0.22	0.36	2**
Filters	0	0	0	0.11	0.11	0
Incompressible	0	0	0	0	0	0
Ion exchange resin	0	0	0	0	0	0
Category B*	0	0	0	0	0	0

* defined by dose at the outer surface of container : (Category A) ＜ 2 mSv/h ≦ (Category B),
** 200-liter drum.

Table 2 Radioactive liquid waste generated in FY 2009.

Amounts / Items	Amounts of generation in each periods (m^3)					Number of package /drum
	1st quarter	2nd quarter	3rd quarter	4th quarter	Total	
Category A*	11.12	19.28	5.94	6.11	42.45	
1)Inorganic	11.12	19.28	5.94	6.01	42.35	treatment
2)Organic	0	0	0	0	0	0
Organic	0	0	0	0	0	0
Oil	0	0	0	0	0	0
3)Sludge	0	0	0	0	0	0
4)Evaporation residue	0	0	0	0.10	0.10	1
Category B*	0	0	0	0	0	0

* defined by concentrations in Bq/cm^3 (β, γ) : (Category A) ＜ 3.7×10^1 ≦ (Category B) ＜ 3.7×10^4.

Appendix

Appendix 1 List of Publication ····· 189
A1.1 Publication in Journal ····· 189
A1.2 Publication in Proceedings ····· 202
Appendix 2 List of Related Patents ····· 210
Appendix 3 List of Related Press-Release and TV Programs ····· 212
Symbol used in the Appendix 1 to 3 ····· 213
Appendix 4 Type of Research Collaboration and Facilities Used for Research ·· 214
Appendix 5 A Typical Example of Abbreviation Name for Organizations in Japan Atomic Energy Agency (JAEA) ····· 216

This is a blank page.

Appendix 1. List of Publication

A 1.1 Publications in Journal

09J001 1-03 C, T

S. Abo, N. Masuda, F. Wakaya, S. Onoda,
T. Hirao, T. Ohshima, T. Iwamatsu and M. Takai
"Evaluation of soft error rates using nuclear probes in bulk and SOI SRAMs with a technology node of 90 nm"
Nucl. Instrum. Meth. Phys. Res. 268 (2010) 2074-2077.

09C002 1-04 C

S. Kuboyama, N. Ikeda, Y. Satoh,
T. Hirao and T. Tamura
"Averaged LET Spectra for SEE Rate Prediction for Power Devices"
IEEE Trans. Nucl. Sci. 56 (2009) 2056-2060.

09J003 1-06 I

J-H. Park, A. Wakahara, H. Okada, Y. Furukawa,
Y-T. Kim, H-J. Chang, J. Song, S. Shin, J-H. Lee,
S. Sato, and T. Ohshima
"Study of Ion-Beam-Induced Damage and Luminescence Properties in Terbium-Implanted AlGaN"
Jap. J. Appl. Phys. 49 (2010) 032401.

09J004 1-07 T

S. Onoda, N. Iwamoto, S. Ono, S. Katakami,
M. Arai, K. Kawano and T. Ohshima
"Transient Response of Charge Collection by Single Ion Strike in 4H-SiC MESFETs"
IEEE Trans. Nucl. Sci. 56 (2009) 3218-3222.

09J005 1-07 T

N. Iwamoto, S. Onoda, T. Ohshima, K. Kojima,
A. Koizumi, K. Uchida and S. Nozaki
"Charge Collection Efficiency of 6H-SiC P+N Diodes Degraded by Low-Energy Electron Irradiation"
Mater. Sci. Forum 645-648 (2010) 921-924.

09J006 1-07 I

T. Tomita, M. Iwami, M. Yamamoto, M. Deki,
S. Matsuo, S. Hashimoto, Y. Nakagawa, T. Kitada,
T. Isu, S. Saito, K. Sakai, S. Onoda and T. Ohshima
"Electronic properties of femtosecond laser induced modified spots on single crystal silicon carbide"
Mater. Sci. Forum 645-648 (2010) 239-242.

09J007 1-07 T, I

Kin Kiong Lee, Jamie S. Laird, T. Ohshima,
S. Onoda, T. Hirao and H. Itoh
"Current Transient Effect in N-channel 6H-SiC MOSFET Induced by Heavy Ion Irradiation"
Mater. Sci. Forum 645-648 (2010) 1013-1016.

09J008 1-07 E

F. Yan, R. P. Devaty, W. J. Choyke, K. Danno,
G. Alfieri, T. Kimoto, S. Onoda, T. Ohshima,
S. A. Reshanov, S. Beljakowa,
B. Zippelius and G. Pensl
"Thermal histories of defect centers as measured by low temperature photoluminescence in n and p-type 4H SiC epilayers generated by irradiation with 170 KeV or 1 MeV electrons"
Mater. Sci. Forum 645-648 (2010) 419-422.

09J009 1-07 E

S. A. Reshanov, S. Beljakowa, M. Weidner,

B. Zippelius, G. Pensl, K. Danno, G. Alfieri,
T. Kimoto, S. Onoda T. Ohshima, Fei Yan,
R. P. Devaty and W. J. Choyke
"Thermal stability of defect centers in n- and p-type 4H-SiC epilayers generated by irradiation with high -energy electrons"
Mater. Sci. Forum 645-648 (2010) 423-426.

09J010 1-07 E
S. Beljakowa, S. A. Reshanov, B. Zippelius,
M. Krieger, G. Pensl, K. Danno, T. Kimoto,
S. Onoda, T. Ohshima, Fei Yan,
R. P. Devaty and W. J. Choyke
"Shallow defects observed in as - grown and electron-irradiated or He+-implanted Al-doped 4H-SiC epilayers"
Mater. Sci. Forum 645-648 (2010) 427-430.

09J011 1-07 G
Y. Tanaka, Y. Tanaka, S. Onoda, A. Takatsuka,
T. Ohshima and T. Yatsuo
"Radiation hardness evaluation of SiC-BGSIT"
Mater. Sci. Forum 645-648 (2010) 941-944,

09J012 1-10 E
H. Matsuura, H. Yanagisawa, K. Nishino,
Y. Myojin, T. Nojiri,
Y.i Matsuyama, and T. Ohshima
"Mechanisms of changes of hole concentration in Al-doped 6H-SiC by electron irradiation and annealing"
Physica B 404 (2009) 4755-4757.

09J013 1-12 E
N. T. Son, C. G. Hemmingsson, T. Pakova,
K. R. Evans, A. Usui, N. Morishita, T. Ohshima,
J. Isoya, B. Monemar and E. Janzén
"Identification of the gallium vacancy-oxygen pair defect in GaN"
Phys. Rev. B 80 (2009) 153202 (4 pages).

09J014 1-12 E
N. T. Son, E. Janzén, N. Morishita, H. Hanaya,
H. Takizawa, T. Ohshima and A. Gali
"Identification of Frenkel-pair defect in electron-irradiated 3C SiC"
Phys. Rev. B 80 (2009) 125201 (8 pages) .

09J015 1-12 O
G. Balasubramanian, P. Neumann, D. Twitchen,
M. Markham, R. Kolesov, N. Mizuochi, J. Isoya,
J. Achard, J. Beck, J. Tissler, V. Jacques,
F. Jelezko and J. Wrachtrup
"Ultralong spin coherence time in isotopically engineered diamond"
Nature Materials, 8 (2009) 383-387.

09J016 1-12 T, E
A. M. Edmonds, T. Umeda, J. Isoya, H. Sumiya,
H. Kanda, T. Taniguchi, N. Morishita, H. Hanaya,
S. Onoda and T. Ohshima
"Continuous-wave and pulsed EPR studies of ensembles of NV centers"
The 61st Diam. Conf., University of Warwick (2010).

09J017 1-13 C, T, G
Y. Sugo, M. Taguchi, Y. Sasaki,
K. Hirota and T. Kimura
"Radiolysis Study of Actinide Complexing Agent by Irradiation with Helium Ion Beam"
Radiat. Phys. Chem. 78 (12) (2009) 1140-1144.

09J018 1-13 G
Y. Sasaki, Y. Sugo, S. Suzuki,
Y. Kitatsuji and T. Kimura
"Development of extraction and separation method of total actinides using TODGA (Contract research)"
JAEA-Research 2009-005.

09J019 1-13 G
Y. Morita, Y. Sasaki, T. Asakura, Y. Kitatsuji,
Y. Sugo and T. Kimura
"Development of a New Extractant and a New Extraction Process for Minor Actinide Separation"
IOP Conf. Ser.: Mater. Sci. Eng. 9 (2010) 012057.

09J020 1-26 T, S, I
Y. Abe and S. Jitsukawa
"Phase transformation of Cu precipitate in Fe-Cu alloy studied using self-guided molecular dynamics"
Phil. Mag. Lett. 89, 9 (2009) 535-543.

09J021 1-26 T, S, I
S. jitsukawa, K. Suzuki, N. Okubo,
M. Ando and K. Shiba
"Irradiation effects on reduced activation ferritic/martensitic steels – tensile, impact, fatigue properties and moldeling"
Nucl. Fusion 49 (2009) 115006.

09J022 1-30 C
N. Nuryanthi, T. Yamaki, H. Koshikawa,
M. Asano, K. Enomoto, S. Sawada, Y. Maekawa,
K.-O. Voss, C. Trautmann and R. Neumann
"Poly(vinylidene fluoride)-Based Ion Track Membranes with Different Pore Diameters and Shapes: SEM Observations and Conductometric Analysis"
Electrochemistry 78 (2010) 146-149.

09J023 1-30 C
T. Yamaki, M. Asano, H. Koshikawa, Y. Maekawa,
R. Neumann, C. Trautmann and K.-O. Voss
"High-Sensitivity Ion Track-Etching of Poly(vinylidene fluoride) Membranes"
GSI Sci. Rep. 2008 (2009) 350.

09J024 1-32 C
T. Yamaki
"Quantum Beam Technology: A Versatile Tool for Developing Polymer Electrolyte Fuel-Cell Membranes"
J. Power Sources, in press.

09J025 1-33 G
S. Hasegawa, K Sato, T. Narita, Y. Suzuki,
S. Takahashi N. Morishita, and Y. Maekawa
"Radiation-Induced Graft Polymerization of Styrene into a Poly(ether ether ketone) Film for Polymer Electrolyte membranes"
J. Memb. Sci. 354 (1-2) (2009) 74-80.

09J026 1-34 E, G
S. Sawada, T. Yamaki, S. Kawahito, M. Asano,
A. Suzuki, T. Terai, and Y. Maekawa
"Thermal Stability of Proton Exchange Fuel-Cell Membranes Based on Crosslinked-Polytetrafluoroethylene for Membrane-Electrode Assembly Preparation"
Polym. Degrad. Stabil. 94 (2009) 344–349.

09J027 1-34 E, G
S. Sawada, A. Kawasuso, M. Maekawa, A. Suzuki,

T. Terai and Y. Maekawa
“Positron Annihilation Lifetime Study of Graft-Type Fluorinated Polymer Electrolyte Membranes”
Mater. Sci. Forum 607 (2009) 70-72.

09J028 2-03 O
M. Takigami, A. Hiroki, N. Nagasawa, T. Kasahara, S. Takigami and M. Tamada
“Effects of CMC Molar Mass on Mechanical Properties of CMC-Acid Gel”
Trans. Mater. Res. Soc. Jpn. 34 (3) (2009) 391-394.

09J029 2-08 E, G, O
S. Saiki, N. Nagasawa, A. Hiroki, N. Morishita, M. Tamada, Y. Muroya, H. Kudo and Y. Katsumura
“ESR study on carboxymethyl chitosan radicals in an aqueous solution”
Radiat. Phys. Chem. 79 (2010) 276-278.

09J030 3-01
赤松 憲
“放射線 DNA 損傷の分析科学的諸問題と対策－DNA の放射線化学変化と生物応答の関係理解のために―”
放射線化学、No.89、(2010) 3-8.

09J031 3-02 C
N. Shikazono, P. O’Neill
“Biological consequences of potential repair intermediates of clustered base damage site in Escherichia coli”
Mutat. Res. 669 (2009) 162-168.

09J032 3-04 O
S. Kitamura, F. Matsuda, T. Tohge, K. Yonekura-Sakakibara, M. Yamazaki, K. Saito and I. Narumi
“Metabolic profiling and cytological analysis of proanthocyanidins in immature seeds of rabidopsis thaliana flavonoid accumulation mutants”
Plant J. (in press) DOI: 10.1111/j.1365-313X. 2010.04174.x

09J033 3-09 C
E. Kondo, M. Nakayama, N. Kameari, N. Tanikawa, Y. Morita, Y. Akita, Y. Hase, A. Tanaka and H. Ishizaka
“Red–purple flower due to delphinidin 3,5-diglucoside, a novel pigment for Cyclamen spp., generated by ion-beam irradiation”
Plant Biotechnol. 26 (2009) 565–569.

09J034 3-09 C
Y. Hase, M. Okamura, D. Takeshita, I. Narumi and A. Tanaka
“Efficient induction of flower-color mutants by ion beam irradiation in petunia seedlings treated with high sucrose concentration”
Plant Biotechnol. 27 (2010) 99-103.

09J035 3-18 G, C
A.N. Sakamoto, T.T.L. Vo, V. Puripunyavanich, Y. Hase, Y. Yokota, N. Shikazono, M. Nakagawa, I. Narumi and A. Tanaka
“A UVB-hypersensitive mutant in Arabidopsis thaliana is defective in the DNA damage response”
Plant J. 60 (2009) 509-517.

09J036 3-28 3-29 G
亀谷 宏美、小川 英之、中村 秀夫、下山 雄平、鵜飼 光子

“照射ナツメグ(Myristica fragrans)の ESR による検知“
Radioisotopes, 58 (2009) 179-185.

09J037 3-28 3-29 G
鵜飼 光子、亀谷 宏美、今村 太郎、
宮ノ下 明大、等々力 節子、下山 雄平
“照射害虫の ESR 信号”
Radioisotopes, 58 (2009) 799-806.

09J038 3-28 3-29 G
桜庭 一宏、鵜飼 光子
“学習指導要領改訂(2009)と放射線教育”
食品照射, 43 (2009) 17-23.

09J039 3-28 3-29 G
亀谷 宏美、鵜飼 光子
“長期間保存した照射黒胡椒のラジカル”
食品照射, 43 (2009) 1-4.

09J040 3-28 3-29 G
小川 英之、鵜飼 光子、 A. Lund、下山 雄平
“照射誘導ラジカルの緩和挙動”
食品照射, 43 (2009) 5-8.

09J041 3-28 3-29 G
菊地 正博、小川 英之、森下 憲雄、鵜飼 光子、
小林 泰彦、下山 雄平
“照射マンゴーに誘起されるラジカルの緩和現象”
食品照射, 43 (2009) 9-13.

09J042 3-28 3-29 G
M. Ukai, H. Kameya,
H. Nakamura and Y. Shimoyama
“Radical scavenging activities of plant food of alkyl-oxy radical and superoxide radical”
Food Sci. Tech. Res. 15 (2009) 619-624.

09J043 3-28 3-29 G
M. Kikuch, M. S. Hussain, N. Morishita, M. Ukai,
Y. Kobayashi and Y. Shimoyama
“ESR Study of free radicals in mango”
Spectrochim. Acta A 75 (2010) 310-313.

09J044 3-30 C
T. Funayama, K. Fukamoto, T. Sakashita,
Y. Yokota, M. Suzuki and Y. Kobayashi
“Development of new cell targeting system for heavy-ion microbeam systems at JAEA-Takasaki”
J. Radiat. Res. 50 (2009) A123.

09J045 3-30 C
C. Fournier, P. Barberet, T. Pouthier, S. Ritter,
B. Fischer, K. O. Voss, T. Funayama, N. Hamada,
Y. Kobayashi and G. Taucher-Scholz
“No evidence for DNA and early cytogenetic damage in bystander cells following heavy ion micro-irradiation at two facilities”
Radiat. Res. 171 (200) 530-540.

09J046 3-30 C
Y. Kobayashi, T. Funayama, N. Hamada,
T. Sakashita, T. Konishi, H. Imaseki, K. Yasuda,
M. Hatashita, K. Takagi, S. Hatori, K. Suzuki,
M. Yamauchi, S. Yamashita, M. Tomita,
M. Maeda, K. Kobayashi, N. Usami and L. Wu
“Microbeam Irradiation Facilities for Radiobiology in Japan and China”
J. Radiat. Res. 50 (2009) A29-A47

09J047 3-32 C, G
T. Sakashita, T. Takanami, S. Yanase, N. Hamada,
M. Suzuki, T. Kimura, Y. Kobayashi,
N. Ishii and A. Higashitani
“Radiation Biology of Caenorhabditis elegans:

Germ Cell Response, Aging and Behavior”
J. Radiat. Res., 51 (2010) 107-121.

09J048 3-33 C
W. S. Al-Jahdari, Y. Suzuki, Y. Yoshida
N. Hamada, K. Shirai S. E. Noda, T. Funayama,
T. Sakashita, Y. Kobayashi, S. Saito,
F. Goto and T. Nakano
“The radiobiological effectiveness of carbon-ion beams on growing neurons”
Int. J. Radiat. Biol. 85 (2009) 700-709.

09J049 3-43 O
T. Sakashita, T. Takanami, S. Yanase, N. Hamada,
M. Suzuki, T. Kimura, Y. Kobayashi,
N. Ishii and A. Higashitani
“Radiation Biology of Caenorhabditis elegans: Germ Cell Response, Aging and Behavior”
J. Radiat. Res. 51 (2010) 107-121.

09J050 3-47 C
S. Ishii, N. Suzui, S. Ito, N. S. Ishioka, N. Kawachi,
N. Ohtake, T. Ohyama and S. Fujimaki
“Real-time imaging of nitrogen fixation in an intact soybean plant with nodules using 13N-labeled nitrogen gas”
Soil Sci. Plant Nutr. 55 (2009) 660-666.

09J051 3-47 C
S. Fujimaki, S. Ishii and N. S. Ishioka
“Non-invasive imaging and analyses of transport of nitrogen nutrition in intact plants using a positron-emitting tracer imaging system (PETIS). In:"Nitrogen Assimilation in Plants"”
T. Ohyama, K. Sueyoshi eds., Research Signpost (in press) 著書.

09J052 3-47 C
藤巻 秀、石井 里美、大山 卓爾
“空気中の窒素を養分にするマメ科植物の「根粒」の機能の画像化”
放射線と産業 124 (2009) 33-35（総説）.

09J053 3-48 C
S. Fujimaki, N. Suzui, N. S. Ishioka, N. Kawachi,
S. Ito, M. Chino and S. Nakamura
“Tracing Cadmium from Culture to Spikelet: Noninvasive Imaging and Quantitative Characterization of Absorption, Transport, and Accumulation of Cadmium in an Intact Rice Plant”
Plant Physiol. 152 (2010) 1796-1806.

09J054 3-48 C
河地 有木、石井 里美、石岡 典子、藤巻 秀
“11CO2 と植物用ポジトロンイメージング装置を用いたダイズ植物の根粒に対する光合成産物移行のリアルタイム解析”
伊藤小百合, 鈴井伸郎. Radioisotopes 59 (2010) 145-154.

09J055 3-51
H. Hanaoka, H. Tominaga, K. Yamada, P. Paudyal,
Y. Iida, S. Watanabe, B. Paudyal, T. Higuchi,
N. Oriuch and K. Endo
“Evaluation of 64Cu-labeled DOTA-D-Phe1-Tyr3-octreotide (64Cu-DOTA-TOC) for imaging somatostatin receptor-expressing tumors”
Ann. Nucl. Med. 23 (2009) 559-567.

09C056 3-51 C
S. Watanabe, H. Hanaoka, J. Liang, Y. Iida,
K. Endo and N. S. Ishioka
“PET Imaging of Norepinephrine Transporter (NET)-Expressing Tumors Using

76Br-meta-Bromobenzylguanidine (76Br-MBBG)"
J. Nucl. Med. (2010) in press.

09J057 3-52 C

P. Paudyal, B. Paudyal, H. Hanaoka, N. Oriuchi,
Y. Iida, H. Yoshioka, H. Tominaga, Sa. Watanabe,
Sh. Watanabe, N. S. Ishioka and K. Endo
"Imaging and biodistribution of Her2/neu expression in non-small cell lung cancer xenografts with (64)Cu-labeled trastuzumab PET"
Cancer Sci. 101 (2010) 1045-1050.

09J058 3-54 S

T. Satoh, M. Oikawa and T. Kamiya
"Three-dimensional measurement of elemental distribution in minute samples by combination of in-air micro-PIXE and STIM"
Nucl. Instrum. Meth. B 267 (2009) 2125-2127.

09J059 3-55 T

Y. Kawamura, K. Ishii, S. Matsuyama,
M. Nakhostin, M. Fujiwara, M. Watanabe,
S. Okura, N. Hamada, S. Tsuboi, K. Yamanaka,
Y. Hashimoto, M. Fujikawa, G. Catella, Y. Hatori,
K. Fujiki, H. Yamazaki, R. Ortega,
G. Deves and A. Carmona
"3D IMAGING OF HUMAN CELLS BY USING PIXE-μ-CT"
Int. J. PIXE, Vol.19 Nos 1&2 (2009) 29-37.

09J060 3-55 T

S. Matsuyama, K. Ishii, M. Fujiwara, Y. Kikuchi,
M. Nakhostin, Y. Kawamura, S. Tsuboi,
K. Yamanaka, M. Watanabe, S. Ohkura,
Y. Hashimoto, M. Fujikawa, G. Catella, K. Fujiki,
Y. Hatori, N. Hamada, S. Tanino, H. Abe,
Y. Watanabe and H. Yamazaki
"CHARACTERIZATION OF CORROSION LAYER OF CARBON STEEL BY MICRO-PIXE/RBS ANALYSIS"
Int. J. PIXE, Vol.19 Nos 1&2 (2009) 61-66.

09J061 3-55 T

S. Matsuyama, K. Ishii, M. Fujisawa,
Y. Kawamura, S. Tsuboi, K. Yamanaka,
M. Watanabe, Y. Hashimoto, S. Ohkura,
M. Fujikawa, T. Nagaya, K. Komatsu,
H. Yamazaki and Y. Kikuchi
"Upgrading of the 4.5 MV Dyanamitron accelerator at Tohoku University for microbeam and nanobeam applications"
Nucl. Instrum. Meth. Phys. Res. B 267 (2009) 2060- 2064.

09J062 3-55 T

石井 慶造
"マイクロPIXEによる準単色X線ミクロンCT"
放射線 Vol.34, No.4 (2009) 266-272.

09J063 3-57 C

H. Yamamoto, Y. Iwami, S. Ebisu, M. Nomachi,
K. Yasuda, T. Sakai and T. Kamiya
"Development of a System for Measuring Fluoride Distribution in Teeth Using a Nuclear reaction"
Int. J. PIXE 19 (1&2) (2009) 91-102.

09C064 3-57 C

H. Komatsu, H. Yamamoto, M. Nomachi,
K. Yasuda, Y. Matsuda, M. Kinugawa,
T. Kijimura, H. Sano, T. Satou,
S. Oikawa and T. Kamiya
"Fluorine Uptake into Human Enamel around Fluoride-containing Dental Materials during Cariogenic pH Cycling"

Nucl. Instrum. Meth. Phys. Res. B 267 (2009) 2136-2139.

09J065 3-58

N. Tanaka, H. Kimura, A. Faried, M. Sakai, A. Sano, T. Inose, M. Sohda, K. Okada, M. Nakajima, T. Miyazaki, M. Fukuchi, H. Kato, T. Asao, H. Kuwano, T. Satoh, M. Oikawa, T. Kamiya and K. Arakawa
"Quantitative analysis of cisplatin sensitivity of human esophageal squamous cancer cell lines using in-air micro-PIXE"
Cancer Sci. (2010). [Epub ahead of print]

09J066 3-59

S. Harada, S. Ehara, K. Ishii, A. Tanaka, T. Satoh, S. Matsuyama, H. Yamazaki, Y. Komori, T. Kamiya, T. Arakawa, M. Saitoh, M. Oikawa and K. sera
"Targeted Delivery of Chemotherapeutic Agents by using Improved Radiosensitive Liquid-Core Microcapsules and Assessment of Their Antitumor Effect"
Int. J. Radiat. Oncol., Biol. Phys. 175 (2009) 455-462.

09J067 3-60 S

S. Matsuzaki, Y. Shimizu, K. Dobashi, T. Nagamine, T. Satoh, T. Ohkubo, A. Yokoyama, Y. Ishii, T. Kamiya, K. Arakawa, S. Makino, M. Utsugi, T. Ishizuka, S. Tanaka, K. Shimizu and M. Mori.
"Analysis on the co-localization of asbestos bodies and Fas or CD163 expression in asbestos lung tissue by in-air micro-pixe"
Int. J. Immunopathol. Pharmacol. 23(1) (2010) 1-11.

09J068 3-60 S

Y. Shimizu, K. Dobashi, T. Kusakbe, T. Nagamine, M. Oikawa, T. Satoh, J. Haga, Y. Ishii, T. Ohkubo, T. Kamiya, K. Arakawa, T. Sano, S. Tanaka, K. Shimizu, S. Matsuzaki, M. Utsug and M. Mori.
"In-air micro-particle induced X-ray emission analysis of asbestos and metals in lung tissue"
Int. J. Immunopathol. Pharmacol. 21(3) (2008) 567-76.

09C069 3-61 S

H. Takada, T, Nagamine, Y. Tokita, M. Oikawa, T. Satoh, T. Kamiya, K. Arakawa and M. IHA
"In-Air Micro-PIXE Analysis for Metal Elements in Rat Hepatocytes Treated With Fucoidan"
Int. J. PIXE 19 (1-2) (2009) 47-54.

09J070 4-01 S, I

A. Inouye, S. Yamamoto, S. Nagata, M. Yoshikawa andT. Shikama
"Hydrogen retention induced by ion implantation in tungsten trioxide films"
Nucl. Instrum. Meth. Phys. Res. B 267 (2009) 1480-1483.

09J071 4-05 I, E

M. Kishimoto, H. Abe and H. Uchida
"Combinational Effect of Charged Particle Irradiation and Alkaline Pretreatment on Hydriding Property of a Mm-Ni Based Alloy"
Int. J. Hydrogen Energy, submitted.

09J072 4-05 I

H. Abe, S. Aone, R. Morimoto, H. Uchida and T. Ohshima
"Improvement of Hydrogen Absorption Characteristics of Pd using Irradiation of Heavy

Ions”
J. Surf. Sci., submitted.

09J073 4-05 I, E
S. Ohnuki, H. Abe, H. Uchida and Y. Matsumura
“Irradiation Effects on Hydrogen Absorption Rate of Metal Hydride”
J. Surf. Sci., submitted.

09J074 4-08 C
S. Watanabe, S. Seki, M. Sugimoto, M. Yoshikawa, S. Tagawa, S. Tsukuda and S. Tanaka
“Sugar Nanowires Based on Cyclodextrin Prepared by Single Particle Nano-fabrication Technique”
Radiat. Phys. Chem., 78 (2009) 1071-1075.

09J075 4-08 4-11 C
S. Tsukuda, S. Seki, M. Sugimoto, A. Idesaki, S. Tagawa and S. Tanaka
“Formation of hybrid nano-structures by ion beam irradiation to the sol-gel film”
J. Photopolym. Sci. Tech. 22 (2009) 245-248.

09J076 4-08 C
A. Idesaki, M. Sugimoto and M. Yoshikawa
“Synthesis Of A Catalyst-Loaded SiC Material from Si-Based Polymer”
Ceram. Trans. 213 (2010) in press.

09J077 4-08 C
M. Sugimoto, A. Idesaki, M. Yoshikawa, S. Watanabe and S. Seki
“Synthesis of Ceramic Nano Fiber from Precursor Polymer by Single Particle Nano-fabrication Technique”
Ceram. Trans. 213 (2010) in press.

09J078 4-10 E, G
M. Narisawa, R. Sumimoto, K. Kita, H. Mabuchi, Y.W. Kim, M. Sugimoto and M. Yoshikawa
“Investigation of Curing Process on Melt Spun Polymethylsilsesquioxane Fiber as Precursor for Silicon Oxycarbide Fibers”
Adv. Mater. Res. 66 (2009) 1-4.

09J079 4-10 E, G
K. Kita, M. Narisawa, H. Mabuchi, M. Itoh, M. Sugimoto and M. Yoshikawa
“Synthesis of SiC based Fibers with Continuous Pore Structure by Melt- spinning and Controlled Curing Method”
Adv. Mater. Res. 66 (2009) 5-8.

09J080 4-10 E, G
K. Kita, M. Narisawa, H. Mabuchi, M. Itoh, M. Sugimoto and M. Yoshikawa
“Formation of Continuous Pore Structures in Si-C-O Fibers by Adjusting the Melt Spinning Condition of Polycarbosilane - Polysiloxane Polymer Blend”
J. Am. Ceram. Soc. 92 (2009) 1192-1197.

09J081 4-10 E, G
K. Kita, M. Narisawa, A. Nakahira, H. Mabuchi, M. Sugimoto and M. Yoshikawa
“Synthesis and properties of ceramic fibers from polycarbosilane/polymethylphenylsiloxane polymer blends”
J. Mater. Sci. 45 (2010) 3397-3404.

09J082 4-10 E, G
M. Narisawa, R. Sumimoto, K. Kita, Y. Satoh, H. Kado, H. Mabuchi, M. Sugimoto, M. Yoshikawa and Y. Kim

"Evaluation of heat stability of Si-O-C fibers derived from polymethylsilsesquioxane"
Ceram. Trans. 213 (2010) in press.

09J083 4-10 E, G

K. Kita, M. Narisawa, H. Mabuchi, M. Itoh, M. Sugimoto and M. Yoshikawa
"Investigation of nano porous SiC based fibers synthesized by precursor method"
Ceram. Trans. 213 (2010) in press.

09J084 4-13 I

Y. Kasukabe, Y. Watanabe, S. Yamamoto, M. Yoshikawa and Y. Fujino
"Characterization of Heating and Nitriding Processes of Titanium Thin Films Grown on NaCl (001) Substrate Held at Room Temperature"
e-J. Surf. Sci. Nanotech. 7 (2009) 625-632.

09J085 4-16

T. Osawa, M. Ono, F. Esaka, S. Okayasu, Y. Iguchi, T. Hao, M. Magara and T. Mashimo
"Mass-dependent isotopic fractionation of a solid tin under a strong gravitational field"
Europhys. Lett. 85 (2009) 64001.

09J086 4-16

M. Ono, M. Sueyoshi, S. Okayasu, T. Hao, F. Esaka, T. Osawa, Y. Iguchi and T. Mashimo
"Development of special rotor for centrifugal separation of isotopes in solid pure metals"
Rev. Sci. Instrum. 80 (2009) 083908.

09J087 4-16

T. Hao, M. Ono, S. Okayasu, S. Sakai, K. Narumi, Y. Hiraiwa, H. Naramoto and Y. Maeda
"RBS study of diffusion under strong centrifugal force in bimetallic Au/Cu thin films"
Nucl. Instrum. Meth. Phys. Res. B 268 (2010) 1867.

09J088 4-17 S

M. Miyao, K. Hamaya, T. Sadoh, H. Itoh and Y. Maeda
"Molecular Beam Epitaxial Growth of Ferromagnetic Heusler Alloys for Group-IV Semiconductor Spintronic Devices"
Thin Solid Films 518 (2010) S273-S277.

09J089 4-18 O

M. Maekawa, Y. Yabuuchi and A. Kawasuso
"Evaluation of stainless steel under tensile stress using positron microbeam"
J. Phys.: Conf. Ser., (2010) to be printed.

09J090 4-22

M. Kayama, H. Nishido and K. Ninagawa
"Impurities effect on cathodoluminescence in tridymite and cristobalite"
J. Mineral. Petrol. Sci., 104 (2009) 401-406.

09J091 4-22

M. Kayama H. Nishido and K. Ninagawa
"Cathodoluminescence characterization of tridymite and cristobalite: Effects of electron irradiation and sample temperature"
Am. Mineral. 94 (2009) 1018-1028.

09J092 4-22

M. Kayama H. Nishido and K. Ninagawa
"Cathodoluminescence of feldspar minerals and assignment of luminescence centers"
Adv. ESR Appl. 25 (2009) 13-18.

09J093 4-22

T.Usami, S. Toyoda, H. Bahadur,
A. K. Srivastava and H. Nishido
"Characterization of the E1′ center in quartz: Role of aluminum hole centers and oxygen vacancies"
Physica B: Condensed Matter, 404 (2009) 3819-3823.

09J094 4-22

K. Zhumadilov, A. Ivannikov, D. Zharlyganova, Z. Zhumadilov, V. Stepanenko, K. Apsalikov, M. R. Ali, A. Zhumadilova, S. Toyoda, S. Endo, K. Tanaka, T. Okamoto and M. Hoshi
"ESR dosimetry study on population of settlements nearby Ust-Kamenogorsk city" Kazakhstan,
Radiat. Envir. Biophys. 48 (2009) 419-425.

09J095 4-22

T. Usami, S. Toyoda and H. Bahadur
"The effect of Al center to the formation of E1' center in Quartz"
Lumin. Appl. (ICLA-2008), Vol-18 (2009) 162-164.

09J096 4-26 4-27 O

Y. Fukaya, A. Kawasuso and A. Ichimiya
"Inelastic scattering processes in reflection high-energy positron diffraction from a Si(111)-7×7 surface"
Phys. Rev. B 79 (2009) 193310 (4 pages).

09J097 4-26 4-27 O

Y. Fukaya, I. Matsuda, M. Hashimoto, H. Narita, A. Kawasuso and A. Ichimiya
"Metal Co-Adsorption Induced $\sqrt{21}\times\sqrt{21}$ Superstructure on Si(111) Surface Studied by Reflection High-Energy Positron Diffraction"
e-J. Surf. Sci. Nanotechnol. 7 (2009) 432-435.

09J098 4-26 4-27 O

M. Hashimoto, Y. Fukaya,
A. Kawasuso and A. Ichimiya
"Phase Transition of In/Si(111) Surface Studied by Reflection High-Energy Positron Diffraction"
e-J. Surf. Sci. Nanotechnol. 7 (2009) 436-440.

09J099 4-28 G

T. Kondoh, A. Asano, J. Yang, K. Norizawa, K. Takahashi, M. Taguchi, R. Nagaishi, R. Katoh and Y. Yoshida
"Pulse Radiolysis Study of Ion-species Effects on the Solvated Electron in Alkylammonium Ionic Liquids"
Radiat. Phys. Chem. 78 (2009) 1157-1160.

09J100 4-29 C

S. Nakagawa, M. Taguchi,
K. Hirota and T. Murakami
"Degradation of hydroxymaleimide in 2-propanol by irradiation of energetic heavy ions (II)"
Radiat. Phys. Chem. 79 (2010) 890-893.

09J101 4-30 C

M. Taguchi, A. Kimura, R. Watanabe and K. Hirota
"Estimation of yields of hydroxyl radicals in water under various energy heavy ions"
Radiat. Res. 171 (2009) 254-263.

09J102 4-30 C

M. Taguchi, G. Baldacchino, S. Kurashima, A. Kimura, Y. Sugo, Y. Katsumura, and K. Hirota
"Transient absorption measurement system using pulsed energetic ion"
Radiat. Phys. Chem. 78 (2009) 1169-1174.

09J103 4-30 C
G. Baldacchino, T. Maeyama , S. Yamashita,
M. Taguchi, A. Kimura,
Y. Katsumura and T. Murakami
"Determination of the Time-dependent OH-Yield by Using a Fluorescent Probe. Application to Heavy Ion Irradiation"
Chem. Phys. Lett. 468 (2009) 275-279.

09J104 4-30 C
M. Alam, F. Miserque, M. Taguchi,
L. Boulanger, and J. P. Renault
"Tuning hydrogen production during oxide irradiation through surface grafting"
J. Mater. Chem. 19 (2009) 4261-4267.

09J105 4-30 C
S. Yamashita, M. Taguchi,
G. Baldacchino and Y. Katsumura
"Radiation chemistry of liquid water with heavy ions: Steady-state and pulse radiolysis studies"
Charged particle and photon interactions with matter-recent advances, applications and interfaces, in press.

09J106 4-31 C
T. Kondoh, A. Asano, J. Yang, K. Norizawa,
K. Takahashi, M. Taguchi, R. Nagaishi,
R. Katoh and Y. Yoshida
"Pulse radiolysis study of ion-species effects on the solvated electrons in alkyl ammonium ionic liquids"
Radiat. Phys. Chem. 78 (2009) 1157-1160.

09J107 4-34 C
Y. Shikaze, Y. Tanimura,
J. Saegusa and M. Tsutsumi
"Development of highly efficient proton recoil counter telescope for absolute measurement of neutron fluences in quasi-monoenergetic neutron calibration fields of high energy"
Nucl. Instrum. Meth. Phys. Res. A 615 (2010) 211-219.

09J108 4-35 C
H. Harano, T. Matsumoto, Y. Tanimura,
Y. Shikaze, M. Baba and T. Nakamura
"Monoenergetic and quiasi-monoenergetic neutron reference fields in Japan"
Radiat. Meas. (in printing).

09J109 4-41 I
V. Lavrentiev, J. Vacik,
H. Naramoto and K. Narumi
"Polymerization of solid C60 under C60+ cluster ion bombardment"
Appl. Phys. A 95 (2009) 867-873.

09J110 4-41
V. Lavrentiev, J. Vacik,
H. Naramoto and K. Narumi
"Fullerene nanostructure design with cluster ion impacts"
J. Alloys Comp. 483 (2009) 479-483.

09J111 4-42 T
N. Fujita, S. Kosugi, Y. Zushi, T. Matsui,
Y. Saitoh and A. Iwase
"Effect of energetic heavy ion irradiation on the structure and magnetic properties of FeRh thin films"
Nucl. Instrum. Meth. Phys. Res. B 267 (2009) 921-924.

09J112 4-47 S

Y. Seki, Y. Furuta, H. Nishikawa, T. Watanabe, T. Nakata, T. Satoh, Y. Ishii and T. Kamiya
"Electroplating using high-aspect-ratio microstructures fabricated by proton beam writing"
Microelectron. Eng. 86, Issues 4-6 (2009) 945-948.

09J113 4-47 S

Y. Furuta, H. Nishikawa, T. Satoh, Y. Ishii, T. Kamiya, R. Nakao and S. Uchida
"Fabrication and evaluation of 3D-electric micro filters using proton beam writing"
Microelectron. Eng. 86, Issues 4-6 (2009) 1396-1400.

09J114 4-47 S

Y. Furuta, H. Nishikawa, T. Satoh, Y. Ishii, T. Kamiya, R. Nakao and S. Uchida
"Applications of microstructures fabricated by proton beam writing to electric-micro filters"
Nucl. Instrum. Meth. Phys. Res. B 267 (2009) 2285–2288.

09J115 4-47 S

西川宏之
"集束プロトンビーム描画による高アスペクト比構造の加工とその応用"
放射線、Vol.35, No.2 (2009) 77-86.

09J116 4-47 S

西川宏之
"マイクロビームによる高アスペクト比微細加工"
特集解説 放射線と産業(雑誌) No.122, (2009) 19-23.

09J117 4-50 C

S. Kurashima, K. Yoshida, M. Oikawa, T. Satoh, N. Miyawaki, T. Yuyama, S. Okumura, H. Kashiwagi, I. Ishibori, T. Nara, T. Kamiya, M. Fukuda and W. Yokota
"Quick change of ion species of heavy-ion microbeam by cocktail beam acceleration technique with the JAEA AVF cyclotron"
Nucl. Instrum. Meth. B 267 (2009) 2024-2027.

09J118 4-50 C

S. Kurashima, T. Yuyama, N. Miyawaki, H. Kashiwagi, S. Okumura and M. Fukuda
"Useful technique for analysis and control of the acceleration beam phase in the azimuthally varying field cyclotron"
Rev. Sci. Instrum. 81 (2010) 033306.

09J119 4-51 T

Y. Saitoh, A. Chiba and K. Narumi
"Transmissions of cluster ions through a tandem accelerator on several stripper gases"
Rev. Sci. Instrum 80 (2009) 106104.

09J120 4-51 I

山田 圭介、大越 清紀、齋藤 雄一、織茂 貴雄、大前 昭臣、山田 尚人、水橋 清
"TIARA イオン注入装置におけるイオン生成法の開発"
JAEA-Tech. 2008-090.

A 1.2 Publication in Proceedings

09C001 1-01 C, T, I, E
M. Imaizumi, T. Ohshima, and T. Takamoto
"Radiation Resistance of InGaP/GaAs Dual-Junction Thin-Film Space Solar Cell"
Proc. 34th IEEE Photovoltaic Specialists Conf. [Philadelphia, USA] (2009) To be issued.

09C002 1-01 C, T, I, E
S. Sato, H. Sai, M. Imaizumi K. Shimazaki, M. Kondo, and T. Ohshima
"Anomalous Photoconductivity Variations of Solar Cell Quality a-Si:H Thin Films Induced by Proton Irradiation"
Proc. 34th IEEE Photovoltaic Specialists Conf. [Philadelphia, USA] (2009) To be issued.

09C003 1-03 C, T
N. Masuda, S. Abo, F. Wakaya, T. Iwamatsu, T. Hirao, S. Onoda, T. Ohshima, and M. Takai
"Soft error tolerance in SOI-SRAM analyzed by oxygen ion probe"
Proc. Int. Workshop Adv. Mater. Nanotechnol. 2009 (IWAMN 2009) (2009) 65.

09C004 1-03 C, T
平尾 敏雄、小野田 忍、牧野 高紘、大島 武
"マイクロビームを用いた最新 SOI メモリセルの SEU 発生挙動の観測"
第 22 回タンデム加速器及びその周辺技術の研究会 報告集 ［つくば］(2009/07) 9.

09C005 1-04 C
A.Maru, H.Shindou T. Ebihara, A. Makihara, T. Hirao and S.Kuboyama
"90 nm バルク CMOS プロセスの宇宙適用性の検討"
第 1 回 半導体材料・デバイスフォーラム (2010/02)

09C006 1-05 C, T, I
高橋 芳浩
"宇宙用半導体デバイス開発に関する基礎研究"
日大理工学術講演会, S4-17 (2009/11) 37-40.

09C007 1-05 C, T, I
大脇 章弘、竹安 秀徳、岡崎 勇志、松岡 将太、高橋 芳浩
"SOI 基板上の pn ダイオードにおける重イオン照射誘起電流"
日大理工学術講演会, M-1 (2009/11) 1051-1052.

09C008 1-05 C, T, I
竹安 秀徳、大脇 章弘、岡崎 勇志、松岡 将太、高橋 芳浩
"SOI デバイスの重イオン照射誘起電流制御に関する検討"
日大理工学術講演会, M-2 (2009/11) 1053-1054.

09C009 1-05 C, T, I
高橋 芳浩
"SOI デバイスの重イオン照射誘起電流"
第 1 回半導体材料・デバイスフォーラム (2010/02) 20-23.

09C010 1-06 I
J. H. Park, H. Okada, A. Wakahara, Y. Furukawa, Y. T. Kim, J. H.Song, H. J. Chang, S. Sato and T. Ohshima
"Effect of ion-beam-induced damage on luminescence properties in Tb implanted AlxGa1-xN"
2009 Asia-Pacific Workshop Fund. Appl. Adv.

Semicond. Dev., [Busan, Korea] (2009/06).

09J011 1-12 E

J. Isoya, T. Umeda, N. Mizuochi, N. T. Son,
E. Janzén, and T. Ohshima
“Comparison of Structure Relaxation in Fundamental Defects Between Diamond and SiC”
The 60th De Beers Diam. Conf., University of Warwick (2009).

09J012 1-12 E

磯谷 順一、大島 武、小野田 忍、森下 憲雄、谷口 尚、渡邊 賢司、神田 久生、角谷 均
“NV センターの量子情報処理・磁束計への応用の課題と欠陥制御”
第 23 回ダイヤモンドシンポジウム、［千葉工業大学］(2009/11).

09J013 1-12 E

磯谷 順一、角谷 均、中村 和郎、花屋 博秋、佐伯 誠一、小野田 忍、大島 武、森下 憲雄、島田 愛子、水田 幸男
“ダイヤモンド中の[NV]-センターのアンサンブル系のスピン緩和：T1，T2*，T2”
第 48 回電子スピンサイエンス学会年会、［神戸大学］(2009/11).

09J014 1-12 E

磯谷 順一、中村 和郎、角谷 均、谷口 尚、神田 久生
“FT-ESR を用いたダイヤモンド中の窒素の高感度定量”
第 57 回応用物理学関係連合講演会、［東海大学］(2010/03).

09J015 1-12 E, T

磯谷 順一、大島 武、小野田 忍、森下 憲雄、花屋 博明、谷口 尚、渡邊 賢司、神田 久生、角谷 均
“ダイヤモンドの NV センターの高濃度作成とスピン緩和”
日本物理学会第 65 会年次大会、［岡山大学］(2010/03).

09C016 1-06 I

T. Hata, H. Okada A. Wakahara Y. Furukawa,
S. Sato and T. Ohshima
“Electrical- and Emission- Characteristics Dependence on Ion Implantation Conditions of Eu-Doped Light Emitting AlGaN/GaN HEMT”
Int. Symp. Adv. Plasma Sci. Appl. (ISPlasma2010), [Nagoya, Japan] (2010/03).

09C017 1-13 G

Y. Sasaki, Y. Sugo, M. Saeki,
Y. Morita and A. Ohashi
“Extraction of technetium(VII) and rhenium(VII) by the new reagent,
2-(Imino)bis(N,N-dialkylacetamide) (IDAA) ”
Proc. Int. Conf. Asia-Pacific Symp. Radiochem. (APSORC-09), [Napa, USA] (2009).

09C018 1-27

I. Ioka, Y. Ishijima, K. Usami, N. Sakuraba,
Y. Kato and K. Kiuchi
“Susceptibility of IASCC for Extra High Purity Austenitic Stainless Steel”
Proc. 14th Int. Conf. Fusion Reactor Mater. [Sapporo, Japan] ICFRM14 (2008) 255.

09C019 1-30 C, I

T. Yamaki, S. Yamamoto,
T. Hakoda and H. Koshikawa
“Ion Beam Modification of Pt Electrocatalyst

Nanoparticles for Polymer Electrolyte Membrane Fuel Cells”
Mater. Res. Soc. Symp. Proc., 1217 (2010) Y08-26.

09C020 1-31 C
H. Koshikawa, H. Usui and Y. Maekawa
“Thermally stable polyimide/Cu hybrid membranes using ion track technique”
16th Int. Conf. Surf. Mod. Mater. by Ion Beams, (SMMIB 2009) [Tokyo, Japan] (2009/09) 5.

09C021 1-33 G
S. Hasegawa, H. Iwase, S. Koizumi,
M. Ohnuma and Y. Maekawa
“Morphology-Controlled Graft Polymerization in Poly(ether ether ketone) films”
58th Symp. Macromolecules.

09C022 1-34 E, G
S. Sawada, A. Kawasuso,
M. Maekawa and Y. Maekawa
“Free-Volume Structure of Fluoropolymer-Based Radiation-Grafted Electrolyte Membranes Investigated by Positron Annihilation Lifetime Spectroscopy”
Abst. Adv. Sci. Res. Symp. 2009 (ASR 2009) [Tokai, Japan] (2009) 25.

09C023 1-34 E, G
S. Sawada, T. Yamaki, M. Asano, A. Suzuki,
T. Terai and Y. Maekawa
“Water Diffusion in Fluoropolymer-Based Fuel-Cell Electrolyte Membranes Investigated by Radioactivated-Tracer Permeation Technique”
Abst. Asia-Pacific Symp. Radiochem. ’09, (APSORC ‘09) [Napa Valley, USA] (2009) PO-2-11-22.

09C024 2-03 O
M. Takigami, N. Nagasawa, Y. Maehara,
S. Takigami and M.Tamada
“Preparation of CMC-Acid Gel and Its Application”
Proc. 15th Gums Stabil. Food Ind. [Wexham, UK] (2009) 427-434.

09C025 3-26 C
増渕 隆、上山 修、佐藤 勝也、長谷 純宏、
鳴海 一成
“イオンビームによる新規酵母の育種”
第6回イオンビーム育種研究会大会、13-14 (2009).

09C026 3-56
K. Endo, Y Shibata, T Yamamoto, K Nakai,
A Matsumura, T Sato, M Oikawa, K Arakawa,
T Kamiya and K Ishii
“THE CAPABILITIES AND LIMITATIONS IN THE ANALYSIS OF BORON MICRO-DISTRIBUTION IN TUMOR CELLS USING PIGE”
13th Int. Congr. Neutron Capture Therapy “A new option against cancer”, [Florence, Italy] (2008/11) 258-260.

09C027 3-60 S
松崎 普一、清水 泰生、土橋 邦生、草壁 孝彦、
長嶺 竹明、及川 將一、神谷 富裕、佐藤 隆博、
芳賀 潤一、大久保 猛、石井 保行、荒川 和夫、
石塚 全、森 昌朋
“In air micro-PIXE を用いた肺内吸入金属と炎症性蛋白発現の解析”
日本呼吸器学会雑誌 47 (2009) 252

09C028 3-61 S
時田 佳治、菊地 弘記、長嶺 竹明、佐藤 隆博、
神谷 富裕、荒川 和夫

“ヒト赤血球を用いた大気マイクロ PIXE 測定試料の作製”
第 25 回 PIXE シンポジウム抄録集 (2009) 18.

09C029 4-04 I
A. V. Umenyi, M. Honmi, K. Miura, O. Hanaizumi, S. Yamamoto, A. Inouye and M. Yoshikawa
“UV and visible light emitting fused-silica substrates fabricated by Si-ion implantation”
16th Int. Conf. Surf. Modif. Mater. by Ion Beams, [Tokyo, Japan] (2009) PA-24.

09C030 4-04 I
S. Kawashiri, M. Honmi, A. V. Umenyi, T. Shinagawa, K. Miura, O. Hanaizumi, S. Yamamoto, A. Inouye and M. Yoshikawa
“Novel photonic crystal waveguides utilizing Si-ion implantation”
5th Int. Symp. Silicon Sci. & 1st Int. Conf. Adv. Micro-Device Eng. [Kiryu, Japan] (2009) 1P19.

09C031 4-04 I
A. V. Umenyi, S. Kawashiri, K. Miura and O. Hanaizumi
“FDTD analysis of fused-silica substrates fabricated by Si-ion implantation for photonic crystals devices”
5th Int. Symp. Silicon Sci. & 1st Int. Conf. Adv. Micro-Device Eng. [Kiryu, Japan] (2009) 1P20.

09C032 4-04 S
Y. Machida, M. Uehara, K. Miura, O. Hanaizumi, Y. Ishii, T. Satoh, K. Takano, T. Ohkubo, A. Yamazaki, A. Inouye, M. Koka, A. Yokoyama, T. Kamiya, T. Kojima and H. Nishikawa
“Fabrication of polymer optical waveguides using proton beam writing”
5th Int. Symp. Silicon Sci. & 1st Int. Conf. Adv. Micro-Device Eng. [Kiryu, Japan] (2009) 2P27.

09C033 4-04 I
三浦 健太、本美 勝史、花泉 修、山本 春也、井上 愛知、吉川 正人
“Si イオン注入により発現する溶融石英基板からの紫外発光”
第 42 回照明学会全国大会、[札幌]、113 (2009).

09C034 4-04 S
三浦 健太、町田 裕貴、上原 政人、花泉 修、石井 保行、佐藤 隆博、高野 勝昌、大久 保猛、山崎 明義、井上 愛知、江夏 昌志、横山 彰人、神谷 富裕、小嶋 拓治、西川 宏之
“プロトンビーム描画による波長 1.5μm 帯用 PMMA 導波路の試作”
第 70 回応用物理学会学術講演会、[富山]、(2009) 8a-ZN-6.

09C035 4-04 S
三浦 健太、町田 裕貴、上原 政人、花泉 修、石井 保行、佐藤 隆博、高野 勝昌、大久保 猛、山崎 明義、井上 愛知、江夏 昌志、横山 彰人、神谷 富裕、小嶋 拓治、西川 宏之
“プロトンビーム描画による波長 1.5mm 帯用シングルモード PMMA 導波路”
電子情報通信学会光エレクトロニクス研究会、[東京]、(2009) OPE2009-165.

09C036 4-04 S
三浦 健太、町田 裕貴、上原 政人、花泉 修、石井 保行、佐藤 隆博、高野 勝昌、大久保 猛、山崎 明義、井上 愛知、江夏 昌志、横山 彰人、神谷 富裕、小嶋 拓治、西川 宏之
“プロトンビーム描画による波長 1.5μm 帯用 PMMA 導波路の試作(II)”

第 57 回応用物理学関係連合講演会、[平塚]、(2010) 18p-P6-3.

09C037 4-17 S

Y. Maeda, Y. Hiraiwa, K. Narumi, A. Kawasuso, Y. Terai, Y. Ando, K. Ueda, T. Sadoh, K. Hamaya and M. Miyao
"Site Preference of Atoms in Heusler Alloys Fe3Si and Fe2MnSi Grown on Ge(111) toward Realization of Ge Channel Spin Transistors"
Mater. Res. Soc. Proc. 1119E (2009) 1119-L05-02-07.

09C038 4-17 S

Y. Maeda
"Aspects of Applications of Semiconducting and Ferromagnetic Silicides to Photonic and Spin Devices"
Proc. 14th JSAP Meeting Semicond. Silicides & Related Mater. (2009) 22-25.

09C039 4-22

M. Kayama, T. Nakazato, H. Nishido, K. Ninagawa and A. Gucsik
Cathodoluminescence Characterization of Maskelynite and Alkali Feldspar in Shergottite (Dhofar 019). "Micro-Raman Spectroscopy and Luminescence Studies in the Earth and Planetary Sciences"
Am. Insti. Phys. Conf. Proc., Gucsik A. (Ed) AIP 1163 (2009) 135-140.

09C040 4-22

T. Okumura, A. Gucsik, H. Nishido, K. Ninagawa and S. Toyoda
Cathodoluminescence microcharacterization of ballen silica in impactites. "Micro-Raman Spectroscopy and Luminescence Studies in the Earth and Planetary Sciences"
Am. Insti. Phys. Conf. Proc., Gucsik A. (Ed) AIP 1163 (2009) 148-154.

09C041 4-22

A. Gucsik, Sz. Berczi, T. Okumura, H. Nishido, K. Ninagawa and Sz. Nagy
Scanning Electron Microscope-Cathodoluminescence Properties of Fayalite and Forsterite from Kaba CV3 Chondrite: Application to Mineralogy of IDPs. "Micro-Raman Spectroscopy and Luminescence Studies in the Earth and Planetary Sciences"
Am. Insti. Phys. Conf. Proc., Gucsik A. (Ed) AIP 1163 (2009) 168-174.

09C042 4-22

S. Toyoda, K. Hosogi, K. Nagashima, Y. Isozaki, Y. Sun and R. Tada
Paramagnetic defects in quartz as the proxies for provenance of Aeolian and fluvial sediments,
Proc. Int. Conf. Lumin. Appl. (ICLA-2008) 18 (2009) 165-167.

09J043 4-22

M. Kayama A. Gucsik, H. Nishido, K. Ninagawa and A. Tsuchiyama
Cathodoluminescence and Raman Spectroscopic Characterization of Experimentally Shocked Plagioclase.
"Micro-Raman Spectroscopy and Luminescence Studies in the Earth and Planetary Sciences"
Am. Inst. Phys. Conf. Proc., Gucsik A. (Ed) AIP 1163 (2009)86-95.

09C044 4-28 G

Y. Kumagai, R. Nagaishi,
R. Yamada and Y. Katsumura
“Effect of Silica Gel on Radiation-induced Reduction of Dichromate Ion”
2nd Anniv. Symp. GoNERI's Foundation - Steps toward Leading the World in Nuclear Education of Universities, Global COE on Nuclear Education and Research Initiative (GoNERI), the University of Tokyo (2009) 135-139.

09C045 4-28 G

Y. Kumagai, R. Nagaishi, R. Yamada,
Y. Muroya and Y. Katsumura
“Effects of Silica Particles on Reactions of Radiolytic Products of Water”
Radiat. Chem. 21st Century - A Visionary Meeting, Notre Dame Radiat. Lab., University of Notre Dame, [IN, USA] (2009) XXX.

09C046 4-28 G

永石 隆二、青柳 登、田口 光正、近藤 孝文、楊 金峰、吉田 陽一
“チオシアン酸イオンを含んだ混合イオン液体中の放射線分解生成物の反応挙動”
大阪大学産業科学研究所量子ビーム科学研究施設、平成 21 年度報告書、(2010) 19.

09C047 4-28 G

近藤 孝文、楊 金峰、法澤 公寛、管 晃一、吉田 陽一、永石 隆二、田口光正、高橋 憲司、加藤 隆二
“イオン液体-水溶液混合系における微粒子生成”
大阪大学産業科学研究所量子ビーム科学研究施設、平成 21 年度報告書、(2010) 36-37.

09C048 4-29 C

S. Nakagawa, M. Taguchi,
K. Hirota and T. Murakami
“LET effect on irradiation of hydroxymaleimide in 2-propanol (4)”
Proc. 52nd Ann. Meeting Jap. Soc. Radiat. Chem., [Fukui, Japan] (2009/09) 109-110.

09C049 4-35 C

H. Harano, T. Matsumoto, J. Nishiyama,
A. Uritani and K. Kudo
“Accelerator-based neutron fluence standard at the National Metrology Institute of Japan”
Proc. 20th Int. Conf. Appl. Accel. Res. Ind., [Fort Worth, USA] AIP 1099 (2009) 915.

09C050 4-36 C

K. Shimada, M. Morev, T. Abe, M. Hirota,
Y. Koike, T. Iimoto and T. Kosako
“Study of the Dosimetry on High-Energy Neutron Using Solid State Track Detector with Multiple Radiator”
2nd Joint Int. Symp. Nucl. Sci. Tech.

09C051 4-36 C

K. Shimada, M. Morev, T. Abe, M. Hirota,
Y. Koike, T. Iimoto and T. Kosako
“Measuring Method of Neutron from 1 MeV to 100 MeV Using a Solid State Nuclear Track Detector with Multi-Layer Radiators”
GoNERI 2nd year symposium.

09C052 4-47 S

Y. Shiine, H. Nishikawa, Y. Furuta,
K. Kanamitsu, T. Satoh, Y. Ishii, T. Kamiya,
R. Nakao and S. Uchida
“Fabrication of Dielectrophoretic Devices Using

Poly-dimethylsiloxane Microstructures by Proton Beam Writing”
35th Int. Conf. Micro & Nano Eng. (MNE), [Ghent, Belgium] (2009/09) P-LIFE-23.

09C053 4-47 S
Y. Shiine, H. Nishikawa, Y. Furuta, T. Sato, Y. Ishii, T. Kamiya, R. Nakao, and S. Uchida
“Development of Dielectrophoretic Devices with High-Aspect Ratio Microstructures Using Proton Beam Writing”
16th Int. Conf. Surf. Mod. Mater. by Ion Beams, (2009/09) PB-33.

09C054 4-47 S
椎根 康晴、西川 宏之、古田 祐介、佐藤 隆博、石井 保行、神谷 富裕、中尾 亮太、内田 論
“集束プロトンビーム描画による PDMS マイクロ流路を有する誘電泳動デバイスの作製”
2009 年秋季第 70 回応用物理学会学術講演会, ［富山］, Vol. 2, 11a-ZF-5 (2009/09) 632.

09C055 4-47 S
西川 宏之、渡辺 徹、関 佳裕、佐藤 隆博、石井 保行、神谷 富裕
“集束プロトンビーム描画による PMMA 母型を用いた高アスペクト比 Ni 電鋳”
2010 年春季 第 57 回 応用物理学関係連合講演会, ［平塚］, (2010/03) 17p-W-13.

09C056 4-50 C
Y. Yuri, T. Ishizaka, T. Yuyama, S. Okumura, I. Ishibori, W. Yokota, S. Watanabe, S. Kubono, and Y. Ohshiro
“FORMATION OF A UNIFORM ION BEAM USING MULTIPOLE MAGNETS”
Proc. 23rd Part. Accel. Conf., [Vancouver, Canada] (2009) TH6PFP082.

09C057 4-50 C
N. Miyawaki, S. Okumura, S. Kurashima, H. Kashiwagi, K. Yoshida, Y. Yuri, T. Yuyama, T. Ishizaka, I. Ishibori, T. Nara and W. Yokota
“Characteristics of beam phase in the JAEA AVF cyclotron”
Proc. Part. Accel. Soc. Meeting 2009, [Ibaraki, Japan] (2009/08) 183-185.

09C058 4-50 C
I. Ishibori, T. Nara, S. Kurashima, K. Yoshida, T. Yuyama, T. Ishizaka, S. Okumura, N. Miyawaki, H. Kashiwagi, Y. Yuri, W. Yokota, T. Yoshida, K. Akaiwa, S. Ishiro, T. Yoshida, S. Kano, A. Ihara, K. Takano, S. Mochizuki and H. Saitoh
“Present Status of AVF Cyclotron at JAEA”
Proc. Part. Accel. Soc. Meeting 2009, [Ibaraki, Japan] (2009/08) 687-689.

09C059 4-50 C
H. Kashiwagi, N. Miyawaki, S. Okumura, I. Ishibori, S. Kurashima, Y. Yuri, T. Ishizaka, T. Yuyama , K. Yoshida, T. Agematsu, T. Nara and W. Yokota
“Phase-space collimator for transverse acceptance measurement”
Proc. Part. Accel. Soc. Meeting 2009, [Ibaraki, Japan] (2009/08) 244-246.

09C060 4-50 C
S. Okumura, N. Miyawaki, T. Yuyama, T. Ishizaka, S. Kurashima, H. Kashiwagi, K. Yoshida, I. Ishibori, Y. Yuri, T. Nara, W. Yokota, M. Fukuda and T. Nakajima
“MAGNETIC FIELD MEASUREMENT

SYSTEM FOR QUICK CHANGE OF THE
CYCLOTRON MAGNETIC FIELD”
Proc. Part. Accel. Soc. Meeting 2009, [Ibaraki,
Japan] (2009/08) 572-574.

09C061 4-51 T, S, I
千葉 敦也、宇野 定則、山田 圭介、横山 彰人、
上松 敬、北野 敏彦、高山 輝充、織茂 貴雄、
江夏 昌志、青木 勇希、山田 尚人、齋藤 勇一、
石井 保行、佐藤 隆博、大久 保猛
“TIARA 静電加速器の現状”
第 22 回「タンデム加速器およびその周辺技術の
研究会」報告集,［つくば］, UTTAC-J-18, 2009
ISSN 1880-4756 (2009/07).

09C062 4-51 S
横山 彰人、石井 保行、千葉 敦也、宇野 定則、
上松 敬、高山 輝充、江夏 昌志
“MeV 級プロトンビームによる発光を利用したエミ
ッタンス測定Ⅱ”
第 22 回「タンデム加速器およびその周辺技術の
研究会」報告集,［つくば］, UTTAC-J-18, 2009
ISSN 1880-4756 (2009/07).

Appendix 2

List of Related Patents

09PAT001 2-02
植木 悠二、玉田 正男(原子力機構・量子ビーム)
梅村 知也、小林 博治(名古屋大学・エコトピア科学研究所)
「極性化合物分離用双性イオン型有機ポリマー系モノリスカラム及びその製造方法」
出願番号:特願 2009-164010 号

09PAT002 2-03
瀧上 眞知子(群馬県産業支援機構)、尾崎 益雄、明田 川康、柴田 卓弥(ウイーグル㈱)、瀧上 昭治(瀧上昭治)、長澤 尚胤、廣木 章博、笠井 昇、吉井 文男、玉田 正男(原子力機構・量子ビーム)
「腐植様着色物質を含有する排水の処理方法および処理システム」
出願番号:特願 2009-276386 号

09PAT003 2-04
佐藤 利弘(㈱日本コンタクトレンズ)、廣木 章博、長澤 尚胤、玉田 正男(原子力機構・量子ビーム)
「コンタクトレンズ、及びその製造方法」
出願番号:特願 2010-068944 号

09PAT004 3-09
長谷 純宏、鳴海 一成、田中 淳(原子力機構・量子ビーム)、岡村 正愛、竹下 大学(キリンアグリバイオ㈱)、
「花色変異体植物の作出方法」
出願番号:特願 2009-160996 号

09PAT005 4-03
田口 富嗣、樹神 克明、社本 真一(原子力機構・量子ビーム)
「単結晶炭化ケイ素ナノチューブの製造方法」
出願番号:特願 2009-145979 号

09PAT006 4-03
田口 富嗣、樹神 克明、社本 真一(原子力機構・量子ビーム)
「アモルファス炭化ケイ素ナノチューブの製造方法」
出願番号:特願 2009-145980 号

09PAT007 4-05
織茂 聡、大道 博行、阿部 浩之(原子力機構・量子ビーム)、内田 裕久(東海大学・工学部)
「レーザー駆動陽子線を用いた水素吸蔵材料製造」
出願番号:特願 2010-106216 号

09PAT008 4-09 4-10
杉本 雅樹、北 憲一郎、武山 昭憲、吉川 正人、成澤 雅紀、間渕 博(原子力機構・量子ビーム)
「ポリマーブレンドによる多孔質セラミックス及びその製造方法」
出願番号:特願 2009-128693 号
出願日:2009 年 05 月 28 日

09PAT009 4-47
西川 宏之、古田 祐介、椎根 康晴、内田 諭、神谷 富裕、石井 保行、佐藤 隆博(芝浦工業大学、首都大学東京、原子力機構による共同出願)
「三次元誘電泳動デバイス」
出願番号:特願 2010-10945 号
出願日:2010 年 1 月 21 日

09PAT010　4-48

酒井　卓郎、松林　政仁、安田　良、飯倉　寛、林田
洋寿（原子力機構・量子ビーム）

「中性子集光素子」

出願番号：特願 2009―202581 号

出願日：2009 年 9 月 2 日

Appendix 3

List of Related Press-Release and TV Programs

09NP001　1-27
平成 20 年 12 月 12 日、電気新聞、電気新聞、日刊工業新聞、化学工業日報、鉄鋼新聞、フジサンケイビジネスアイに掲載
「合金製造で新技術」

09NP002　1-27
平成 21 年 10 月 28 日、日経産業新聞に掲載
「ステンレス鋼耐食性3倍の高純度」

09NP003　2-03
平成 22 年 1 月 26 日、上毛新聞に掲載
「家畜ふん尿を脱色　回収物は肥料に」

09NP004　2-03
平成 22 年 2 月 4 日、化学工業日報に掲載
「植物由来弾性ゲル　医療・化粧品への応用期待」

09NP005　3-47
平成 21 年 3 月 17 日発表、日刊工業、上毛、毎日、日経産業に掲載
植物ポジトロンイメージング技術により共生的窒素固定の観測に成功
－微生物が空気から作る肥料をダイズの生産に活かす－

09TV001　3-09
平成 21 年 12 月 22～24 日、朝日新聞(埼玉版)、毎日新聞(埼玉版)、読売新聞(埼玉版)、産経新聞(埼玉版)、日経新聞(埼玉版)、上毛新聞、埼玉新聞、日本農業新聞、その他共同通信が配信した地方紙
「青色まで後一歩、赤紫のシクラメン開発」

Symbol used in the Appendix 1 to 3

An example of symbol expression is written as following.

09	J	119	4-51	T
①	②	③	④-⑤	⑥

① Number of last two orders in fiscal year

② Kind of publication

- **J** : Publication in Journal
- **C** : Publication as Proceedings
- **NP** : Press-Release (Newspaper)
- **TV** : TV Programs
- **PA** : Patent

③ Consecutive numbers for the kind of publication

④-⑤ Paper number

④ Classification number of research field

- **1** : Space, nuclear and energy engineering
- **2** : Environment conservation and resource security
- **3** : Biotechnology and medical application
- **4** : Advanced materials, analysis and novel technology

⑤ Consecutive number every research field

⑥ Accelerators or irradiation facilities utilized for the research

- **C** : AVF Cyclotron
- **T** : 3 MV Tandem Electrostatic Accelerator
- **S** : 3 MV Single-ended Electrostatic Accelerator
- **I** : 400 kV Ion Implanter
- **E** : 2 MV Electron Accelerator
- **G** : Co-60 Gamma-ray Irradiation Facilities
- **O** : Off-line (Research without the utilization of irradiation facilities)

Appendix 4 Type of Research Collaboration and Facilities Used for Research

Paper Number	Type of Research Collaboration*1					Irradiation Facilites*2						Paper Number	Type of Research Collaboration*1					Irradiation Facilites*2					
	Joint Res.	Entr. Res.	Coop.	JAEA Inter.	Com. Use	C	T	S	I	E	G		Joint Res.	Entr. Res.	Coop.	JAEA Inter.	Com. Use	C	T	S	I	E	G
1-01	●					◎	◎		◎			3-02				●		◎					
1-02				●		◎						3-03				●		◎					
1-03	●					◎	◎					3-04	●OL										
1-04	●					◎						3-05	●					◎					
1-05	●					◎	◎					3-06				●		◎					
1-06	●								◎			3-07	●					◎					
1-07	●										◎	3-08	●					◎					
1-08					●	◎						3-09		●				◎					
1-09					●				◎		◎	3-10	●					◎					
1-10	●									◎	◎	3-11	●					◎					
1-11	●							◎	◎			3-12	●					◎					
1-12	●						◎			◎	◎	3-13	●					◎					
1-13				●		◎	◎				◎	3-14	●					◎					
1-14		●									◎	3-15	●					◎					
1-15				●							◎	3-16	●					◎					
1-16				●							◎	3-17	●					◎					
1-17				●							◎	3-18		●				◎					
1-18	●										◎	3-19	●					◎					
1-19	●										◎	3-20	●					◎					
1-20	●										◎	3-21	●					◎					
1-21				●			◎					3-22	●					◎					
1-22				●							◎	3-23	●					◎					
1-23	●							◎				3-24				●		◎					
1-24				●				◎				3-25	●					◎					
1-25				●		◎				◎	◎	3-26	●					◎					
1-26			●				◎	◎	◎			3-27				●							◎
1-27				●			◎	◎	◎			3-28	●										◎
1-28				●			◎	◎				3-29	●										◎
1-29				●			◎					3-30				●		◎					
1-30				●		◎			◎			3-31				●		◎					◎
1-31				●							◎	3-32				●		◎					◎
1-32				●		◎						3-33	●					◎					
1-33	●										◎	3-34	●					◎					
1-34	●									◎	◎	3-35	●					◎					
⋮	⋮	⋮	⋮	⋮	⋮	⋮	⋮	⋮	⋮	⋮	⋮	3-36	●					◎					
2-01				●						◎		3-37	●					◎					
2-02	●										◎	3-38	●					◎					
2-03	●										◎	3-39	●					◎					
2-04	●									◎		3-40	●					◎					
2-05				●						◎		3-41	●					◎					
2-06				●						◎		3-42	●					◎					
2-07	●									◎		3-43	●OL										
2-08				●						◎	◎	3-44	●					◎					
2-09				●							◎	3-45	●					◎					
⋮	⋮	⋮	⋮	⋮	⋮	⋮	⋮	⋮	⋮	⋮	⋮	3-46	●					◎					
3-01				●			◎				◎	3-47	●					◎					

Paper Number	Type of Research Collaboration[*1]					Irradiation Facilites[*2]						Paper Number	Type of Research Collaboration[*1]					Irradiation Facilites[*2]					
	Joint Res.	Entr. Res.	Coop.	JAEA Inter.	Com. Use	C	T	S	I	E	G		Joint Res.	Entr. Res.	Coop.	JAEA Inter.	Com. Use	C	T	S	I	E	G
3-48	●					◎						4-24	●OL										
3-49	●					◎						4-25				●OL							
3-50	●					◎						4-26	●OL										
3-51	●					◎						4-27				●OL							
3-52				●OL								4-28				●							◎
3-53	●					◎						4-29	●					◎					
3-54			●					◎				4-30				●		◎					
3-55			●					◎				4-31	●					◎					
3-56			●					◎				4-32	●					◎					
3-57			●					◎				4-33	●					◎					
3-58			●					◎				4-34	●					◎					
3-59			●					◎				4-35	●					◎					
3-60			●					◎				4-36					●	◎					
3-61			●					◎				4-37					●	◎					
3-62			●					◎				4-38				●						◎	
⋮	⋮	⋮	⋮	⋮	⋮	⋮	⋮	⋮	⋮	⋮	⋮	4-39			●				◎				
4-01				●				◎	◎			4-40			●				◎				
4-02					●				◎			4-41			●				◎	◎	◎		
4-03				●			◎		◎			4-42			●				◎				
4-04	●							◎	◎			4-43			●				◎				
4-05	●						◎		◎			4-44			●				◎				
4-06	●							◎				4-45			●				◎				
4-07				●					◎			4-46	●					◎		◎		◎	◎
4-08	●					◎						4-47	●						◎	◎			
4-09				●						◎	◎	4-48				●				◎			
4-10	●									◎	◎	4-49				●		◎					
4-11					●	◎						4-50				●		◎					
4-12					●				◎		◎	4-51				●			◎	◎	◎		
4-13					●				◎			4-52				●		◎					
4-14				●			◎	◎	◎			⋮	⋮	⋮	⋮	⋮	⋮	⋮	⋮	⋮	⋮	⋮	⋮
4-15					●					◎		5-01						◎	◎	◎	◎		
4-16				●				◎				5-02						◎					
4-17	●							◎				5-03							◎	◎	◎		
4-18				●OL						◎		5-04										◎	◎
4-19				●			◎					5-05										◎	◎
4-20	●							◎				5-06						◎	◎	◎	◎	◎	◎
4-21					●			◎		◎		5-07						◎	◎	◎	◎		
4-22					●		◎					5-08						◎	◎	◎	◎		
4-23	●					◎						⋮	⋮	⋮	⋮	⋮	⋮	⋮	⋮	⋮	⋮	⋮	⋮

[*1] Type of Research Collaboration

Joint Res. : Joint research with external users

Entr. Res. : Research entrusted to JAEA

Coop. Res. : Cooperative research with plural universities through The University of Tokyo

JAEA Inter. : JAEA internal use

Com. Use : Common use based on "JAEA-facility-use"

OL : Off line (research without the use of irradiation facilities)

[*2] Utilization of Irradiation Facilities

C : AVF Cyclotron System

T : 3 MV Tandem Electrostatic Accelerator

S : 3 MV Single-ended Electrostatic Accelerator

I : 400 kV Ion Implanter

E : 2 MV Electron Accelerator

G : Co-60 Gamma-ray Irradiation Facilities

Appendix 5　A Typical Example of Abbreviation Name for Organizations in Japan Atomic Energy Agency (JAEA)

◆ Directorate, Center, Institute, etc.

QuBS（量子ビーム応用研究部門）: Quantum Beam Science Directorate
NSED（原子力基礎工学研究部門）: Nuclear Science and Engineering Directorate
FRDD（核融合研究開発部門）: Fusion Research and Development Directorate
GIRDD（地層処分研究開発部門）: Geological Isolation Research and Development Directorate
ANSRD（次世代原子力システム研究開発部門）: Advanced Nuclear System Research and Development Directorate
NCBD（バックエンド推進部門）：Nuclear Cycle Backend Directorate
NSRC（安全研究センター）: Nuclear Safety Research Center
NFCEL（核燃料サイクル工学研究所）: Nuclear Fuel Cycle Engineering Laboratories
NERCC（原子力エネルギー基盤連携センター）:Nuclear Engineering Research Collaboration Center
J-PARC（ J-PARC センター）: J-PARC Center
TARRI（高崎量子応用研究所）: Takasaki Advanced Radiation Research Institute
NSRI（原子力科学研究所）: Nuclear Science Research Institute
KPSI（関西光科学研究所）: Kansai Photon Science Institute

◆ Division, Unit, Department, etc.

・Environment and Industrial Materials Research Division, QuBS, JAEA
（量子ビーム応用研究部門、環境・産業応用研究開発ユニット）
・Radiation-Applied Biology Division, QuBS, JAEA
（量子ビーム応用研究部門、バイオ応用技術研究ユニット）
・Neutron Material Research Center, QuBS, JAEA
（量子ビーム応用研究部門、中性子物質科学研究ユニット）
・Neutron Technology R&D Center, QuBS, JAEA
（量子ビーム応用研究部門、中性子産業利用技術研究ユニット）
・Advanced Photon Research Center, QuBS, JAEA
（量子ビーム応用研究部門、レーザー応用技術研究ユニット）
・Division of Environment and Radiation Sciences, NSED, JAEA
（原子力基礎工学研究部門、環境・放射線工学ユニット）
・Division of Fuels and Materials Engineering, NSED, JAEA
（原子力基礎工学研究部門、燃料・材料工学ユニット）

・Research Coordination and Promotion Office, NSED, JAEA
（原子力基礎工学研究部門、研究推進室）
・Division of ITER Project, FRDD, JAEA
（核融合研究開発部門、ITER プロジェクトユニット）
・Division of Fusion Energy Technology, FRDD, JAEA
（核融合研究開発部門、核融合エネルギー工学研究開発ユニット）
・Advanced Science Research Center, JAEA
（先端基礎研究センター）
・Department of Advanced Radiation Technology, TARRI, JAEA
（高崎量子応用研究所、放射線高度利用施設部）
・Department of Radiation Protection, NSRI, JAEA
（原子力科学研究所、放射線管理部）
・Accelerator Division, J-PARC, JAEA
（J-PARC センター、加速器ディビジョン）
・Safety Division, J-PARC, JAEA
（J-PARC センター、安全ディビジョン）
・LWR Long-term Reliability Research Unit, NSRC, JAEA
（安全研究センター、軽水炉長期化対応研究ユニット）
・Geological Isolation Research Unit, GIRDD, JAEA
（地層処分研究開発部門、地層処分基盤研究開発ユニット）
・Nuclear Cycle Engineering Department, NFCEL, JAEA
（核燃料サイクル工学研究所　サイクル工学試験部）
・Plutonium Fuel Development Center, NFCEL, JAEA
（核燃料サイクル工学研究所　プルトニウム燃料技術開発センター）
・Advanced Reprocessing Unit, ANSRD, JAEA
（次世代原子力システム研究開発部門　次世代再処理システムユニット）
・Industrial Collaboration Promotion Department, JAEA
（産学連携推進部）
・Nuclear Cycle Backend Technology Development Unit, NCBD, JAEA
（バックエンド推進部門　バックエンド技術開発ユニット）

This is a blank page.

国際単位系（SI）

表１．SI 基本単位

基本量	SI 基本単位	
	名称	記号
長さ	メートル	m
質量	キログラム	kg
時間	秒	s
電流	アンペア	A
熱力学温度	ケルビン	K
物質量	モル	mol
光度	カンデラ	cd

表２．基本単位を用いて表されるSI組立単位の例

組立量	SI 基本単位	
	名称	記号
面積	平方メートル	m^2
体積	立法メートル	m^3
速さ，速度	メートル毎秒	m/s
加速度	メートル毎秒毎秒	m/s^2
波数	毎メートル	m^{-1}
密度，質量密度	キログラム毎立方メートル	kg/m^3
面積密度	キログラム毎平方メートル	kg/m^2
比体積	立方メートル毎キログラム	m^3/kg
電流密度	アンペア毎平方メートル	A/m^2
磁界の強さ	アンペア毎メートル	A/m
量濃度(a)，濃度	モル毎立方メートル	mol/m^3
質量濃度	キログラム毎立法メートル	kg/m^3
輝度	カンデラ毎平方メートル	cd/m^2
屈折率(b)	（数字の） 1	1
比透磁率(b)	（数字の） 1	1

(a) 量濃度（amount concentration）は臨床化学の分野では物質濃度（substance concentration）ともよばれる。
(b) これらは無次元量あるいは次元１をもつ量であるが、そのことを表す単位記号である数字の１は通常は表記しない。

表３．固有の名称と記号で表されるSI組立単位

組立量	SI 組立単位			
	名称	記号	他のSI単位による表し方	SI基本単位による表し方
平面角	ラジアン(b)	rad	1 (b)	m/m
立体角	ステラジアン(b)	sr(c)	1 (b)	m^2/m^2
周波数	ヘルツ(d)	Hz		s^{-1}
力	ニュートン	N		m kg s^{-2}
圧力，応力	パスカル	Pa	N/m^2	m^{-1} kg s^{-2}
エネルギー，仕事，熱量	ジュール	J	N m	m^2 kg s^{-2}
仕事率，工率，放射束	ワット	W	J/s	m^2 kg s^{-3}
電荷，電気量	クーロン	C		s A
電位差（電圧），起電力	ボルト	V	W/A	m^2 kg s^{-3} A^{-1}
静電容量	ファラド	F	C/V	m^{-2} kg^{-1} s^4 A^2
電気抵抗	オーム	Ω	V/A	m^2 kg s^{-3} A^{-2}
コンダクタンス	ジーメンス	S	A/V	m^{-2} kg^{-1} s^3 A^2
磁束	ウエーバ	Wb	Vs	m^2 kg s^{-2} A^{-1}
磁束密度	テスラ	T	Wb/m^2	kg s^{-2} A^{-1}
インダクタンス	ヘンリー	H	Wb/A	m^2 kg s^{-2} A^{-2}
セルシウス温度	セルシウス度(e)	℃		K
光束	ルーメン	lm	cd sr(c)	cd
照度	ルクス	lx	lm/m^2	m^{-2} cd
放射性核種の放射能(f)	ベクレル(d)	Bq		s^{-1}
吸収線量，比エネルギー分与，カーマ	グレイ	Gy	J/kg	m^2 s^{-2}
線量当量，周辺線量当量，方向性線量当量，個人線量当量	シーベルト(g)	Sv	J/kg	m^2 s^{-2}
酸素活性	カタール	kat		s^{-1} mol

(a)SI接頭語は固有の名称と記号を持つ組立単位と組み合わせても使用できる。しかし接頭語を付した単位はもはやコヒーレントではない。
(b)ラジアンとステラジアンは数字の１に対する単位の特別な名称で、量についての情報をつたえるために使われる。実際には、使用する時には記号rad及びsrが用いられるが、習慣として組立単位としての記号である数字の１は明示されない。
(c)測光学ではステラジアンという名称と記号srを単位の表し方の中に、そのまま維持している。
(d)ヘルツは周期現象についてのみ、ベクレルは放射性核種の統計的過程についてのみ使用される。
(e)セルシウス度はケルビンの特別な名称で、セルシウス温度を表すために使用される。セルシウス度とケルビンの単位の大きさは同一である。したがって、温度差や温度間隔を表す数値はどちらの単位で表しても同じである。
(f)放射性核種の放射能（activity referred to a radionuclide）は、しばしば誤った用語で"radioactivity"と記される。
(g)単位シーベルト（PV,2002,70,205）についてはCIPM勧告2（CI-2002）を参照。

表４．単位の中に固有の名称と記号を含むSI組立単位の例

組立量	SI 組立単位		
	名称	記号	SI 基本単位による表し方
粘度	パスカル秒	Pa s	m^{-1} kg s^{-1}
力のモーメント	ニュートンメートル	N m	m^2 kg s^{-2}
表面張力	ニュートン毎メートル	N/m	kg s^{-2}
角速度	ラジアン毎秒	rad/s	m m^{-1} s^{-1}=s^{-1}
角加速度	ラジアン毎秒毎秒	rad/s^2	m m^{-1} s^{-2}=s^{-2}
熱流密度，放射照度	ワット毎平方メートル	W/m^2	kg s^{-3}
熱容量，エントロピー	ジュール毎ケルビン	J/K	m^2 kg s^{-2} K^{-1}
比熱容量，比エントロピー	ジュール毎キログラム毎ケルビン	J/(kg K)	m^2 s^{-2} K^{-1}
比エネルギー	ジュール毎キログラム	J/kg	m^2 s^{-2}
熱伝導率	ワット毎メートル毎ケルビン	W/(m K)	m kg s^{-3} K^{-1}
体積エネルギー	ジュール毎立方メートル	J/m^3	m^{-1} kg s^{-2}
電界の強さ	ボルト毎メートル	V/m	m kg s^{-3} A^{-1}
電荷密度	クーロン毎立方メートル	C/m^3	m^{-3} sA
表面電荷	クーロン毎平方メートル	C/m^2	m^{-2} sA
電束密度，電気変位	クーロン毎平方メートル	C/m^2	m^{-2} sA
誘電率	ファラド毎メートル	F/m	m^{-3} kg^{-1} s^4 A^2
透磁率	ヘンリー毎メートル	H/m	m kg s^{-2} A^{-2}
モルエネルギー	ジュール毎モル	J/mol	m^2 kg s^{-2} mol^{-1}
モルエントロピー，モル熱容量	ジュール毎モル毎ケルビン	J/(mol K)	m^2 kg s^{-2} K^{-1} mol^{-1}
照射線量（X線及びγ線）	クーロン毎キログラム	C/kg	kg^{-1} sA
吸収線量率	グレイ毎秒	Gy/s	m^2 s^{-3}
放射強度	ワット毎ステラジアン	W/sr	m^4 m^{-2} kg s^{-3}=m^2 kg s^{-3}
放射輝度	ワット毎平方メートル毎ステラジアン	$W/(m^2$ sr)	m^2 m^{-2} kg s^{-3}=kg s^{-3}
酵素活性濃度	カタール毎立方メートル	kat/m^3	m^{-3} s^{-1} mol

表５．SI 接頭語

乗数	接頭語	記号	乗数	接頭語	記号
10^{24}	ヨタ	Y	10^{-1}	デシ	d
10^{21}	ゼタ	Z	10^{-2}	センチ	c
10^{18}	エクサ	E	10^{-3}	ミリ	m
10^{15}	ペタ	P	10^{-6}	マイクロ	μ
10^{12}	テラ	T	10^{-9}	ナノ	n
10^{9}	ギガ	G	10^{-12}	ピコ	p
10^{6}	メガ	M	10^{-15}	フェムト	f
10^{3}	キロ	k	10^{-18}	アト	a
10^{2}	ヘクト	h	10^{-21}	ゼプト	z
10^{1}	デカ	da	10^{-24}	ヨクト	y

表６．SIに属さないが、SIと併用される単位

名称	記号	SI 単位による値
分	min	1 min=60s
時	h	1h =60 min=3600 s
日	d	1 d=24 h=86 400 s
度	°	1°=(π/180) rad
分	’	1’=(1/60)°=(π/10800) rad
秒	”	1”=(1/60)’=(π/648000) rad
ヘクタール	ha	$1ha=1hm^2=10^4m^2$
リットル	L, l	$1L=11=1dm^3=10^3cm^3=10^{-3}m^3$
トン	t	$1t=10^3$ kg

表７．SIに属さないが、SIと併用される単位で、SI単位で表される数値が実験的に得られるもの

名称	記号	SI 単位で表される数値
電子ボルト	eV	$1eV=1.602\ 176\ 53(14)\times10^{-19}J$
ダルトン	Da	$1Da=1.660\ 538\ 86(28)\times10^{-27}kg$
統一原子質量単位	u	1u=1 Da
天文単位	ua	$1ua=1.495\ 978\ 706\ 91(6)\times10^{11}m$

表８．SIに属さないが、SIと併用されるその他の単位

名称	記号	SI 単位で表される数値
バール	bar	$1\ bar=0.1MPa=100kPa=10^5Pa$
水銀柱ミリメートル	mmHg	1mmHg=133.322Pa
オングストローム	Å	$1\ Å=0.1nm=100pm=10^{-10}m$
海里	M	1 M=1852m
バーン	b	$1\ b=100fm^2=(10^{-12}cm)2=10^{-28}m^2$
ノット	kn	1 kn=(1852/3600)m/s
ネーパ	Np	SI単位との数値的な関係は、対数量の定義に依存。
ベル	B	
デジベル	dB	

表９．固有の名称をもつCGS組立単位

名称	記号	SI 単位で表される数値
エルグ	erg	$1\ erg=10^{-7}$ J
ダイン	dyn	$1\ dyn=10^{-5}$N
ポアズ	P	$1\ P=1\ dyn\ s\ cm^{-2}=0.1Pa\ s$
ストークス	St	$1\ St=1cm^2\ s^{-1}=10^{-4}m^2\ s^{-1}$
スチルブ	sb	$1\ sb=1cd\ cm^{-2}=10^4cd\ m^{-2}$
フォト	ph	$1\ ph=1cd\ sr\ cm^{-2}\ 10^4lx$
ガル	Gal	$1\ Gal=1cm\ s^{-2}=10^{-2}ms^{-2}$
マクスウェル	Mx	$1\ Mx = 1G\ cm^2=10^{-8}Wb$
ガウス	G	$1\ G=1Mx\ cm^{-2}=10^{-4}T$
エルステッド(c)	Oe	1 Oe ≙ $(10^3/4\pi)A\ m^{-1}$

(c) ３元系のCGS単位系とSIでは直接比較できないため、等号「 ≙ 」は対応関係を示すものである。

表10．SIに属さないその他の単位の例

名称	記号	SI 単位で表される数値
キュリー	Ci	$1\ Ci=3.7\times10^{10}Bq$
レントゲン	R	$1\ R=2.58\times10^{-4}C/kg$
ラド	rad	$1\ rad=1cGy=10^{-2}Gy$
レム	rem	$1\ rem=1\ cSv=10^{-2}Sv$
ガンマ	γ	1γ=1 nT=10-9T
フェルミ		1フェルミ=1 fm=10-15m
メートル系カラット		1メートル系カラット = 200 mg = 2×10-4kg
トル	Torr	1 Torr = (101 325/760) Pa
標準大気圧	atm	1 atm = 101 325 Pa
カロリー	cal	1cal=4.1858J（「15℃」カロリー），4.1868J（「IT」カロリー）4.184J（「熱化学」カロリー）
ミクロン	μ	1 μ =1μm=10^{-6}m

（第8版，2006年改訂）

この印刷物は再生紙を使用しています